Investigating the Intrinsic Role of Programmed Death Ligand-1 in Human Cancers
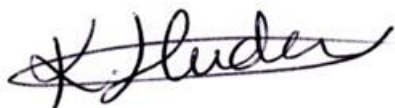
Katie Victoria Hudson

A thesis submitted in partial fulfilment of the requirements of Sheffield Hallam University for the degree of Doctor of Philosophy

November 2022

Declaration

I, Katie Victoria Hudson, confirm that I have not been enrolled for another award of the university, or other academic or professional organisation, whilst undertaking my research degree. I confirm that none of the material contained in the thesis has been used in any other submission for an academic award. I confirm that the work presented in this thesis is my own and where information has been derived from other sources, I confirm that this has been indicated in the thesis. I confirm that the work undertaken towards the thesis has been conducted in accordance with the SHU Principles of Integrity in Research and the SHU Research Ethics Policy. The word count of the thesis is 70,042.

Name	Katie Victoria Hudson
Award	PhD
Date of Submission	November 2022
Faculty	Health and Wellbeing
Director(s) of Studies	Dr Rebecca Leyland

Abstract

Programmed death-ligand 1 (PD-L1) expression is a survival mechanism employed by tumours to mediate immune evasion and tumour progression. PD-1/PD-L1-targeted therapies have revolutionised the cancer therapy landscape due to their ability to promote durable anti-tumour immune responses in select patients with advanced cancers. However, some patients are unresponsive, hyperprogressive or develop resistance. The exact mechanisms for this are still unclear. Recently, a pro-tumorigenic role of PD-L1 to send pro-survival signals in cancer cells is becoming apparent in some cancers. Better characterisation of the three-dimensional (3D) architecture of solid tumours by utilising 3D cell culture could provide an environment that more closely recapitulates *in vivo* human tumours for investigating tumour-intrinsic PD-L1 signalling and immunotherapy responses. The role of PD-L1 and how approved immunotherapies may influence its role needs to be fully explored in all cancer types using *in vitro* cell culture systems that better model tumour heterogeneity compared to standard monolayer cell culture.

Within this thesis, human breast prostate and colorectal cancer cell lines were firstly characterised for their expression of immune-inhibitory proteins (PD-L1, PD-1 and PD-L2), immunological proteins (DR4, DR5 and Fas) and tumorigenic proteins (CD44 and HIF1α) at basal level in two-dimensional (2D) monolayer cell culture, before being investigated in two different 3D cell culture models (hanging drop and alginate hydrogel beads) of varying *in vitro* complexity. In doing this, we were able to demonstrate that cancer cells alter their gene and protein expression levels and develop hypoxia in a 3D environment that more closely mimics human *in vivo* solid tumours. Cancer cells in 3D reduced their expression of death receptors and antigen presenting machinery which would reduce their susceptibility to immune-mediated cell death and could ultimately hinder their response to immunotherapy.

Thereafter, we investigated the biological effects of therapeutically approved anti-PD-L1 monoclonal antibody Atezolizumab, before comparing PD-L1 blockade with PD-L1 knockdown in high PD-L1 expressing breast cancer cells cultured in 2D monolayer and 3D cell culture models. PD-L1 blockade using Atezolizumab demonstrated modest effects on breast cancer cell growth, proliferation, viability, and metabolism in our functional assays, but did reduce the phosphorylation of molecules involved in the PI3K/AKT and MAPK/ERK signalling pathways. PD-L1 knockdown, on the other hand, revealed the importance of PD-L1 expression for the spheroid-

forming capabilities of breast cancer cells in our 3D cell culture models. PD-L1 knockdown also potentiated the modest biological effects on breast cancer cell growth, proliferation, viability, and metabolism observed by Atezolizumab treatment. Additionally, cytokine modulation of PD-L1 expression was investigated in combination with PD-L1 blockade and PD-L1 knockdown in our studies. Utilising the 3D alginate model for the culture of breast cancer cells revealed a potential benefit of combining cytokines with PD-L1 targeting for the treatment of breast cancer which warrants further investigation.

Altogether this thesis provides new insights into: (1) the expression of immunological and tumorigenic proteins by diverse human cancer cells; (2) how PD-L1 blockade with Atezolizumab may influence PD-L1 intrinsic signalling in breast cancer cells; and (3) how PD-L1 may exhibit a pro-tumour role in breast cancer cells, not only in 2D monolayer but for the first time in two different 3D cell culture models.

Table of Contents

List of Figures

Figure 3.1 *In vitro* model complexity and physiological relevance of 3D versus 2D cancer models for oncology and immuno-oncology research.

Figure 3.2 Human breast, prostate and colorectal cancer cell lines form viable hanging drop 3D spheroids.

Figure 3.3 Each cancer cell line forms highly viable 3D spheroids of similar size at day 3 of culture.

Figure 3.4 Human breast, prostate and colorectal cancer cell lines grow in alginate hydrogel beads to form viable monoclonal 3D spheroid colonies at day 10.

Figure 3.5 Human breast, prostate, and colorectal cancer cell lines are highly viable in alginate hydrogel beads at day 3, 6 and 10.

Figure 3.6 Human breast, prostate, and colorectal cancer 3D alginate spheroid colony diameters are greater than 100 μm at day 10.

Figure 3.7 Normal oxygen concentrations were detected in 2D monolayer cultures of human breast, prostate, and colorectal cancer cells.

Figure 3.8 Hypoxia detected in most cancer cell lines cultured in 3D hanging drop spheroids at day 3.

Figure 3.9 Hypoxia was not detected in images taken of whole alginate hydrogel beads at day 10.

Figure 3.10 Hypoxia was detected in all cancer cell lines cultured in 3D spheroid colony aggregates.

Figure 3.11 3D cancer hanging drop spheroids show altered PD-L1 mRNA and protein expression when compared to cancer cells cultured in 2D monolayers.

Figure 3.12 Cancer cell PD-L1 mRNA and protein expression in 3D alginate spheroid colonies was altered compared to cancer cells cultured in 2D monolayers.

Figure 3.13 PD-L1 expression can be detected throughout LNCaP, SW480 and SW620 3D hanging drop spheroids.

Figure 3.14 PD-L1 expression can be detected throughout MDA-MB-231, LNCaP, PC3, and SW620 3D alginate spheroid colonies.

Figure 3.15 SW480 cells express an increased frequency and MFI of PD-1 protein expression in 3D spheroid colonies compared to 2D-cultured cells.

Figure 3.16 Representative flow cytometry plots display PD-1 expression amongst cancer cell lines in 2D and 3D cell culture models.

Figure 3.17 MDA-MB-231 and PC3 cells display decreased PD-L2 mRNA and/or protein expression in 3D cell culture models compared to 2D-cultured cells.

Figure 3.18 Representative flow cytometry plots display PD-L2 expression amongst cancer cell lines in 2D and 3D cell culture models.

Figure 3.19 The frequency of HLA-ABC expression on MCF-7 cells is significantly reduced in 3D cell culture models compared to 2D-cultured cells.

Figure 3.20 Representative flow cytometry plots display cell surface HLA-ABC expression amongst cancer cell lines in 2D and 3D cell culture models.

Figure 3.21 DR4 mRNA and/or protein expression is significantly altered in some cancer cell lines cultured in 3D cell culture models compared to their 2D monolayer counterparts.

Figure 3.22 Representative flow cytometry plots display DR4 protein expression amongst cancer cell lines in 2D and 3D cell culture models.

Figure 3.23 MDA-MB-231 cells display altered DR5 expression in 3D cell culture models compared to their monolayer counterparts.

Figure 3.24 Representative flow cytometry plots display DR5 protein expression amongst cancer cell lines in 2D and 3D cell culture models.

Figure 3.25 Some cancer cells display altered Fas expression at mRNA and/or protein level in 3D cell culture models compared to their monolayer counterparts.

Figure 3.26 Representative flow cytometry plots display Fas protein expression amongst cancer cell lines in 2D and 3D cell culture models.

Figure 3.27 Most cancer cells display altered CD44 expression at mRNA and/or protein level in 3D cell culture models compared to their monolayer counterparts.

Figure 2.28 Representative flow cytometry plots display cell surface CD44 protein expression amongst cancer cell lines in 2D and 3D cell culture models**.**

Figure 3.29 Cancer cells display comparable levels of HIF1α protein expression in 3D cell culture models compared to their monolayer counterparts.

Figure 3.30 Representative flow cytometry histograms display HIF1α protein expression amongst cancer cell lines in 2D and 3D cell culture models.

Figure 4.1 The proposed mechanism of action of PD-L1 in tumour cell signalling.

Figure 4.2 Timeline of Atezolizumab treatment strategies with or without IFNγ and/or TNFα for 2D- and 3D-cultured breast cancer cells.

Figure 4.3 Atezolizumab completely blocks PD-L1 detection on the cell surface of MDA-MB-231 cells cultured in monolayer in a dose-dependent manner.

Figure 4.4 Atezolizumab almost completely blocks PD-L1 detection on the cell surface of MDA-MB-231 cells cultured in 3D hanging drop spheroids in a dose-dependent manner.

Figure 4.5 Atezolizumab partially blocks PD-L1 detection on the cell surface of MDA-MB-231 cells cultured in 3D alginate spheroid colonies in a dose-dependent manner.

Figure 4.6 Atezolizumab does not affect PD-L1 mRNA levels in MDA-MB-231 cells cultured in 2D monolayer and 3D cell culture models.

Figure 4.7 MDA-MB-231 cells treated with Atezolizumab for 3 or 6 days appear to be less confluent than untreated cells.

Figure 4.8 Atezolizumab treatment does not significantly affect the percentage surface area of the wells covered by MDA-MB-231 cells after 3 or 6 days of culture.

Figure 4.9 Atezolizumab treatment had no significant effect on the expression of Ki67 by MDA-MB-231 cells cultured in monolayer.

Figure 4.10 Atezolizumab-mediated blockade of PD-L1 has minimal effect on the viability of MDA-MB-231 cells at day 3 and 6 of culture.

Figure 4.11 Atezolizumab significantly decreases the level of ATP produced by MDA-MB-231 cells after 6 days.

Figure 4.12 MDA-MB-231 cells form 3D hanging drop spheroids of similar diameter whether treated with or without Atezolizumab.

Figure 4.13 Untreated 3D hanging drop spheroids visually display a higher density of Hoechst 33342 positive cells throughout the spheroid after 6 days of culture.

Figure 4.14 Atezolizumab has no effect on the frequency and level of Ki67 expressed by cells cultured in 3D hanging drop spheroids for 3 or 6 days.

Figure 4.15 Atezolizumab-mediated blockade of PD-L1 does not significantly induce apoptotic cell death in cells cultured in 3D hanging drop spheroids after 3 and 6 of culture.

Figure 4.16 Atezolizumab significantly reduced the level of ATP produced by 3D hanging drop spheroids after 6 days.

Figure 4.17 MDA-MB-231 cells form 3D spheroid colonies in alginate hydrogel beads of similar diameter whether treated with or without Atezolizumab.

Figure 4.18 MDA-MB-231 cells grow similarly in alginate hydrogel beads to form 3D spheroid colonies whether treated with or without Atezolizumab.

Figure 4.19 Atezolizumab has no effect on the frequency and level of Ki67 expressed by MDA-MB-231 cells after being cultured in 3D alginate spheroid colonies for 3, 6 and 10 days.

Figure 4.20 Treatment of 3D alginate spheroid colonies with Atezolizumab does not significantly induce apoptotic cell death at day 3, 6 or 10 of culture.

Figure 4.21 Atezolizumab significantly reduces the level of ATP produced by cells cultured in 3D alginate spheroid colonies for 6 and 10 days.

Figure 4.22 MDA-MB-231 cells treated with Atezolizumab demonstrated 21 main differences in kinase phosphorylation compared to untreated cells.

Figure 4.23 The phosphorylation of p53 isoforms, STAT molecules and Src family kinases were affected by Atezolizumab treatment in MDA-MB-231 cells.

Figure 4.24 Atezolizumab altered the phosphorylation levels of several kinases associated with the PI3K/AKT/mTOR and MAPK/ERK signalling pathway in MDA-MB-231 cells.

Figure 4.25 Atezolizumab in combination with modulatory cytokines has no significant effect on the viability of MDA-MB-231 cells cultured in 2D monolayer.

Figure 4.26 Atezolizumab in combination with modulatory cytokines has no significant effect on the viability of MDA-MB-231 3D hanging drop spheroids.

Figure 4.27 Atezolizumab in combination with modulatory cytokines does not induce a significant amount of cell death in MDA-MB-231 3D alginate spheroid colonies at day 3.

Figure 5.8 MDA-MB-231 cells transfected with the 1319 plasmid demonstrate EmGFP positivity and express the lowest frequency and level of PD-L1 expression compared to WT and scrambled control cells.

Figure 5.9 MDA-MB-231 cells seeded at 200,000 cells/well demonstrate the highest stable transfection efficacy 14 days post-transfection.

Figure 5.10 MDA-MB-231 cells transfected with the 1319 plasmid form EmGFP positive colonies in a clonogenic assay.

Figure 5.11 Flow cytometry confirms isolated MDA-MB-231 colonies transfected with the 1319 plasmid express high levels of EmGFP.

Figure 5.12 MDA-MB-231 colonies transfected with the 1319 plasmid display significantly reduced levels of PD-L1 mRNA compared to WT and scrambled control cells.

Figure 5.13 MDA-MB-231 colonies transfected with the 1319 plasmid display significantly reduced levels of PD-L1 protein compared to WT and scrambled control cells.

Figure 5.14 MDA-MB-231 WT cells form colonies in a clonogenic assay.

Figure 5.15 MDA-MB-231 WT colonies display comparable levels of PD-L1 expression to the MDA-MB-231 heterogeneous cell population.

Figure 5.16 MDA-MB-231 PD-L1 knockdown cells display approximately a 70% reduction in PD-L1 mRNA and protein expression compared to WT cells.

Figure 5.17 PD-L1 knockdown cells cultured in monolayer appear less confluent than WT, Atezolizumab-treated WT and scrambled control cells after 3 days of culture.

Figure 5.18 PD-L1 knockdown cells cultured in monolayer appear less confluent than WT, Atezolizumab-treated WT and scrambled control cells after 6 days of culture.

Figure 5.19 PD-L1 knockdown cells cover a smaller percentage surface area of the well in a 96-well plate after 3 and 6 days of culture compared to WT, Atezolizumab-treated WT, and scrambled control cells.

Figure 5.20 PD-L1 knockdown cells display a lower MFI for Ki67 expression compared to WT, Atezolizumab-treated WT, and scrambled control cells at day 3 and 6 of culture.

Figure 5.21 PD-L1 knockdown cells display significantly more cell death after 3 days of culture compared to WT, Atezolizumab-treated WT and scrambled control cells.

Figure 5.22 PD-L1 knockdown cells display significantly more cell death than WT cells after 6 days of culture.

Figure 5.23 PD-L1 knockdown cells display significantly reduced cellular metabolic activity after 3 and 6 days of culture compared to Atezolizumab-treated WT cells.

Figure 5.24 PD-L1 knockdown 3D spheroids exhibited the smallest diameter after 3 and 6 days of culture.

Figure 5.25 PD-L1 knockdown 3D spheroids exhibit a smoother and more spherical outer surface topology after 3 days of culture.

Figure 5.26 PD-L1 knockdown 3D spheroids visually display a smoother outer surface topology and lower density of Hoechst 33342 positive cells in the outer region of the spheroid after 6 days of culture.

Figure 5.27 Ki67 expression is not significantly altered in PD-L1 knockdown cells cultured for 3 or 6 days in 3D spheroids compared to WT, Atezolizumab-treated WT, and scrambled control cells.

Figure 5.28 PD-L1 knockdown 3D spheroids display significantly more cell death compared to WT and scrambled control 3D spheroids at day 3 of culture.

Figure 5.29 Atezolizumab-treated WT and PD-L1 knockdown 3D spheroids display significantly more cell death compared to WT and scrambled control 3D spheroids at day 6 of culture.

Figure 5.30 PD-L1 knockdown 3D spheroids display significantly reduced levels of ATP after culture for 6 days compared to WT, Atezolizumab-treated WT and scrambled control 3D spheroids.

Figure 5.31 PD-L1 knockdown cells exhibit the smallest diameter at day 3, 6 and 10 of culture in alginate.

Figure 5.32 WT, Atezolizumab-treated WT, scrambled control and PD-L1 knockdown cells remain single cells or form cell clusters within alginate at day 3 of culture.

Figure 5.33 Only WT, Atezolizumab-treated WT and scrambled control cells begin to form 3D spheroid colonies within the alginate after 6 days.

Figure 5.34 PD-L1 knockdown cells display a similar frequency and level of Ki67 expression after 3, 6 and 10 days of culture in alginate.

Figure 5.35 Atezolizumab-treated WT and PD-L1 knockdown cells display significantly reduced detectable PD-L1 expression after 3 and 6 days of culture in alginate.

Figure 5.36 After 3 days of culture in alginate, no difference was observed in the amount of cell death amongst all cells.

Figure 5.37 PD-L1 knockdown cells display significantly more cell death compared to WT and scrambled control cells after being cultured for 6 days in alginate.

Figure 5.38 PD-L1 knockdown cells display significantly more cell death compared to WT, Atezolizumab-treated WT and scrambled control cells after being cultured in alginate for 10 days.

Figure 5.39 PD-L1 knockdown cells display significantly reduced ATP levels after 6 and 10 of culture in alginate compared to WT, Atezolizumab-treated WT and scrambled control cells.

Figure 5.40 PD-L1 knockdown cells display 22 main differences in kinase phosphorylation compared to WT, Atezolizumab-treated WT and scrambled control cells.

Figure 5.41 PD-L1 knockdown alters the phosphorylation levels of p53 isoforms, STAT molecules, Src family kinases and Wnt signalling molecules.

Figure 5.42 PD-L1 knockdown alters the phosphorylation levels of PI3K/AKT/mTOR and MAPK/ERK signalling molecules.

Figure 5.43 TNFα does not enhance the cell death phenotype observed by PD-L1 knockdown in MDA-MB-231 cells in monolayer cell culture.

Figure 5.44 TNFα does not enhance the cell death phenotype observed by Atezolizumab and PD-L1 knockdown in MDA-MB-231 3D spheroids.

Figure 5.45 TNFα enhances the cell death phenotype observed by PD-L1 knockdown cells after only 3 days of being cultured in alginate hydrogel beads.

Figure 6.1 A schematic representation of the proposed mechanism of PD-L1 intrinsic signalling following Atezolizumab treatment in TNBC cells.

Figure 6.2 A schematic representation of the proposed effects of PD-L1 knockdown in TNBC cells.

List of Tables

Publications, Funding applications, Conferences attended, Communications and Other relevant activities

Publications:

Published reviews:

Hudson K. Cross N. Jordan-Mahy N. and Leyland R. The extrinsic and intrinsic roles of PD-L1 and its receptor PD-1: Implications for immunotherapy treatment. *Front Immunol.* 2020 Oct; doi: 10.3389/fimmu.2020.568931 *(Impact factor: 6.429).*

Manuscripts in preparation:

Hudson K. Cross N. Jordan-Mahy N. and Leyland R. Programmed death-ligand 1 expression in human cancer three-dimensional cell culture models. *Cancer Immunol. Immunother. (Impact factor: 6.968)*

Hudson K. Cross N. Jordan-Mahy N. and Leyland R. Inhibition of programmed death-ligand 1 in three-dimensional tumour models of human breast cancer induces cell death, reduces cell proliferation, and prevents spheroid formation. *Cancer Immunol. Immunother. (Impact factor: 6.968)*

Applications for funding:

British Society of Immunology Travel Grant (£700) – **successful** November 2019

British Association of Cancer Research (£800)- **unsuccessful** November 2019

British Society of Immunology Bursary (£250) - **successful** October 2021

Oral Presentations:

Doctoral Training Alliance, 3D Cell Culture Training Course: 17th-18th May (2019). Presentation title: Expression of immuno-inhibitory proteins in 2D and 3D culture by human cancer cell lines. Sheffield Hallam University, Sheffield, UK.

Poster Presentations:

British Society for Immunology (BSI): 28th Nov-2nd Dec (2021). Abstract title: Investigation of the intrinsic role of PD-L1 in human breast cancer models. Edinburgh International Conference Centre, Edinburgh, UK.

American Association of Cancer Research (AACR): 10th-15th April (2021). Abstract title: Characterisation of 3D models of human breast, prostate and colorectal cancer. Virtual.

British Society for Immunology (BSI): 1st-2nd December (2020). Abstract title: Characterisation of 3D models of human breast cancer and the effects of PD-L1 blockade with Atezolizumab with or without TNFα on cancer cell viability. Virtual conference/presentation. Virtual.

European Association of Cancer Research (EACR)-American Association of Cancer Research (AACR)- Associação Portuguesa de Investigação em Cancro (ASPIC): 02nd-04th March (2020). Abstract title: Exploring the Intrinsic Role of Programmed Death-Ligand 1 in Human Cancers using 2D and 3D Cell Culture Systems. Lisbon Congress Centre, Lisbon, Portugal.

British Association of Cancer Research (BACR): 1st-3rd July (2019). Abstract title: Programmed death-ligand 1 expression in human cancer cell lines in two-dimensional and three-dimensional cell culture systems. Nottingham Conference Centre, Nottingham, UK.

Relevant courses and workshops:

Flow Cytometry Webinars 1-4 with Derick Davis, Francis Crick Cancer Research Institute, London, UK **(2020)**.

Stem Ambassador Training, Sheffield Hallam University, Sheffield, UK **(2019)**.

Doctoral Training Alliance, 3D Cell Culture Training Course, Sheffield Hallam University, Sheffield, UK **(2019)**.

Faculty of Health and Wellbeing PhD workshop series, Sheffield Hallam University, Sheffield, UK **(2018-2019)**.

Abbreviations

PD-L1	Programmed death ligand 1
PD-1	Programmed death 1
PD-L2	Programmed death ligand 2
HIF1α	Hypoxia-inducible factor 1 alpha
IFNγ	Interferon gamma
TNFα	Tumour necrosis factor alpha
DR4	Death receptor 4
DR5	Death receptor 5
Fas	Fas-associated protein
HPRT1	Hypoxanthine-guanine phosphoribosyltransferase 1
TBP	TATA-box protein
RT-qPCR	Real time quantitative polymerase chain reaction
2D	Two-dimensional
3D	Three-dimensional
RPMI	Roswell Park Memorial Institute
DMEM	Dulbecco's Modified Eagle Medium
FBS	Foetal Bovine Serum
PBS	Phosphate buffer saline
ATCC	American Type Culture Collection
TNBC	Triple negative breast cancer
HLA-ABC	Human leukocyte antigen A, B and C (also known as MHC-1)
MFI	Median fluorescent intensity
TRAIL	TNF-related apoptosis-inducing ligand
PI	Propidium iodide
PE	Phycoerythrin
APC	Allophycocyanin
FITC	Fluorescein isothiocyanate
NK cells	Natural killer cells
MDSCs	Myeloid-derived suppressor cells
MIA	Multiple image alignment
OCT	Optimal cutting temperature
DAB	3,3-Diaminobenzidine
NS	Not significant
ND	Not detected

NSCLC	Non-small cell lung cancer
HKG	Housekeeping gene
HSP27	Heat shock protein 27
MMPs	Matrix metalloproteinases
WT	Wild-type
CSC	Cancer stem cell
BRAF	v-raf murine sarcoma viral oncogene homolog B1
EGFR	Epidermal growth factor receptor
KRAS	Kirsten rat sarcoma viral oncogene homolog
TCR	T cell receptor
Tregs	Regulatory T cells
ECM	Extracellular matrix
APCs	Antigen presenting cells
CTLA4	Cytotoxic T leukocyte antigen 4
CDK4/6	Cyclin-dependent kinase 4/6
3'UTR	3' untranslated region
HDACs	Histone deacetylases
TGFβ	Transforming growth factor beta
TAA	Tumour-associated antigen
EMT	Epithelial to mesenchymal transition
IL	Interleukins

Acknowledgements

I would like to take this opportunity to firstly thank my supervisor's Dr. Rebecca Leyland, Dr. Neil Cross and Dr. Nikki Jordan-Mahy, for the opportunity to work on this PhD project. Your guidance and encouragement throughout the entirety of my PhD has been extraordinary. Through the highs and lows of my PhD journey, you have been there to support my every move and I will forever be very grateful. The whole experience for me has been life changing and I have you all to thank for where I am in my career today.

Dr. Rebecca Leyland, I do not think I could have asked for a better Director of Studies. You have been the most inspirational role model for me in terms of your dedication and ambition to succeed in research. Throughout my PhD you have always encouraged me to push myself which has given me the confidence I needed to become an independent researcher. I am so appreciative of all the time you put aside to help and support me. I will truly miss working with you.

Dr. Neil Cross, firstly I need to thank you massively for encouraging me to apply for this PhD. Without you informing me about it I would have missed the opportunity because I was travelling around Thailand. Whilst it was not the easiest PhD application to write whilst on my travels, you did everything you could to make sure I was in with a shot, and I will always be grateful. You are the most knowledgeable person I know; I do not think there is anything you do not know. Thank you for sharing your knowledge with me, supporting me throughout my PhD, being there for me throughout writing my thesis, and I hope one day I can be as successful as you in my field of research.

Dr. Nikki Jordan-Mahy 'my PhD mum', throughout my PhD you have been so compassionate and understanding through the hard times that I have experienced. Your continuous words of encouragement and how much you believe in me has got me where I am today. Especially through my writing period, I cannot thank you enough. I know for a fact I could not have done it without your constant support and inspiration. Your patience, time, and dedication to help me write my thesis has truly been extraordinary. I will never forget this hard time of my life, writing and working full time, and I believe I have you to thank for making it that bit easier. Anyone would be lucky to have you as their supervisor.

With that, I would also like to thank all staff and students, old and new, in the BMRC. Just the smallest bit of advice or comfort from anyone has helped me along the way, and I have learnt so much, and for that I am extremely grateful. I will truly miss being a part of such a talented and inspirational scientific community. I would like to say a big thank you to PhD students: Lucy Flint, Cristiana De Matos, Filipe Hanson and Rachel Hodgson. You have all played a big role in my PhD experience whether it's been helping me in the lab or offering a shoulder to cry on. You were always the people I could go too when times were hard, and you would always make me feel better by making me laugh.

Lastly, a massive thank you to my friends and family for their patience and support throughout my PhD. I have not been the best company to be around at times, but I could always rely on you to make me feel better. Connor, my partner, and best friend, you have been with me for the last 12 years and have seen me at my best and my worst, thank you for continuing to love and support me like you do. Most of all, thank you to my mum and dad for always believing in me, even when I did not. You both continue to be my biggest inspiration in life, and I owe everything to you both. You will both be glad I finally finished my PhD!

1. Introduction

1.1 General Introduction

Cancer is a serious global health problem responsible for one in six deaths worldwide. In 2020, there were approximately 10 million cancer deaths globally (Debela *et al.*, 2021). Conventional therapeutic strategies, such as surgery, chemotherapy and radiotherapy have been the gold standard treatment for cancer patients for several decades, but they are invasive and have severe toxicity effects in some patients (Vanneman and Dranoff, 2012). Over many years research efforts have been focused on developing targeted therapies that have equal or improved treatment efficacy, whilst causing less damage to healthy cells and thus less toxicities for the cancer patients. The entry of targeted therapies into the clinic for the treatment of multiple different cancer types has substantially improved overall patient survival (Debela *et al.,* 2021). However, some patients, like those with triple negative breast cancer (TNBC) remain limited to chemotherapy treatment due to TNBC lacking targetable biomarkers, unlike other breast cancer subtypes with targetable hormone receptors (Feng *et al.,* 2018).

Cancer immunotherapy is an example of targeted therapy which has revolutionized the cancer therapy landscape due to its capability to deliver unprecedented clinical benefit in many advanced cancers (Wang *et al.*, 2019; Hudson *et al.,* 2020). Cancer immunotherapies work to re-establish immune-mediated tumour eradication (Beatty and Gladney, 2015). Monoclonal antibodies targeting immune checkpoint molecules such as programmed death-1 (PD-1) and programmed death-ligand 1 (PD-L1) have made by far the largest contribution to these advancements in immunotherapy (Wang *et al.,* 2019; Hudson *et al.,* 2020).

PD-L1 is an immune checkpoint inhibitor that binds to its receptor PD-1 expressed by T cells, B cells, dendritic cells, and monocytes (Freeman *et al.,* 2000). PD-L1 is expressed by T cells, B cells, natural killer (NK) cells, dendritic cells, macrophages, myeloid-derived suppressor cells (MDSCs) and many other cell types such as epithelial and endothelial cells (Johnson and Dong, 2017; Dong *et al.,* 2019). The PD-1/PD-L1 signalling axis regulates immune responses to prevent exacerbated activation and autoimmunity (Dong *et al.,* 2002; Dong *et al.,* 2019). Many tumours exploit this mechanism by overexpressing PD-L1 (Hino *et al.,* 2010; Maine *et al.,* 2013; Muenst *et al.,* 2014). Recently, tumours have also been shown to express PD-1 (Yao *et al.,* 2018; Wang *et al.,* 2020). PD-L1 binding to PD-1 on immune cells

induces inhibitory responses which in turn can promote immune evasion and tumour progression (Dong *et al.,* 2002).

Elevated expression of PD-L1 on tumours has been reported to strongly correlate with advanced disease state and unfavourable prognosis in melanoma (Hino *et al.,* 2010), breast (Muenst *et al.,* 2014), gastric (Fashoyin-Aje *et al.,* 2019), ovarian (Maine *et al.,* 2013), liver (Zeng *et al.,* 2011), kidney (Thompson *et al.,* 2006), pancreatic (Nomi *et al.,* 2007) and bladder (Inman *et al.,* 2007) cancer. Immunotherapies targeting the PD-1/PD-L1 signalling axis have become the first-line treatment for some cancers due to their ability to promote durable anti-tumour immune responses in select patients with advanced cancers (Fehrenbacher *et al.,* 2016; Rosenberg *et al.,* 2016; Balar *et al.,* 2017), leading to their approval by the USA Food and Drug Administration (FDA). Although PD-1/PD-L1-targeted therapies have demonstrated clinical benefits across a broad range of cancers, some patients are unresponsive, hyperprogressive or develop resistance (Wang *et al.,* 2019). The objective response rate of anti-PD-L1 monoclonal antibodies alone is approximately 15% in non-small-cell lung cancer (NSCLC) (Garon *et al.,* 2015; Fehrenbacher *et al.,* 2016), approximately 20% in urothelial carcinomas (Balar *et al.,* 2017; Powles *et al.,* 2017) and approximately 30% in Merkel cell carcinomas (Kaufman *et al.,* 2016; Kaufman *et al.,* 2018). Consequently, novel therapeutic strategies are required to enhance patient response rates through combining PD-1/PD-L1-targeted therapy with other immune approaches, small molecule inhibitors, chemotherapy, or other modalities (Yi *et al.,* 2022).

Patients considered eligible for PD-1/PD-L1-targeted therapy are those that present with PD-L1-positive tumours, circulating PD-1 positive/CD8+ T cells and/or tumours with high mutational burden (Balar *et al.,* 2017; Yi *et al.,* 2018). However, patient tumours that have shown to lack PD-L1 have also responded positively to PD-1/PD-L1-targeted therapy (Dong *et al.,* 2019; Chocarro de Erauso *et al.,* 2020), suggesting that either blocking PD-L1 expression on tumours is not required for anti-tumour responses and inhibition of PD-L1 on immune cells alone may be sufficient or that more sensitive approaches to detecting PD-L1 expression on tumours is required. Conversely, some tumours with high PD-L1 expression have shown to be unresponsive to PD-1/PD-L1-targeted therapy (Bai *et al.,* 2017), likely due to the lack of immune stimulatory cells present in the tumour microenvironment to elicit an effective anti-tumour immune response, but reasons for this remain to be fully

elucidated. However, patients that are intrinsically unresponsive to PD-1/PD-L1-targeted therapy can also demonstrate 'primary resistance' whereby their tumours display inadequate T cell infiltration, T cell exclusion, impaired interferon gamma (IFNγ) receptor signalling and/or local immune suppression (Bai *et al.,* 2017; Jiang *et al.,* 2019). Patients that initially respond to PD-1/PD-L1-targeted therapy also show 'acquired resistance' whereby their tumours display loss of T cell function and/or disrupted antigen processing and presentation (Tumeh *et al.,* 2014; Bai *et al.,* 2017).

In recent years, approximately 10% of cancer patients have experienced pseudoprogression in response to PD-1/PD-L1-targeted therapy, whereby patients temporally exhibit rapid progression of their condition before responding successfully to treatment (Kocikowski *et al.,* 2020). On the other hand, some patients have experienced hyperprogression in response to PD-1/PD-L1-targeted therapy, which is characterised by rapid deterioration of their condition upon initialisation of treatment without a successful response; giving patients less than 2 months to live from onset (Kocikowski *et al.,* 2020). The reasons for pseudoprogression and hyperprogression in response to PD-1/PD-L1-targeted therapy remain speculative and need to be explored. It is also important for clinicians to be able to distinguish between the two types of responses to inform patient selection for therapy. Further insight into the role of PD-L1 and PD-1 in the tumour microenvironment could allow the identification of more appropriate biomarkers predictive of clinical efficacy to PD-1/PD-L1-targeted therapy necessary to ensure patients receive the maximum clinical benefit whilst avoid immune-related adverse effects (Yi *et al.,* 2018; Wang *et al.,* 2019), pseudoprogression and hyperprogression (Kocikowski *et al.,* 2020).

Most research investigating the tumorigenic role of PD-L1, and PD-1 has been carried out in human or mouse cancer cell lines grown in two-dimensional (2D) monolayer cell culture (Hudson *et al.,* 2020). Accordingly, there is an urgent need for more relevant *in vitro* models capable of closely mimicking the heterogeneity of the tumour microenvironment during *in vivo* conditions, thus allowing a more predictive *in vitro* evaluation of the role of PD-L1 and PD-1, PD-1/PD-L1-targeted therapy, potential combination strategies and immune cell-cancer cell interactions.

1.2 Immune systems role in cancer

The tumour microenvironment consists of extracellular matrix (ECM) components and diverse cell populations such as T cells, B cells, NK cells, macrophages, dendritic cells, fibroblasts, and endothelial cells (Gajewski *et al.,* 2013). Crosstalk

between cancer cells and accessory cells fuels and shapes tumour development. Although immune cells such as NK, CD8+ and CD4+ T cells which migrate to the tumour display anti-tumour activity, over time the tumour microenvironment becomes immunosuppressive, favouring the emergence of tumour promoting cells such as regulatory T cells (Tregs), MDSCs and M2 macrophages (Beatty and Gladney, 2015). This is known as the phenomenon cancer immuno-editing which involves three phases: elimination, equilibrium, and escape (Figure 1.1).

In the elimination phase, innate and adaptive immunity work together to destroy cancer cells before they become clinically apparent. Hence why patients that are immunocompromised due to other clinical illnesses such as HIV are more susceptible to develop cancer as their immune system fails to respond (Prakash *et al.,* 2002). Genetic aberrations that occur within normal healthy cells can be hereditary or induced through exposure to carcinogens, radiation, chronic inflammation, or viruses (Beatty and Gladney, 2015). It is these genetic changes that predict the cancer cells fate for either immune destruction or entering dynamic equilibrium with immune cells which ultimately leads to immune escape by employing a selection pressure that forces cancer cells to mutate and adapt further to evade the immune system defences.

During the early stages of tumour development, cytotoxic immune cells including NK cells, CD8+ and CD4+ T cells migrate to the tumour, recognise, and eliminate the more immunogenic cancer cells (Teng *et al.,* 2015). Cancer cells with a high mutational burden are normally considered immunogenic because of the high number of neo-antigens presented in the major histocompatibility complex class 1 (MHC-1) molecules on their cell surface which leads to immune cell activation (Aptsiauri *et al.,* 2007). The direct interaction of the T cell receptor (TCR) binding to an antigenic peptide presented on an MHC molecule on antigen presenting cells (APCs) or tumour cells is necessary for T cell activation. Hence why PD-1 positive CD8+ T cells tend to be present in tumours characterised by a high mutation burden such as metastatic melanoma (Tumeh *et al.,* 2014; Gros *et al.,* 2014) and colorectal cancer (Llosa *et al.,* 2015), and thus why these tumours positively correlate with a clinical response to PD-1/PD-L1-targeted therapies (Larkin *et al.,* 2015; Overman *et al.,* 2017).
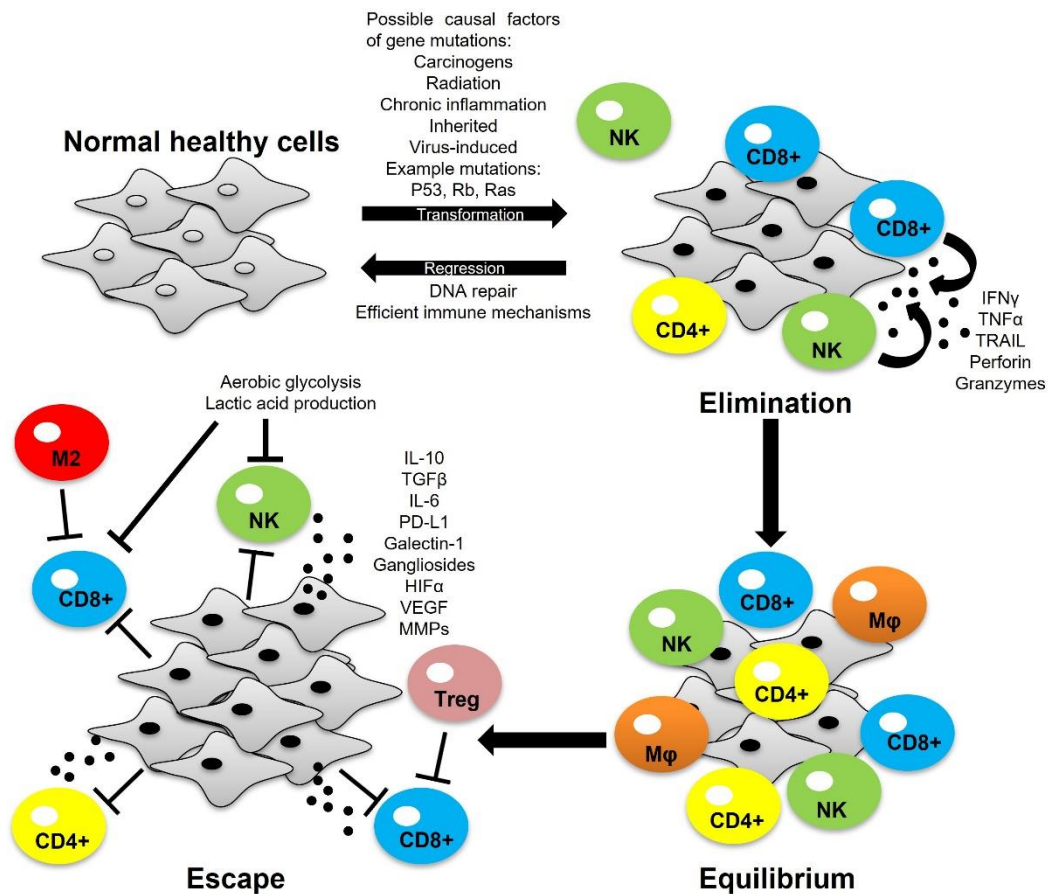
Figure 1.1 The process of cancer immuno-editing: elimination, equilibrium, and escape. Normal healthy cells transform into tumour cells through acquiring mutations that allows for uncontrolled growth of the cell. In the elimination phase, immune cells can recognize and eliminate tumour cells by inducing apoptosis via granule and/or receptor-mediated mechanisms. Some tumour cells avoid immune destruction and enter dynamic equilibrium with immune cells whereby the immune system elicits a potent enough response to contain the tumour cells but not enough to eradicate them. During this phase tumour cells develop increased genetic instability and undergo immune selection, whereby the immune cells eliminate those tumour cells susceptible to immune-mediated killing, whilst selecting those tumour cells with mechanisms to evade the immune system. These selected tumour cells can now proliferate freely and expand leading to immune escape. Interferon gamma (IFN-γ), tumour necrosis factor alpha (TNF-α), tumour necrosis factor-related apoptosis-inducing ligand (TRAIL), interleukin 10 (IL-10), interleukin 6 (IL-6), transforming growth factor beta (TGF-β), hypoxic inducible factor 1/2 alpha (HIF-1/2α), vascular endothelial growth factor (VEGF), matrix metalloproteinases (MMPs). Image taken from Hudson *et al.,* (2020).

1.2.1 Immune-mediated cancer cell killing

CD8+ T cells trigger apoptosis in cancer cells by specifically recognising and binding an antigenic peptide presented in the MHC-1 molecule on the surface of cancer cells using their unique TCR (de Visser *et al.,* 2006). CD8+ T cells induce apoptosis through the release of granules (granzyme and perforin molecules) and death receptor-mediated mechanisms (Maher and Davies, 2004). Similarly, NK cells, dendritic cells and macrophages mediate cancer cell apoptosis but elicit a non-specific response. Death receptor-mediated mechanisms to induce cancer cell death involve the tumour necrosis factor (TNF) receptor superfamily and their respective ligands. The six human death receptors (DRs) include: TNF-R1, Fas, TRAIL-R1 (DR4), TRAIL-R2 (DR5), DR3 and DR6 which are stimulated by TNF, FasL, TRAIL and TL1A, respectively (Loetscher *et al.,* 1990; Itoh *et al.,* 1991; Sheridan *et al.,* 1997; Migone *et al.,* 2002). The ability of these receptors to induce cancer cell death made them interesting to explore for therapeutic targeting (Walczak *et al.,* 2013).

1.2.1.1 Death receptors in cancer

Since the discovery of TNF in 1975 it has emerged as a therapeutic target for many inflammatory diseases due to its capability to induce chronic inflammation when present at high levels (Walczak *et al.,* 2013). Treatment of patients suffering with rheumatoid arthritis, Crohn's disease and psoriasis are treated with TNF blockers which show a success rate often higher than 50%. For cancer treatment however, the success of TNF treatment has been limited, despite the direct induction of cancer cell death, the role of TNF is contradictory in cancer and lethal systemic toxicities induced by TNF stimulation raise many clinical concerns (Montfort *et al.,* 2019). Regardless, ways to directly target the TNF to the tumour through using oncolytic viruses and conjugated peptides, has demonstrated the ability of TNF, specifically TNFα to synergise with anti-PD-1 therapy in melanoma, lymphoma and prostate cancer mouse models (Curnis *et al.,* 2000; Calcinotto *et al.,* 2012; Cervera-Carrascon *et al.,* 2018; Elia *et al.,* 2018).

The lack of early promise of TNF led to the discovery of death receptors: Fas, DR4 and DR5 (Trauth *et al.,* 1989; Wiley *et al.,* 1995; Clayer *et al.,* 2001). Subsequently, this led to the development of anti-Fas, anti-DR4 and anti-DR5 monoclonal antibodies as well as recombinant TRAIL that were shown to bind the death receptors on the surface of cancer cells and induce apoptosis in many different types of cancer cells. Indeed, many tumours express Fas, DR4 and DR5 at high levels (Trauth *et al.,*

1989; Wiley *et al.,* 1995), suggesting they would be exquisitely sensitive to death receptor-induced apoptosis. Importantly, TRAIL seemed the most promising death-inducing ligand, due to its ability to specifically kill cancer cells, but not normal healthy cells *in vitro* (Wiley *et al.,* 1995; Pitti *et al.,* 1996; Walczak *et al.,* 1999). Despite this, clinical evaluation of targeting these death receptors using monotherapy did not produce striking results (Bianco *et al.,* 2003; Modiano *et al.,* 2012; Kelley and Ashkenazi, 2004; Herbst *et al.,* 2010). This is most likely due to cancer cells developing resistance mechanisms to reduce their susceptibility to death receptor-mediated killing (Todaro *et al.,* 2008; Newsom-Davis *et al.,* 2009). From these clinical investigations, however, it was evident that death receptor targeting has the potential to show promising clinical results when used in combination with other anti-cancer therapies. For example, intratumoral delivery of FasL was shown to stimulate pro-inflammatory signals and reduced the immunosuppressive tumour microenvironment by abrogating tumour-promoting macrophages and Tregs, whilst releasing CD8+ T cells from their immunosuppressive state (Modiano and Bellgrau, 2016). Hence raising the possibility of the therapeutic potential of FasL to synergise with immunotherapies such as PD-1/PD-L1-targeted therapies. Similarly, Hendricks *et al.,* (2016) showed the potential synergy of co-targeting PD-L1 and TRAIL using a bi-specific protein. In this study melanoma cells undergo PD-L1-directed TRAIL-mediated apoptosis and in a co-culture with T cells the bi-specific protein augmented T cell activation (Hendricks *et al.,* 2016). The cooperation of TRAIL and PD-L1 targeting therefore warrants further investigation as the cancer specific nature of TRAIL makes it appealing to potentially reduce the immune adverse effects observed in some patients treated with immunotherapies.

1.2.1.2 Death receptor-mediated activation of extrinsic and intrinsic apoptotic pathways

Depending on their status of stimulation, TRAIL and FasL can be expressed by various cells of the immune system, amongst them NK cells, T cells, NK T cells, dendritic cells and macrophages (Walczak, 2013). TRAIL and FasL binding to their receptors are important for maintenance of immune homeostasis. The fact that cancer cells express DR4, DR5 and Fas makes them susceptible to immune-mediated cancer cell killing. TRAIL and FasL binding causes receptor trimerization and clustering of the intracellular death domain (Elmore, 2007). This leads to the recruitment of Fas-associated death domain and binding of pro-caspase-8 leading to the formation of the death-inducing signalling complex. This in turn activates caspase

8 leading to apoptosis either via the extrinsic or intrinsic apoptotic pathway. In the extrinsic apoptotic pathway, caspase-8 directly cleaves caspase 3 and initiates the caspase cascade, ultimately leading to apoptosis. Cross-talk between the death-receptor (extrinsic) pathway and the mitochondrial (intrinsic) pathway has been reported (Igney and Krammer 2002). BID, a BH3 domain-containing proapoptotic Bcl2 family member, is present in the cytosol and a proximal substrate of caspase 8. Activated caspase 8 cleaves BID forming truncated BID (tBID) which then translocates to the mitochondria initiating the intrinsic apoptotic pathway (Li *et al.,* 1998). Tumour cells can acquire resistance to apoptosis by the expression of anti-apoptotic proteins (such as c-FLIP) or by the downregulation or mutation of pro-apoptotic proteins (such as Bid) and receptors (such as DR4, DR5 and Fas). Figure 1.2 demonstrates the mechanisms of immune-mediated cancer cell killing and highlights with red asterisks where cancer cells can undergo adaptations to avoid immune recognition and cell death (Figure 1.2).

1.2.2 Immune evasion mechanisms

Tumour immune escape refers to the phenomenon by which tumour cells can grow and metastasise by avoiding recognition and elimination by the immune system, which is an important hallmark of cancer to promote survival and development (Hanahan and Weinberg, 2011). There are a variety of mechanisms employed by tumours to mediate immune evasion including: (i) loss of antigenicity either by acquisition of defects in antigen processing and presentation or through the loss of immunogenic antigens leading to reduced antigen presentation in the MHC-1 molecules (Beatty and Gladney, 2015; Teng *et al.,* 2015); (ii) development of immunosuppressive mechanisms such as the expression of PD-L1 resulting in direct inhibition of immune cell function (Dong *et al.,* 2002; Teng *et al.,* 2015); and (iii) creation of an immunosuppressive microenvironment by secretion of pro-tumorigenic cytokines such as transforming growth factor beta (TGF-β) and interleukin (IL)-10 that recruit and activate immune cells and other cells such as cancer-associated fibroblasts and endothelial cells that function to inhibit anti-tumour immunity via direct and indirect mechanisms (Gajewski *et al.,* 2013).
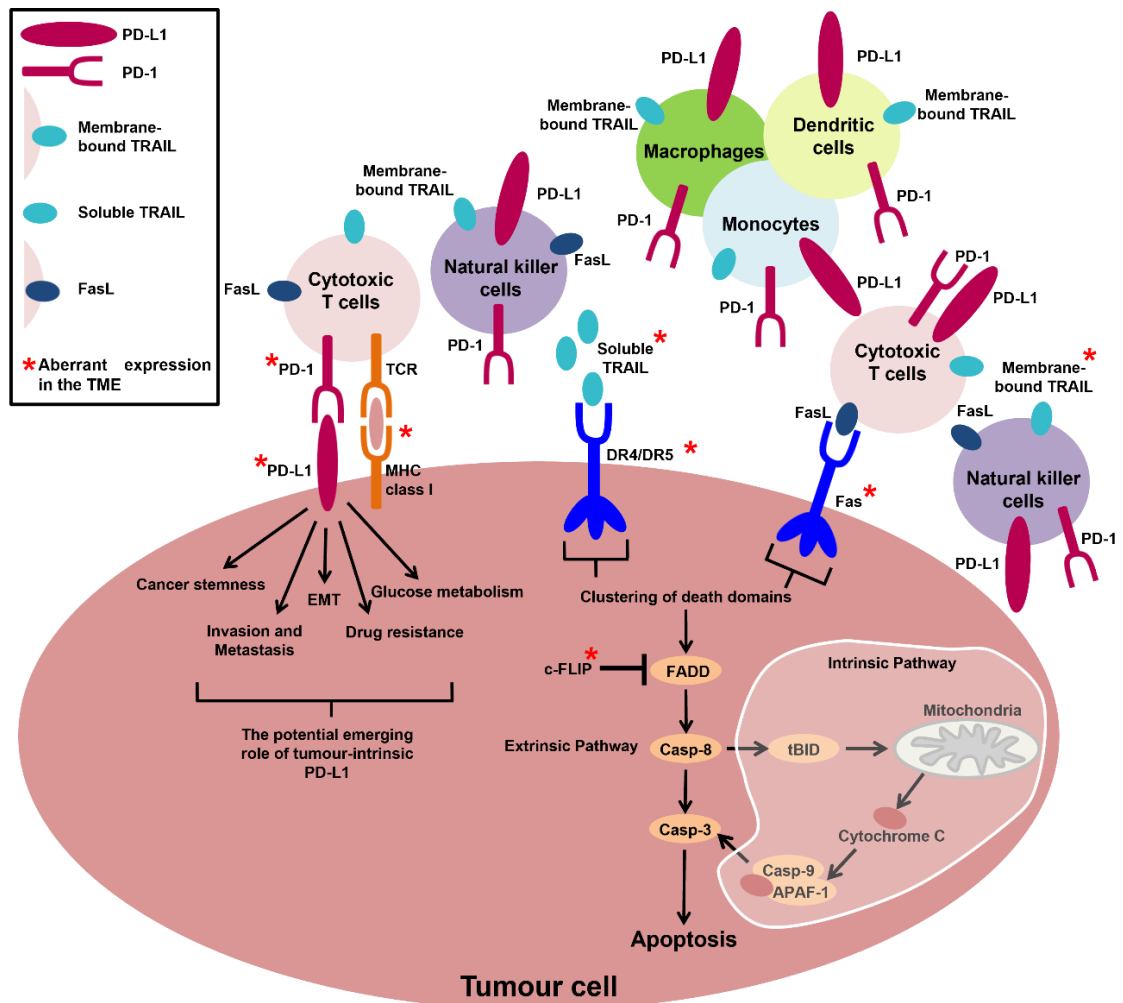
Figure 1.2 Immune evasion mechanisms employed by cancer cells. In the tumour microenvironment, cancer cells and immune cells exhibit overexpression of immune-inhibitory proteins such as PD-L1 and PD-1 to inhibit immune cell effector functions. More recently, there is an emerging role that PD-L1 sends pro-survival signals in some cancer cells to promote tumour initiation, invasion, and metastasis, epithelial to mesenchymal transition, drug resistance and regulate glucose metabolism. Cancer cells can also reduce their susceptibility to immune-mediated killing by reducing their immunogenicity through downregulating or acquiring mutations in antigen presentation machinery (such as MHC complex I) or cell surface death receptors (DR4, DR5 and Fas). PD-1/PD-L1-targeted therapies, death receptor agonists, recombinant human TRAIL and FasL have been shown to promote apoptosis in cancer cells. Red asterisks are used to highlight the aberrant expression of certain proteins expressed by cancer cells and immune cells observed in the tumour microenvironment which mediates immune evasion.

Leukocyte infiltration into the tumour stroma and their subsequent activation is essential for successful immune-mediated elimination of malignant cells. Predominantly, CD8+ T cells play a pivotal role in anti-tumour immunity and their presence in the tumour stroma correlates with a positive prognosis in multiple solid tumours including breast (Mahmoud *et al.,* 2011), colorectal (Galon *et al.,* 2006), bladder (Sharma *et al.,* 2007) and ovarian cancer (Sato *et al.,* 2005). CD8+ T cells, CD4+ T cells, B cells and NK cells induce immuno-protective inflammatory responses by secreting IFN-γ, tumour necrosis factor (TNF)-α, IL-17 and IL-2 (Gajewski *et al.,* 2013). The cytotoxic effect of these cells is dependent on their ability to penetrate the tumour stroma and become activated (Li *et al.,* 2018).

Solid tumours are often poorly vascularized creating an oxygen and nutrient gradient so that some cancer cells exist in a hypoxic environment, whilst others exist in a vascularized area with sufficient oxygen (Noman *et al.,* 2015). Hypoxia contributes to immune tolerance of tumour cells by impeding the homing of immunocompetent cells into tumours and inhibiting their anti-tumour responses. Besides immune cells being unable to compete for nutrients limiting their ability to function effectively, tumour-associated macrophages, Tregs and MDSCs preferentially infiltrate and home to hypoxic regions and elicit their immunosuppressive functions (Noman *et al.,* 2015; Li *et al.,* 2018). Tumour-associated macrophages upregulate hypoxia inducible factors which induce the expression of proangiogenic molecules such as vascular endothelial growth factor (VEGF). Whilst VEGF is well-known to support tumour cell growth and metastasis (Li *et al.,* 2018), it can also inhibit T cell function (Ziogas *et al.,* 2012), prevent dendritic cell differentiation and activation (Gabrilovich *et al.,* 1996) and facilitate the recruitment of Tregs and MDSCs to the tumour microenvironment (Yang *et al.,* 2018). Hypoxia-driven expression of forkhead box P3 (FoxP3) is the key regulator in the development and function of Tregs (Clambey *et al.,* 2012). High abundance of FoxP3 positive cells in the tumour microenvironment correlates with poor prognosis in most solid tumours, particularly when this coincides with a low abundance of CD8+ T cells (Shang *et al.,* 2015). Tregs secrete TGF-β and IL-10, suppressing CD8+ T cells and NK cell effector function, whilst promoting tumour-associated macrophages and MDSCs immunosuppressive function. MDSCs induce T cell anergy by producing IL-6, IL-10 and reactive oxygen species and expressing high levels of PD-L1 (Noman *et al.,* 2015). Hypoxia has been shown to increase the expression of PD-L1 on MDSCs, tumour-associated macrophages, dendritic cells and tumour cells, demonstrating how it is a potent driver of immune evasion in the

tumour microenvironment (Johnson and Dong, 2017). Recently, it has been reported that PD-L1 blockade downregulates signalling pathways associated with hypoxia and tumour growth (Saleh *et al.,* 2019). Because the immunosuppressive function of immune cells can be enhanced by hypoxia, it highlights how regulating the expression of PD-L1 could help to manipulate the aforementioned immune evasion mechanisms in the tumour microenvironment.

1.3   Immune checkpoint signalling in cancer

Immune checkpoint molecules expressed on T cells such as cytotoxic T lymphocyte antigen 4 (CTLA-4) and PD-1 regulate immune responses by dampening T cell activation to prevent exacerbated activation and autoimmunity (Hanahan and Weinberg, 2011; Buchbinder and Desai, 2016). During cancer development anti-tumour immunity is suppressed and immunotherapies targeting CTLA-4 and PD-1 signalling axes have been developed to reactivate T cells to induce immune-mediated tumour eradication (Khair *et al.,* 2019). Normally, T cell activation requires two signals. Signal one is the TCR recognising and binding to an antigenic peptide presented on an MHC molecule on antigen presenting cells (APCs) or tumour cells. The second is a co-stimulatory signal through CD28 on T cells binding to CD80/CD86 on APCs. CTLA-4 prevents T cell activation by competing with the co-stimulatory molecule CD28 for the CD80/CD86 on APCs (Hodi *et al.,* 2010). Ipilimumab is a CTLA-4 inhibitor approved for the treatment of advanced or unresectable melanoma (Hodi *et al.,* 2010; Pacheco *et al.,* 2019). Unlike CTLA-4 expression restricted to T cells, PD-1 is expressed by activated T cells, B cells and monocytes. PD-1 binds to its two ligands, PD-L1 and PD-L2, expressed primarily by APCs and tumour cells (Freeman *et al.,* 2000). The function of PD-L2 however is not as widely known as PD-L1 (Qin *et al.,* 2019). Activated PD-1 on T cells through PD-L1 binding counteracts the downstream signalling of the TCR and CD28 co-stimulatory signal by phosphorylating the cytoplasmic immunoreceptor tyrosine-based switch motif leading to the recruitment of Src homology region 2 domain containing phosphatases 1 and 2 (SHP1/2) and slam-associated protein (Qin *et al.,* 2019; Peled *et al.,* 2018). SHP1/2 dephosphorylate the TCR and CD28 proximal signalling molecules including ZAP70 and PI3K, respectively, inhibiting T cell activation, cytokine production and promoting pro-apoptotic molecule expression, ultimately resulting in T cell anergy or apoptosis (Figure 1.3) (Jiang *et al.,* 2019). The overexpression of PD-L1 in many cancers causes functionally exhausted and unresponsive T cells, promoting immune

evasion and tumour progression (Freeman *et al.,* 2000; Hino *et al.,* 2010; Maine *et al.,* 2013; Muenst *et al.,* 2014) and abrogating PD-L1 expression on tumour cells can enhance sensitivity to T cell killing (Teo *et al.,* 2015; Wu *et al.,* 2019).
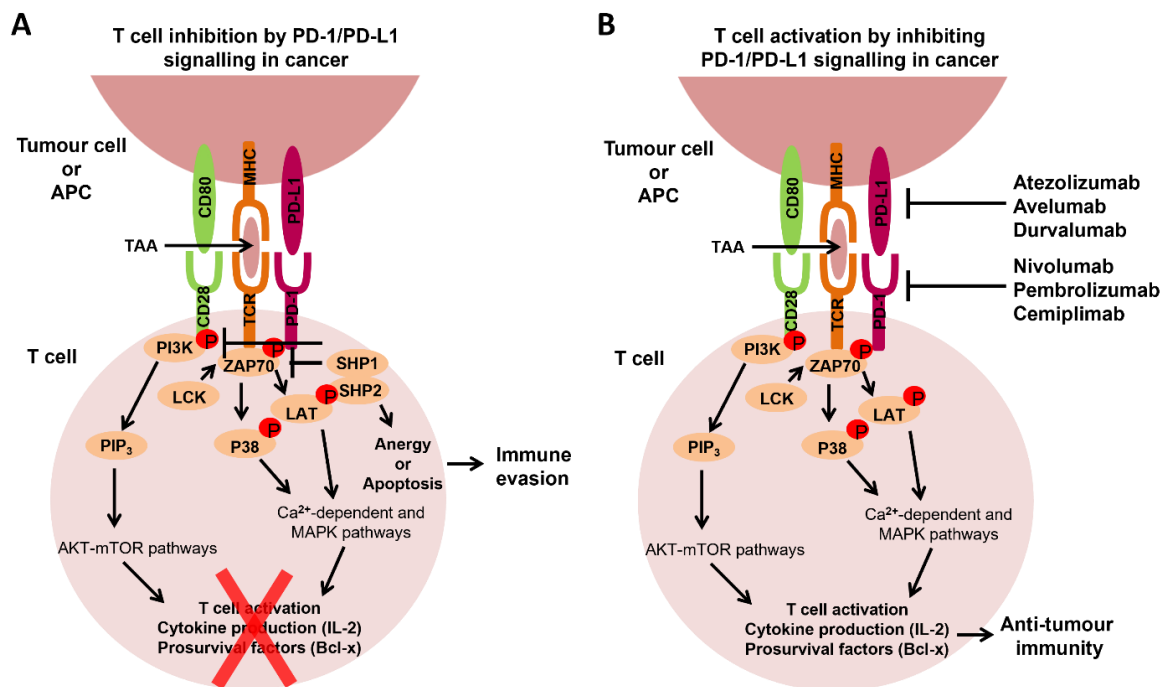
Figure 1.3 The extrinsic function of the PD-1/PD-L1 signalling axis in cancer. T cells play an important role in modulating immune responses against tumour cells, but tumours can exhibit immune inhibitory mechanisms like overexpressing PD-L1 to avoid T cell-mediated killing. **(A)** When PD-L1 binds to PD-1 expressed on the surface of T cells, T cells become inactivated through the recruitment of SHP1/2 which subsequently inhibits TCR and CD28 co-stimulatory signalling by preventing the phosphorylation of ZAP70 and PI3K, leading to T cell anergy or apoptosis and ultimately immune evasion. **(B)** Monoclonal antibodies targeting the PD-1/PD-L1 signalling axis have been developed to restore immune-mediated eradication of the tumour. PD-1/PD-L1 blockade allows co-stimulatory signal transduction from the TCR and CD28 on T cells upon interaction with APCs or tumour cells. TCR binding to the tumour-associated antigen (TAA) in the MHC complex leads to the phosphorylation of ZAP70, which then phosphorylates P38 and LAT resulting in activation of calcium-dependent and MAPK pathways. Simultaneously, CD80 binding to CD28 phosphorylates PI3K which activates PIP3 leading to AKT-mTOR pathway activation. These signalling pathways promote T cell activation, cytokine production and pro-survival factor expression stimulating anti-tumour immunity. Image taken from Hudson *et al.,* (2020).

1.4 Immunotherapies targeting the PD-1/PD-L1 signalling axis

1.4.1 Monotherapy PD-1/PD-L1 checkpoint blockade

PD-1/PD-L1-targeted therapies yield remarkable anti-tumour immune responses with limited side effects in select patients with advanced cancers (Wang *et al.,* 2019). They have shown to increase the proliferation of tumour-infiltrating lymphocytes and develop a more clonal TCR repertoire within the T cell population directed against the tumour (Tumeh *et al.,* 2014). Currently there are six approved monoclonal antibodies for the targeting of PD-1 (Table 1.1) and PD-L1 (Table 1.2) for the treatment of multiple cancers as single agents; some of which have gained accelerated approval and emerged as front-line treatments for some cancers (Khair *et al.,* 2019). In 2014, the FDA approved the first anti-PD-1 monoclonal antibody, Nivolumab, for treatment of patients with unresectable or metastatic melanoma and disease progression following Ipilimumab (anti-CTLA-4), based on the CA209037 clinical trial data where Nivolumab alone achieved 31.7% objective response rate (Weber *et al.,* 2015). Subsequently, Nivolumab was approved for the first-line treatment of metastatic melanoma (Weber *et al.,* 2017) and second-line treatment for NSCLC (Brahmer *et al.,* 2015) and renal cell carcinoma (Motzer *et al.,* 2015) following successful phase I-III clinical trials. Nivolumab has also been approved for classic Hodgkin lymphoma (Ansell *et al.,* 2015), head and neck squamous cell carcinoma (Ferris *et al.,* 2017), bladder cancer (Sharma *et al.,* 2017) and colorectal cancer with microsatellite instability or mismatch repair deficiency (Overman *et al.,* 2017). Similarly, the anti-PD-1 monoclonal antibody Pembrolizumab is approved for the first-line treatment of metastatic melanoma (Robert *et al.,* 2015) and NSCLC (Garon *et al.,* 2015) and second-line treatment for metastatic head and neck squamous cell carcinoma (Bauml *et al.,* 2017) and refractory classical Hodgkin's lymphoma (Chen *et al.,* 2017). In addition, it has also been approved for gastric/gastroesophageal junction adenocarcinomas (Fashoyin-Aje *et al.,* 2019), cervical cancer (Chung *et al.,* 2019) and primary mediastinal large B-cell lymphoma (Zinzani *et al.,* 2017). Pembrolizumab is also the first therapy to be approved for the treatment of all solid tumours with high mutation burden (Patnaik *et al.,* 2015). More recently, Nivolumab and Pembrolizumab have gained accelerated approval for many more cancers (Table 1.1). Cemiplimab represents a newly approved anti-PD-1 monoclonal antibody for the treatment of metastatic cutaneous squamous cell carcinoma (Markham and Duggan, 2018). Atezolizumab was the first anti-PD-L1 monoclonal antibody to be approved for treatment of advanced NSCLC and

metastatic urothelial carcinoma. Atezolizumab promoted a tolerable and durable objective response rate of 23% and 15% in NSCLC (Fehrenbacher *et al.,* 2016; Horn *et al.,* 2018) and in metastatic urothelial carcinoma, respectively (Rosenberg *et al.,* 2016; Petrylak *et al.,* 2018), whilst anti-PD-L1 monoclonal antibodies Avelumab and Durvalumab are approved for the treatment of Merkel cell carcinoma (Kaufman *et al.,* 2016; Kaufman *et al.,* 2018) and NSCLC (Antonia *et al.,* 2018), respectively and are both approved for treatment of metastatic urothelial carcinoma (Powles *et al.,* 2017; Patel *et al.,* 2017). Furthermore, these PD-1/PD-L1-targeted therapies are also being investigated for treatment of colorectal, prostate, and breast cancer as well as haematological malignancies as monotherapy and in combination with conventional and targeted therapies and have shown promising results in clinical trials (Yi *et al.,* 2022).

1.4.2   Co-inhibitory checkpoint blockade

Ipilimumab (anti-CTLA4) alone has shown to increase the overall survival of metastatic melanoma patients but is associated with severe immune-related adverse events and low patient response rates (Buchbinder and Desai, 2016). Some tumours present with T cell defective PD-1 following anti-PD-1 therapy, rendering them resistant, however, this coincides with increased expression of other immune checkpoints on the T cell surface (Grywalska *et al.,* 2018). Combining anti-CTLA-4 with anti-PD-1 has shown to synergistically activate anti-tumour immunity, enhancing clinical efficacy whilst improving tolerability and overcoming resistance (Hodi *et al.* 2010). Anti-CTLA-4 combined with anti-PD-1 was first approved for treatment of metastatic melanoma (Weber *et al.,* 2016) and was subsequently approved for metastatic renal cell carcinoma (Motzer *et al.,* 2018), colorectal cancer with high microsatellite instability and mismatch repair aberrations (Overman *et al.,* 2018), PD-L1 positive NSCLC (Hellmann *et al.,* 2019), hepatocellular carcinoma (Yau *et al.,* 2020), and malignant pleural mesothelioma (Baas *et al.,* 2021).

Other dual immune checkpoint blockade strategies which involve combining PD-1/PD-L1-targeted therapies with monoclonal antibodies targeting TIM-3, LAG-3, PVRIG and TIGIT are still in clinical trials, having not yet been approved by the FDA (Yi *et al.,* 2022).

Table 1.1 FDA approved single agent use of PD-1-targeted therapy for a broad range of cancer types.

Drug	Drug Target	Study Name (Identifier)	Population	Refs
Nivolumab	PD-1	NCT01844505	Metastatic melanoma	Larkin *et al.,* 2015
		NCT01642004	Advanced non-small cell lung cancer	Brahmer *et al.,* 2015
		NCT01668784	Advanced renal-cell carcinoma	Motzer *et al.,* 2015
		NCT01592370	Relapsed/refractory classical Hodgkin's lymphoma	Ansell *et al.,* 2015
		NCT02488759	Recurrent or metastatic head and neck squamous cell carcinoma	Ferris *et al.,* 2017
		NCT02387996	Metastatic urothelial carcinoma	Sharma *et al.,* 2017
		NCT02060188	Colorectal cancer with MSI-H and dMMR aberrations	Overman *et al.,* 2017
		NCT01658878	Advanced hepatocellular carcinoma	El-Khoueiry *et al.,* 2017
		NCT01928394	Metastatic small cell lung cancer	Antonia *et al.,* 2016
		NCT02569242	Unresectable Advanced or Recurrent Esophageal Cancer	Kato *et al.,* 2019
Pembrolizumab	PD-1	NCT01866319	Metastatic melanoma	Robert *et al.,* 2015
		NCT01295827	Advanced non-small cell lung carcinoma	Garon *et al.,* 2015
		NCT02255097	Recurrent or metastatic head and neck cancers	Bauml *et al.,* 2017
		NCT02453594	Adults and paediatric patients with refractory classical Hodgkin's lymphoma	Chen *et al.,* 2017
		NCT02335424	Metastatic urothelial carcinoma	Balar *et al.,* 2017
		NCT01295827	Unresectable or metastatic MSI-H or dMMR solid tumours	Patnaik *et al.,* 2015

Table 1.1 Continued…

Drug	Drug Target	Study Name (Identifier)	Population	Refs
Pembrolizumab	PD-1	NCT02335411	Recurrent locally advanced or metastatic gastric or gastroesophageal junction adenocarcinoma	Fashoyin-Aje *et al.,* 2019
		NCT02628067	Recurrent or metastatic cervical cancer	Chung *et al.,* 2019
		NCT02576990	Adults and paediatric patients with refractory or relapsed primary mediastinal large B-cell lymphoma	Zinzani *et al.,* 2017
		NCT02702414	Advanced hepatocellular carcinoma	Zhu *et al.,* 2018
		NCT02267603	Adult and paediatric recurrent locally Merkel cell carcinoma	Nghiem *et al.,* 2016
		NCT02054806	Advanced small cell lung cancer	Ott *et al.,* 2017
		NCT03284424	Advanced Cutaneous Squamous Cell Carcinoma	Grob *et al.,* 2020
		NCT02628067	Advanced Endometrial Cancer	Marabelle *et al.,* 2020
		NCT02563002	Colorectal cancer with MSI-H and dMMR aberrations	André *et al.,* 2020
Cemiplimab	PD-1	NCT02760498	Metastatic cutaneous squamous cell carcinoma	Markham *et al.,* 2018

Table 1.1 Anti-PD-1 monoclonal antibodies approved for the treatment of multiple cancer types as single agents. PD-1 checkpoint inhibitors currently approved by the FDA include Nivolumab, Pembrolizumab, and Cemiplimab for a broad range of cancers. For each drug displayed in the table, the cancer types to which they were approved for treatment are shown in order of approval. MSI-H, High microsatellite instability; MMR, mismatch repair. Table updated and adapted from Hudson *et al.,* (2020).

Table 1.2 FDA approved single agent use of PD-L1-targeted therapy for a broad range of cancer types.

Drug	Drug Target	Study Name (Identifier)	Population	Refs
Atezolizumab	PD-L1	NCT01375842	Metastatic urothelial carcinoma	Petylak *et al.,* 2018
		NCT01903993	Advanced non-small cell lung carcinoma	Fehrenbacher *et al.,* 2016
Avelumab	PD-L1	NCT02155647	Merkel cell carcinoma	Kaufman *et al.,* 2018
		NCT01772004	Metastatic urothelial carcinoma	Patel *et al.,* 2017
Durvalumab	PD-L1	NCT01693562	Advanced urothelial carcinoma	Powles *et al.,* 2017
		NCT02125461	Unresectable stage III non-small cell lung carcinoma	Antonia *et al.,* 2018

Table 1.2 Anti-PD-L1 monoclonal antibodies approved for the treatment of multiple cancer types as single agents. PD-L1 checkpoint inhibitors currently approved by the FDA include Atezolizumab, Avelumab and Durvalumab for a broad range of cancers. For each drug displayed in the table, the cancer types to which they were approved for treatment are shown in order of approval. Table adapted from Hudson *et al.,* (2020).

1.4.3   PD-1/PD-L1 checkpoint blockade combined with chemotherapy

The ability of tumour cells to develop resistance to chemotherapy is a major obstacle in prolonging patient survival. Emerging evidence suggests PD-L1 promotes chemotherapy resistance in melanoma, lymphoma, breast cancer and other cancers (Ghebeh *et al.,* 2010; Li *et al.,* 2017; Wu *et al.,* 2018) suggesting coupling PD-1/PD-L1 blockade with chemotherapy has the potential to increase clinical efficacy. Tumours unresponsive to PD-1/PD-L1-targeted therapy often lack sufficient tumour-associated antigens to present to T cells, meaning T cells are unable to recognise and become activated to exert their cytotoxicity. For example, tumours with few somatic mutations such as pancreatic, TNBC and prostate cancer appear more resistant to PD-1/PD-L1-targeted therapy, compared to tumours with high mutational burden (Patnaik *et al.,* 2015). Chemotherapy has been shown to stimulate anti-tumour immune responses (Pacheco *et al.,* 2019). For example, chemotherapy-induced killing of tumour cells releases tumour associated antigens into the tumour

microenvironment, leading to T cell activation and thus tumour cell killing. PD-1/PD-L1 blockade frees T cells for activation and therefore combining the two would enhance tumour cell killing, not only in tumours known to respond to PD-1/PD-L1-targeted therapy, but those considered less immunogenic and otherwise resistant. Multiple types of chemotherapy including cisplatin (Ohtsukasa *et al.,* 2003), doxorubicin (Ghebeh *et al.,* 2010) and gemcitabine (Plate *et al.,* 2005) have been shown to promote lymphocyte infiltration, induce PD-L1 expression on tumour cells, deplete immunosuppressive cells such as Tregs and MDSCs and promote maturation and activation of APCs. The improvement in the tumour microenvironment following chemotherapy treatment suggests an attractive synergy between chemotherapy and PD-1/PD-L1 blockade.

Preclinical evaluation of PD-1/PD-L1-targeted therapy in combination with chemotherapy has demonstrated promising results (Ghebeh *et al.,* 2010; Li *et al.,* 2017; Wu *et al.,* 2018); however, there is only moderate support of this evidence in the human population. So far only three cancer types have gained FDA approval for treatment with chemotherapy regimens combined with PD-1/PD-L1-targeted therapy. In advanced non-squamous NSCLC, Pembrolizumab combined with platinum-doublet chemotherapy achieved an objective response rate of 61.4% leading to its approval in 2017 (Gadgeel *et al.,* 2017). Later in a phase 3 trial evaluating pembrolizumab combined with standard chemotherapy in NSCLC patients, the combination was also approved for squamous NSCLC (Paz-Ares *et al.,* 2018). Similarly, Atezolizumab combined with platinum-doublet chemotherapy and bevacizumab (an angiogenesis inhibitor) gained approval by the FDA based on the results of IMpower150 for advance non-squamous NSCLC (Socinski *et al.,* 2018). Additionally, Atezolizumab combined with nanoparticle-bound albumin (nab)-paclitaxel gained approval by the FDA for TNBC in 2018 (Schmid *et al.,* 2018). This combination promoted a higher median progression-free (7.2 months versus 5.5 months) and overall survival (21.3 months versus 17.6 months) than Atezolizumab plus placebo. More recently, Atezolizumab in combination with nab-paclitaxel and carboplatin or carboplatin and etoposide have been approved for the treatment of non-squamous NSCLC (West *et al.,* 2019) and extensive-stage small-cell lung cancer (Mansfield *et al.,* 2020), respectively. Despite the current lack of FDA approved PD-1/PD-L1-targeted therapies for combination with chemotherapy, there are several undergoing clinical developments for multiple different cancers including

melanoma (Khair *et al.,* 2019), NSCLC (Pacheco *et al.,* 2019), gastric (Sun *et al.,* 2021), colorectal and breast cancer (Grywalska *et al.,* 2018).

In light of this, triple combination with other anti-cancer agents would further enhance clinical efficacy. Chemotherapy has shown to sensitise tumour cells to TRAIL and Fas receptor-mediated apoptosis. For instance, tumour-selective recombinant TRAIL or death receptor agonists have shown cooperation with conventional and targeted therapies in many pre-clinical and clinical studies (Leong *et al.,* 2009; Qiao *et al.,* 2018). One study explored the combination of PD-L1 inhibition and TRAIL using a bi-functional fusion protein in melanoma cells and demonstrated synergistic PD-L1-directed TRAIL-mediated tumour cell apoptosis via increasing T cell activation (Hendriks *et al.,* 2016). By combining tumour-selective TRAIL with PD-L1 blockade alone or in combination with chemotherapy offers a novel approach to enhance the efficacy of PD-L1/PD-1 checkpoint inhibition without affecting the toxicity profile.

1.4.4   PD-L1 checkpoint blockade combined with radiotherapy

Like chemotherapeutic agents, radiotherapy can also induce immunogenic cell death and enhance anti-tumour immune responses (Hwang *et al.,* 2018; Romano *et al.,* 2021; Yi *et al.,* 2022). Not only is this immune response inflicted locally but also systemically. Many preclinical and clinical studies have demonstrated that radiotherapy could synergise with PD-1/PD-L1-targeted therapies (Yi *et al.,* 2022; Yu *et al.,* 2022). For example, radiotherapy has been reported to increase T cell infiltration and expand the TCR repertoire in the tumour microenvironment (Lim *et al.,* 2014). It has also been shown to upregulate the expression of PD-L1 (Deng *et al.,* 2014) and MHC-1 (Wang *et al.,* 2017) on tumour cells, making them more susceptible to PD-1/PD-L1-targeted therapies and increasing their likeness to be recognised and eliminated by CD8+ T cells through TCR binding.

The safety and efficacy of PD-1/PD-L1-targeted therapies with radiotherapy alone and in combination with chemotherapy have been evaluated in several solid tumour types (Yi *et al.,* 2022). Whilst these combinations have demonstrated promising clinical outcomes and superiority over PD-1/PD-L1 monotherapy in phase 1 and 2 trials, none yet have gained FDA approval. More research is required to optimise radioimmunotherapy regimens in terms of dose, fractionation, and tumour volume to allow the optimal type and magnitude of local and systemic anti-tumour immune response (Romano *et al.,* 2021), which is highly likely to be cancer type specific.

1.4.5 PD-1/PD-L1 checkpoint blockade combined with targeted therapy

Oncogenic driver mutations participate in immunosuppression. Mutant v-raf murine sarcoma viral oncogene homolog B1 (BRAF) proto-oncogene and epidermal growth factor receptor (EGFR) correlate with poor prognosis and low patient response to PD-1/PD-L1-targeted therapy in melanoma (Simeone *et al.,* 2015) and NSCLC (Hellmann *et al.,* 2018), respectively. These mutations have shown to regulate PD-1 and PD-L1 expression in different tumour cell types (Dong *et al.,* 2018). Monoclonal antibodies targeting oncogenic driver mutations modulate the tumour microenvironment via antibody-dependent cellular cytotoxicity and promote anti-tumour immune responses. Erlotinib is an example of an EGFR inhibitor currently under clinical investigation for treatment of NSCLC patients in combination with PD-1/PD-L1-targeted therapy (Gettinger *et al.,* 2018). The immune-stimulatory effects on the tumour microenvironment showed the potential to increase the efficacy of PD-1/PD-L1 blockade, but so far, the immune-related adverse effects are outweighing the positive clinical outcomes (Oshima *et al.,* 2018) and these combinations require further investigation.

Vascular targeting drugs are also under clinical investigation for treatment of cancer patients in combination with PD-1/PD-L1-targeted therapy (Yi *et al.,* 2022). Vascular targeting drugs have been shown to increase PD-L1 expression and modulate anti-tumour immunity through the recruitment of CD8+ T cells to the tumour microenvironment and reduce immunosuppressive cells such as Tregs and MDSCs (Yang *et al.,* 2018). Axitinib, Cabozantinib, Bevacizumab and Lenvatinib are vascular targeting drugs that have gained FDA approval in combination with PD-1/PD-L1-targeted therapies either alone or combined with chemotherapy for multiple different cancers including advanced NSCLC (Socinski *et al.,* 2018), endometrial carcinoma (Makker *et al.,* 2019), hepatocellular carcinoma (Finn *et al.,* 2018), and renal cell carcinoma (Mortez *et al.,* 2020; Choueiri *et al.,* 2021). Many other targeted therapies are undergoing clinical investigation for their cooperation with PD-1/PD-L1-targeted therapies including PARP inhibitors, cyclin-dependent kinase 4/6 (CDK4/6) inhibitors and many more (Reviewed: Yi *et al.,* 2022).

Whilst immunotherapies targeting the PD-1/PD-L1 signalling axis have demonstrated unprecedented success has monotherapy and in combination with conventional and targeted therapies in the clinic, the fact remains; there are a large percentage of non-

responders or initial responders that acquire resistance (Yi *et al.,* 2018; Wang *et al.,* 2019). Most research associated with PD-L1 and PD-1 has been focused on their extrinsic role to inhibit the immune system, but more recently a tumour-intrinsic role of PD-L1 and PD-1 is emerging in some cancer types; however, these roles remain to be fully characterised in all cancers. Important questions to be addressed are the contribution of tumorigenic expression of PD-L1 and PD-1 to intrinsic signalling, whether monoclonal antibodies targeting the PD-1/PD-L1 signalling axis work sufficiently to block this new and emerging role of PD-L1 and PD-1 and whether the intrinsic roles of these proteins are contributing significantly to resistance, relapse to treatment, and hyperprogressive responses in patients.

1.5   Mechanisms affecting PD-L1 expression in tumours

The tumour-intrinsic PD-L1 pathway is aberrantly activated in many cancers (Hino *et al.,* 2010; Maine *et al.,* 2013; Muenst *et al.,* 2014; Ju *et al.,* 2020). There are several intrinsic and extrinsic mechanisms responsible for PD-L1 regulation in tumour cells, including genetic alterations, epigenetic modifications, oncogenic and tumour suppressor signals, inflammatory cytokines, and other factors (Figure 1.4) (Reviewed by Dong *et al.,* 2018; Chen *et al.,* 2019; Hudson *et al.,* 2020).
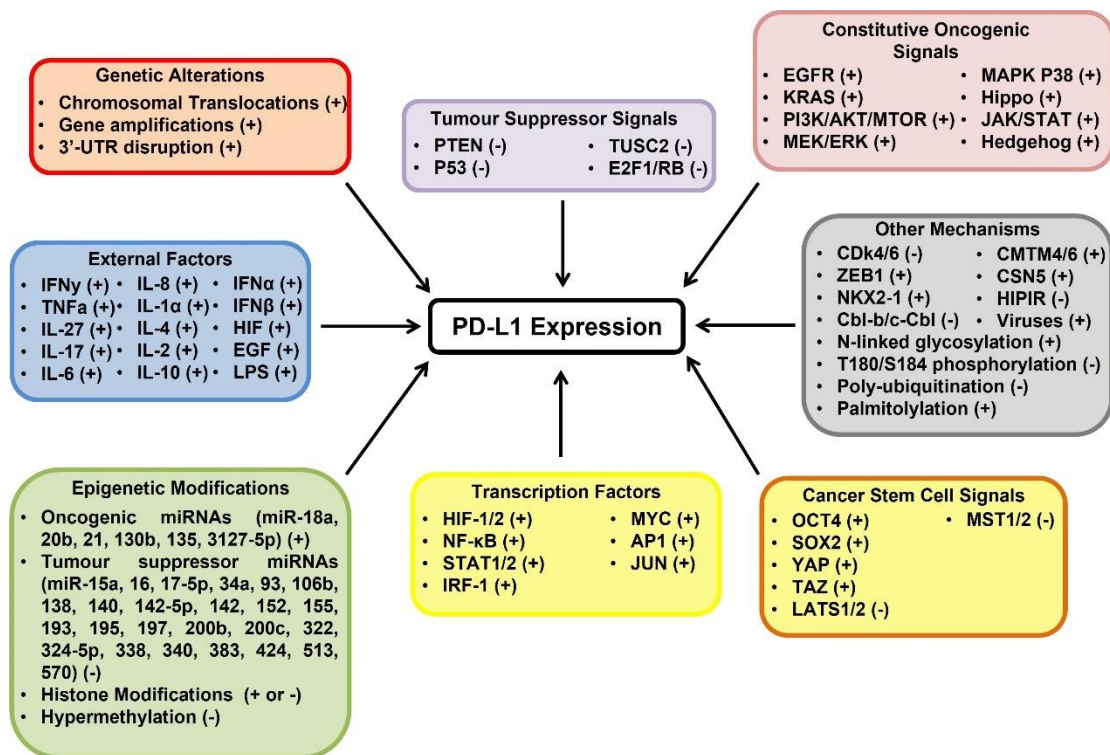
Figure 1.4 The mechanisms of PD-L1 activation and inactivation in cancer. The diagram highlights the many mechanisms behind PD-L1 regulation in tumour cells and whether the proposed mechanisms have been shown to upregulate (+) or downregulate (−) the expression of PD-L1. PD-L1 expression is regulated at the transcriptional, post transcriptional, translational, and post translational level in tumour cells. Many mechanisms have been shown to modulate PD-L1 expression including genetic aberrations, epigenetic modifications, oncogenic and tumour suppressor signals, and extrinsic factors. Image updated from Hudson *et al.,* (2020).

1.5.1 Genetic aberrations of PD-L1

Several tumours harbour genetic aberrations of the chromosome 9p24.1 which *CD274,* the gene for PD-L1, resides ultimately affecting the expression of PD-L1 (Twa *et al.,* 2014; Budczies *et al.,* 2016; Kogure and Kataoka, 2017). Increased copy number alterations on chromosome 9p correlates directly with increased PD-L1 expression (Budczies *et al.,* 2016) and frequently occurs in primary mediastinal B-cell lymphoma (63%) (Green *et al.,* 2010), classical Hodgkin lymphoma (40%) (Ansell *et al.*, 2015), triple-negative breast cancer (29%) (Barrett *et al.,* 2015), and soft tissue carcinomas (21.1%) (Budczies *et al.,* 2017). A recent study analysing 9,771 tumour samples from 22 cancer types revealed a high frequency of copy number gains in bladder, cervical, colorectal, ovarian, and head and neck cancer (more than 15% of

tumours), but only a low frequency in pancreatic, renal cell and papillary thyroid carcinoma (less than 5% of tumours) (Budczies *et al.,* 2016). In addition, copy number gains are also less frequently observed in gastric cancer (15%) (Bass *et al.,* 2014), NSCLC (5.3%) (Ikeda *et al.,* 2016), small cell lung cancer (1.9%) (George *et al.,* 2017), and diffuse large B-cell lymphoma (3%) (Georgiou *et al.,* 2016). PD-L1 copy number gains are associated with substantial therapeutic activity in some cancers due to the high levels of tumour PD-L1 and increased immune infiltrates that they have shown to promote (Ansell *et al.,* 2015; Inoue *et al.,* 2016). There is some evidence to suggest that PD-L1 chromosomal translocations influence PD-L1 overexpression in certain diffuse large B cell lymphomas (Twa *et al.,* 2014; Georgiou *et al.,* 2016). Disruption of the 3' untranslated region (UTR) of PD-L1 is another mechanism by which some tumours such as adult T-cell leukaemia/lymphoma, diffuse large B-cell lymphoma, and gastric cancer display marked elevation of aberrant PD-L1 transcripts that have become stabilised by truncation of the 3'UTR (Wang *et al.,* 2012; Kogure and Kataoka, 2017; Ju *et al.,* 2020). PD-L1 deletions however are more frequently observed in tumours than copy number gains (31% vs. 12%); particularly in melanoma and NSCLC where greater than 50% of tumours harbour PD-L1 deletions (Budczies *et al.,* 2016). PD-L1 deletions, like PD-L1 copy number gains, are associated with a high tumour mutational load and poor prognosis, but the clinical significance of PD-L1 deletions is not yet clear (Barrett *et al.,* 2015; Budczies *et al.,* 2016).

1.5.2   Epigenetic mechanisms modulate PD-L1 expression

Epigenetic modifications including microRNAs (miRNAs), promoter DNA methylation, and histone modifications have been shown to modulate PD-L1 expression in different cancers (Zheng *et al.,* 2016; Dong *et al.,* 2018; Lv *et al.,* 2020). A number of miRNAs have been identified to directly or indirectly influence PD-L1 expression (Dong *et al.,* 2018; Shen *et al.*, 2019); the majority of which inhibit PD-L1 expression by tumour cells. One miRNA identified across multiple cancers to inhibit PD-L1 expression is miR-200c which directly binds to the 3'UTR of PD-L1 in hepatocellular carcinoma (Sun *et al.,* 2018), acute lymphoid leukaemia (Pyzer *et al.,* 2017) and NSCLC (Chen *et al.,* 2014). Additionally, in NSCLC reduced miR-197 expression promotes chemoresistance via regulating the CKS1B/STAT3 signalling pathway to promote PD-L1 expression (Fujita *et al.,* 2015). The miR-197/PD-L1 axis has also been reported of clinical significance in oral squamous cell carcinoma, but

here PD-L1 was found to be a positive prognostic factor due to its expression positively correlating with tumour-infiltrating lymphocytes (Ahn *et al.,* 2017). Other inhibitory miRNAs are highlighted in Figure 1.4. miRNAs that positively regulate PD-L1 expression include miR-135 (Wang and Zhang, 2018) and miR-3127-5p in NSCLC (Tang *et al.,* 2018) and miR-18a in cervical cancer (Dong *et al.,* 2018). In colorectal cancer PTEN is directly targeted by miRNAs miR-130b, miR-20b and miR-21 to indirectly induce PD-L1 expression via PI3K-AKT-mTOR pathway activation (Zhu *et al.,* 2014).

Recently, PD-L1 promoter methylation has been shown to negatively correlate with PD-L1 expression in multiple cancer types including acute myeloid leukaemia (Goltz *et al.,* 2017), glioblastoma (Heiland *et al.,* 2017), melanoma (Micevic *et al.,* 2018), head and neck cancer (Franzen *et al.,* 2017), colorectal cancer (Goltz *et al.,* 2017), gastric cancer (Lv *et al.,* 2020) and prostate cancer (Gevensleben *et al.,* 2016). The methylation status of the PD-L1 promoter has clinical significance for predicting the outcome of PD-1/PD-L1-targeted therapy (Gevensleben *et al.,* 2016; Goltz *et al.,* 2017; Franzen *et al.,* 2017; Goltz *et al.,* 2017; Micevic *et al.,* 2018; Lv *et al.,* 2020). For example, in NSCLC patients, anti-PD-1 therapy enhanced PD-L1 promoter methylation and reduced PD-L1 expression which mediated resistance to anti-PD-1 immunotherapy Nivolumab in NSCLC patients (Zhang *et al.,* 2017). In addition, histone modifications including methylation and acetylation can modulate PD-L1 expression in some cancers (Linenlaf *et al.,* 2016; Booth *et al.,* 2017; Bae *et al.,* 2018; Wang *et al.,* 2018; Xiao *et al.,* 2019). The histone methyltransferase, enhancer of zeste 2 polycomb repressive complex 2 subunit has been shown to supress PD-L1 expression through mediating trimethylation of the PD-L1 promotor in hepatoma cells (Xiao *et al.,* 2019). Moreover, histone deacetylases (HDACs) have been reported to regulate PD-L1 expression (Zheng *et al.,* 2016; Booth *et al.,* 2017; Wang *et al.,* 2018). In lung cancer, HDAC inhibition has been shown to augment PD-1/PD-L1-targeted therapy through the enhancement of PD-L1 expression (Zheng *et al.,* 2016; Briere *et al.,* 2018).

1.5.3 Constitutive oncogenic signalling regulates PD-L1 expression

Oncogenic and tumour suppressor signalling pathways have been shown to regulate PD-L1 expression (Cao *et al.,* 2017; Janse Van Rensburg *et al.,* 2018). Oncogenic signals derived from aberrant receptors, effector molecules and transcription factors

lead to the overexpression of PD-L1 by tumours and are associated with poor prognosis and patient response to PD-1/PD-L1-targeted therapy (Jiang *et al.,* 2013; Hellman *et al.,* 2018; Janse Van Rensburg *et al.,* 2018; Ju *et al.,* 2020). PI3K-AKT-mTOR and RAS-MAPK pathway activation is evidently linked to constitutive PD-L1 regulation in many cancers (Akbay *et al.,* 2013; Lastwika *et al.,* 2016; Almozyan *et al.,* 2017; Ju *et al.,* 2020). Loss of PTEN (a tumour suppressor that negatively regulates PI3K-AKT-mTOR signalling) or mutations in *PIK3CA* (a catalytic subunit of PI3K) leads to elevated PD-L1 expression via constitutive P13K-ATK-mTOR pathway activation in squamous cell lung carcinoma (Xu *et al.,* 2014; McGowan *et al.,* 2017), NSCLC (Lastwika *et al.,* 2016), gliomas (Parsa *et al.,* 2007), colorectal cancer (Song *et al.,* 2013), prostate cancer (Crane *et al.,* 2009) and breast cancer (Mittendorf *et al.,* 2014). Some tumours harbour mutations in RAS, BRAF and EGFR and exhibit constitutive RAS-MAPK pathway activation and consequently overexpress PD-L1 (Akbay *et al.,* 2013; Jiang *et al.,* 2013; Simeone *et al.,* 2015; Hellman *et al.,* 2018). BRAF and EGFR mutations correlate with PD-L1 expression, poor prognosis and low patient response to PD-1/PD-L1-targeted therapy in melanoma (Jiang *et al.,* 2013; Simeone *et al.,* 2015) and NSCLC (Hellman *et al.,* 2018), respectively. Moreover, oncogenic transcription factors including MYC (Maeda *et al.,* 2017), STAT (Marzec *et al.,* 2008), NFκB (Gowrishankar *et al.,* 2015; Jin *et al.,* 2019), IRF-1 (Lee *et al.,* 2006), AP-1 (Green *et al.,* 2012) and HIF (Noman *et al.,* 2014; Barsoum *et al.,* 2014) have been reported to modulate PD-L1 expression at the transcriptional level. MYC expression is found elevated in 70% of cancers (Dang *et al.,* 2012) and has recently been shown to bind to the PD-L1 promoter transcriptionally inducing PD-L1 expression (Casey *et al.,* 2016). Like MYC, other oncogenic reprogramming factors have been implicated in PD-L1 regulation. OCT4 and SOX2 have both been shown to upregulate PD-L1 expression in cervical cancer (Dong *et al.,* 2018) and hepatocellular carcinoma (Zhong *et al.,* 2017), respectively, highlighting the necessity of PD-L1 expression for tumour reprogramming functions.

1.5.4   Post-translational modifications modulate PD-L1 expression

Posttranslational modifications have recently been recognised to modulate PD-L1 expression in some cancers, namely, N-linked glycosylation, phosphorylation and poly-ubiquitination (Li *et al.,* 2016; Mezzadra *et al.,* 2017; Zhang *et al.,* 2018; Hsu *et al.,* 2018; Wang *et al.,* 2019). Mass spectrometry analysis revealed that PD-L1 expressed by human tumour tissues and cancer cell lines (including breast,

melanoma, lung and colorectal) was highly glycosylated at the asparagine residues of four NXT motifs in the PD-L1 extracellular domain (Li *et al.,* 2016). This N-linked glycosylation was shown to be responsible for PD-L1 protein stability; giving PD-L1 a four-fold longer half-life compared to non-glycosylated PD-L1 (Li *et al.,* 2016). Phosphorylation and poly-ubiquitination of PD-L1 has the opposite effect to glycosylation in that they both reduce PD-L1 expression. In breast and cervical cancer, cyclin D-CDK4 kinase was shown to destabilise PD-L1 via phosphorylating cullin 3-speckle type POZ protein E3 ligase, leading to PD-L1 ubiquitination; ultimately reducing PD-L1 expression (Zhang *et al.,* 2018). Likewise, ubiquitin E3 ligases Cbl-b and Cbl-c negatively regulate PD-L1 expression by inactivating STAT, AKT and ERK signalling in NSCLC cells (Wang *et al.,* 2018).

1.5.5   Extrinsic factors promote PD-L1 expression

Interferon gamma signalling in the tumour microenvironment is primarily responsible for PD-L1 upregulation by tumour cells in most cancer types (Moon *et al.,* 2017; Zhang *et al.,* 2017; Garcia-Diaz *et al.,* 2017; Li *et al.,* 2018; Imai *et al.,* 2019; Chen *et al.,* 2019). This may be due in part to secretion of IFNγ from tumour specific T-cells within the tumour microenvironment. A study investigating IFNγ-mediated PD-L1 upregulation in multiple cancers including melanoma, renal cell carcinoma, head and neck cancer and NSCLC, found that IFNγ was able to induce mRNA and protein PD-L1 expression by tumour cells regardless of constitutive PD-L1 expression (Chen *et al.,* 2019). Although, IFNγ is a dominant driver of PD-L1 expression in various tumours, the mechanism by which IFNγ mediates PD-L1 upregulation appears to be distinct among different cancer types. For example, transcription factors JAK/STAT1, IRF-1 and NFκB are responsible for IFNγ-induced PD-L1 expression in hematopoietic tumours (Bellucci *et al.,* 2015), lung cancer (Lee *et al.,* 2006) and melanoma (Gowrishankar *et al.,* 2015), respectively. IFNγ signalling is often associated with a positive patient response to PD-1/PD-L1-targeted therapy in metastatic melanoma, NSCLC, head and neck cancer, gastric cancer and urothelial carcinoma (Ayers *et al.,* 2017; Karachaliou *et al.,* 2018; Yi *et al.,* 2018). Moreover, loss of function mutations in molecules involved in the IFNγ signalling pathway such as JAK1, JAK2 and β2-microglobulin have been identified to render tumour cells unresponsive to IFNγ signalling and mediate intrinsic or acquired resistance to PD-1-targeted therapy (Zartesky *et al.,* 2016; Shin *et al.,* 2017; Alavi *et al.,* 2018).

Other inflammatory cytokines shown to promote PD-L1 expression by tumour cells include: TNFα in breast (Lim *et al.,* 2016), prostate, colorectal cancer (Wang *et al.,* 2017) and hepatocellular carcinoma (Li *et al.,* 2018); IL-27 in lung, prostate and ovarian cancer (Carbotti *et al.,* 2015); and TGFβ in breast (Alsuliman *et al.,* 2015) and lung cancer (Kurimoto *et al.,* 2016). Additionally, some cytokines have been shown to work synergistically to upregulate PD-L1 expression in tumours such as TNFα with IFNγ (Yee *et al.,* 2017) and with IL-17 (Wang *et al.,* 2017). Besides inflammatory cytokines extrinsically modulating PD-L1 expression, hypoxia in the tumour microenvironment selectively elevates PD-L1 expression via HIF-1α activation in melanoma, breast, lung, thyroid, and prostate cancer (Barsoum *et al.,* 2014; Johnson and Dong, 2017; Zhou *et al.,* 2019).

Despite the tremendous efforts of scientific researchers to provide insight into the mechanisms behind PD-L1 signal activation in cancer, the regulation of PD-L1 expression by tumours remains to be fully elucidated in all cancer types. Understanding the mechanisms of tumorigenic PD-L1 expression and signalling in different cancer types may provide therapeutic opportunities to alleviate PD-L1-induced intratumoral immunosuppression and overcome resistance to PD-1/PD-L1-targeted therapy and chemotherapy. For greater improvement in the efficacy of PD-1/PD-L1-targeted therapy, it is necessary to identify and target tumour-intrinsic mechanisms that are both responsible for controlling PD-L1 expression and promoting tumour progression and resistance to cancer treatment.

1.6 Tumour-intrinsic PD-L1 signalling

To date, there are less than twenty publications investigating the intrinsic role of PD-L1 in tumours: predominantly using RNA interference approaches in two dimensional (2D)-cultured mouse or human cancer cell lines and immunocompromised mouse models. There is an emerging role of PD-L1 to send pro-survival signals within tumour cells to promote cancer initiation, metastasis, development, and resistance to therapy (Illustrated previously in Figure 1.2 Section 1.2.1.2). However, how these emerging pro-survival signals are conveyed intracellularly from cell surface PD-L1 is largely unknown. There is accumulating evidence that intracellular regions of PD-L1 are responsible for transducing survival signals in tumour cells (Azuma *et al.,* 2008; Gato-Cañas *et al.,* 2017; Escors *et al.,* 2018). Three conserved amino acid sequences including RMLDVEKC, DTSSK and QFEET motifs have been reported

and shown to be located in the intracellular domain of PD-L1. RMLDVEKC and DTSSK motifs were reported to be associated with regulating PD-L1 stability and signal transduction due to the discovery of two specific phosphorylation sites located in the motifs (Lim *et al.,* 2016; Gato-Cañas *et al.,* 2017). Gato-Cañas *et al.,* (2017) demonstrated that the RMLDVEKC motif was required to inhibit IFN-mediated cytotoxicity towards tumour cells via directly preventing STAT3 phosphorylation and caspase-mediated apoptosis. Another study also demonstrated that tumour cells expressing PD-L1 were refractory to Fas- and protein kinase inhibitor Staurosporine-mediated apoptosis (Azuma *et al.,* 2008), which could suggest that the intracellular motifs of PD-L1 may be involved in crosstalk with other signalling pathways; in particular signalling pathways that control tumour cell survival. Other studies have shown that PD-L1 agonists can induce crosslinking between PD-L1 and CD80/CD86 to transduce reverse signalling (Kim *et al.,* 2008; Chaudhri *et al.,* 2018; Zhao *et al.,* 2019). Recently, PD-L1 has been shown to form a heterodimer with CD80, a shared ligand with CTLA-4 and CD28, in *cis* on APCs and tumour cells. This heterodimer was reported to weaken CD80:CTLA4 interaction, but not CD80:CD28 binding indicating that PD-L1 may prevent CTLA-4 inhibitory signals (Chaudhri *et al.,* 2018; Zhao *et al.,* 2019). Furthermore, overexpression of CD80 on PD-L1 positive tumour cells was shown to blunt the pro-tumour role of PD-L1 (Haile *et al.,* 2011). The above studies support the notation that PD-L1 reverse signalling exists in tumour cells. Research efforts should expand on this emerging concept of PD-L1 reverse signalling which has the potential to identify new mechanisms of PD-L1-targeted immunotherapy.

1.6.1 Tumour-intrinsic PD-L1 is associated with cancer initiation

PD-L1 expression has been shown to correlate with the cancer stem cell (CSC)-like characteristics including the expression of CD44 and/or CD133 at high levels on tumour cells. Human head and neck (Lee *et al.,* 2016), lung (Nishino *et al.,* 2017) and colorectal (Zhi *et al.,* 2015) cancer cells that have CSC-like characteristics (CD44^{high}/CD133^{high}) were shown to preferentially express PD-L1 compared to CD44^{low}/CD133^{low} cancer cells in immunocompromised mouse models either inoculated with a patient-derived xenograft or human cancer cell lines mixed with Matrigel®, respectively. In breast and lung cancer cells CD44 was shown to be a key regulator of PD-L1 expression following shRNA-directed knockdown of CD44 *in vitro* and *in vivo* using a metastatic breast cancer xenograft mouse model (Kong *et al.,*

2019). Additionally, primary tumour samples from breast and lung cancer patients expressed high levels of PD-L1 correlating with CD44 positivity (Kong *et al.,* 2019), suggesting that CD44 regulation of PD-L1 expression observed *in vitro* could be similar to that of an *in vivo* human tumour.

OCT4 and Nanog are transcription factors critical for pluripotency and tumorigenesis Dong *et al.,* 2018). PD-L1 has been shown to promote OCT4 and Nanog expression via PI3K/AKT pathway in breast CSCs (Almozyan *et al.,* 2017). PD-L1 knockdown compromised the capability of breast CSCs to self-renew themselves *in vitro* and *in vivo* using immune deficient nude mice. CSCs ability to self-renew and differentiate into heterogeneous lineages of cancer cells is thought to be responsible for drug resistance and relapse in cancer development and progression (Dong *et al.,* 2018). A recent study showed that breast cancer stemness is regulated by miR-873 directly suppressing PD-L1 expression and thus PI3K/AKT and ERK1/2 signalling in breast cancer cells, which reduced CSC-like characteristics and enhanced chemosensitivity (Gao *et al.,* 2019). Tumour PD-L1 has also been shown to promote the tumour-initiating cell generation in immunocompromised murine melanoma and ovarian cancer mouse models; a phenotype which was also verified in a human ovarian cancer cell xenograft mouse model (Gupta *et al.,* 2016; Kari *et al.,* 2019). This mechanism of intrinsic PD-L1 to drive tumour stemness was associated with increased mTORC1 signalling (Gupta *et al.,* 2016); a signalling pathway later shown to be triggered by reduced actin cytoskeleton polymerisation which was directly mediated by intrinsic PD-L1 (Kari *et al.,* 2019). PD-L1 silencing in cancer cells increased actin cytoskeletal polymerisation and reduced mTORC1 signalling compared to cells expressing PD-L1. However, CSC-like characteristics including high aldehyde dehydrogenase activity, reduced production of reactive oxygen species and a dormant state in the cell cycle were favoured following knockdown of PD-L1 in cholangiocarcinoma cell tumours inoculated into mice compared to high PD-L1 expressing tumours (Tamai *et al.,* 2014), indicating that intrinsically PD-L1 may have different roles in different cancer types. Moreover, the CSC-like phenotype is shown to be associated with epithelial to mesenchymal transition (EMT) (Dong *et al.,* 2018). Chen *et al.,* (2014) indirectly knocked down PD-L1 via the microRNA-200/ZEB1 axis in lung adenocarcinoma cells and found that PD-L1 expression correlated with EMT. Low miRNA-200 expressing cells transplanted into a synergetic

immunocompetent mouse model exhibited decreased intratumoural CD8+ T cells and increased metastatic potential due to lack of control over PD-L1 regulation.

1.6.2 Tumour-intrinsic PD-L1 and the promotion of tumour growth, invasion, and metastasis

Besides EMT playing a key role in invasion and metastasis, it can alter the tumour immune microenvironment to immunosuppressive and influence response to PD-1/PD-L1-targeted therapies (Mak *et al.,* 2016). PD-L1 knockdown in cultured human gastric cancer cell lines SGC-7901 and AGS reduced cell proliferation, migration, invasion and apoptosis and induced cell cycle arrest *in vitro* and reduced tumour growth and EMT phenotypic marker expression in immunocompromised mice *in vivo* compared to gastric tumours expressing PD-L1 (Li *et al.,* 2017). Similarly, in cultured human Jurkat lymphoid leukaemia cells and Raji lymphoma cells, PD-L1 knockdown by lentiviral transduction reduced their invasive ability via downregulation of ECM-degrading enzymes, MMP 2 and 9 (Li *et al.,* 2012). PD-L1 silencing in murine B16 melanoma cells has also been shown to slow tumour growth and reduce metastases to the lungs of immunocompetent mice as well as immunodeficient mice via mechanisms that increase autophagy and reduce mTORC1 signalling (Clark *et al.,* 2016). These findings may be linked to the intrinsic functions of PD-L1 to promote tumour stemness via mTORC1 signalling (Gupta *et al.,* 2016; Kari *et al.,* 2019). Tumour-initiating cells induced by intrinsic PD-L1 signalling are likely to show higher metastatic potential due to their self-renewal capabilities. Interestingly, the same therapeutic effect to reduce lung metastasis was absent in murine ovarian ID8agg cancer cells lacking PD-L1, in immunocompromised mice (Clark *et al.,* 2016), suggesting the effects of intrinsic PD-L1 may be tumour specific, and warrant further investigation. A recent study which knocked down PD-L1 in NCI-H1299 and Calu-1 cells, showed enhanced proliferation in comparison to control cells (Wang *et al.,* 2020), suggesting a tumour suppressor role of PD-L1. Indeed, PD-L1 expression has been shown to correlate with EMT markers in many solid tumours including gastric, lung, breast, colon and other common cancers (Mak *et al.,* 2016; Chen *et al.,* 2017). With consideration co-targeting of EMT vulnerabilities, and PD-1/PD-L1 signalling axis may have the potential to improve clinical efficacy of immunotherapy by limiting the shift of the tumour microenvironment from immunostimulatory to immunosuppressive during tumour development.

1.6.3 Tumour-intrinsic PD-L1 and regulation of metabolic processes

Within the tumour microenvironment, nutrient competition between tumour cells and immune cells may regulate tumour progression, and PD-L1 has been reported to directly regulate the metabolism of several cancer cell lines (Cham *et al.,* 2008; Chang *et al.,* 2015). Lactate derived from tumours can suppress the function of T cells by disrupting aerobic glycolysis, a process required for optimal T cell function (Cham *et al.,* 2008). It has been reported that checkpoint blockade could induce an increase in the glucose concentration within a progressive tumour mouse model, which correlated with glycolytic capacity in tumour infiltrating lymphocytes and increased IFNγ production (Chang *et al.,* 2015). Interestingly, treatment of B16 melanoma, MC38 colon cancer and sarcoma cancer cell lines *in vitro* with anti-PD-L1 antibodies was shown to reduce aerobic glycolysis mechanisms, including reduced glycolysis enzymes and Akt phosphorylation, indicating a tumour intrinsic role for PD-L1 in enhancing tumour glycolysis. The same results were achieved by shRNA mediated knockdown of PD-L1 (Chang *et al.,* 2015), strongly suggesting that PD-L1 itself was the modulator of glycolysis in cancer cells. Hypoxic inducible factor, HIF-1α is a well-known modulator of glycolysis in cancer cells (Al Tameemi *et al.,* 2019). The reduced glycolytic activity of cancer cells caused by PD-L1 blockade would subsequently induce an adaptive hypoxic response and stimulate the production of HIF-1α. HIF-1α also directly modulates immune cell activity in the tumour microenvironment to favour tumour growth and induces PD-L1 expression on tumour cells and immune cells; indirectly mediating immune escape and tumour progression (Johnson and Dong, 2017). Under hypoxic conditions PD-L1 expression was directly induced by HIF-1α on MDSCs in B16-F10 tumour-bearing mice, and PD-L1 blockade increased MDSC-mediated T cell activation by downregulating IL-10 and IL-6 expression (Noman *et al.,* 2014). Dual blockade of PD-L1 and HIF-1α could further reduce the glycolytic activity of cancer cells caused by PD-L1 blockade and enhance anti-tumour immunity, ultimately leading to cancer cell death.

1.6.4 Tumour-intrinsic PD-L1 facilitates resistance to anti-cancer therapies

PD-L1 exhibits an anti-apoptotic role in MDA-MB-231 breast cancer cells and silencing PD-L1 in these cells increased cancer cell apoptosis and enhanced cancer cell susceptibility to doxorubicin-induced apoptosis *in vitro* and *in vivo* (Ghebeh *et al.,* 2010), suggesting that PD-L1 not only prevents cancer cell apoptosis, but also promotes chemotherapy resistance. Likewise, CRISPR/Cas9 knockout of PD-L1

enhanced the sensitivity of human osteosarcoma KHOS and MNNG/HOS cells to doxorubicin and paclitaxel and compromised their ability to form three-dimensional (3D) spheroids *in vitro* (Liao *et al.,* 2017). Further characterisation of the role of PD-L1 in chemotherapy resistance in MDA-MB-231 breast cancer cells discovered that PD-L1 knockdown suppresses the expression of multidrug resistance 1/P-glycoprotein (MDR1/P-gp) via PI3K/AKT pathway *in vitro* (Liu *et al.,* 2017); recognising this has an additional therapeutic target. In fact, PD-1/PD-L1 interaction increased survival of breast cancer cells when exposed to doxorubicin (Liu *et al.,* 2017), suggesting that PD-1/PD-L1-targeted therapy may increase chemotherapy efficacy by inhibiting MDR1/P-gp expression which usually confers resistance in breast cancer cells. Moreover, through culturing of breast (MDA-MB-231 and 4T1) and prostate (DU145) cancer cell lines with recombinant PD-1 or Jurkat T cells it has been shown how PD-1/PD-L1 interactions results in increased resistance to doxorubicin and docetaxel (Black *et al.,* 2016). Subsequent knockdown or blockade of PD-1 restored tumour cell chemo-sensitivity and reduced their metastatic potential in a synergistic breast cancer mouse model. This suggests that blockade of intrinsic pathways is beneficial for therapy. Conversely, human colorectal cancer cells harbouring a *BRAF^{V600E}* mutation showed that the depletion of PD-L1 suppresses chemotherapy-induced apoptosis through the down regulation of BIM and BIK BH3-only proteins (Feng *et al.,* 2019), even though depletion alone reduced tumour growth. The effect of PD-L1 on chemosensitivity was confirmed in *BRAF^{V600E}* mutant MC38 murine tumour xenografts, where PD-L1 knockout cells were less sensitive to chemotherapy due to the suppression of pro-apoptotic molecules, BIM and BIK, compared to parental cells expressing PD-L1. This study highlights the importance of understanding the role of PD-L1 in each cancer type and its subtypes to design effective treatment regimens that will benefit cancer patients.

The tumour-intrinsic role of PD-L1 appears to be similar across all cancer types investigated in the literature to date, with the exceptions of cholangiocarcinoma and contradictory evidence in lung cancer, in that PD-L1 promotes tumour growth and development. However, the molecular mechanisms of PD-L1 exerting pro-tumour activity appear to be distinct amongst different cancer types. Notably, all except one report investigating the intrinsic role of PD-L1 in lung cancer demonstrates a pro-tumour role of PD-L1. In this one study, the cells utilised were mesenchymal lung cancer cell lines which harboured Kirsten rat sarcoma viral oncogene homolog

(KRAS) and/or p53 mutations, suggesting that the tumour cells metastatic capacity and mutational status may not be determining factors as to whether PD-L1 exhibits a pro-tumour or anti-tumour role in lung cancer. Furthermore, Wang *et al.,* (2020) showed that PD-L1 expression reduces lung cancer cell proliferation, which may suggest that although PD-L1 expression limits tumour cell proliferation it may still affect other tumour characteristics that influence tumour progression. The reasons behind this potential role of PD-L1 in lung cancer warrants further investigation.

1.7   Tumour-intrinsic PD-1 signalling

Similar to PD-L1, the expression of PD-1 on T cells and its role to inhibit the immune system is well characterised, but recent studies have found intrinsic expression of PD-1 on tumour cells including melanoma (Kleffel *et al.,* 2015), hepatic carcinoma (Li *et al.,* 2017), ovarian (Osta *et al.,* 2018), bladder (Osta *et al.,* 2018), lung (Du *et al.,* 2018; Wang *et al.,* 2020) and colorectal (Wang *et al.,* 2020) cancer cells. In melanoma B16 tumours, a subpopulation of PD-1 expressing cancer cells were identified to modulate downstream mTOR signalling and promote tumorigenesis independent of adaptive immunity, in an *in vivo* mouse model lacking an adaptive immune system (Figure 1.5A) (Kleffel *et al.,* 2015). This effect was abrogated with anti-PD-1 therapy, tumour-specific PD-1 knockdown and mutagenesis of intracellular signalling motifs downstream of PD-1, strongly suggesting an intrinsic function of PD-1 to promote tumorigenesis in melanoma. Similar to intrinsic PD-1 in melanoma cells, intrinsic PD-1 in liver cancer cells has been reported to mediate tumorigenesis in immunocompromised mice via regulating mTOR signalling (Figure 1.5A) (Li *et al.,* 2017) and thus combined inhibition of PD-1 and mTOR may be a potential therapeutic strategy for melanoma and liver cancer. Moreover, anti-PD-1 therapy reduced the cell growth of ovarian ES2 and bladder RT4 cancer cell lines cultured in 2D in the absence of adaptive immunity (Osta *et al.,* 2018), implying that PD-1 expression is potentially oncogenic.

Interestingly in murine NSCLC M109 cells, intrinsic PD-1 exhibited an anti-tumour role in immunocompromised mice and when NSCLC cells were treated with anti-PD-1 therapy they demonstrated increased proliferation and tumour growth (Figure 1.5B) (Du *et al.,* 2018). Consistent with this, silencing of PD-1 or therapeutic antibody blockade of PD-1 on the surface of NSCLC and colorectal cancer cells increased proliferation *in vitro* via activating PI3K and MAPK pathways (Wang *et al.,* 2020),

suggesting that PD-1 could be involved in development of resistance to immunotherapy blockade in NSCLC and could provide one explanation for why patients with NSCLC can display hyperprogressive disease following treatment with anti-PD-1 therapy (Champiat *et al.,* 2017; Wang *et al.,* 2020). The latter findings also suggest that the tumour suppressor role of PD-1 on cancer cells may not be limited to NSCLC. Although, Wang *et al.,* demonstrated that PI3K and MAPK pathways were activated following anti-PD-1 therapy in NSCLC cells *in vitro* and *in vivo*, their study also showed that PD-1/PD-L1 dysfunction did not activate mTOR, illustrating that the mechanism behind tumour-intrinsic PD-1 to either induce or inhibit tumour growth may be different. However, mTOR activation has been shown to occur in the only two studies investigating tumour-intrinsic PD-1 where PD-1 has a pro-tumour role, which may suggest that mTOR signal activation is necessary for PD-1 to exhibit tumorigenic activity. Therefore, the molecular mechanism behind tumour-intrinsic PD-1 needs to be elucidated in other cancer types to confirm this potential role of mTOR in PD-1 signalling in tumour cells. Furthermore, studies investigating the role of tumour-intrinsic PD-1 in tumours have utilised tumour cell lines that exhibit invasive and metastatic potential. The metastatic potential of cells does not seem to be a factor in determining whether PD-1 is pro- or anti-tumorigenic and nor is it associated with enhanced tumour-intrinsic PD-1 activity (Kleffel *et al.,* 2015). Additionally, studies have used both poorly- and well-differentiated tumour cells which have been shown to have the same PD-1-intrinsic function, implying that the differentiated state of the cell is also not a contributing factor to the role of PD-1 in tumours. Yao *et al.,* reanalysed cancer transcriptomic and proteomic data from The Cancer Genomic Atlas Project and The Cancer Cell Line Encyclopedia Dataset to find that tumour-intrinsic PD-1 expression is widespread in many cancer types. This heterogeneity may explain the differential therapeutic effects of anti-PD-1 drugs and could provide crucial information required when selecting suitable patients for treatment dependent on the cancer cell type. However, further work in different cancers and tumour models could also shed more light into this area.

So far, most evidence for PD-L1 and PD-1 signalling in cancer cells is based on 2D cell culture models using murine and human cancer cells and immunodeficient mouse models that can fail to fully recapitulate the human *in vivo* tumour (Hoarau-Véchot *et al.,* 2018; Wang *et al.,* 2019). Therefore, more relevant models capable of recapitulating the heterogeneity of the tumour microenvironment during *in vivo*

conditions could allow further predictive *in vitro* evaluation of the tumour-intrinsic role of PD-L1 and PD-1, and how these roles may be affected by immunotherapy treatment and influence immune cell function.
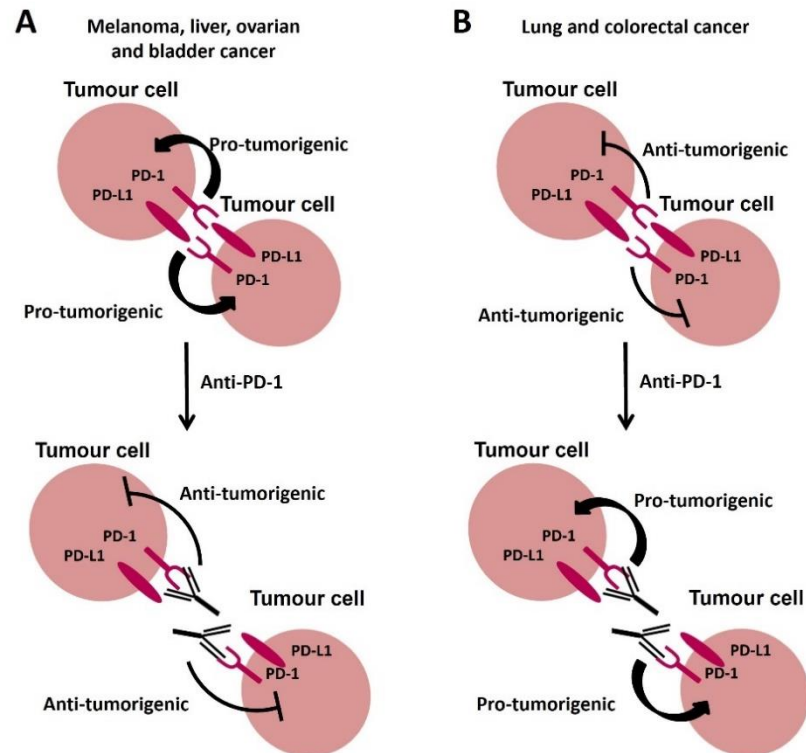
Figure 1.5 The new and emerging role of PD-1 signalling in cancer. (A) Intrinsic PD-1 signalling has been shown to promote tumorigenesis in melanoma, liver, and bladder cancer cells. Anti-PD-1 therapy abrogates this effect inhibiting tumour growth. **(B)** Intrinsic PD-1 signalling in NSCLC and colorectal cancer cells has been shown to inhibit tumorigenesis. Anti-PD-1 therapy preventing PD-1 signalling promotes tumour progression in NSCLC and colorectal cancer cells. Image adapted from Hudson *et al.,* 2020.

1.8 Immunotherapy blockade of intrinsic PD-L1 and PD-1 signalling

Recent reports discussed above suggest that the emerging intrinsic role of PD-L1 is largely pro-tumorigenic in several cancers, but that in lung cancer and cholangiocarcinoma, it may act as a tumour suppressor gene. Likewise, the new emerging tumour intrinsic role of PD-1 has also been reported to have differential roles in different cancer cell types and this remains to be further investigated. However, there are currently a limited number of reports investigating how immunotherapeutic drugs potentially modulate these intrinsic pathways.

Theivanthiran *et al.,* (2021) demonstrated that PD-1 blockade on CD8+ T cells in a syngeneic mouse model was able to activate a PD-L1-NLRP3 inflammasome signalling pathway in tumour cells that promoted MDSC recruitment and infiltration into the tumour microenvironment. MDSCs induced T cell anergy through producing IL-6, IL-10 and reactive oxygen species (Noman *et al.,* 2015), thus dampening the immune response and promoting resistance to anti-PD-1 therapies. The effect of the immunotherapy drug Atezolizumab was measured on MDA-MB-231 breast cancer cells (Saleh *et al.,* 2019). In this study, RNA-Seq was utilised to assess the modulation of gene expression after treatment with Atezolizumab and it was reported that genes promoting cell migration, metastasis, EMT, cell growth and hypoxia were downregulated whilst anti-apoptosis genes were upregulated. This suggests that Atezolizumab may be able to modulate the signaling of PD-L1 in this cell line to some extent at the level of gene expression. Similarly, Chen *et al.,* (2021) demonstrated using homemade anti-PD-L1 antibodies that PD-L1 blockade reduced tumor metastasis in an immunocompetent TNBC mouse model (Chen *et al.,* 2021). In contrast, Wang *et al.,* (2020) investigated the effects of anti-PD-1 antibodies Nivolumab and Pembrolizumab or the anti-PD-L1 antibody Atezolizumab on Calu-1, SW480, HT-29, BxPC-3, SK-BR-3, and U-2 OS cells. All immunotherapy drugs were shown to increase cell proliferation compared to isotype control *in vitro.* To verify these findings *in vivo,* human lung cancer cells were inoculated into immunocompromised mice. Similar to *in vitro* studies, monoclonal antibody administration to block PD-1 or PD-L1 activated PI3K and MAPK pathways by phosphorylating AKT and ERK1/2, respectively, promoting tumour cell growth *in vivo.* Furthermore, a very recent study showed that PD-L1 engagement with cellular ligands and Atezolizumab was able to promote increased oncolytic viral infections in prostate cancer cells via suppressing type I interferon responses and inducing a pro-glycolytic shift in cancer cells (Hodgins *et al.,* 2022). These few studies suggest that immunotherapeutic antibodies may be able to modulate the intrinsic function of PD-L1 and PD-1 and potentially highlights an alternative mechanism by which tumours may develop resistance to PD-1/PD-L1 targeting therapy through co-expressing PD-L1 and its receptor PD-1. Moreover, understanding the mechanisms of tumour-intrinsic signalling may give insight into potential therapeutic combinations with PD-1/PD-L1-targeted therapies. For example, Hodgins *et al.,* (2022) study mentioned above illustrates a novel mechanism by which therapeutic monoclonal antibodies can enhance oncolytic virus uptake, and therefore supports the use of these antibodies

in combination with oncolytic virotherapy. The ability of immunotherapy drugs to modulate the intrinsic PD-L1 and PD-1 pathway in other cancers in more heterogeneous tumour models could also provide further important insight into the mechanism of immunotherapy treatment.

1.9 Modelling tumour heterogeneity to further elucidate intrinsic roles of PD-L1 and PD-1

Tumour heterogeneity makes it challenging to identify novel therapeutic targets and potential biomarkers of immunotherapy response that could substantially enhance therapeutic efficacy (Wang *et al.,* 2019). The scientific basis for numerous clinical trials has derived from 2D cell culture models and animal models, which can fail to fully replicate the human tumour microenvironment due to lack of heterogeneity and species-to-species variability, respectively, which could account for lack of transferability of PD-1/PD-L1-targeted antibodies into the clinic (Hoarau-Véchot *et al.,* 2018; Wang *et al.,* 2019). Furthermore, most evidence to date exploring the intrinsic role of PD-L1 and PD-1 has been based on 2D cell culture models using murine or human cancer cell lines or animal models, and thus limit the capacity to explore these roles in a relevant human tumour setting (Hudson *et al.,* 2020). Given the emerging intrinsic roles of PD-L1 and PD-1 and the differences between cancer types, utilising models which closely mimic the heterogeneity of the human tumour microenvironment could allow a more predictive *in vitro* evaluation of the intrinsic role of PD-L1 and PD-1 in cancer and modulation by anti-cancer therapeutics. For example, human cancer cells implemented into different 3D cell culture models have shown to exhibit characteristics that more closely mimic *in vivo* human tumours, such as changes in morphology, proliferation, gene and protein expression and response to treatment (Hoarau-Véchot *et al.,* 2018). Table 1.3 demonstrates only a few of many studies that have shown the benefits of using different 3D cell culture models to mimic the characteristics of an *in vivo* human tumour more closely.

Table 1.3 Examples of 3D cell culture models that recapitulate biological characteristics of an *in vivo* human tumour.

Cancer Model	Cell line	3D Model	Results
Breast	MDA-MB-231	Alginate Scaffold	Cancer cells present with CSC-like phenotype by increasing the expression of CD44, CD24 and inducing expression of ALDH1 in 3D
		Multicellular Spheroids	3D spheroids displayed a pH gradient; an acidic tumour microenvironment facilitating drug resistance
	MCF-7	Collagen Scaffold	High expression of CSC-associated properties such as CD44
		Multicellular Spheroids	Higher expression of HIF-1α and P-gp induced cancer cell resistance to doxorubicin
Prostate	LNCaP	Collagen Scaffold	In 3D cancer cells displayed higher resistance to docetaxel than in 2D
		Multicellular Spheroids	In 3D spheroids, cancer cells were more resistant to docetaxel and secreted elevated levels of PSA than in 2D
		Multicellular Spheroids	In 3D spheroids, cancer cells had higher E-cadherin expression than 2D
	PC3	Collagen Scaffold	In 3D cancer cells displayed higher resistance to docetaxel and expressed lower levels of MMP1 and MMP9 than in 2D
Colorectal	SW480	Laminin-rich ECM	The ECM interactions reduced proliferative rate of cells (225 genes were expressed at significantly different levels in 2D vs 3D)
		Multicellular Spheroids	In 3D cancer cells exhibited increased activation of metabolic pathway (glycolysis), increased HIF-1α expression and reduced MAPK signalling.
	SW620	Multicellular Spheroids	AKT and mTOR signalling was drastically reduced in 3D compared to 2D
		Multicellular Spheroids	Therapeutic efficacy of 5-FU was significantly reduced in 3D compared to 2D

Table 1.3. Examples of 3D cell culture models utilised in preclinical research to better mimic the characteristics of an *in vivo* human tumour than conventional 2D cell culture. Human cancer cells have been implemented into various 3D cell culture models that facilitate the formation of spheroids that exhibit characteristics that resemble human tumours.

1.9.1   The benefits of using 3D cell culture models in cancer immunology

Many researchers use 2D cell cultures as the *in vitro* pre-clinical model for testing of anti-cancer drugs before proceeding to *in vivo* trials due to their simplicity, cost-effectiveness, and compatibility with high throughput screening platforms (Law *et al.,* 2021). However, the results attained from 2D *in vitro* models have limited clinical translatability to human tumours, which may in part explain why over 90% of potential anti-cancer drugs result in translational failure in clinical trials (Law *et al.,* 2021). Cancer cells cultured in 2D monolayer are grown on a hard, rigid plastic surface which aberrantly alters the cells behaviour, gene and protein expression, and drug sensitivity (Knight and Przybors, 2015). Additionally, unlike solid tumours, monolayer cultured cells demonstrate limited cell-to-cell interactions, cell-to-ECM interactions, and drug resistance, whilst also lack concentration gradients of soluble metabolites, oxygen and pH which together support tumour survival *in vivo* (Law *et al.,* 2021). 3D cell culture systems on the other hand offers a more physiological environment for pre-clinical testing of anti-cancer drugs and exploring cancer cells and their interactions with other cell types that exist in the tumour microenvironment (Figure 1.6). 3D cell culture systems mimic the 3D architecture, nutrient gradient, cell-cell and cell-ECM interactions, gene and protein expression and drug sensitivity of *in vivo* solid tumours (Breslin and O'Driscoll, 2013; Knight and Przybors, 2015; Lazzari *et al.,* 2017; Hoarau-Véchot *et al.,* 2018; Di Modugno *et al.,* 2019; Boucherit *et al.,* 2020). Indeed, different 3D cell culture systems have been used to make advancements in cancer immunology in which 2D cell culture fail to do so as effectively (Fitzgerald *et al.,* 2021). The most common 3D models used in cancer immunology include tumour spheroids, organoids, and microfluidic chips.

Figure 1.6 The physiological differences between 2D and 3D cell culture models. Cancer cells cultured in 2D monolayer cell culture display aberrant characteristics due to being grown on a stiff surface that poorly resembles the physiological conditions *in vivo.* In comparison, 3D cell culture models display many characteristics that closely resembles that of an *in vivo* human tumour. Image taken from Law *et al.,* (2021).

1.9.2   The use of tumour spheroids in cancer immunology

There are many different techniques employed to generate 3D tumour spheroids. The most conventional approach is through the aggregation of cancer cell lines via attachment prevention techniques (Law *et al.,* 2021). Such methods include the use of attachment prevention surfaces such as commercial ultra-low attachment plates and matrix coatings like agarose, or the suspension of cells within a droplet of liquid termed 'hanging drop' (Kelm *et al.,* 2003; Friedrich *et al.,* 2009). These cell aggregation methods are well characterised to generate robust tumour spheroids with diameters over 200 µM promoting the development of a hypoxic core; an important characteristic of *in vivo* human tumour that influences tumour development and immune cell function (Kelm *et al.,* 2003; Boucherit *et al.,* 2020). Alternatively, 3D tumour spheroids can be created by embedding cancer cell lines in different

biological and synthetic hydrogels. Biological hydrogels include plant-derived alginate and animal derived-collagen, Matrigel, and gelatin. Synthetic hydrogels include hyaluronic acid and biopolymer hydrogels. Hydrogel scaffolds promote a single-cell suspension to proliferate into isogenic spheroid populations to enable a more natural development of cultures that resemble *in vivo* properties (Knight and Przybors, 2015). Using hydrogel scaffolds can bring external ECM properties to facilitate the structure of a cellular environment and development of cell-ECM and cell-cell interactions found *in vivo*. The stiffness of hydrogels can also be modified to resemble the pathological stiffness of solid tumours that is well known to shape tumour development (Law *et al.,* 2021).

Whilst 3D tumour spheroids themselves generated using cancer cell lines are a homogenous cell population and do not properly model the cancer-immune microenvironment due to the lack of immune cells, they offer the opportunity to perform screening of immunotherapy drugs to assess drug penetrance (Fitzgerald *et al.,* 2021). Because cancer cells cultured in 2D monolayer are a single layer of cells it makes it impossible to assess drug penetrance this way. Unlike small molecule inhibitors that readily penetrate tumours, larger monoclonal antibodies of which many immunotherapy drugs are can have heterogeneous tumour distribution which can ultimately limit their therapeutic efficacy (Fitzgerald *et al.,* 2021). Lui *et al.,* (2018) demonstrated the time-dependent penetration and heterogeneous distribution of the EGFR-targeting monoclonal antibody Cetuximab in HT-29 and DLD-1 colorectal cancer spheroids using mass spectrometry imaging and fluorescent microscopy; observations which were in accordance with former *in vivo* studies (Lui *et al.,* 2018). Additionally, the delivery of trastuzumab, a HER2-targeting monoclonal antibody via immunoliposomes was shown to reduce the proliferation of MDA-MB-231 breast cancer cells culture in 3D spheroids to the same extent as MDA-MB-231 breast cancer tumours in an *in vivo* mouse model (Rodallec *et al.,* 2018), highlighting the benefits of using 3D spheroids for the assessment of the biological effects of immunotherapy drugs.

Many studies have used 3D tumour spheroids to assess immune cell infiltration has this is an important factor to ensure the efficacy of immunotherapies. Mark *et al.,* (2020), recently demonstrated that the cytotoxic capability of NK cells was reduced 5.6-fold in K562 leukemic cell 3D tumour spheroids formed in a collagen matrix compared to their 2D counterparts, due to the NK cells not being able to efficiently

migrate into the tumour mass. The use of cytokines to promote the migration of NK cells into colorectal cancer 3D tumour spheroids has been shown to increase NK-mediated cancer cell lysis (Courau *et al.,* 2019). However, the increased NK cell migration was accompanied by an increase in cancer cells expression of inhibitory receptors including MICA/B and NKG2A. Monoclonal antibodies targeting these receptors re-established NK cell-mediated lysis. This previously has been shown to be the case in a melanoma mouse model (De Andrade *et al.,* 2018).

Furthermore, 3D tumour spheroids have been used to understand the complex cancer cell-immune cell interactions which can lead to tumour growth and immune escape. It was found that ovarian cancer 3D spheroids co-cultured with monocytes demonstrated a higher invasive phenotype and lower sensitivity to chemotherapy compared to cancer spheroids alone (Raghavan *et al.,* 2019). Many studies have since shown that the mechanism by which monocytes can influence tumour progression is due to cancer cells being able to promote the polarisation of monocytes to M2-type immunosuppressive macrophages which in turn suppress the effector function of CD8+ and CD4+ T cells in the tumour microenvironment leading to immune escape and drug resistance. This has been demonstrated in ovarian, pancreatic and melanoma 3D spheroids and *in vivo* mouse models (Kuen *et al.,* 2017; Chandrakesan *et al.,* 2020). These studies further highlight the importance of utilising 3D tumour spheroids for elucidating immune evasion mechanisms in cancer.

1.9.3   The use of other 3D cell culture systems used in cancer immunology

Unlike 3D tumour spheroids, organoids are formed from stem cells or progenitor cells which expand and differentiate to make multicellular and heterogeneous clusters containing cell types with similar phenotypes to the original human organ from which they were derived (Fitzgerald *et al.,* 2021). By incorporating autologous immune cells into tumour-derived organoids, many researchers have been able to provide invaluable insight into the mechanisms of antigen presentation (Chakrabarti *et al.,* 2018), develop immunotherapies such as CAR-T cell therapy (Leuci *et al.,* 2020) and investigate personalised immunotherapy treatment (Votanopoulos *et al.,* 2020). Votanopoulos *et al.,* (2020) utilised melanoma tumour biopsies and lymph node specimens from the same patients to co-culture *ex vivo* and was able to demonstrate that the organoid models from 6 out of the 7 patients correctly reflected the clinical response to anti-PD-1 and anti-CTLA4 monoclonal antibodies.

Whilst patient-derived organoids are more clinically relevant models than 3D tumour spheroids derived from cancer cell lines, they are difficult to obtain and are low throughput. 3D tumour spheroids grown using scaffold-free or scaffold-based methods provides the opportunity to investigate cancer immunology and immunotherapy responses in a high throughput manner whilst still mimicking more closely the tumour heterogeneity than that seen in 2D monolayer cultures.

1.9.4 The use of cancer-immune cell co-cultures and 3D cell culture models to further elucidate intrinsic roles of PD-L1 and PD-1

So far there has been limited use of 3D cell culture models to investigate the regulation and tumorigenic roles of PD-L1 and PD-1 (Hudson *et al.,* 2020). The very few studies which have, demonstrate their vast importance. In breast and lung cancer cell lines cultured in 3D cell culture models, PD-L1 expression has been reported to be affected by the extracellular matrix stiffness (Azadi *et al.,* 2019; Miyazawa *et al.,* 2018). Therefore, mimicking the different pathological tissue stiffness observed across different cancer types through modifying 3D scaffolds may better enable the investigations of PD-L1 and immunotherapy responses, as we could presume that PD-L1 expression levels would more closely mimic the levels found in solid tumours. Lanuza *et al.,* (2018) also investigated three different colorectal cancer cell lines cultured in 3D spheroids and showed that PD-L1 expression only altered in 2 out of the 3 cell lines, suggesting that PD-L1 modulation in a 3D environment may be cancer cell type specific. Collectively, these three studies demonstrate how the culturing of cancer cells in a 3D environment is important to better understand PD-L1 modulation in a more representative human context. The exact mechanisms by which the extracellular matrix and other features of a 3D environment may modulate PD-L1 warrants further investigation in all cancers as therapeutic targeting of these mechanisms could improve the efficacy of PD-1/PD-L1-targeted therapies.

In recent studies, 3D models have been shown to resemble the tumour immune microenvironment for the investigation of the PD-1/PD-L1 signalling axis. A tumour-immune co-culture was utilised to assess the efficacy of immunotherapies Nivolumab and Durvalumab in ovarian cancer cell lines (Natoli *et al.,* 2020). Through using this model, researchers showed how chemotherapy resistant ovarian cancer cells were less responsive to nivolumab treatment due to reduced expression of MHC-1, rendering CD8+ T cells less capable of being activated. Furthermore, Neal *et al.,* (2018) demonstrated the ability to culture *ex vivo* 3D organoids for a period of 28

days that still exhibited the same TCR repertoire as the original tumour. In this model, they were able to show that anti-PD-1 antibody treatment induced CD8+ T cell expansion in 83% of organoids derived from anti-PD-1 responsive patients versus only 14% in organoids derived from anti-PD-1 unresponsive patients (Neal *et al.,* 2018), indicating how this model could be extremely valuable to help elucidate the mechanisms of immunotherapy resistance in unresponsive patients in a personalised manner.

1.10 Summary

PD-1/PD-L1 checkpoint blockade is at the cutting edge of research offering cancer patients hope for new treatment regimens with potential to have substantial clinical benefit and prolong survival. PD-1/PD-L1-targeted therapies reactivate the immune system to induce immune-mediated tumour eradication, and although they have demonstrated success as single agents, they have also shown cooperation with conventional and targeted therapies in the clinic. Unfortunately, most patients are unresponsive or develop resistance to PD-1/PD-L1-targeted therapy. Further elucidating the tumour intrinsic role of PD-L1 and its receptor PD-1 in all cancer types by using relevant human tumour models will help understand the basis for or lack of response to immunotherapy and may allow the identification of novel therapeutic targets and biomarkers to enhance clinical efficacy.

1.11 Aims and objectives of this thesis

The aim of this PhD project was to further elucidate the tumorigenic role of PD-L1 through utilising anti-PD-L1 immunotherapy drug Atezolizumab and PD-L1 knockdown strategies in human cancer cell lines cultured in 2D and 3D cell culture models. To achieve this, the following objectives were investigated:

- Determine the basal level of PD-L1 expression and its modulation by immunological cytokines in 2D-cultured human breast, prostate, and colorectal cancer cell lines.

- Characterise human cancer cell lines for other immunological and tumorigenic marker expression.

- Validate the growth and viability of human cancer cell lines in two 3D cell culture models and measure PD-L1 expression, along with other immunological and tumorigenic markers to compare to 2D monolayer cultures.

- Explore the phenotypic effects of therapeutic anti-PD-L1 monoclonal antibody Atezolizumab on human breast cancer cells cultured in 2D and 3D models.

- Knockdown PD-L1 in human breast cancer cells and assess the phenotypic changes in 2D and 3D models compared to PD-L1 blockade with Atezolizumab.

2. Characterisation and immune modulation of human breast, prostate, and colorectal cancer cells in standard 2D monolayer culture

2.1 Introduction

Cancer cells express different molecules intracellularly and extracellularly which can facilitate their ability to survive and develop within the tumour microenvironment (Mirabelli *et al.,* 2019). Many of these molecules can mediate immune evasion by direct or indirect inhibition of immune cell effector functions. The overexpression of PD-L1 is one such mechanism employed by tumours to evade immune-mediated killing by directly binding its receptor PD-1 expressed by CD8+ T cells and other cell types in the tumour microenvironment, including cancer cells (Freeman *et al.,* 2000; Dong *et al.,* 2002). Downregulation of HLA-ABC and death receptor expression such as DR4, DR5 and Fas; are another mechanism tumour cells may employ to reduce their immunogenicity and prevent cell death induced by CD8+ T cells and other immune cells (Beatty and Gladney, 2015; Garrido *et al.,* 2019). Within solid tumours hypoxia develops and whilst cancer cells adapt to survive, other cell types such as immune cells suffer as a consequence and can switch from tumour-suppressive to tumour-supportive phenotypes (Noman *et al.,* 2015). Hypoxia and cytokine-release such as IFNγ and TNFα in the tumour microenvironment can regulate the expression of tumour cell surface markers to favour tumour progression (Tsai and Wu, 2012; Showalter *et al.,* 2017). Alternatively, tumour cells can acquire mutations in the HLA-ABC gene or antigen-presenting machinery impeding immune recognition (Shukla *et al.,* 2015; Schaafsma *et al.,* 2021). Similarly, mutations can occur in genes encoding death receptors DR4, DR5 and Fas preventing cancer cell apoptosis (Lee *et al.,* 1999; Shin *et al.,* 2001). Additionally, CD44, a cell surface adhesion molecule, overexpressed by cancer cells has been shown to promote tumorigenesis (Senbanjo and Chellaiah, 2017) as well as interact with the Fas-induced cell death pathway to facilitate the survival of cancer cells (Yasuda *et al.,* 2001).

Since mouse and human cancer cell lines provide the basis for cancer immunology research studies (Mirabelli *et al.,* 2019), it is important to have knowledge of the different immunological and tumorigenic markers that they express. Plus, understand how their expression compares to *in vivo* solid tumours. This would improve preclinical predictive validity of data produced using *in vitro* cancer cell line models;

and ultimately increase the transition from preclinical monolayer cultures to more complex *in vitro* and *in vivo* models of human cancer.

2.1.1 Aims

In the following chapter the aim was to characterise human breast, prostate, and colorectal cancer cell lines grown in 2D monolayer cell culture for immunological and tumorigenic marker expression. The objectives were to assess baseline levels of several immunological and tumorigenic markers expressed by each cell line at mRNA and protein levels. Firstly, the mRNA expression and protein production of baseline PD-L1 was assessed before the effect of IFNγ and TNFα on cell surface PD-L1 protein expression was subsequently measured. In addition, the expression of PD-1, PD-L2, HLA-ABC, DR4, DR5, Fas, CD44 and HIF1α mRNA and/or protein were examined in each cell line.

2.1.2 Hypotheses

It was hypothesised that human breast, prostate, and colorectal cancer cell lines would express differential levels of baseline PD-L1 depending on the cancer cell type at mRNA and protein levels; and that PD-L1 protein expression could be modulated by culturing 2D monolayer cancer cell lines with cytokines (IFNγ and TNFα). Additionally, it was hypothesised that cancer cell lines cultured in 2D cell culture would express differential levels of other immunological and tumorigenic markers depending on the cancer cell type at mRNA and protein levels.

2.2 Materials and Methods

2.2.1 Cell lines and culture conditions

Human breast (MDA-MB-231 and MCF-7), prostate (LNCaP and PC3) and colorectal (SW480 and SW620) cancer cell lines were purchased from American Type Culture Collection (ATCC). Breast and prostate cancer cell lines were cultured in Roswell Park Memorial Institute (RPMI 1640) medium and colorectal cancer cell lines were cultured in Dulbecco's modified Eagle's medium (DMEM). All media was supplemented with 10% foetal bovine serum (FBS) and 1% penicillin-streptomycin. Cells were maintained in standard culture conditions (5% CO_2, 37°C) and grown to 80-90% confluency in monolayer before being used experimentally. For each experiment, the cell concentration of live cells was determined using a haemocytometer and trypan blue stain. All cell culture materials were supplied by Gibco™ (ThermoFisher Scientific). Cell lines were regularly tested for mycoplasma using the EZ-PCR™ Mycoplasma Detection Kit (Biological Industries) and the MycoAlert™ Mycoplasma Detection Kit (Lonza) and were confirmed to be mycoplasma free. Cells were below passage 30 for all experiments.

2.2.2 RNA extraction and quantification, cDNA synthesis and real-time quantitative polymerase chain reaction

Monolayer cells (5×10^5) were seeded in a T25 flask and cultured for 72 hours before being harvested and lysed using 500 µL BL-TG buffer (4M Guanidine thiocyanate, 0.01M Tris, 1% 1-Thioglycerol, Promega) for total RNA extraction using the ReliaPrep™ RNA Miniprep System (Promega), according to the manufactures protocol. RNA purity and quantity was assessed by using a NanoDrop 1000 (ThermoFisher Scientific). First-strand complementary DNA (cDNA) was generated from 1 µg of total RNA with the High-Capacity RNA-to-cDNA™ Kit (ThermoFisher Scientific). Real-time quantitative polymerase chain reaction (RT-qPCR) was performed using TaqMan® Assays in 10 µL reaction mixtures. TaqMan Assay reaction mixtures contained: 5 µL of TaqMan® Fast Advance (Applied Biosystems), 2.5 µL nuclease-free H_2O, 0.5 µL primer-probe (TaqMan Gene Expression Assays, FAM, ThermoFisher Scientific) (Table 2.1) and 2 µL cDNA or water for a no template control. Hypoxanthine guanine phosphoribosyl transferase gene (HPRT1) and TATA-box binding protein (TBP) were used as housekeeping genes (HKGs). All primer-probes were purchased from Life Technologies Limited (ThermoFisher Scientific). MicroAmp™ Optical 96-Well Reaction Plates were used for all RT-qPCR

experiments (ThermoFisher Scientific). The TaqMan qPCR thermal profile consisted of an initial activation step of 10 minutes at 95°C, followed by 40 cycles of 30 seconds denaturation at 95°C and 1 minute annealing at 60°C. RT-qPCR was performed using the QuantStudio 3 Detection System (QuantStudio Design and Analysis Software, Applied Biosystems). Since baseline mRNA levels of immunological and tumorigenic markers were being assessed under the same experimental conditions for each cancer cell line, relative expression was calculated using the ΔCT method which compares the expression level of the gene of interest to the expression level of HKGs (HPRT1 and TBP) for each cancer cell line. The ΔCT method calculation used:

$$Relative\ expression = 2^{-(GOI\ Ct - HKG\ Ct)}$$

Table 2.1 TaqMan primer-probes for RT-qPCR.

Species	Gene of Interest	Assay ID
Human	*HPRT1*	Hs99999909_m1
	TBP	Hs99999910_m1
	CD274 (PD-L1)	Hs00204257_m1
	CD273 (PD-L2)	Hs00228839_m1
	CD279 (PD-1)	Hs01550088_m1
	CD261 (DR4)	Hs00269492_m1
	CD262 (DR5)	Hs00366278_m1
	CD95 (Fas)	Hs00163653_m1
	CD44	Hs01075864_m1
	HIF1A (HIF1α)	Hs00153153_m1

Table 2.1 TaqMan primer-probes for RT-qPCR used throughout the study. All primer-probe assays were selected that crossed exon boundaries and that were validated for 100% amplification efficacy. The genes detected using the primer-probes included: HPRT1 (*HPRT1*); TBP (*TBP*); PD-L1 (*CD274*); PD-L2 (*CD273*); DR4 (*CD261*); DR5 (*CD262*); Fas (*CD95*); CD44 antigen (*CD44*); and HIF1α (*HIF1A*).

2.2.3 Flow Cytometry

2.2.3.1 Cell surface staining

Cells were seeded at 5 x 10^5 cells/well in 6-well plates and cultured to 90% confluency before being harvested for flow cytometry to assess cell surface protein expression. Firstly, cells were washed with phosphate buffered saline (PBS) containing 2% FBS, before being re-suspended and labelled with Fc block (Human TruStain FcX™; Biolegend) at 1:100 dilution for 10 minutes. Cells were subsequently labelled with Allophycocyanin (APC) anti-human PD-L1 (clone 29E.2A3; Biolegend), APC anti-human PD-L2 (clone 24F.10C12PE; 2B Scientific Limited), Phycoerythrin (PE) anti-human PD-1 (clone: EH12.1; BD Biosciences), Fluorescein isothiocyanate (FITC) anti-human HLA-ABC (clone G46-2.6; BD Biosciences), APC anti-human DR4 (clone DJR1; Biolegend), PE anti-human DR5 (clone DJR2-4; Biolegend), PE anti-human Fas (clone DX2; Biolegend) and APC anti-human CD44 (clone IM7; eBiosciences) antibodies or their matched isotype controls for 30 minutes. All antibodies were used at optimised dilutions (Table 2.2) which were determined by performing titrations of each antibody (Appendix Figure 9.1). Isotype controls were used at the same optimised dilution as its matched antibody isotype. Fc block, antibody and isotype dilutions were made in PBS containing 2% FBS. Finally, cells were washed with PBS containing 2% FBS twice before being placed into flow cytometry tubes in a final volume of 200 μL for data acquisition. Data was acquired using either a FACSCalibur (BD Biosciences) with CellQuest™ Pro Software v.5.2.1 (BD Biosciences) or a CytoFLEX (Beckman Coulter, IN, USA) with CytExpert Software (Beckman Coulter). Data was analysed using FlowJo 10 Software (FlowJo, LLC). The overall percentage expression of each positively stained sample run was determined by subtracting the isotype control percentage. The median fluorescent intensity (MFI) of each positively stained sample run was determined by dividing by the value of the isotype control.

Table 2.2 Antibodies used throughout the study for identifying specific cell surface and intracellular antigens by flow cytometry.

Type of Staining	Antigen	Label	Isotype	Manufacturer	Dilution
Cell Surface	PD-L1	APC	Mouse IgG2b, κ	Biolegend	1:100
	PD-L2	APC	Mouse IgG2a, κ	Elabscience	1:100
	PD-1	PE	Mouse IgG1, κ	BD Biosciences	1:25
	HLA-ABC	FITC	Mouse IgG1, κ	BD Biosciences	1:50
	DR4	APC	Mouse IgG1, κ	Biolegend	1:50
	DR5	PE	Mouse IgG1, κ	Biolegend	1:50
	Fas	PE	Mouse IgG1, κ	Biolegend	1:50
	CD44	APC	Rat IgG2b, κ	eBiosciences	1:25
Intracellular Staining	HIF1α	PE	Mouse IgG2b, κ	Biolegend	1:50

Table 2.2 Antibodies used for flow cytometry to identify cell surface and intracellular antigens expressed by cancer cells. Columns illustrate the antigens recognised by the antibody, the fluorophore with which the antibody is labelled and detected by flow cytometry, the isotype of the antibody, the manufacturer and the optimised working dilution of the antibody used.

2.2.3.2 Cytokine modulation of PD-L1 expression

Low PD-L1 expressing SW620 colorectal cancer cells were seeded at 5×10^5 cells/well in 6-well plates and incubated with recombinant human interferon gamma (IFNγ) (Biolegend) or recombinant tumour necrosis factor alpha (TNFα) (Bio-Techné) at concentrations ranging from 5 ng/ml to 0 ng/ml in 10-fold dilutions for 48 hours to determine the lowest dose of each cytokine that could significantly induce PD-L1 expression. For subsequent experiments, all cancer cell lines were treated with 0.5 ng/ml IFNγ and/or 5 ng/ml TNFα for 48 hours before assessing cell surface PD-L1 expression using flow cytometry as described above. For MDA-MB-231 and LNCaP cancer cells, 10 ng/ml of each cytokine was also investigated as described above.

2.2.3.3 Intracellular staining of HIF-1α

Cells were seeded at 5 x 10^5 cells/well in 6-well plates and cultured for 72 hours before being harvested for flow cytometry to assess HIF1α protein expression by intracellular staining. Firstly, cell suspensions were placed into flow cytometry tubes (BD Biosciences), and then washed with cell staining buffer (Biolegend). The resulting pellet in the residual volume of approximately 100 μL was dissociated by pulse vortexing and then cells were fixed and permeabilised using the eBiosciences Foxp3/Transcription Factor Staining Buffer Set (eBiosciences), according to the manufacturer's protocol. Following fixation, permeabilization and subsequent wash steps, 1 μL of FC block was added to each tube (1:100 dilution) and incubated for 10 minutes before labelling with PE mouse anti-human HIF1α antibody (Clone 546-16; Biolegend) or its matched isotype control at the optimised dilution (1:50). Fc block, isotype and antibody dilutions were made in 1X permeabilization buffer supplied with the set from eBiosciences. After 30 minutes incubation, cells were washed twice with 1X permeabilization buffer and resuspended in 200 μL cell staining buffer for flow cytometric analysis as described above.

2.2.4   Statistical analysis

Statistical analysis was performed using Prism version 7.03 (GraphPad Software, Inc.). A Shapiro-Wilk normality test was used to determine whether data had a parametric or non-parametric distribution. As the data was non-parametric it is represented here as median ± range and each independent experiment as 3 technical repeats (n=3). Statistical analysis was undertaken using a Kruskal-Wallis followed by a Dunn's multiple comparisons test. P-values less than 0.05 were considered significant (*P<0.05 and **P<0.01).

2.3 Results

2.3.1 Human breast, prostate, and colorectal cancer cell lines express differential levels of PD-L1 at mRNA and protein level

Six human cancer cell lines including two breast (MDA-MB-231 and MCF-7), two prostate (LNCaP and PC3) and two colorectal (SW480 and SW620) were assessed to determine the basal level of PD-L1 expression at mRNA and protein level under standard *in vitro* culture conditions. PD-L1 mRNA (Figure 2.1A) and protein (Figure 2.1B and Figure 2.1C) expression was differentially expressed across all human cancer cell lines investigated.

MDA-MB-231 TNBC cells expressed high levels of PD-L1 mRNA and protein in comparison to MCF-7 luminal-derived hormone-expressing breast cancer cells which expressed one of the lowest levels of PD-L1 amongst the cancer cell lines investigated. Almost all MDA-MB-231 cells expressed PD-L1 (99.5% ± 0.159), whereas only 4% (± 1.818) of MCF-7 cells expressed PD-L1.

Lymph node-derived, LNCaP, and bone-derived, PC3, metastatic prostate cancer cells both expressed low levels of PD-L1 mRNA and protein. Whilst only 8.6% (± 8.24) of LNCaP cells expressed low levels of cell surface PD-L1, 77.5% (± 31.73) of PC3 cells expressed the low level of PD-L1 on their cell surface.

SW480 primary-derived colorectal cancer cells expressed higher levels of PD-L1 mRNA and protein than SW620 lymph node-derived metastatic colorectal cancer cells originating from the same tumour. SW480 cells expressed the second highest level of PD-L1 mRNA amongst the cancer cell lines investigated and over one quarter of their cell population expressed PD-L1 on their cell surface (27% ± 1.655) at a moderate level. In contrast, SW620 cells displayed low PD-L1 mRNA and protein levels and the frequency of which PD-L1 was expressed on their cell surface was only 3% (± 1.544).

Figure 2.1 Human breast, prostate, and colorectal cancer cell lines express differential levels of PD-L1 at mRNA and protein level. PD-L1 (*CD274*) **(A)** gene and **(B)** protein expression was measured by RT-qPCR and flow cytometry, respectively, for MDA-MB-231, MCF-7, LNCaP, PC3, SW480 and SW620 cancer cell lines. The percentage of PD-L1 protein expression is shown (left) alongside the MFI (right). **(C)** Representative flow cytometry histograms show the isotype control (grey) relative to the PD-L1 positive populations (pink). Data is presented as median ± range. n=3 independent experiments each with 3 technical repeats.

2.3.2 IFNγ and TNFα synergistically upregulate cell surface PD-L1 in some human cancer cell line

Next, it was determined whether PD-L1 protein expression could be modulated on the cell surface of human cancer cell lines cultured under standard culture conditions. Human cancer cells were treated with the lowest significant dose of IFNγ (Appendix Figure 9.2A) and TNFα (Appendix Figure 9.2B) that could induce cell surface PD-L1 expression, either alone or in combination which was determined by treating low PD-L1-expressing SW620 colorectal cancer cells with a range of cytokine concentrations. Our data showed that PD-L1 expression could be upregulated by individual cytokines and synergistically upregulated when treated with both cytokines in combination in 4 out of the 6 cancer cell lines (Figure 2.2A-F).

MDA-MB-231 breast (Figure 2.2A) and LNCaP prostate cancer cells (Figure 2.2C) were the only cells that demonstrated no statistically significant alterations to PD-L1 expression (p=0.092 and p=0.125, respectively) when treated with individual or both cytokines, although these cells did demonstrate a slight increase in PD-L1 expression with cytokine treatment. Interestingly, LNCaP cells displayed an increase in PD-L1 expression when treated with TNFα alone, but PD-L1 expression by IFNγ-treated cells was found to be comparable to that of untreated cells, even with the addition of TNFα in the combined cytokine treatment. Additionally, a subsequent experiment was performed using higher cytokine concentrations to treat MDA-MB-231 and LNCaP cells to achieve maximum response. There were still no statistically significant changes to baseline PD-L1 protein expression (Appendix Figure 9.3A and B). In fact, the percentage of expression and the MFI of PD-L1 expression for both MDA-MB-231 and LNCaP cells treated with 10 ng/ml cytokines was comparable to that of those treated with cytokines at the lowest significant dose to induce PD-L1 expression.

MCF-7 breast cancer cells displayed a significant increase in the frequency of cells expressing PD-L1 when treated with IFNγ (30.9% ± 11.6, p=0.033) alone or in combination with TNFα (62.5% ± 21.4, p=0.0041) compared to untreated control cells (4.65% ± 2.12) (Figure 2.2B). This was accompanied by an increase in the MFI of PD-L1 expression in IFNγ-treated MCF-7 cells which was further increased in MCF-7 cells treated with IFNγ and TNFα combined compared to the untreated control cells.

Similarly, PC3 prostate cancer cells exhibited a significant increase in the proportion of cells expressing PD-L1 when treated with both cytokines (93.2% ± 5.06, p=0.043) compared to untreated control cells (79% ± 6.7) but exhibited no statistically significant change (p=0.062) in the MFI of PD-L1 expression following cytokine treatment (Figure 2.2D).

The SW480 colorectal cancer cells displayed no statistically significant change in the frequency (p=0.076) or MFI (p=0.055) of PD-L1 expression with cytokine treatment alone or in combination, although they did show a trend increase in the proportion of cells expressing PD-L1 with IFNγ alone (51.99% ± 41.7) and in combination with TNFα (90.1% ± 51.5) compared to untreated control cells (14.9% ± 16) (Figure 2.2E).

Lastly, SW620 colorectal cancer cells displayed a significant increase in the MFI of PD-L1 expression as well as in the proportion of cells expressing PD-L1 following treatment with IFNγ (59.23% ± 18.45, p=0.024) and IFNγ and TNFα combined (85.8% ± 14.2, p=0.0067) compared to untreated control cells (1.6% ± 1.2) (Figure 2.2F). The level and frequency of PD-L1 expression by SW620 cells was significantly increased following treatment with both cytokines, compared to individual cytokines alone.

2.3.3 Human breast, prostate and colorectal cancer cell lines also express differential levels of immunological and tumorigenic markers

Since baseline PD-L1 was expressed at very different levels amongst the six cancer cell lines investigated, it was next determined whether this was the case for the expression of other immunological (PD-1, PD-L2, HLA-ABC, DR4, DR5 and Fas) and tumorigenic (CD44 and HIF1α) markers at mRNA and/or protein levels.

2.3.3.1 PD-1 expression is only detectable in colorectal cancer cell lines

PD-1, the receptor for PD-L1 and PD-L2, was investigated here at mRNA (Figure 2.3A) and protein (Figure 2.3B and C) levels. PD-1 was only found to be expressed at very low levels in SW480 and SW620 colorectal cancer cells at mRNA level. Interestingly, PD-1 expression was only found to be expressed on the cell surface of 1.2% (± 0.37) of SW480 cells at very low levels but was not found to be expressed on the cell surface of SW620 cells. PD-1 expression was not detectable at mRNA or protein levels in human breast and prostate cancer cell lines.
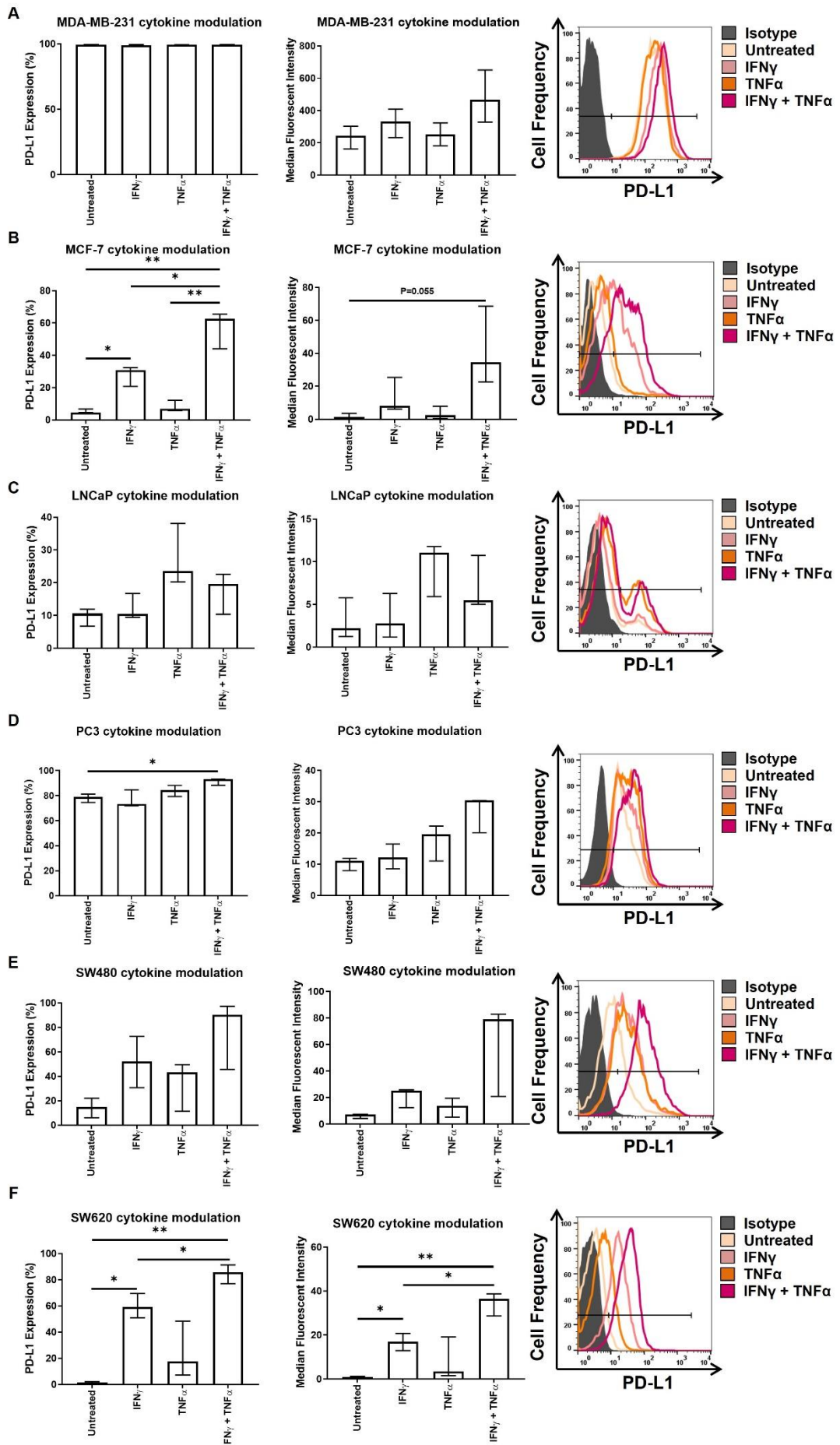
Figure 2.2 IFNγ and TNFα act synergistically to upregulate PD-L1 expression in some cancer cell lines. The effect of IFNγ and/or TNFα on cell surface PD-L1 expression by **(A)** MDA-MB-231, **(B)** MCF-7, **(C)** LNCaP, **(D)** PC3, **(E)** SW480 and **(F)** SW620 cells was assessed by flow cytometry. The percentage of PD-L1 expression is shown (left) alongside the MFI (right). Representative flow cytometry histograms show the isotype control (grey) relative to PD-L1 positive cells, untreated (beige) or treated with IFNγ (light pink), TNFα (orange) or the combination (dark pink). Data is presented as median ± range. n=3 independent experiments each with 3 technical repeats. Data was analysed by a Kruskal-Wallis followed by Dunn's multiple comparisons test (*P<0.05 and **P<0.01).
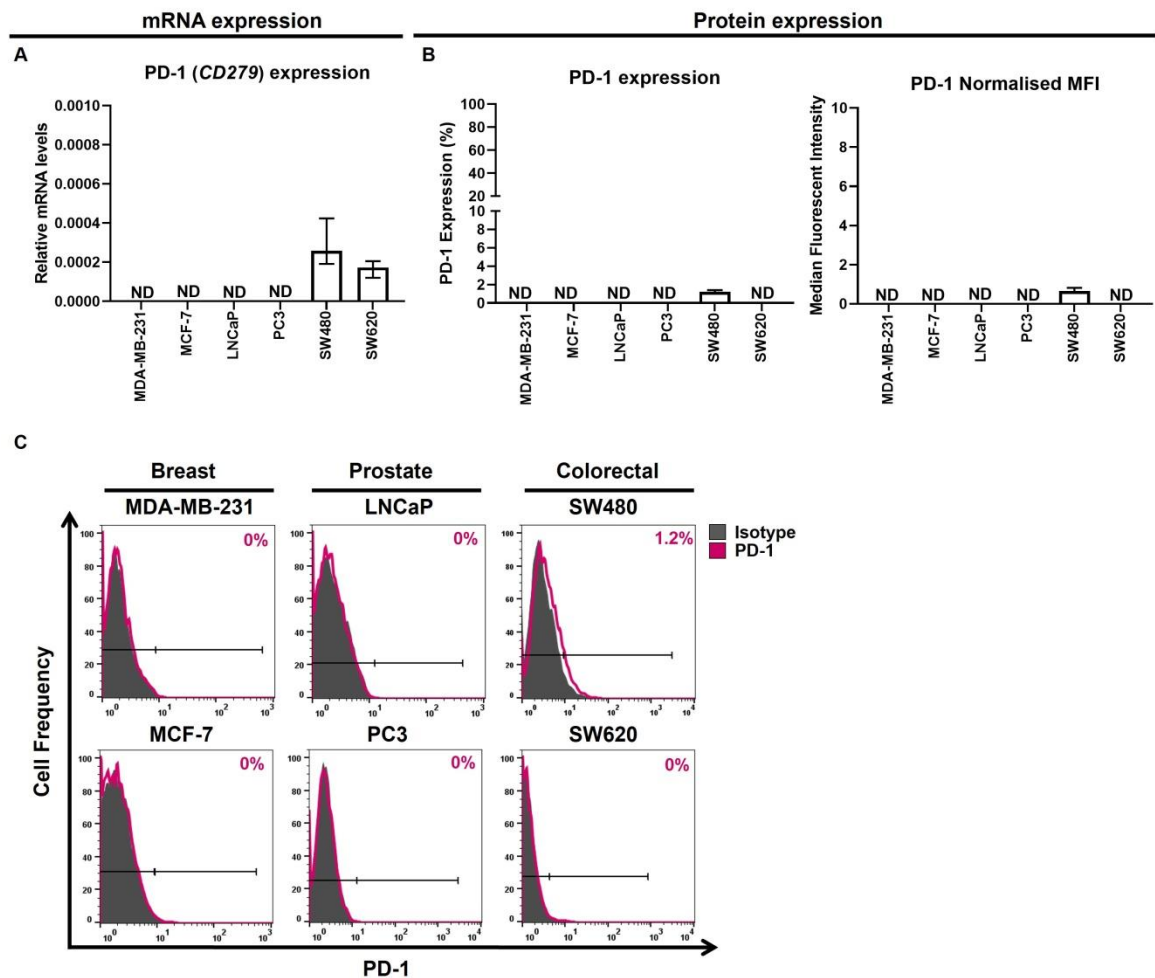
Figure 2.3 Colorectal cancer cell lines express low levels of PD-1. PD-1 (*CD279*) **(A)** gene and **(B)** protein expression was measured by RT-qPCR and flow cytometry, respectively, by MDA-MB-231, MCF-7, LNCaP, PC3, SW480 and SW620 cancer cell lines. The percentage of PD-1 expression is shown (left) alongside the MFI (right). **(C)** Representative flow cytometry histograms show the isotype control (grey) relative to the PD-1 positive populations (pink). Data is presented as median ± range. n=3 independent experiments each with 3 technical repeats. ND indicates gene and/or protein expression was not detected.

2.3.3.2 PD-L2 is differentially expressed amongst human cancer cell lines

The expression of PD-L2, another ligand for PD-1 besides PD-L1, was also investigated here and was shown to be expressed at differential levels amongst the six cancer cell lines examined at mRNA (Figure 2.4A) and protein (Figure 2.4B and C) levels.

MDA-MB-231 breast cancer cells expressed the highest levels of PD-L2 mRNA and protein in comparison to MCF-7 breast cancer cells and other cancer cells investigated. 59.2% (± 8.01) of MDA-MB-231 cells expressed PD-L2 on their cell surface, whilst MCF-7 breast cancer cells expressed low levels of PD-L2 at mRNA and protein levels, with only 4.1% (± 2.79) of cells expressing PD-L2 at this low level.

For LNCaP prostate cancer cells, PD-L2 expression was not detectable at mRNA or protein levels. In contrast, PC3 prostate cancer cells expressed the second highest level of PD-L2 mRNA and protein amongst the cell lines investigated. The proportion of PD-L2-expressing PC3 cells was variable between experiments ranging from low to moderate (5.25% ± 29.8).

SW480 primary colorectal cancer cells expressed consistently low levels of PD-L2 at mRNA and protein levels, with only a small proportion of cells expressing PD-L2 on their cell surface (2.07% ± 4.44). Meanwhile, SW620 metastatic colorectal cancer cells did not express detectable levels of PD-L2 at mRNA or protein levels.

2.3.3.3 HLA-ABC is expressed in a high proportion of breast, prostate, and colorectal cancer cells

So far, this study has shown that cancer cells express one or more immune inhibitory molecules, including PD-L1, PD-L2 and/or PD-1 at mRNA and protein levels, therefore it was next determined whether cancer cells expressed immune co-stimulatory molecules HLA-A, HLA-B and HLA-C (HLA-ABC) antigens. All cancer cells investigated here displayed a high proportion (>80%) of cells expressing HLA-ABC (Figure 2.5A and B).

MDA-MB-231 breast cancer cells expressed the highest level of HLA-ABC. 97.4% (± 4.1) of the cell population expressed HLA-ABC at a substantially high level. Likewise, a high proportion of HLA-ABC-expressing cells were seen in MCF-7 (96.27% ± 10.39), LNCaP (82.7% ± 7.14), PC3 (95.27% ± 10.24), SW480 (91.2% ±14.48) and SW620 (94.6% ± 8.09) cancer cell lines. However, these cancer cell lines demonstrated only low to moderate MFI for HLA-ABC expression.

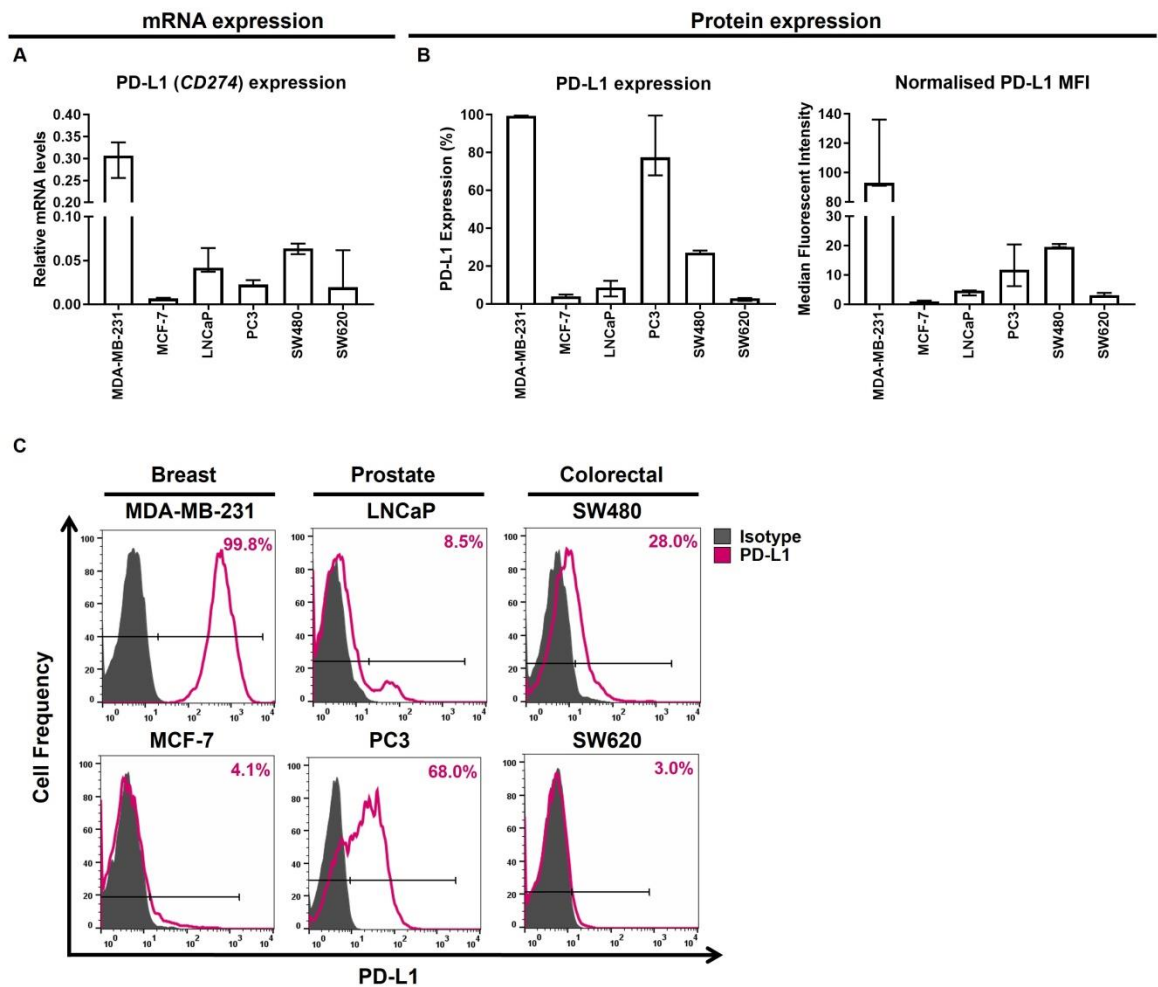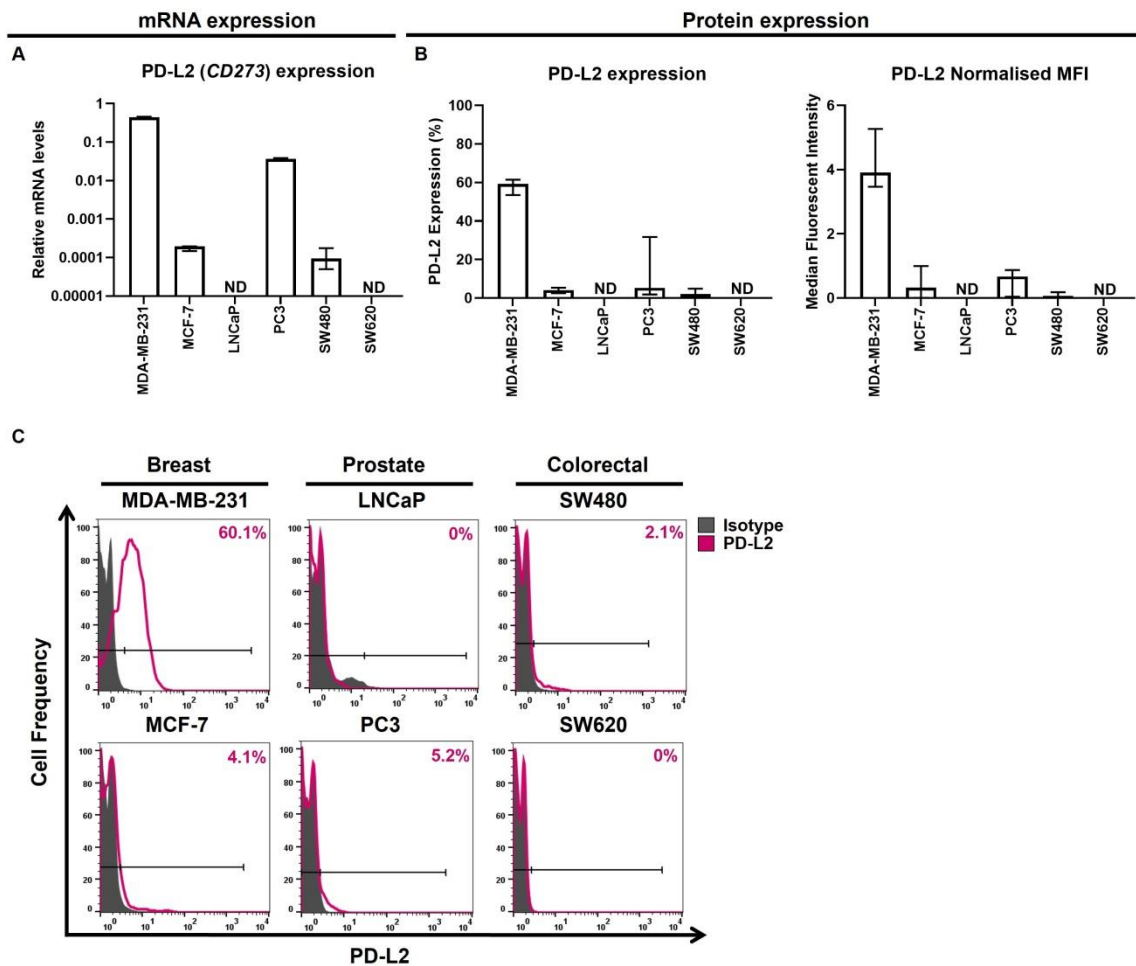**Figure 2.4 Human breast, prostate, and colorectal cancer cell lines express differential levels of PD-L2.** PD-L2 (*CD273*) **(A)** gene and **(B)** protein expression was measured by RT-qPCR and flow cytometry, respectively, for MDA-MB-231, MCF-7, LNCaP, PC3, SW480 and SW620 cancer cell lines. The percentage of PD-1 expression is shown (left) alongside the MFI (right). **(C)** Representative flow cytometry histograms show the isotype control (grey) relative to the PD-L2 positive populations (pink). Data is presented as median ± range. n=3 independent experiments each with 3 technical repeats. ND indicates gene and/or protein expression was not detected.
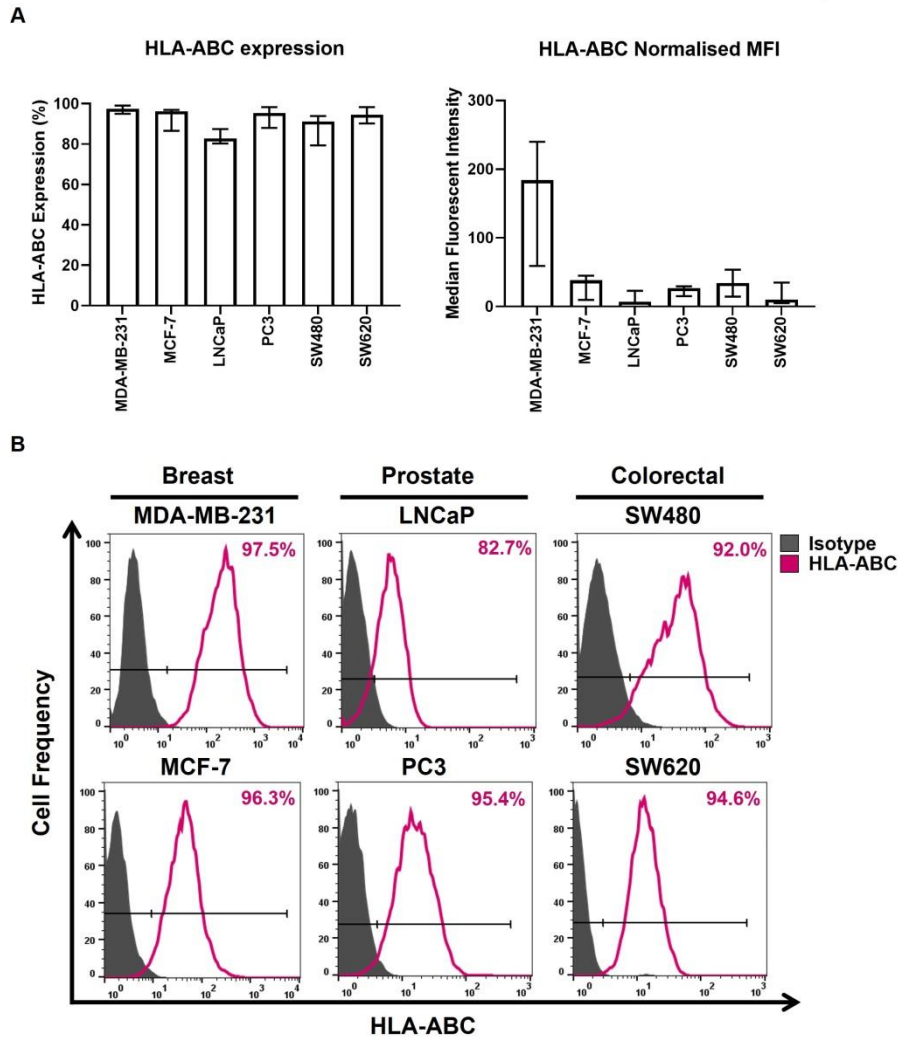
Figure 2.5 Human breast, prostate, and colorectal cancer cell lines express relatively high levels of cell surface HLA-ABC. (A) Flow cytometric analysis was used to measure the cell surface HLA-ABC expression by MDA-MB-231, MCF-7, LNCaP, PC3, SW480 and SW620 cancer cell lines. The percentage of HLA-ABC expression is shown (left) alongside the MFI (right). **(B)** Representative flow cytometry histograms show the isotype control (grey) relative to the HLA-ABC positive populations (pink). Data is presented as median ± range. n=3 independent experiments each with 3 technical repeats.

2.3.3.4 Death receptors are expressed at differential levels by human cancer cell lines

To further characterise cancer cells in standard monolayer cell culture and determine their immunogenic status, mRNA and protein expression measurements of DR4 (Figure 2.6A-C), DR5 (Figure 2.7A-C) and Fas (Figure 2.8A-C) were taken and were found to be differentially expressed amongst the different cancer cell lines.

2.3.3.4.1 DR4 expression by cancer cell lines

MDA-MB-231 and MCF-7 breast cancer cells expressed low levels of DR4 at mRNA and protein levels; with only 15.5% (± 4.77) and 4.5% (± 8.22) of cells, respectively, expressing DR4 in the whole cell population. In contrast, 61.1% (± 13.47) of LNCaP and 52.4% (± 15.9) of PC3 prostate cancer cells expressed moderate levels of DR4 protein. LNCaP cells also displayed a higher level of DR4 mRNA expression than PC3 cells. SW480 and SW620 colorectal cancer cells expressed similar levels of DR4 mRNA and protein. Accordingly, the frequency of DR4-expressing cells was also similar amongst SW480 and SW620 cells, expressing 41.8% (± 10.6) and 62.75% (± 12.94) of DR4, respectively.

2.3.3.4.2 DR5 expression by cancer cell lines

MDA-MB-231 breast cancer cells displayed moderate levels of DR5 mRNA and protein expression, and this was found in 89.64% (± 10.99) of the cell population. MCF-7 breast cancer cells expressed a lower level of DR5 mRNA and protein in 55.29% (± 13.3) of the cell population.

DR5 mRNA and protein expression was found to be the highest in LNCaP prostate cancer cells. This was also the case for the proportion of LNCaP cells expressing DR5 (97.1% ± 3.21). PC3 prostate cancer cells also expressed high levels of DR5 mRNA and protein on 92.56% (± 4.12) of its cell population.

Likewise, SW480 and SW620 colorectal cancer cells were shown to express similar levels of DR5 expression at mRNA and protein level. SW480 cells expressed DR5 in 89.76% (± 26.8) of the cell population. Similarly, SW620 cells displayed a high proportion of cells expressing DR5 (95.04% ± 0.43).
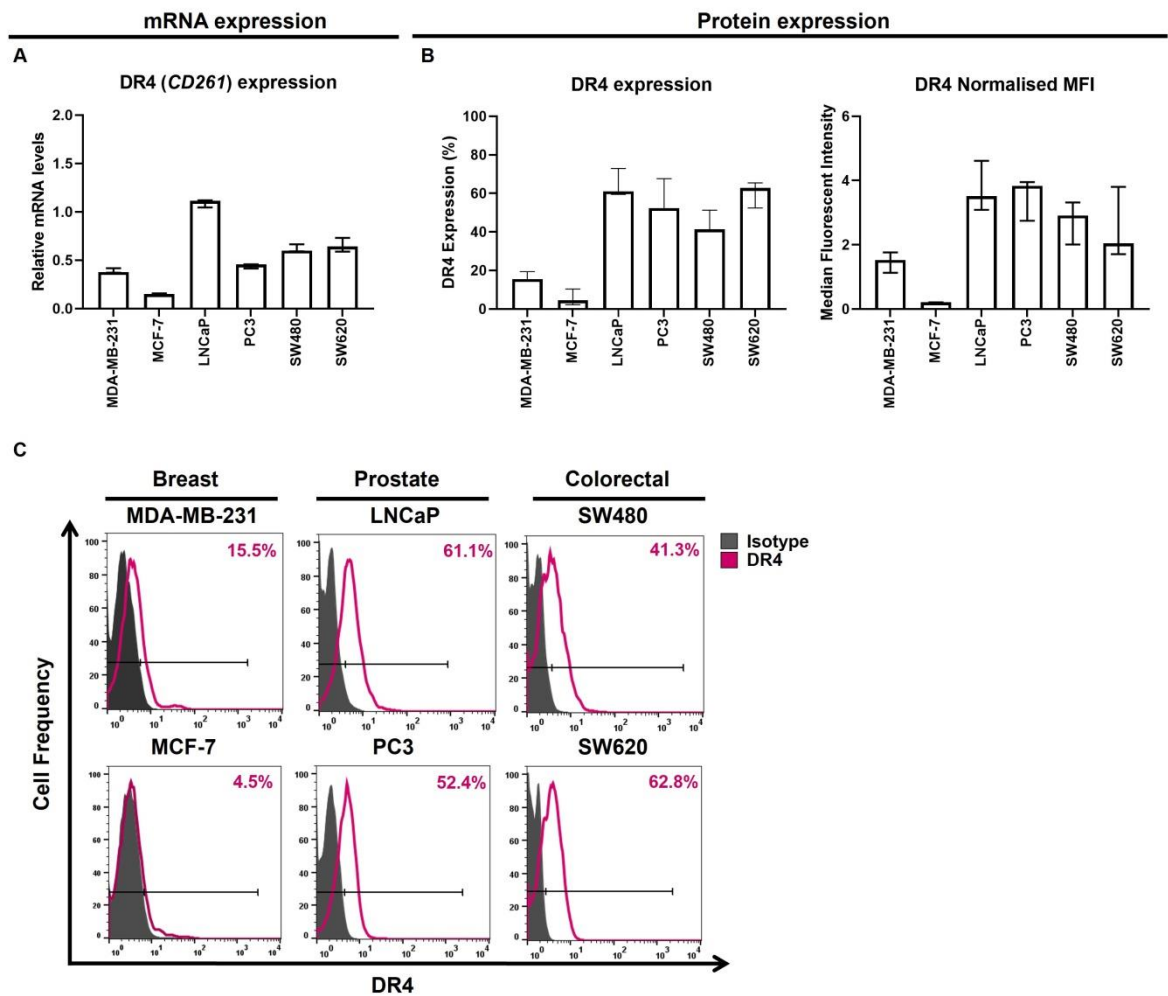
Figure 2.6 Human breast, prostate, and colorectal cancer cell lines express low to moderate levels of DR4 expression at mRNA and protein levels. DR4 (*CD261*) **(A)** gene and **(B)** protein expression was measured by RT-qPCR and flow cytometry, respectively, for MDA-MB-231, MCF-7, LNCaP, PC3, SW480 and SW620 cancer cell lines. The percentage of DR4 expression is shown (left) alongside the MFI (right). **(C)** Representative flow cytometry histograms show the isotype control (grey) relative to the DR4 positive populations (pink). Data is presented as median ± range. n=3 independent experiments each with 3 technical repeats.
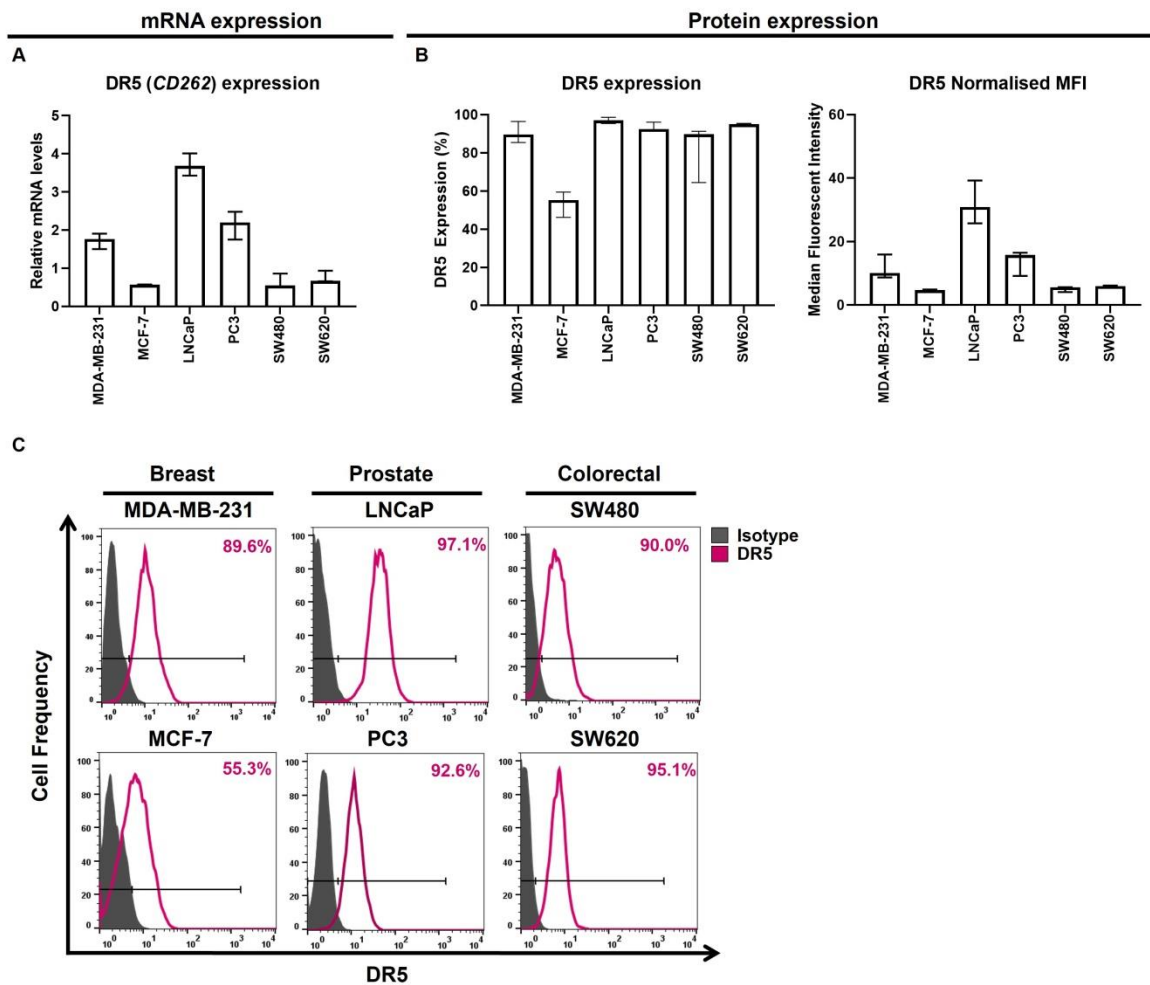
Figure 2.7 Human breast, prostate, and colorectal cancer cell lines express high proportions of cell surface DR5 at a moderate to high mRNA and protein levels. DR5 (*CD262*) **(A)** gene and **(B)** protein expression was measured by RT-qPCR and flow cytometry, respectively, for MDA-MB-231, MCF-7, LNCaP, PC3, SW480 and SW620 cancer cell lines. The percentage of DR5 expression is shown (left) alongside the MFI (right). **(C)** Representative flow cytometry histograms show the isotype control (grey) relative to the DR5 positive populations (pink). Data is presented as median ± range. n=3 independent experiments each with 3 technical repeats.

2.3.3.4.3   Fas expression by cancer cell lines

MDA-MB-231 and MCF-7 breast cancer cells were found to express Fas mRNA and protein at relatively low levels. Only 14.7% (± 8.81) of MDA-MB-231 cells expressed Fas protein and MCF-7 cells expressed a similar proportion of Fas protein (23.3% ± 9.21).

LNCaP prostate cancer cells displayed the second highest level of Fas mRNA and the highest level of Fas protein, although only 47.5% (± 18.88) of LNCaP cells expressed this higher level of Fas expression. In contrast, PC3 prostate cancer cells showed low levels of Fas mRNA and protein expression in a small proportion of cells (20.1% ± 15.89).

Interestingly, SW480 colorectal cancer cells displayed the highest level of Fas mRNA and the highest proportion of cells expressing Fas on their cell surface (60.99% ± 24.13). SW480 cells also showed the second highest expression of Fas protein. Oppositely, SW620 colorectal cancer cells expressed the lowest levels of Fas mRNA and protein, and this low expression was only found on 19.5% (± 5.62) of the SW620 cell population.

2.3.3.5   Tumorigenic marker, CD44 is expressed at relatively high levels by cancer cell lines

Human breast, prostate and colorectal cancer cell lines were further investigated for their expression of the tumorigenic maker, CD44, a cell surface adhesion molecule. The expression of standard CD44 and variant isoforms of CD44 by cancer cells cultured in monolayer were measured at mRNA (Figure 2.9A) and protein (Figure 2.9B and C) levels.

MDA-MB-231 breast cancer cells expressed the highest level of CD44 at mRNA and protein level and displayed the highest proportion of cells expressing CD44 (99.26% ± 1.07). MCF-7 breast, PC3 prostate, SW480 and SW620 colorectal cancer cells, also expressed high levels of CD44 at mRNA and protein level and the proportion of cells expressing CD44 were higher than 80% for all these cancer cells (94.8% ± 8.25, 98.86% ± 1.02, 82.71% ± 29.15, 92.1% ± 8.85, respectively). Interestingly, CD44 mRNA expression by LNCaP prostate cancer cells was detected at low levels, and CD44 protein expression was not detectable on the surface of these cells.
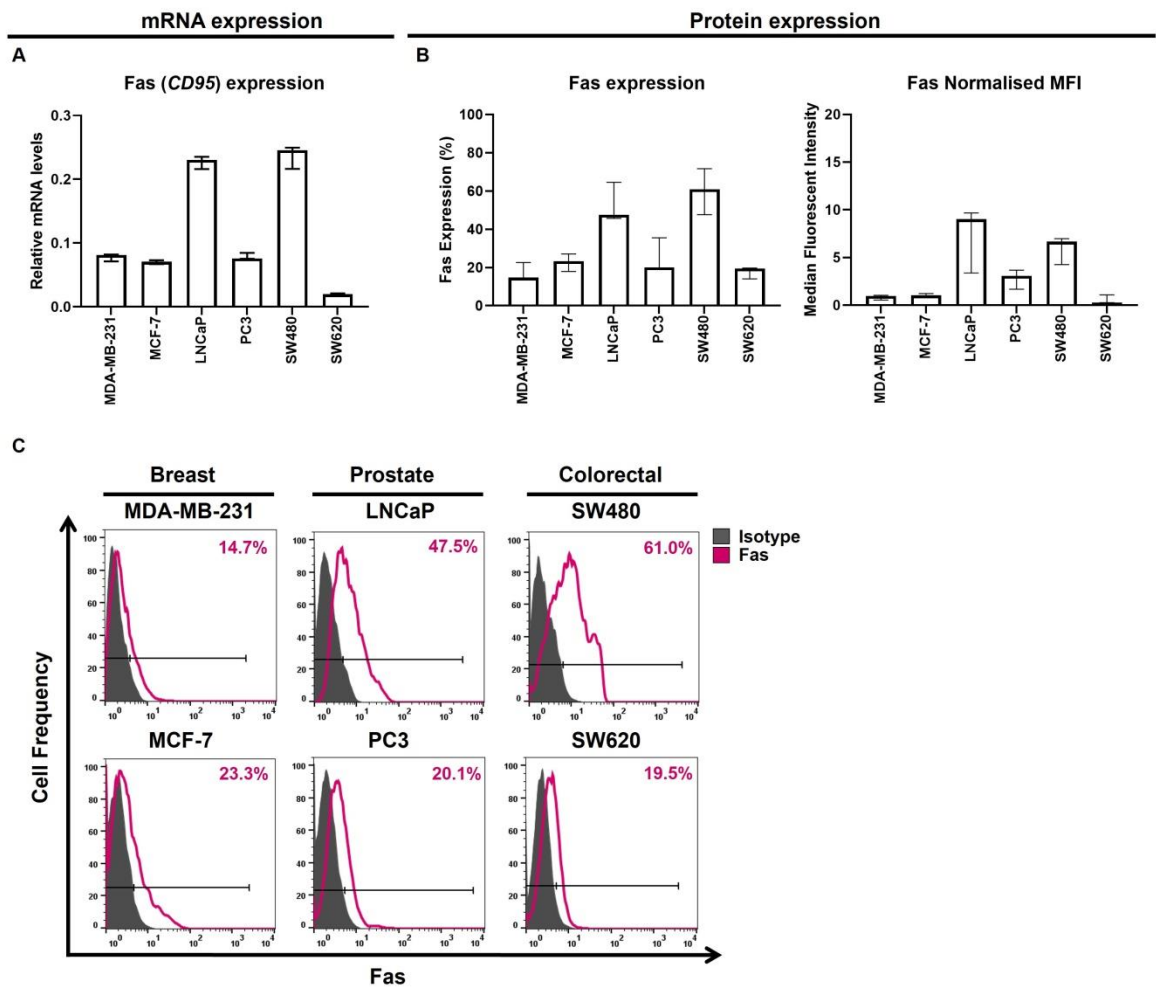
Figure 2.8 Human breast, prostate and colorectal cancer cell lines express low levels of Fas mRNA and protein in 2D cell culture. Fas (*CD95*) **(A)** gene and **(B)** protein expression was measured by RT-qPCR and flow cytometry, respectively, for MDA-MB-231, MCF-7, LNCaP, PC3, SW480 and SW620 cancer cell lines. The percentage of Fas expression is shown (left) alongside the MFI (right). **(C)** Representative flow cytometry histograms are displayed show the isotype control (grey) relative to the Fas positive populations (pink). Data is presented as median ± range. n=3 independent experiments each with 3 technical repeats.
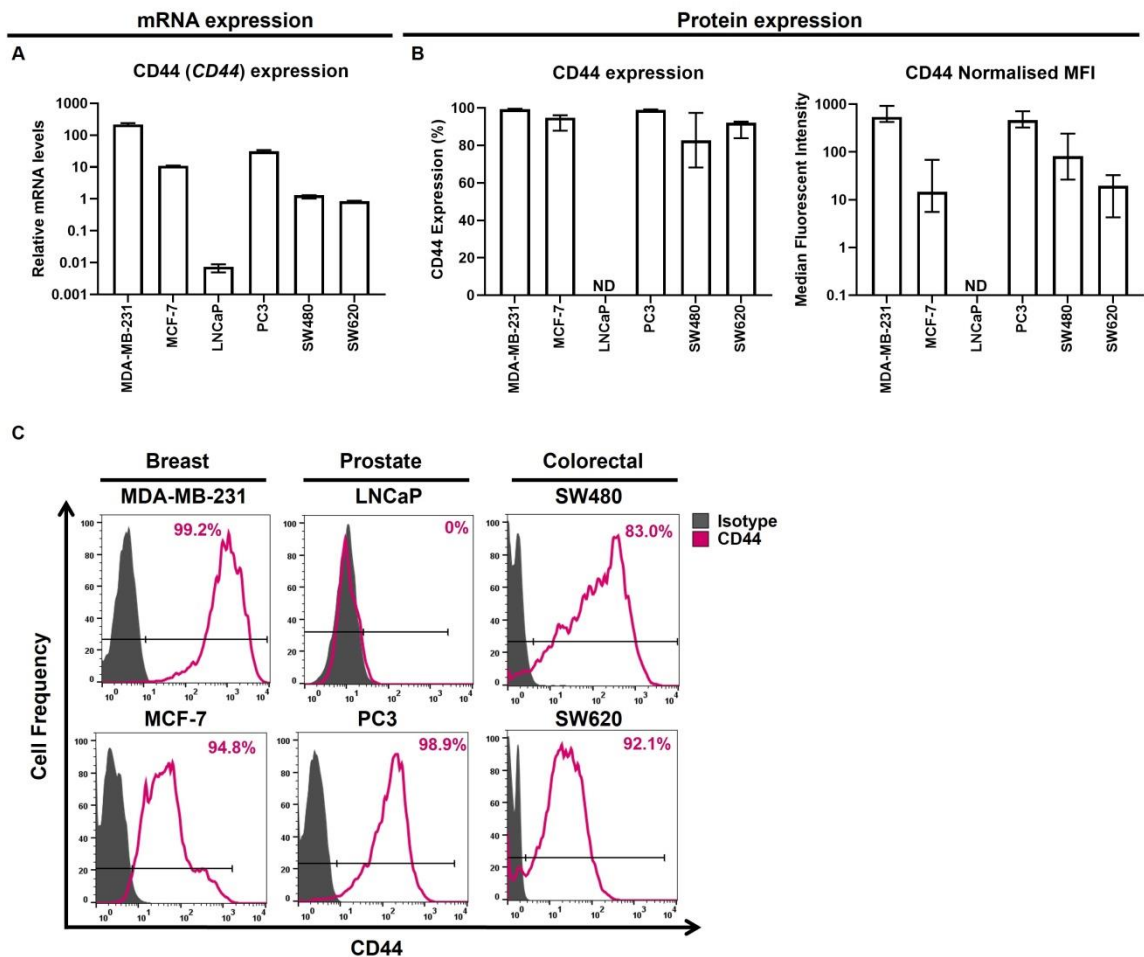
Figure 2.9 Human breast, PC3 prostate and colorectal cancer cells express relatively high levels of CD44 at mRNA and/or protein level. CD44 (*CD44*) **(A)** gene and **(B)** protein expression was measured by RT-qPCR and flow cytometry, respectively, for MDA-MB-231, MCF-7, LNCaP, PC3, SW480 and SW620 cancer cell lines. The percentage of CD44 expression is shown (left) alongside the MFI (right). **(C)** Representative flow cytometry histograms show the isotype control (grey) relative to the CD44 positive populations (pink). Data is presented as median ± range. n=3 independent experiments each with 3 technical repeats.

2.3.3.6 Tumorigenic marker, HIF1α is expressed differentially by cancer cell lines

Since our study was interested in utilising 3D cell culture models in subsequent experiments to mimic solid tumour physiology more closely in that a hypoxic environment was generated, baseline HIF1α mRNA (Figure 2.10A) and protein (Figure 2.10B) was assessed in cancer cells cultured in 2D monolayer. Interestingly, baseline HIF1α mRNA expression was detected in all cancer cell lines investigated at relatively high levels despite being grown in normoxic conditions. In all the cancer cells, over 80% of the cell populations were HIF1α positive, but expressed HIF1α protein at low levels. MDA-MB-231 breast cancer cells expressed the highest level of HIF1α mRNA and protein expression. MDA-MB-231 cells also displayed the highest proportion of cells expressing HIF1α (97.4% ± 6.92). In contrast, MCF-7 breast cancer cells displayed the lowest proportion of cells expressing HIF1α (80.4% ± 14.51). In LNCaP prostate cancer cells 89.6% (± 19.51) of cells expressed HIF1α protein. Similarly, 94.7% (± 15.1) of PC3 prostate cancer cells expressed HIF1α protein. Furthermore, SW480 colorectal cancer cells expressed the lowest level of HIF1α mRNA and protein, but this low level of expression was found in 86.6% (± 36.19) of the cell population. Likewise, SW620 cells also displayed a high percentage of cells expressing HIF1α (93.7% ± 1.27) and a low MFI for HIF1α protein expression.
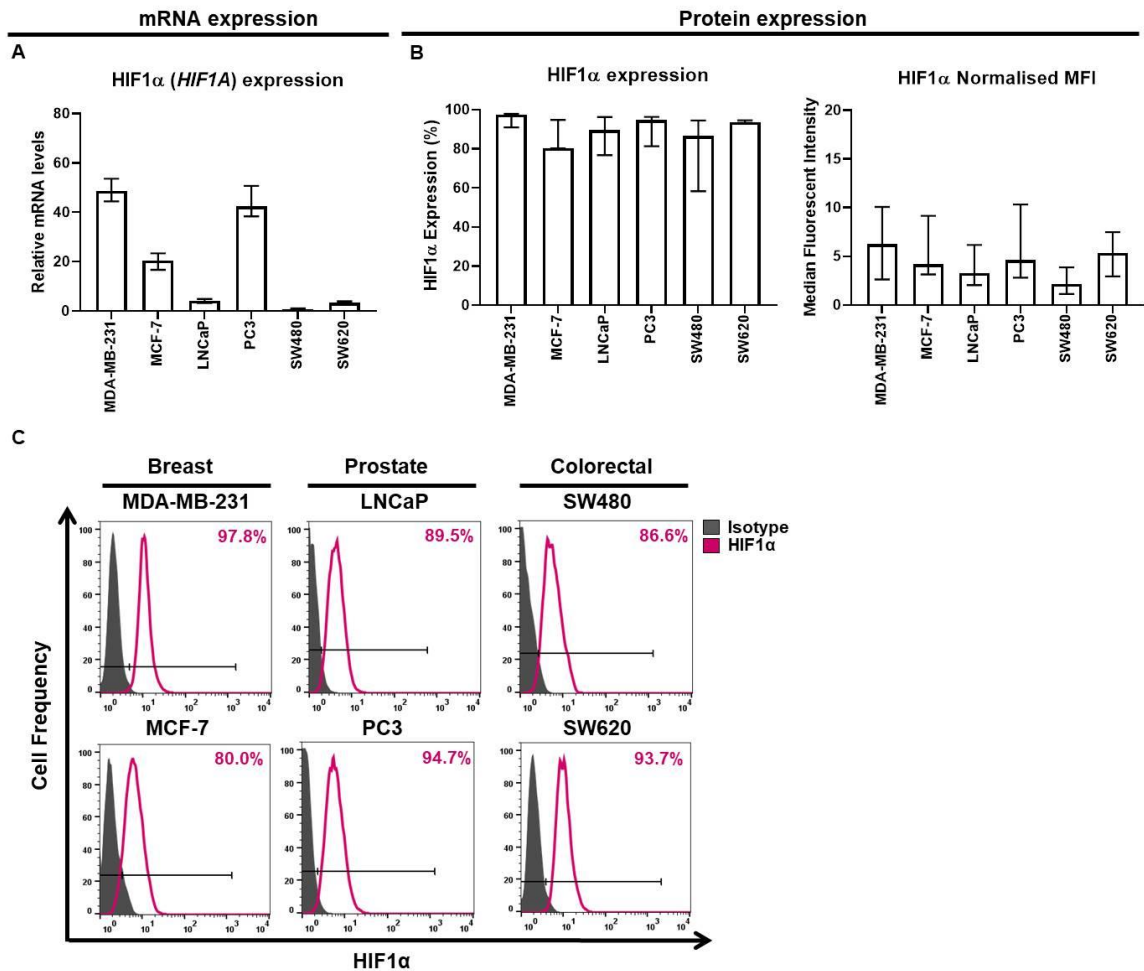
Figure 2.10 Human breast, prostate and colorectal cancer cells cultured in 2D monolayer under normoxic conditions express differential levels of HIF1α at mRNA and/or protein level. HIF1α (*HIF1A*) **(A)** gene and **(B)** protein expression was measured by RT-qPCR and flow cytometry, respectively, for MDA-MB-231, MCF-7, LNCaP, PC3, SW480 and SW620 cancer cell lines. The percentage of HIF1α expression is shown (left) alongside the MFI (right). **(C)** Representative flow cytometry histograms show the isotype control (grey) relative to the HIF1α positive populations (pink). Data is presented as median ± range. n=3 independent experiments each with 3 technical repeats.

2.4   Discussion

Cancer cell lines are invaluable *in vitro* model systems heavily used for preclinical research to gain mechanistic and therapeutic insight (Mirabelli *et al.,* 2019). In order to select the most appropriate cancer cell line when designing an experiment, it is vital to know the molecular and cellular alterations featured in each cell line such as their mutational status and gene and protein expression profiles which can be predictive of their response to treatment and interactions with specific cell types within the tumour microenvironment. Although the Cancer Cell line Encyclopaedia is a widely available source encompassing the characterisation of 947 cancer cell lines (Barretina *et al.,* 2012; Garnett *et al.,* 2012), the extent to which it covers gene and protein expression profiles of specific immunological and tumorigenic markers is limited (Nusinow *et al.,* 2020). However, regardless of whether the expression data required is publicly available, it is necessary to verify gene and protein expression before commencing studies due to the possibility that cancer cell lines can become cross contaminated or mycoplasma positive affecting their biological phenotypes. Here, we characterised six mycoplasma free human cancer cell lines for their expression of immunological and tumorigenic markers including PD-L1, PD-1, PD-L2, HLA-ABC, DR4, DR5, Fas, CD44 and HIF1α at mRNA and protein levels to aid in our downstream application of each cell line.

The basal expression levels of PD-L1 by human cancer cell lines were found to be in accordance with the published literature, in that, MDA-MB-231 breast and PC3 prostate cancer cells expressed high levels of PD-L1 (Soliman *et al.,* 2014; Martin *et al.,* 2015). Whilst LNCaP prostate and SW480 colorectal cancer cells expressed low to moderate levels of PD-L1 (Song *et al.,* 2013; Martin *et al.,* 2015); and MCF-7 breast and SW620 colorectal cancer cells expressed low levels of PD-L1 (Song *et al.,* 2013; Soliman *et al.,* 2014).

Cytokine driven PD-L1 upregulation on the surface of cancer cells is a well-documented mechanism that occurs in the tumour microenvironment during the development of the adaptive immune response to prevent cancer cells being recognised and destroyed by tumour-specific CD8+ T cells (Lee *et al.,* 2006; Pardoll, 2012). IFNγ in particular, is a potent modulator of PD-L1 expression. The endogenous expression of transcription factor, IRF-1, has been found responsible for constitutive PD-L1 expression and induction of PD-L1 following IFNγ stimulation (Lee *et al.,* 2006). Our data confirms that human breast, prostate and colorectal

cancer cells investigated here have the potential to demonstrate adaptive immune resistance. Pro-inflammatory cytokines, IFNγ and TNFα, were able to individually increase cell surface PD-L1 expression on cancer cells and work synergistically together in some of the cancer cell lines to further increase cell surface PD-L1 expression. This synergistic effect was only previously observed in human dermal lymphatic endothelial cells (Yee *et al.,* 2017). TNFα-mediated induction of miR-155 expression was reported to be responsible for driving PD-L1 expression in these cells which was then shown to be enhanced by the addition of IFNγ (Yee *et al.,* 2017).

PD-1 and PD-L2 expression was found amongst the human cancer cell lines investigated, further illustrating the extent of cancer cells to express immune inhibitory molecules in order to survive within the tumour microenvironment. Whilst PD-1 expression on melanoma, ovarian, liver and bladder cancer cells has been reported to elicit an anti-tumour role in response to anti-PD-1 therapy (Kleffel *et al.,* 2015; Li *et al.,* 2017; Osta *et al.,* 2018), in NSCLC and colorectal cancer cells anti-PD-1 therapy has been shown to promote tumour progression via activating PI3K and MAPK pathways (Du *et al.,* 2018; Wang *et al.,* 2020). This tumour-suppressive role of PD-1 in these cancer types could be responsible for the hyperprogressive disease observed in a minority of patients with NSCLC following treatment with anti-PD-1 therapy (Kocikowski *et al.,* 2020). Consistent with our study, Wang *et al.,* (2020) showed that SW480 colorectal cancer cells expressed cell surface PD-1 and as a result they were able to show that anti-PD-1 therapy enhanced SW480 cell proliferation.

So far, compared to PD-L1, the functional role of PD-L2 in cancer cells remains largely unknown (Qin *et al.,* 2019). Here, we showed 4 out of 6 cancer cell lines expressed PD-L2 which may suggest its expression has some survival advantage towards the tumour. Indeed, a meta-analysis of solid tumour patients revealed that high PD-L2 expression may promote metastasis and predict unfavourable prognosis, particularly in hepatocellular carcinoma (Yang *et al.,* 2019). Similarly, Marinelli *et al.,* (2020) showed that PD-L2 positive endometrial cancer cell lines displayed a high migratory capacity, increased AKT pathway activation and reduced sensitivity to chemotherapy compared to PD-L2 negative control cells. Nevertheless, the presence of PD-L2 expression, similar to PD-L1, on tumour and stromal cells in the tumour microenvironment has been shown to positively correlate with immunotherapy response in some cancers (Yang *et al.,* 2019).

The presentation of tumour-associated neo-antigens in MHC molecules by APCs or tumour cells is necessary for T cell activation and immune-mediated killing of cancer cells, as well as predicting immunotherapy response (Bai *et al.,* 2017; Yi *et al.,* 2018). MHC class 1 molecules (HLA-ABC) were expressed at moderate to high levels amongst the human cancer cell lines investigated here, suggesting that these cell lines may demonstrate sufficient antigen presentation with the ability to elicit an immune response in the tumour microenvironment (Garrido *et al.,* 2016).

Importantly, cancer cells can also undergo death receptor-mediated apoptosis by TRAIL and FasL binding to DR4/DR5 and Fas, respectively (Shin *et al.,* 2001). Anti-cancer agents targeting these death receptors are currently under preclinical and clinical investigation because of their specificity to induce apoptosis in cancer cells (Ashkenazi *et al.,* 2008; Herbst *et al.,* 2010; Villa-Morales and Fernández-Piqueras, 2012; Hendricks *et al.,* 2016). In our study, cancer cell lines displayed low to moderate DR4 expression and higher expression of DR5. The lower expression of DR4 by cancer cells compared to DR5 could be a survival mechanism. For example, although DR5 has a higher affinity for TRAIL, TRAIL binding does not correlate with DISC formation which is necessary for cancer cell apoptosis. However, TRAIL does bind to DR4, and this has been shown to be more effective at inducing apoptosis than TRAIL binding to DR5 (Thorburn, 2007; Tur *et al.,* 2008); which could in part explain why cancer cells express lower levels of DR4 and high levels of DR5. Furthermore, cancer cells were shown to express moderate to high levels of death receptor Fas, suggesting that these cancer cells may be susceptible to Fas/FasL-mediated apoptosis. This expression data suggests that the cancer cells investigated in this study may be sensitive to TRAIL and FasL receptor agonists.

In solid tumours, hypoxia develops due to deficiencies in oxygen throughout the tumour tissue, with HIF-1α expression playing a vital role in the regulation of many genes involved in cellular metabolic and survival pathways in response to hypoxia (Noman *et al.,* 2015). HIF1α is continuously synthesised but rapidly degraded under normoxic conditions. HIF1α only becomes stable in reduced oxygen concentrations resulting in its translocation to the nucleus, heterodimerization with arylhydrocarbon receptor nuclear translocator, DNA binding and promotion of target gene transcription (Kallio *et al.,* 1997). Overexpression of HIF1α is well established in cancer cells to facilitate tumour progression (Shi *et al.,* 2010). Here, in all six human cancer cell lines cultured under normoxic conditions, we demonstrated HIF1α mRNA

expression as expected, but also showed that almost 100% of the cells expressed low but detectable levels of HIF1α protein. Whilst we would expect HIF1α degradation under normoxic conditions, hence, not to detect HIF1α protein via intracellular staining, normoxic activation of HIF by oncogenes (Chan *et al.,* 2003), growth factors and cytokines (Hellwig-Burgel *et al.,* 1999; Zhou *et al.,* 2003), and small signalling molecules such as nitric oxide (Metzen *et al.,* 2003) has been reported previously. Additionally, Shi *et al.,* (2010) showed that MDA-MB-231 breast cancer cells expressed the highest level of HIF1α compared to other breast cancer cells, including MCF-7 cells also investigated here, which was accompanied by a faster growth rate. Whilst abrogating HIF1α expression in MDA-MB-231 cells, significantly suppressed cell proliferation and increased apoptosis (Shi *et al.,* 2010). Overall, these findings illustrate the importance of HIF1α in tumour growth and survival and demonstrates that HIF1α may become stabilised in cancer cell lines by other factors other than hypoxia.

Lastly, in this study the expression of CD44, a cell surface adhesion protein and cancer stem cell marker (Senbanjo and Chellaiah, 2017), was also assessed amongst human cancer cell lines due to its previously reported association with PD-L1 expression (Zhi *et al.,* 2015; Nishino *et al.,* 2017; Kong *et al.,* 2019). CD44 was found to be expressed amongst all cell lines at mRNA and protein levels, except for LNCaP prostate cancer cells. Although in LNCaP cells CD44 was expressed at mRNA level this was not translated to protein levels, this correlates with previous findings on CD44 expression in LNCaP cells (Tai *et al.,* 2011; Li *et al.,* 2017). Importantly, cell lines expressing high levels of PD-L1 mRNA or protein (MDA-MB-231 and PC3 cells) displayed the highest levels of CD44 expression. CD44 expression on cancer cells is associated with increased invasive potential, drug resistance and may indicate a cancer stem cell phenotype when co-expressed with CD133 and other cancer stem cell markers (Zhi *et al.,* 2015; Nishino *et al.,* 2017; Senbanjo and Chellaiah, 2017).

All together this expression data shown here validates what has already been shown in the literature or provides new insight into different immunological and tumorigenic markers expressed in a panel of diverse cancer types cultured in 2D monolayer cell culture, and acts as a basic platform for future cancer immunology research to aid in experimental design.

3. Characterisation of 3D cell culture models of human breast, prostate, and colorectal cancer

3.1 Introduction

Whilst human cancer cell lines cultured in 2D monolayer cell culture provide high throughput *in vitro* systems that have been instrumental to the advancements of cancer immunology research. They fail to fully recapitulate *in vivo* human solid tumours due to their lack of heterogeneity (Boucherit *et al.,* 2020). Scaffold-free and scaffold-based 3D cell culture models created with human cancer cells are advantageous alternatives to standard 2D monolayer cell culture (Figure 3.1) (Hudson *et al.,* 2020; Boucherit *et al.,* 2020).
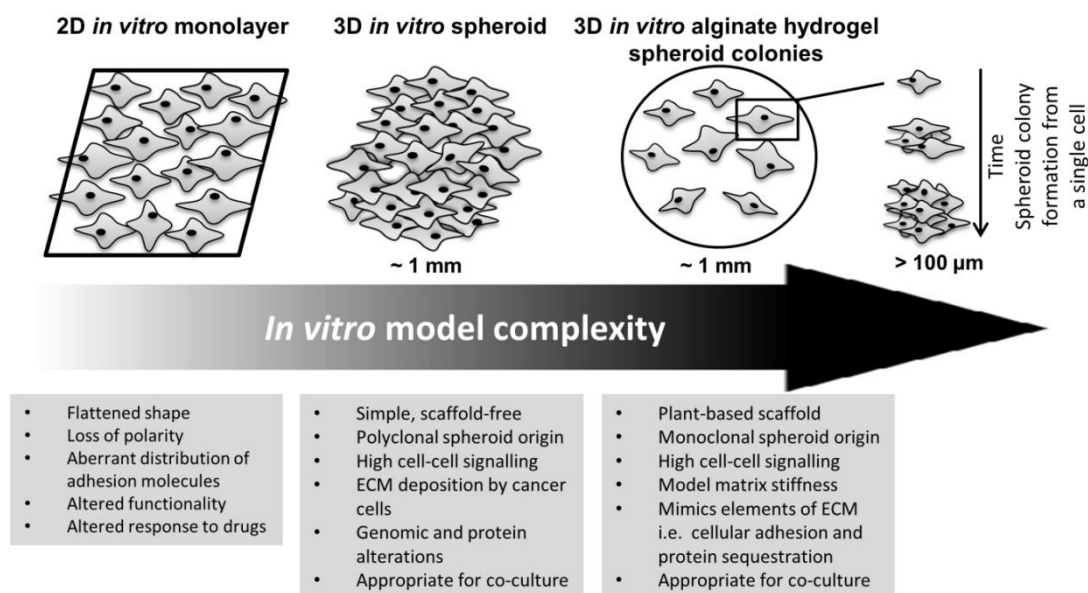
Figure 3.1 *In vitro* model complexity and physiological relevance of 3D versus 2D cancer models for oncology and immuno-oncology research.

Importantly, 3D *in vitro* and *ex vivo* (patient-derived) models, have similar biological characteristics to native tumour tissue; having a comparable 3D architecture with a nutrient gradient compromising a proliferative outer layer, a quiescent inner layer and a necrotic core; a hypoxic microenvironment; cell-cell and cell-extracellular matrix signalling; genomic and protein alterations; and a predictive response to treatment (Breslin and O'Driscoll, 2013; Knight and Przybors, 2015; Lazzari *et al.,* 2017; Hoarau-Véchot *et al.,* 2018; Di Modugno *et al.,* 2019; Boucherit *et al.,* 2020). These

3D cell culture models also allow the opportunity to alter the cell composition in order to study different aspects of the tumour microenvironment (Boucherit *et al.,* 2020). Indeed, these 3D models could be used to study PD-1/PD-L1-targeted therapies and their interplay within the tumour microenvironment.

PD-1/PD-L1-targeted therapies have yielded remarkable anti-tumour immune responses in select patients with advanced cancers, but the majority of patients have been shown to be unresponsive, hyperprogressive or develop resistance (Fehrenbacher *et al.,* 2016; Rosenberg *et al.,* 2016; Balar *et al.,* 2017; Chen *et al.,* 2017). The exact mechanisms for this are still unclear. The new and emerging roles of both PD-L1 and its receptor PD-1 to send pro-survival signals in tumour cells may be in part responsible for the lack of response to PD-1/PD-L1-targeted therapies, and requires further investigation (Hudson *et al.,* 2020). Hence, there is urgent need for more relevant *in vitro* oncology models, capable of closely mimicking the heterogeneity of the tumour microenvironment during *in vivo* conditions. This could allow a more predictive *in vitro* evaluation of the tumour-intrinsic role of PD-L1 and PD-1, and their response to PD-1/PD-L1-targeted therapy, plus enable the evaluation of potential combination strategies and cancer cell-immune cell interactions.

3.1.1 Aims

The aims of this chapter were to characterise two 3D cell culture models (hanging drop and alginate hydrogel beads) of human breast, prostate, and colorectal cancers and compare them to their 2D monolayer counterparts. Assessment was made of cell growth and viability and the spheroid diameter. Using immunofluorescence and immunohistochemistry, assessment was made of the hypoxic area and PD-L1 expression, respectively, in the 3D tumour models. Immunological (PD-L1, PD-1, PD-L1, HLA-ABC, DR4, DR5 and Fas) and tumorigenic (CD44 and HIF1α) marker expression was also assessed at the mRNA and protein levels using RT-qPCR and flow cytometry, respectively, in the 3D models compared to their 2D monolayer counterparts.

3.1.2 Hypotheses

It was hypothesised that human breast, prostate, and colorectal cancer cell lines would grow successfully in 3D cell culture models to form viable 3D cancer spheroids that would display a hypoxic core and mimic more closely the architecture and

heterogeneity of solid tumours. It was also hypothesised that PD-L1 expression within 3D cancer spheroids would be localised to the hypoxic core and that its expression by cancer cells would be significantly altered in a 3D cell culture environment compared to 2D-cultured cells. Similarly for PD-1, PD-L2, HLA-ABC, DR4, DR5, Fas, CD44 and HIF1α expression, it was hypothesised that a 3D cell culture environment would alter the levels at which they were expressed by cancer cells compared to when they were cultured in monolayer.

3.2   Materials and Methods

3.2.1   Establishing 2D and 3D cultures

All human breast, prostate and colorectal cancer cell lines were cultured as described in Chapter 2, Section 2.2.1. For experiments, monolayer 2D cell cultures were established in flat-bottom 6-well plates at a seeding density of 5 x 10^5 cells/well. 3D cell cultures were established using the hanging drop method to form 3D spheroid aggregates (Knight and Przybors, 2015) and alginate hydrogel beads to generate 3D spheroid monoclonal colonies (Arhoma *et al.,* 2017).

3.2.1.1   Hanging drop method

To generate 3D spheroids using the hanging drop method the lid of a Petri dish was inverted and 10 μL of cell suspension containing 10,000 cells was pipetted drop-by-drop onto the lid. The bottom of the petri dish was filled with PBS to act as a hydration chamber to which the inverted lid was placed on top. The droplets were monitored daily for spheroid formation via microscopy and were harvested for downstream analysis at day 3 by pipetting 10 mL of complete medium gently onto the lid and collecting all the spheroids, with a single spheroid being generated per droplet.

3.2.1.2   Alginate hydrogel beads

To form 3D spheroid colonies using alginate hydrogel beads, cell lines were suspended in 1.2% w/v sterile sodium alginate (Merck) in 0.15 M sodium chloride at optimised seeding densities ranging from 6 x 10^5 cells/ml to 1.2 x 10^6 cells/ml depending on the cell line (Table 4). The alginate-cell mixture was extruded out of a 21G needle (Merck) into 0.2 M calcium chloride to polymerise the alginate into beads and encapsulate the cells. Following 10 minutes incubation at 37°C alginate hydrogel beads were washed twice with 0.15 M sodium chloride and once with complete medium before culturing for 3, 6 and 10 days. For long term cultures media was changed every 72 hours. Alginate hydrogel beads were monitored daily for spheroid colony formation via microscopy and harvested at day 3, 6 and 10 for downstream analysis. To release the spheroid colonies into solution, alginate hydrogel beads were immersed in sterile alginate dissolving buffer (55 mM sodium citrate, 30 mM EDTA and 0.15 M sodium chloride) for 10 minutes at 37°C. Spheroid colonies were then washed with PBS in preparation for downstream analysis.

Table 3.1 Optimised cell seeding densities for the optimal formation of 3D spheroid colonies within alginate hydrogel beads.

Cell line	Optimised cell seeding density per 1 mL of alginate
MDA-MB-231	1.0×10^6
MCF-7	1.2×10^6
LNCaP	0.6×10^6
PC3	0.6×10^6
SW480	0.6×10^6
SW620	0.6×10^6

Table 3.1 The number of cells used to form 3D alginate spheroid colonies cultures was dependent on the cancer cell line utilised.

3.2.2 Fluorescent Microscopy

3.2.2.1 Monitoring cell viability in 3D cell culture models

A single spheroid or a whole alginate hydrogel bead for each cell line was harvested and placed in a 96-well plate and stained with Hoechst 33342 (10 µg/mL) (ThermoFisher Scientific) and Propidium Iodide (PI) (10 µg/mL) (Merck) for 20 minutes at 37°C. Fluorescent images were obtained using the Olympus IX81 microscope (Olympus Corporation) and multi-fluorescent images were captured by multiple image alignment (MIA) using the 10X objective lens and the Olympus cellSens Imaging Software (Olympus Corporation). After capturing the image, the full spheroid or alginate hydrogel bead was selected, and the surface area of Hoechst 33342 and PI was measured concurrently. The percentage viability for each spheroid and alginate hydrogel bead was calculated by dividing the surface area of Hoechst 33342 stained cells by the total surface area of Hoechst 33342 and PI stained cells then multiplying by 100. Data acquisition was carried out for 3D spheroids over a time course from day 3 to day 7 to determine the optimal time for 3D spheroids to be used for downstream experiments. At day 3, the spheroid cell viability was quantified for each cell line. For alginate hydrogel beads, data was acquired at day 3, 6 and 10 and cell viability was quantified at each time point. For cell viability of 3D cultures, 4 independent experiments were carried out each with 3 technical repeats.

3.2.2.2 Detecting hypoxia in 3D cell culture models

A single spheroid at day 3 or a whole alginate hydrogel bead at day 10 for each cell line was harvested and placed in a 96-well plate. Subsequently, Image-iT™ Hypoxia

Reagent (ThermoFisher Scientific) was added at a final concentration of 5 µM to each well and incubated at 37°C in a CO_2 incubator for 1 hour. After 40 minutes of the incubation period, Hoechst 33342 was added to each well at a final concentration of 10 µg/mL. 3D-cultures were then visualised using the Olympus IX81 microscope (Olympus Corporation) and multi-fluorescent images were captured by MIA using 10X objective lens and the Olympus cellSens Imaging Software (Olympus Corporation). Some alginate-derived spheroid colonies were dissociated from the alginate using alginate dissolving buffer and cultured in 96-well ultra-low attachment microplates overnight to form 3D spheroid colony aggregates, named aggregoids (Flint *et al.,* 2020). These aggregoids were also assessed for hypoxia as described above. 2D-cultured cells were used as negative controls for hypoxia detection. 2D-cultured cells were seeded at 3 x 10^4 cells/well in 96-well plates, cultured overnight in a CO_2 incubator at 37°C and then treated the same as described above, except cells were only cultured with the Image-iT™ Hypoxia Reagent for 30 minutes to which Hoechst 33342 was added after the initial 10 minutes of the incubation.

3.2.2.3 Measuring 3D spheroid diameter

The diameter of 3D spheroids and 3D spheroid colonies was measured for each cell line using the diameter measurement option in the cellSens Imaging Software (Olympus Corporation). Diameter was measured in micrometres (µM). For 3D spheroids the diameter was assessed at day 3 for all cell lines. For 3D spheroid colonies the diameter was assessed at day 10 for all cell lines. For a non-biased approach to measuring the diameter of 3D spheroid colonies within the alginate bead, 3 spheroid colonies were measured from 5 different areas of the bead including from the 4 corners and centre of the bead. For diameter measurements, 4 independent experiments were carried out each with 3 technical repeats.

3.2.3 RNA extraction and quantification, cDNA synthesis and real-time quantitative polymerase chain reaction

Monolayer cultured cells were harvested and lysed from cell culture T25 flasks at 90% confluency as described in Chapter 2 Section 2.2.2. For 3D spheroids, five Petri dish lids were prepared for each cell line and cultured for 3 days. At day 3, 3D spheroids were flushed from the Petri dish lid, spun down using a benchtop centrifuge at 400 g and the supernatant was removed. For 3D spheroid colonies, approximately 60 alginate beads were prepared for each cell line. The 3D spheroid colonies were released from the alginate using alginate dissolving buffer at day 3, 6

and 10, spun down using a benchtop centrifuge at 400 g and the supernatant was removed. To facilitate cell lysis of 3D cultures, 500 µL BL-TG buffer was added to the pellets. Subsequently, total RNA extraction, cDNA synthesis and RT-qPCR to measure mRNA was performed as described in Chapter 2, Section 2.2.2.

3.2.4   Flow Cytometry

Monolayer cells for each cell line were seeded at 5 x 10^5 cells/well in 6-well plates and cultured for 3 days before being harvested by trypsinisation, placed into Eppendorf tubes and subsequently stained for flow cytometry (as described in Chapter 2, Section 2.2.3.1). 3D-cultures were prepared for flow cytometry as follows: 1 Petri dish of 3D spheroids grown for 3 days provided enough cells to stain 3 samples for flow cytometry. An appropriate number of Petri dishes were prepared for each experiment for each cell line. For 3D spheroid colonies, 12-well plates were prepared, each with 10 beads/well for each sample. Enough beads were generated for each cell line to prepare plates for harvesting cells at day 3, 6 and 10. 2D-cultured cells were plated timely to run concurrently with these timepoints so that 2D cell, 3D spheroid and 3D spheroid colony expression was comparable. 3D-cultures were dissociated into single cell suspensions by treating cells with Trypsin-EDTA 0.25% (ThermoFisher Scientific) for 5 minutes. Once cells were harvested, cells were stained for cell surface and intracellular antigens, and data was acquired as described in Chapter 2 Section 2.2.3.1 Appropriate gating strategies were carried out for each independent experiment including gating on 2D and 3D isotype controls, single cells and live cells. For MDA-MB-231 cells, isotype controls for 2D-cultured cells and 3D alginate spheroid colonies are both displayed on representative flow cytometry plots for DR5 and Fas due to differences in background signal in unstained cells between culture methods. A PE-conjugated isotype control that was a different clone (clone P3.6.2.8.1; eBiosciences) to the original isotype clone used in conjugation with DR5 and Fas antibodies was investigated in 2D-cultured and 3D alginate-cultured cells to exclude non-specific binding as a factor for increased background in 3D isotype controls compared to 2D.

3.2.5   Immunohistochemistry

3.2.5.1 Sample preparation

Hanging drop 3D spheroids for each cell line were carefully transferred into moulds containing a layer of optimal cutting temperature (OCT) compound (VWR) using Axygen 200 µL Wide-Bore pipette tips (Corning). For 3D spheroid colonies, either

whole alginate beads for each cell line at day 10 were transferred into moulds containing OCT, or the 3D spheroid colonies were dissociated from the alginate at day 10. These 3D spheroid colonies in suspension were centrifuged using a benchtop centrifuge at 700 g for 3 minutes and washed twice with PBS before the pellets from each cell line were placed into moulds containing a layer of OCT. Once 3D cultures were located centrally in the moulds they were covered with a layer of OCT and immediately flash frozen in liquid nitrogen before being stored at -80°C until cryostat sectioning.

3.2.5.2 Cryostat sectioning

Sections for immunocytochemistry were warmed to -20°C before being cut using the Leica 1950 UV cryostat (Leica Biosystems), set to -20°C, at a 5 and 10 µm thickness and mounted on a positively charged X-tra® adhesive slide (Leica Biosystems). The slides were fixed in ice cold methanol and then stored at -80°C in an airtight container until stained.

3.2.5.3 Optimisation and controls

MDA-MB-231 breast cancer cells known to express high levels of PD-L1 were used as a positive control for PD-L1 staining. Whilst MCF-7 breast cancer cells known to express negligible levels of PD-L1 were used as a negative control. Cytospins of 2D-cultured breast cancer cells were prepared on positively charged X-tra® adhesive slides and fixed in ice cold methanol for anti-PD-L1 (clone 29E.2A3; Biolegend) antibody optimisation. The following antibody dilutions were investigated: 1:25, 1:50, 1:100, 1:200, 1:400, 1:800. Cytospins for antibody-matched isotype controls and secondary antibody controls were also prepared for each experiment. After the antibody concentration was optimised, the need for a hydration step within the staining protocol was investigated by comparing stained samples that were stained and processed with and without a hydration step in the staining procedure. It was found that the inclusion of the hydration step improved the quality of the staining and was incorporated into the protocol.

3.2.5.4 PD-L1 staining

Sections were stained for PD-L1 expression according to the manufacturer's protocol (Mouse specific HRP/DAB (ABC) Detection Kit, Abcam). 5 and 10 µM sections were rehydrated in 1x Tris Buffered Saline (TBS) for 10 minutes before being treated with a hydrogen peroxide block for 10 minutes. The sections were washed with 1x TBS and further incubated for 10 minutes with a protein block applied. Sections were

washed 3 times with 1x TBS before being incubated for 1 hour with the anti-PD-L1 primary antibody (clone 29E.2A3; Biolegend) diluted 1 in 100 in 1x TBS containing 1% bovine serum albumin (BSA). After 4 washes in 1x TBS the sections were incubated for 10 minutes with biotinylated goat anti-mouse secondary antibody, followed by a further 10 minute incubation with streptavidin peroxidase and 5-minute incubation with 3,3-Diaminobenzidine (DAB). The latter incubation period is followed by 4 washes with 1X TBS and an additional wash step with deionised water, before performing a counterstain with haematoxylin. Sections were immersed in Mayer's haematoxylin (Leica Biosystems) for 1 minute and run under slow running tap water for 30 seconds. The sections were dehydrated in increasing concentrations of alcohol (75% ethanol twice for 5 minutes, 95% ethanol twice for 5 minutes, 100% ethanol twice for 5 minutes) and twice in xylene for 5 minutes before being mounted with a coverslip using DPX mounting medium (Sigma) and allowed to dry. Sections were visualised using an Olympus BX60 Microscope (Olympus). Images were captured using cellSens Imaging Software (Olympus Corporation).

3.2.6 Statistical analysis

Statistical analysis was performed using Prism version 7.03 (GraphPad Software, Inc.). A Shapiro-Wilk normality test was used to determine whether data had a parametric or non-parametric distribution. As the data was non-parametric, for data with 2 groups a Mann-Whitney U test was performed, otherwise, a Kruskal-Wallis with a Dunn's multiple comparisons test was utilised. Data was represented as median ± range. P-values less than 0.05 were considered significant (*P<0.05, **P<0.01, ***P<0.001 and ****P<0.0001). Each independent experiment has 3 technical repeats (n=3).

3.3 Results

3.3.1 Human breast, prostate and colorectal cancer cell lines form viable spheroids using the hanging drop method

Human breast, prostate and colorectal cancer cell lines were investigated to determine whether they could form 3D spheroids using the hanging drop method. Single hanging drop spheroids were harvested at day 3, 4, 5, 6 and 7 and then stained with Hoechst 33342/PI to assess cell viability on each day using fluorescence microscopy. All six cancer cell lines formed viable and intact spheroids from day 3 to day 7 (Figure 3.2). No necrotic core was observed in any of the hanging drop spheroids at each of the time points. Day 3 of culture when the spheroids had fully formed was the time point taken forwarded for investigating 3D spheroids.

At day 3, the 3D hanging drop spheroids of each cell line were highly viable (Figure 3.3A), and percentage viability was quantified (Figure 3.3B). MDA-MB-231, MCF-7, LNCaP, PC3, SW480 and SW620 cancer cell lines displayed a 99.56% (± 0.78), 99.61% (± 2.22), 99.5% (± 1.19), 99.85% (± 0.61), 99.82% (± 2.41) and 99.79% (± 0.5) viability, respectively. At day 3, the diameter of each spheroid was measured concurrently (Figure 3.3C). All cell lines formed hanging drop spheroids with a diameter between 500-1000 µm. The MCF-7 breast cancer cells formed the smallest spheroid diameter of 525.6 µm (± 116.5), whereas the other cancer cell lines formed spheroids of a similar diameter: MDA-MB-231 (830.1 µm ± 118), LNCaP (754.5 µm ± 193.5), PC3 (766.5 µm ± 210), SW480 (808.1 µm ± 148) and SW620 (889.3 µm ± 199.2).
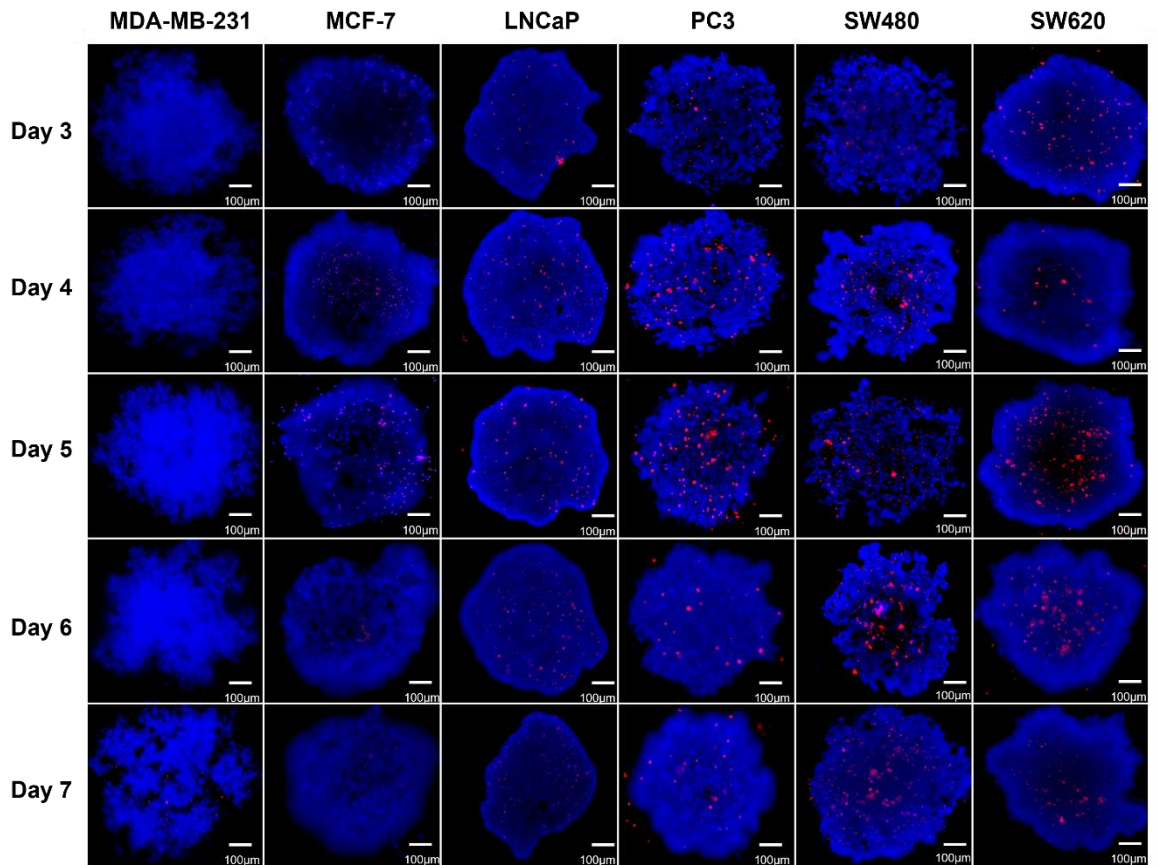
Figure 3.2 Human breast, prostate and colorectal cancer cell lines form viable hanging drop 3D spheroids. Hoechst 33342/PI staining and fluorescent microscopy was used to assess cell viability of hanging drop 3D spheroids from day 3 to 7. Blue Hoechst 33342 staining indicates viable cells, and red PI staining indicates dead cells. Scale bar represents 100 µm. n=4 independent experiments each with 3 technical repeats.
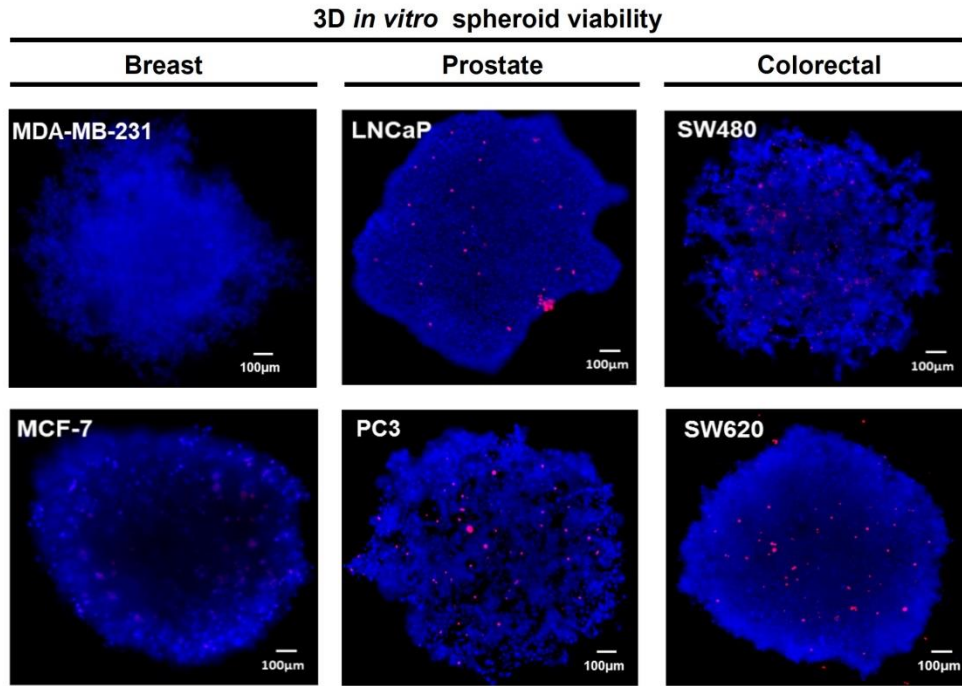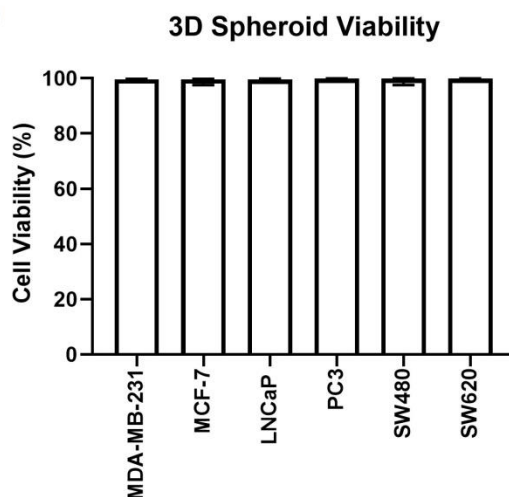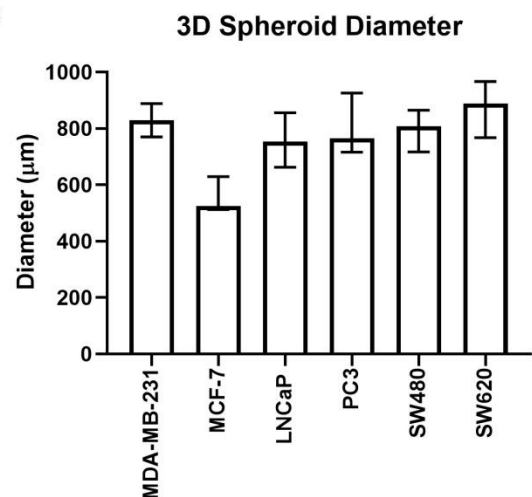
Figure 3.3 Each cancer cell line forms highly viable 3D spheroids of similar size at day 3 of culture. (A) Single hanging drop 3D spheroids were harvested at day 3 of culture and assessment was made of: cell viability using fluorescence microscopy following Hoechst 33342/PI staining (Scale bar represents 100 μm), **(B)** percentage of viable cells and **(C)** spheroid diameter. Data was presented as median ± range, n=4 independent experiments each with 3 technical repeats.

3.3.2 Human breast, prostate and colorectal cancer cell lines grow successfully in alginate hydrogel beads to form monoclonal spheroid colonies

After successfully being able to grow 3D cancer spheroids using a scaffold free-based method, it was next determined whether the six cancer cell lines would grow in scaffold-based alginate hydrogel beads. The ability of the cancer cells to proliferate from a single cell to form monoclonal 3D spheroid colonies was monitored at day 3, 6 and 10 by Hoechst 33342/PI staining via fluorescence microscopy (Figure 3.4). Here, all cancer cell lines grew successfully in the alginate hydrogel beads and remained highly viable over the 10 days in culture. Hoechst 33342/PI staining did not reveal areas of pronounced cell death caused by the fabrication procedure. The viability of cancer cell lines grown in alginate was quantified. Each cancer cell line displayed a median viability greater than 90% at day 3, 6 and 10 (Figure 3.5). Also, alginate hydrogel beads facilitated the formation of 3D spheroid colonies that reached a diameter of approximately 100-150 µm at day 10 for each cancer cell line (Figure 3.6). MCF-7 breast cancer cells demonstrated the smallest 3D spheroid colony diameter at day 10 (107.9 µm ± 26.7), followed by LNCaP (112.4 µm ± 41.82), SW620 (120.9 µm ± 26), MDA-MB-231 (121.7 µm ± 28.3), SW480 (126.7 µm ± 30.9), and finally PC3 cells which demonstrated the largest 3D spheroid colony diameter of 143.9 µm (± 53.8) at day 10.

Figure 3.4 Human breast, prostate and colorectal cancer cell lines grow in alginate hydrogel beads to form viable monoclonal 3D spheroid colonies at day 10. Human cancer cells encapsulated in alginate hydrogel were grown in culture for 10 days. Cell viability was assessed by Hoechst 33342/PI staining of cancer cells growing in alginate hydrogel at day 3, 6 and 10. Scale bar represents 500 µm. The white boxes represent spheroid colonies within the alginate at day 10 with a diameter greater than 100 µm. n=4 independent experiments each with 3 technical repeats.
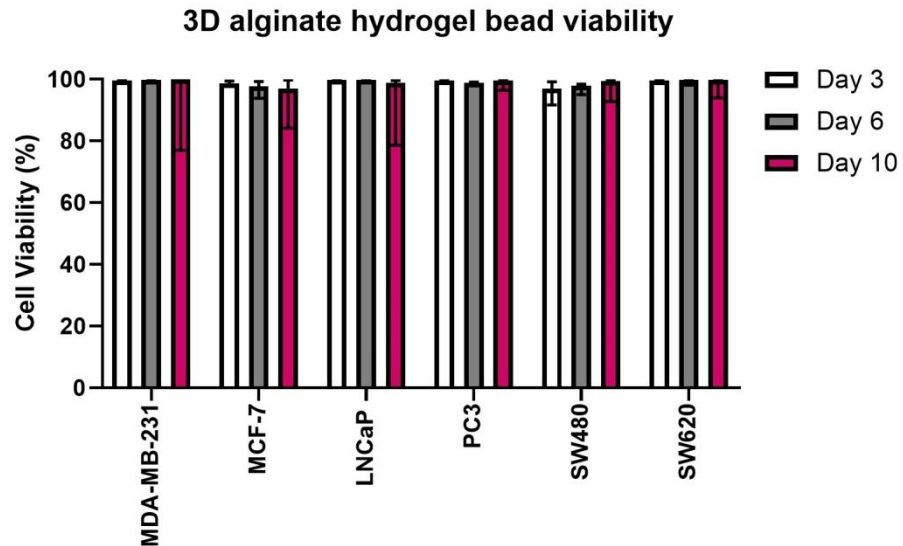
3D alginate hydrogel bead viability

Figure 3.5 Human breast, prostate, and colorectal cancer cell lines are highly viable in alginate hydrogel beads at day 3, 6 and 10. Hoechst 33342/PI and fluorescent microscopy were used to quantify the viability of cancer cells grown in alginate hydrogel beads for 3, 6 and 10 days. Data is presented as median ± range. n=4 independent experiments each with 3 technical repeats.

3D alginate spheroid colony diameter at day 10
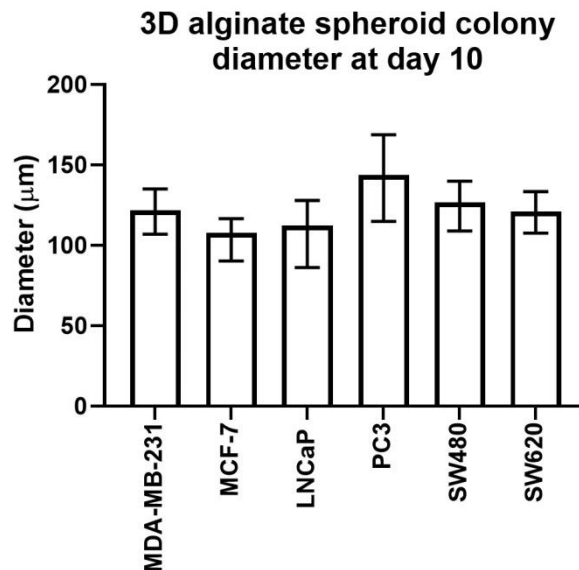
Figure 3.6 Human breast, prostate, and colorectal cancer 3D alginate spheroid colony diameters are greater than 100 µm at day 10. The diameters of individual 3D alginate spheroid colonies were measured after 10 days in culture. Data is presented as median ± range. n=4 independent experiments each with 3 technical repeats.

3.3.3 Hypoxia was detected in some cancer cell lines cultured in 3D hanging drop spheroids at day 3 and 3D alginate spheroid colonies at day 10

To determine whether 3D hanging drop spheroids at day 3 and 3D alginate spheroid colonies at day 10 developed a hypoxic environment, both 3D cultures were treated with a fluorogenic compound (Image-iT™ Hypoxia Reagent) that fluoresces in the presence of low oxygen concentrations. 3D cultures were stained concurrently with Hoechst 33342. 2D-cultured cells plated in 6-well plates for each cancer cell line were used as a negative control that represented normal oxygen concentrations and therefore no fluorescence was detected by these 2D-cultured cells (Figure 3.7).

In some 3D hanging drop spheroids however, fluorescence was detected demonstrating a hypoxic environment developing within these cultures at day 3 (Figure 3.8). MDA-MB-231 breast, PC3 prostate and SW480 and SW620 colorectal cancer cell 3D hanging drop spheroids all demonstrated a strong signal for low oxygen concentrations which was predominantly localised to the core of each of the 3D spheroids. For MCF-7 breast 3D hanging drop spheroids low oxygen levels were detected, located centrally to the core of the spheroid, but the signal was much weaker. In contrast, LNCaP prostate 3D hanging drop spheroids displayed normal levels of oxygen comparable to that of 2D-cultured LNCaP cells.

In 3D alginate spheroid colonies, fluorescent signals for low oxygen concentration were not detectable for each of the cancer cell lines, and therefore showed similar results to that of their 2D monolayer counterparts (Figure 3.9). To determine whether 3D spheroid colonies can display low oxygen concentrations and to exclude the alginate from acting as a barrier to entry of the fluorogenic compound used, 3D spheroid colonies were dissociated from the alginate, cultured overnight in 96-well ultra-low attachment plates, and assessed for low oxygen concentrations. When 3D spheroid colonies aggregated together forming aggregoids, low oxygen concentrations were detected in all cancer cell lines after less than 24 hours of being cultured (Figure 3.10).
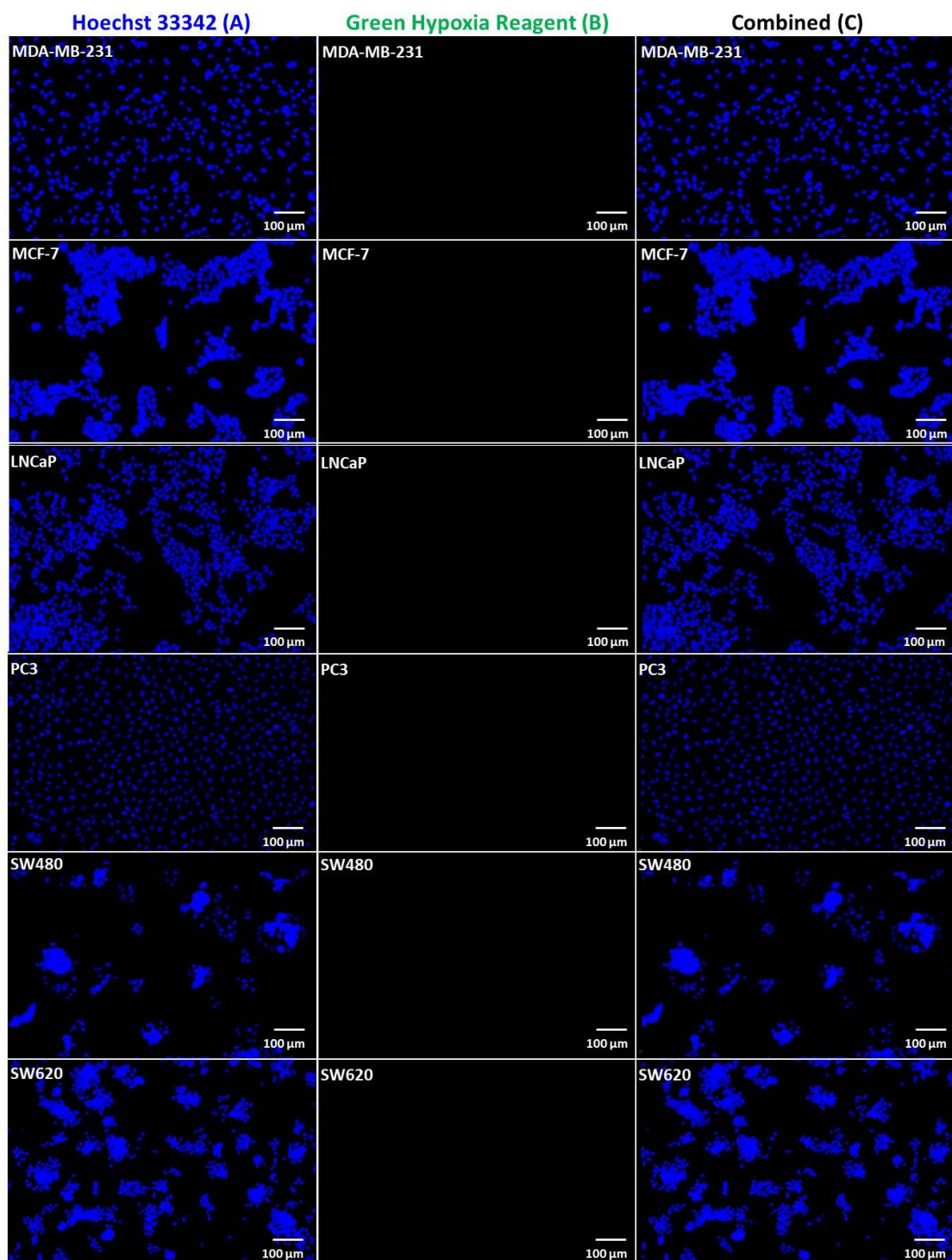
Figure 3.7 Normal oxygen concentrations were detected in 2D monolayer cultures of human breast, prostate, and colorectal cancer cells. (A) Hoechst 33342 (blue) and **(B)** hypoxia reagent (green) staining and fluorescent microscopy was used to assess cell viability and hypoxia, respectively. **(C)** Hoechst 33342 and hypoxia reagent-stained cells were shown combined. Scale bar represents 100 μm. n=1 independent experiment with 3 technical repeats.
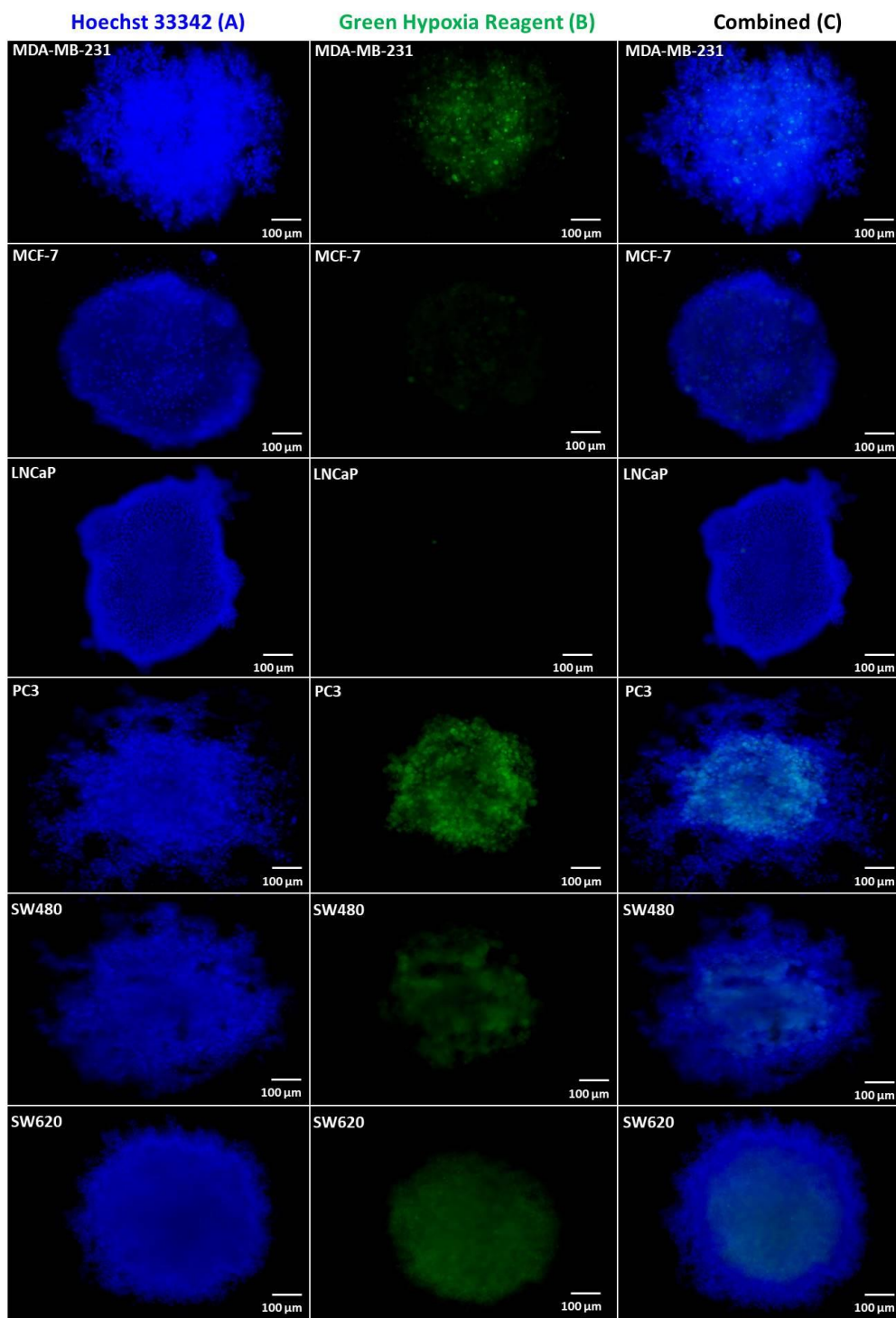
Figure 3.8 Hypoxia detected in most cancer cell lines cultured in 3D hanging drop spheroids at day 3. (A) Hoechst 33342 (blue) and **(B)** hypoxia reagent (green) staining and fluorescent microscopy was used to measure cell viability and hypoxia, respectively. **(C)** Hoechst 33342 and hypoxia reagent combined images show MDA-MB-231, MCF-7, PC3, SW480 and SW620 3D hanging drop spheroids had a hypoxic core. Scale bar represents 100 µm. n=1 independent experiment with 3 technical repeats.

3D Spheroid Colonies in Alginate Hydrogel Beads
Hoechst 33342/Hypoxia Reagent
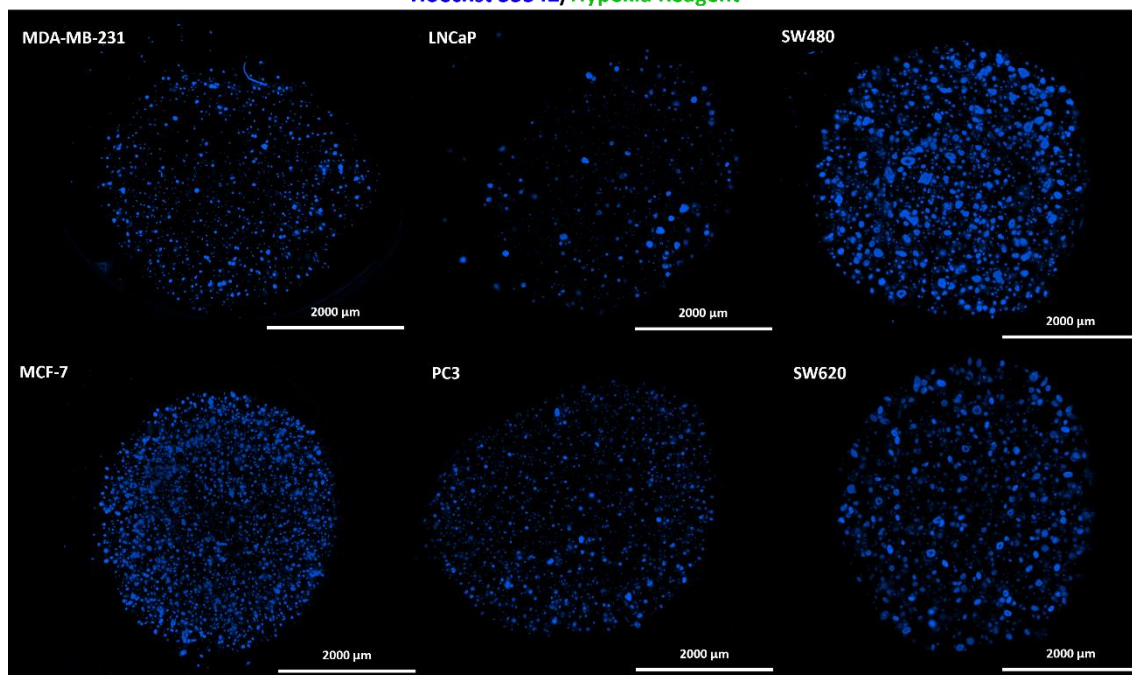
Figure 3.9 Hypoxia was not detected in images taken of whole alginate hydrogel beads at day 10. Hoechst 33342 (blue) and hypoxia reagent (green) staining and fluorescent microscopy was used to measure cell viability and hypoxia, respectively, in cancer cells grown in alginate hydrogel beads. No green fluorescence indicative of hypoxia was detected in any of the cell lines. Scale bar represents 100 µm. n=1 independent experiment with 3 technical repeats.

Figure 3.10 Hypoxia was detected in all cancer cell lines cultured in 3D spheroid colony aggregates. 3D spheroid colonies dissociated from the alginate hydrogel beads for each cancer cell line were cultured overnight before being stained with Hoechst 33342 (blue) and hypoxia reagent (green) and visualised by fluorescent microscopy. Each cell line showed a hypoxic region (green) within the aggregoids. Scale bar represents 100 µm. n=1 independent experiment with 3 technical repeats.

3.3.4 Hanging drop 3D cancer spheroids display altered PD-L1 expression when compared to cancer cell lines in 2D cell culture

The expression of PD-L1 at mRNA and protein levels was determined by RT-qPCR and flow cytometry, respectively, for all six human cancer cell lines grown in standard 2D cell culture and 3D hanging drop spheroids. Our data revealed that PD-L1 mRNA and/or protein expression altered in all human cancer cell lines grown in 3D spheroids compared to their 2D counterparts (Figure 3.11A-M and Table 3.2). Appropriate gating strategies were performed including single cell and live cell gating for each experiment (Figure 3.11A).

MDA-MB-231 breast cancer cells exhibited a significant decrease in the level of PD-L1 mRNA ($p=0.05$) (Figure 3.11B) and protein ($p=0.05$) (Figure 3.11C) expression in hanging drop 3D cell culture, compared to 2D-cultured cells. Meanwhile, in MCF-7 breast cancer cells displayed a significant increase ($p=0.05$) in the frequency of cells expressing PD-L1 in 3D cell culture, but the level of PD-L1 mRNA ($p=0.1$) (Figure 3.11D) and protein ($p=0.35$)(Figure 3.11E) expression was similar to 2D-cultured cells.

In the LNCaP prostate cancer cells they showed no difference in PD-L1 expression at mRNA level ($p=0.1$) (Figure 3.11F) but did display a significant increase ($p=0.05$) in the proportion of cells expressing PD-L1, and the level of PD-L1 protein on their cell surface in 3D cell culture compared to 2D (Figure 3.11G). PC3 prostate cancer cells demonstrated a significant decrease ($p=0.05$) in the level of PD-L1 expression at mRNA (Figure 3.11H) level and in the percentage of cells expressing cell surface PD-L1 (Figure 3.11I).

In the SW480 colorectal cancer cells they exhibited a significant decrease ($p=0.05$) in the mRNA level of PD-L1 (Figure 3.11J). Interestingly, the frequency of SW480 cells expressing PD-L1 and the level of PD-L1 protein on the cell surface significantly increased ($p=0.05$) in 3D cell culture (Figure 3.11K). SW620 colorectal cancer cells exhibit a significant increase ($p=0.05$) in the proportion of cells expressing PD-L1 and the level of PD-L1 protein on the cell surface in 3D (Figure 3.11M), but the level of PD-L1 mRNA expression was similar to 2D-cultured cells ($p=0.5$) (Figure 3.11L).
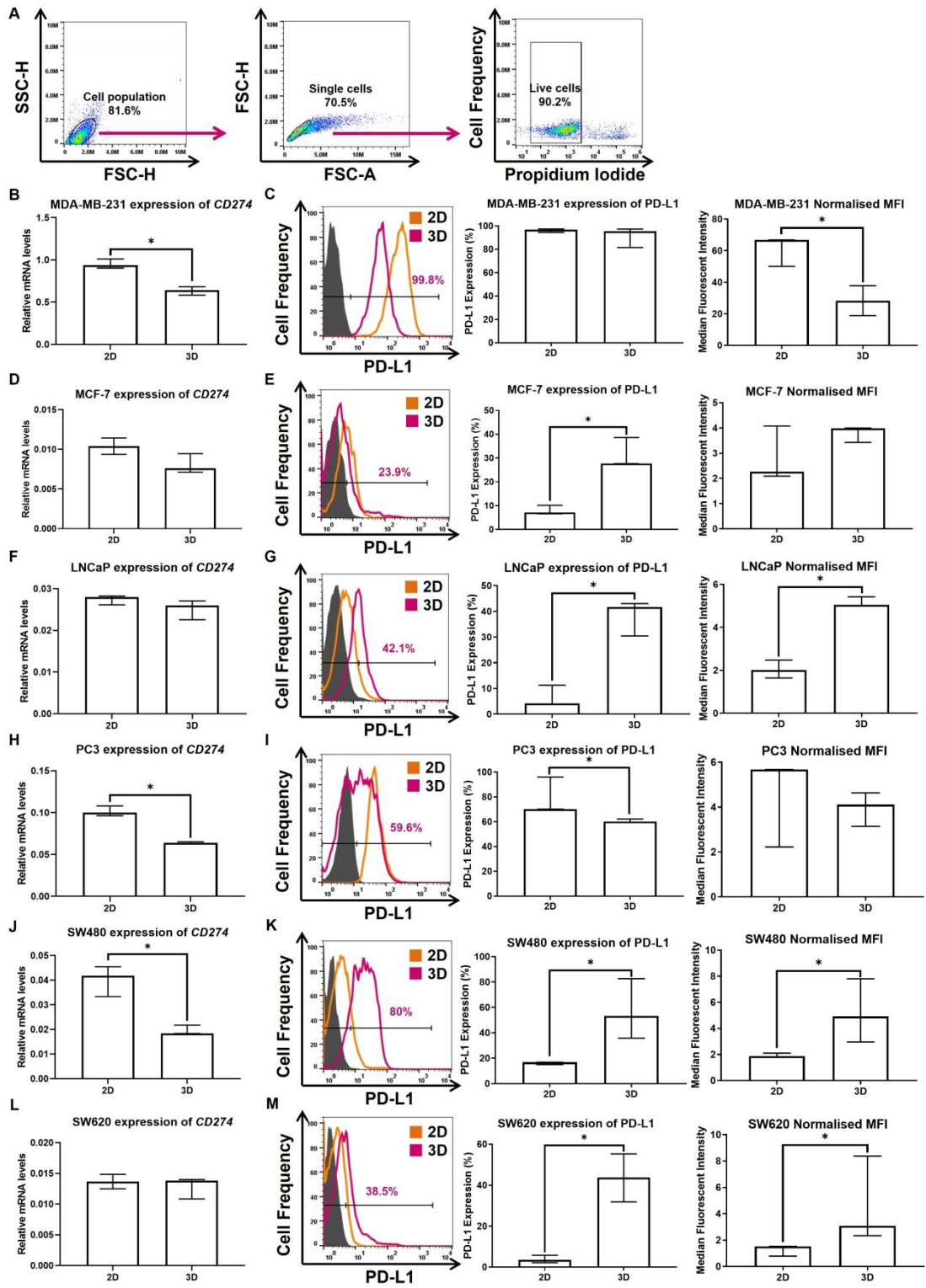
A

B MDA-MB-231 expression of *CD274*

C MDA-MB-231 expression of PD-L1 · MDA-MB-231 Normalised MFI

D MCF-7 expression of *CD274*

E MCF-7 expression of PD-L1 · MCF-7 Normalised MFI

F LNCaP expression of *CD274*

G LNCaP expression of PD-L1 · LNCaP Normalised MFI

H PC3 expression of *CD274*

I PC3 expression of PD-L1 · PC3 Normalised MFI

J SW480 expression of *CD274*

K SW480 expression of PD-L1 · SW480 Normalised MFI

L SW620 expression of *CD274*

M SW620 expression of PD-L1 · SW620 Normalised MFI

Figure 3.11 3D cancer hanging drop spheroids show altered PD-L1 mRNA and protein expression when compared to cancer cells cultured in 2D monolayers. PD-L1 mRNA and cell surface protein expression was measured by RT-qPCR and flow cytometry, respectively, in 2D-cultured cells and 3D hanging drop spheroids at day 3. **(A)** For flow cytometry, appropriate gating strategies including single cell and live cell gating were performed for each experiment. PD-L1 mRNA and cell surface protein expression was measured for MDA-MB-231 **(B, C)**, MCF-7 **(D, E)**, LNCaP (**F, G)**, PC3 (**H, I**), SW480 (**J, K**) and SW620 (**L, M**) at day 3. Representative flow cytometry histograms are displayed for each cell line showing the isotype control (grey) relative to the PD-L1 positive populations for cells grown in 2D (orange) and 3D (pink) cell culture. The percentage of PD-L1 positive cells (left) is shown alongside the normalised MFI (right) for each cell line. Data is presented as median ± range. n=3 independent experiments each with 3 technical repeats. Data was analysed by a Mann-Whitney U test (*P<0.05).

3.3.5 Cancer 3D spheroid colonies generated in alginate hydrogel beads exhibit altered PD-L1 expression compared to cancer cell lines in 2D cell culture

To evaluate whether the alterations observed in PD-L1 expression were consistent across different *in vitro* 3D cell culture models, we investigated the expression of PD-L1 at mRNA and protein levels in a second, more complex alginate hydrogel bead 3D cell culture model that incorporates a biologically inert scaffold and relies on clonal growth rather than aggregation of cells. For 3D spheroid colonies formed in alginate, PD-L1 expression at mRNA and protein level was assessed at day 3, 6 and 10 using RT-qPCR and flow cytometry, respectively (Figure 3.12A-M). PD-L1 expression in day 10 3D alginate spheroid colonies is summarised in Table 5. For flow cytometry experiments appropriate gating strategies were performed including single cell and live cell gating for each experiment (Figure 3.12A).

MDA-MB-231 breast cancer 3D spheroid colonies displayed a significant decrease in the frequency of cells expressing PD-L1 and the level of PD-L1 expressed at mRNA (Figure 3.12B) and protein (Figure 3.12C) levels over time, when compared to cells in standard 2D cell culture. MCF-7 breast cancer 3D spheroid colonies showed a significant decrease in the mRNA expression of PD-L1 at each time point (Figure 3.12D). However, they displayed a significant increase in the frequency of cells expressing cell surface PD-L1 at all time points in 3D in comparison to 2D-cultured cells (Figure 3.12E).

Similarly, LNCaP prostate cancer 3D spheroid colonies grown in alginate showed a significant decrease in PD-L1 mRNA (Figure 3.12F) and exhibited a significant increase in the frequency of cells expressing PD-L1 at each time point in 3D compared to 2D cell culture (Figure 3.12G). PC3 prostate cancer cells displayed a significant decrease in PD-L1 mRNA expression when grown in 3D spheroid colonies compared to 2D-cultured cells at all time points (Figure 3.12H). The proportion of cells expressing PD-L1 and the level at which PD-L1 protein was expressed in 3D spheroid colonies was comparable to that of 2D-cultured cells (Figure 3.12I).

Likewise, SW480 colorectal cancer cells grown in alginate displayed a significant decrease in PD-L1 mRNA expression compared to 2D-cultured cells at all time points (Figure 3.12J). The frequency of PD-L1 protein and MFI was similar to 2D-cultured cells when SW480 cells were grown in alginate (Figure 3.12K). Furthermore, SW620 colorectal cancer cells grown in 3D spheroid colonies exhibited a significant

124

decrease in PD-L1 mRNA expression at day 3 and 6 which was followed by a significant increase at day 10 compared to mRNA levels in 2D-cultured cells (Figure 3.12L). SW620 3D spheroid colonies also showed a significant increase in the frequency of cells expressing PD-L1 compared to 2D-cultured cells at day 10 (Figure 3.12M).

3.3.6 Immunohistochemical PD-L1 localisation within 3D hanging drop spheroids and 3D alginate spheroid colonies

To investigate the localisation of PD-L1 expression in 3D cultures, first the anti-PD-L1 antibody and staining method required optimisation. Different antibody concentrations were investigated (Appendix Figure 9.4) followed by the need for a hydration step in the staining protocol (Appendix Figure 9.5) using cytospins of MDA-MB-231 breast cancer cells expressing high levels of PD-L1 (positive control) and MCF-7 breast cancer cells expressing low levels of PD-L1 (negative control). Importantly, only haematoxylin stain was observed in the isotype control and secondary antibody control samples, indicating that the observed brown staining in these samples was due to the anti-human PD-L1 antibody binding specifically to PD-L1 on MDA-MB-231 breast cancer cells. The optimal PD-L1 antibody concentration was determined to be 1:100 dilution, and PD-L1 staining was improved with the incorporation of a hydration step.

Subsequently, cytospins of cancer cells and cryostat sections of 3D cultures were prepared and stained with anti-human PD-L1 antibody and Haematoxylin. Appropriate controls were used for each cell culture model investigated (Appendix Figure 9.6A-F) and 2D monolayer cells were stained concurrently (Appendix Figure 9.7A-F).

3.3.6.1 PD-L1 staining of 3D hanging drop spheroids

MDA-MB-231 3D hanging drop spheroids were too fragile to isolate intact spheroids for flash freezing, and to allow cryostat sections to be prepared and subsequent staining for PD-L1 expression. However, all the other cell lines formed individual 3D hanging drop spheroids, which could be harvested intact for downstream PD-L1 staining (Figure 3.13A-E).

MCF-7 (Figure 3.13A) and PC3 (Figure 3.13C) 3D hanging drop spheroids did not display detectable levels of PD-L1 via immunohistochemistry, comparable to their 2D monolayer counterparts. PD-L1 expression was detected on LNCaP (Figure 3.13B),

SW480 (Figure 3.13D) and SW620 (Figure 3.13E) cells cultured in 3D hanging drop spheroids. PD-L1 was detected throughout the 3D spheroids and not localised to a particular area.

3.3.6.2 PD-L1 staining of 3D alginate spheroid colonies

To assess PD-L1 staining within 3D alginate spheroid colonies, whole alginate beads were frozen, cryostat sectioned and assessed for PD-L1 expression and localisation via immunohistochemistry (Figure 3.14A-F). MDA-MB-231 3D spheroid colonies displayed the highest level of PD-L1 protein amongst all the cancer cell lines (Figure 3.14A).

A strong brown stain for PD-L1 was also found in PC3 3D spheroid colonies (Figure 3.14D), although this was not consistent throughout the alginate beads (Data not shown). In LNCaP (Figure 3.14C) and SW620 (Figure 3.14F) 3D spheroid colonies, the stain for PD-L1 was found to be the weakest amongst those found positive for PD-L1 via immunohistochemistry. PD-L1 expression by immunohistochemistry was not detected in MCF-7 (Figure 3.14B) and SW480 (Figure 3.14E) 3D spheroid colonies. Furthermore, in those cell lines that exhibited PD-L1 positivity by immunohistochemistry, they did not show any particular localisation of PD-L1 within the 3D spheroid colonies formed in alginate.
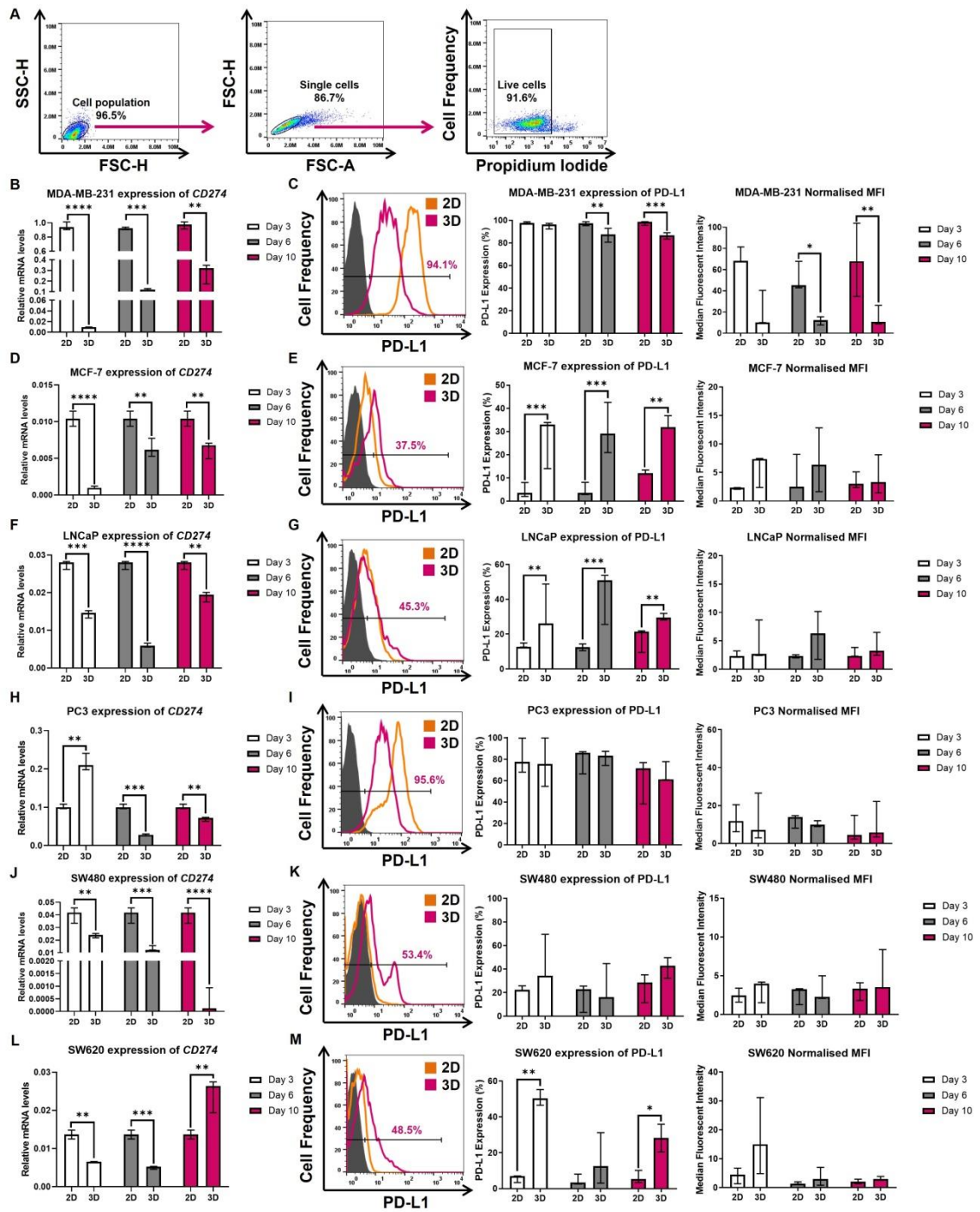
Figure 3.12 Cancer cell PD-L1 mRNA and protein expression in 3D alginate spheroid colonies was altered compared to cancer cells cultured in 2D monolayers. 3D alginate spheroid colonies and 2D-cultured cells were harvested at day 3, 6 and 10 and assessed for PD-L1 mRNA and cell surface protein expression using RT-qPCR and flow cytometry, respectively. **(A)** For flow cytometry, appropriate gating strategies including single cell and live cell gating were performed for each experiment. PD-L1 mRNA and cell surface protein expression was measured for MDA-MB-231 (**B, C**), MCF-7 (**D, E**), LNCaP (**F, G**), PC3 (**H, I**), SW480 (**J, K**) and SW620 (**L, M**) at day 3, 6 and 10. Representative flow cytometry histograms are displayed for each cell line showing the isotype control (grey) relative to the PD-L1 positive populations for cells grown in 2D (orange) and 3D (pink) cell culture. The percentage of cells expressing PD-L1 (left) is shown alongside the normalised MFI (right) for each cell line. Data is presented as median ± range. n=3 independent experiments each with 3 technical repeats. Data was analysed by a Kruskal-Wallis followed by Dunn's multiple comparisons test (*P<0.05, **P<0.01, ***P<0.001 and ****P<0.0001).

3D Hanging Drop Spheroids
Haematoxylin/PD-L1
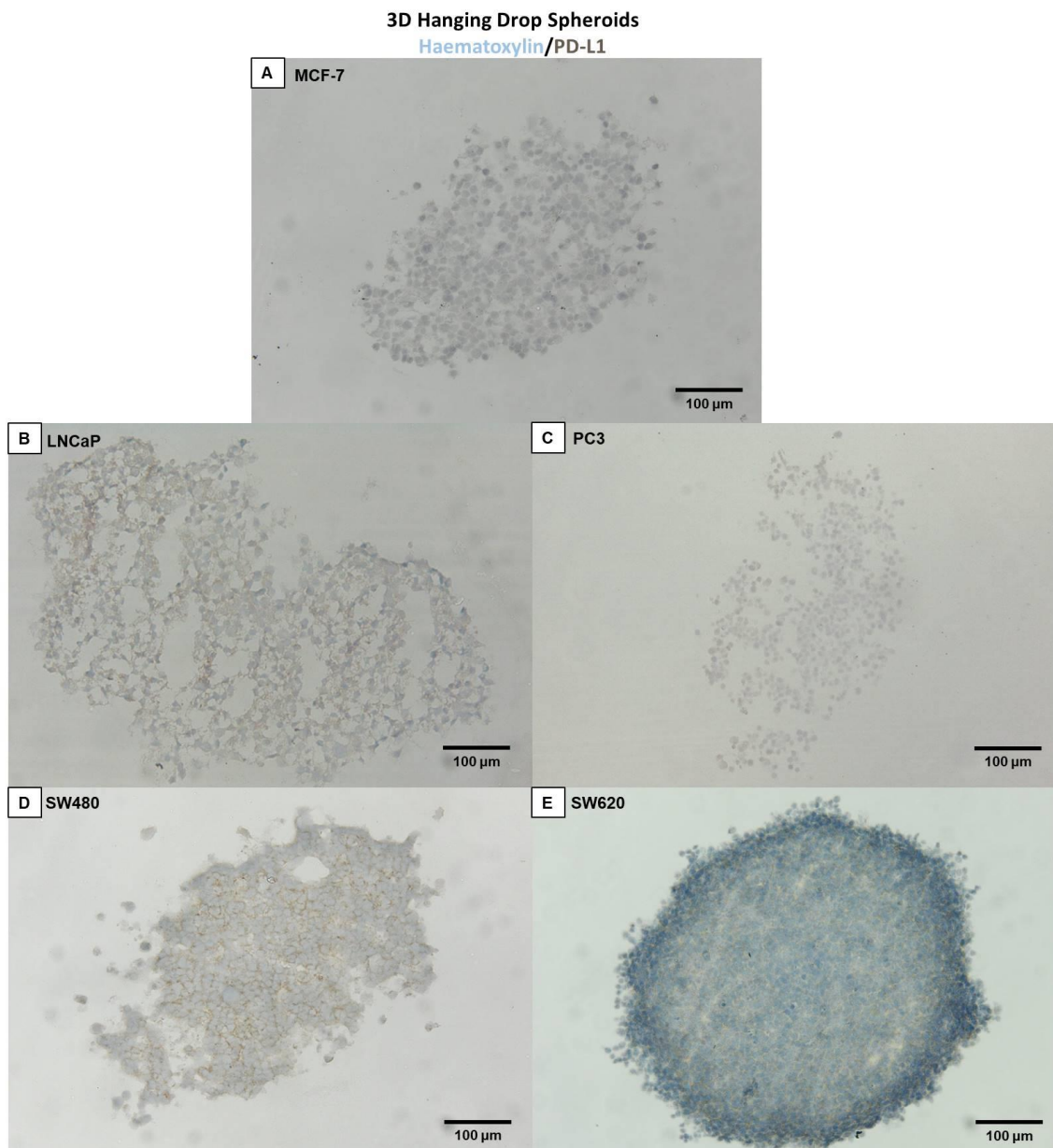
Figure 3.13 PD-L1 expression can be detected throughout LNCaP, SW480 and SW620 3D hanging drop spheroids. Immunohistochemical staining of PD-L1 was performed on MCF-7 **(A)**, LNCaP **(B)**, PC3 **(C)**, SW480 **(D)** and SW620 **(E)** cancer cells cultured in 3D hanging drop spheroids for 3 days to assess PD-L1 localisation. Scale bar represents 100 μm. n=3 independent experiments, each with 3 technical repeats.
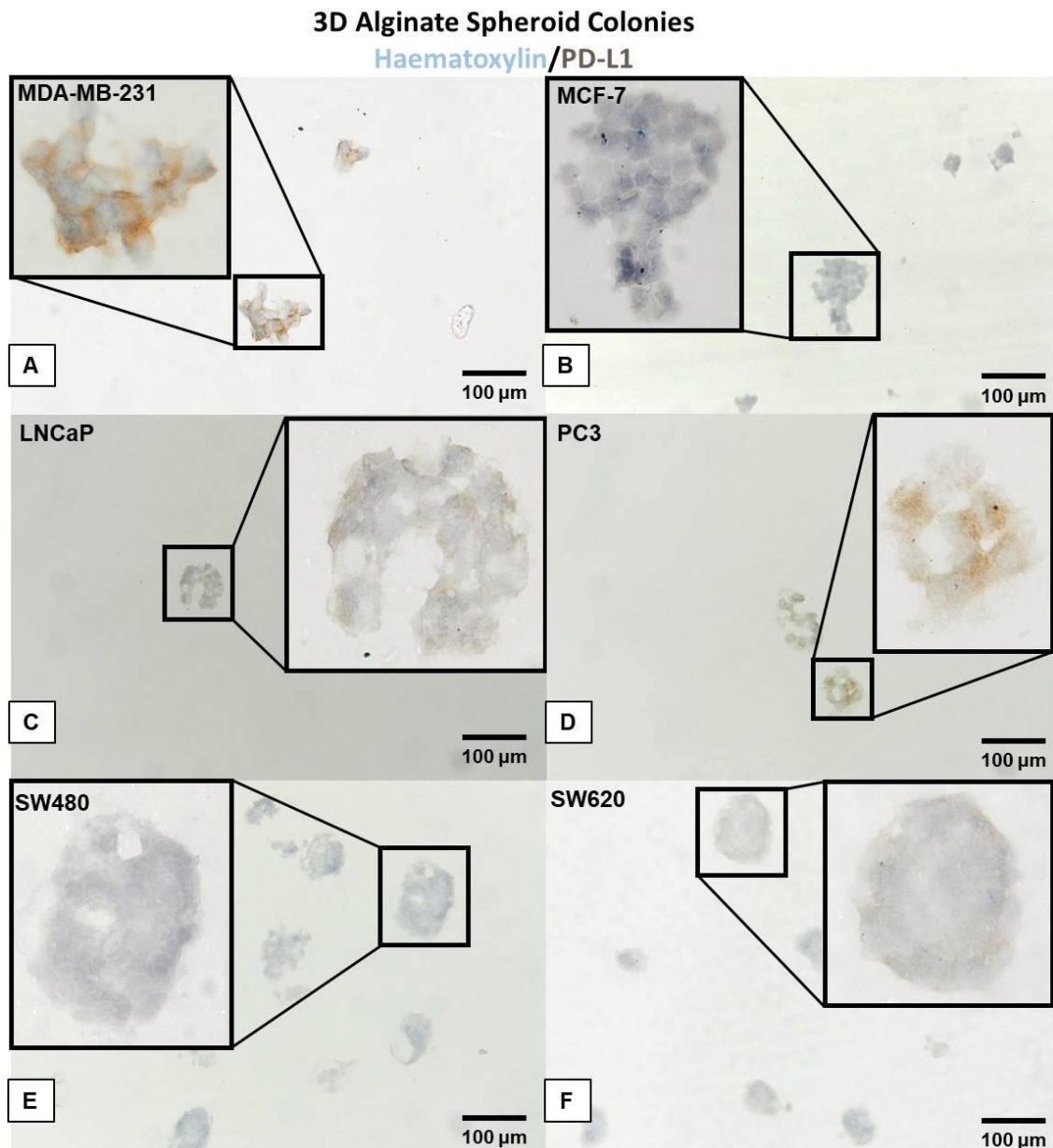
3D Alginate Spheroid Colonies
Haematoxylin/PD-L1

Figure 3.14 PD-L1 expression can be detected throughout MDA-MB-231, LNCaP, PC3, and SW620 3D alginate spheroid colonies. Immunohistochemical staining of PD-L1 was performed on MDA-MB-231 **(A)**, MCF-7 **(B)**, LNCaP **(C)**, PC3 **(D)**, SW480 **(E)** and SW620 **(F)** cancer cells cultured in 3D alginate spheroid colonies for 10 days to assess PD-L1 localisation. Images of whole alginate bead sections were captured. Single 3D spheroid colonies in the black box were taken using the 40X objective. Scale bar represents 100 μm. n=3 independent experiments each with 3 technical repeats.

3.3.7 Human breast, prostate, and colorectal cancer cell lines express altered levels of immunological and tumorigenic markers in 3D cell culture models compared to their 2D monolayer counterparts

Since PD-L1 mRNA and protein expression by cancer cell lines altered in 3D cell culture models when compared to their 2D monolayer counterparts, it was next determined whether the expression of other immunological (PD-1, PD-L2, HLA-ABC, DR4, DR5 and Fas) and tumorigenic (CD44 and HIF1α) markers at mRNA and/or protein levels changed in a 3D cell culture environment compared to 2D-cultured cells.

For 3D spheroids formed by hanging drop, the expression of immunological and tumorigenic markers was assessed and compared to 2D-cultured cells at day 3, whereas for 3D spheroid colonies formed in alginate, the expression of these markers was assessed and compared to 2D-cultured cells at day 10. Single cell gating was performed for all flow cytometry experiments as shown above (Section 3.3.4 and 3.5.5).

3.3.7.1 PD-1 expression was found in a higher proportion of SW480 colorectal cancer cells cultured in 3D spheroid colonies compared to 2D

As observed in Chapter 2 Figure 2.3, colorectal cancer cell lines, SW480 and SW620, were the only cells found to express PD-1 in 2D cell culture at mRNA level (Figure 3.15A and Table 3.2). Also, the level of PD-1 mRNA expressed by SW480 and SW620 cells in 3D cell culture models was comparable to that of 2D-cultured cells. SW620 cells were found not to express detectable levels of cell surface PD-1 in 2D cell culture and neither did cells in either 3D cell culture models (Figure 3.15B and C). Interestingly, SW480 cells displayed a significant increase in the frequency and MFI of PD-1 expression when cultured in 3D spheroid colonies formed in alginate compared to their 2D monolayer counterparts. However, in 3D hanging drop spheroids, SW480 cells no longer displayed detectable levels of cell surface PD-1 compared to 2D-cultured cells. Representative flow cytometry plots showing the expression of PD-1 in 3D hanging drop spheroids and alginate 3D spheroid colonies compared to 2D-cultured cells are found in Figure 3.16A and B, respectively.
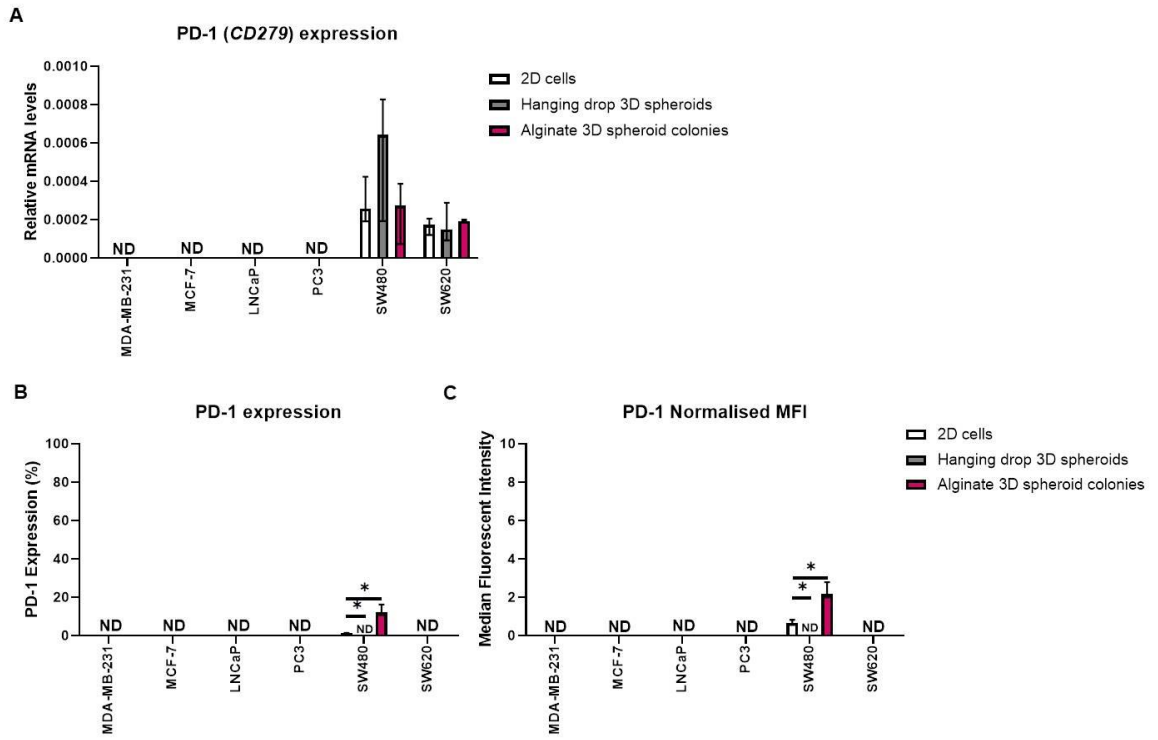
Figure 3.15 SW480 cells express an increased frequency and MFI of PD-1 protein expression in 3D spheroid colonies compared to 2D-cultured cells. PD-1 **(A)** gene and **(B, C)** protein expression was measured in cancer cells cultured in 2D monolayer, 3D hanging drop spheroids and 3D alginate spheroid colonies. **(B)** Shows the percentage of PD-1 expression and **(C)** shows the MFI for each cell line. Data is presented as median ± range. n=3 independent experiments each with 3 technical repeats. Data was analysed by a Kruskal-Wallis followed by Dunn's multiple comparisons test (*P<0.05). ND indicates gene or protein expression not detected.
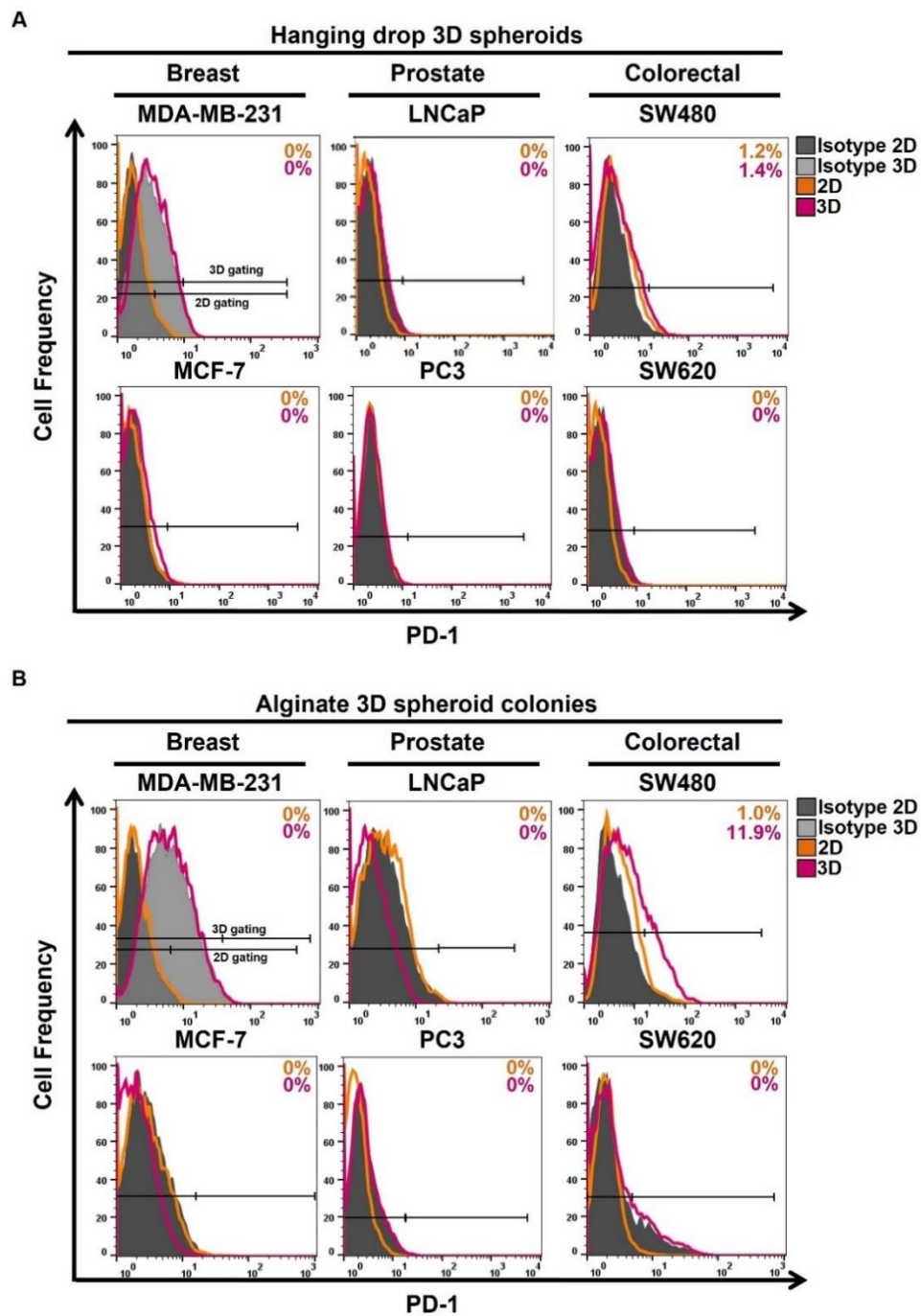
Figure 3.16 Representative flow cytometry plots display PD-1 expression amongst cancer cell lines in 2D and 3D cell culture models. Representative flow cytometry histograms are displayed for **(A)** 3D hanging drop spheroids (pink) and **(B)** 3D alginate spheroid colonies (pink) to show PD-1 positive populations relative to the isotype control (grey) and 2D monolayer cells (orange). Histograms for MDA-MB-231 3D cultures are presented with both 2D and 3D (light grey) isotype controls. n=3 independent experiments each with 3 technical repeats.

3.3.7.2 PD-L2 expression was significantly decreased in MDA-MB-231 and PC3 cancer cells cultured in 3D cell culture models compared to 2D cell culture

Human breast, prostate and colorectal cancer cell lines displayed differential expression of PD-L2 at mRNA (Figure 3.17A) and protein (Figure 3.17B and C) levels in 2D cell culture compared to in 3D cell culture models (Table 5). Representative flow cytometry histograms illustrate the expression of PD-L2 in 3D hanging drop spheroids (Figure 3.18A) and alginate 3D spheroid colonies (Figure 3.18B) compared to 2D-cultured cells.

MDA-MB-231 breast cancer cells displayed a significant reduction in the level of PD-L2 mRNA and in the proportion of cells expressing cell surface PD-L2 in both 3D cell culture models compared to 2D-cultured cells. In 3D spheroids formed by hanging drop, MDA-MB-231 cells displayed a greater decrease in PD-L2 mRNA compared to 2D-cultured cells than 3D spheroid colonies formed in alginate. In terms of the percentage of cells expressing PD-L2 and the MFI of PD-L2 protein expression, the variability in its expression between experiments in 3D hanging drop spheroids is less than that of 3D alginate spheroid colonies.

In contrast, PC3 prostate cancer cells showed a greater decrease in PD-L2 mRNA when cultured in 3D alginate spheroid colonies when compared to 3D hanging drop spheroids and 2D-cultured cells, although PD-L2 mRNA expression was still significantly reduced in 3D hanging drop spheroids compared to 2D-cultured cells. Additionally, PC3 cells did not display any significant changes in cell surface PD-L2 expression.

MCF-7 breast, and SW480 colorectal cancer cells displayed comparable levels of PD-L2 expression at mRNA and protein levels in 2D and 3D cell culture models. Similar to findings in Chapter 2 Figure 2.4, LNCaP prostate, and SW620 colorectal cancer cells exhibited no detectable levels of PD-L2 expression at mRNA and protein levels in 2D cell culture which was also found to be the case when these cancer cells were cultured in 3D cell culture models.
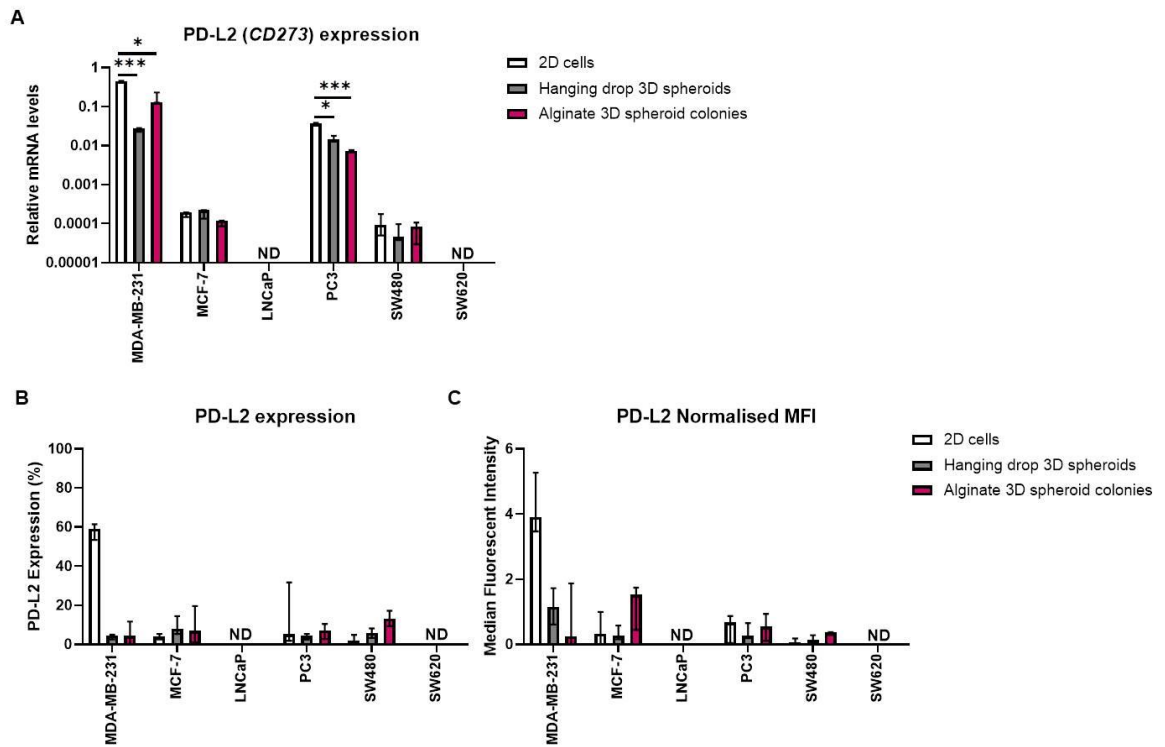
Figure 3.17 MDA-MB-231 and PC3 cells display decreased PD-L2 mRNA and/or protein expression in 3D cell culture models compared to 2D-cultured cells. PD-L2 **(A)** gene and **(B, C)** protein expression was measured in cancer cells cultured in 2D monolayer, 3D hanging drop spheroids and 3D alginate spheroid colonies. **(B)** Shows the percentage of PD-L2 expression and **(C)** shows the MFI for each cell line. Data is presented as median ± range. n=3 independent experiments each with 3 technical repeats. Data was analysed by a Kruskal-Wallis followed by Dunn's multiple comparisons test (*P<0.05 and ***P<0.001). ND indicates gene or protein expression was not detectable.

Figure 3.18 Representative flow cytometry plots display PD-L2 expression amongst cancer cell lines in 2D and 3D cell culture models. Representative flow cytometry histograms are displayed for **(A)** 3D hanging drop spheroids (pink) and **(B)** 3D alginate spheroid colonies (pink) to show PD-L2 positive populations relative to the isotype control (grey) and 2D monolayer cells (orange). n=3 independent experiments each with 3 technical repeats.

3.3.7.3 Human MCF-7 breast cancer cells cultured in 3D cell culture models display reduced HLA-ABC protein expression compared to 2D-cultured cells

Human MCF-7 breast cancer cells displayed a significant reduction in the proportion of cells expressing HLA-ABC protein in both 3D cell culture models compared to their 2D monolayer counterparts (Figure 3.19A and Table 3.2). The proportion of HLA-ABC-expressing cells was lower in MCF-7 cells cultured in 3D hanging drop spheroids than 3D alginate spheroid colonies.

For LNCaP prostate and SW480 colorectal cancer cells, the proportion of HLA-ABC expressing cells was reduced in both 3D cell culture models but due to variation in HLA-ABC protein expression between independent experiments no statistically significant alterations could be observed for these cells.

For MDA-MB-231 breast, PC3 prostate and SW620 colorectal cancer cell lines the proportion of HLA-ABC expressing cells was comparable to that of 2D-cultured cells. The MFI of HLA-ABC expression in 3D-cultured cells was comparable to that of 2D-cultured cells for all cancer cell lines (Figure 3.19B and Table 3.2). Representative flow cytometry histograms illustrate the expression of HLA-ABC protein in 3D hanging drop spheroids (Figure 3.20A) and alginate 3D spheroid colonies (Figure 3.20B) compared to 2D-cultured cells.
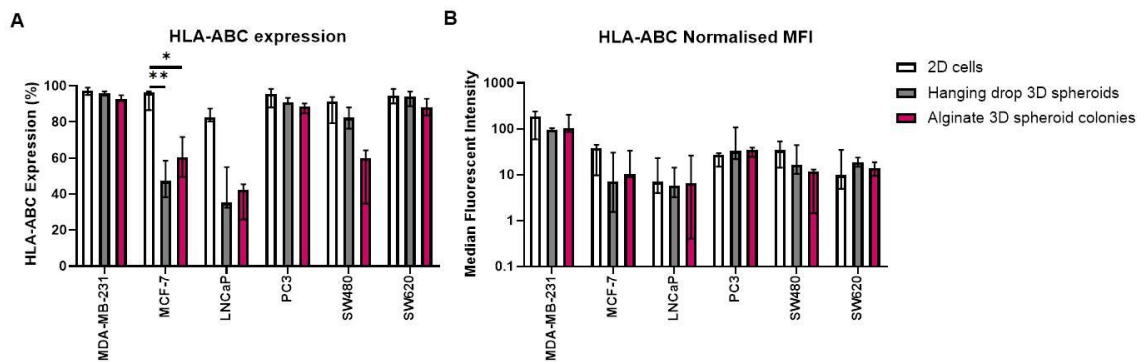
Figure 3.19 The frequency of HLA-ABC expression on MCF-7 cells is significantly reduced in 3D cell culture models compared to 2D-cultured cells. HLA-ABC protein expression was measured on cancer cells cultured in 2D cell culture, 3D hanging drop spheroids and 3D alginate spheroid colonies. **(A)** Shows the percentage of HLA-ABC expression and **(B)** shows the MFI for each cell line. Data is presented as median ± range. n=3 independent experiments each with 3 technical repeats. Data was analysed by a Kruskal-Wallis followed by Dunn's multiple comparisons test (*P<0.05 and **P<0.01).
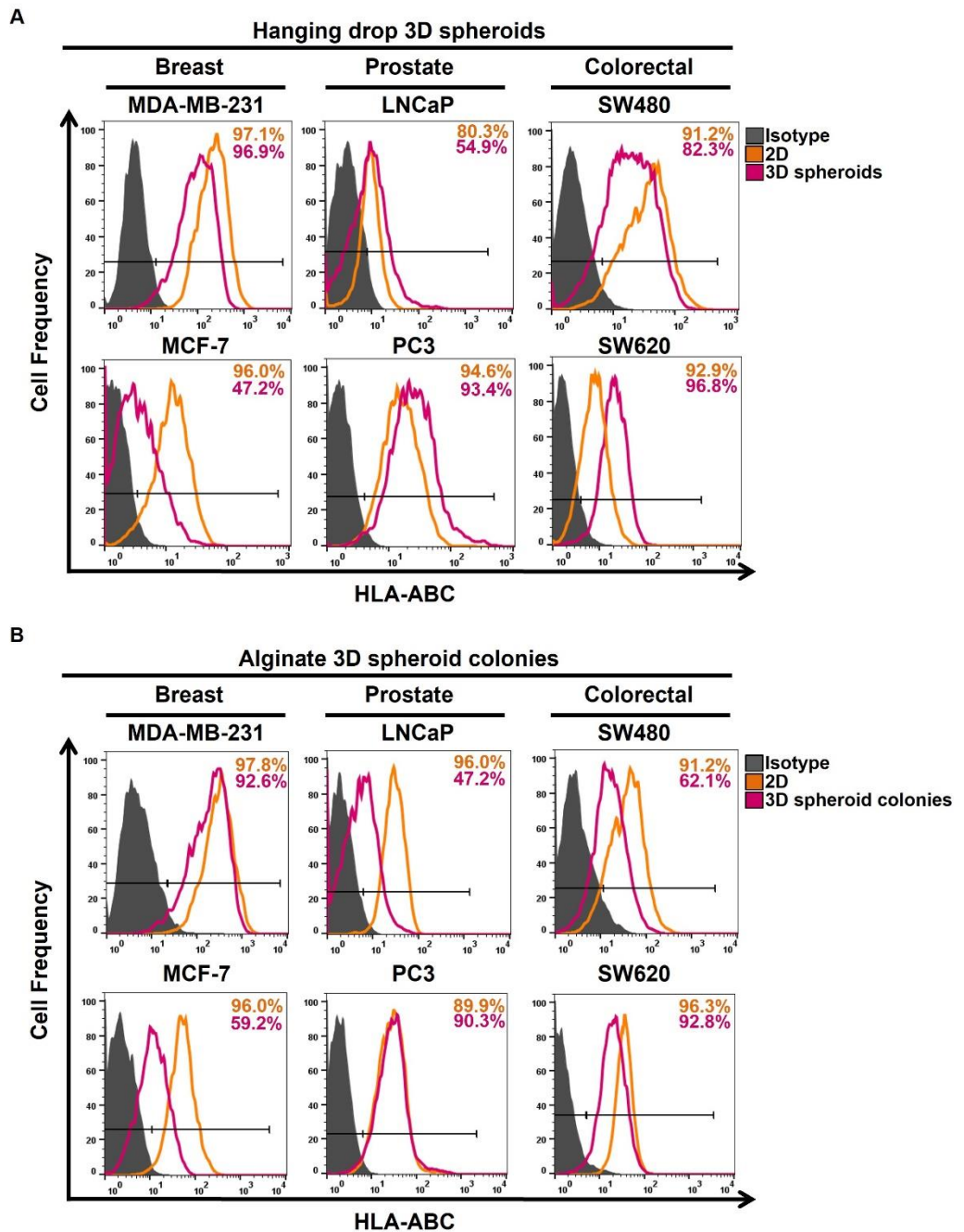
Figure 3.20 Representative flow cytometry plots display cell surface HLA-ABC expression amongst cancer cell lines in 2D and 3D cell culture models. Representative flow cytometry histograms are displayed for **(A)** 3D hanging drop spheroids (pink) and **(B)** 3D alginate spheroid colonies (pink) to show HLA-ABC positive populations relative to the isotype control (grey) and 2D monolayer cells (orange). n=3 independent experiments each with 3 technical repeats.

3.3.7.4 Some cancer cells expressed altered levels of death receptors in 3D cell culture models compared to their 2D monolayer counterparts

To further characterise cancer cells in 3D cell culture models and determine whether their immunogenic status alters in a 3D environment compared to in 2D monolayer cell culture, the expression of DR4, DR5, and Fas by cancer cell lines was measured following culture in 3D hanging drop spheroids for 3 days and 3D alginate spheroid colonies for 10 days.

3.3.7.4.1 DR4 expression in 3D cell culture models compared to 2D-cultured cells

The altered expression of DR4 mRNA and protein by cancer cell lines observed in 3D cell culture models compared to 2D-cultured cells differs depending on the 3D cell culture model used and cancer cell lineage (Figure 3.21A-C and Table 3.2). MDA-MB-231 breast cancer cells displayed a significant increase in DR4 mRNA expression when cultured in 3D hanging drop spheroids compared to 2D-cultured cells, but when cultured in 3D alginate spheroid colonies DR4 mRNA expression was found to be significantly reduced compared to 2D-cultured cells (Figure 3.21A). In contrast, MCF-7 breast cancer cells showed similar significant alterations to downregulate DR4 mRNA expression in each of the 3D cell culture models compared to their 2D monolayer counterparts. MDA-MB-231 and MCF-7 cells did not however show any significant alterations to DR4 protein expression (Figure 3.21B and 3.21C).

LNCaP prostate cancer cells demonstrated a significant decrease in DR4 mRNA expression when cultured in 3D hanging drop spheroids compared to 2D-cultured cells, whereas DR4 mRNA expression was shown to be significantly increased in 3D alginate spheroid colonies compared to 2D-cultured cells. However, LNCaP DR4 protein expression did not alter in either 3D cell culture model. Whilst PC3 prostate cancer cells demonstrated no statistically significant change to DR4 mRNA expression in 3D cell culture models. They were the only cancer cells that showed a significantly reduced proportion of cells expressing DR4 protein compared to 2D-cultured cells.

Finally, the SW480 and SW60 colorectal cancer cells cultured in 3D cell culture models displayed comparable DR4 expression at mRNA and protein levels compared to 2D-cultured cells. Representative flow cytometry histograms illustrating the expression of DR4 in 3D hanging drop spheroids and alginate 3D spheroid colonies compared to 2D-cultured cells are shown in Figure 3.22A and B.

Figure 3.21 DR4 mRNA and/or protein expression is significantly altered in some cancer cell lines cultured in 3D cell culture models compared to their 2D monolayer counterparts. DR4 **(A)** gene and **(B, C)** protein expression was measured in cancer cells cultured in 2D cell culture, 3D hanging drop spheroids and 3D alginate spheroid colonies. **(B)** Shows the percentage of DR4 expression and **(C)** shows the MFI for each cell line. Data is presented as median ± range. n=3 independent experiments each with 3 technical repeats. Data was analysed by a Kruskal-Wallis followed by Dunn's multiple comparisons test (*P<0.05, **P<0.01 and ***P<0.001).

Figure 3.22 Representative flow cytometry plots display DR4 protein expression amongst cancer cell lines in 2D and 3D cell culture models. Representative flow cytometry histograms are displayed for **(A)** 3D hanging drop spheroids (pink) and **(B)** 3D alginate spheroid colonies (pink) to show DR4 positive populations relative to the isotype control (grey) and 2D monolayer cells (orange). n=3 independent experiments each with 3 technical repeats.

3.3.7.4.2 DR5 expression in 3D cell culture models compared to 2D-cultured cells

DR5 expression was only found to be significantly altered in MDA-MB-231 breast cancer cells cultured in 3D cell culture models compared to 2D-cultured cells at mRNA (Figure 3.23A) and protein (Figure 3.23B and C) levels out of all the six cancer cell lines investigated (Table 3.2).

MDA-MB-231 cells in 3D hanging drop spheroids demonstrated a significant increase in DR5 mRNA expression compared to 2D-cultured cells, whereas in 3D alginate spheroid colonies DR5 mRNA expression was significantly decreased compared to 2D-cultured cells. Interestingly, the proportion of MDA-MB-231 cells expressing DR5 protein was significantly decreased in both 3D cell culture models, although more so when the cells were cultured in the 3D alginate spheroid colonies. Representative flow cytometry histograms illustrate the expression of DR5 in 3D hanging drop spheroids (Figure 3.24A) and alginate 3D spheroid colonies (Figure 3.24B) compared to 2D-cultured cells for all cancer cell lines.
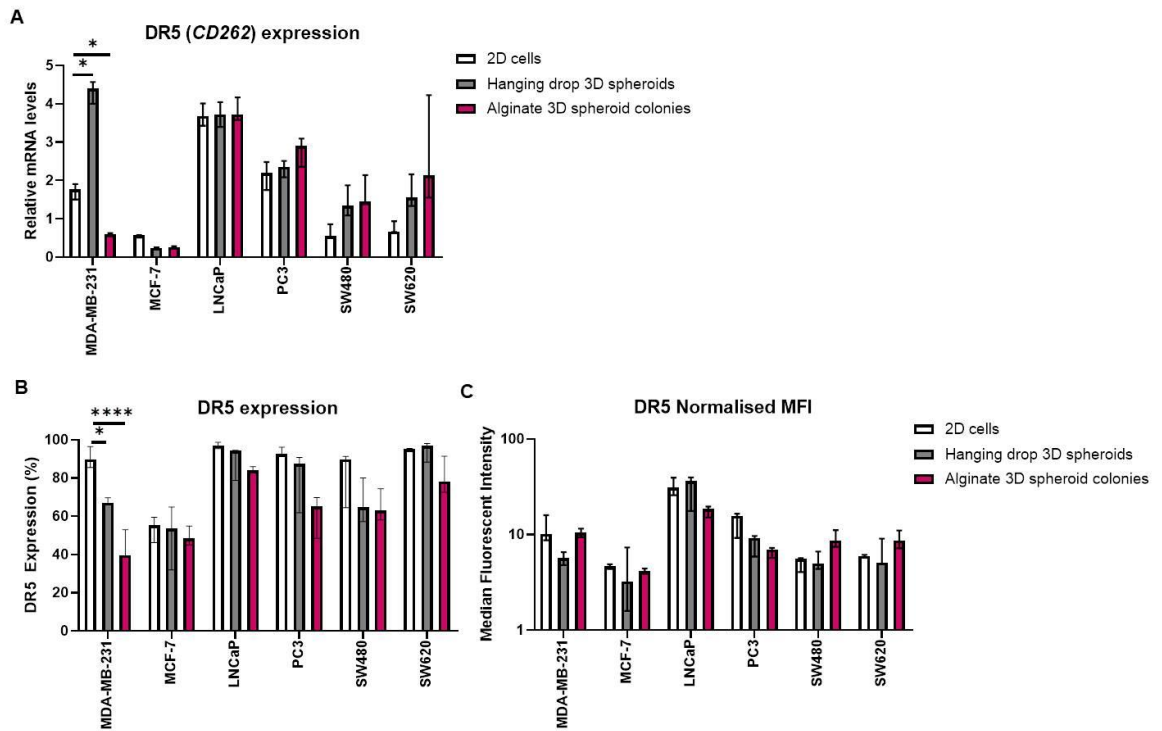
Figure 3.23 MDA-MB-231 cells display altered DR5 expression in 3D cell culture models compared to their monolayer counterparts. DR5 **(A)** gene and **(B, C)** protein expression was measured in cancer cells cultured in 2D cell culture, 3D hanging drop spheroids and 3D alginate spheroid colonies. **(B)** Shows the percentage of DR4 expression and **(C)** the MFI for each cell line. Data is presented as median ± range. n=3 independent experiments each with 3 technical repeats. Data was analysed by a Kruskal-Wallis followed by Dunn's multiple comparisons test (*P<0.05 and ****P<0.0001).
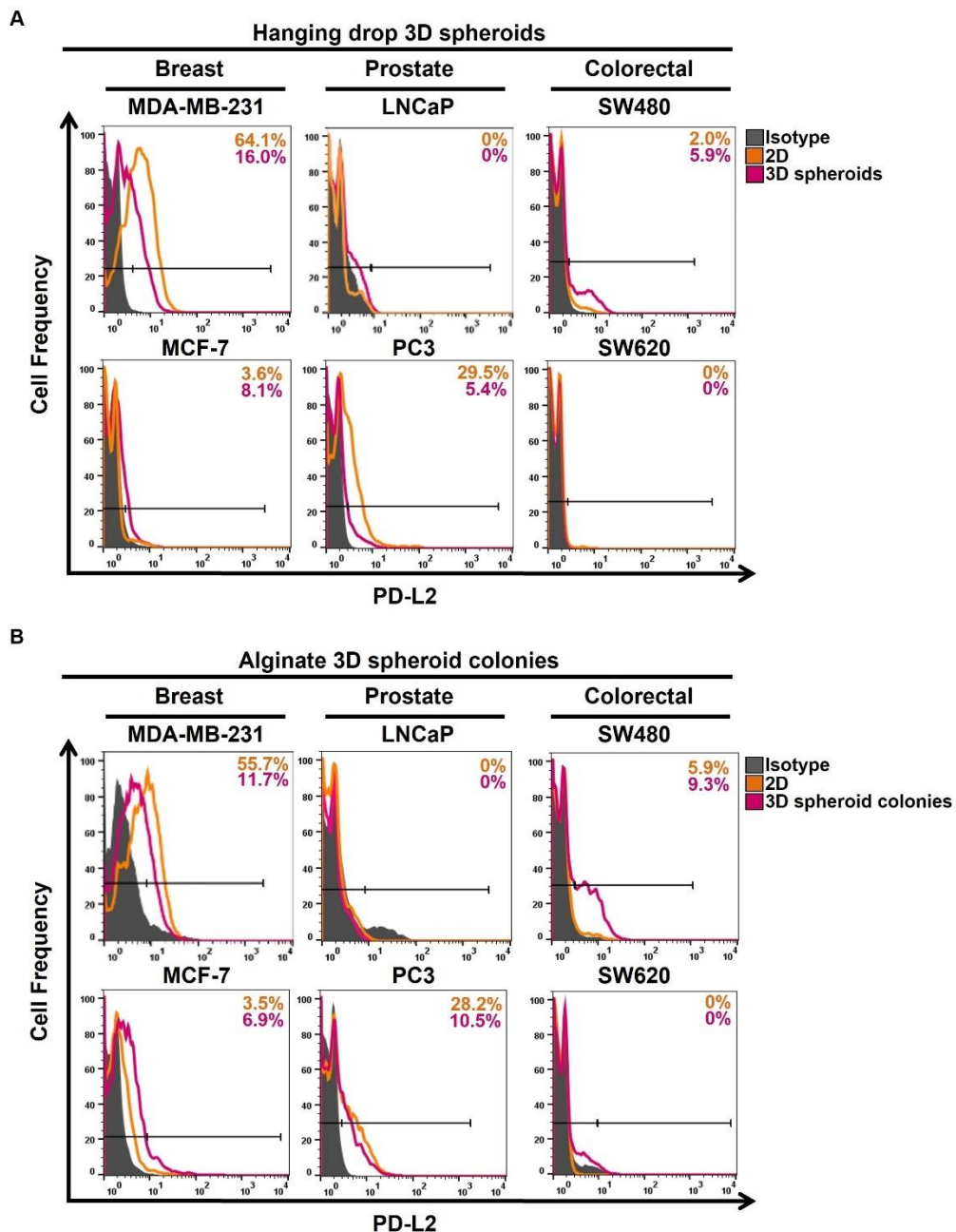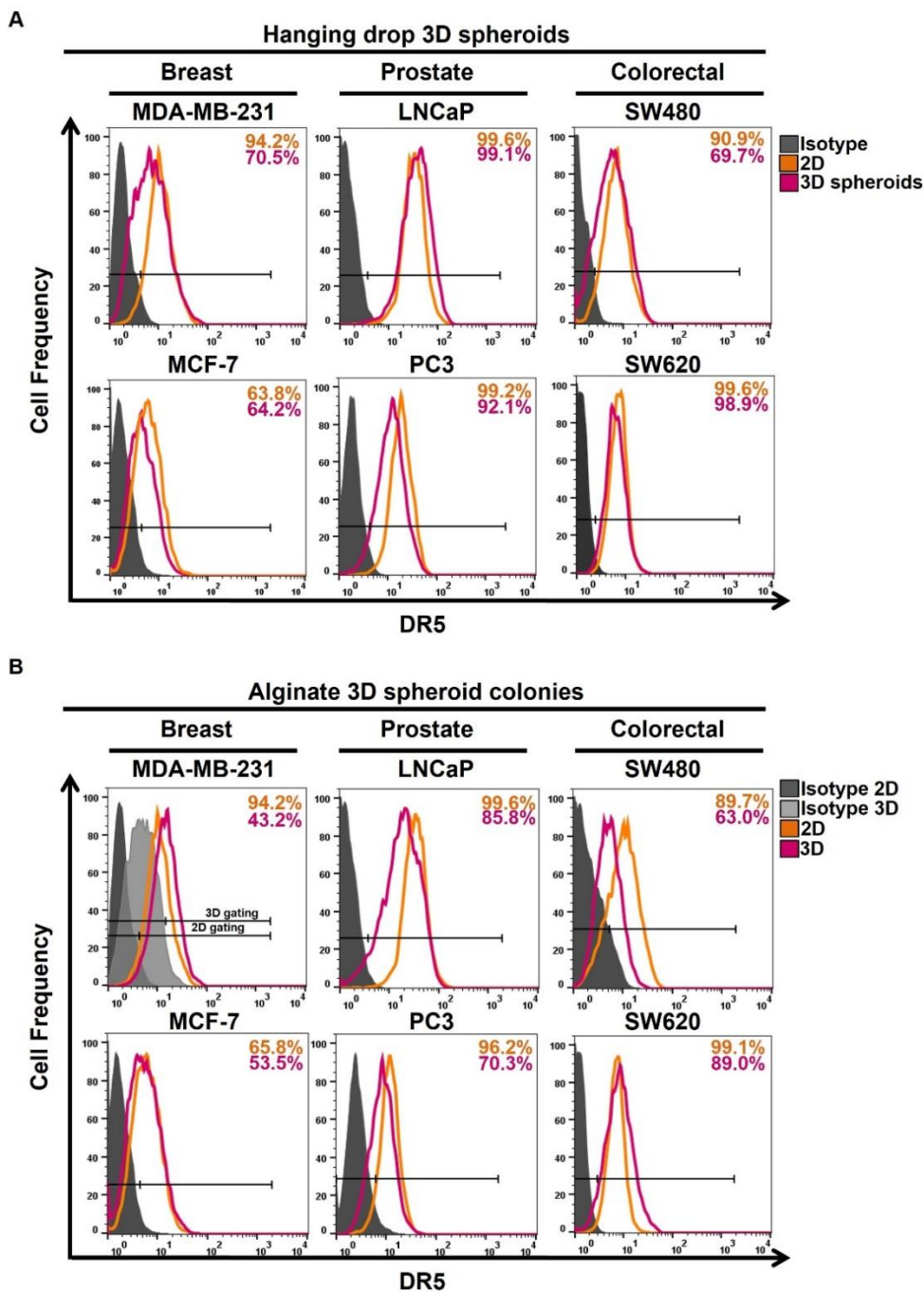
Figure 3.24 Representative flow cytometry plots display DR5 protein expression amongst cancer cell lines in 2D and 3D cell culture models. Representative flow cytometry histograms are displayed for **(A)** 3D hanging drop spheroids (pink) and **(B)** 3D alginate spheroid colonies (pink) to show DR5 positive populations relative to the isotype control (grey) and 2D monolayer cells (orange). Histograms for MDA-MB-231 3D cultures are presented with both 2D and 3D (light grey) isotype controls. n=3 independent experiments, each with 3 technical repeats.

3.3.7.4.3 Fas expression in 3D cell culture models compared to 2D-cultured cells

In four out of the six cancer cell lines investigated, Fas mRNA expression was found to be significantly altered when cells were cultured in 3D cell culture models compared to their 2D monolayer counterparts (Figure 3.25A and Table 3.2).

MCF-7 breast, LNCaP prostate and SW480 colorectal cancer cells all demonstrated a significant reduction in Fas mRNA expression when cultured in 3D cell culture models compared to 2D-cultured cells. For MCF-7 and LNCaP cells, Fas mRNA expression was found to be expressed at the lowest levels in 3D hanging drop spheroids compared to 3D alginate spheroid colonies and 2D-cultured cells. For SW480 cells, Fas mRNA was found to be expressed at the lowest levels in 3D alginate spheroid colonies compared to 3D hanging drop spheroids and 2D-cultured cells. Whilst PC3 prostate cancer cells demonstrated a significant decrease in Fas mRNA expression when cultured in 3D hanging drop spheroids like the three other cancer cell lines mentioned above, PC3 cells showed a significant increase in Fas mRNA expression when cultured in 3D alginate spheroid colonies compared to 2D-cultured cells.

In terms of protein expression, only SW480 cells demonstrated significantly altered levels of Fas (Figure 3.25B and C and Table 3.2). The proportion of SW480 cells expressing Fas protein on their cell surface was found to be significantly reduced in 3D alginate spheroid colonies compared to 3D hanging drop spheroids and 2D-cultured cells which demonstrated a similar percentage of Fas-expressing cells within the cell population. Representative flow cytometry histograms illustrating the expression of Fas in 3D hanging drop spheroids and 3D alginate spheroid colonies compared to 2D-cultured cells can be found in Figure 3.26A and B).
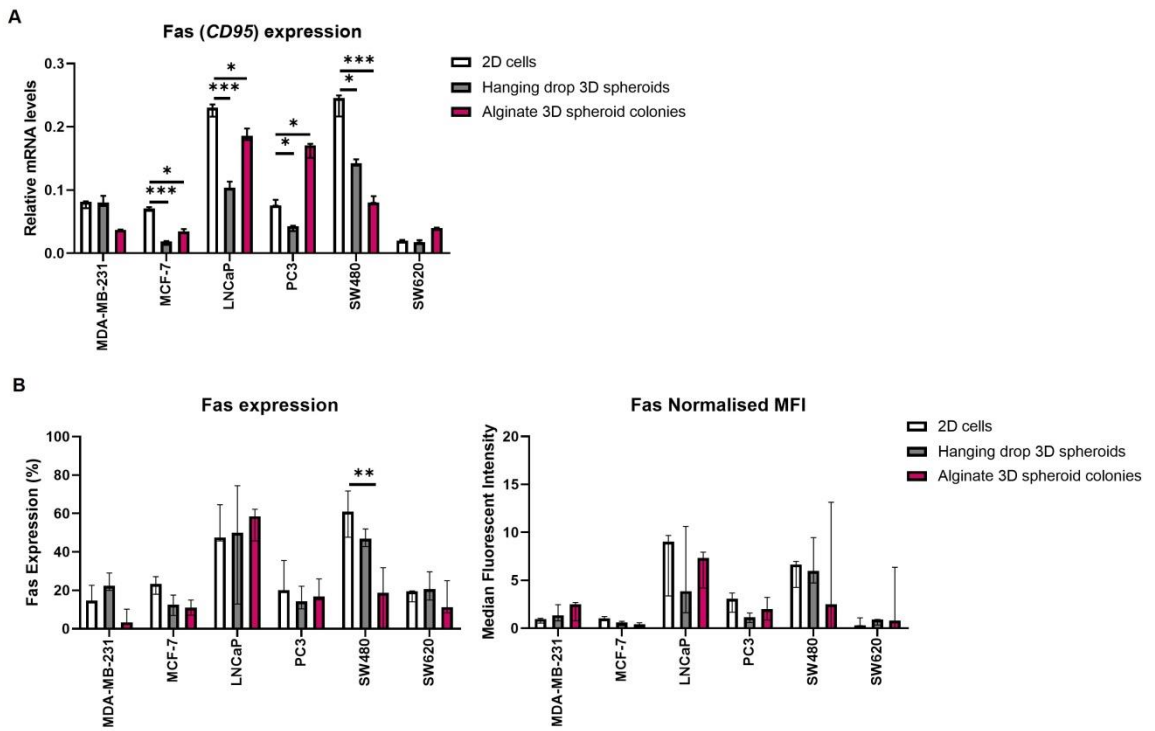
Figure 3.25 Some cancer cells display altered Fas expression at mRNA and/or protein level in 3D cell culture models compared to their monolayer counterparts. Fas **(A)** gene and **(B, C)** protein expression was measured in cancer cells cultured in 2D cell culture, 3D hanging drop spheroids and 3D alginate spheroid colonies. **(B)** Shows the percentage of Fas expression and **(C)** shows the MFI for each cell line. Data is presented as median ± range. n=3 independent experiments each with 3 technical repeats. Data was analysed by a Kruskal-Wallis followed by Dunn's multiple comparisons test (*P<0.05, **P<0.01, ***P<0.001).
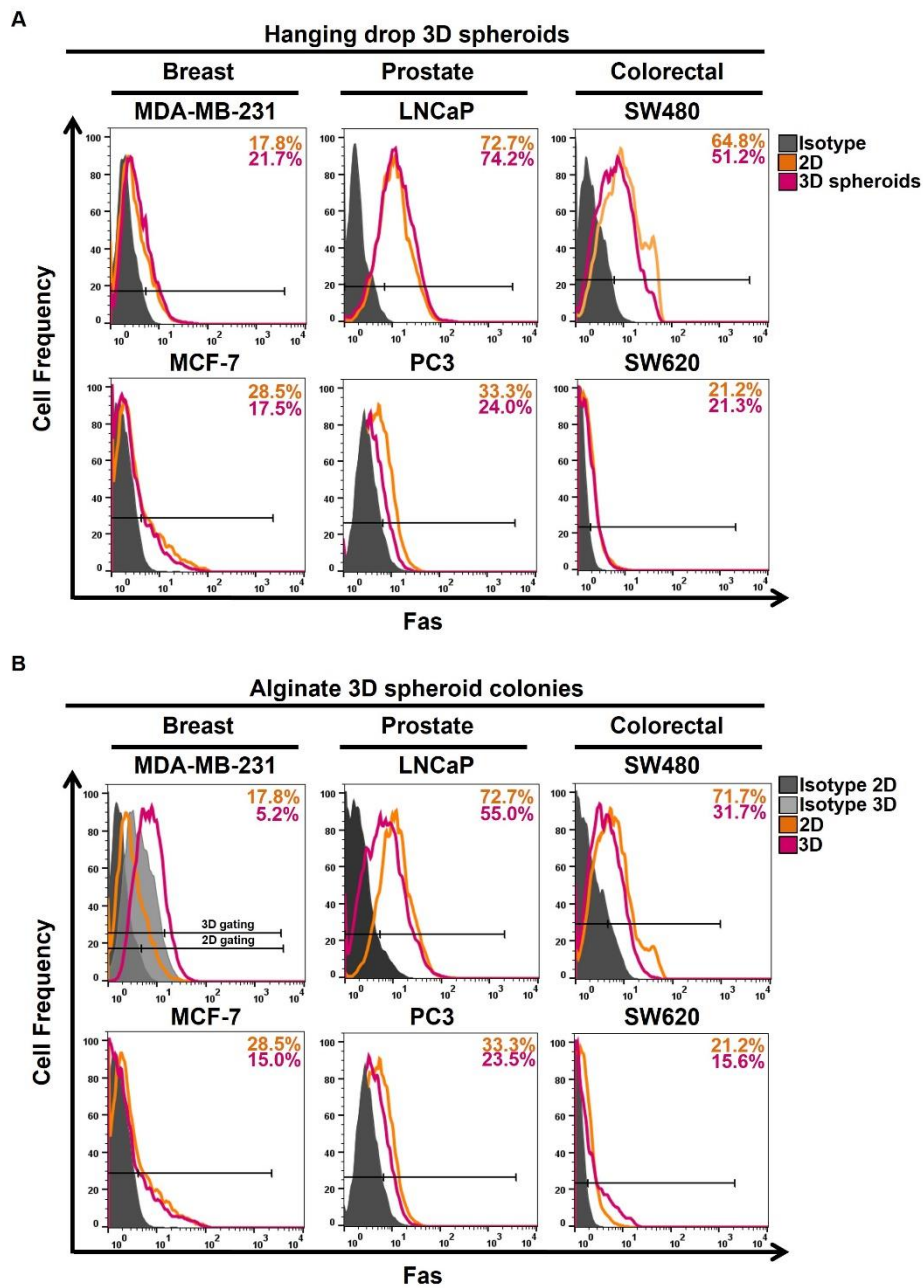
Figure 3.26 Representative flow cytometry plots display Fas protein expression amongst cancer cell lines in 2D and 3D cell culture models. Representative flow cytometry histograms are displayed for **(A)** 3D hanging drop spheroids (pink) and **(B)** 3D alginate spheroid colonies (pink) to show Fas positive populations relative to the isotype control (grey) and 2D monolayer cells (orange). Histograms for MDA-MB-231 3D cultures are presented with both 2D and 3D (light grey) isotype controls. n=3 independent experiments, each with 3 technical repeats.

3.3.7.5 Tumorigenic marker, CD44 was expressed at significantly altered in some cancer cell lines cultured in 3D cell culture models compared to 2D-cultured cells

Human breast, prostate and colorectal cancer cell lines were further investigated for their expression of tumorigenic marker, CD44, in 3D cell culture models compared to their 2D monolayer counterparts. Only MDA-MB-231 breast cancer cells demonstrated a significant decrease in CD44 mRNA expression when cultured in 3D cell culture models compared to their 2D monolayer counterparts (Figure 3.27A and Table 3.2).

In contrast, MCF-7 breast and SW480 and SW620 colorectal cancer cell lines demonstrated a significant increase in the level of CD44 mRNA expression in 3D cell culture models compared to 2D-cultured cells. Interestingly, prostate cancer cell lines (LNCaP and PC3) in 3D cell culture models expressed comparable levels of CD44 mRNA expression to their 2D-cultured cells. As shown in Chapter 2 Figure 2.9, CD44 protein was found not to be expressed at detectable levels in 2D-cultured LNCaP cells which was also found to be the case for CD44 protein expression by LNCaP cells cultured in 3D cell culture models (Figure 3.27B and C). Furthermore, out of the six cancer cell lines only SW620 demonstrated altered CD44 protein expression in 3D cell culture models compared to 2D-cultured cells (Table 3.2). SW620 colorectal cancer cells displayed a significantly lower proportion of CD44 expressing cells in 3D hanging drop spheroids, which was found to be even lower in 3D alginate spheroid colonies, compared to 2D-cultured cells, which was the opposite effect observed for these cells at mRNA levels. Representative flow cytometry histograms illustrating the expression of cell surface CD44 protein in 3D hanging drop spheroids and 3D alginate spheroid colonies compared to 2D-cultured cells can be found in Figure 3.28A and B.
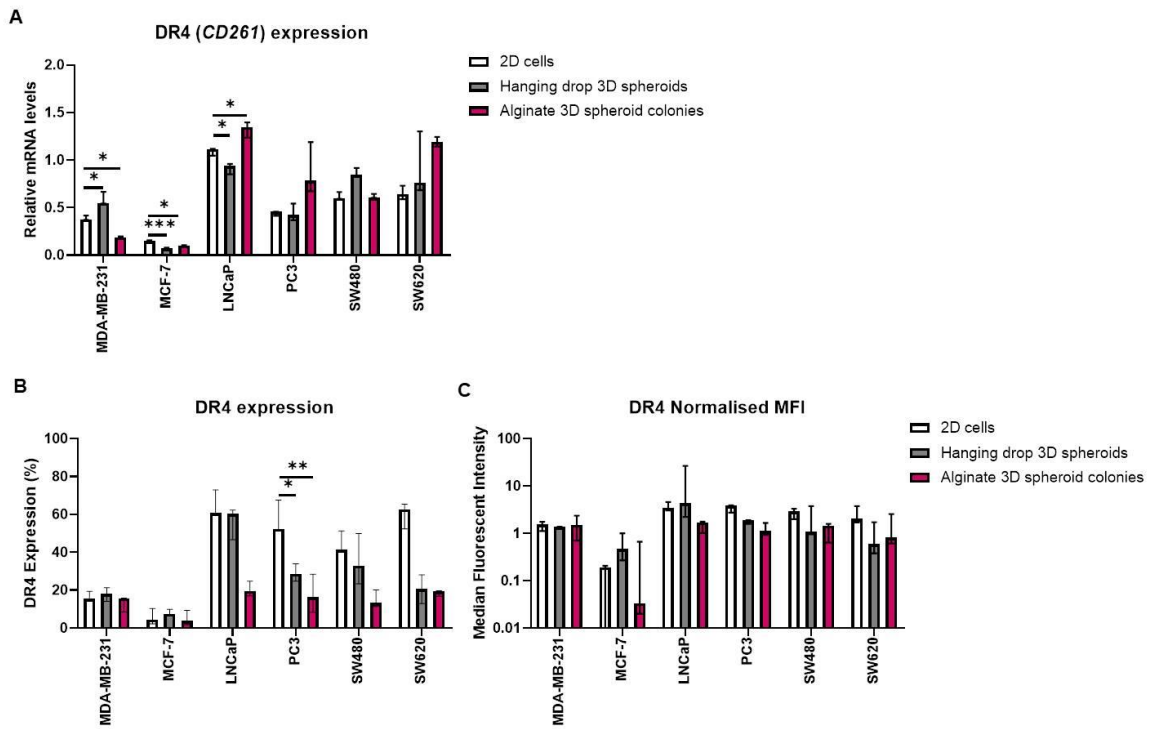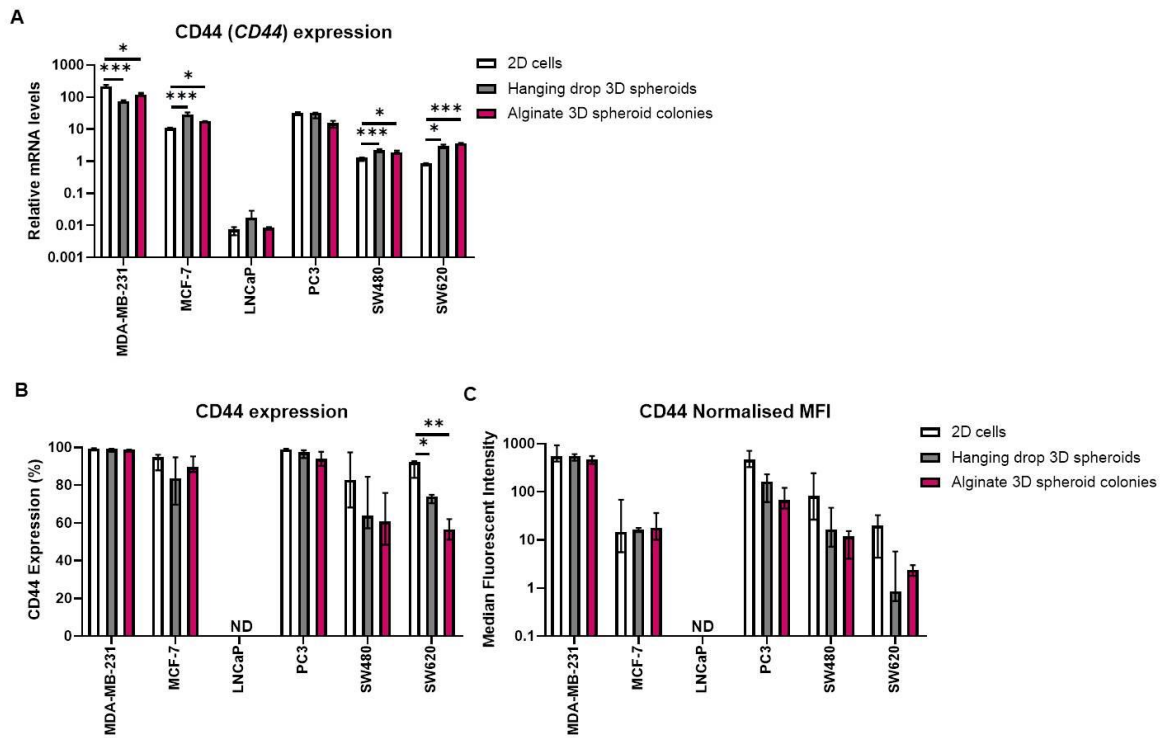
Figure 3.27 Most cancer cells display altered CD44 expression at mRNA and/or protein level in 3D cell culture models compared to their monolayer counterparts. CD44 **(A)** gene and **(B, C)** protein expression was measured in cancer cells cultured in 2D cell culture, 3D hanging drop spheroids and 3D alginate spheroid colonies. **(B)** Shows the percentage of CD44 and **(C)** shows the MFI for each cell line. Data is presented as median ± range. n=3 independent experiments each with 3 technical repeats. Data was analysed by a Kruskal-Wallis followed by Dunn's multiple comparisons test (*P<0.05, **P<0.01 and ***P<0.001). ND indicates that protein expression was not detectable.
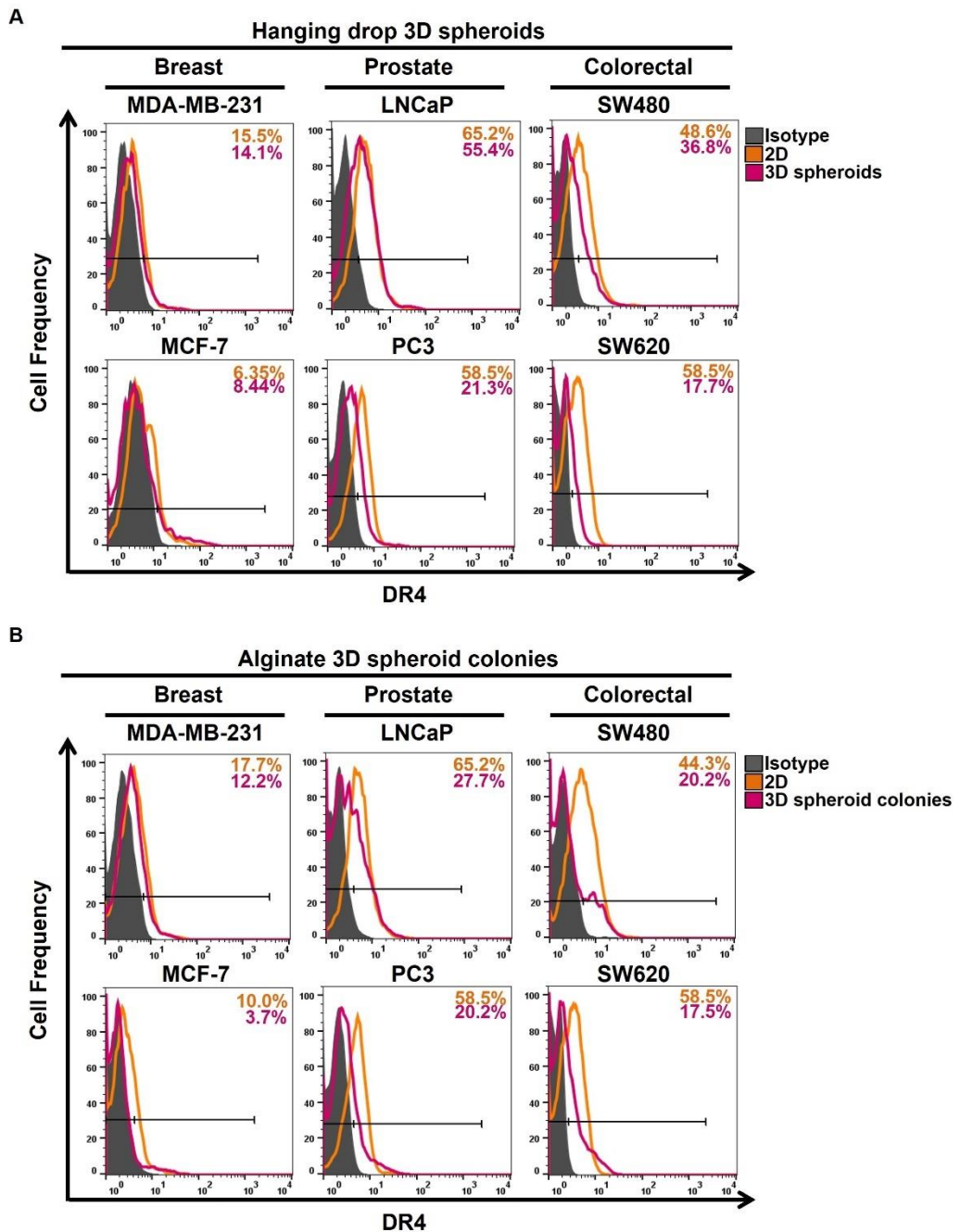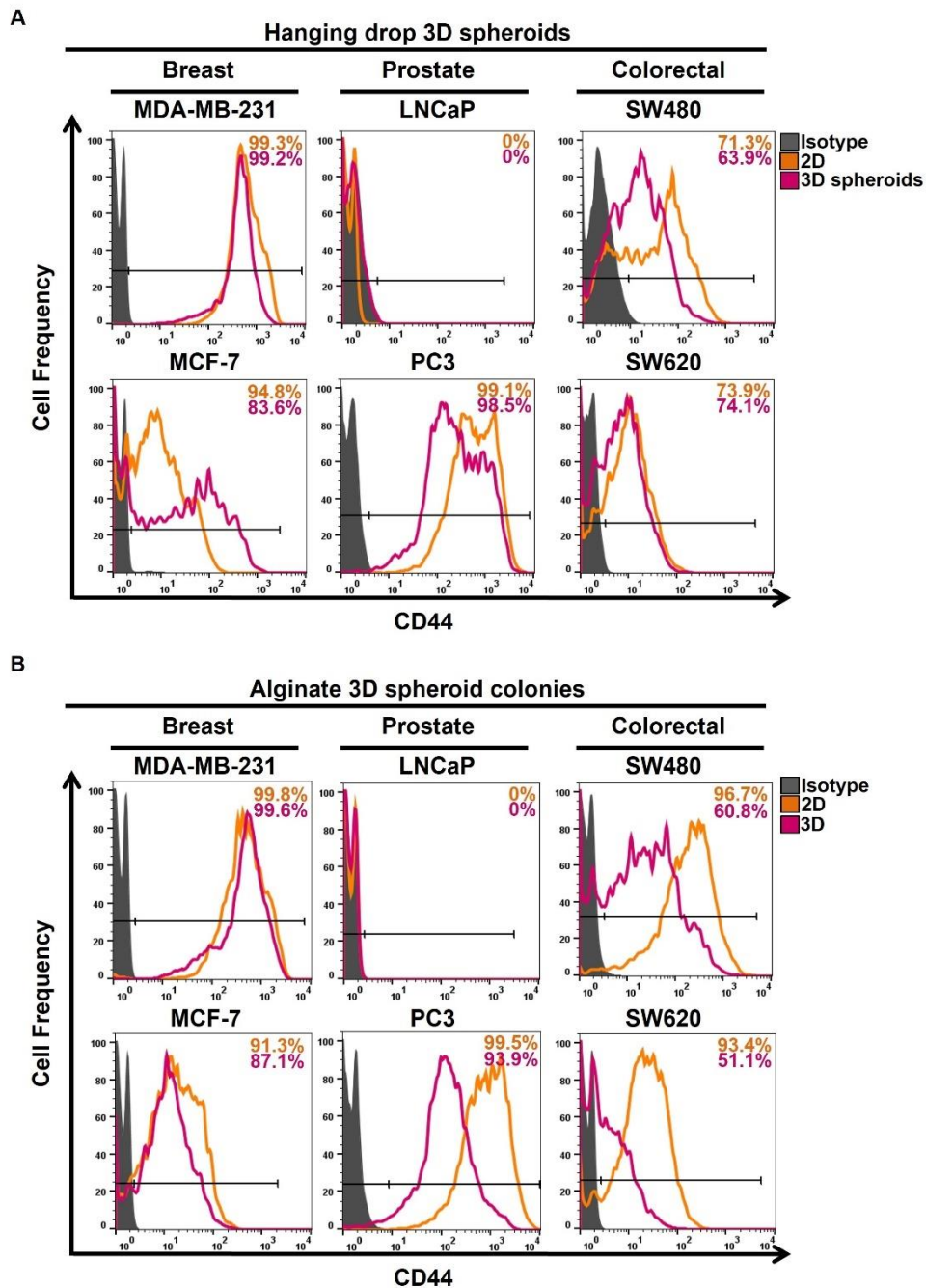
Figure 2.28 Representative flow cytometry plots display cell surface CD44 protein expression amongst cancer cell lines in 2D and 3D cell culture models. Representative flow cytometry histograms are displayed for **(A)** 3D hanging drop spheroids (pink) and **(B)** 3D alginate spheroid colonies (pink) to show CD44 positive populations relative to the isotype control (grey) and 2D monolayer cells (orange). n=3 independent experiments each with 3 technical repeats.

3.3.7.6 Tumorigenic HIF1α expression levels by most cancer cell lines cultured in 3D cell culture models were comparable to that of 2D-cultured cells

Next, HIF1α mRNA and protein expression by cancer cell lines was measured to determine whether the low oxygen concentrations that may develop within 3D cell culture models could trigger any changes to its expression. Surprisingly, MDA-MB-231 breast cancer cells showed significantly reduced levels of HIF1α mRNA expression in 3D hanging drop spheroids compared to 2D-cultured cells (Figure 3.29A and Table 3.2). However, MDA-MB-231 cells cultured in 3D alginate spheroid colonies demonstrated no changes to HIF1α mRNA expression compared to 2D-cultured cells.

LNCaP prostate cancer cells was the only cancer cell line to demonstrate significantly increased HIF1α mRNA expression in both 3D cell culture models compared to 2D cultured cells. In LNCaP cells, the HIF1α mRNA levels were higher in 3D hanging drop spheroids than in 3D alginate spheroid colonies compared to 2D-cutlured LNCaP cells. In terms of the proportion of HIF1α protein expressed within the different cell line populations and the level by which it is expressed at protein level, remained unchanged in all cancer cell lines investigated in 3D cell culture models compared to 2D (Figure 3.29B and C and Table 3.2). Representative flow cytometry histograms illustrating the expression of HIF1α protein in 3D hanging drop spheroids and 3D alginate spheroid colonies compared to 2D-cultured cells can be found in Figure 3.30A and B, respectively. In both colorectal cancer cell lines cultured in 3D alginate spheroid colonies, flow cytometry histograms showed a small percentage of the cell populations expressed higher level of HIF1α protein compared to the rest of the population.
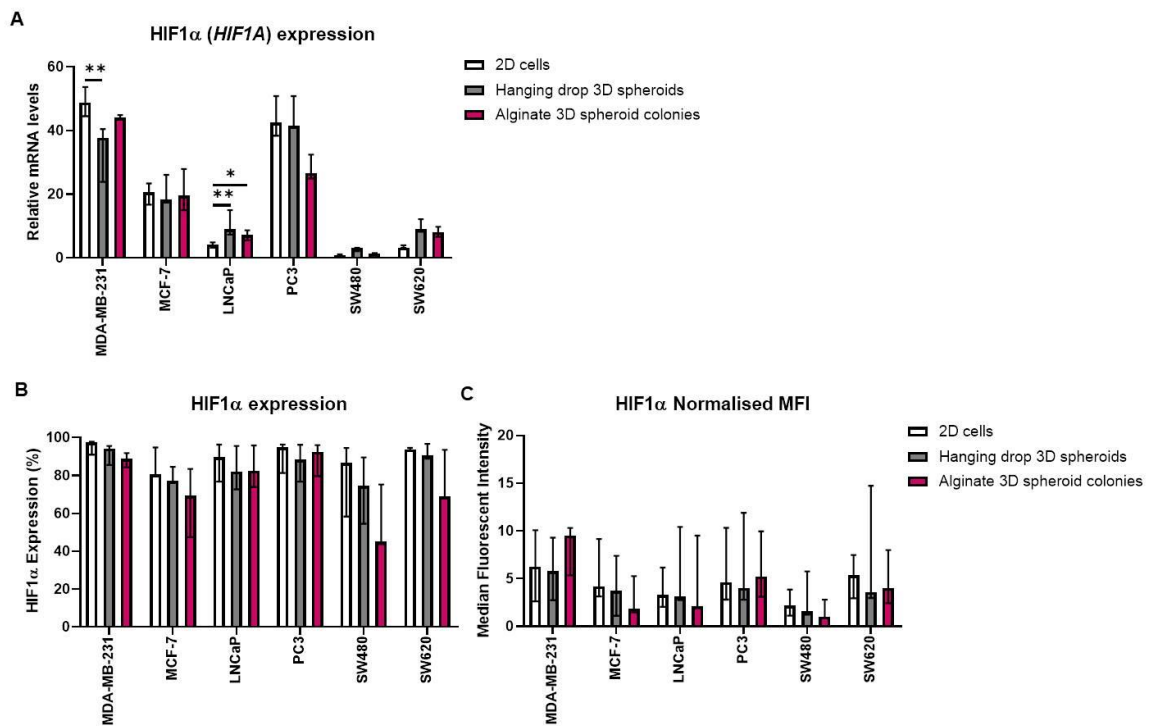
Figure 3.29 Cancer cells display comparable levels of HIF1α protein expression in 3D cell culture models compared to their monolayer counterparts. HIF1α **(A)** gene and **(B, C)** protein expression was measured in cancer cells cultured in 2D cell culture, 3D hanging drop spheroids and 3D alginate spheroid colonies. **(B)** Shows the percentage of HIF1α and **(C)** shows the MFI for each cell line. Data is presented as median ± range. n=3 independent experiments each with 3 technical repeats. Data was analysed by a Kruskal-Wallis followed by Dunn's multiple comparisons test (*P<0.05 and **P<0.01).
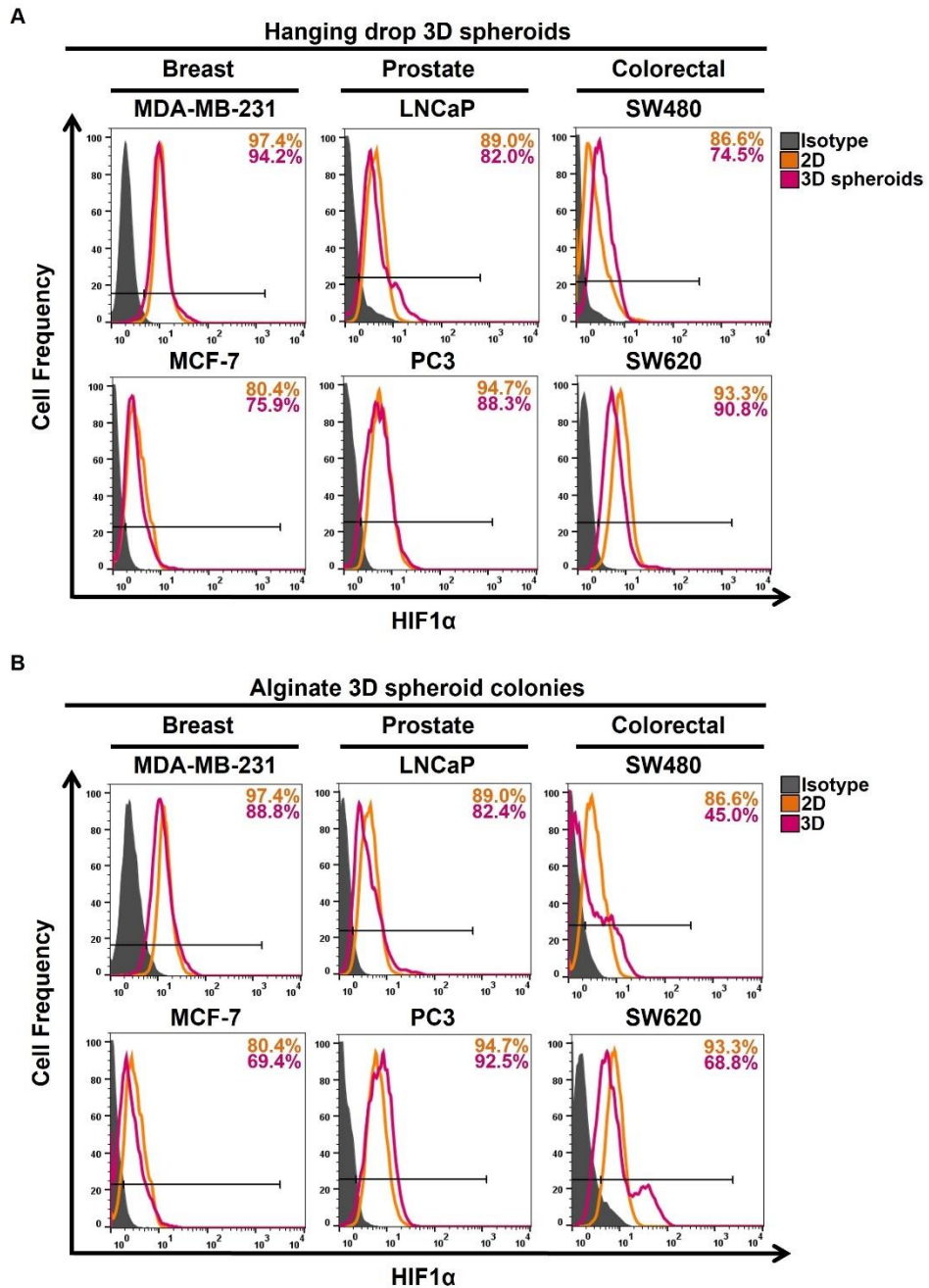
Figure 3.30 Representative flow cytometry histograms display HIF1α protein expression amongst cancer cell lines in 2D and 3D cell culture models. Representative flow cytometry histograms are displayed for **(A)** 3D hanging drop spheroids (pink) and **(B)** 3D alginate spheroid colonies (pink) to show HIF1α positive populations relative to the isotype control (grey) and 2D monolayer cells (orange). n=3 independent experiments each with 3 technical repeats.

Table 3.2 Summary table of immunological and tumorigenic markers expressed by human cancer cell lines cultured in 3D cell culture models compared to their 2D monolayer counterparts.

Cell lines	Hanging drop 3D spheroids versus 2D cultures at day 3			Alginate 3D spheroid colonies versus 2D cultures at day 10		
	mRNA	Protein		mRNA	Protein	
		%	MFI		%	MFI
PD-L1 expression						
MDA-MB-231	↓P<0.05	NS P>0.05	↓P<0.05	↓P<0.01	↓P<0.001	↓P<0.01
MCF-7	↓P<0.05	↑P<0.05	NS P>0.05	↓P<0.01	↓P<0.01	NS P>0.05
LNCaP	NS P>0.05	↑P<0.05	↑P<0.05	↓P<0.01	↑P<0.01	NS P>0.05
PC3	↓P<0.05	↑P<0.05	NS P>0.05	↓P<0.01	NS P>0.05	NS P>0.05
SW480	↓P<0.01	↑P<0.05	↑P<0.05	↓P<0.0001	NS P>0.05	NS P>0.05
SW620	NS P>0.05	↑P<0.05	↑P<0.05	↑P<0.01	↑P<0.05	NS P>0.05
PD-1 expression						
MDA-MB-231	ND	ND	ND	ND	ND	ND
MCF-7	ND	ND	ND	ND	ND	ND
LNCaP	ND	ND	ND	ND	ND	ND
PC3	ND	ND	ND	ND	ND	ND
SW480	NS P>0.05	ND	ND	NS P>0.05	↑P<0.05	↑P<0.05
SW620	NS P>0.05	ND	ND	NS P>0.05	ND	ND
PD-L2 expression						
MDA-MB-231	↓P<0.001	NS P>0.05	NS P>0.05	↓P<0.05	NS P>0.05	NS P>0.05
MCF-7	NS P>0.05	NS P>0.05	NS P>0.05	NS P>0.05	NS P>0.05	NS P>0.05
LNCaP	ND	ND	ND	ND	ND	ND
PC3	↓P<0.05	NS P>0.05	NS P>0.05	↓P<0.001	NS P>0.05	NS P>0.05
SW480	NS P>0.05	NS P>0.05	NS P>0.05	NS P>0.05	NS P>0.05	NS P>0.05
SW620	ND	ND	ND	ND	ND	ND

Table 3.2. Continued…

Cell lines	Hanging drop 3D spheroids versus 2D cultures at day 3			Alginate 3D spheroid colonies versus 2D cultures at day 10		
	mRNA	Protein		mRNA	Protein	
		%	MFI		%	MFI
HLA-ABC expression						
MDA-MB-231	-	NS P>0.05	NS P>0.05	-	NS P>0.05	NS P>0.05
MCF-7	-	↓P<0.05	NS P>0.05	-	↓P<0.05	NS P>0.05
LNCaP	-	NS P>0.05	NS P>0.05	-	NS P>0.05	NS P>0.05
PC3	-	NS P>0.05	NS P>0.05	-	NS P>0.05	NS P>0.05
SW480	-	NS P>0.05	NS P>0.05	-	NS P>0.05	NS P>0.05
SW620	-	NS P>0.05	NS P>0.05	-	NS P>0.05	NS P>0.05
DR4 expression						
MDA-MB-231	↑P<0.05	NS P>0.05	NS P>0.05	↓P<0.05	NS P>0.05	NS P>0.05
MCF-7	↓P<0.05	NS P>0.05	NS P>0.05	↓P<0.05	NS P>0.05	NS P>0.05
LNCaP	↓P<0.05	NS P>0.05	NS P>0.05	↑P<0.05	NS P>0.05	NS P>0.05
PC3	NS P>0.05	↓P<0.05	NS P>0.05	NS P>0.05	↓P<0.05	NS P>0.05
SW480	NS P>0.05	NS P>0.05	NS P>0.05	NS P>0.05	NS P>0.05	NS P>0.05
SW620	NS P>0.05	NS P>0.05	NS P>0.05	NS P>0.05	NS P>0.05	NS P>0.05
DR5 expression						
MDA-MB-231	↑P<0.05	↓P<0.05	NS P>0.05	NS P>0.05	↓P<0.0001	NS P>0.05
MCF-7	NS P>0.05	NS P>0.05	NS P>0.05	NS P>0.05	NS P>0.05	NS P>0.05
LNCaP	NS P>0.05	NS P>0.05	NS P>0.05	NS P>0.05	NS P>0.05	NS P>0.05
PC3	NS P>0.05	NS P>0.05	NS P>0.05	NS P>0.05	NS P>0.05	NS P>0.05
SW480	NS P>0.05	NS P>0.05	NS P>0.05	NS P>0.05	NS P>0.05	NS P>0.05
SW620	NS P>0.05	NS P>0.05	NS P>0.05	NS P>0.05	NS P>0.05	NS P>0.05

Table 3.2. Continued…

Cell lines	Hanging drop 3D spheroids versus 2D cultures at day 3			Alginate 3D spheroid colonies versus 2D cultures at day 10		
	mRNA	Protein		mRNA	Protein	
		%	MFI		%	MFI
Fas expression						
MDA-MB-231	NS P>0.05	NS P>0.05	NS P>0.05	NS P>0.05	NS P>0.05	NS P>0.05
MCF-7	↓P<0.001	NS P>0.05	NS P>0.05	↓P<0.05	NS P>0.05	NS P>0.05
LNCaP	↓P<0.001	NS P>0.05	NS P>0.05	↓P<0.05	NS P>0.05	NS P>0.05
PC3	↓P<0.05	NS P>0.05	NS P>0.05	NS P>0.05	NS P>0.05	NS P>0.05
SW480	↓P<0.05	NS P>0.05	NS P>0.05	↓P<0.001	↓P<0.01	NS P>0.05
SW620	NS P>0.05	NS P>0.05	NS P>0.05	NS P>0.05	NS P>0.05	NS P>0.05
CD44						
MDA-MB-231	↓P<0.001	NS P>0.05	NS P>0.05	↓P<0.05	NS P>0.05	NS P>0.05
MCF-7	↑P<0.001	NS P>0.05	NS P>0.05	↑P<0.05	NS P>0.05	NS P>0.05
LNCaP	NS P>0.05	ND	ND	NS P>0.05	ND	ND
PC3	NS P>0.05	NS P>0.05	NS P>0.05	NS P>0.05	NS P>0.05	NS P>0.05
SW480	↑P<0.001	NS P>0.05	NS P>0.05	↑P<0.05	NS P>0.05	NS P>0.05
SW620	↑P<0.05	↓P<0.05	NS P>0.05	↑P<0.001	↓P<0.01	NS P>0.05
HIF1α						
MDA-MB-231	↓P<0.001	NS P>0.05	NS P>0.05	NS P>0.05	NS P>0.05	NS P>0.05
MCF-7	NS P>0.05	NS P>0.05	NS P>0.05	NS P>0.05	NS P>0.05	NS P>0.05
LNCaP	↑P<0.001	NS P>0.05	NS P>0.05	↑P<0.05	NS P>0.05	NS P>0.05
PC3	NS P>0.05	NS P>0.05	NS P>0.05	NS P>0.05	NS P>0.05	NS P>0.05
SW480	NS P>0.05	NS P>0.05	NS P>0.05	NS P>0.05	NS P>0.05	NS P>0.05
SW620	NS P>0.05	NS P>0.05	NS P>0.05	NS P>0.05	NS P>0.05	NS P>0.05
Colour Key: Black shows NS (no significant) change, red shows a significant decrease, green shows a significant increase, blue shows genes/proteins ND (not detected)						

3.4 Discussion

There is currently heightened interest in understanding the role of PD-L1 in the tumour and the tumour microenvironment, since targeting the PD-1/PD-L1 signalling axis has revolutionised the cancer therapy landscape, yet challenges remain, and need addressing to improve patient response and overcome resistance mechanisms in all cancers. Over recent years 3D cell culture models have been reported to have more physiological relevant functions for oncology and immune-oncology studies than standard 2D monolayer cell culture in terms of defence response to treatment and immune system modulation. Additionally, whilst the use of *in vivo* mouse models is paramount to testing the efficacy and systemic effects of therapeutic drugs before human clinical trials, unless humanised mouse models are utilised, they are problematic for investigating the PD-1/PD-L1 signalling axis in a human context and hence for the testing of human anti-PD-1/PD-L1 monoclonal antibody therapies. Indeed, the expression of immune checkpoint molecules by tumours *in vivo* have been reported to differ from their expression in 2D monolayer cell culture models (Rom-Jurek *et al.,* 2018; Boucherit *et al.,* 2020). This highlights the importance of utilising more robust human 3D cell culture models to mimic characteristics of the tumour more closely to measure immunotherapy and tumour responses (Hudson *et al.,* 2020). To this end, here we investigated whether PD-L1 expression by six human cancer cell lines could be modulated at mRNA and protein level when grown in two different 3D cell culture models of varying *in vitro* complexity as opposed to standard 2D cell culture. Other immunological and tumorigenic markers (PD-1, PD-L2, HLA-ABC, DR4, DR5, Fas, CD44 and HIFα) were also investigated alongside PD-L1.

Whilst 2D cell culture provides opportunities to explore the biological functions of cancer cells in an easy and high throughput manner, cancer cells display aberrant characteristics when grown in monolayer, which fails to mimic those observed in *in vivo* human tumours. Many studies have shown that PD-L1 expression by human cancer cells differs *in vivo* compared to their *in vitro* monolayer counterparts (Gatalica *et al.,* 2014; Rom-Jurek *et al.,* 2018). In the present study, we utilised a scaffold-free (hanging drop method) and a scaffold-based (alginate hydrogel bead) system to form 3D spheroids and 3D spheroid colonies, respectively, to assess PD-L1 expression by human cancer cells compared to their 2D monolayer counterparts. These 3D cell culture models have previously been reported to sustain an oxygen and nutrient gradient (Muller-Klieser and Sutherland, 1982; Alessandri *et al.,* 2013; Nunes *et al.,*

2019), encourage increased extracellular matrix deposition (Lee and Mooney, 2012; Rios de la Rosa *et al.,* 2018), facilitate genomic and protein alterations (Souza *et al.,* 2017; Souza *et al.,* 2018) and demonstrate increased resistance to anti-cancer therapies (Luca *et al.,* 2013; Riedl *et al.,* 2017; Takahashi *et al.,* 2020; Boucherit *et al.,* 2020), similar to that observed in *in vivo* human tumours.

We have demonstrated here it was possible to grow all six cell lines using both 3D cell culture methods. However, it is important to note that there were technical difficulties maintaining hanging drop cultures of MDA-MB-231 cells for subsequent immunohistochemical analysis, although analysis by flow cytometry from 3D hanging drop spheroids was straight forward. In contrast, the use of the 3D alginate model was more amenable for subsequent immunohistochemistry, but cells needed a longer culture period for single cells to form colonies. Furthermore, the release of cells from alginate was required prior to flow cytometry analysis, however here we have shown that this was possible without adversely effecting cell viability. Importantly, our 3D models show the development of hypoxic regions, particularly in hanging drop spheroids which is a key feature of tumours that requires modelling *in vitro* (Noman *et al.,* 2014; Barsoum *et al.,* 2014; Scharping *et al.,* 2017). Both 3D cell culture models have great potential in recreating the cancer tumour microenvironment, its variation in cellular composition, molecular microenvironment and 3D architecture and stiffness, and thus create a more realistic model of *in vivo* cancer tumours. Hence, this will enable us to elucidate the intrinsic role of PD-L1 in cancer.

Using these models, we found that PD-L1 expression was altered in a 3D environment compared to cells cultured in monolayer. Additionally, the expression of other immunological and tumorigenic markers (PD-1, PD-L2, HLA-ABC, DR4, DR5, Fas, CD44 and HIFα) were also found to change in cancer cells grown in 3D cell culture models compared to their 2D monolayer counterparts.

Here, we show new data that PD-L1 mRNA expression was reduced in breast, prostate and colorectal cancer cells grown in both 3D cell culture models compared to their 2D monolayer counterparts. This reduced PD-L1 expression in 3D culture was also observed on the cell surface of MDA-MB-231 breast and PC3 prostate cancer cells. It is well documented that TNBCs have the highest PD-L1 expression among all breast cancer subtypes (Soliman *et al.,* 2014; Gatalica *et al.,* 2014). Consistent with this, MDA-MB-231 TNBC cells in 3D cultures still expressed the

highest level of PD-L1 compared to MCF-7 luminal A breast cancer 3D cultures, despite their reduced expression. A study analysing PD-L1 expression on human tumour samples demonstrated that 59% of TNBCs expressed PD-L1 compared to 33% of the luminal A subtypes (Gatalica *et al.,* 2014). In the same study, out of 20 prostate and 87 colon tumour samples only 25% and 21% were shown to express PD-L1, respectively. This study indicates that PD-L1 is heterogeneously expressed among human cancers *in vivo* and that PD-L1 expression is only found in a small percentage of tumour samples. Martin *et al.,* (2015) also demonstrated the paucity of PD-L1 expression in human prostate cancer cell lines (including LNCaP and PC3 cancer cells) and human prostate samples to find that PD-L1 was expressed at very low levels across all samples (Martin *et al.,* 2015). In line with our study, it was recently reported that human breast cancer cell lines (BT-474, MDA-MB-231, SK-BR-3, and JIMT-1) that had been implemented into immunodeficient and humanized mouse models developed tumours that displayed diminished PD-L1 expression compared to their 2D *in vitro* counterparts (Rom-Jerek *et al.,* 2018). The downregulation of PD-L1 expression by cancer cells *in vivo* was thought to be associated with the cell density and compactness of the tumour, and the lower proliferative rate of the cancer cells, as opposed to the aberrantly reduced cell-cell contact and higher proliferative rate cancer cells exhibit in 2D culture, respectively (Satelli *et al.,* 2016; Clark *et al.,* 2016; Rom-Jerek *et al.,* 2018). With the increased cell-cell contact and the reduced proliferative status of cancer cells that is observed in 3D cell culture, we can postulate that this may in part explain our observations and implies that our 3D cancer models may be able to recapitulate PD-L1 expression to that of an *in vivo* tumour for the first time. To further support our data, more recently, substrate stiffness has been reported to modulate PD-L1 expression in lung (Miyazawa *et al.,* 2018) and breast (Azadi *et al.,* 2019) cancer cells, highlighting how mechanical cues in the tumour microenvironment can also influence PD-L1 expression. These studies showed that softer substrates facilitated a decrease in PD-L1 expression. Therefore, considering monolayer cells are cultured on hard plastic with stiffness in the gigapascal range which is not comparable to human soft tissues, either healthy or pathological, therefore it is not unexpected that in 3D cultures where cancer cells are in suspension (hanging drop 3D spheroids, elastic moduli <0.1Kilopascal, KPa) or in 1.2% alginate (3D spheroid colonies, elastic moduli of ~5-10KPa) that PD-L1 expression was reduced, where the stiffness is more physiologically relevant to *in vivo* tumour tissue.

Furthermore, Rom-Jerek *et al.,* (2018) also found that PD-L1 was not expressed ubiquitously across the tumour. Similarly in *in vivo* human tumours not all cancer cells show uniform PD-L1 expression and their PD-L1 status is likely to vary from any one time given the influence of the tumour microenvironment (Tumeh *et al.,* 2014; Ribas and Hu-Lieskovan, 2016). In the present study, we attempted to assess the localisation of PD-L1 expression within our 3D cell culture models to determine whether PD-L1 expression was ubiquitously expressed amongst the human cancer cell lines investigated here in 3D. We found that for most cancer cell lines this was possible and that PD-L1 expression was located throughout both 3D cultures but that its expression was not found expressed on every cell. Additionally, PD-L1 expression detected was variable amongst independent experimental repeats for each cancer cell line cultured in both 3D models, indicating heterogeneity within each cancer cell line population over the period of investigation. Furthermore, PD-L1 localisation within the 3D models was not localised to the hypoxic core which we originally hypothesised. This could be a result of the wrong time point assessed has 3D cultures may require an extended time course under hypoxic conditions to alter PD-L1 distribution. Further work would be required to refine the staining procedure and a larger sample size would allow conclusive assumptions to be made regarding PD-L1 localising within our 3D cultures.

Although cancer cells in this study present with reduced PD-L1 expression at mRNA level in a 3D culture environment compared to their 2D counterparts, some cancer cells including MCF-7 breast, LNCaP prostate, SW480 and SW620 colorectal cancer cells displayed an increased proportion of cells expressing cell surface PD-L1 at a higher MFI in 3D in at least one or both of the 3D cell culture models compared to 2D-cultured cells. This could suggest that other intrinsic and extrinsic factors that regulate PD-L1 are playing a role in the 3D environment to promote PD-L1 protein expression on a higher proportion of the cancer cells (Hudson *et al.,* 2020). Within the literature, only one previous publication has investigated PD-L1 expression in 2D versus 3D cell culture (Lanuza *et al.,* 2018). In this study, only colorectal cancer cell lines (HCT116, HT29 and Caco-2) were assessed; none of which we studied here and only one 3D model was used. They showed HT26 and Caco-2 colorectal cancer cells displayed increased MFI of PD-L1 expression in 3D cell culture, whilst the HCT116 displayed similar MFI to 2D-cultured cells. These results, along with ours, may suggest that PD-L1 regulation in a 3D environment is dependent on the cancer cells being implemented and highlights the heterogeneity among different cancer

types. Many factors that have been shown to positively correlate with PD-L1 expression in native human tumours exist in 3D spheroids and potentially could account for the increases in cell surface PD-L1 we observe in this study. Some of these include: increased expression of HIFs (HIF-1α and HIF-2α) (Noman *et al.,* 2014; Barsoum *et al.,* 2014; Scharping *et al.,* 2017); increased expression of GLUT-1 (Young *et al.,* 2011); increased activation of oncogenic signalling pathways such as phosphatidylinositol 3-kinase (PI3K)/AKT and mitogen-activated protein kinase (MAPK) pathways (Riedl *et al.,* 2017; Dong *et al.,* 2018) and increased pro-inflammatory cytokine secretion such as IFN-γ and interleukin 10 (Mahon *et al.,* 2015).

Alternatively, the prevalence of PD-L1 expression in patient tumours has been reported to be higher in metastatic tumours compared to primary tumours in some cancers (Wang *et al.,* 2016). In 3D culture, MCF-7, LNCaP and SW620 cancer cells derived from metastatic tumours displayed increased PD-L1 protein expression which could potentially reflect their metastatic phenotype *in vivo.* However, SW480 cancer cells derived from a primary tumour also displayed increased PD-L1 protein expression in 3D culture to similar levels of its metastatic counterpart SW620 cancer cells. This once again highlights tumour heterogeneity and demonstrates how PD-L1 expression can vary, particularly amongst primary and metastatic tumours. In some cancers including breast (Tawfik *et al.,* 2018) and urothelial carcinomas (Burgess *et al.,* 2019), primary- and secondary-derived tumours have been shown to express similar levels of PD-L1. In colorectal cancer specifically, the status of PD-L1 positivity and how this reflects the tumour stage remains to be elucidated.

A consistency in the expression pattern of PD-L1 was observed across both 3D cell culture models in this study which was also the case PD-L2 expression. PD-L2 expression was either found to be unaltered in a 3D cell culture environment or significantly downregulated. Interestingly, MDA-MB-231 and PC3 cells that exhibited a significant decrease in PD-L2 expression in both 3D cell culture models, also displayed a significant decrease in PD-L1 expression in 3D compared to 2D monolayer cultured cells. This may imply that there is interplay between these immune-inhibitory molecules to modulate each other's expression in these cancer cell lines.

However, the other immunological markers investigated here demonstrated differences in their expression patterns depending on the 3D cell culture model

implemented. Indeed, the different 3D cancer models used have distinctive characteristics in that the hanging drop method facilitates heterogeneous aggregation of cancer cells (Knight and Przybors, 2015), whereas the alginate hydrogel beads simulate the formation of clonal spheroids, whereby cancer cells are being selected for survival characteristics and their ability to self-renew and proliferate from a single cell (Florczyk *et al.,* 2016). Recently, transcription factor NRF2 has been shown to be a prerequisite for clonal formation in order to protect cancer cells from oxidative stress that develops during tumorigenesis (Takahashi *et al.,* 2020). If NRF2 expressing cells are being selected for in the alginate model, this could subsequently alter the level of genes and proteins expressed, and therefore may be responsible for the differences we observe in this study when comparing the expression data from the alginate model to the 3D hanging drop model and 2D cell culture. The changes in the expression of PD-1 protein by colorectal SW480 cells and in the expression of DR4 and DR5 mRNA expression by MDA-MB-231 breast and LNCaP prostate cells in this study illustrate how different 3D models can influence different cancer cell characteristics depending on the cancer type. In the alginate model, PD-1 was upregulated on the surface of SW480 cells compared to 2D-cultured cells and 3D spheroids. Conversely, DR4 and DR5 were downregulated by MDA-MB-231 cells in the alginate model whereas they were upregulated in the hanging drop model compared to 2D-cultured cells. Collectively, these findings could indicate that these specific cancer cell lines are being selected for clonal expansion in the alginate model to ultimately increase the expression of genes and proteins that would likely be advantageous for cancer cell survival (i.e. tumour-PD-1 expression could intrinsically promote cancer cell survival (Hudson *et al.,* 2020)), as well as decrease the expression of immunological markers that would otherwise increase their susceptibility to immune-mediated cell death in the tumour microenvironment (i.e. downregulating death receptors could make cancer cells less susceptible to immune-mediated killing and resistant to drugs that target death receptors (Shin *et al.,* 2001; Martínez-Lostao *et al.,* 2015; Chandrasekaran *et al.,* 2014). Reduced expression of death receptor Fas and HLA-ABC was also observed in our study, suggesting the possibility that cancer cells have the tendency to reduce their immunogenic status when cultured in a 3D environment which more closely mimics that of an *in vivo* human tumour (Ashkenazi *et al.,* 2008; de Carvalho-Neto *et al.,* 2013; Peter *et al.,* 2015; Dhatchinamoorthy *et al.,* 2021). In support of this statement, Chandrasekaran *et al.,* (2014) demonstrated how breast cancer (BT20 and MCF-7)

3D tumour spheroids were more resistant to TNF-alpha-related-apoptosis-inducing-ligand (TRAIL)-mediated apoptosis than 2D-cultured cells due to their downregulation of DR4 and DR5. Restoring DR4 and DR5 expression via COX-2 inhibition increased TRAIL-mediated apoptosis in 3D cultures (Chandrasekaran *et al.,* 2014). In the same study, cells in 3D culture were shown to exhibit high CD44 expression, a cancer stem cell-like characteristic that facilitates tumorigenic processes such as proliferation, invasion and metastasis (Senbanjo and Chellaiah, 2017). In our study 4 out of the 6 cancer cell lines upregulate CD44 mRNA in 3D cell culture models compared to 2D, once again this highlights the need for using 3D cell culture over 2D cell culture to mimic *in vivo* tumour characteristics.

Hypoxic conditions are well-known to promote HIF1α expression by cancer cells in that it prevents HIF1α degradation (Noman *et al.,* 2015). Whilst hypoxic regions were detected in our 3D cell culture models for most cancer cell lines, to our surprise, only LNCaP prostate cancer cells demonstrated an increase in HIF1α mRNA expression. Although our data may seem to contradict the literature in that hypoxic conditions should upregulate HIF1α expression, it has been reported that during prolonged exposure to hypoxia, cancer cells may exhibit reduced levels of HIF1α expression thought to be caused by a feedback mechanism that augments HIF-1α degradation under hypoxic conditions (Marxsen *et al.,* 2004). This could imply that HIF1α expression may have been increased at some point of the cancer cells culture period in 3D, but at the time expression was assessed it could have returned to basal levels. Alternatively, low oxygen concentrations detected in this study by the hypoxia reagent used may not be indicative of very low oxygen levels as what may be induced by using a hypoxic chamber. For example, Doublier *et al.,* 2012 demonstrated that MCF-7 cells cultured in monolayer under hypoxic conditions (1% oxygen) expressed higher levels of HIF1α protein compared MCF-7 cells cultured in monolayer and 3D spheroids under normoxic conditions (17% oxygen). This may suggest that the extent to which our 3D models may induce hypoxia may not be sufficient to upregulate HIF1α in all cancer cell lines investigated here.

In summary, there are several key regulators of PD-L1 expression that have previously been reported (Hudson *et al.,* 2020) and many of these regulators can be influenced by growing cancer cells in 3D (Riedl *et al.,* 2017; Souza *et al.,* 2018), and thus may contribute to the changes in PD-L1 observed in this study. Further investigations are required to determine the exact mechanism of PD-L1 up- or down-

regulation in each cancer cell line in 3D, compared to conventional 2D monolayer. Importantly, the alterations to PD-L1 expression by cancer cells that we observed were consistent across two different 3D cell culture models, which suggests that the mechanisms for regulating PD-L1 expression in 3D cell culture is intrinsic to these cancer cells. Both 3D models explored in this study present with advantages over 2D monolayer culture, allowing better mimicking of *in vivo* conditions for the investigation of PD-L1. The further characterisation performed in this study to assess other immunological markers expressed by human cancer cells in 3D cell culture models compared to 2D-cultured cells provides a platform for future oncology and immuno-oncology studies investigating anti-cancer therapies which may target these markers either alone or in combination with PD-L1-targeted therapy.

4. Investigating the effects of the anti-PD-L1 immunotherapy drug Atezolizumab on 2D- and 3D-cultured breast cancer cells

4.1 Introduction

Atezolizumab was the first anti-PD-L1 immunotherapy drug to be approved for the treatment of advanced NSCLC and metastatic urothelial carcinoma in 2016 (Fehrenbacher *et al.,* 2016; Rosenberg *et al.,* 2016) and has since gained approval for the treatment of extensive-stage small cell lung cancer (Horn *et al.,* 2018), melanoma (Gutzmer *et al.,* 2020) and TNBC (Schmid *et al.,* 2018), either as single agents or in combination with other anti-cancer therapies. Atezolizumab is an Fc-engineered, humanised immunoglobulin monoclonal antibody that directly binds to PD-L1 and provides dual blockade of the PD-1 and B7.1 receptors found on T cells and antigen presenting cells; to ultimately reactivate the immune system without inducing antibody-dependent cellular cytotoxicity (Markham *et al.,* 2016). This unique design of Atezolizumab prevents effector immune cells that express PD-L1 from being targeted for destruction once bound by Atezolizumab by active immune cells, and therefore promotes maximal opportunity for establishment of the immune system in its fight against the cancer cells.

Whilst the role of PD-L1 to inhibit the immune system is well established and that blocking PD-L1 inhibitory activity with monoclonal antibodies such as Atezolizumab can induce immune-mediated tumour eradication (Shah *et al.,* 2018; Hudson *et al.,* 2020), more recently the role of PD-L1 to send pro-survival signals is emerging in some cancer types (Figure 4.1) (Dong *et al.,* 2018; Hudson *et al.,* 2020); however, this role remains to be fully characterised in all cancers. Importantly, it is unclear whether monoclonal antibodies targeting the PD-1/PD-L1 signalling axis work sufficiently to block this new and emerging role of PD-L1, and whether this intrinsic role is contributing significantly to drug resistance, relapse to treatment, and hyperprogressive responses observed in cancer patients (Yi *et al.,* 2018; Wang *et al.,* 2019).
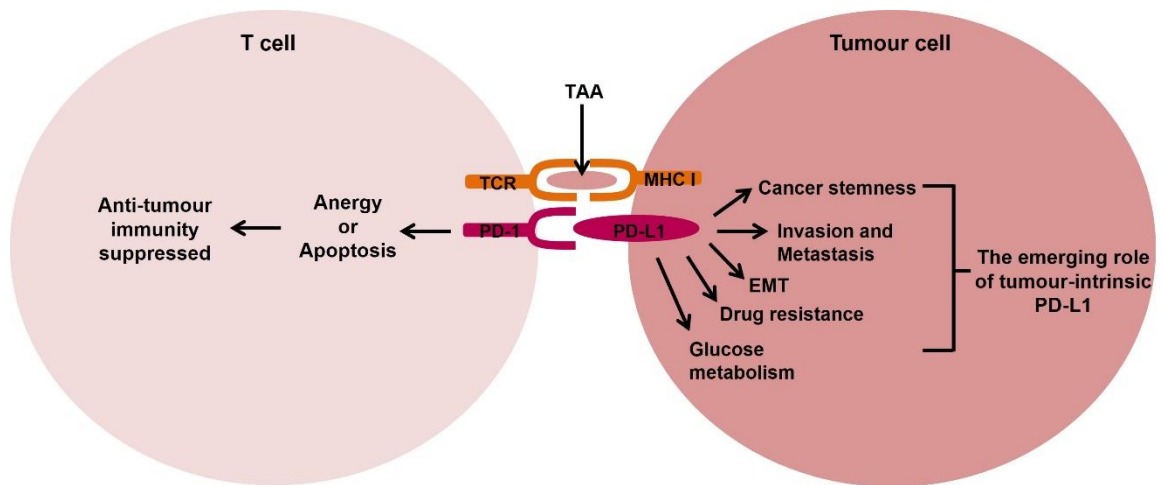
Figure 4.1 The proposed mechanism of action of PD-L1 in tumour cell signalling. In select cancer types, there is an emerging role of PD-L1 to send pro-survival signals in tumour cells. PD-L1 signalling in some tumour cells has been shown to promote cancer initiation, epithelial to mesenchymal transition (EMT), invasion and metastasis, regulate glucose metabolism, and contribute to drug resistance. TAA; Tumour-associated antigen.

There are currently a limited number of reports investigating how immunotherapeutic drugs potentially modulate the intrinsic pathway of PD-L1 (Hudson *et al,* 2020). Four studies identified to investigate the tumorigenic role of PD-L1 by treatment of cancer cells with Atezolizumab have used 2D cell culture models which poorly recapitulate the characteristics of an *in vivo* solid tumour, and therefore are less likely to provide predictive responses to what would be observed *in vivo* (Saleh *et al.,* 2019; Ali *et al.,* 2019; Wang *et al.,* 2020; Chen *et al.,* 2021). Investigating intrinsic PD-L1 signalling and responses to anti-PD-L1 immunotherapy drugs in diverse cancer types and in more heterogeneous tumour models could provide further important insight into the mechanism of immunotherapy treatment.

4.1.1 Aims

In this chapter, the aims were to investigate the direct agonistic biological effects of the anti-PD-L1 immunotherapy drug, Atezolizumab on human breast cancer cells cultured in 2D monolayer and 3D cell culture models. Firstly, the effects of Atezolizumab on PD-L1 mRNA and protein expression were examined. Secondly, the effects of Atezolizumab on the growth, proliferation, and cell viability of breast cancer cells in 2D and 3D cell culture models were investigated. In addition, the effect of Atezolizumab on the phosphorylation levels of several kinases was also explored as an indicator of how it may influence intracellular signalling in breast

cancer cells. Lastly, the cell viability of 2D- and 3D-cultured breast cancer cells was assessed following treatment with Atezolizumab alone or in combination with modulatory cytokines.

4.1.2   Hypotheses

It was hypothesised that Atezolizumab binding to PD-L1 on the surface of 2D- and 3D-cultured human breast cancer cells would ultimately influence the growth, proliferative capacity, and viability of breast cancer cells, and in turn affect intracellular signalling via influencing kinase activity. Additionally, through combining Atezolizumab treatment with cytokine modulation of PD-L1 expression, it was hypothesised that there may be an increase in cell death in 2D and 3D cell culture models of human breast cancer.

4.2 Materials and Methods

4.2.1 Cell lines and cell culture methods

MDA-MB-231 and MCF-7 breast cancer cell lines were used for all subsequent experiments due to their PD-L1 expression status being high and low, respectively. Monolayer cells were cultured and maintained as described in Chapter 2 Section 2.2.1. 3D hanging drop spheroids and 3D alginate spheroid colonies were generated as described in Chapter 3 Section 3.2.1.1 and 3.2.1.2.

4.2.2 Atezolizumab dose response curve for 2D and 3D cultures

MDA-MB-231 breast cancer cells known to express high baseline levels of PD-L1 were treated with Atezolizumab (Selleckchem) in 2D monolayer and 3D cell culture models. Monolayer MDA-MB-231 cells were seeded in 6-well plates at 5×10^5 cells/well and incubated overnight to allow cells to adhere before being treated with Atezolizumab at concentrations between 0 to 10 nM for 1 hour (Table 4.1). Following the preparation and culture of 3D spheroids for 3 days and 3D spheroid colonies for 10 days they were treated with 0 to 40 nM concentrations of Atezolizumab for 1 hour (Table 4.1). PD-L1 expression was assessed by flow cytometry with or without Atezolizumab treatment as described in Chapter 2 Section 2.2.3.1. Isotype controls were prepared for each of the different concentrations of Atezolizumab investigated for both 2D monolayer and 3D cultures.

Table 4.1 Atezolizumab concentrations used to generate dose response curves for the different cell culture methods.

Cell culture method	Concentrations of Atezolizumab (nM)
2D monolayer	0, 0.003125, 0.00625, 0.0125, 0.025, 0.05, 0.1, 0.2, 0.4, 1, 5, 10
3D hanging drop spheroids	0, 0.025, 0.05, 0.1, 0.2, 0.4, 1, 5, 10, 20
3D alginate spheroid colonies	0, 0.025, 0.05, 0.1, 0.2, 0.4, 1, 5, 10, 20, 40

Table 4.1 Concentrations of Atezolizumab used to generate a dose response curve in 2D monolayer and 3D cell cultures. Concentrations ranging between 0-40 nM of Atezolizumab were used to assess the dose response of MDA-MB-231 cells cultured in 2D and 3D cell culture models.

4.2.3 Atezolizumab effects on PD-L1 mRNA expression in 2D and 3D cultures

MDA-MB-231 cells were grown to 90% confluency in two T25 flasks for 3 days. Cells in one T25 flask were treated with 10 nM Atezolizumab for 1 hour or 3 days before being lysed for RNA extraction as described in Chapter 2 Section 2.2.2. For assessment of 3D cultures, 10 Petri dish lids were prepared with 3D spheroids by the hanging drop method and 120 alginate beads were made for 3D spheroid colony formation. 3D spheroids cultured for 3 days, and 3D spheroid colonies cultured for 10 days were treated with 10 nM Atezolizumab for 1 hour before being harvested and lysed for RNA extraction as described in Chapter 3 Section 3.2.3. Subsequently, total RNA extraction, cDNA synthesis and RT-qPCR were performed to detect PD-L1 mRNA as described in Chapter 2, Section 2.2.2. A comparison was made of the effects of Atezolizumab treatment on PD-L1 mRNA compared to untreated 2D monolayer and 3D cultures and PD-L1 expression was calculated using the ΔΔCT method. The ΔΔCT method considers gene expression levels relative to the HKGs in treated vs untreated conditions.

4.2.4 Effects of Atezolizumab on growth and proliferation of breast cancer cells in 2D and 3D cell culture models

4.2.4.1 Fluorescent microscope images of 2D and 3D cultures

For monolayer cell culture, cells were seeded at 3×10^4 cells/well in a 96-well plate and cultured with or without 10 nM Atezolizumab for 3 and 6 days. 3D spheroids were generated by seeding 100 µL of 10,000 cells/well in 96-well ultra-low attachment plates and cultured with or without 10 nM Atezolizumab for 3 and 6 days. Alginate hydrogel beads were prepared, and one bead was seeded with 100 µL of medium per well in a 96-well plate. Alginate hydrogel beads were cultured with or without 10 nM Atezolizumab for 3, 6 and 10 days. At each time point to be assessed, 2D and 3D cultures were stained with Hoechst 33342 (10 µg/mL) and PI (10 µg/mL) for 20 minutes at 37°C before being visualised using the BioTek Cytation 5 Cell Imaging Multimode Reader (Agilent). Multi-colour fluorescent images using DAPI and Texas Red filters were captured using the Gen5 software (Agilent). The Gen5 software was set up to take images of 2D and 3D cultures using Z-stack and montage modes. For cells cultured in 2D monolayer only, the surface area of the wells in a 96-well plate covered by Hoechst 33342/PI positive cells was determined using the image processing software ImageJ 1.5i (Java) to compare the wells of untreated and

Atezolizumab-treated cells after 3 and 6 days of culture. The data was expressed as a percentage of the untreated control cells.

4.2.4.2 Diameter measurements of 3D cultures

The diameter of 3D spheroids and 3D spheroid colonies was measured for untreated and Atezolizumab-treated cultures using the diameter measurement option in the cellSens Imaging Software as described in Chapter 3 Section 3.2.2.3.

4.2.4.3 Intracellular staining of cell proliferation marker Ki67 in 2D and 3D cultures

Single cell suspensions were made from 2D- and 3D-cultured cells treated with or without 10 nM Atezolizumab via trypsinisation. Subsequently, cells were washed with cell staining buffer (Biolegend) and slowly resuspended in 70% ethanol for 1 hour at 4°C to fix and permeabilise the cells. Cells were then washed with cell staining buffer twice and resuspended in 100 µL Fc block for 10 minutes before labelling with 4 µL of PerCP-Cy™5.5 mouse anti-human Ki-67 antibody (1:25 dilution) (Clone B56; BD Biosciences) or PerCP-Cy™5.5 Mouse IgG1 κ isotype control (BD Biosciences). The optimised antibody concentration was determined by titrating the antibody prior to experiments (Appendix Figure 9.1). After 30 minutes incubating, cells were washed twice with cell staining buffer and resuspended in cell staining buffer for flow cytometric analysis. Data was acquired using the FACSCalibur (Becton Dickson) with CellQuest Pro Software v.5.2.1 and analysed as described in Chapter 2 Section 2.2.3.1.

4.2.5 Effects of Atezolizumab on breast cancer cell viability and metabolic activity in 2D and 3D cell culture models

4.2.5.1 Assessment of apoptosis using Annexin V/PI staining

MDA-MB-231 cells were seeded in 24-well plates at 1×10^5 cells/well for 2D monolayer cell culture, 3D spheroids were formed by seeding 100 µL of 10,000 cells/well in 96-well ultra-low attachment plates, and 10 freshly made alginate hydrogel beads were seeded in each well of 12-well plates for 3D spheroid colony formation. 2D-cultured cells and 3D spheroids were maintained and treated in culture before being harvested at day 3 and 6 of culture for downstream analysis, whereas 3D spheroid colonies were maintained and treated in culture before being harvested for downstream analysis after 3, 6 and 10 days. 2D and 3D cell culture models were untreated or treated with 10 nM Atezolizumab with or without IFNγ and/or TNFα. Two

Atezolizumab treatment strategies were used (Figure 4.2A and B). In treatment strategy 1, cultures were either seeded in untreated medium or medium containing 10 nM Atezolizumab from day 0 (day of seeding) (Figure 4.2A). In these cultures, medium with or without 10 nM Atezolizumab was replaced every 3-4 days. In treatment strategy 2, some cultures left untreated were later treated with 10 nM Atezolizumab for 1 hour before harvesting at each time point (Figure 4.2B). In these cultures, medium was also replaced every 3-4 days. Prior to the Atezolizumab treatment for 1 hour, some cultures were treated with IFNγ and/or TNFα for 48 hours to modulate PD-L1 expression. MCF-7 breast cancer cells cultured in 2D and 3D alginate spheroid colonies were treated in the same way as MDA-MB-231 breast cancer cultures for the assessment of apoptosis via Annexin V/PI staining.

After 3, 6 (2D cells, 3D spheroids and 3D spheroid colonies) and 10 (3D spheroid colonies only) days of culture, cells in single cell suspension were stained with Annexin V (FITC) and PI (Biolegend), according to the manufacturer's protocol. A titration experiment was performed on the Annexin V stain to determine the optimal volume. The volume of Annexin V used to stain all samples in each experiment was 3 µL Annexin V in 100µL Annexin V binding buffer supplied with the kit. Data was acquired using the FACSCalibur (Becton Dickson) with CellQuest Pro Software v.5.2.1 (Becton Dickson). Data was analysed using FlowJo software v.9.9.6 (Treestar). Appropriate gating of single cell populations was carried out for each sample run in each independent experiment. The percentage of non-apoptotic/viable (AV-/PI-), early apoptotic (AV+/PI-), late apoptotic (AV+/PI+) and necrotic (AV-/PI+) cells was determined for each sample run in each independent experiment after applying appropriate compensation using single colour controls that were run alongside each experiment. Cell surface staining of PD-L1 as described in Chapter 2 Section 2.2.3.1 was performed simultaneously alongside Annexin V and PI staining to determine the degree of PD-L1 blockade in Atezolizumab-treated 2D and 3D cultures treated with or without IFNγ and/or TNFα.
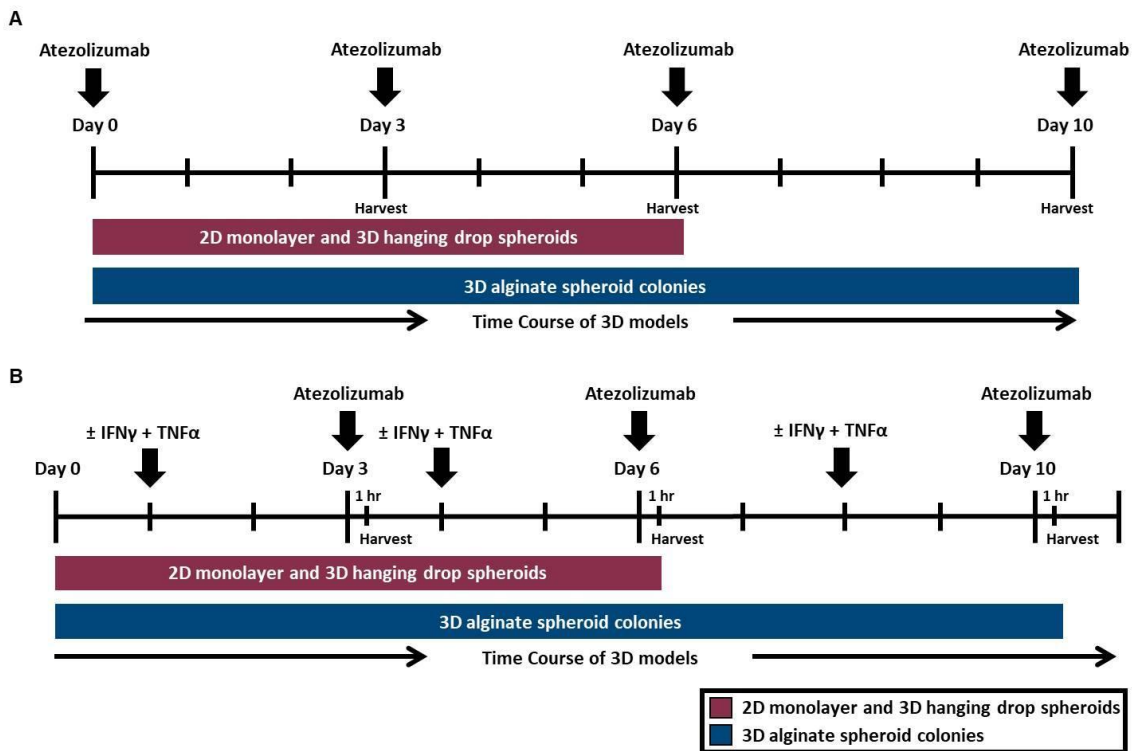
Figure 4.2 Timeline of Atezolizumab treatment strategies with or without IFNγ and/or TNFα for 2D- and 3D-cultured breast cancer cells. (A) Breast cancer cells in 2D monolayer and 3D cultures were treated with or without 10 nM Atezolizumab at day 0 and were cultured for 3, 6 or 10 days before being harvested for analysis. **(B)** 2D and 3D cultures were treated with 10 nM Atezolizumab for 1 hour before being harvested on day 3, 6 or 10. Some cultures were treated with IFNγ and/or TNFα 48 hours prior to dosing with 10 nM Atezolizumab for 1 hour at each time point before harvesting for analysis. Untreated or Atezolizumab-treated medium was replaced every 3 to 4 days for all cultures.

4.2.5.2 Assessment of cellular activity using CellTiter-Glo in 2D and 3D cultures

Monolayer MDA-MB-231 cells were seeded at 3 x 10^5 cells/well in white opaque 96-well plates (ThermoFisher Scientific) and cultured for 3 and 6 days. For 3D spheroids, cells were seeded at 10,000 cells/well in 100 μL of medium in white opaque 96-well plates that were pre-coated with 30 μL 1% agarose (Merck) and allowed to dry. 3D spheroids were also cultured for 3 and 6 days. For 3D spheroid colonies, 1 whole bead was placed in each well of a white opaque 96-well plate in 100 μL of medium and cultured for 3, 6 and 10 days with regular medium changes every 3-4 days. 2D and 3D cultures were untreated or treated with 10 nM Atezolizumab with or without

IFNγ and/or TNFα as described above. Following culture of untreated and treated 2D-cultured cells, the CellTiter-Glo® Cell Viability Assay (Promega) was used to measure ATP levels via luminescent detection, according to the manufacturer's protocol. For 3D-cultured cells, the CellTiter-Glo® 3D Cell Viability Assay (Promega) was used to measure ATP levels in untreated and treated 3D cultures, according to the manufacturer's protocol. Standard curves were generated immediately prior to adding the CellTiter-Glo® reagent to samples of interest using ATP disodium salt (Promega) to ensure ATP levels of the 2D and 3D cultures were kept below the 10 µM limit of the assay linearity. A concentration range of 0-10 µM ATP was used for the standard curve. The luminescent signal was read using the CLARIOstar Microplate Reader (BMG LABTECH). The luminescent signal given from 2D, and 3D cultures was normalised to the luminescent signal from wells that contained culture medium and CellTiter-Glo® reagent only and is presented in relative luminescent units (RLU).

4.2.5.3 Assessment of caspase 3 activity in 3D alginate spheroid colonies

3D alginate spheroid colonies were left untreated or treated with 10 nM Atezolizumab for 1 hour with or without IFNγ and/or TNFα 48 hours previous as described above. These were then harvested after 6 and 10 days of culture, prepared into single cell suspensions for detecting caspase 3 activity via flow cytometry using the NucView® 488 Caspase-3 Substrate staining protocol (Biotium). Some 3D alginate spheroid colonies were treated with 10% DMSO for 24 hours before being harvested for analysis to generate a positive control for apoptosis. For staining, 2×10^4 cells in 200 µL medium was transferred into pre-labelled flow cytometry tubes, stained with 5 µM Casapse-3 substrate solution, mixed well and then incubated at room temperature for 30 minutes. The samples were then analysed by flow cytometry as described in Chapter 2 Section 2.2.3.1.

4.2.6   Effects of Atezolizumab on cellular signalling using a protein profiler array

MDA-MB-231 cells were passaged into four T175 flasks and grown to 90% confluency. Two of these T175 flasks were treated with 10 nM Atezolizumab for 6 days. Cells were harvested, counted and 1×10^7 cells were solubilised in 1 mL lysis buffer supplied with the Human Phospho-Kinase Array Kit (Bio-Techné). The lysis buffer was supplemented with 10 µg/mL Pepstatin (Bio-Techné), 10 µg/mL Aprotinin (Bio-Techné) and 10 µg/mL Leupeptin (Bio-Techné). The cell lysates were mixed by

pipetting before being rocked gently on ice for 30 minutes. Cell lysates were then centrifuged at 14,000 g for 5 minutes and the resulting supernatant was transferred into a clean labelled Eppendorf tube. To determine the amount of protein isolated from the untreated and Atezolizumab-treated cells, the Coomassie Plus (Bradford) Assay was performed according to the manufacturer's protocol (ThermoFisher). A protein standard curve was generated using albumin standards (ThermoFisher) prepared to concentrations ranging from 0 µg/mL to 2000 µg/mL. The unknown protein samples were assessed undiluted, diluted 1 in 5 and 1 in 10 with dH$_2$O to ensure that they would fit within the linear range of the assay so that the protein concentration could be determined. In a 96-well plate, 5 µL of each standard and each sample was added to the wells in triplicate followed by 250 µL of Coomassie Plus Reagent (ThermoFisher). The plate was placed onto a plate shaker to mix the contents of the wells for 30 seconds before being incubated for 10 minutes at room temperature. The absorbance was then measured at a wavelength of 595 nm using a CLARIOstar Microplate Reader (BMG LABTECH). Each absorbance value was normalised to the average of the blank (0 µg/mL). A standard curve was generated, and protein concentrations of samples were extrapolated.

For the array, 250 µg of protein was used per assay set (membranes A and B) and the array was carried out as stated in the manufacturer's protocol. The Array was adapted to be detected by infrared imaging rather than X-ray and this was done by substituting the Streptavidin-HRP for IRDye 800CW Streptavidin (LI-COR). Array images were captured using the LI-COR Oddyssey Imaging System (LI-COR) and processed using the Image Studio Lite Software (LI-COR). The intensity for each spot was determined and normalised by subtracting the intensity of the background control. Graphs of spot intensities were prepared for untreated and Atezolizumab-treated cells.

4.2.7   Statistical analysis

Statistical analysis was performed using Prism version 7.03 (GraphPad Software, Inc.) as described in Chapter 2 and 3. Data shown here was determined to be non-parametric and hence was represented as median ± range. P-values less than 0.05 were considered significant (*P<0.05, **P<0.01, ***P<0.001 and ****P<0.0001). Each independent experiment has 3-6 technical repeats which are indicated in the figure legends.

4.3 Results

4.3.1 Atezolizumab blocks PD-L1 on the cell surface of breast cancer cells in a dose-dependent manner in both 2D and 3D cell culture models

In order to assess the effects of Atezolizumab on cancer cell viability in 2D and 3D cell culture models and determine its mechanism of action in MDA-MB-231 breast cancer cells, first, the optimal dose sufficient to block PD-L1 on the surface of cancer cells cultured in 2D monolayer and 3D cell culture was determined by flow cytometry. As already shown in Chapter 2 Figure 2.1, almost 100% of MDA-MB-231 cells expressed PD-L1 on their cell surface when cultured in monolayer. However, the ability to detect PD-L1 on MDA-MB-231 cells by flow cytometry was specifically prevented by 1 hour of Atezolizumab treatment in a dose-dependent manner (Figure 4.3A and B). Treating cells with 10 nM Atezolizumab was able to completely block detection of PD-L1 on the surface of MDA-MB-231 cells using the anti-human PD-L1 antibody in 2D cell culture (Figure 4.3C).

For 3D hanging drop spheroids, 10 nM Atezolizumab was able to block almost all detectable levels of PD-L1 on the cell surface of MDA-MB-231 cells with only 8.81% (± 5.318) of cells being detected for PD-L1 expression (Figure 4.4A-C). A higher concentration of 20 nM Atezolizumab was used to treat 3D hanging drop spheroids to determine whether a higher dose would achieve complete blockade of cell surface PD-L1, but similar levels were still detected by flow cytometry (Figure 4.2A and B).

Similarly, for 3D alginate spheroid colonies treated with 10 nM Atezolizumab, PD-L1 expression in 21.7% (± 6.95) of the cells remained detectable by flow cytometry (Figure 4.5A-C). Even when increased concentrations of Atezolizumab (20 nM and 40 nM) were investigated, PD-L1 on the cell surface of MDA-MB-231 cells remained only partially blocked by Atezolizumab in 3D alginate spheroid colonies (Figure 4.5A and B).
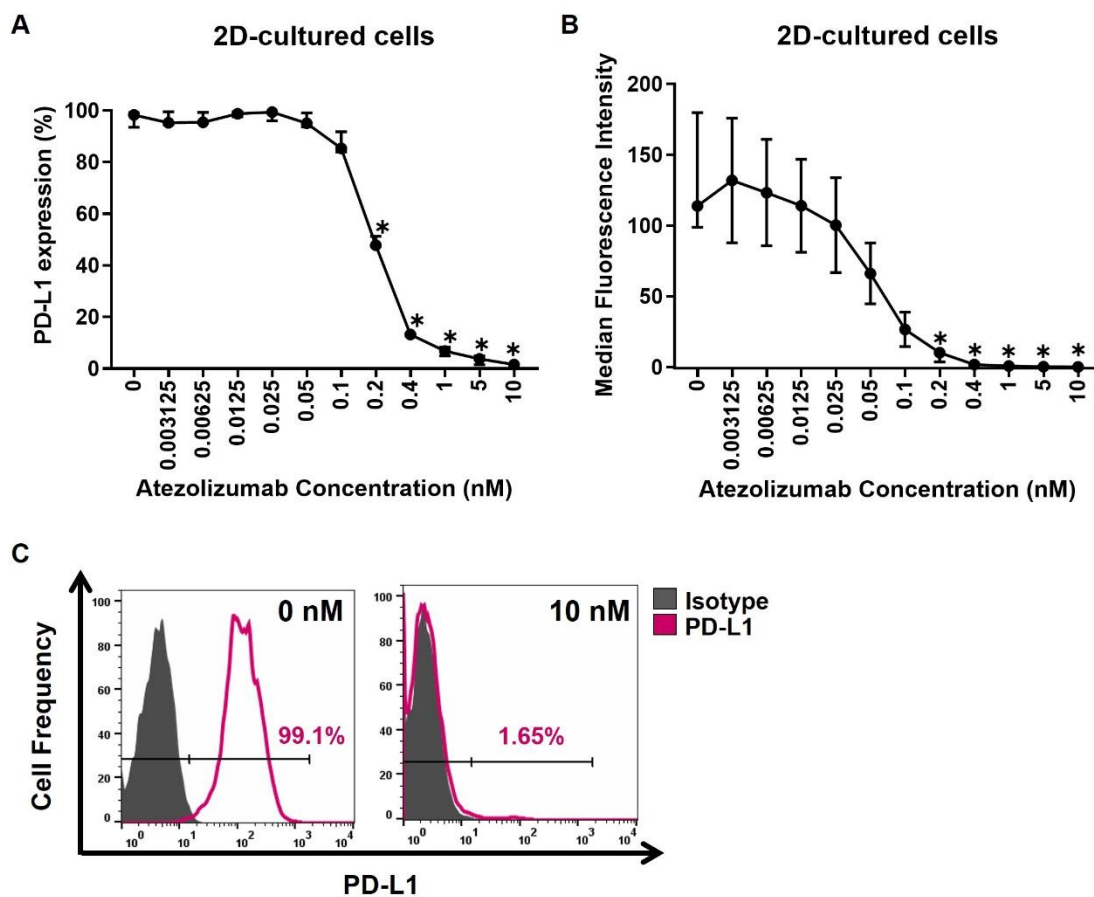
Figure 4.3 Atezolizumab completely blocks PD-L1 detection on the cell surface of MDA-MB-231 cells cultured in monolayer in a dose-dependent manner. The degree of PD-L1 blockade after 1 hour of Atezolizumab treatment at different concentrations (0 to 10 nM) on MDA-MB-231 cells cultured in monolayer was determined by flow cytometry. **(A)** The percentage of cells expressing PD-L1 and **(B)** the MFI of detectable PD-L1 expression is shown for each concentration investigated. **(C)** Representative flow cytometry histograms of 0 and 10 nM concentrations are shown to demonstrate the degree of PD-L1 blockade by Atezolizumab. Data is presented as median ± range. n=3 independent experiments each with 3 technical repeats. Data was analysed by a Kruskal-Wallis followed by Dunn's multiple comparisons test (*P<0.05).

Figure 4.4 Atezolizumab almost completely blocks PD-L1 detection on the cell surface of MDA-MB-231 cells cultured in 3D hanging drop spheroids in a dose-dependent manner. The degree of PD-L1 blockade after 1 hour of Atezolizumab treatment at different concentrations (0 to 20 nM) on MDA-MB-231 cells cultured in 3D hanging drop spheroids was determined by flow cytometry. **(A)** The percentage of cells expressing PD-L1 and **(B)** the MFI of detectable PD-L1 expression is shown for each concentration investigated. **(C)** Representative flow cytometry histograms of 0 and 10 nM concentrations are shown to demonstrate the degree of PD-L1 blockade by Atezolizumab. Data is presented as median ± range. n=3 independent experiments each with 3 technical repeats. Data was analysed by a Kruskal-Wallis followed by Dunn's multiple comparisons test (*$p < 0.05$).

Figure 4.5 Atezolizumab partially blocks PD-L1 detection on the cell surface of MDA-MB-231 cells cultured in 3D alginate spheroid colonies in a dose-dependent manner. The degree of PD-L1 blockade after 1 hour of Atezolizumab treatment at different concentrations (0 to 40 nM) on MDA-MB-231 cells cultured in 3D alginate spheroid colonies was determined by flow cytometry. **(A)** The percentage of cells expressing PD-L1 and **(B)** the MFI of detectable PD-L1 expression is shown for each concentration investigated. **(C)** Representative flow cytometry histograms of 0 and 10 nM concentrations are shown to demonstrate the partial blockade of PD-L1 by Atezolizumab. Data is presented as median ± range. n=3 independent experiments each with 3 technical repeats. Data was analysed by a Kruskal-Wallis followed by Dunn's multiple comparisons test (*$P < 0.05$).

4.3.2 Atezolizumab does not affect PD-L1 mRNA expression levels by breast cancer cells in 2D and 3D cell culture models

Next, it was determined whether blocking PD-L1 with 10 nM Atezolizumab on the cell surface of MDA-MB-231 cells influenced PD-L1 mRNA levels when cells were grown in monolayer and 3D cultures. RT-qPCR experiments to measure PD-L1 mRNA levels showed that 10 nM of Atezolizumab treatment for 1 hour did not significantly affect PD-L1 mRNA levels in monolayer or 3D cell cultures (Figure 4.6). Importantly, this experiment also verified the differential levels of PD-L1 mRNA observed amongst the different cell culture models observed in Chapter 3 Figures 3.11 and 3.12.

4.3.3 Atezolizumab has no significant effect on the growth and proliferation of MDA-MB-231 cells cultured in 2D monolayer cell culture

To determine whether Atezolizumab treatment could influence the growth and proliferation of MDA-MB-231 cells cultured in 2D monolayer, firstly cells seeded into 96-well plates were cultured with or without Atezolizumab for 3 or 6 days before being stained with Hoechst 33342/PI. Hoechst 333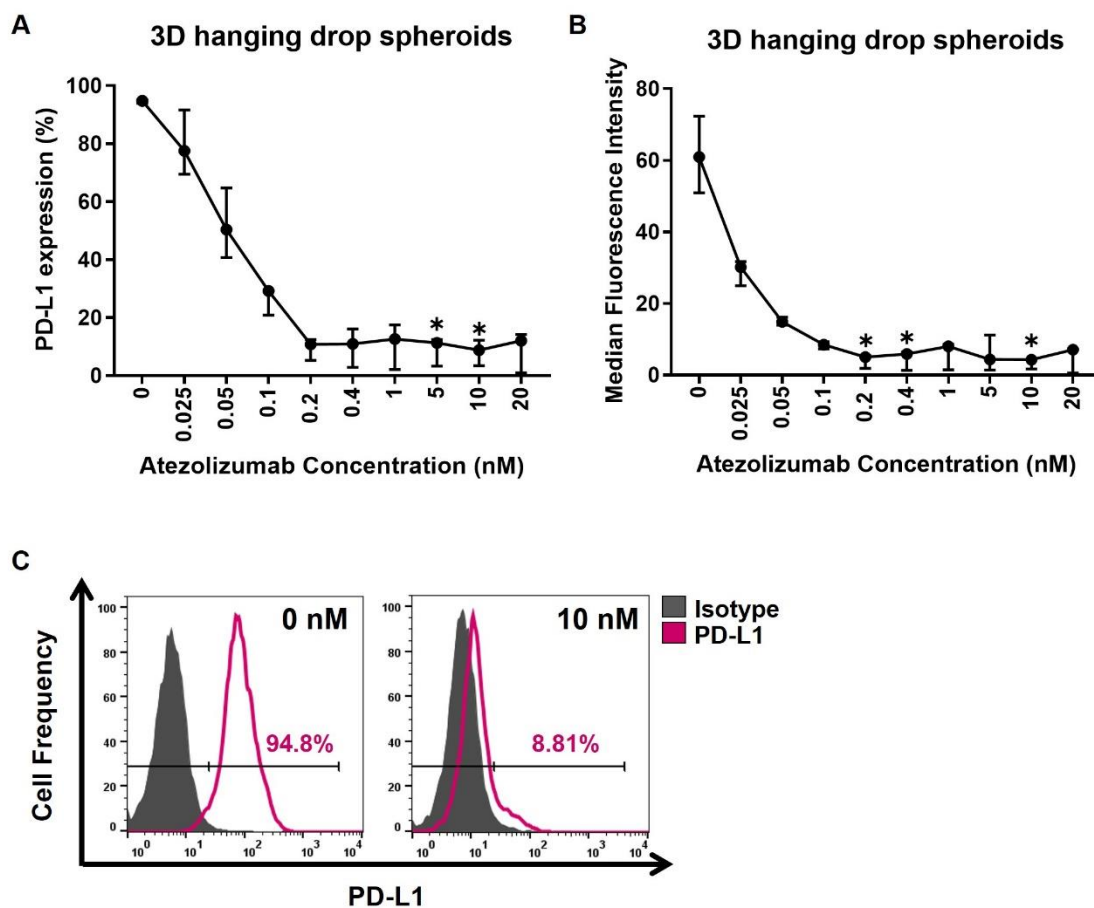42/PI images showed that Atezolizumab-treated cells seeded at the same cell density as untreated cells appeared to be less confluent after 3 and 6 days (Figure 4.7). To verify this observation, the surface area covered by Hoechst 33342/PI positive cells was calculated for untreated and Atezolizumab-treated cells and expressed as a percentage of the control (untreated cells). However, the percentage surface area covered by untreated and Atezolizumab-treated cells was found not to be statistically significantly different after 3 (Figure 4.8A) or 6 (Figure 4.8B) days of culture.

The expression of the cell proliferation marker, Ki67 was also investigated in MDA-MB-231 cells treated with or without Atezolizumab in monolayer cell culture to further assess whether Atezolizumab has any effect on cell proliferation. Atezolizumab-treated cells demonstrated a similar frequency and level of Ki67 protein expression compared to untreated cells after 3 (Figure 4.9A) and 6 (Figure 4.9B) days of culture. At day 6 however, the median MFI for Ki67 expression by Atezolizumab-treated cells was lower than that observed in untreated cells, but this was not significant.
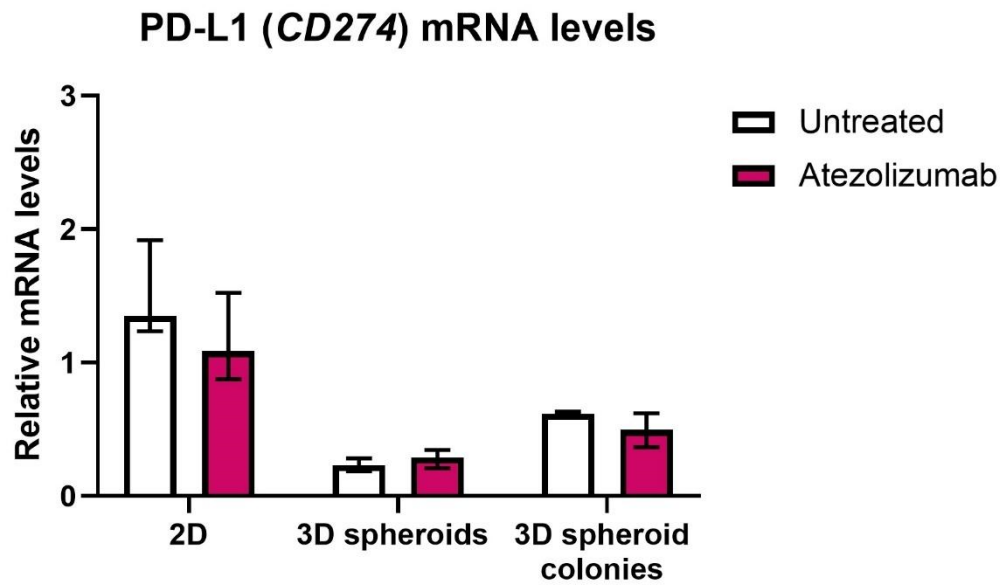
PD-L1 (*CD274*) mRNA levels

Figure 4.6 Atezolizumab does not affect PD-L1 mRNA levels in MDA-MB-231 cells cultured in 2D monolayer and 3D cell culture models. RT-qPCR was used to determine the level of PD-L1 mRNA expressed by untreated and Atezolizumab-treated cells cultured in 2D monolayer, 3D hanging drop spheroids and 3D alginate spheroid colonies, relative to HKGs. Data is presented as median ± range. n=3 independent experiments each with 3 technical repeats. Statistical analysis was undertaken using a Mann-Whitney U-test on each cell culture method.
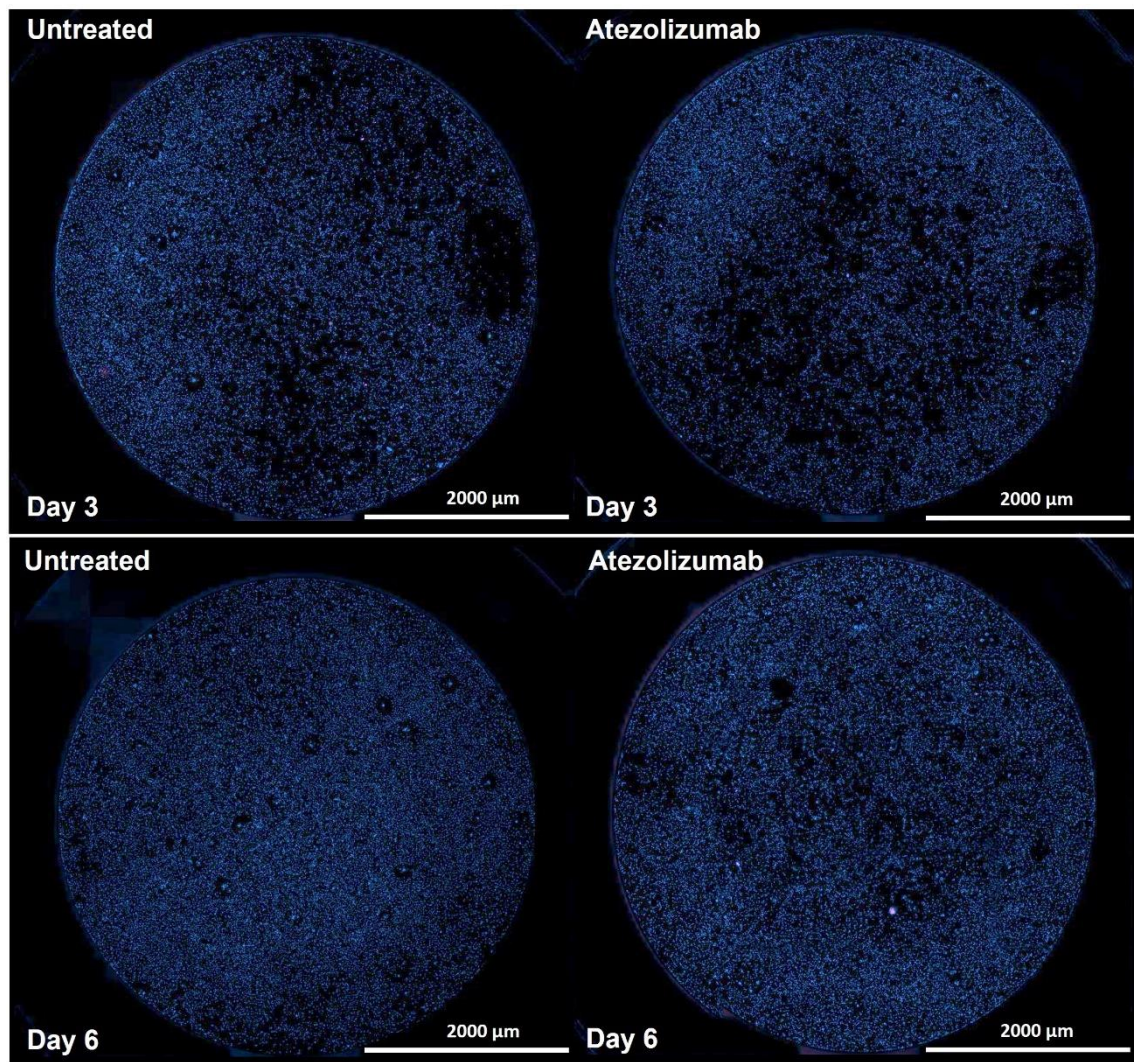
Figure 4.7 MDA-MB-231 cells treated with Atezolizumab for 3 or 6 days appear to be less confluent than untreated cells. Low magnification images of wells containing untreated and Atezolizumab-treated cells were captured using the 4X objective lens at day 3 and 6 of culture after being stained with Hoechst 33342/PI. Scale bar represents 2000 µm. n=3 independent experiments each with 3 technical repeats.
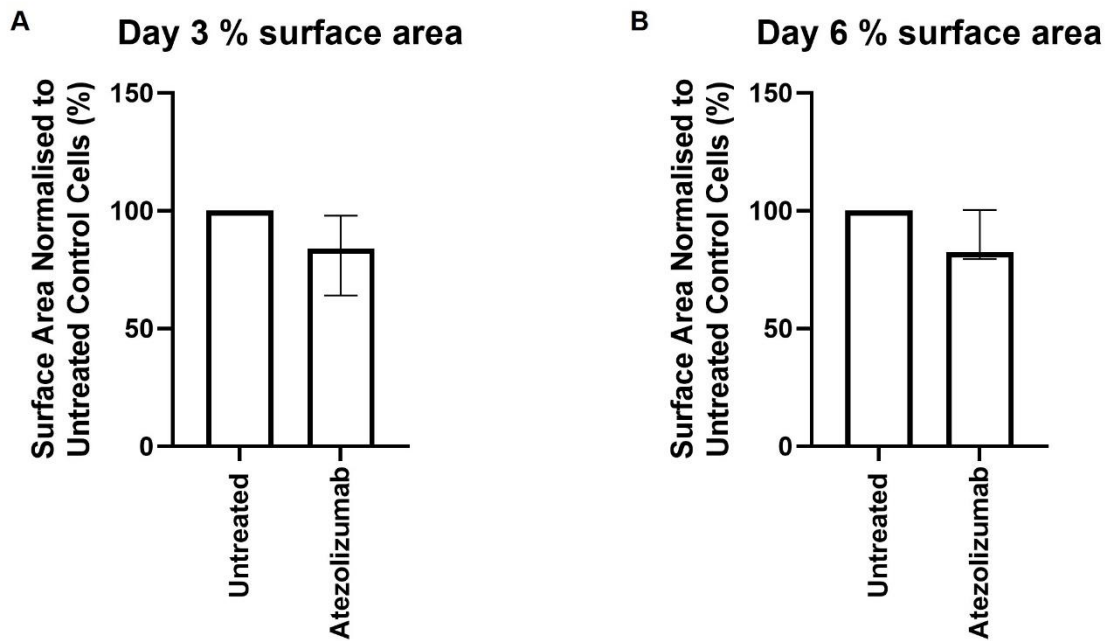
Figure 4.8 Atezolizumab treatment does not significantly affect the percentage surface area of the wells covered by MDA-MB-231 cells after 3 or 6 days of culture. The surface area of the wells covered with untreated and Atezolizumab-treated cells stained with Hoechst 33342/PI was determined at **(A)** day 3 and **(B)** day 6 of culture. Data is expressed as a percentage of the untreated control cells and is presented as median ± range. n=3 independent experiments each with 3 technical repeats. Data was analysed by a Mann-Whitney U-test.
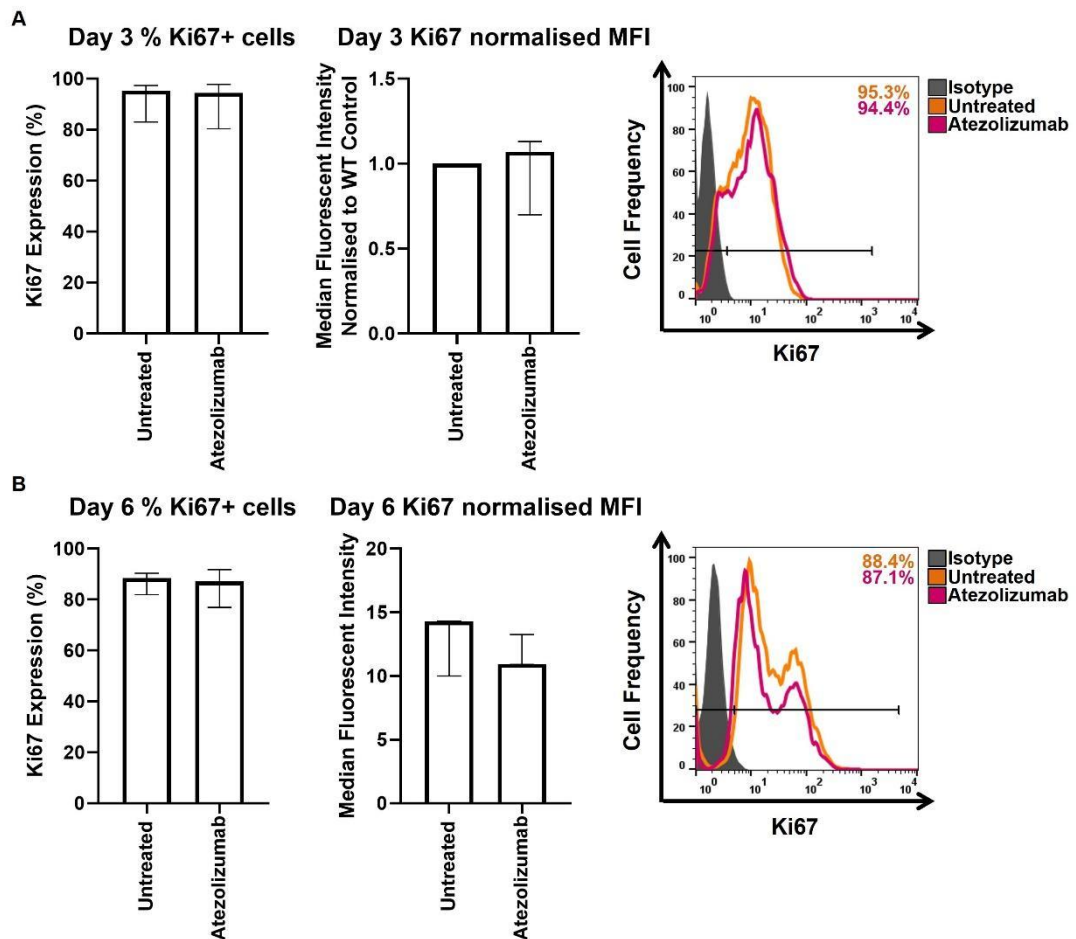
Figure 4.9 Atezolizumab treatment had no significant effect on the expression of Ki67 by MDA-MB-231 cells cultured in monolayer. Ki67 protein expression was measured by untreated and Atezolizumab-treated cells at **(A)** day 3 and **(B)** day 6 of culture. The percentage of cells expressing Ki67 protein is displayed (left) alongside the MFI (right). Representative flow cytometry histograms illustrate the isotype control (grey) relative to the Ki67 positive population for untreated (orange) and Atezolizumab-treated (pink) cells. Data is presented as median ± range. n=3 independent experiments each with 3 technical repeats. Data was analysed by a Mann-Whitney U-test.

4.3.4 Atezolizumab treatment for 6 days shows signs to induce some cell death of MDA-MB-231 cells cultured in 2D monolayer cell culture

Despite Atezolizumab having no significant effect on confluence and Ki67 expression of MDA-MB-231 cells cultured in monolayer, it was still of interest to determine whether Atezolizumab influenced the viability of MDA-MB-231 cells. Parallel with investigating the cell viability of MDA-MB-231 cells, the expression of PD-L1 was assessed by flow cytometry to ensure that Atezolizumab was blocking PD-L1 detection on the surface of cancer cells for all cell viability experiments so that it could be assumed that any changes to cell viability would likely be a result of the Atezolizumab treatment (Appendix Figure 9.8). As described previously in this Chapter, Section 4.3.1, 1 hour of 10 nM Atezolizumab treatment was sufficient to block PD-L1 on the surface of MDA-MB-231 cells cultured in monolayer. Because of this, the effects of Atezolizumab on cell viability was assessed following 3 and 6 days of Atezolizumab treatment, as well as at day 3 and day 6 after 1 hour of Atezolizumab treatment to determine whether prolonged exposure to Atezolizumab had any pronounced effects on breast cancer cell viability.

MDA-MB-231 cells treated with or without Atezolizumab as described above were subsequently stained with Annexin V/PI to assess cellular apoptosis and necrosis. Only MDA-MB-231 cells treated with Atezolizumab for 6 days showed signs of necrosis, but this was not significant compared to untreated cells (Figure 4.10A and B). The percentage of necrotic cells doubled in cells treated with Atezolizumab for 6 days compared to untreated cells.

4.3.5 Atezolizumab treatment for 6 days affects the cellular activity of MDA-MB-231 breast cancer cells cultured in monolayer

In order to validate the effects observed by Atezolizumab on the viability of MDA-MB-231 cells, cellular ATP production was measured as an indicator of cell viability following 3 and 6 days of treatment. As expected from the data above, ATP levels after 3 days of Atezolizumab treatment were comparable to that of the ATP levels of untreated cells (Figure 4.11A). However, following 6 days of Atezolizumab treatment, cells exhibited significantly lower levels of ATP compared to untreated cells ($p=0.05$) (Figure 4.11B), which correlated with the Annexin V/PI cell viability data.
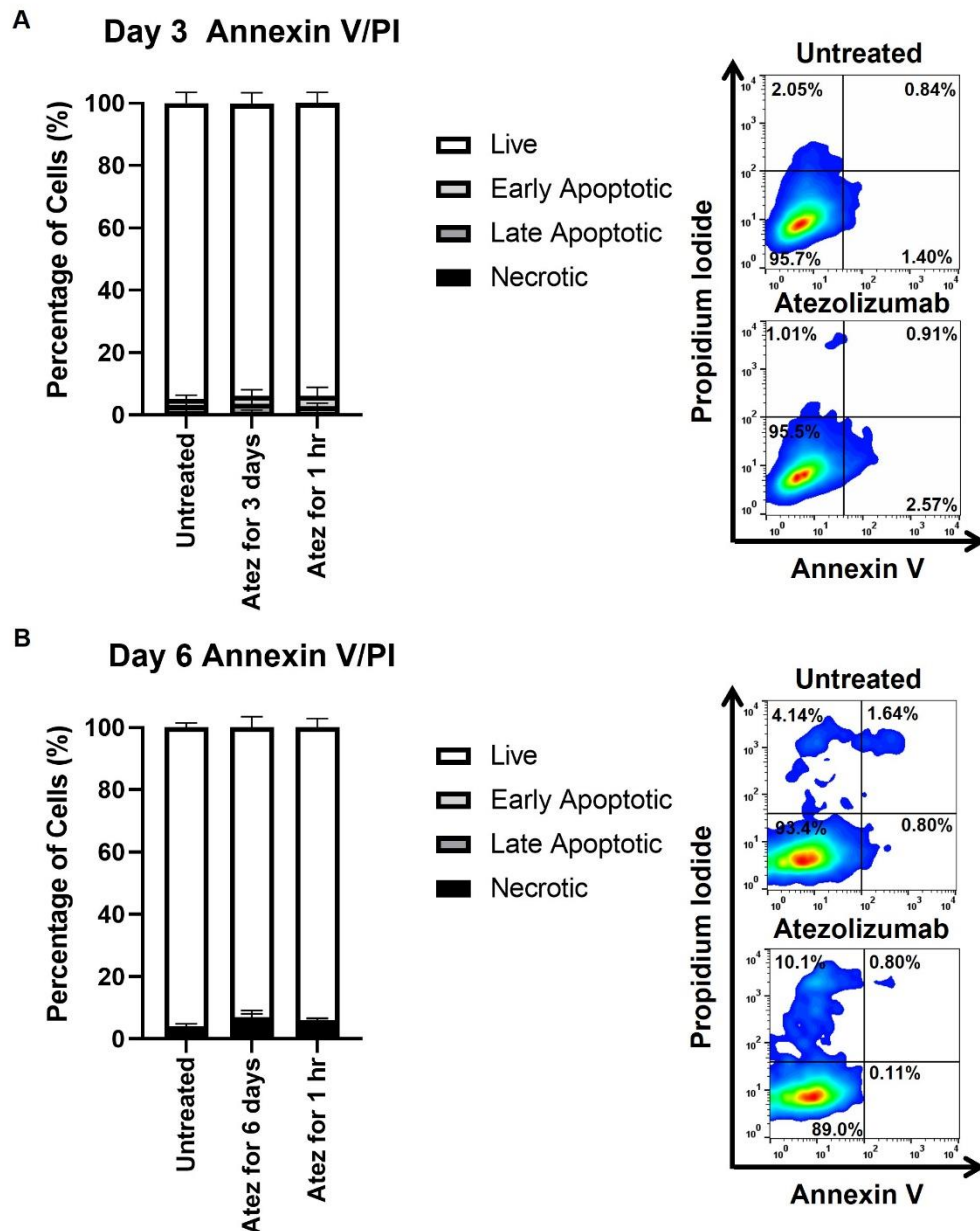
Figure 4.10 Atezolizumab-mediated blockade of PD-L1 has minimal effect on the viability of MDA-MB-231 cells at day 3 and 6 of culture. Annexin V/PI staining was used to assess the viability of untreated MDA-MB-231 cells compared to **(A)** cells treated with Atezolizumab for 3 days or 1 hour at day 3 of culture, and **(B)** cells treated with Atezolizumab for 6 days or 1 hour at day 6 of culture. Representative flow cytometry plots show the effects of Atezolizumab on cancer cell viability at day 3 and 6 of culture compared to untreated cells. Data is presented as median ± range. n=3 independent experiments each with 3 technical repeats. Data was analysed by a Kruskal-Wallis comparing the percentage of non-viable cells in untreated versus Atezolizumab-treated cells.
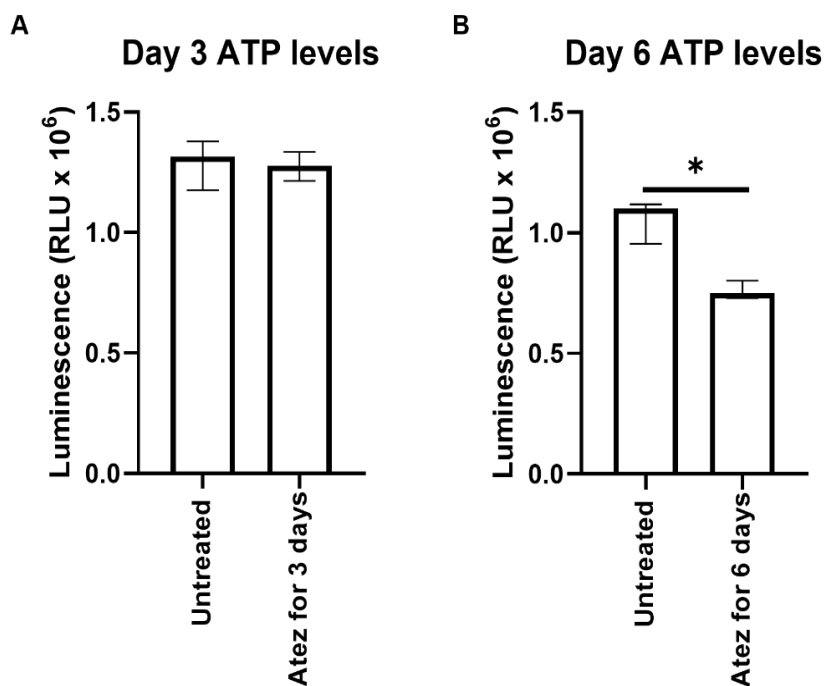
Figure 4.11 Atezolizumab significantly decreases the level of ATP produced by MDA-MB-231 cells after 6 days. The cellular activity by untreated and Atezolizumab-treated MDA-MB-231 cells was measured as an indicator of viability after **(A)** 3 and **(B)** 6 days of culture. Data is presented as median ± range. n=3 independent experiments each with 6 technical repeats. Data was analysed by a Mann-Whitney U test (*P<0.05).

4.3.6 Atezolizumab has minimal effect on the growth and proliferation of MDA-MB-231 breast cancer cells cultured in hanging drop 3D spheroids

Although Atezolizumab treatment had no significant effects on the growth and proliferation of 2D monolayer MDA-MB-231 cells, it was next determined whether Atezolizumab could affect the growth and proliferation of MDA-MB-231 cells cultured in 3D hanging drop spheroids. It was first determined whether Atezolizumab treatment affected the diameter of 3D hanging drop spheroids over a 7-day period by comparing Atezolizumab-treated to untreated 3D spheroids. However, whether 3D spheroids were treated with or without Atezolizumab, they displayed comparable diameters at each time point investigated (Figure 4.12).

Representative images of 3D spheroids stained with Hoechst 33342/PI not only further demonstrated the similarity in the diameter between those treated and untreated, but importantly highlighted apparent differences in staining patterns at day 3 and 6 of culture (Figure 4.13). After 3 days of culture, 3D spheroids treated with or without Atezolizumab exhibited similar staining patterns throughout the spheroids, however after 6 days untreated 3D spheroids displayed a higher density of cells stained with Hoechst 33342 throughout the 3D spheroid, which could only be observed in the outermost layer of those spheroids treated with Atezolizumab.

To further investigate the growth of MDA-MB-231 cells in 3D spheroids formed by hanging drop, the expression of Ki67 was measured to determine whether Atezolizumab affects their proliferative capacity. Atezolizumab-treated 3D spheroids displayed similar expression levels of Ki67 protein compared to untreated 3D spheroids after 3 (Figure 4.14A) and 6 (Figure 4.14B) days, however it is important to note a great deal of heterogeneity in the Atezolizumab-treated hanging drop spheroids at 3 or 6 days.
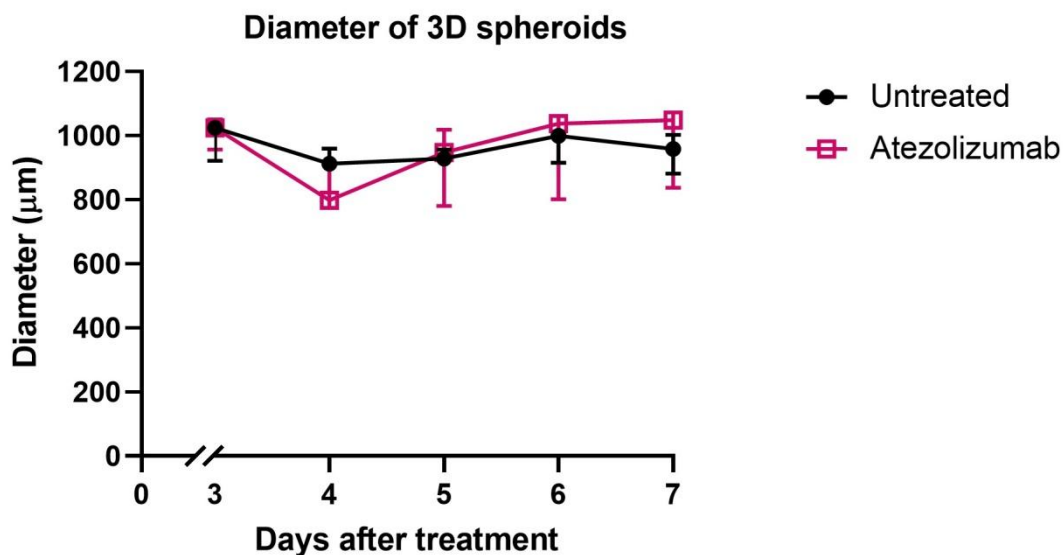
Figure 4.12 MDA-MB-231 cells form 3D hanging drop spheroids of similar diameter whether treated with or without Atezolizumab. The diameter of 3D hanging drop spheroids untreated or treated with Atezolizumab was measured from day 3 to day 7. Data is presented as median ± range. n=4 independent experiments each with 3 technical repeats. Statistical analysis was undertaken using Mann-Whitney U-tests to compare untreated and treated 3D spheroid diameters at each time point.
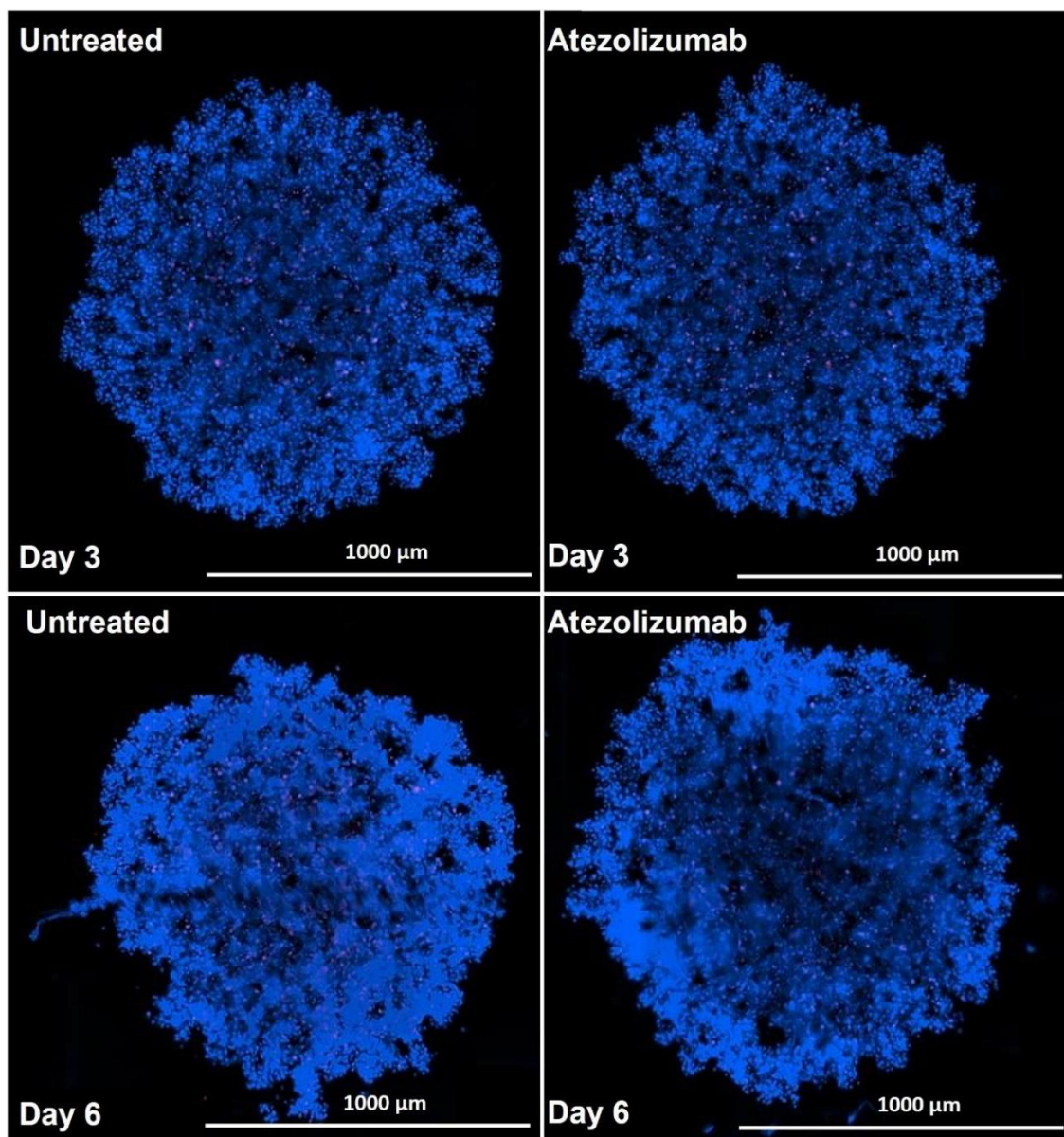
Figure 4.13 Untreated 3D hanging drop spheroids visually display a higher density of Hoechst 33342 positive cells throughout the spheroid after 6 days of culture. Z-stack images of untreated and Atezolizumab-treated 3D hanging drop spheroids stained with Hoechst 33342/PI were captured by fluorescent microscopy after 3 and 6 days of culture. Scale bar represents 1000 μm. n=3 independent experiments, each with 3 technical repeats.
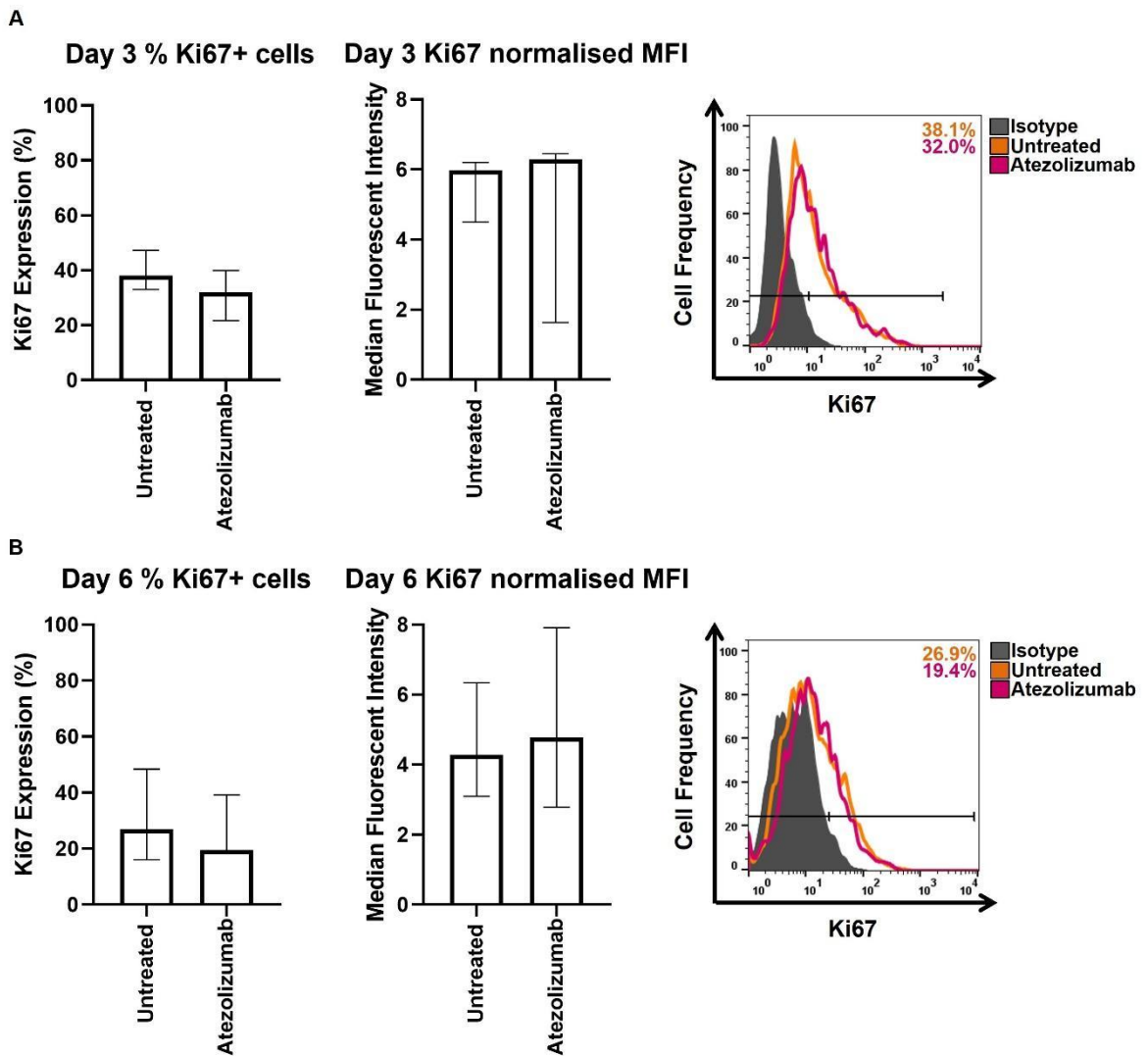
Figure 4.14 Atezolizumab has no effect on the frequency and level of Ki67 expressed by cells cultured in 3D hanging drop spheroids for 3 or 6 days. Flow cytometry was used to measure Ki67 protein expressed by untreated and Atezolizumab-treated cells cultured in 3D hanging drop spheroids for **(A)** 3 and **(B)** 6 days. The percentage of cells expressing Ki67 protein is displayed (left) alongside the MFI (right). Representative flow cytometry histograms illustrate the isotype control (grey) relative to the Ki67 positive population for untreated (orange) and Atezolizumab-treated (pink) 3D hanging drop spheroids. Data is presented as median ± range. n=3 independent experiments each with 3 technical repeats. Data was analysed using a Mann-Whitney U-test.

4.3.7 Atezolizumab does not significantly affect the viability of MDA-MB-231 3D hanging drop spheroids after 6 days of culture

MDA-MB-231 3D hanging drop spheroids were treated with Atezolizumab for 3 and 6 days, or for 1 hour at day 3 and 6 of culture before the cell viability was assessed. PD-L1 blockade by Atezolizumab was verified by flow cytometry (Appendix Figure 9.8). Annexin V/PI staining of 3D spheroids showed a small proportion of cells were undergoing all forms of cell death, this was observed in both untreated and Atezolizumab treated cells, at all treatment regimens and time points, and there were no significant differences in their proportion of cells in the difference stages of cell death (Figure 4.15A and B). However, in Atezolizumab-treated 3D spheroids more apoptotic cell death was observed after 1 hour of treatment at both timepoints and after 6 days of treatment.

4.3.8 Atezolizumab treatment for 6 days affects the cellular activity of MDA-MB-231 cells cultured in 3D hanging drop spheroids

To further investigate the effects of Atezolizumab treatment on MDA-MB-231 3D hanging drop spheroid viability, ATP levels were measured in untreated and Atezolizumab-treated 3D spheroids at 3 and 6 days. Atezolizumab-treated 3D spheroids did not display a statistically significant difference in ATP levels compared to those untreated after 3 days of culture (Figure 4.16A), but after 6 days of culture with Atezolizumab treatment, 3D spheroids showed significantly reduced ATP levels compared to those untreated ($p=0.05$) (Figure 4.16B).
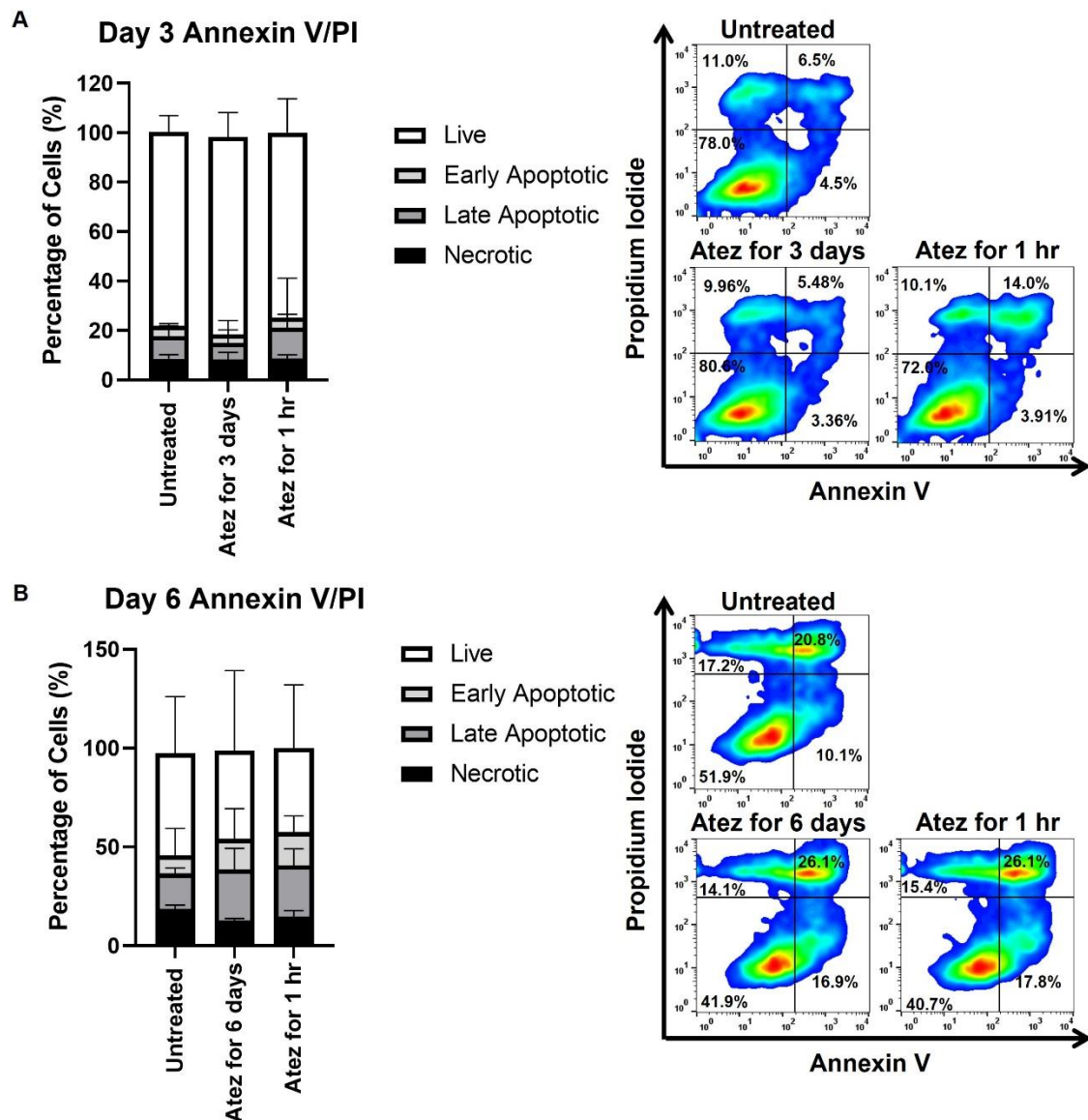
Figure 4.15 Atezolizumab-mediated blockade of PD-L1 does not significantly induce apoptotic cell death in cells cultured in 3D hanging drop spheroids after 3 and 6 of culture. Annexin V/PI staining was used to assess the viability of untreated cells cultured in 3D hanging drop spheroids compared to **(A)** cells treated with Atezolizumab for 3 days or for 1 hour at day 3 of culture and **(B)** cells treated for 6 days or for 1 hour at day 6 of culture. Representative flow cytometry plots demonstrate the effects of Atezolizumab on cancer cell viability in 3D hanging drop spheroids. Data is presented as median ± range. n=3 independent experiments each with 3 technical repeats. Data was analysed by a Kruskal-Wallis test comparing the percentage of non-viable untreated cells versus Atezolizumab-treated cells.
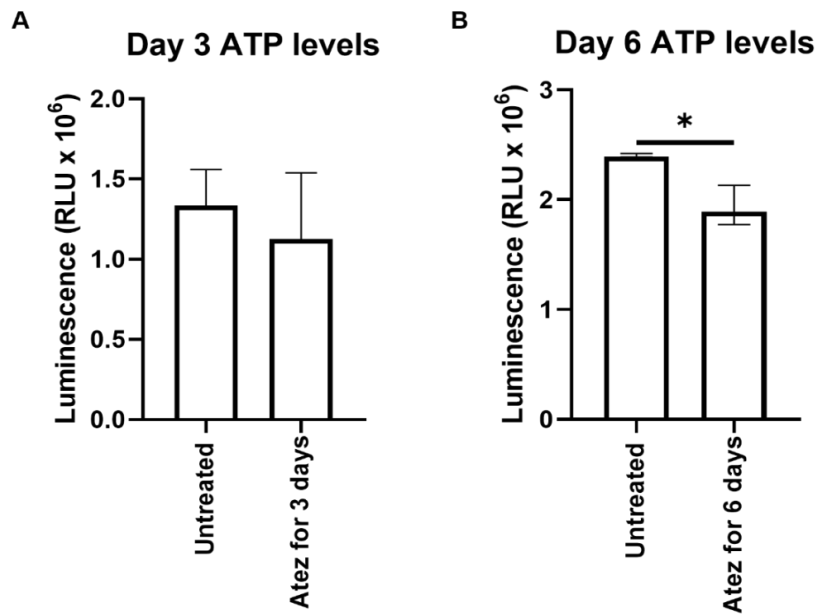
Figure 4.16 Atezolizumab significantly reduced the level of ATP produced by 3D hanging drop spheroids after 6 days. The cellular activity of cells cultured in 3D hanging drop spheroids treated with or without Atezolizumab for **(A)** 3 and **(B)** 6 days was assessed by measuring ATP levels as an indicator of cell viability. Data is presented as median ± range. n=3 independent experiments each with 6 technical repeats. Data was analysed by a Mann-Whitney U test (*P<0.05).

4.3.9 Atezolizumab does not affect the growth of MDA-MB-231 3D spheroids colonies that form in alginate hydrogel beads

Next, it was determined whether Atezolizumab treatment had any effect on the growth and proliferation of MDA-MB-231 3D spheroid colonies grown in alginate hydrogel beads. Firstly, the diameters of untreated and Atezolizumab-treated 3D alginate spheroid colonies were measured over a time course of 10 days (Figure 4.17). It was shown that the colonies grew from single cells (approximately 20 µm) from day 0 over 10 days to form colonies with a diameter of approximately 100 µm. Atezolizumab treatment did not affect the diameter of colonies that formed in alginate as the diameters were comparable to those untreated at each time point assessed. Representative images of whole alginate hydrogel beads stained with Hoechst 33342/PI after 3, 6 and 10 days of culture also demonstrated the similarities in the growth of untreated and Atezolizumab-treated 3D spheroid colonies over the time course investigated (Figure 4.18).

Ki67 protein expression by untreated and Atezolizumab-treated 3D alginate spheroid colonies was also assessed to evaluate whether Atezolizumab treatment could affect cell proliferation of MDA-MB-231 cells. However, Atezolizumab treatment had no effect on the expression of Ki67 protein by cells cultured in 3D alginate spheroid colonies for 3 (Figure 4.19A), 6 (Figure 4.19B) or 10 (Figure 4.19C) days compared to those untreated.
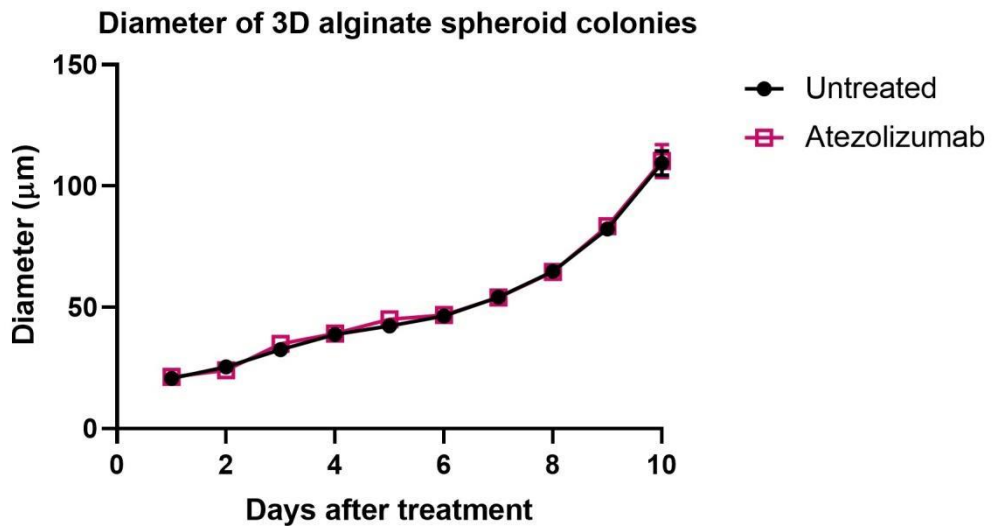
Figure 4.17 MDA-MB-231 cells form 3D spheroid colonies in alginate hydrogel beads of similar diameter whether treated with or without Atezolizumab. The diameter of 3D alginate spheroid colonies untreated or treated with Atezolizumab was measured over a time course of 10 days. Data is presented as median ± range. n=3 independent experiments each with 3 technical repeats. Data was analysed by performing Mann-Whitney U-tests for each time point assessed comparing untreated and treated 3D alginate spheroid colony diameters.
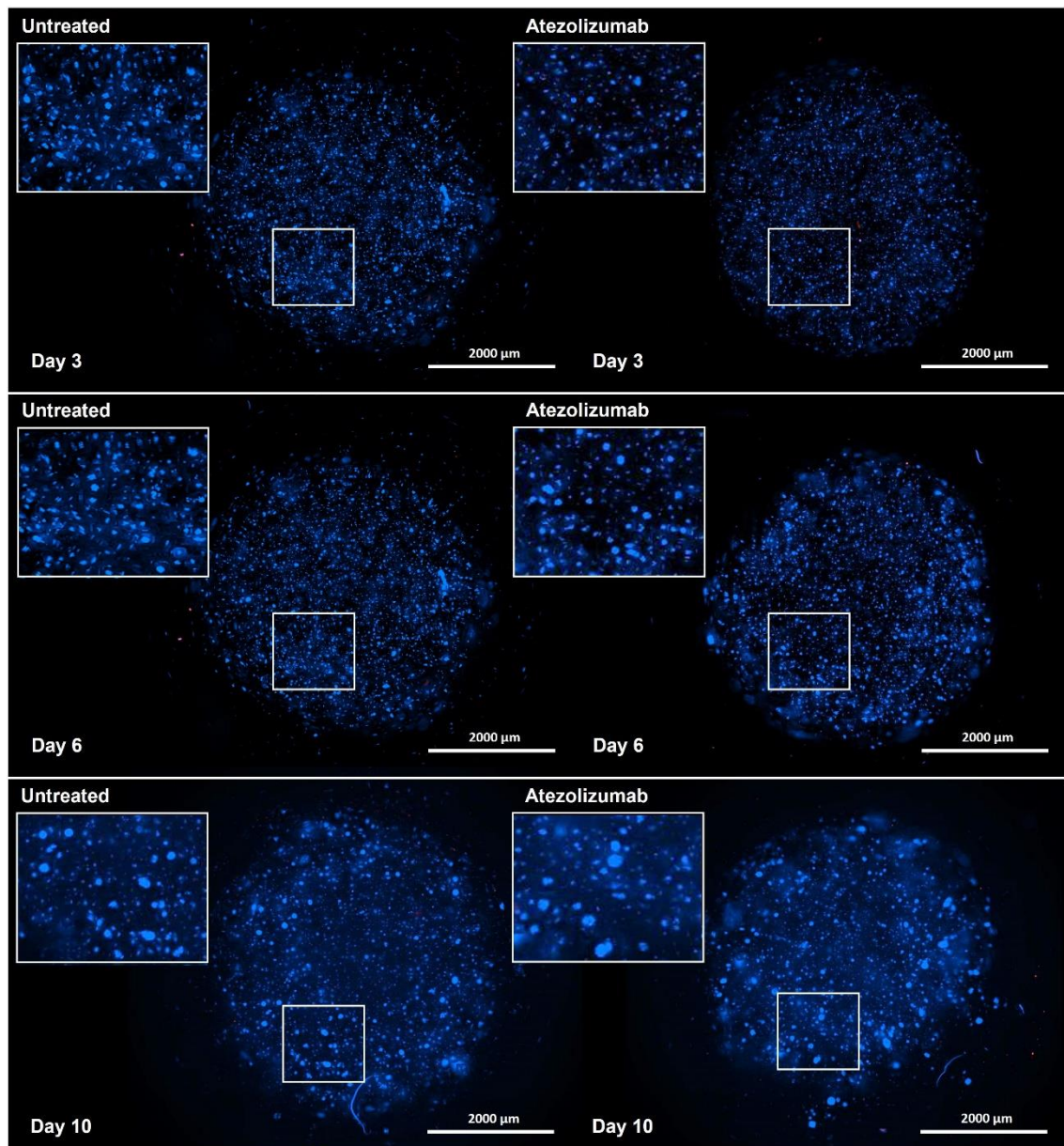
Figure 4.18 MDA-MB-231 cells grow similarly in alginate hydrogel beads to form 3D spheroid colonies whether treated with or without Atezolizumab. Z-stack images of whole alginate hydrogel beads were captured after they were stained with Hoechst 33342/PI at day 3, 6 and 10 of culture to demonstrate the growth of 3D spheroid colonies within the alginate beads treated with or without Atezolizumab. Scale bar represents 2000 μm. n=3 independent experiments, each with 3 technical repeats.
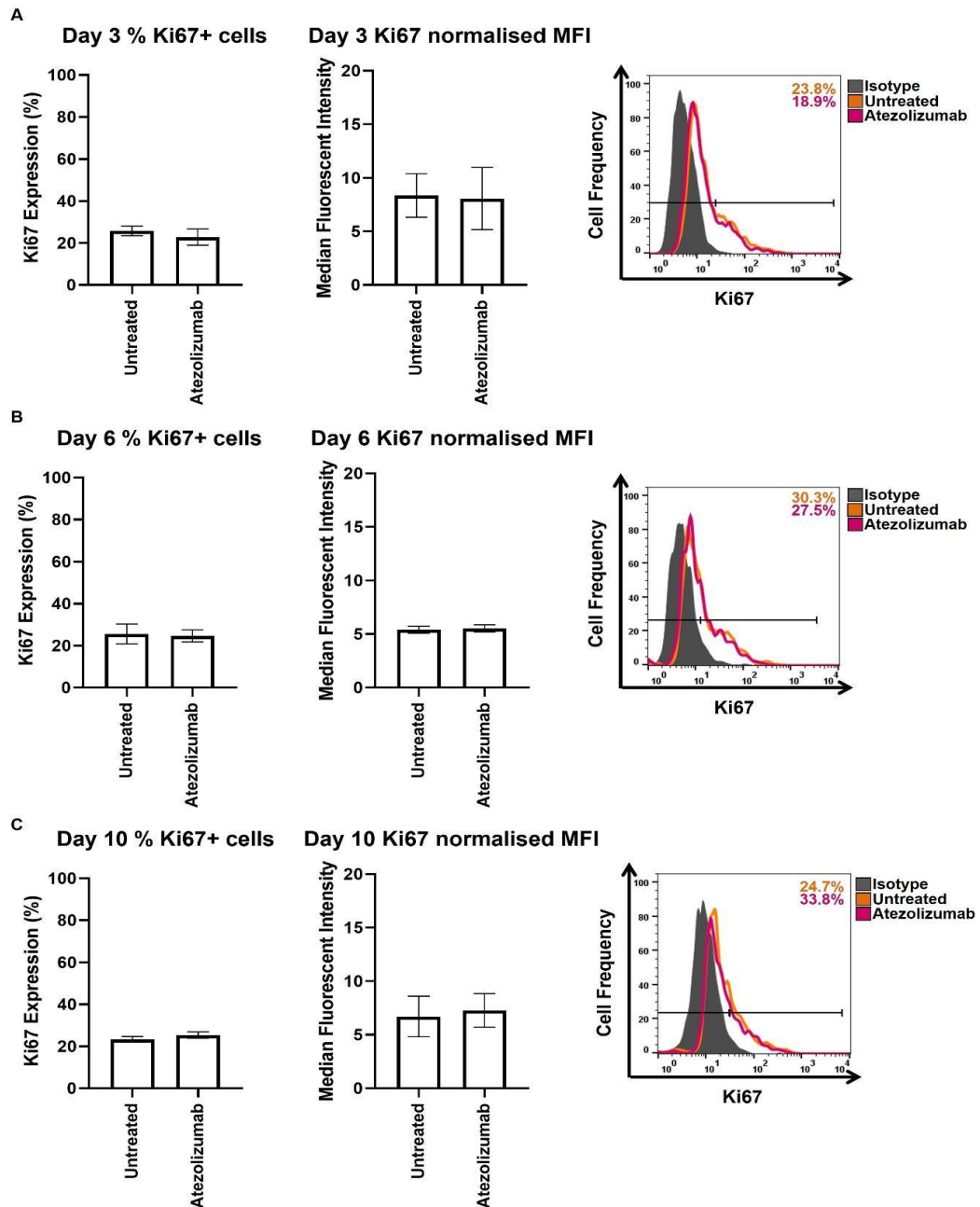
Figure 4.19 Atezolizumab has no effect on the frequency and level of Ki67 expressed by MDA-MB-231 cells after being cultured in 3D alginate spheroid colonies for 3, 6 and 10 days. Flow cytometry was used to measure Ki67 protein expressed by untreated and Atezolizumab-treated cells cultured in 3D alginate spheroid colonies for **(A)** 3, **(B)** 6 and **(C)** 10 days. The percentage of cells expressing Ki67 protein is displayed (left) alongside the MFI (right). Representative flow cytometry histograms illustrate the isotype control (grey) relative to the Ki67 positive population for untreated (orange) and Atezolizumab-treated (pink) 3D alginate spheroid colonies. Data is presented as median ± range. n=3 independent experiments each with 3 technical repeats. Data was analysed using a Mann-Whitney U-test.

4.3.10 Atezolizumab shows signs to induce some cell death in 3D alginate spheroid colonies after 3, 6 and 10 days of culture

The effects of Atezolizumab on the viability of MDA-MB-231 3D spheroids colonies grown in alginate hydrogel beads after 3, 6 or 10 days of culture was next investigated. PD-L1 blockade was once again verified by flow cytometry (Appendix Figure 9.8).

Atezolizumab treatment of alginate spheroid colonies did induce some apoptotic cell death in 3D spheroid colonies in comparison to those untreated at day 3 (Figure 4.20A), 6 (Figure 4.20B) and 10 (Figure 4.20C) of culture. The highest levels of cell death were observed after 3 days of culture in Atezolizumab-treated 3D alginate spheroid colonies. 44.4% of cells treated with Atezolizumab for 3 days and 46.8% of cells treated with Atezolizumab for 1 hour at day 3 of culture were found to be apoptotic or necrotic, compared to only 26.1% of cells found in those untreated. However, these levels of total cell death were not significantly different from the untreated control cells at all timepoints assessed.

4.3.11 Atezolizumab treatment for 6 or 10 days affects the cellular activity of MDA-MB-231 breast cancer cells cultured in 3D alginate spheroid colonies

To further validate the effects of Atezolizumab treatment on the viability of 3D alginate spheroid colonies, ATP measurements were taken after 3, 6 and 10 days of culture. Interestingly, no significant effects on the ATP levels were found for Atezolizumab-treated 3D alginate spheroid colonies after 3 days of culture compared to those untreated (Figure 4.21A), despite observing the highest amount of cell death via Annexin V/PI staining at day 3. However, the levels of ATP produced by Atezolizumab-treated 3D alginate spheroid colonies after 6 (Figure 4.21B) and 10 (Figure 4.21C) days of culture were significantly reduced compared to those untreated ($p=0.05$).

A

Day 3 Annexin V/PI
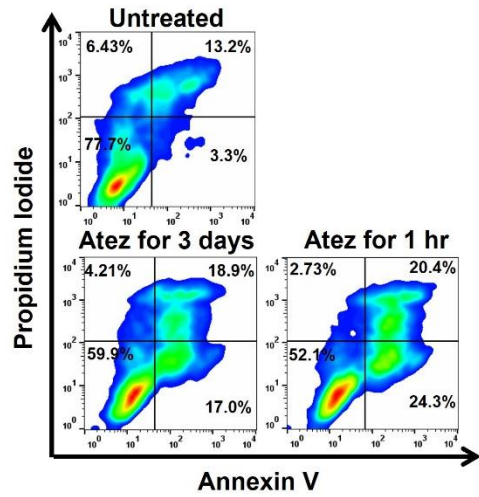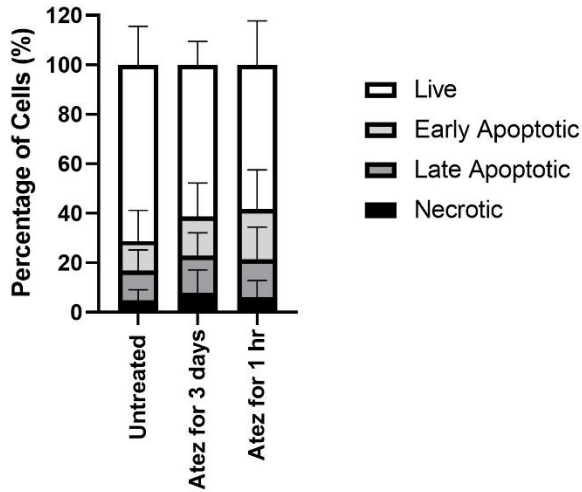
B

Day 6 Annexin V/PI
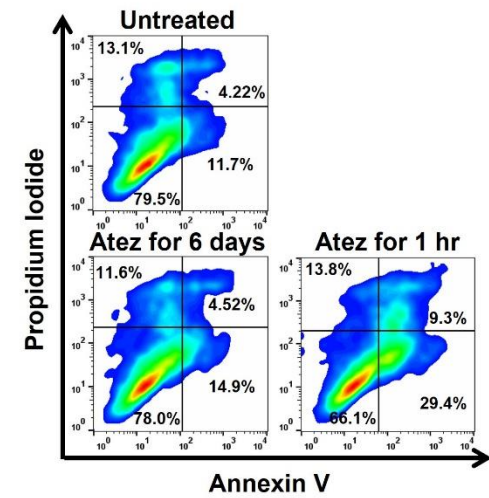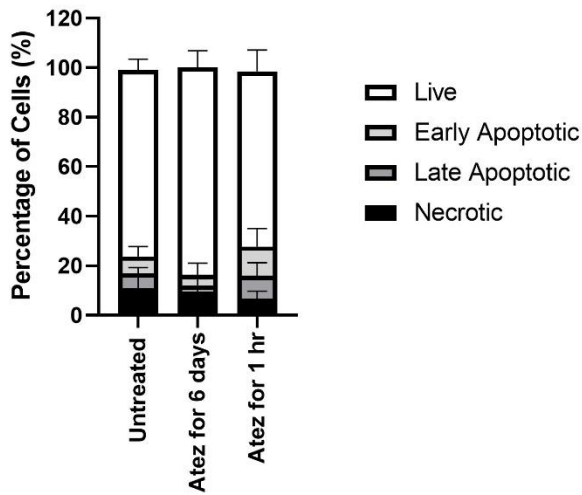
C

Day 10 Annexin V/PI
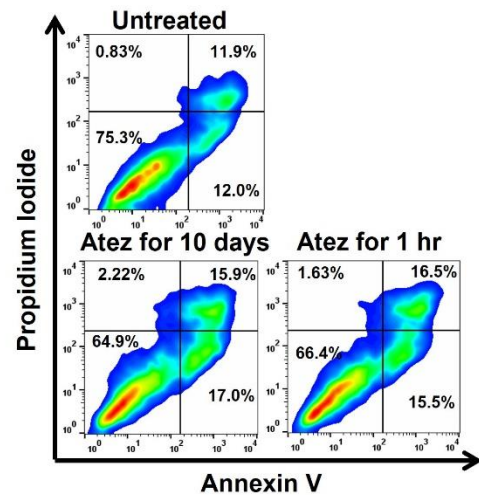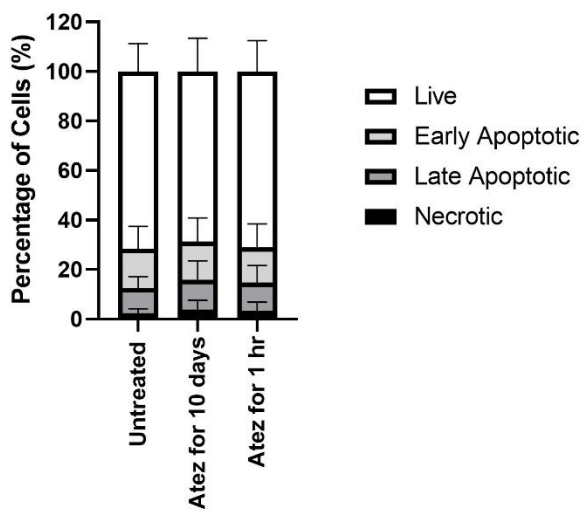
Figure 4.20 Treatment of 3D alginate spheroid colonies with Atezolizumab does not significantly induce apoptotic cell death at day 3, 6 or 10 of culture. Annexin V/PI staining was used to assess the viability of MDA-MB-231 cells cultured in 3D alginate spheroid colonies untreated or treated with Atezolizumab for **(A)** 3, **(B)** 6 and **(C)** 10 days or for 1 hour at **(A)** day 3, **(B)** day 6 and **(C)** day 10 of culture. Representative flow cytometry plots are displayed for each timepoint assessed and demonstrate the effects of Atezolizumab on the viability of cells cultured in 3D alginate spheroid colonies. Data is presented as median ± range. n=3 independent experiments each with 3 technical repeats. Data was analysed using a Kruskal-Wallis comparing the percentage of non-viable cells in untreated versus Atezolizumab-treated cells.

A **Day 3 ATP levels**

B **Day 6 ATP levels**

C **Day 10 ATP levels**
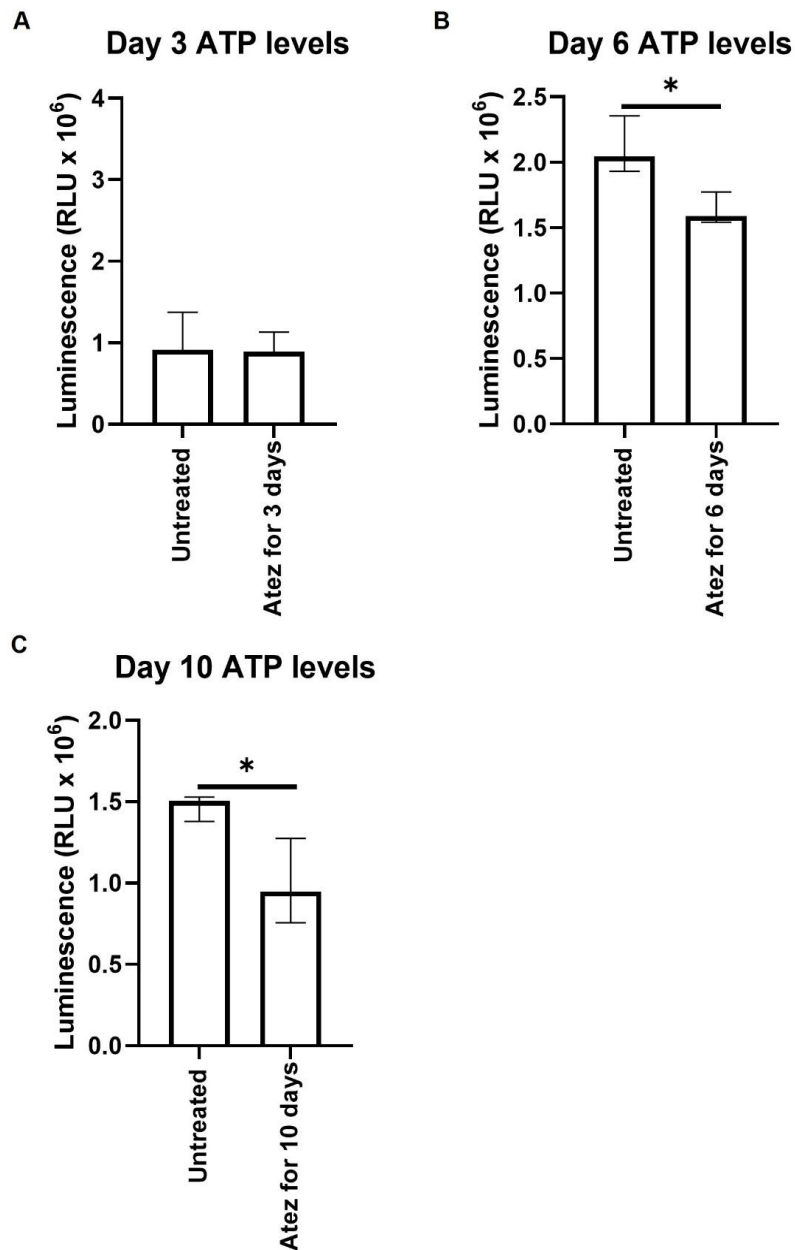
Figure 4.21 Atezolizumab significantly reduces the level of ATP produced by cells cultured in 3D alginate spheroid colonies for 6 and 10 days. The cellular activity of MDA-MB-231 cells cultured in 3D alginate spheroid colonies treated with or without Atezolizumab was assessed by measuring ATP levels at **(A)** day 3, **(B)** 6, and **(C)**10 of culture**.** Data is presented as median ± range. n=3 independent experiments each with 6 technical repeats. Data was analysed by a Mann-Whitney U test (*P<0.05).

4.3.12 MDA-MB-231 breast cancer cells exhibit altered levels of kinase phosphorylation following Atezolizumab treatment

To determine whether Atezolizumab influences tumour-intrinsic signalling and further understand the mechanism of action of Atezolizumab in MDA-MB-231 breast cancer cells, the relative levels of phosphorylation at 37 kinase phosphorylation sites and 2 related total proteins were measured using a Human Phospho-Kinase Array. Out of the 37 kinase phosphorylation sites and 2 total proteins assessed, MDA-MB-231 cells treated with Atezolizumab demonstrated 21 main alterations to kinase phosphorylation in comparison to untreated cells (Figure 4.22). Figure 4.22 highlights using numbers the main differences observed in kinase phosphorylation between untreated and Atezolizumab-treated cells. These annotated numbers displayed on the membrane correspond to the annotated numbers displayed on the graphs in Figure 4.25, 4.26, 4.27, 4.28 and 4.29. Kinase phosphorylation sites in MDA-MB-231 cells that remained unchanged or showed similar levels of phosphorylation following Atezolizumab treatment can be found in the Appendix (Appendix Figure 9.9). Appendix Table 9.1 displays the coordinates of each target and control on the protein profiler array membranes A and B.

MDA-MB-231 cells treated with Atezolizumab displayed an increase in the p53 isoforms phosphorylated at S15 which was accompanied by a decrease in the p53 isoforms phosphorylated at S46 compared to untreated cells (Figure 4.23A). Likewise, the phosphorylation of 5 Signal Transducer and Activator of Transcription (STAT) molecules was also assessed, although only STAT3 (Y705, S727) and STAT1 (Y701) phosphorylation was found to be substantially altered following Atezolizumab treatment (Figure 4.23B). STAT3 phosphorylation was substantially reduced, whereas STAT1 phosphorylation was substantially increased in Atezolizumab-treated cells compared to those untreated. Similarly, Src family kinases, Src and Yes were shown to exhibit increased phosphorylation at sites Y419 and Y412, respectively in cells treated with Atezolizumab (Figure 4.23C). Lck, also a Src family kinase, however, was found to display reduced phosphorylation levels in cells treated with Atezolizumab compared to those untreated.

The phosphorylation of molecules associated with P13K/AKT/mTOR signalling was also affected by Atezolizumab treatment in MDA-MB-231 cells (Figure 4.24A). Phosphorylation sites of AKT (T308), p70 S6 kinase (T389, T421/S424), Chk-2 (T68), PLC-γ1 (Y783), GSKβ (S9) and GSKα/β (S21/S9) displayed reduced levels of

phosphorylation in cells treated with Atezolizumab compared to untreated cells. Additionally, Atezolizumab treatment was also shown to reduce the phosphorylation of molecules involved in ERK signalling (Figure 4.24B). Phosphorylated ERK1/2 (T202/Y204, T185/Y187) was substantially reduced in cells treated with Atezolizumab compared to those untreated. Reduced ERK1/2 phosphorylation was accompanied by a reduction in MSK1/2 (S376/S360), RSK1/2 (S221/S227), RSK1/2/3 (S380/S386/S377), and p38α (T180/Y182) phosphorylation.
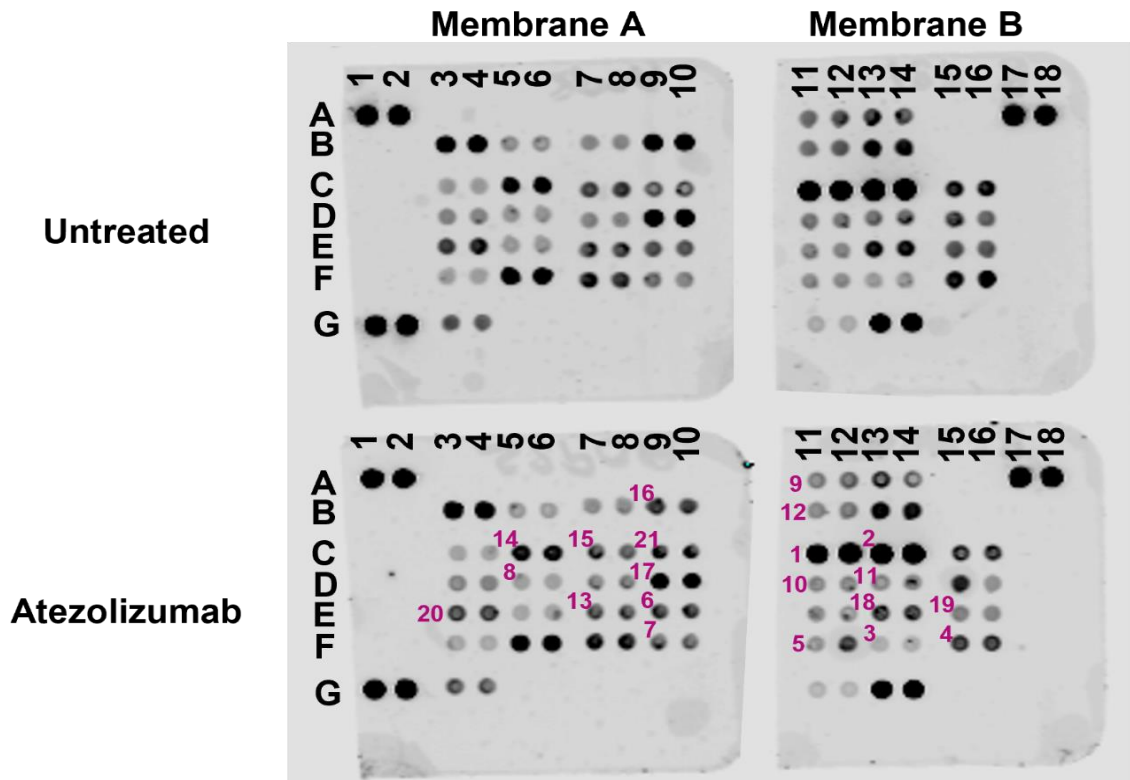
Figure 4.22 MDA-MB-231 cells treated with Atezolizumab demonstrated 21 main differences in kinase phosphorylation compared to untreated cells. The Human Phospho-Kinase Array was utilised to measure relative levels of phosphorylation of 37 kinase phosphorylation sites and 2 related total proteins in MDA-MB-231 cells treated with or without Atezolizumab. Array membranes A and B that had been treated with cell lysate from untreated and Atezolizumab-treated cells were scanned with LI-COR Odyssey® Infrared Imaging System. The annotated numbers (pink) displayed on membranes A and B highlight the 21 main changes in phosphorylation levels detected in Atezolizumab-treated cells compared to untreated cells. Each number is located to the left of the target spots that are in duplicate.
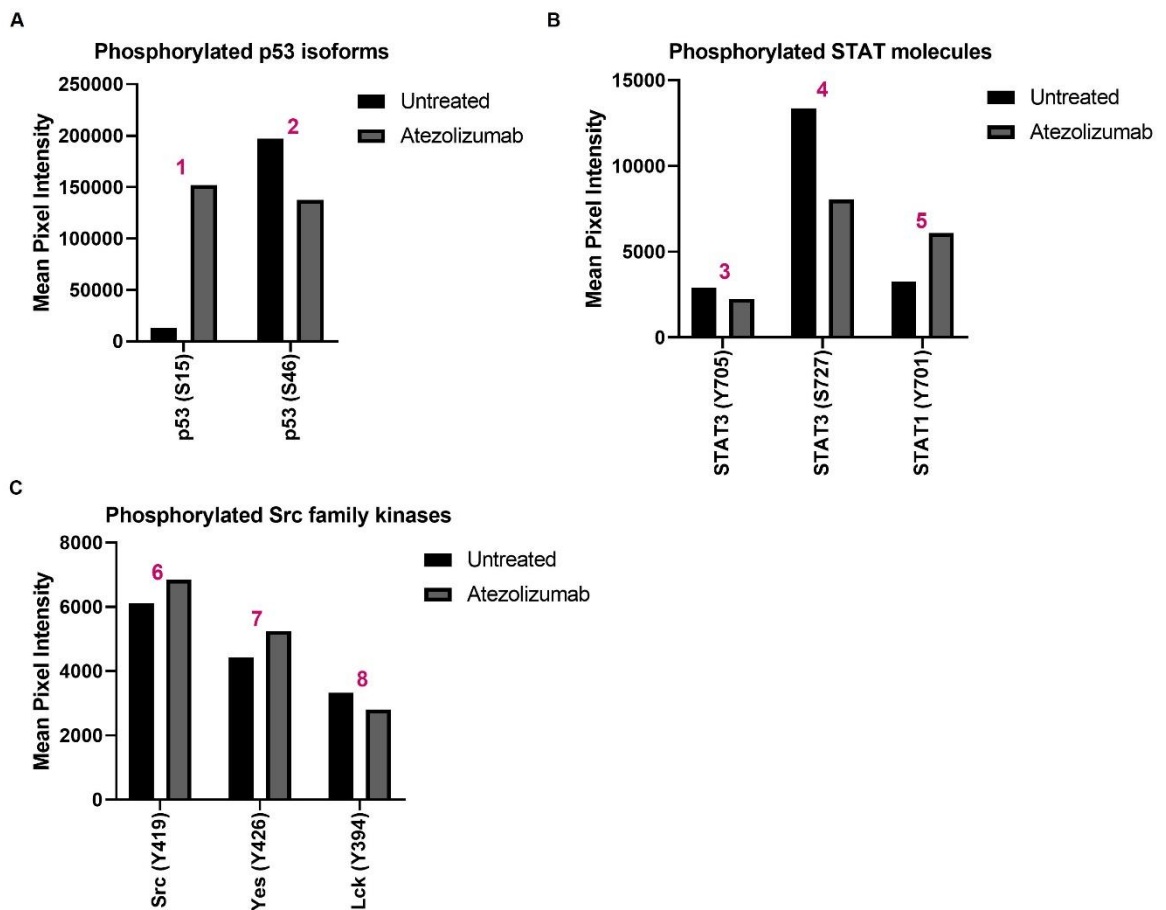
A

Phosphorylated p53 isoforms

B

Phosphorylated STAT molecules

C

Phosphorylated Src family kinases

Figure 4.23 The phosphorylation of p53 isoforms, STAT molecules and Src family kinases were affected by Atezolizumab treatment in MDA-MB-231 cells. The effects of Atezolizumab on the phosphorylation levels of **(A)** p53 isoforms, **(B)** STAT molecules and **(C)** Src family kinases was assessed in MDA-MB-231 cells by performing a Human Phospho-Kinase Array. The annotated numbers displayed on the graph correspond to annotated numbers on the array membrane in Figure 4.22. Data represents n=1 independent experiment with 2 technical repeats shown as the mean pixel intensity.
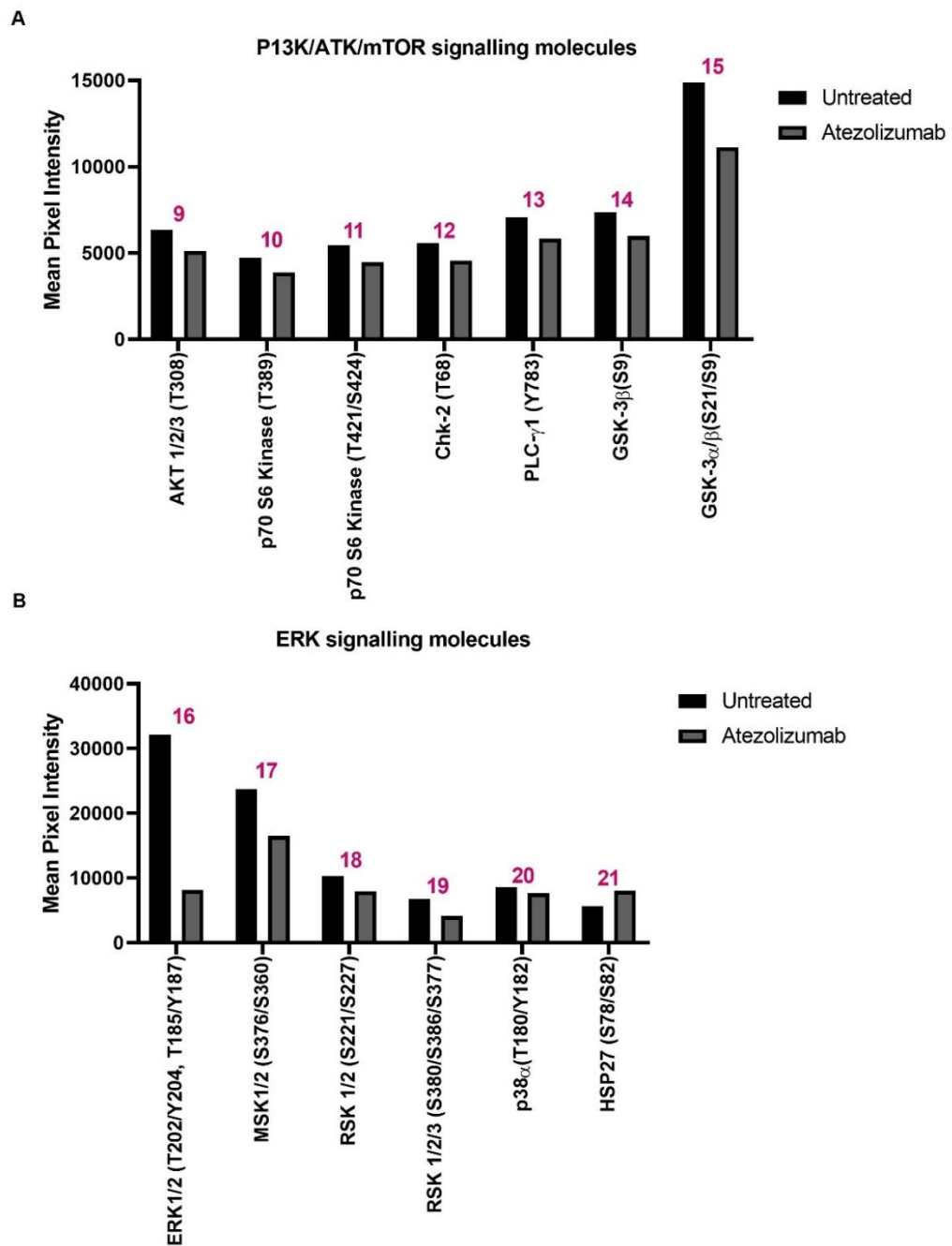
Figure 4.24 Atezolizumab altered the phosphorylation levels of several kinases associated with the PI3K/AKT/mTOR and MAPK/ERK signalling pathway in MDA-MB-231 cells. The effects of Atezolizumab on the phosphorylation levels of different kinases involved in the **(A)** PI3K/AKT/mTOR and **(B)** MAPK/ERK signalling pathways were assessed in MDA-MB-231 cells by performing a Human Phospho-Kinase Array. The annotated numbers displayed on the graph correspond to annotated numbers on the array membrane in Figure 4.22. Data represents n=1 independent experiment with 2 technical repeats shown as the mean pixel intensity.

4.3.13 Investigating the effects of Atezolizumab in combination with IFNγ and/or TNFα on cell viability of 2D- and 3D-cultured breast cancer cells

Since Atezolizumab treatment alone was shown to have no statistically significant effects on the cell viability of 2D- and 3D-cultured MDA-MB-231 cells, combining Atezolizumab treatment with modulatory cytokines was next investigated to determine whether there could be an enhanced effect to induce cancer cell death in 2D monolayer and 3D breast cancer models. MDA-MB-231 and MCF-7 breast cancer cells cultured in monolayer and 3D cell culture models were treated with cytokines, IFNγ and/or TNFα, 48 hours prior to Atezolizumab treatment for 1 hour before assessing the cell viability. PD-L1 blockade by Atezolizumab with or without cytokine modulation was verified for both cell lines in 2D and 3D cell culture models (Appendix Figure 9.10 and 9.11).

4.3.13.1 Atezolizumab in combination with modulatory cytokines has no effect on the viability of 2D-cultured MDA-MB-231 cells

Atezolizumab treatment alone for 1 hour was shown not to induce significant amounts of cell death in cells cultured in 2D monolayer as shown previously in Figure 4.10 (p=0.99) (Figure 4.25A). However, a high percentage of necrosis was observed in cells treated with IFNγ and TNFα compared to untreated cells (Figure 4.25B and C). When Atezolizumab was combined with both cytokines, the median percentage of necrotic cells was higher (8.95% ± 7.4) compared to both cytokines alone (3.9% ± 7.95), but this was not statistically significant (p=0.99).

4.3.13.2 Atezolizumab in combination with modulatory cytokines has no effect on the viability of MDA-MB-231 3D hanging drop spheroids

The effects of cytokine modulation for 48 hours prior to treatment with Atezolizumab for 1 hour on cancer cell viability was next assessed in MDA-MB-231 3D hanging drop spheroids. As shown previously in Figure 4.15, Atezolizumab treatment alone for 1 hour was shown to induce more apoptotic cell death in 3D spheroids, than observed in those untreated although this was found not to be significant (Figure 4.26A and C). Also, there was no significant enhanced effect on cell viability observed in 3D spheroids when cytokines were combined with Atezolizumab as opposed to cytokines alone. Similar to the effects observed in 2D-cultured cells, IFNγ and TNFα combined induced significant amounts of apoptotic cell death in 3D spheroids (0.034), as did TNFα alone (0.045), compared to untreated 3D spheroids

which was not significantly affected by the addition of Atezolizumab (Figure 4.26B and C).
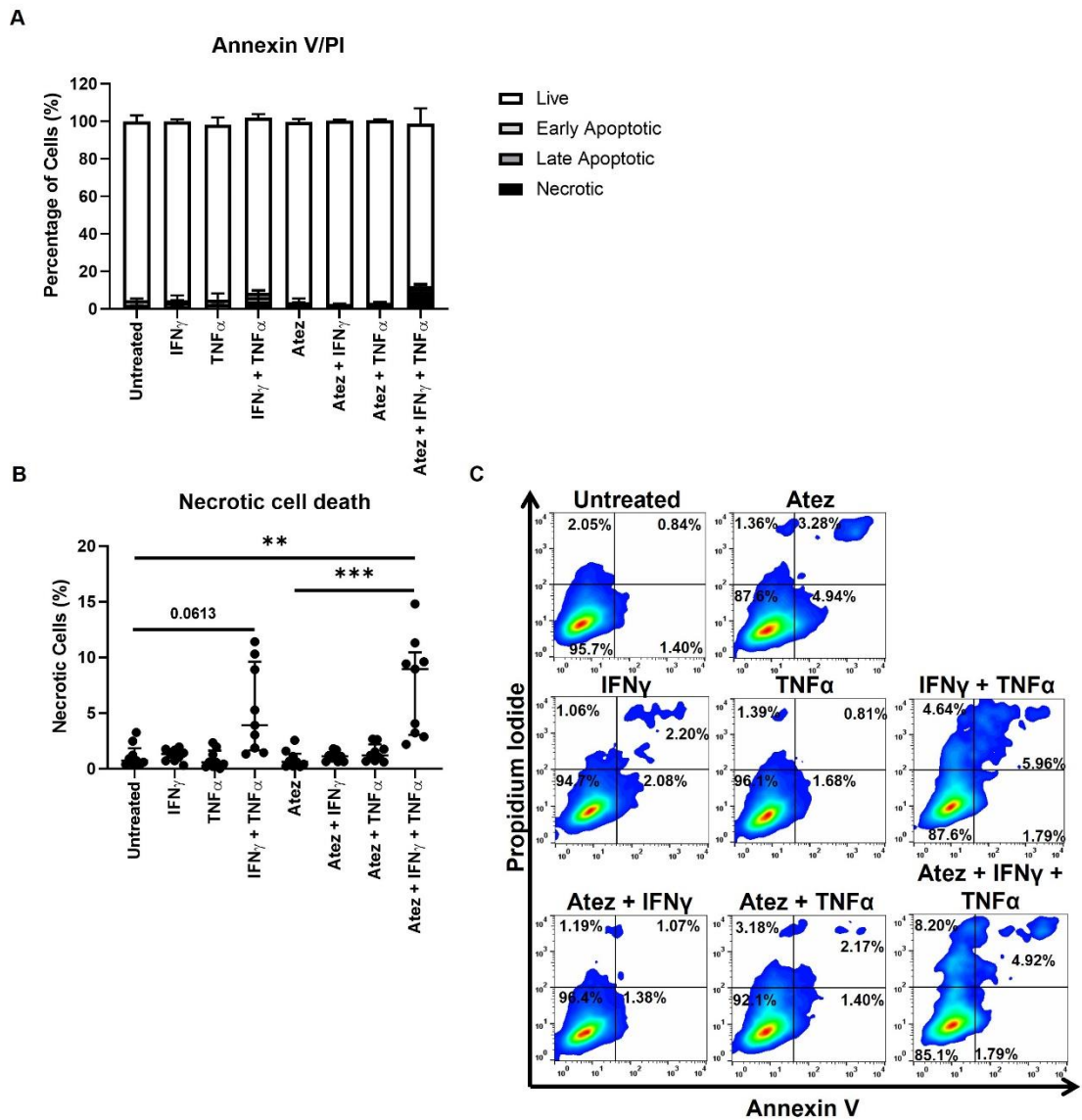
Figure 4.25 Atezolizumab in combination with modulatory cytokines has no significant effect on the viability of MDA-MB-231 cells cultured in 2D monolayer. Monolayer-cultured MDA-MB-231 cells were treated with Atezolizumab for 1 hour with or without cytokine modulation for 48 hours previous. **(A)** Cellular viability was then assessed by Annexin V/PI staining. **(B)** The percentage of necrotic cells (AV-/PI+) is shown separately for statistical analysis. **(C)** Representative flow cytometry plots demonstrate the effects of Atezolizumab on cell viability with or without prior cytokine modulation compared to those untreated and treated with cytokines alone. Data is presented as median ± range. n=3 independent experiments each with 3 technical repeats. Data was analysed by a Kruskal-Wallis followed by Dunn's multiple comparisons test (**P<0.01 and ***P<0.001).
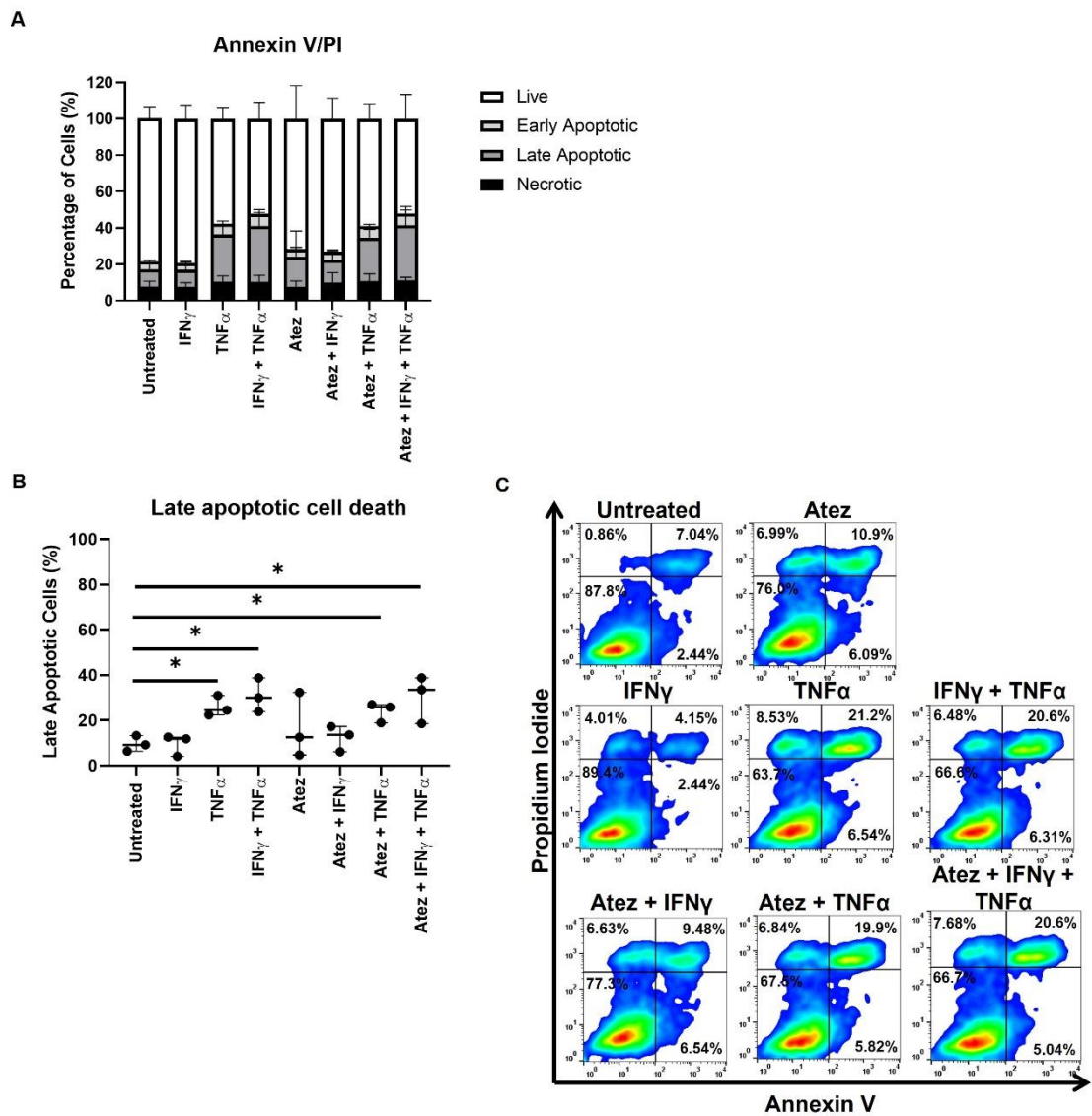
Figure 4.26 Atezolizumab in combination with modulatory cytokines has no significant effect on the viability of MDA-MB-231 3D hanging drop spheroids.
(A) Cell viability was assessed by staining MDA-MB-231 cells in 3D hanging drop spheroids using Annexin V/PI following treatment with Atezolizumab for 1 hour, with or without cytokine modulation for 48 hours previous. **(B)** The percentage of late apoptotic cells (AV+/PI+) is shown separately for statistical analysis. **(C)** Representative flow cytometry plots demonstrate the effect of Atezolizumab with or without prior cytokine modulation on the viability of 3D spheroids compared to those untreated or treated with cytokines alone. Data is presented as median ± range. n=3 independent experiments each with 3 technical repeats. Data was analysed by a Kruskal-Wallis followed by Dunn's multiple comparisons test (*P<0.05).

4.3.13.3 Atezolizumab treatment combined with TNFα ± IFNγ may enhance cancer cell death in MDA-MB-231 3D alginate spheroid colonies

The effects of cytokine modulation for 48 hours prior to treatment with Atezolizumab for 1 hour on cellular viability and cellular activity was lastly assessed in MDA-MB-231 3D alginate spheroid colonies after 3, 6 and 10 days of culture.

4.3.13.1.1 Effects of Atezolizumab combined with TNFα ± IFNγ on the viability of 3D alginate spheroid colonies after 3 days of culture

Whether 3D alginate spheroid colonies were treated with cytokines alone, Atezolizumab alone or the combinations, cell death was found not to be significantly affected compared to those untreated after 3 days of culture (Figure 4.27A and B). Interestingly, 3D alginate spheroid colonies treated with Atezolizumab and TNFα displayed a higher median percentage of late apoptotic cells (31.7% ± 22.45) compared to those untreated (12.2% ± 8.84) or treated with Atezolizumab (11.7% ± 18.13) or TNFα (6.22% ± 32.3) alone (Figure 4.27C). Additionally, 3D alginate spheroid colonies treated with Atezolizumab and both cytokines demonstrated a trend increase in the percentage of necrotic cells, compared to those untreated or treated with Atezolizumab or both cytokines alone (Figure 4.27D). Although both these data sets were found not to be significant.
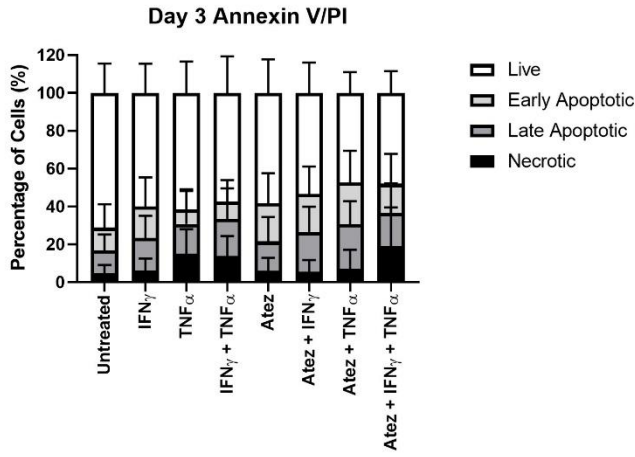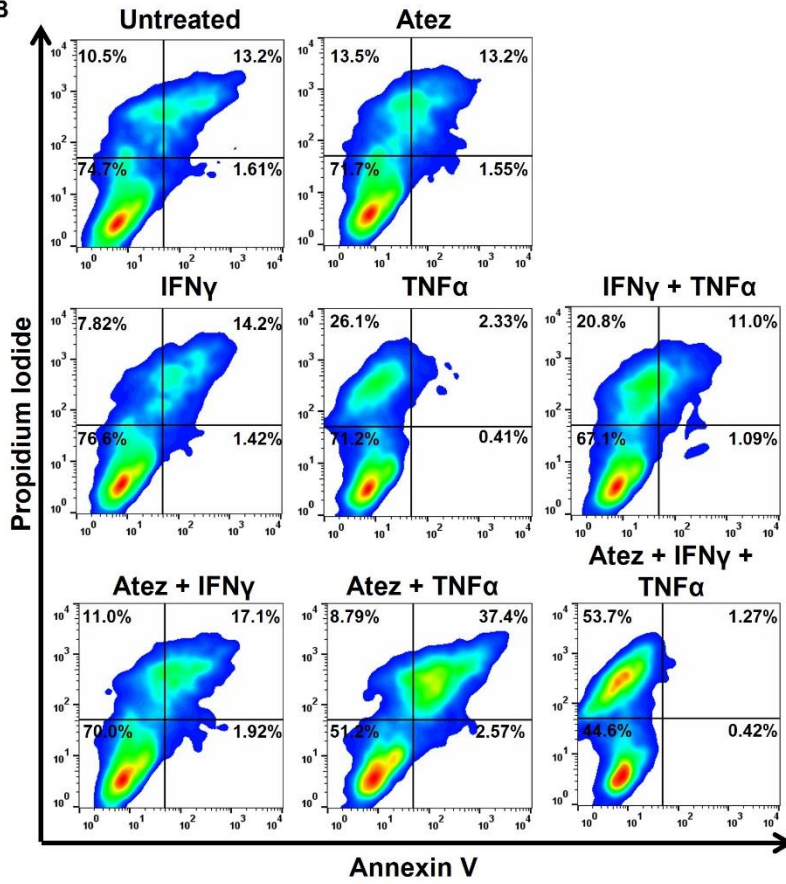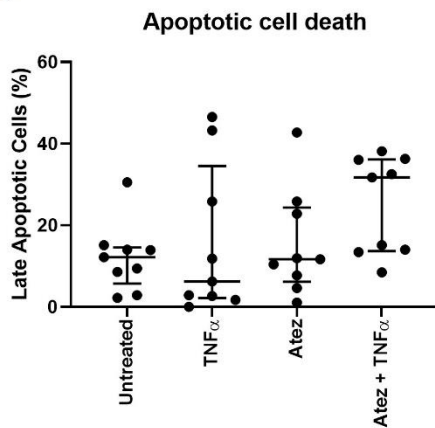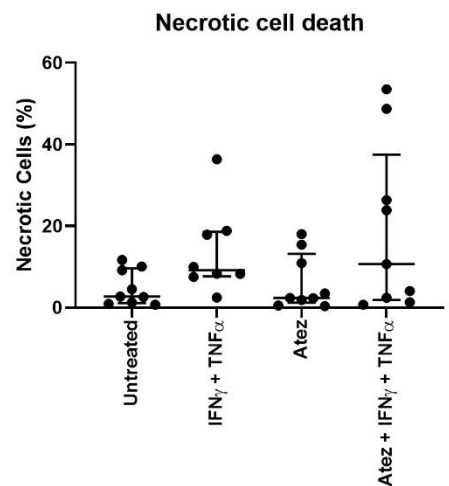
A Day 3 Annexin V/PI

Legend: Live, Early Apoptotic, Late Apoptotic, Necrotic

Groups: Untreated, IFNγ, TNFα, IFNγ + TNFα, Atez, Atez + IFNγ, Atez + TNFα, Atez + IFNγ + TNFα

B Propidium Iodide vs Annexin V

Untreated: 10.5%, 13.2%, 74.7%, 1.61%
Atez: 13.5%, 13.2%, 71.7%, 1.55%
IFNγ: 7.82%, 14.2%, 76.6%, 1.42%
TNFα: 26.1%, 2.33%, 71.2%, 0.41%
IFNγ + TNFα: 20.8%, 11.0%, 67.1%, 1.09%
Atez + IFNγ: 11.0%, 17.1%, 70.0%, 1.92%
Atez + TNFα: 8.79%, 37.4%, 51.2%, 2.57%
Atez + IFNγ + TNFα: 53.7%, 1.27%, 44.6%, 0.42%

C Apoptotic cell death — Late Apoptotic Cells (%)

Groups: Untreated, TNFα, Atez, Atez + TNFα

D Necrotic cell death — Necrotic Cells (%)

Groups: Untreated, IFNγ + TNFα, Atez, Atez + IFNγ + TNFα

Figure 4.27 Atezolizumab in combination with modulatory cytokines does not induce a significant amount of cell death in MDA-MB-231 3D alginate spheroid colonies at day 3. (A) Cell viability was assessed by staining MDA-MB-231 cells with Annexin V/PI that had been cultured in 3D alginate spheroid colonies and treated with Atezolizumab for 1 hour with or without cytokine modulation 48 hours prior. **(B)** Representative flow cytometry plots demonstrate the effect of Atezolizumab with or without prior cytokine modulation on the viability of 3D alginate spheroid colonies compared to those untreated. **(C)** The percentage of late apoptotic cells (AV+/PI+) is shown separately to compare cells untreated or treated with TNFα alone, Atezolizumab alone, and the combination. **(D)** The percentage of necrotic cells (AV-/PI+) is also shown separately to compare cells untreated or treated with both cytokines alone, Atezolizumab alone, and the combination. Data is presented as median ± range. n=3 independent experiments each with 3 technical repeats. Data was analysed by a Kruskal-Wallis test and Dunn's multiple comparisons test.

4.3.13.1.2 Effects of Atezolizumab combined with TNFα on the viability and cellular activity of 3D alginate spheroid colonies after 6 days of culture

At day 6 of culture, Atezolizumab-treated 3D alginate spheroid colonies displayed more cell death than those untreated (Figure 4.28A and B). Although, TNFα alone did not induce cell death in 3D alginate spheroid colonies at day 6 of culture, the percentage of late apoptotic cells was enhanced when TNFα was combined with Atezolizumab (13.8% ± 10.8), compared to those untreated (4.97% ± 2.98), treated with Atezolizumab alone (12% ± 10.45) and TNFα alone (5.28% ± 4.59) (Figure 4.28C). However, the viability effects of this combined treatment were highly variable amongst alginate cultures and hence found to be not significant.

The effect that Atezolizumab and TNFα had on 3D alginate spheroid colony viability alone and combined was further investigated by assessing apoptosis via measuring caspase 3 positivity (Figure 4.29A), as well as cellular metabolic activity via measuring ATP levels after 6 days of culture (Figure 4.29B). Caspase 3 positivity was significantly increased in 3D alginate spheroid colonies treated with TNFα alone (p=0.0036), Atezolizumab alone (0.039) and Atezolizumab and TNFα combined (p=0.017) compared to those untreated. However, caspase 3 positivity did not differ significantly between 3D alginate spheroid colonies treated with Atezolizumab and TNFα combined compared to TNFα alone. Similarly, Atezolizumab-treated 3D alginate spheroid colonies with or without TNFα showed a trend decrease in ATP production compared to those untreated and treated with TNFα alone. Also, ATP levels were comparable between Atezolizumab-treated 3D alginate spheroid colonies and those treated with the combination.
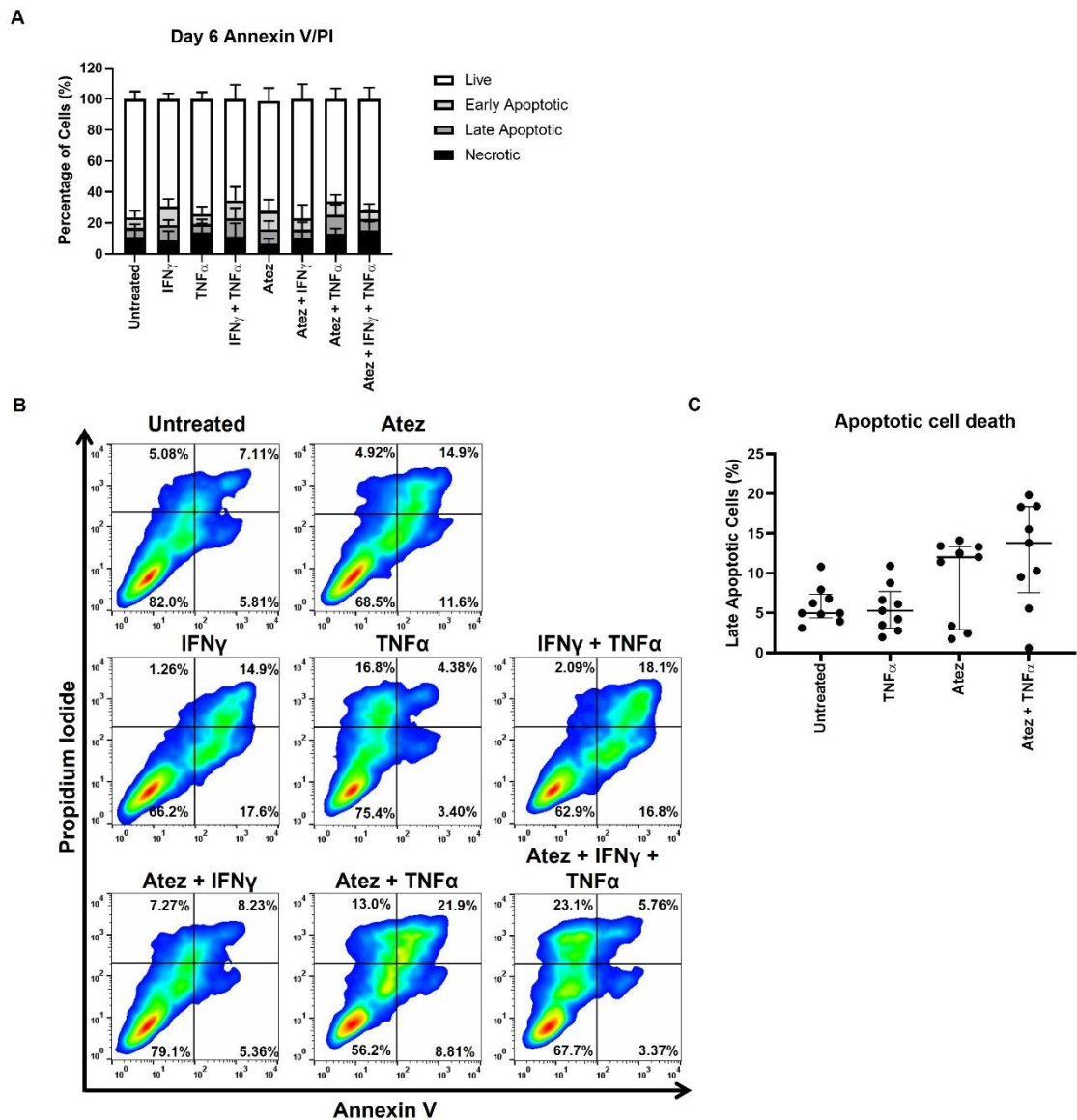
Figure 4.28 Combining Atezolizumab with TNFα may show signs to induce apoptotic cell death in MDA-MB-231 3D alginate spheroid colonies after 6 days of culture. MDA-MB-231 cells cultured in 3D alginate spheroid colonies were treated with Atezolizumab for 1 hour with or without cytokine modulation for 48 hours previous at day 6 of culture. **(A)** Cellular viability was then assessed by Annexin V/PI staining. **(B)** Representative flow cytometry plots demonstrate the effect of Atezolizumab with or without prior cytokine modulation on cell viability compared to cells untreated or treated with cytokines alone. **(C)** The percentage of late apoptotic cells (AV+/PI+) is shown separately to compare cells untreated or treated with TNFα alone, Atezolizumab alone, or combined. Data is presented as median ± range. n=3 independent experiments each with 3 technical repeats. Data was analysed by a Kruskal-Wallis test and a Dunn's multiple comparisons test.
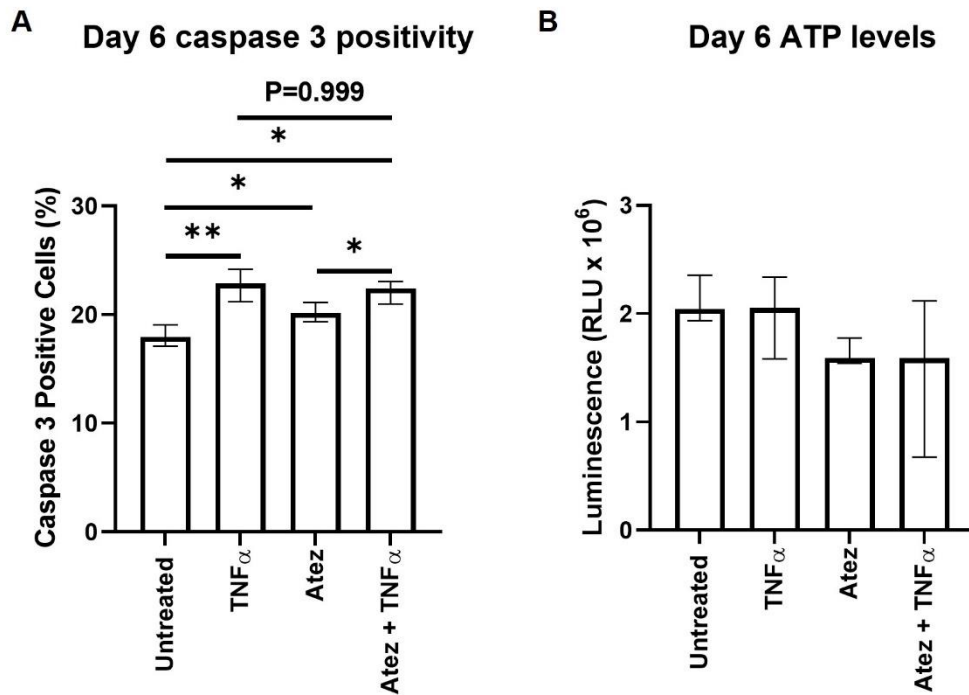
**Figure 4.29 Atezolizumab and TNFα alone or combined increases caspase 3 positive cells in 3D alginate spheroid colonies at day 6 of culture but has no significant effect on ATP production.** To assess whether Atezolizumab treatment with or without TNFα influenced cellular caspase 3 or metabolic activity in MDA-MB-231 3D alginate spheroid colonies at day 6 of culture, **(A)** caspase 3 positivity and **(B)** ATP levels were measured, respectively. Data is presented as median ± range. n=3 independent experiments each with 2 technical repeats. Data was analysed by a Kruskal-Wallis followed by Dunn's multiple comparisons test (*P<0.05 and **P<0.01).

4.3.13.1.3 Effects of Atezolizumab combined with TNFα ± IFNγ on the viability and cellular activity of 3D alginate spheroid colonies after 10 days of culture

The Annexin V/PI viability data at day 10 for untreated and treated 3D spheroid colonies was comparable to that of the viability data at day 3 and 6 for untreated and treated 3D alginate spheroid colonies. Atezolizumab-treated 3D spheroid colonies in combination with TNFα alone or IFNγ and TNFα combined displayed a trend increase in apoptotic cell death in comparison to 3D alginate spheroid colonies untreated and treated with Atezolizumab or cytokines alone at day 10 of culture (Figure 4.30A and B). In 3D alginate spheroid colonies at day 10 of culture however, it was Atezolizumab in combination with IFNγ and TNFα that demonstrated the greatest effect to induce cell death compared to Atezolizumab in combination with TNFα alone (Figure 4.30B and C).

The effects of Atezolizumab treatment in combination with cytokines on the viability of 3D alginate spheroid colonies was further investigated by measuring apoptosis via caspase 3 positivity and cellular metabolic activity via ATP levels at day 10 of culture. Caspase 3 positivity in 3D alginate spheroid colonies treated with Atezolizumab in combination with both cytokines was significantly increased compared to those untreated (p=0.0079), treated with Atezolizumab alone (p=0.0477) and the cytokine combination alone (p=0.0342) after 10 days of culture (Figure 4.31A). Similarly, ATP levels in 3D alginate spheroid colonies treated with Atezolizumab and both cytokine modulations were significantly reduced after 10 days of culture compared to those untreated (p=0.027) (Figure 4.31B). Importantly, 3D alginate spheroid colonies treated with Atezolizumab and both cytokines displayed significantly reduced levels of ATP compared to those treated with both cytokines alone (p=0.042). Moreover, 3D alginate spheroid colonies treated with Atezolizumab and both cytokines showed slightly reduced ATP levels in comparison to those treated with Atezolizumab alone, although this was not found to be statistically significant. Conclusively, these results correlate with the Annexin V/PI staining of 3D alginate spheroid colonies showing that Atezolizumab in combination with cytokines may induce cell death in MDA-MB-231 cells cultured in alginate cultures.

To determine whether these significant changes observed in the cell viability and metabolic activity of MDA-MB-231 3D alginate spheroid colonies were likely due to PD-L1 upregulation following cytokine modulation, mRNA levels of PD-L1 were

measured in untreated, IFNγ-treated, TNFα-treated and IFNγ-/TNFα-treated 3D spheroid colonies at day 10 of culture with or without Atezolizumab treatment (Figure 4.31C). 3D alginate spheroid colonies displayed significantly upregulated PD-L1 mRNA following treatment with IFNγ and TNFα combined (p=0.0006). The levels of PD-L1 modulation were comparable following the addition Atezolizumab treatment at mRNA level.
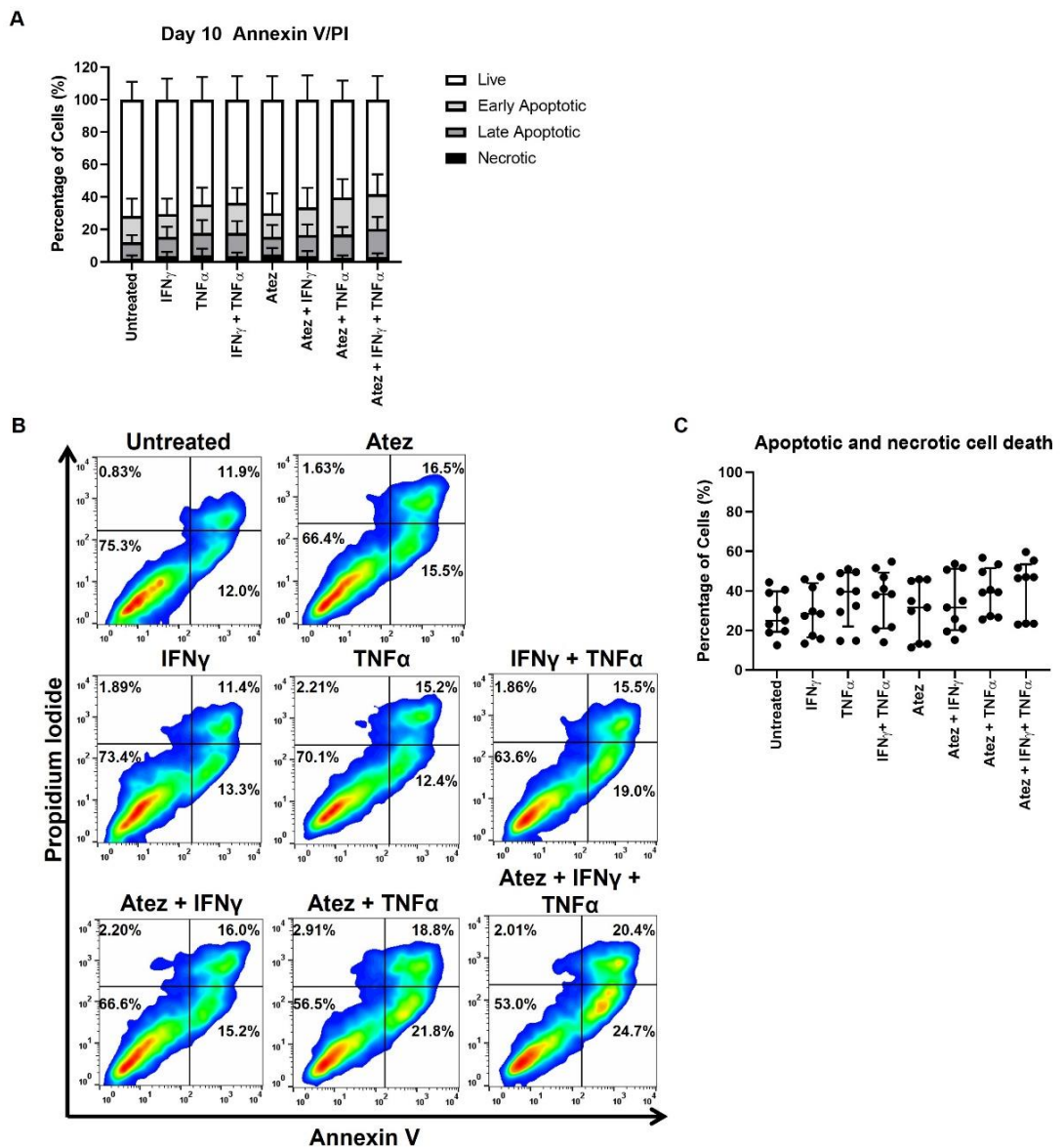
Figure 4.30 Atezolizumab alone and in combination with cytokines may show signs to induce cell death in MDA-MB-231 3D alginate spheroid colonies at day 10 of culture. MDA-MB-231 cells cultured in 3D alginate spheroid colonies were treated with Atezolizumab for 1 hour with or without cytokine modulation for 48 hours previous at day 10 of culture. **(A)** Cellular viability was assessed by Annexin V/PI staining. **(B)** Representative flow cytometry plots demonstrate the effects of Atezolizumab with or without cytokine treatment on the viability of cells cultured in 3D alginate spheroid colonies. **(C)** The percentage of non-viable cells (AV+/PI-, AV+/PI+, AV-/PI+) is shown separately to compare cell death amongst the different treatment groups. Data is presented as median ± range. n=3 independent experiments each with 3 technical repeats. Data was analysed by a Kruskal-Wallis test and a Dunn's multiple comparisons test.
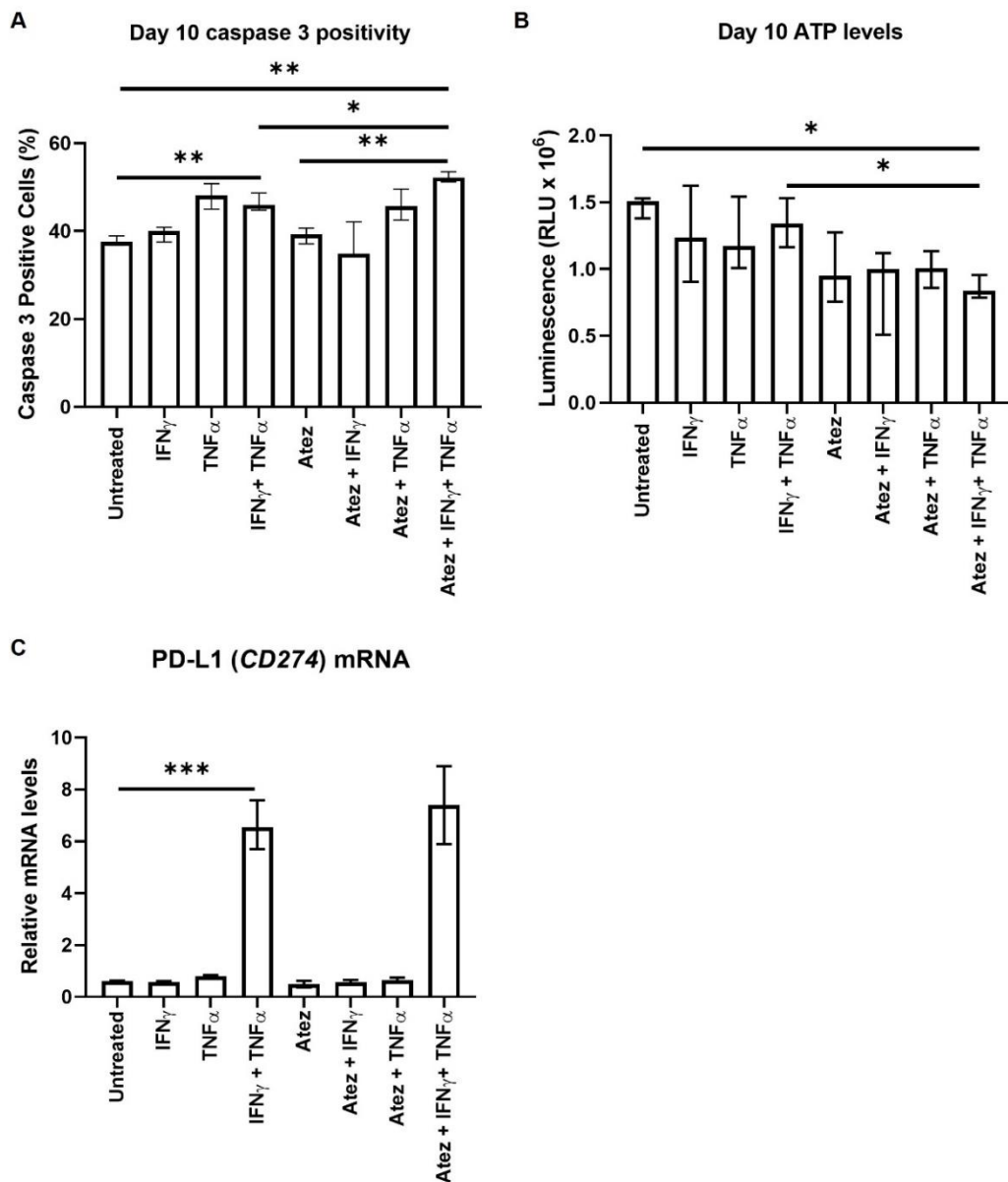
Figure 4.31 Atezolizumab in combination with IFNγ and TNFα induces significant apoptotic cell death and reduces ATP production in MDA-MB-231 3D alginate spheroid colonies at day 10 of culture which is likely due to increased PD-L1 mRNA expression. To assess cellular apoptosis and metabolic activity and determine whether the changes in both these biological process may be due to PD-L1 upregulation in response to treatment, **(A)** caspase 3 positivity, **(B)** ATP production and **(C)** PD-L1 mRNA levels were measured in day 10 3D alginate spheroid colonies treated with or without Atezolizumab in combination with cytokine modulation. Data is presented as median ± range. n=3 independent experiments each with 3 technical repeats. Data was analysed by a Kruskal-Wallis followed by Dunn's multiple comparisons test (*P<0.05, **P<0.01 and ***P<0.001). Only significant values which are relevant to the most important findings are displayed.

4.3.13.4 Atezolizumab treatment in combination with modulatory cytokines may induce a similar cell death phenotype in low PD-L1 expressing MCF-7 breast cancer cells

It was next determined whether Atezolizumab alone or in combination with modulatory cytokines was able to bind PD-L1 and effect the cell viability of low PD-L1 expressing MCF-7 breast cancer cells cultured in 2D monolayer and 3D alginate spheroid. Indeed, 2D-cultured and 3D-cultured MCF-7 breast cancer cells treated with Atezolizumab with or without cytokines demonstrated reduced detectable levels of PD-L1 expression by flow cytometry compared to cells untreated or treated with cytokines alone (Appendix Figure 9.11). As observed in monolayer MDA-MB-231 cells (Figure 4.10), Atezolizumab was shown to have no effect on MCF-7 cell viability despite complete blockade of PD-L1 (Figure 4.32A and B), which may be due to low expression of PD-L1. However, TNFα treatment alone or combined with IFNγ induced cell death compared to untreated cells more so than when combined with Atezolizumab.

Because Atezolizumab treatment combined with TNFα or both cytokines combined showed signs to affect the viability and activity of MDA-MB-231 3D alginate spheroid colonies after 10 days of culture, the effects of these treatment combination were assessed in MCF-7 3D spheroid colonies after 10 days of culture to determine whether a similar phenotype could be observed. Untreated MCF-7 3D alginate spheroid colonies after 10 days of culture displayed a high percentage of cell death (Figure 4.33A). Despite this, the percentage of cell death was greater in MCF-7 3D alginate spheroid colonies treated Atezolizumab and both cytokines compared to those untreated or treated with Atezolizumab alone and both cytokines alone (Figure 4.33B and C).
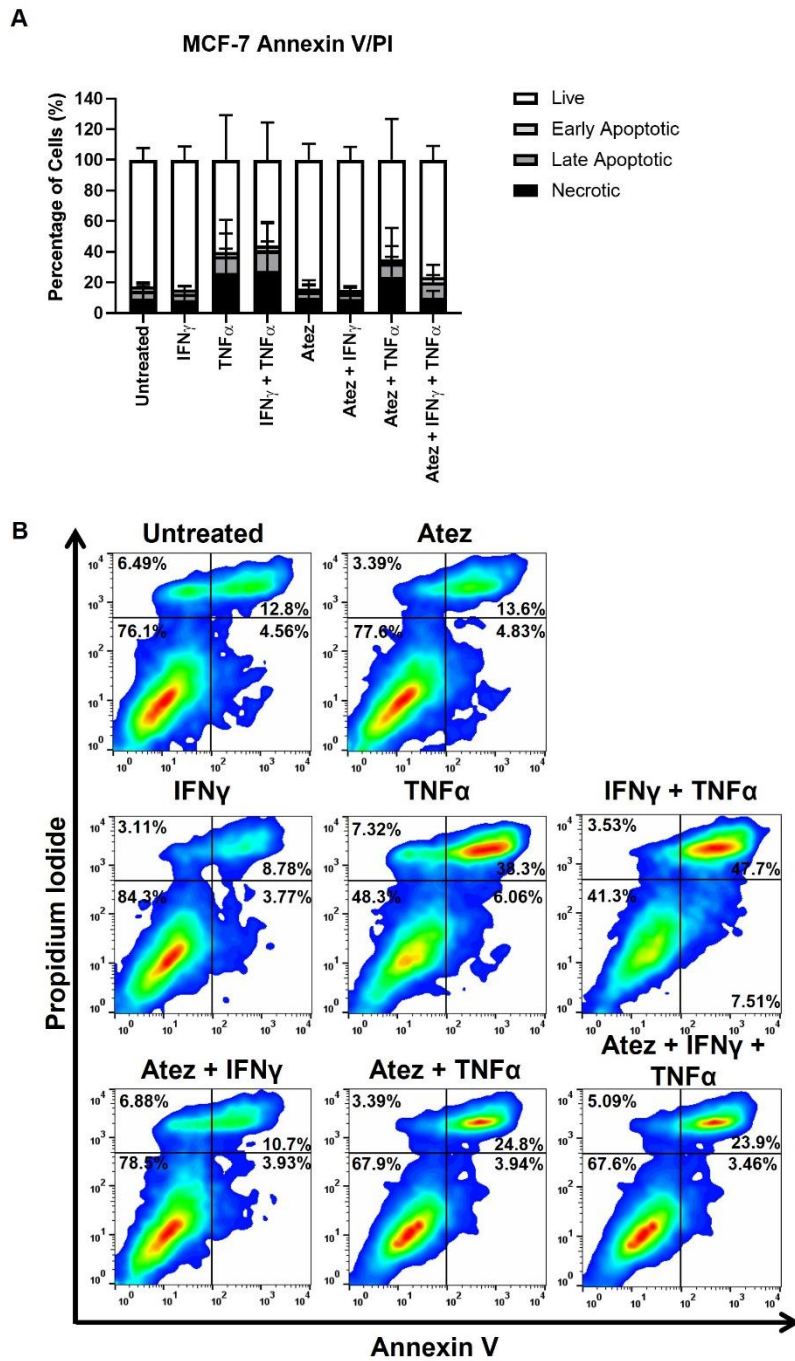
Figure 4.32 Atezolizumab with or without cytokine treatment has no effect on the viability of MCF-7 cells cultured in 2D monolayer. (A) The viability of MCF-7 cells cultured in 2D monolayer was assessed using Annexin V/PI staining following treatment with Atezolizumab for 1 hour with or without cytokine modulation 48 hours previous. **(B)** Representative flow cytometry plots showing the effects of treatment on cell viability. Data is presented as median ± range. n=3 independent experiments each with 3 technical repeats. Data was analysed by a Kruskal-Wallis comparing all treatment groups.
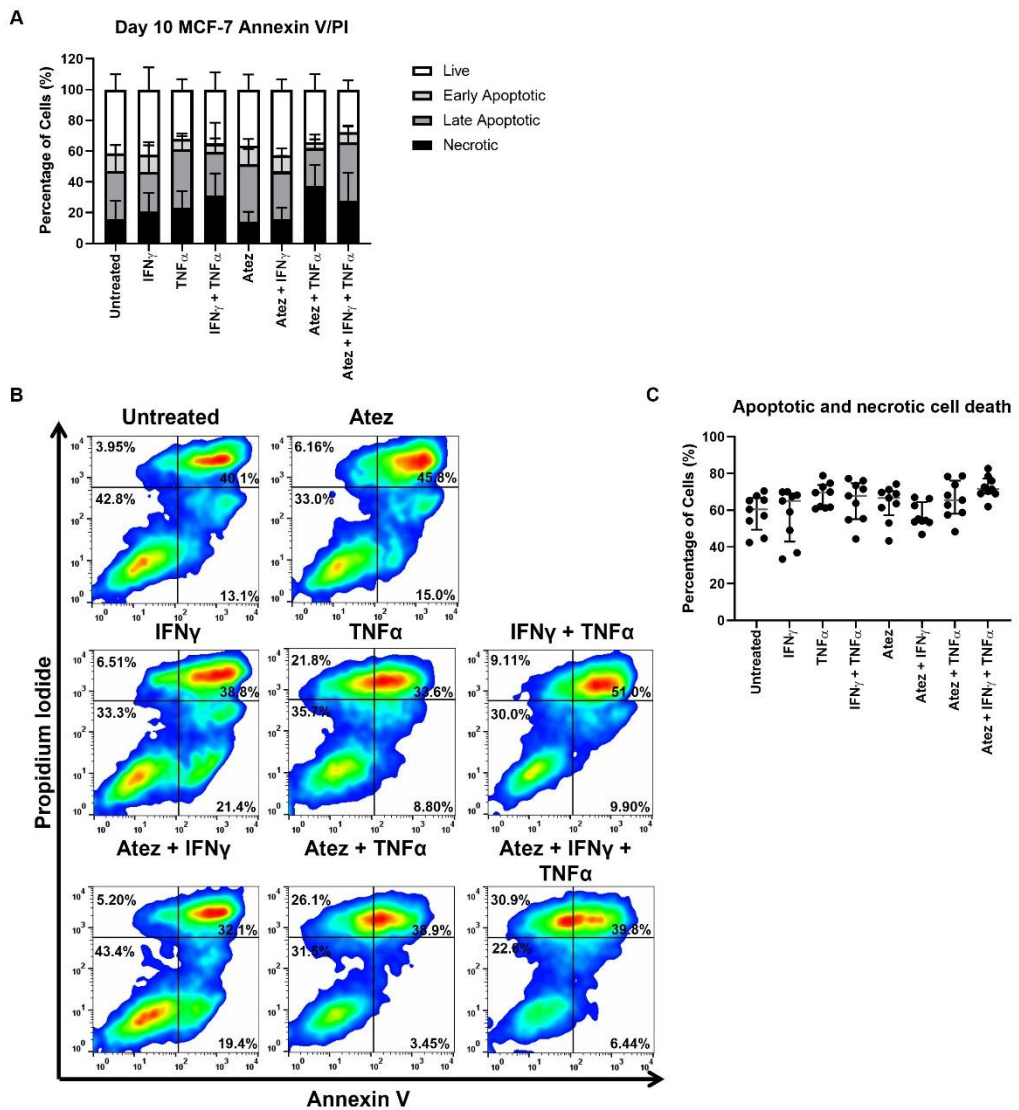
Figure 4.33 MCF-7 cells cultured in 3D alginate spheroid colonies for 10 days display the highest percentage of cell death following treatment with Atezolizumab in combination with IFNγ and TNFα. (A) MCF-7 3D alginate spheroid colonies were stained with Annexin V/PI to assess cell viability following treatment with Atezolizumab with or without cytokines 48 hours previous. **(B)** Representative flow cytometry plots demonstrate the effect of Atezolizumab with or without cytokines on the viability of 3D alginate spheroid colonies. **(C)** The percentage of non-viable cells (AV+/PI-, AV+/PI+, AV-/PI+) is shown separately to compare cell death amongst the different treatment groups. Data is presented as median ± range. n=3 independent experiments each with 3 technical repeats. Data was analysed by a Kruskal-Wallis comparing all the treatments.

4.4 Discussion

It is well regarded in the literature that the growth of human cancer cell lines in 3D cell culture models is a more stringent and representative approach to perform *in vitro* drug screening. 3D cell cultures possess several *in vivo* features of tumours that would influence treatment responses such as, cell-cell interaction, production/deposition of extracellular matrix, hypoxia, drug penetration and resistance; that 2D monolayer cell cultures cannot reproduce. In Chapter 3 of this thesis, we have already demonstrated that gene and protein expression profiles are altered in 3D cell culture models, which would also influence the tumours response to treatment. In this chapter, we show that the capability of anti-PD-L1 immunomodulatory drug, Atezolizumab, to block PD-L1 on the surface of cancer cells and the subsequent phenotypic effects it has intrinsically on the cancer cells differs in 2D and 3D cell culture models of breast cancer.

To assess the ability of Atezolizumab to block PD-L1 on the surface of cancer cells by flow cytometry, it was first necessary to understand the binding sites of Atezolizumab to PD-L1 to select a detection antibody that binds to the same epitope. Zhang *et al.,* (2017) demonstrated through crystallisation that Atezolizumab binds the front β-sheet of the PD-L1 IgV domain through three complementary determining region (CDR) loops from the heavy chain and one CDR loop from the light chain (Zhang *et al.,* 2017). Whilst it is well understood that the binding of Atezolizumab to PD-L1 blocks its interaction with PD-1, more recently, it has been reported to prevent PD-L1 forming heterodimers with CD80 in *cis* (Chaudhri *et al.,* 2018; Sansom and Walker, 2019). The antibody clone, 29E.2A3, used to detect PD-L1 in this study has been shown to recognise an epitope on PD-L1 within the PD-L1-CD80 binding region (Haile *et al.,* 2011).

Consequently, we were able to observe a dose-response to Atezolizumab treatment in our MDA-MB-231 2D and 3D cell culture models. Importantly, the efficiency of Atezolizumab to bind PD-L1 on MDA-MB-231 cells cultured in monolayer was higher than on MDA-MB-231 cells cultured in 3D hanging drop spheroids and 3D alginate spheroid colonies despite their reduced cell surface PD-L1 expression already in a 3D environment. Out of the two 3D models, Atezolizumab was less efficient at blocking PD-L1 on MDA-MB-231 cells cultured in alginate. Previous studies have reported that culturing cancer cells in 3D alters the spatial organisation of cell surface proteins that makes them less accessible to being targeted, and that the size of the

3D structures influences drug diffusion (Edmondson *et al.,* 2014). Additionally, the loose aggregation of MDA-MB-231 cells that form in hanging drop spheroids could make them more susceptible to being bound by Atezolizumab than those cultured in alginate (Imamura *et al.,* 2015). Imamura *et al.,* (2015) showed that breast cancer cell lines that developed dense 3D spheroids (BT-549, BT-474 and T47D) demonstrated greater resistance to chemotherapies, paclitaxel and doxorubicin, compared to those that formed loose 3D spheroids (MDA-MB-231, HCC-1954 and MCF-7). This was likely due to the increased accessibility of the chemotherapy drugs to the cancer cells.

Regardless, it was clear from our data that Atezolizumab was able to penetrate the 3D structures to an extent where only a small percentage of cells were being detected for PD-L1 expression, in which otherwise would be approximately 90% of the cells. To note, we also showed that Atezolizumab binding to the epitope of PD-L1 did not affect PD-L1 mRNA levels in MDA-MB-231 breast cancer cells which is in accordance with the published literature (Saleh *et al.,* 2019; Ali *et al.,* 2019). A recent study used Fourier Transform Infrared spectroscopy analysis to reveal stress-induced chemical alterations in both protein and lipid structure of MDA-MB-231 cells following Atezolizumab treatment (Ali *et al.,* 2019). Authors showed Atezolizumab altered the conformation of PD-L1 affecting its structure and function and prevented any further ability for it to bind PD-1, leading to sustained T cell activation (Ali *et al.,* 2019). Another study demonstrated that Avelumab, an approved anti-PD-L1 monoclonal antibody with a native Fc region, was internalised short after binding to PD-L1 and FcγR *in vitro* and *in vivo* (Jin *et al.,* 2021). Jin *et al.,* (2021) also showed that Atezolizumab was internalised but at a slower rate in comparison to Avelumab. Their studies *in vivo* using mice and cynomolgus monkeys showed that PD-L1 binding played the dominant role that led to Avelumab and Atezolizumab internalisation (Jin *et al.,* 2021). Additionally, an anti-PD-L1 monoclonal antibodies targeting glycosylated PD-L1 demonstrated the ability to induce PD-L1 internalisation due to N-linked glycosylation being a necessary post-translational modification for PD-L1 to maintain its stability (Li *et al.,* 2016; Park *et al.,* 2021). Very recently, Hodgins *et al.,* (2022) demonstrated the capability of Atezolizumab to enhance oncolytic virus infections in mouse prostate cancer cells *in vitro* and *in vivo* via intrinsic signalling mechanisms. Whilst Atezolizumab is thought to be an antagonist, merely acting as a blocking agent, the above studies support the notation that

Atezolizumab and other therapeutic monoclonal antibodies may have potential to signal intrinsically to the cancer cells.

Several recent studies have investigated the possibility of an intrinsic role of PD-L1 in cancer cells across diverse cancer types (reviewed: Hudson *et al.,* 2020) Indeed, from the current literature it is becoming apparent that PD-L1 may be capable of sending pro-survival or anti-tumour signals within cancer cells to promote or inhibit tumour progression, respectively, through studies using predominantly RNA interference approaches in 2D-cultured mouse or human cancer cell lines and immunocompromised mouse models. However, the effect of intrinsic PD-L1 signalling is not fully conclusive in any cancer and the evidence is limited to whether approved therapeutic monoclonal antibodies affect PD-L1 signalling intrinsically. It is imperative that the role of PD-L1 is elucidated in all cancer types to aid in the correct selection of patients to treat with therapeutic anti-PD-L1 monoclonal antibodies.

To our knowledge, only 5 studies have investigated the effects of anti-PD-L1 monoclonal antibodies on intrinsic PD-L1 signalling. Saleh *et al.,* (2019) was the first to report the ability of Atezolizumab to bind PD-L1 on monolayer-cultured MDA-MB-231 breast cancer cells and induce cell death and transcriptomic changes, independent of the immune system. In our study, we were unable to detect any significant changes to cell viability in Atezolizumab-treated monolayer-cultured MDA-MB-231 cells compared to untreated cells, but there were signs of necrosis induced by Atezolizumab after 6 days as well as significantly reduced ATP levels in accordance with Saleh *et al.,* (2019) findings that Atezolizumab may reduce MDA-MB-231 cell viability. Indeed, this study showed that Atezolizumab could downregulate genes involved in ATP synthesis (Saleh *et al.,* 2019). To support these findings, here by performing Phospho-Kinase array we showed that Atezolizumab-treated cells had increased phosphorylation of p53 at S15 that has been shown to occur in response to metabolic stress via AMPK protein kinase activation (Jones *et al.,* 2005; Loughery *et al.,* 2014). Whilst phosphorylation of p53 at S15 has also be found to trigger transcription of apoptosis-related genes, the phosphorylation of p53 at S46 and S392 was reduced in Atezolizumab-treated cells. Phosphorylated S46 and S392 has been shown to correlate with apoptosis induction (Oda *et al.,* 2000; Castrogiovanni *et al.,* 2018). This data may suggest that Atezolizumab may elicit metabolic changes to the cells via mechanisms that avoids effecting cancer cell

viability to a degree that cannot be significantly detected by performing phenotypical functional assays.

Importantly, here we were able to show for the first time that Atezolizumab was able to induce signs of reduced viability and significant reductions in ATP synthesis in 3D hanging drop spheroids and 3D alginate spheroid colonies. The effect of Atezolizumab to induce apoptotic and necrotic cell death in MDA-MB-231 cells grown in alginate was most noticeable at day 3 and reduced over the time course of 10 days, which could suggest at the earlier timepoints cells were most vulnerable as single cells and once they became more established into 3D spheroid colonies, they appeared more resistant to Atezolizumab-induced cell death. Moreover, whilst in Saleh *et al.,* (2019) study Atezolizumab-treated cells showed significantly higher cell death compared to untreated cells, they did not display significantly higher cell death compared to cells treated with an IgG control. This could suggest indirect antibody toxicity towards the cells as opposed to direct effect of PD-L1 binding and inducing cell death intrinsically.

Atezolizumab effects on growth of MDA-MB-231 cells assessed by fluorescent staining and Ki67 expression analysis were lacking in this study in both 2D and 3D cell culture models. Mohan *et al.,* (2019) also showed that Atezolizumab was unable to inhibit the growth of TNBC cell lines (MDA-MB-231 and BT20) but was able supress invasion and motility through the inhibition of focal adhesion kinase phosphorylation which was not assessed in this study. In contrast, other studies have shown contradictory evidence of PD-L1 blockade effecting cell growth and proliferation. Saleh *et al.,* (2019) demonstrated a reduction in cell proliferation following Atezolizumab treatment. Controversially, Calu-1 lung cancer cells exhibited increased proliferation via increased AKT and ERK phosphorylation in an *in vivo* immunocompromised mouse model following treatment with Atezolizumab (Wang *et al.,* 2020).

Using RNA-Seq, Saleh *et al.,* (2019) illustrated that genes involved in promoting cell migration, metastasis, EMT, cell growth and hypoxia were downregulated whilst apoptosis genes were upregulated after MDA-MB-231 cells were treated with Atezolizumab. Chen *et al.,* 2021 showed that PD-L1 intrinsically promotes EMT via suppressing p38-MAPK activity and the destruction of EMT transcription factor Snail through using homemade anti-PD-L1 antibodies that promote degradation of PD-L1 in an immunocompetent TNBC mouse model. Antibody treatment suppressed

tumour metastasis to the lungs by increasing E-cadherin expression and reducing p38-MAPK activity and Snail expression (Chen *et al.,* 2021). Similarly, here using a Phospho-Kinase array, we demonstrated that Atezolizumab treatment reduced the phosphorylation of molecules involved PI3K/AKT and MAPK/ERK signalling pathways responsible for cell proliferation, survival, migration, and invasion (Guo *et al.,* 2020; Rascio *et al.,* 2021). Phosphorylated ERK1/2 in MDA-MB-231 cells was the most reduced kinase following Atezolizumab treatment. In colorectal cancer cells, phosphorylated ERK was also shown to be substantially reduced following PD-L1 blockade in a colon CT26 tumour *in vivo* mouse model (Passariello *et al.,* 2019). PD-L1 positive tumour cell lines have been shown to have a constitutively high degree of phosphorylation of ERK1/2 and P38 compared to PD-L1 negative tumour cells leading to aggressive and invasive phenotypes (Massi *et al.,* 2014) which could explain why blocking PD-L1 on MDA-MB-231 cells resulted in a reduction of both phosphorylated ERK1/2 and P38.

Collectively, the above data suggests that Atezolizumab may be able to modulate the signalling of PD-L1 in MDA-MB-231 breast cancer cells to some extent at the level of gene expression and post-translational modifications; in favour of preventing tumour progression which may not be limited to breast cancer.

Since the degree of cell death induced by Atezolizumab was limited in this study, we next wanted to determine whether the upregulation of PD-L1 with cytokine modulation could enhance the cell death phenotype observed by breast cancer cells cultured in 2D and 3D models. Indeed, chemotherapeutic agents such as cisplatin, doxorubicin and gemcitabine have been shown to induce PD-L1 expression on tumour cells and work synergistically with anti-PD-L1 monoclonal antibodies to reduce tumour growth and progression (Ghebeh *et al.,* 2010; Ng *et al.,* 2018; Fournel *et al.,* 2019; Del Re *et al.,* 2021). In this study we used IFNγ and/or TNFα to upregulate PD-L1 expression at mRNA and protein level before treating the cells with Atezolizumab. However, these cytokines have previously shown their ability to induce cancer cell apoptosis themselves (Cruceriu *et al.,* 2012; Kotredes and Gamero, 2013), and therefore were also investigated alone alongside them being combined with Atezolizumab.

In MDA-MB-231 2D cells and 3D alginate spheroid colonies, IFNγ and TNFα combined induced cell death. In MDA-MB-231 3D hanging drop spheroids TNFα alone was able to induce cell death. Previously, MDA-MB-231 cells along with other

TNBC cells have shown to be resistant TNFα-mediated apoptosis via NFκB activation and Bcl-2 overexpression (Wang *et al.,* 2012). This suggests that MDA-MB-231 cultured in 3D hanging drop spheroids may change their molecular phenotype that makes them more vulnerable to TNFα-mediated apoptosis. It has been reported that the action of TNFα, whether it elicits a pro-tumour or anti-tumour role, is heavily dependent on the cellular context and specific molecular traits of the cancer cells (Cruceriu *et al.,* 2012). In this study we also investigated 2D- and 3D-cultured ER+ MCF-7 breast cancer cells and they did display sensitivity to TNFα treatment alone, which was in accordance with the literature (Simstein *et al.,* 2003; Donato *et al.,* 2004). Interestingly, when Atezolizumab treatment was added to MDA-MB-231 cells modulated with TNFα, cells displayed the highest amount of cell death amongst the treatment groups in 2D cells and 3D alginate spheroid colonies.

It has recently been shown that TNFα plays a major role in maintaining the stability of PD-L1 on the surface of tumour cells (Lim *et al.,* 2016). TNFα-mediated signalling via the TNF receptor on tumour cells leads to the transcription of CSN5 which stabilises PD-L1 by direct deubiquitination or by inhibiting ubiquitination of PD-L1. This in part could explain why TNFα was able to induce cancer cell death in combination with Atezolizumab as TNFα is maintaining PD-L1 expression in order for Atezolizumab to bind and elicit its anti-tumour role. Here we also showed that the cell death phenotype was the same in MCF-7 breast cancer cells cultured in 3D alginate spheroid colonies suggesting that targeting of PD-L1 in combination with an apoptosis-inducing drug like TNFα could also be beneficial for tumours expressing low PD-L1.

Furthermore, apoptosis-inducing ligands, such as TNFα and TRAIL have demonstrated their ability to improve immunotherapy responses. In a melanoma mouse model, oncolytic viral delivery of TNFα and IL-2 improved the efficacy of anti-PD-1 treatments (Cervera-Carrascon *et al.,* 2018). TNFα coupled to a tissue-specific peptide was also able to reduce tumour growth in murine melanoma and lymphoma models (Curnis *et al.,* 2000), as well as promote the efficacy of adoptive T cell therapy combined with anti-PD-1 therapy in murine melanoma and prostate carcinoma models (Calcinotto *et al.,* 2012; Elia *et al.,* 2018). One study explored the combination of PD-L1 inhibition and TRAIL using a bi-functional fusion protein in melanoma cells and demonstrated synergistic PD-L1-directed TRAIL-mediated tumour cell apoptosis via increasing T cell activation (Hendricks *et al.,* 2016). Whilst TNFα has limitations

as a therapeutic agent due to its well-known systemic toxicity, TRAIL-mediated apoptosis offers a novel approach to enhance the efficacy of PD-L1/PD-1 checkpoint inhibition without affecting the toxicity profile with TRAIL being cancer cell specific.

In summary, this study provides new insight into the intrinsic role of PD-L1 through using the approved anti-PD-L1 immunotherapy drug, Atezolizumab in MDA-MB-231 cells, not only in 2D monolayer-culture but for the first time reported in two different 3D cell culture models. Utilising functional assays, we were able to show that blocking PD-L1 with Atezolizumab was able to manipulate the cancer cells intrinsically resulting in a reduction in viability, ATP synthesis and phosphorylation of a broad range of kinases. Lastly, we were able to demonstrate therapeutic potential of Atezolizumab in combination with TNFα for the treatment of breast cancer in a 3D alginate model that more closely recapitulates that of an *in vivo* human tumour compared to standard 2D cell culture. Regardless, there is still ample research to be done to fully understand the intrinsic role of PD-L1 in breast cancer cells and determine the exact mechanistic actions of Atezolizumab in an immune-independent context.

5. Investigating the biological effects of miRNA-mediated PD-L1 knockdown on MDA-MB-231 breast cancer cells compared to PD-L1 blockade with Atezolizumab

5.1 Introduction

Since most patients treated with immunotherapies targeting the PD-1/PD-L1 signalling pathway are shown to be unresponsive or develop resistance short after treatment initiation, it is important to understand the mechanism of action of the proteins in which they target. Recent scientific efforts have demonstrated the potential of PD-L1 to send pro-survival signals in cancer cells to promote cancer initiation, metastasis, development, and resistance to therapy (Dong *et al.,* 2018; Hudson *et al.,* 2020). The investigations into PD-L1 intrinsic signalling have been predominantly focused on cancer types such as melanoma and NSCLC where PD-1/PD-L1-targeted monotherapies have demonstrated the most success in generating complete patient responses (Larkin *et al.,* 2015; Brahmer *et al.,* 2015; Robert *et al.,* 2015; Fehrenbacher *et al.,* 2016; Antonia *et al.,* 2018). Whilst this research is paramount to gain an understanding to how treatment efficacy can be improved in these cancer types, limited research on PD-L1 intrinsic signalling has taken place on cancer types where PD-1/PD-L1-targeted therapies have the potential to benefit cancer patients. For example, cancer types that present with PD-L1 positivity, circulating PD-1 positive/CD8+ T cells and/or high mutational burden (Yi *et al.,* 2018).

Triple negative breast cancer (TNBC) is one of those cancer types that display high PD-L1 expression shown to correlate with high CD8+ T cells presence in the tumour microenvironment (Sabatier *et al.,* 2015); key features which have prompted clinical investigation of PD-1/PD-L1-targeted therapies alone and in combination with other anti-cancer agents for TNBC patients. Table 5.1 illustrates the vast number of clinical trials using anti-PD-L1 monoclonal antibodies alone or in combination with chemotherapy and/or targeted therapy in TNBC patients (Table 5.1). Whilst several clinical trials have shown objective tumour responses and durable long-term disease control (Bertucci and Gonçalves, 2017), only Atezolizumab in combination with nab-paclitaxel has been approved for the treatment of TNBC patients to date (Schmid *et al.,* 2018), raising questions of why this may be the case. From the sparse literature available to date in TNBC cells, PD-L1 intrinsic signalling has been reported to promote cancer stem cell (CSC)-like characteristics (Almozyan *et al.,* 2017), growth

(Chen *et al.,* 2021) and chemotherapy resistance (Black *et al.,* 2016; Liu *et al.,* 2017). These studies used small interfering RNA (siRNA) to silence PD-L1 in mouse or human 2D-cultured cells and immunocompromised mouse models. Importantly, the tumorigenic role of PD-L1 in TNBC has not yet been investigated in 3D cancer models and only one of the above studies compared the silencing of PD-L1 to their homemade PD-L1 blocking monoclonal antibodies to determine the role of PD-L1 intrinsic signalling in TNBC cells (Chen *et al.,* 2021).

Table 5.1 Clinical trials using anti-PD-L1 monoclonal antibodies in TNBC.

Anti-PD-L1 Antibody	Combined drug (s)	Study Name (Identifier)
Atezolizumab	-	NCT01375842
	Carboplatin and Paclitaxel	NCT02883062
	Paclitaxel	NCT03125902
	nab-paclitaxel	NCT02425891
	AKT inhibitor (Ipatasertib) and paclitaxel	NCT04177108
	BET inhibitor (RO)	NCT03292172
	HDAC inhibitor (Entinostat)	NCT02708680
	PARP inhibitor (Rucaparib)	NCT03101280
	PI3K-gamma inhibitor (IPI-549)	NCT03961698
	VEGF inhibitor (Cabozantinib)	NCT03170960
Durvalumab	-	NCT03356860
	PARP inhibitor (Olaparib)	NCT03544125
	Nab-paclitaxel and Dose-dense Doxorubicin/Cyclophosphamide	NCT02489448
	ATR inhibitor (AZD6738) and PARP inhibitor (Olaparib)	NCT03740893
	Paclitaxel	NCT02628132
	PTK7 inhibitor (PF-06647020)	NCT02222922
Avelumab	-	NCT01772004
	GITR inhibitor (TRX518) and cyclophosphamide	NCT03861403
	PTK7 inhibitor (PF-06647020)	NCT02222922

Table 5.1. Clinical trials using anti-PD-L1 monoclonal antibodies alone or in combination with chemotherapy and/or targeted therapy in TNBC patients. Several clinical studies are ongoing or have been completed for the use of anti-PD-L1 monoclonal antibodies in TNBC with or without other anti-cancer agents. Red highlights the only approved anti-PD-L1 therapy for TNBC in combination with nab-paclitaxel.

It is possible that blocking PD-L1 using monoclonal antibodies may be insufficient in TNBC to completely inhibit the intrinsic signalling mediated by PD-L1 and that other therapeutic approaches to target PD-L1 intrinsically may offer more benefits to breast cancer patients. Hence why the comparisons of PD-L1 knockdown to the effects of therapeutically approved monoclonal antibodies that block PD-L1 at the cell surface is imperative, not only to determining the role of PD-L1 in TNBC cells but to verify the efficacy of monoclonal antibodies in an immune-independent setting for the treatment of TNBC.

5.1.1   Aims

The following chapter aims to further elucidate the tumorigenic role of PD-L1 in human breast cancer cells by utilising 3D cell culture models that are more physiologically relevant to *in vivo* human solid tumours than standard 2D cell culture. To do this, firstly PD-L1 was specifically knocked down in human MDA-MB-231 breast cancer cells by using a miRNA-mediated approach. The biological effects of PD-L1 knockdown on breast cancer cell growth, proliferation, viability, spheroid forming capabilities and intracellular signalling were then explored. With blocking PD-L1 using an anti-PD-L1 immunotherapy drug being the approved therapeutic strategy for targeting tumorigenic PD-L1, the biological effects of the anti-PD-L1 immunotherapy drug Atezolizumab on breast cancer cells were compared to the biological effects of PD-L1 knockdown. Finally, PD-L1 knockdown cells were treated with TNFα to determine whether reduced PD-L1 expression could enhance the cell death induced by TNFα even more so than when TNFα was combined with Atezolizumab as observed in Chapter 4 Section 4.3.13.

5.1.2   Hypotheses

It was hypothesised that PD-L1 knockdown would reduce the growth, proliferation, viability, and spheroid forming capability of MDA-MB-231 breast cancer cells and that this would be reflected in the downstream signalling pathways explored in this study. It was also hypothesised that the biological effects of PD-L1 knockdown in breast cancer cells would be more profound in comparison to blocking PD-L1 with the anti-PD-L1 immunotherapy drug Atezolizumab on the cell surface of cancer cells. Similarly, it was hypothesised that PD-L1 knockdown cells treated with TNFα would exhibit more cell death than breast cancer cells treated with Atezolizumab and TNFα.

5.2 Materials and Methods

5.2.1 Cell lines and culture conditions

Human MDA-MB-231 breast cancer cells were used for all subsequent experiments due to their high PD-L1 expression status. Monolayer cells were cultured and maintained as described in Chapter 2 Section 2.2.1. 3D hanging drop spheroids and 3D alginate spheroid colonies were generated as described in Chapter 3 Section 3.2.1.1 and 3.2.1.2.

5.2.2 miRNA knockdown of PD-L1

5.2.2.1 Oligonucleotide annealing and ligation reaction

Single-oligonucleotides were designed specifically to wild-type PD-L1 (accession number NM_014143) using the Invitrogen BLOCK-iT™ RNAi Designer tool (Table 5.2) (ThermoFisher Scientific). Lyophilized single-oligonucleotides were reconstituted in nuclease-free water to a final concentration of 200 µM. Oligonucleotide annealing, and ligation reactions were carried out according to the manufacturer's protocol (BLOCK-iT™ Pol II miR RNAi Expression Vector Kit with Emerald Green Fluorescent Protein (EmGFP), ThermoFisher Scientific). The pcDNA™6.2-GW/EmGFP-miR vector construct to which the resulting double-stranded oligonucleotide primers was incorporated, and its key features are illustrated in Figure 5.1 and Table 5.3, respectively. For oligonucleotide annealing, 5 µL top oligonucleotide, 5 µL bottom oligonucleotide, 2 µL 10x oligo buffer and 8 µL nuclease-free water was added to 0.5 mL microcentrifuge tube at a final concentration of 50 µM, incubated at 95°C for 4 minutes and left to cool to room temperature before being centrifuged and stored at -20°C. The resulting double-stranded oligonucleotides and the double-stranded miR-*lacZ* positive control oligonucleotide was diluted 5000-fold (10 nM). A 20 µL ligation reaction mixture was prepared for each double-stranded oligonucleotide containing: 4 µL 5x ligation buffer, 2 µL vector (5 ng/ µL), 4 µL double-stranded oligonucleotide (10 nM), 9 µL nuclease-free water and 1 µL T4 ligase. The mixture was incubated for 30 minutes at room temperature and then placed on ice. A negative control was prepared substituting the double-stranded oligonucleotide for nuclease-free water. A positive control was prepared using the ds miR-*lacZ* oligonucleotide provided with the kit.

Table 5.2 Top and bottom oligonucleotides designed specific to wild-type PD-L1 (NM_014143).

Name	Oligonucleotide Sequence	
	Top	**Bottom**
NM_014143_1045	**5'**TGCTGTTAAGTCCCACATTGCCTGCAGTTTTGG CCACTGACTGACTGCAGGCAGTGGGACTTAA**3'**	**5'**CCTGTTAAGTCCCACTGCCTGCAGTCAGTCAG TGGCCAAAACTGCAGGCAATGTGGGACTTAAC**3'**
NM_014143_1264	**5'**TGCTGAAATTAGGGATTCTCAACCCGGTTTTGG CCACTGACTGACCGGGTTGAATCCCTAATTT**3'**	**5'**CCTGAAATTAGGGATTCAACCCGGTCAGTCAG TGGCCAAAACCGGGTTGAGAATCCCTAATTTC**3'**
NM_014143_1319	**5'**TGCTGAACAAATTGAGGCATTGAGTGGTTTTGG CCACTGACTGACCACTCAATCTCAATTTGTT**3'**	**5'**CCTGAACAAATTGAGATTGAGTGGTCAGTCAGT GGCCAAAACCACTCAATGCCTCAATTTGTTC**3'**
NM_014143_1549	**5'**TGCTGAGACCAAGCACCTTACAAATAGTTTTGG CCACTGACTGACTATTTGTAGTGCTTGGTCT**3'**	**5'**CCTGAGACCAAGCACTACAAATAGTCAGTCAGT GGCCAAAACTATTTGTAAGGTGCTTGGTCTC**3'**

Table 5.2 Four different oligonucleotide primers to be ligated for incorporation into the vector construct. Columns illustrate the name of each oligonucleotide primer and the sequences of the top and bottom oligonucleotide which were designed specifically to be ligated into the BLOCK-iT miRNA vector system (pcDNA™6.2-GW/EmGFP-miR) for miRNA-mediated knockdown of PD-L1 in human MDA-MB-231 breast cancer cells.
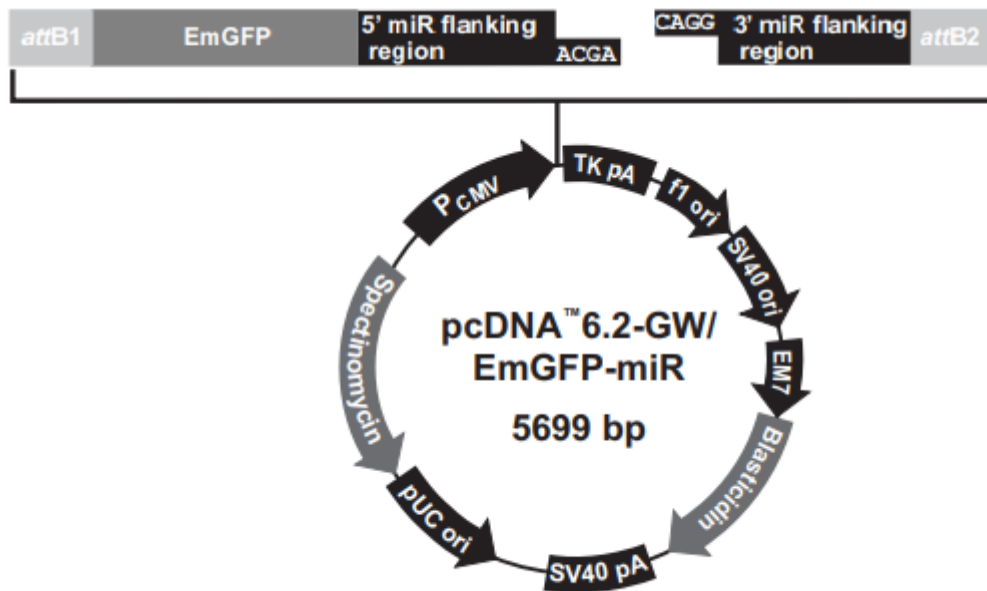
Figure 5.1 The pcDNA™6.2-GW/EmGFP-miR vector construct. The figure illustrates the pcDNA™6.2-GW/EmGFP-miR vector construct to which double-stranded oligonucleotides were incorporated.

5.2.2.2 Transformation of One Shot® TOP10 *E. coli*

One Shot® TOP10 *E. coli* (ThermoFisher) was transformed with the ligated plasmid DNA. One vial of *E. coli* was used per transformation (4x double-stranded oligonucleotides, 1x positive and 1x negative ligation reaction, and 1x positive and 1x negative transformation controls). Sterile Lennox broth (LB) agar was made by adding 35 g LB agar powder (Merck) to a final volume 1 L of deionised water. The LB agar was then dissolved using a heated stirrer and magnetic flea before being sterilised via autoclaving. Subsequently, LB agar plates were prepared with 50 µg/ml spectinomycin or 100 µg/ml ampicillin for the positive control plasmid. 2 µL of ligation reaction was used per vial of *E. coli* which was incubated on ice for 15 minutes; heat shocked at 42°C for 30 seconds and immediately placed back on ice before adding 250 µL of pre-warmed Super Optimal Broth Catabolite repression (SOC) medium supplied with the *E. coli* to each vial and incubating for 1 hour at 37°C horizontally shaking at 200 rpm. Transformed *E. coli* was then plated onto pre-warmed agar plates containing the appropriate selective antibiotics using sterile inoculation loops and incubated at 37°C overnight. The four double-stranded oligonucleotides that form the four different vector constructs are named hereafter collectively as constructs or individually as 1045, 1264, 1319, 1549 (the number given to each top and bottom oligonucleotide, refer to Table 5.2 Section 5.2.2.1).

Table 5.3. Key features of the pcDNA™6.2-GW/EmGFP-miR vector.

Key Feature	Benefit
CMV promoter	Recognised by RNA Polymerase II and controls high-level, constitutive expression of miRNA.
miRNA forward sequencing primer	Allows sequencing of the insert.
EmGFP coding sequence	Allows visual detection of transfected mammalian cells using fluorescence microscopy.
EmGFP forward sequencing primer	Allows sequencing of the insert.
5′ and 3′ miR flanking regions	Allows formation of functional engineered pre-miRNA.
5′ overhangs	Allows ligase-mediated directional cloning of the double-stranded oligonucleotide of interest.
miRNA reverse sequencing primer	Allows sequencing of the insert.
TK polyadenylation signal	Allows transcription termination and polyadenylation of mRNA.
f1 origin	Allows rescue of single-stranded DNA
SV40 early promoter and origin	Allows high-level expression of the selection marker and episomal replication in cells expressing the SV40 large T antigen.
EM7 promoter	Synthetic prokaryotic promoter for expression of the selection marker in Escherichia coli (*E. coli*).
Blasticidin resistance gene	Permits selection of stably transfected mammalian cell lines.
SV40 polyadenylation signal	Allows transcription termination and polyadenylation of mRNA.
pUC origin	Permits high-copy replication and maintenance in *E. coli*.
Spectinomycin resistance gene and promoter	Allows selection of the plasmid in *E. coli*. The promoter allows expression of the spectinomycin resistance gene in *E. coli*.

Table 5.3. The key features and benefits of using the pcDNA™6.2-GW/EmGFP-miR vector for our study to knockdown PD-L1 in human MDA-MB-231 breast cancer cells using a miRNA-mediated approach.

5.2.2.3 Plasmid DNA isolation

Sterile LB was made up by adding 20 g LB powder (Merck) to a final volume of 1 L of deionised water which was then autoclaved to sterilise. Five single colonies from each construct (1045, 1264, 1319 and 1549), the negative control and the positive control, were selected and grown up for 15 hours in 5 mL of sterile LB containing 50 µg/ml spectinomycin or ampicillin (positive control), named hereafter as clones. The bacteria-containing LB was centrifuged at 6800 g for 2 minutes to pellet the bacteria and the plasmid DNA was isolated using the GeneJET Plasmid Miniprep Kit (ThermoFisher Scientific), according to the manufacturer's protocol. DNA quantity and purity was assessed by using a spectrophotometer (NanoDrop 1000, ThermoFisher). Purified plasmid DNA was stored at -20°C until use.

5.2.2.4 Plasmid DNA sequencing

Out of each of the four vector constructs, one clone found to have high-quality plasmid DNA was prepared to be sent off for Sanger Sequencing by the Sanger Sequencing Services at Source Biosciences. The sequencing results were assessed using the National Centre for Biotechnology Information (BLAST) software, to determine whether the inserts were in the correct orientation and that no mutations had occurred within the miRNA sequences during transformation so that they had 100% homology to the target sequence PD-L1.

5.2.2.5 Transfection of human MDA-MB-231 breast cancer cells and selection of stable transfectants

A dose response curve with Blasticidin (0-10 µg/ml) (Fisher Scientific) was generated for MDA-MB-231 breast cancer cells to determine the optimal concentration required to kill non-transfected cells. Cells were cultured to ~80% confluency prior to transfection with plasmid DNA using the Amaxa Cell Line Nucelofector Kit V (Lonza) or Lipofectamine™ 3000 Transfection Reagent (ThermoFisher Scientific). Appropriate controls were used during the transfection process including a negative scrambled miRNA control (pcDNA™6.2-GW/± EmGFPmiR-neg control, ThermoFisher Scientific), GFP positive control (Lonza), antibiotic control (cells minus plasmid DNA treated with antibiotic) and transfection reagent/procedure control (cells treated the same as transfected cells minus plasmid DNA).

5.2.2.5.1 Nucleofection

Cells were harvested and 1×10^6 cells per reaction were centrifuged for 10 minutes and resuspended in 100 µL Nucleofector solution supplied with the Amaxa Cell Line Nucleofector Kit V. Plasmid DNA (2 µg) was added to the solution which was placed into certified cuvettes in the Nucleofector IIb device (Lonza) with the X-013 programme selected. Immediately after transfection the solution was diluted with 500 µL culture medium and transferred to 6-well plates with 900 µL of culture medium for overnight incubation. Blasticidin (10 µg/ml) was added for mammalian selection 24 hours post-transfection and replaced with fresh selection medium every 3 days for 14 days to select for Blasticidin-resistant cells. Transfection efficacy through visualising EmGFP positive cells was monitored daily using fluorescent microscopy.

5.2.2.5.2 Lipofection

Cells were harvested and 150,000 cells/well were seeded into a 24-well plate for overnight culture. For transfection, 25 µL Opti-MEM™ I Reduced Serum Medium (ThermoFisher Scientific) was prepared with 2 µL lipofectamine 3000 reagent. Separately, 25 µL Opti-MEM™ I Reduced Serum Medium was prepared with 0.25 µg of plasmid DNA and 0.5 uL P3000 reagent (ThermoFisher Scientific). The two solutions were then mixed and incubated at room temperature for 15 minutes to form lipid:DNA complexes before 50 µL was added to appropriate wells containing the cells to be transfected, gently mixed by swirling and left to incubate for 24 hours. Cells were then trypsinised and moved up to 6-well plates with fresh medium containing Blasticidin (10 µg/ml) antibiotics for selection which was replaced every 3 days for 14 days to generate a stable cell line.

5.2.2.5.2.1 Selection of stable transfectants

Clonal discs (4.8 mm, ThermoFisher) soaked in Trypsin-EDTA 0.25% were used to isolate individual resistant colonies (10 per construct) from each well that were also identified to express homogenous EmGFP via fluorescent microscopy using the Olympus IX81 microscope. Fluorescent images were captured at 20X objective using the Olympus cellSens Imaging Software and homogenous EmGFP colonies were marked on the plate for removal using clonal discs. Each individual colony was placed in a well of a 24-well plate in selection medium and grown to 90% confluency before being moved to larger culture vessels.

5.2.2.5.2.2   Assessment of PD-L1 knockdown efficacy by flow cytometry

PD-L1 knockdown efficacy for each of the selected colonies per vector construct were assessed by PD-L1 staining via flow cytometry as described in Chapter 2 Section 2.2.3.1. Concurrently, EmGFP expression was assessed by flow cytometry as its expression level should correlate with PD-L1 knockdown efficacy with it being located upstream of the miRNA. Appropriate controls were used for assessing PD-L1 expression by EmGFP positive cells including single colour controls (APC only and FITC only) as well as cells negative for EmGFP. When analysing the data for transfected cells using FlowJo EmGFP positive cells were gated first before PD-L1 expression was assessed.

5.2.2.5.2.3   Lipofection method optimisation

Once the vector construct that most effectively at reduced PD-L1 expression was identified (measured by flow cytometry of PD-L1), the lipofection procedure was optimised using the chosen vector construct to determine where it was possible to yield a higher stable transfection efficacy. Firstly, the densities of cells seeded for the transfection procedure were investigated by plating 100,000, 125,000, 150,000, 175,000 and 200,000 cells in a 24-well plate prior to transfection, whilst all the other steps in the transfection procedure remained the same as above (Section 5.2.2.7). Alongside investigating cell seeding densities, the amount of plasmid DNA used to transfect cells was also investigated at the original seeding density (150,000 cells) as stated above (Section 5.2.2.7) Cells were treated with 0.25 µg, 0.5 µg, 0.75 µg and 1 µg of plasmid DNA, whilst the transfection procedure remained the same as above (Section 5.2.2.7). Following transfection, the cells were monitored for EmGFP expression via fluorescent microscopy and were treated with blasticidin-containing medium 24 hours post-transfection for 14 days in 6-well plates. After selection, cells expressing EmGFP were isolated, grown up and assessed for PD-L1 expression by flow cytometry to assess whether stable transfection efficacy was improved by altering the cell seeding density or the amount of plasmid DNA used in the lipofection procedure.

5.2.2.5.2.4   Confirmation of stable PD-L1 knockdown efficacy using RT-qPCR and Flow Cytometry

Clonal assays of cells that showed the lowest expression of PD-L1 by flow cytometry following optimisation were prepared and monitored for homogenous EmGFP positive colony formation to which 6 of these were then isolated and assessed for

PD-L1 expression by RT-qPCR and flow cytometry. The colony that demonstrated the highest degree of PD-L1 knockdown at mRNA and protein level was expanded in culture, stocks were made, and these cells were used for subsequent experiments to investigate the biological effects of PD-L1 knockdown in MDA-MB-231 cancer cells.

5.2.2.5.2.5 Clonal assay using wild-type MDA-MB-231 cells

To confirm that reduced PD-L1 expression was a result of the miRNA-mediated knockdown experiment and not due to clonal variation of PD-L1 expression in MDA-MB-231 wild-type (WT) cells, a clonal assay using MDA-MB-231 WT cells was performed by seeding 2×10^4 cells/well in a 6-well plate. Colony formation was monitored daily using the Olympus IX81 microscope until individual colonies were ready to be marked for isolation using clonal discs as described above. Images of established WT colonies were captured using the 20X objective lens and the Olympus cellSens Imaging Software. Ten colonies were isolated in total (two from each of the 5 wells of the 6-well plate). The remaining well was used to grow MDA-MB-231 WT cells to 90% confluency to use as a control for heterogeneous PD-L1 expression. All clones were then expanded for assessment of PD-L1 expression by flow cytometry as described in Chapter 2 Section 2.2.3.1. The expression of PD-L1 by each expanded clone was compared to MDA-MB-231 WT cells grown as a heterogeneous population.

5.2.3 Effects of PD-L1 knockdown on cellular growth and proliferation in 2D and 3D cultures

5.2.3.1 Fluorescent microscope images of 2D and 3D cultures

Monolayer-cultured cells and 3D cultures were prepared for MDA-MB-231 WT, scrambled control and PD-L1 knockdown cells. WT cultures were either left untreated or treated with Atezolizumab. Cultures were harvested, stained with Hoechst 33342/PI and images using the 4X objective lens were captured using the BioTek Cytation 5 Cell Imaging Multimode Reader as described in Chapter 4 Section 4.2.4.1. Images of cells cultured in monolayer were analysed using ImageJ to determine the surface area of the wells in a 96-well plate covered by Hoechst 33342/PI positive cells for untreated WT, Atezolizumab-treated WT, scrambled control and PD-L1 knockdown cells after 3 and 6 days of culture. The data was expressed as a percentage of the untreated WT control cells.

5.2.3.2 Diameter measurements of 3D cultures

The diameter of 3D hanging drop spheroids and 3D alginate spheroid colonies was measured for untreated WT, Atezolizumab-treated WT, scrambled control and PD-L1 knockdown cultures using the diameter measurement option in the cellSens Imaging Software as described in Chapter 3 Section 3.2.2.3.

5.2.3.3 Intracellular staining of cell proliferation marker Ki67 in 2D and 3D cultures

Single cell suspensions were made from 2D- and 3D-cultured cells generated from WT, Atezolizumab-treated WT, scrambled control and PD-L1 knockdown cultures via trypsinisation. Subsequently, intracellular staining of Ki67 was performed on 2D- and 3D-cultured cells before being analysed by flow cytometry as described in Chapter 4 Section 4.2.4.3.

5.2.4 Effects of PD-L1 knockdown on cell viability and metabolic activity in 2D and 3D cultures

5.2.4.1 Assessment of apoptosis using Annexin V/Propidium Iodide staining

MDA-MB-231 WT, Atezolizumab-treated WT, scrambled control and PD-L1 knockdown cells were cultured in 2D and 3D cultures, harvested from culture as single cell suspensions, and subsequently labelled with Annexin V (APC) and PI (Biolegend) as described in Chapter 4 Section 4.2.5.1. For scrambled control and PD-L1 knockdown cells that expressed EmGFP, 3-colour flow cytometry was performed whereby EmGFP was detected by the FITC channel, PI was detected by the PE channel, and Annexin V was detected by the APC channel. Single cell gating and single colour controls were used for all experiments to allow appropriate compensation. PD-L1 cell surface expression was assessed parallel to cell viability as described in Chapter 2 Section 2.2.3.1 to ensure that PD-L1 was being blocked by Atezolizumab and that PD-L1 expression remained reduced in PD-L1 knockdown cells.

Additionally, Annexin V/PI staining experiments were repeated with MDA-MB-231 WT, Atezolizumab-treated WT, scrambled control and PD-L1 knockdown cells cultured in 2D and 3D cultures but some cells received TNFα treatment alone for 48 hours prior to flow cytometric analysis as described in Chapter 4 Section 4.2.5.1.

5.2.4.2 Assessment of cellular activity using CellTitre-Glo in 2D and 3D cultures

The CellTiter-Glo® Cell Viability Assay was used to assess ATP production by MDA-MB-231 WT, Atezolizumab-treated WT, scrambled control and PD-L1 knockdown cells that were cultured in monolayer and 3D cell culture models for 3, 6 or 10 days as described in Chapter 4 Section 4.2.5.2.

5.2.4.3 Assessment of cellular activity using MTT assay in 2D-cultured cells

Monolayer MDA-MB-231 WT, Atezolizumab-treated WT, scrambled control and PD-L1 knockdown cells were cultured for 3 and 6 days in 96-well plates at a seeding density of 3 x 10^4 cells/well, before the cellular activity was assessed using the CyQUANT MTT Cell Viability Assay (ThermoFisher Scientific), according to the manufacturer's instructions. Firstly, the manufacturer's standard protocol was compared to the quick protocol provided with the kit to determine which was the most appropriate for subsequent experiments. Both protocols were performed on cells seeded at different densities (1 x 10^4 cells/mL to 5 x 10^4 cells/mL) in a 96-well plate to determine whether each protocol gave the same absorbance values. Following this initial experiment, the quick protocol was used thereafter. To plated cells 100 µL of fresh medium without phenol red (Gibco, ThermoFisher Scientific) was added to each well before adding 10 µL 12 mM MTT and incubating at 37°C for 4 hours. After the incubation 85 µL of the medium was removed from each of the wells and 50 µL of DMSO (ThermoFisher Scientific) was added and mixed thoroughly by pipetting up and down. Cells were incubated for a further 10 minutes at 37°C before reading at 570 nm absorption using a CLARIOstar Microplate Reader (BMG LABTECH).

5.2.5 Effects of PD-L1 knockdown on cellular signalling using a protein profiler array

Two T175 flasks of MDA-MB-231 WT, Atezolizumab-treated WT, scrambled control and PD-L1 knockdown cells were grown to 90% confluency before protein was isolated from the cells and quantified as described in Chapter 4 Section 4.2.6.1. The array was performed as described in Chapter 4 Section 4.2.6.1. Graphs of spot intensities were plotted for WT, Atezolizumab-treated WT, scrambled control and PD-L1 knockdown cells.

5.2.6   Statistical analysis

Statistical analysis was performed using Prism version 7.03 (GraphPad Software, Inc.) as described in previous Chapters. Data shown here was determined to be non-parametric and is represented as median ± range. P-values less than 0.05 were considered significant (*$P<0.05$, **$P<0.01$, ***$P<0.001$ and ****$P<0.0001$). Each independent experiment has 3-6 technical repeats.

5.3 Results

5.3.1 Double-stranded oligonucleotide inserts displayed 100% homology to the original sequences designed to knockdown PD-L1

To confirm that the oligonucleotide inserts were in the correct orientation and displayed the correct sequence following *E. coli* transformation, the clone with the highest DNA purity for each of the four different vector constructs were sent for DNA sequencing (Appendix Figure 9.12). Assessment of the DNA sequencing results using BLAST software revealed that the plasmid DNA for each clone matched 100% homology to the oligonucleotides originally designed to target PD-L1 by miRNA-mediated knockdown (Figure 5.2).

5.3.2 MDA-MB-231 WT cells are sensitive to Blasticidin

Prior to mammalian cell transfection, it was also necessary to determine the sensitivity of MDA-MB-231 WT cells to Blasticidin to find the optimal concentration to use for mammalian cell selection to ultimately produce a stable cancer cell line with PD-L1 knockdown. A dose response curve was established for MDA-MB-231 WT cells in response to different concentrations of Blasticidin (0-10 µg/ml) by measuring the viability of cells over 12 days (Figure 5.3). Cells displayed over 50% cell death after 3 or more days of treatment with 10 µg/ml Blasticidin. Since mammalian selection is normally a process of 10 to 14 days (Mortensen and Kingston, 2001), 10 µg/ml was determined to be the optimal concentration of Blasticidin due all cells being confirmed dead after 12 days. Whilst 100% cell death was also observed with 7.5 µg/ml Blasticidin at day 12, it was decided that 10 µg/ml was more sufficient to ensure that all MDA-MB-231 cells not containing the plasmid DNA were removed from culture before expanding the stably transfected cells.

Figure 5.2 BLAST alignment results. DNA sequencing data was input into BLAST software to determine whether the forward and reverse strand from each vector construct displayed 100% homology to the original expected sequence.
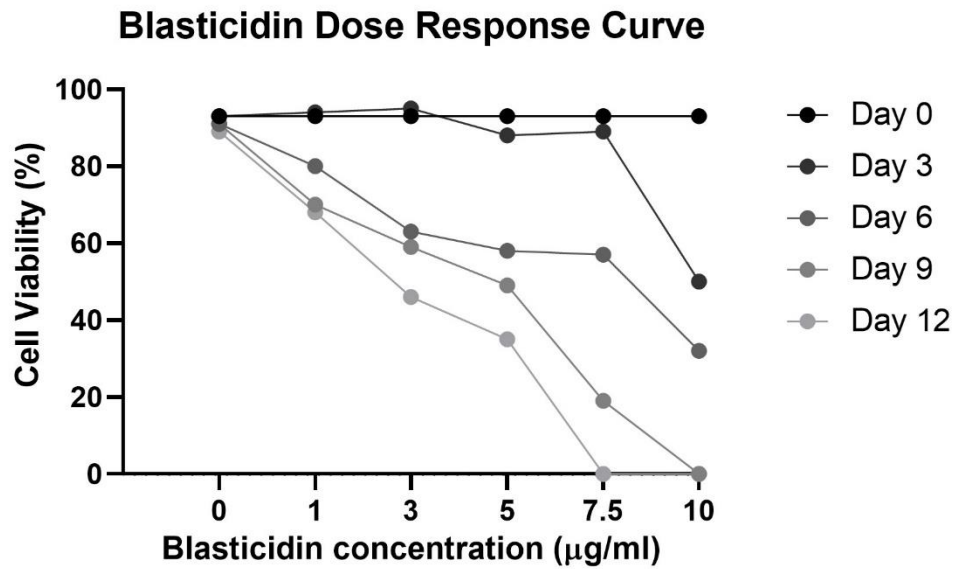
Figure 5.3 MDA-MB-231 WT cells are highly sensitive to 10 µg/ml Blasticidin after 3, 6, 9 and 12 days of culture. Prior to transfection, MDA-MB-231 WT cells were treated with 0-10 µg/ml Blasticidin for 12 days and the viability was assessed every 3 days to determine the optimal concentration necessary to kill non-transfected MDA-MB-231 WT cells. Data is presented as the average percentage viability from 3 technical repeats of n=1 independent experiment.

5.3.3 miRNA-mediated knockdown of PD-L1 in MDA-MB-231 breast cancer cells using the transfection method nucleofection

MDA-MB-231 breast cancer cells transfected with the negative scrambled control, positive control, and vector constructs (1045, 1264, 1319 and 1549) using nucleofection displayed EmGFP expression 24 hours post-transfection (Figure 5.4). Unexpectedly, cells transfected with the negative scrambled control did not display the same high levels of EmGFP expression 24 hours post-transfection compared to the vector constructs. The growth of transfected cells in selection medium and their expression of EmGFP were assessed daily by fluorescent microscopy. After 6 days post-transfection, fewer cells were present in the wells and EmGFP was less frequently expressed in the few cells remaining (Appendix Figure 9.13). Additionally, after selection for 14 days there were no viable transfected cells remaining in the wells (Data not shown). Unfortunately, transfected cells did not produce stable integration of the plasmid DNA into their own genome, and thus only showed transient expression of EmGFP. Moreover, whether transient PD-L1 knockdown was achieved or not in MDA-MB-231 cells was not able to be investigated following transfection using nucleofection as there was not enough viable cells post-transfection to assess PD-L1 expression by flow cytometry.
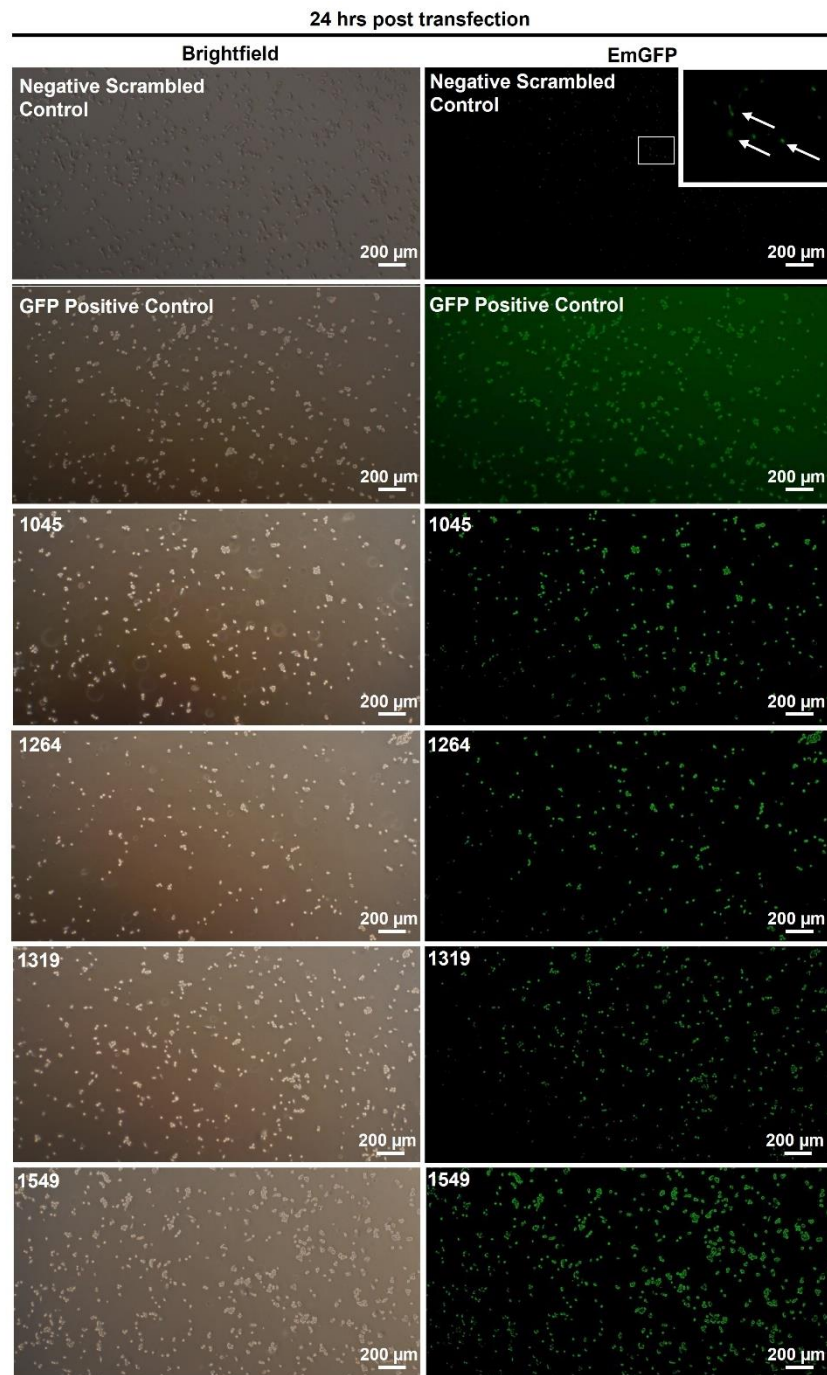
Figure 5.4 MDA-MB-231 cells transfected using nucleofection display EmGFP positivity 24 hours post-transfection. Nucleofection was used to transfect MDA-MB-231 cells with plasmid DNA for the negative scrambled control, GFP positive control and the 4 vector constructs (1045, 1264, 1319 and 1549). EmGFP expression was assessed 24 hours post-transfection. Images were captured and are shown in brightfield and FITC (EmGFP/GFP) separately. The white arrows shown for the negative scrambled control illustrate EmGFP positive cells that can be observed in the main figure in the small white box. Scale bar represents 200 µm. Images represent n=2 transfection procedures.

5.3.4 miRNA-mediated knockdown of PD-L1 in MDA-MB-231 breast cancer cells using the lipofection transfection method

Due to nucleofection being unsuccessful for stable transfection of MDA-MB-231 cells and providing no possibility to measure PD-L1 expression, lipofection was used next as an alternative transfection method. Figure 5.5 demonstrates the gating strategy used to assess EmGFP positivity and PD-L1 expression post-transfection via flow cytometry (Figure 5.5). Transfecting MDA-MB-231 cells with plasmid DNA using lipofection enabled the assessment of EmGFP and PD-L1 expression 24 hours post-transfection (Figure 5.6A-C). The transfection efficacy was assessed by measuring EmGFP positive cells within the transfected cell population. Over 55% of cells transfected with the GFP positive control were GFP positive, whilst cells transfected with the negative scrambled control, 1045, 1264, 1319 and 1549 displayed between 13% and 27% EmGFP positivity 24 hours post-transfection (Figure 5.6A). Within the GFP positive population of all transfected cells the level of PD-L1 expression was comparable to that of the MDA-MB-231 WT and EmGFP positive scrambled control cells 24 hours post-transfection, suggesting that 24 hours post-transfection may be an insufficient time point to observe any effect of miRNA-mediated knockdown on PD-L1 expression (Figure 5.6B and C).

Rather than repeating the transfection procedure, it was next decided to proceed and culture all the transfected cells mentioned above (except GFP positive control) with selection medium to generate stable cell lines harbouring either the plasmid DNA for the negative scrambled control or for miRNA-mediated knockdown of PD-L1, to which then the expression of EmGFP and PD-L1 was assessed again. Following culture in selection medium for 14 days, EmGFP positive cells or colonies were identified by fluorescent microscopy for cells transfected with the four vector constructs (1045, 1264, 1319 and 1549) (Figure 5.7). EmGFP positive cells were also detected by flow cytometry in cells transfected with the negative scrambled control and the four vector constructs (Figure 5.8A and B). All transfected cells displayed a similar proportion of cells expressing PD-L1, except for those transfected with the 1319 vector construct (Figure 5.8C). Cells transfected with the 1319 vector construct also showed the largest shift in PD-L1 MFI compared to WT and negative scrambled control cells, out of all the other vector constructs (Figure 5.8D and E).
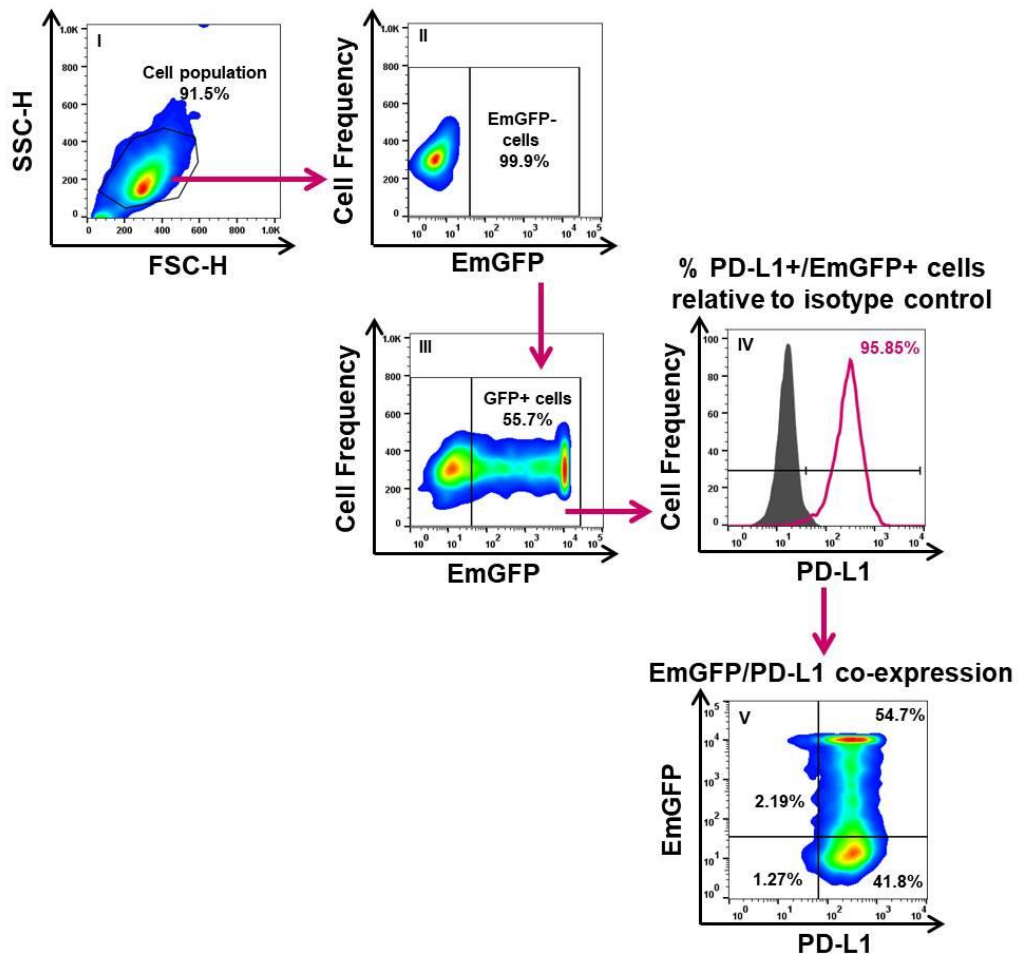
Figure 5.5 Illustrates the gating strategy applied to samples when assessing EmGFP and PD-L1 expression by transfected MDA-MB-231 cells via flow cytometry. (I) Flow cytometry plots demonstrate how the cell population of interest was first gated, followed by **(II)** EmGFP negative and **(III)** EmGFP positive cells. **(IV)** The expression of PD-L1 was then determined for the EmGFP positive cell population by first gating the PD-L1 negative population using the isotype control. **(V)** Co-expression of GFP and PD-L1 was also assessed by gating for both GFP and PD-L1 on the same flow cytometry plot.
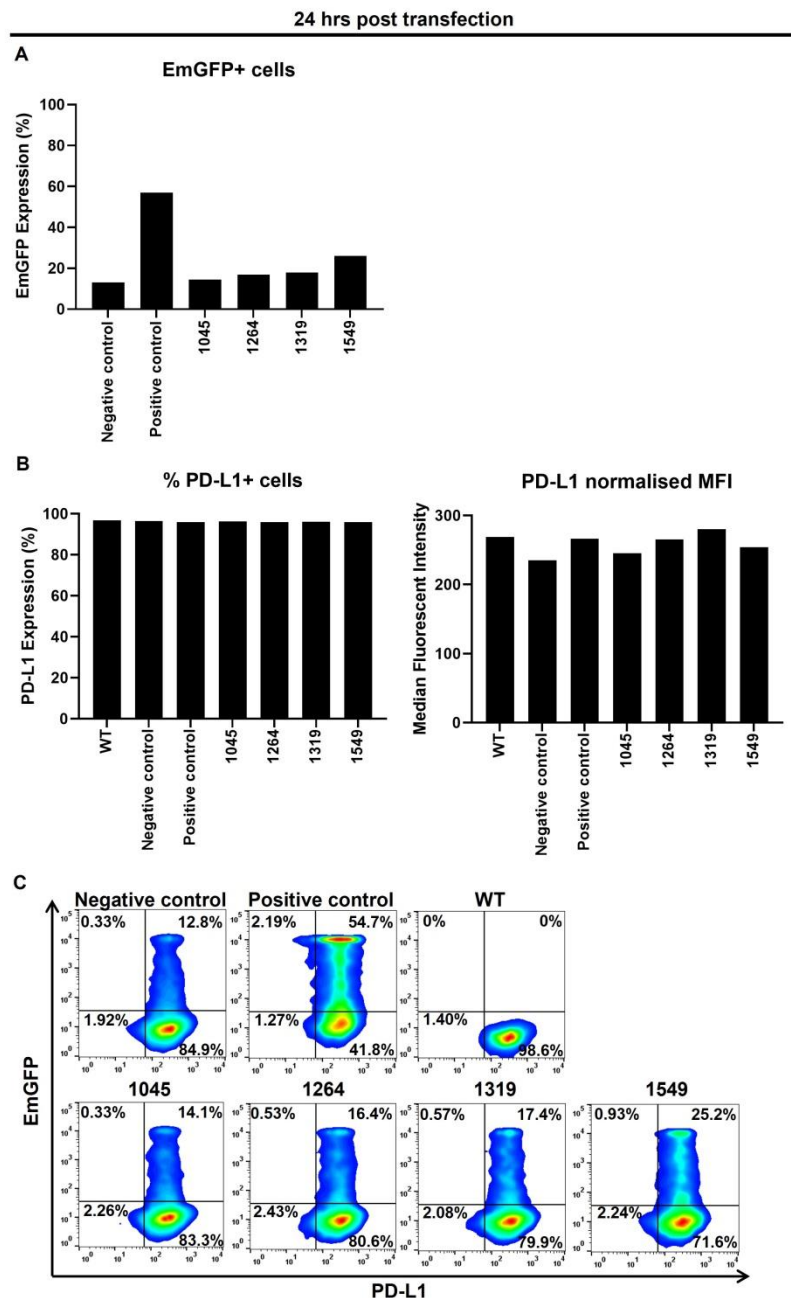
Figure 5.6 EmGFP positive cells were detected in transfected MDA-MB-231 cells 24 hours post-transfection using lipofection but PD-L1 expression remained unchanged compared to WT cells. At 24 hours post-transfection, MDA-MB-231 cells transfected with the plasmid DNA for the negative scrambled control, GFP positive control, 1045, 1264, 1319 and 1549 were assessed for **(A)** EmGFP expression and **(B)** PD-L1 expression. The percentage of cells expressing PD-L1 is shown (left) alongside the MFI for PD-L1 expression (right). **(C)** Representative flow cytometry plots are displayed to show the co-expression of EmGFP and PD-L1 within the cell populations. Data shown here represents n=1 independent experiment.
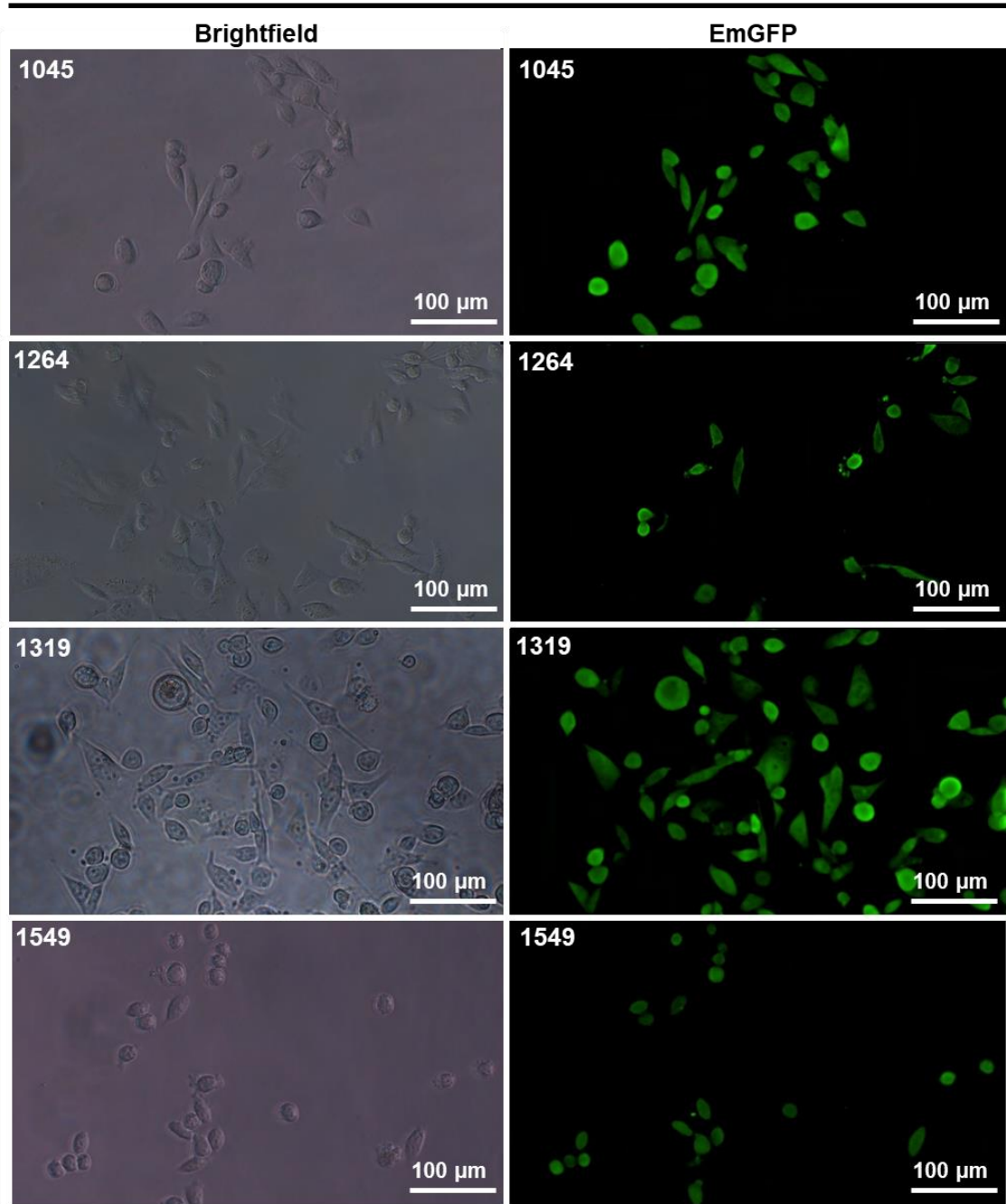
Figure 5.7 14 days post-transfection MDA-MB-231 cells expressing different vector constructs display EmGFP positivity. Fluorescent microscopy was used to identify EmGFP positive cells or EmGFP positive colonies within the cell populations transfected with 1045, 1264, 1319 and 1549 plasmids after 14 days of culture in Blasticidin selection medium. Scale bar represents 100 μm. Images represent n=1 independent experiment.
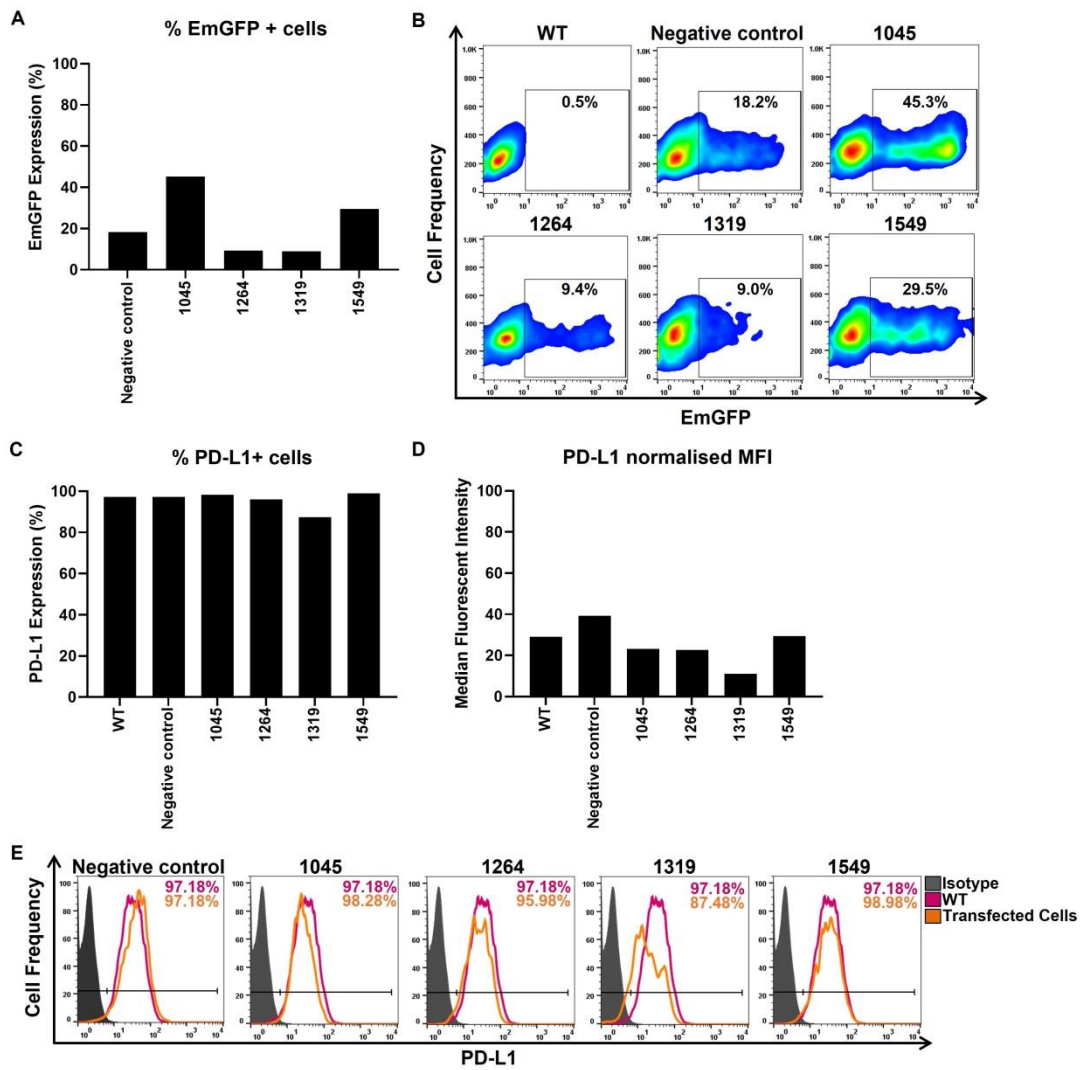
Figure 5.8 MDA-MB-231 cells transfected with the 1319 plasmid demonstrate EmGFP positivity and express the lowest frequency and level of PD-L1 expression compared to WT and scrambled control cells. (A) Flow cytometry was used to confirm the presence of EmGFP expression within the Blasticidin-resistant cell populations. **(B)** Representative flow cytometry plots show the percentage of EmGFP positive cells. **(C)** The frequency and **(D)** the level of PD-L1 expression by EmGFP positive cells was assessed by flow cytometry. **(E)** Representative flow cytometry histograms show PD-L1 expression by transfected cells relative to the isotype control and WT cells. Data represents n=1 independent transfection with 3 technical repeats.

5.3.5 MDA-MB-231 breast cancer cells transfected with the 1319 plasmid demonstrated a significant reduction in PD-L1 expression

Since the 1319 plasmid demonstrated the most promising results for achieving miRNA-mediated PD-L1 knockdown, transfection experiments using the 1319 plasmid were repeated to determine whether the transfection efficacy of stably transfected cells could be improved by altering the cell density or the amount of plasmid DNA used. Interestingly, altering of the cell density used (Figure 5.9A-B) but not the amount of plasmid DNA (Appendix Figure 9.14) improved the stable transfection efficacy as assessed by EmGFP positivity and PD-L1 expression via flow cytometry. MDA-MB-231 cells seeded at 200,000 cells/well displayed the highest EmGFP expression after undergoing stable selection (Figure 5.9A) which correlated with the highest reduction in PD-L1 expression (Figure 5.9B).

With these new stably transfected MDA-MB-231 cells, clonal assays were performed and monitored daily for homogenous EmGFP positive colony formation. Fluorescent microscopy was used to identify 6 colonies that homogenously expressed EmGFP (Figure 5.10). These colonies were isolated and expanded for assessment of EmGFP positivity by flow cytometry as well as PD-L1 mRNA and protein expression by RT-qPCR and flow cytometry, respectively. Isolated colonies displayed high EmGFP expression by flow cytometry (Figure 5.11) which corresponded with significantly reduced levels of PD-L1 expression at mRNA (Figure 5.12) and protein (Figure 5.13A and B) levels ($p < 0.05$), compared to WT and scrambled control cells. It was also confirmed that the significant reduction of PD-L1 expression was a result of the miRNA-mediated knockdown of PD-L1 and unlikely to be due to the clonogenic variation of PD-L1 expression within the MDA-MB-231 cell population (Figure 5.14 and 5.15A-C). Furthermore, colony 6 which displayed the lowest level of PD-L1 expression at both mRNA and protein levels was taken forward for future experiments investigating the biological effects of PD-L1 knockdown on MDA-MB-231 breast cancer cells. In a subsequent verification experiment, PD-L1 mRNA and protein expression by cells in colony 6 were shown to have approximately 70% reduced PD-L1 expression compared to WT cells (Figure 5.16A-C).
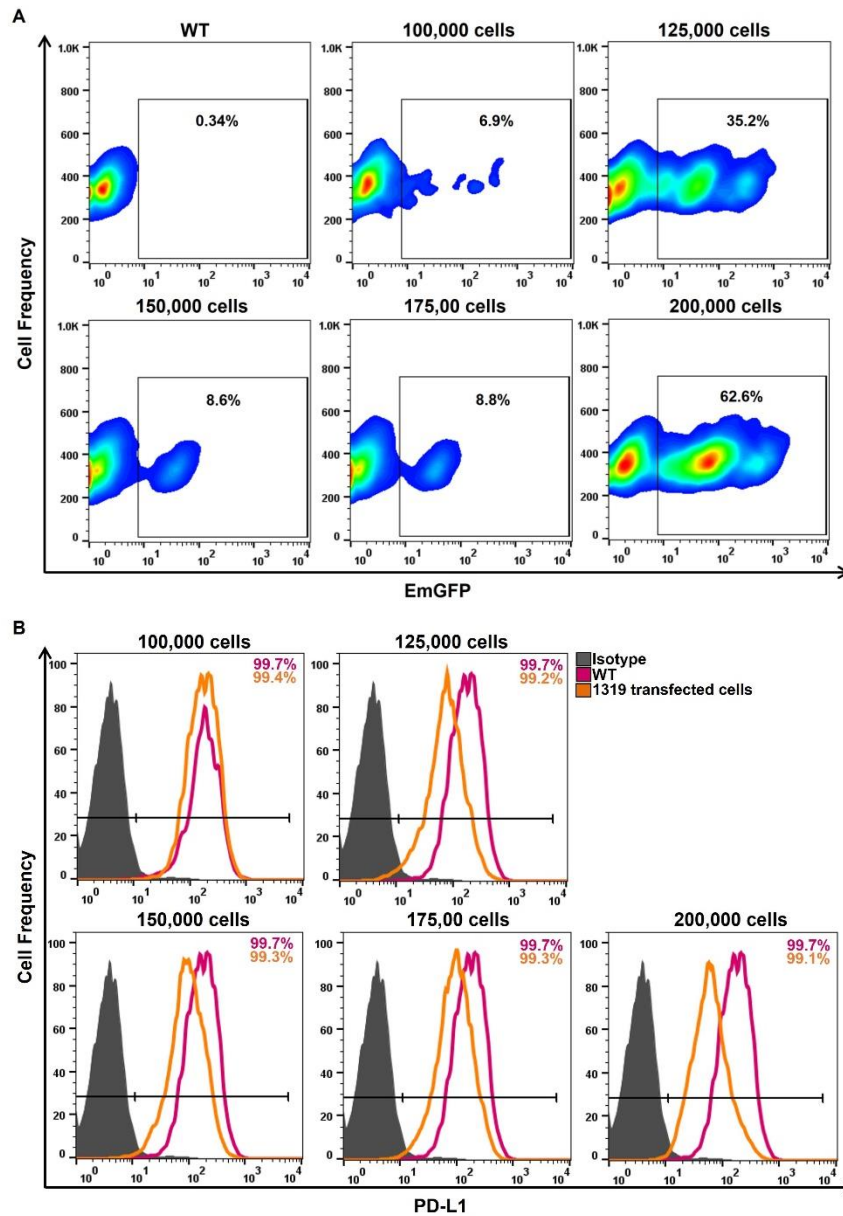
Figure 5.9 MDA-MB-231 cells seeded at 200,000 cells/well demonstrate the highest stable transfection efficacy 14 days post-transfection. MDA-MB-231 cells were seeded at different cell densities; two cell densities above and below the original cell density used (150,000 cells) to determine whether stable transfection efficacy could be improved following stable integration of the 1319 plasmid. **(A)** Flow cytometry plots show the GFP positivity present within the transfected cell population for each cell density investigated. **(B)** Flow cytometry histograms demonstrate the percentage and level of PD-L1 expression by transfected cells at each of the cell densities investigated relative to the isotype control and WT cells. Data represents n=1 independent transfection with 3 technical repeats.
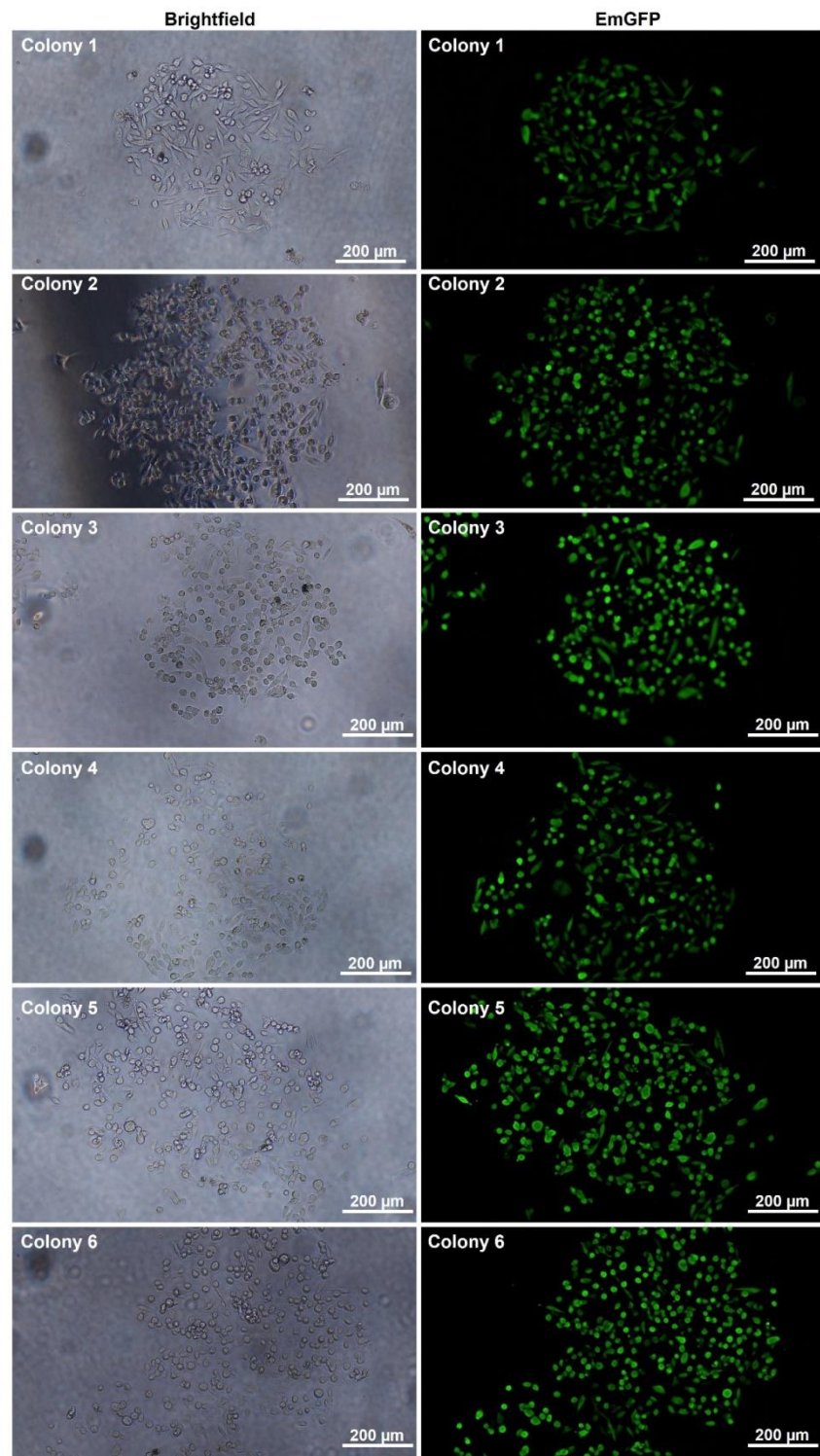
Figure 5.10 MDA-MB-231 cells transfected with the 1319 plasmid form EmGFP positive colonies in a clonogenic assay. Clonogenic assays of MDA-MB-231 cells transfected with the 1319 plasmid were prepared and 6 EmGFP positive colonies were identified by fluorescent microscopy. Brightfield and FITC images were captured of each colony identified. Scale bar represents 200 μm. Images represent n=1 independent experiment.
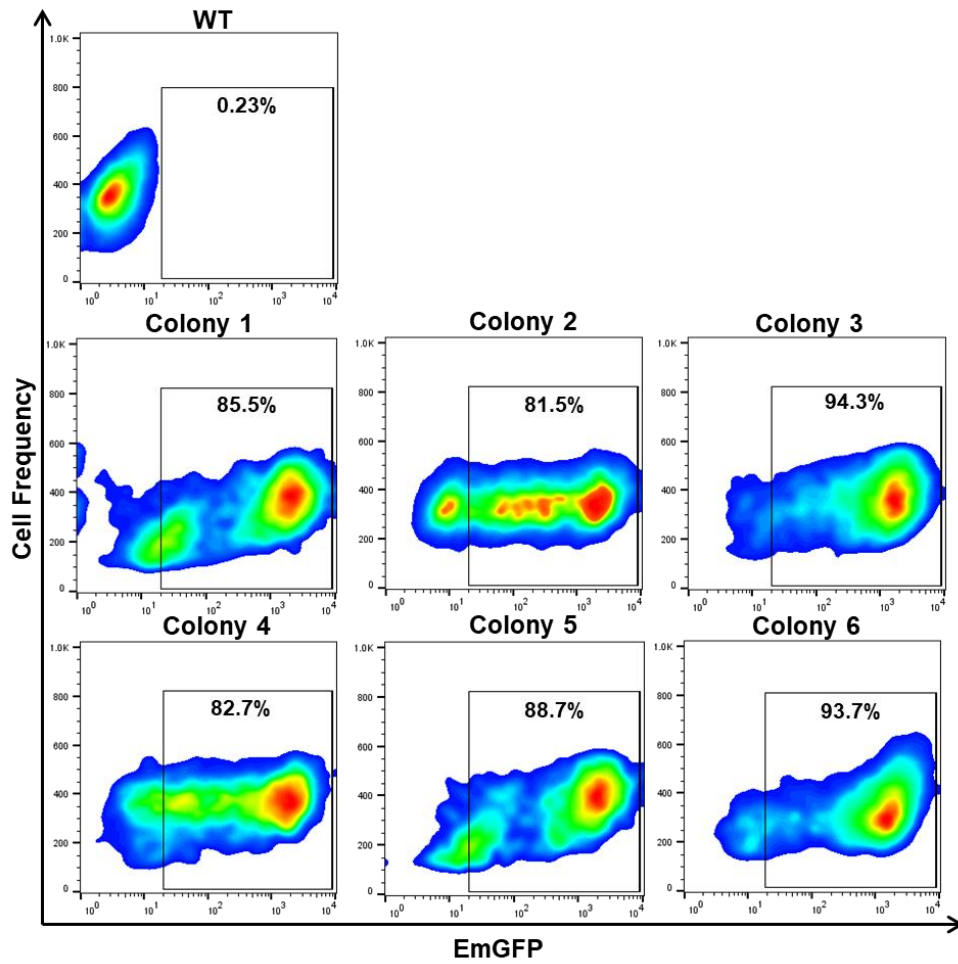
Figure 5.11 Flow cytometry confirms isolated MDA-MB-231 colonies transfected with the 1319 plasmid express high levels of EmGFP. MDA-MB-231 colonies that were identified by fluorescent microscopy were isolated and expanded to confirm the expression of EmGFP by flow cytometry. Representative flow cytometry plots show the percentage and level of EmGFP expression by the 6 colonies compared to EmGFP negative WT cells. Data represents n=1 independent experiment with 3 technical repeats.
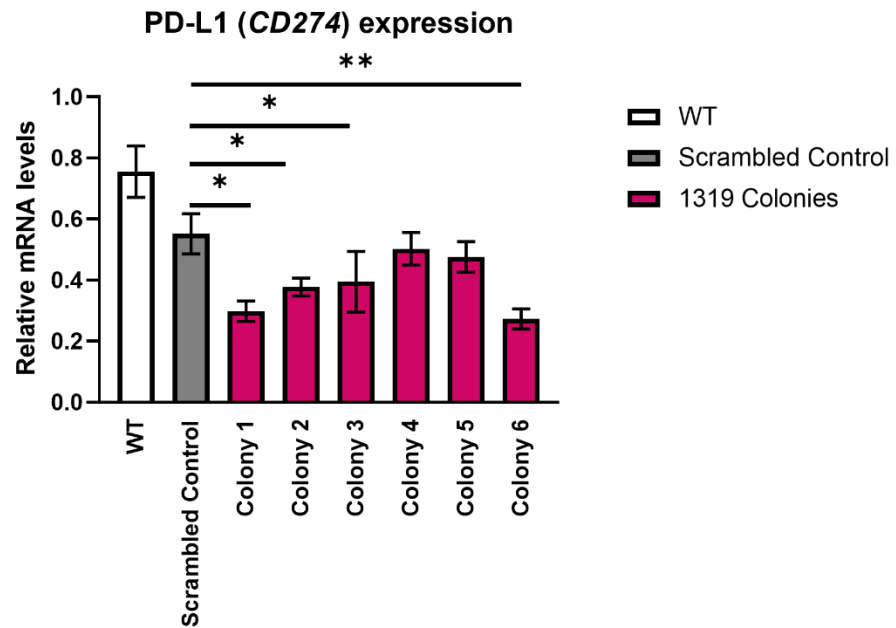
Figure 5.12 MDA-MB-231 colonies transfected with the 1319 plasmid display significantly reduced levels of PD-L1 mRNA compared to WT and scrambled control cells. The 6 GFP positive colonies were assessed for PD-L1 expression at mRNA level by RT-qPCR to ultimately identify the colony that showed the highest reduction in PD-L1 mRNA expression. Data is presented as median ± range. n=3 independent experiments each with 3 technical repeats. Data was analysed using a Kruskal-Wallis followed by Dunn's multiple comparisons test. Significance was displayed only for the scrambled negative control versus 1319 colonies (*P<0.05 and **P<0.01).
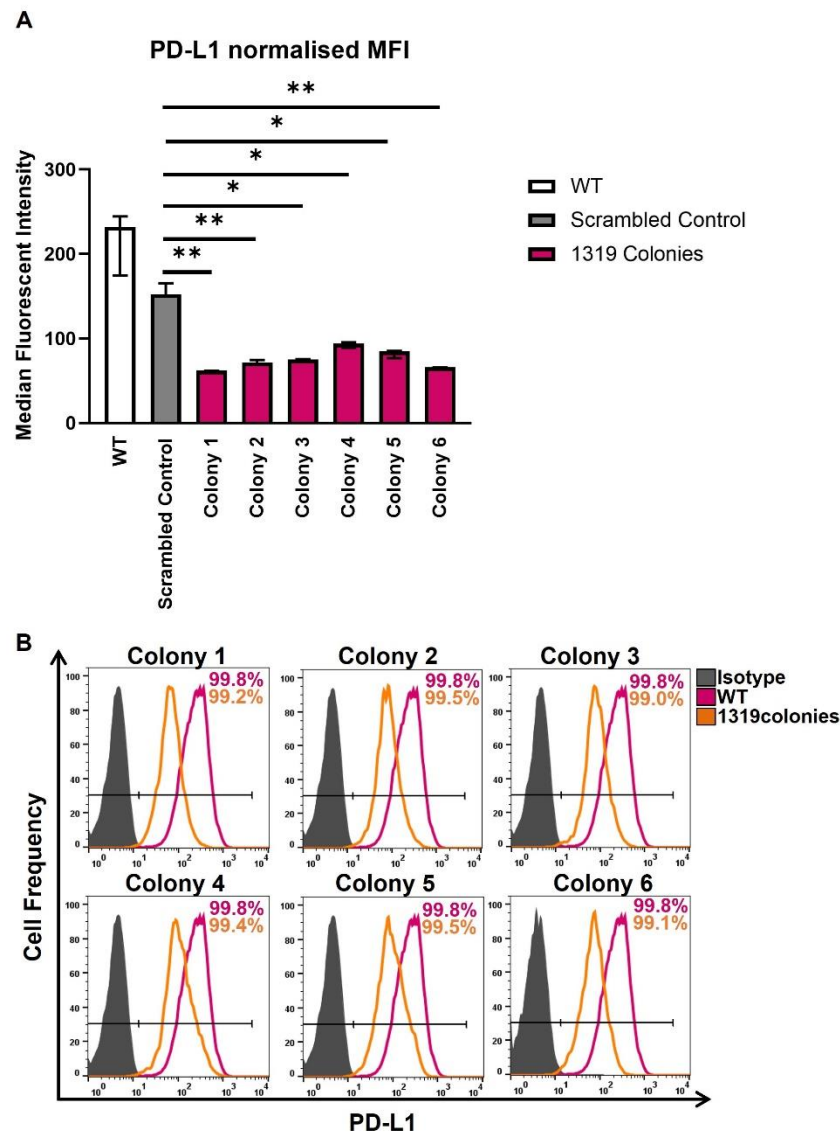
Figure 5.13 MDA-MB-231 colonies transfected with the 1319 plasmid display significantly reduced levels of PD-L1 protein compared to WT and scrambled control cells. (A) The 6 EmGFP positive colonies were assessed for PD-L1 expression at protein level by flow cytometry to identify the colony that showed the highest reduction in the level of PD-L1 protein expression. **(B)** Representative flow cytometry histograms shown for colonies 1 to 6 (orange) demonstrate reduced PD-L1 expression relative to the isotype control (grey) and WT cells (pink). Data is presented as median ± range. n=3 independent experiments each with 3 technical repeats. Data was analysed using a Kruskal-Wallis followed by Dunn's multiple comparisons test. Significance was only displayed for the scrambled negative control versus 1319 colonies (*P<0.05 and **P<0.01).
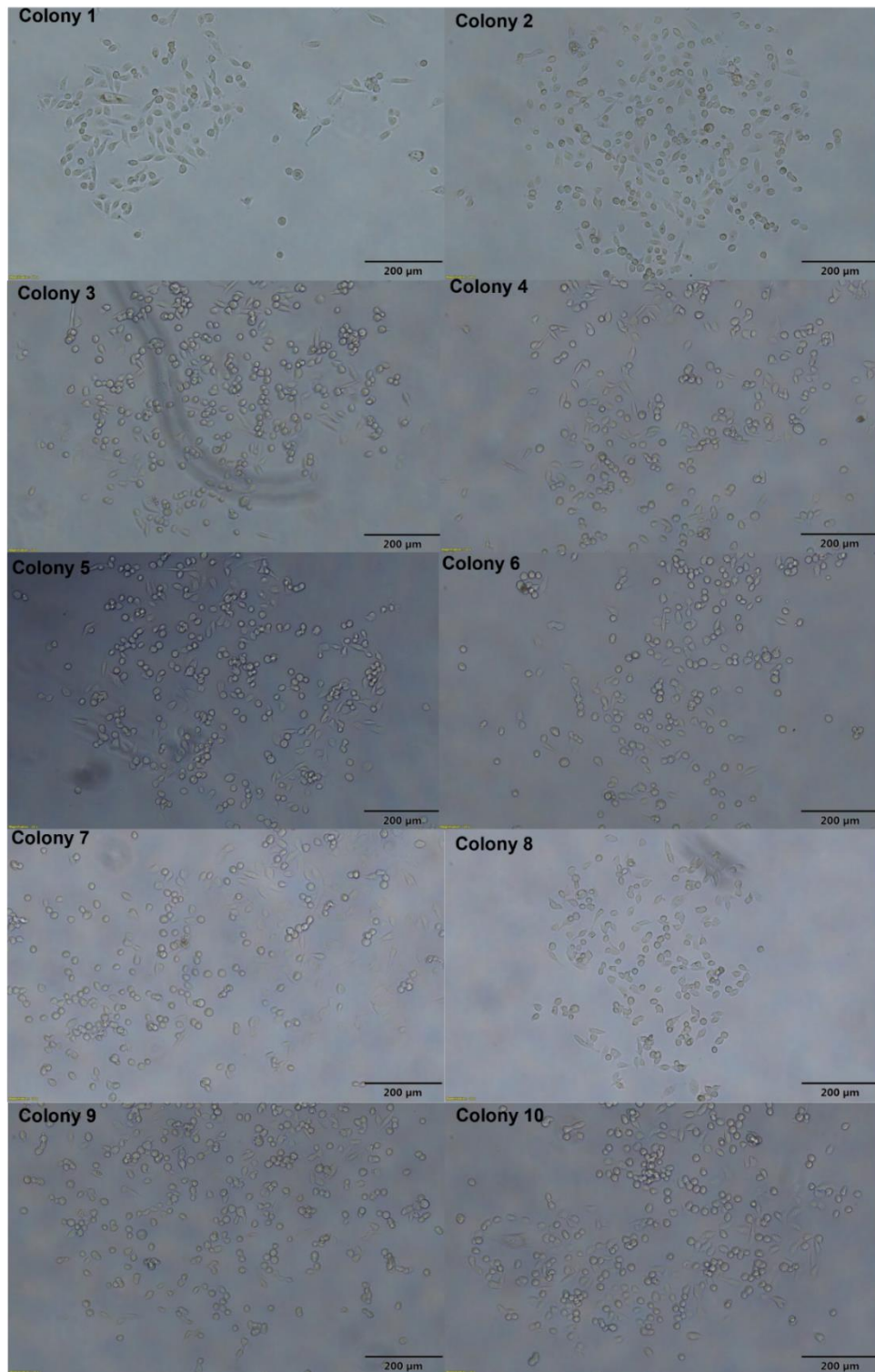
Figure 5.14 MDA-MB-231 WT cells form colonies in a clonogenic assay. MDA-MB-231 WT cells were seeded at clonal density, monitored for colony formation and 10 individual colonies were identified for subsequent isolation. Brightfield images of the 10 individual colonies were captured. Scale bar represents 200 µm. Images represent n=1 independent experiment.
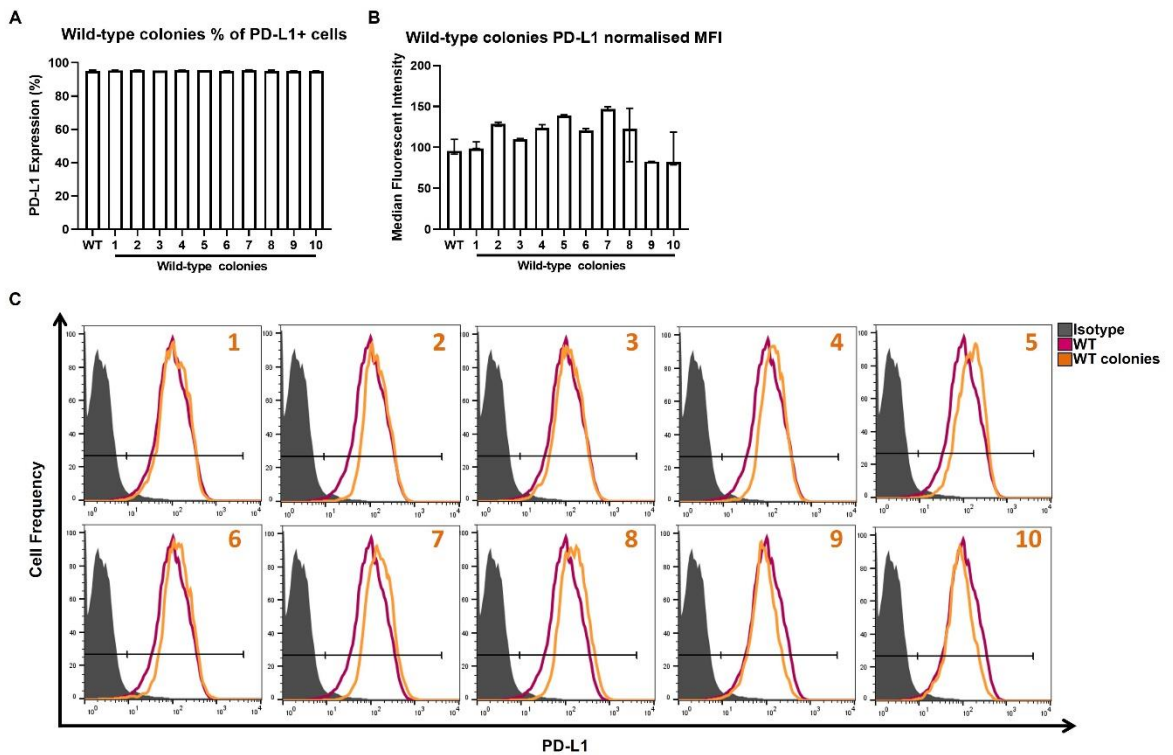
Figure 5.15 MDA-MB-231 WT colonies display comparable levels of PD-L1 expression to the MDA-MB-231 heterogeneous cell population. The 10 MDA-MB-231 WT colonies that were identified in the clonal assay, were expanded to allow the expression of PD-L1 to be assessed by flow cytometry to determine whether PD-L1 expression by these clones varied compared to PD-L1 expression by the heterogeneous MDA-MB-231 WT cell population. **(A)** The percentage of cells expressing PD-L1 is shown alongside **(B)** the MFI of PD-L1 expression. **(C)** Representative flow cytometry histograms show the isotype control (grey) relative to the PD-L1 positive populations for heterogeneous WT cells (pink) and WT colonies (orange). Data is presented as median ± range. n=1 independent experiments with 3 technical repeats.
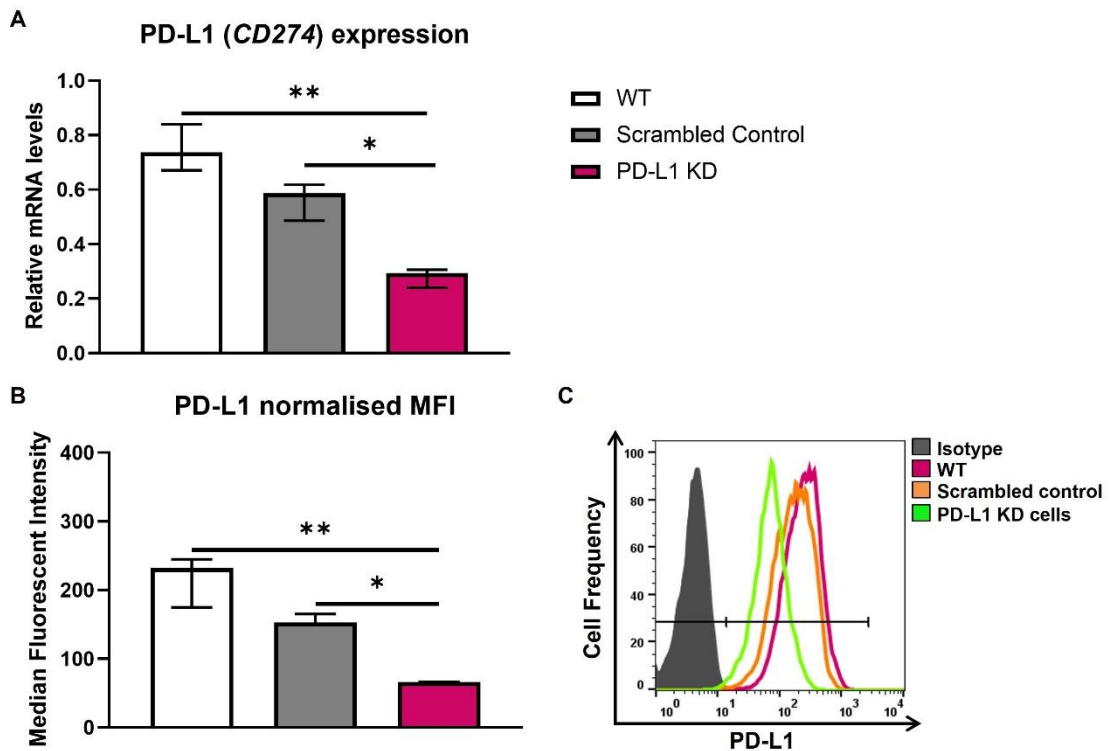
Figure 5.16 MDA-MB-231 PD-L1 knockdown cells display approximately a 70% reduction in PD-L1 mRNA and protein expression compared to WT cells. The MDA-MB-231 colony transfected with the 1319 plasmid DNA found to express the lowest level of PD-L1 mRNA and protein (colony 6) was further assessed for PD-L1 expression at **(A)** mRNA and **(B)** protein levels to confirm the PD-L1 knockdown phenotype. **(C)** A representative flow cytometry histogram shows PD-L1 expression by PD-L1 knockdown cells (green) relative to the isotype control (grey), WT (pink) and negative scrambled control (orange) cells. Data is presented as median ± range. n=3 independent experiments each with 3 technical repeats. Data was analysed by a Kruskal-Wallis followed by Dunn's multiple comparisons test (*P<0.05 and ***P<0.001).

5.3.6 PD-L1 knockdown affects the growth and proliferation of MDA-MB-231 breast cancer cells in 2D cell culture

To investigate the biological effects of PD-L1 knockdown versus PD-L1 blockade with Atezolizumab on MDA-MB-231 cells, it was first determined whether PD-L1 knockdown affected the growth and proliferation of MDA-MB-231 cells cultured in monolayer compared to Atezolizumab treatment. Images of WT, Atezolizumab-treated WT, scrambled control and PD-L1 knockdown cells seeded into 96-well plates were captured after being stained with Hoechst 33342/PI at day 3 (Figure 5.17) and 6 (Figure 5.18) of culture. Although the same number of cells was seeded at both time points assessed, wells containing PD-L1 knockdown cells appeared less confluent compared to wells containing WT, Atezolizumab-treated WT, and scrambled control cells after 3 and 6 days of culture. This difference in the confluency of the wells could also be observed in representative brightfield images taken independently to the fluorescent images after 3 and 6 days of culture in Appendix Figure 9.15. These observations were verified by calculating the percentage surface area covered by Hoechst 33342/PI positive cells after 3 (Figure 5.19A) and 6 (Figure 5.19B) days of culture. The percentage surface area covered by PD-L1 knockdown cells was approximately 60% after 3 (p=0.029) and 6 (p=0.02) days of culture relative to WT control cells (100%), which was found to be statistically significantly different. PD-L1 knockdown cells also exhibited a smaller percentage surface area covered than Atezolizumab-treated WT and scrambled control cells at both time points assessed. Although this data was found not to be significant.

Additionally, the expression of cell proliferation marker Ki67 was also substantially reduced in PD-L1 knockdown cells compared WT, Atezolizumab-treated WT and scrambled control cells after 3 (Figure 5.20A) and 6 (Figure 5.20B) days of culture. After 3 days, 70.5% (± 13.65) of PD-L1 knockdown cells displayed Ki67 expression at a lower MFI compared to WT, Atezolizumab-treated WT and scrambled control cells shown to express Ki67 in 95.3% (± 14.3), 94.4% (± 17.44) and 96.6% (± 7.78) of the cell population, respectively. Similarly, after 6 days, only 61.1% (± 23.3) of PD-L1 knockdown cells were shown to express Ki67 in comparison to WT, Atezolizumab-treated WT and scrambled control cells that were shown to express Ki67 in 88.2% (± 8.27), 87.1% (± 14.82) and 78.4% (± 17.48) of the cell population, respectively.
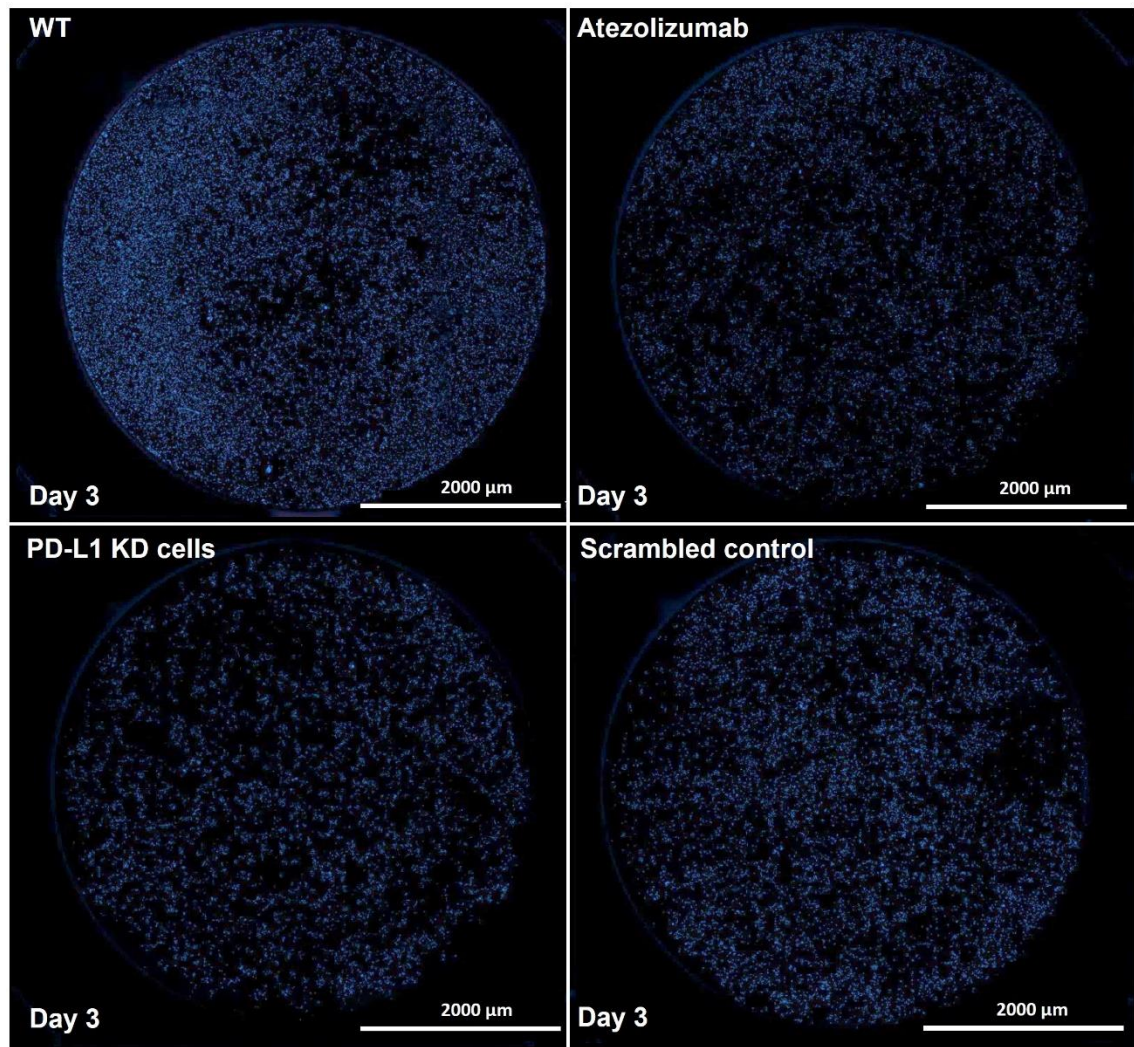
Figure 5.17 PD-L1 knockdown cells cultured in monolayer appear less confluent than WT, Atezolizumab-treated WT and scrambled control cells after 3 days of culture. Low magnification images were captured of MDA-MB-231 WT, Atezolizumab-treated WT, scrambled control and PD-L1 knockdown cells using the 4X objective lens after being cultured for 3 days and subsequently stained with Hoechst 33342/PI. Scale bar represents 2000 μm. Images represent n=3 independent experiments each with 3 technical repeats.
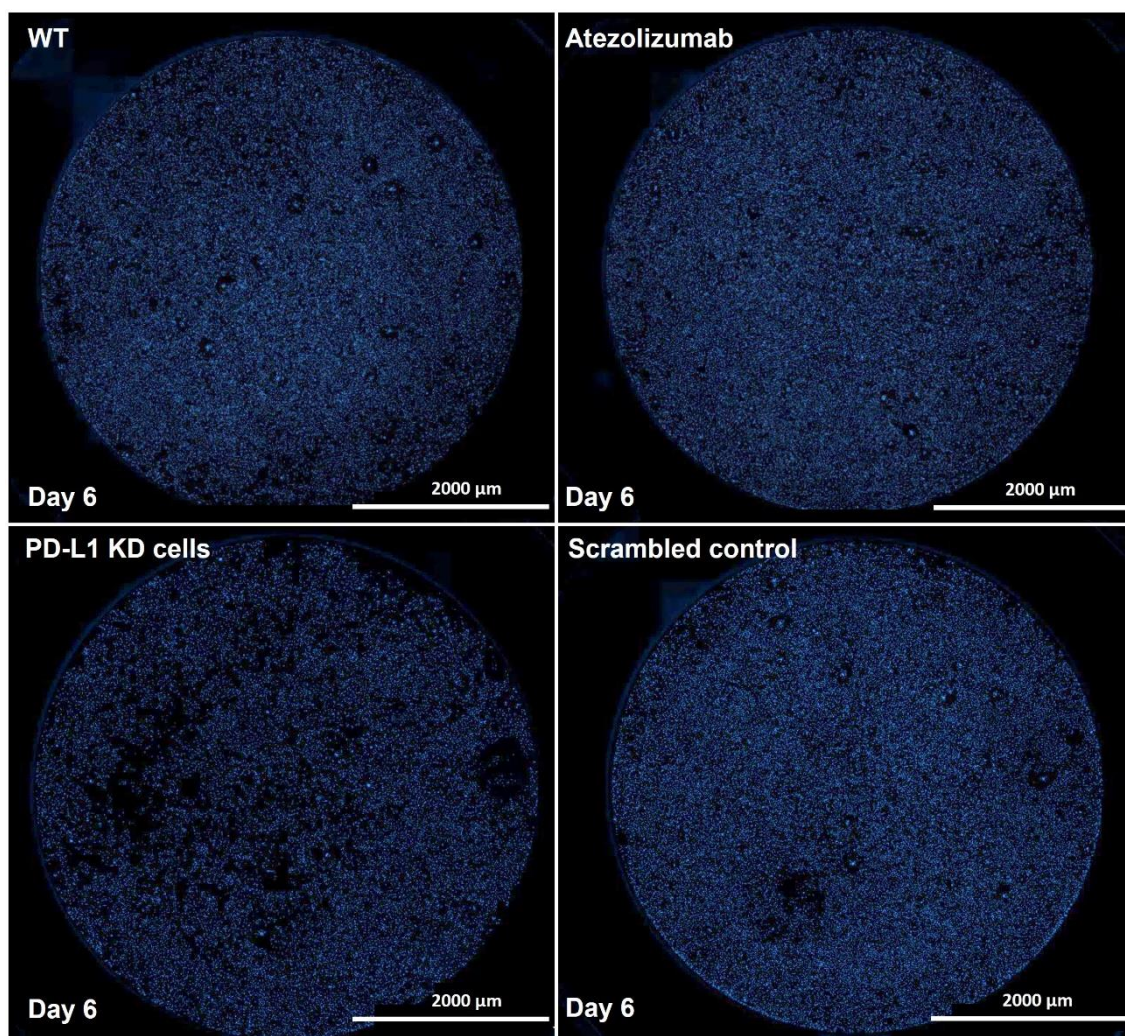
Figure 5.18 PD-L1 knockdown cells cultured in monolayer appear less confluent than WT, Atezolizumab-treated WT and scrambled control cells after 6 days of culture. Low magnification images were captured of MDA-MB-231 WT, Atezolizumab-treated WT, scrambled control and PD-L1 knockdown cells using the 4X objective lens after being cultured for 6 days and subsequently stained with Hoechst 33342/PI. Scale bar represents 2000 µm. Images represent n=3 independent experiments each with 3 technical repeats.
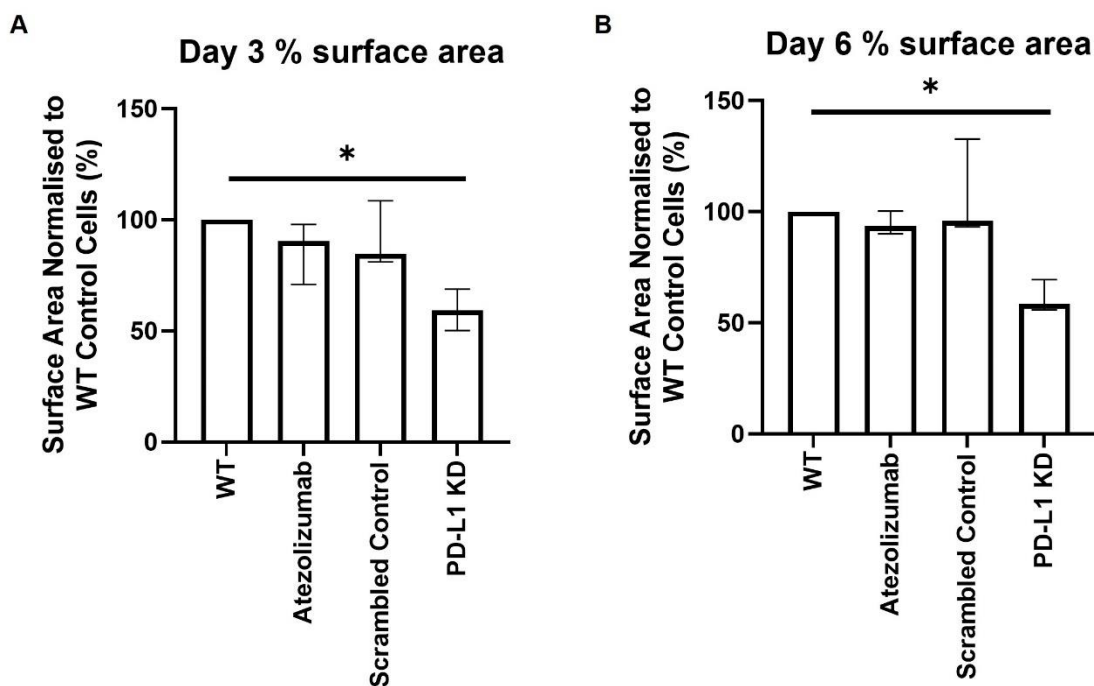
Figure 5.19 PD-L1 knockdown cells cover a smaller percentage surface area of the well in a 96-well plate after 3 and 6 days of culture compared to WT, Atezolizumab-treated WT, and scrambled control cells. The percentage surface area of the wells covered with WT, Atezolizumab-treated WT, scrambled control and PD-L1 knockdown cells that were stained with Hoechst 33342/PI was determined at **(A)** day 3 and **(B)** day 6 of culture. Data is presented as median ± range. n=3 independent experiments each with 3 technical repeats. Data was analysed by a Kruskal-Wallis followed by Dunn's multiple comparisons test (*P<0.05).
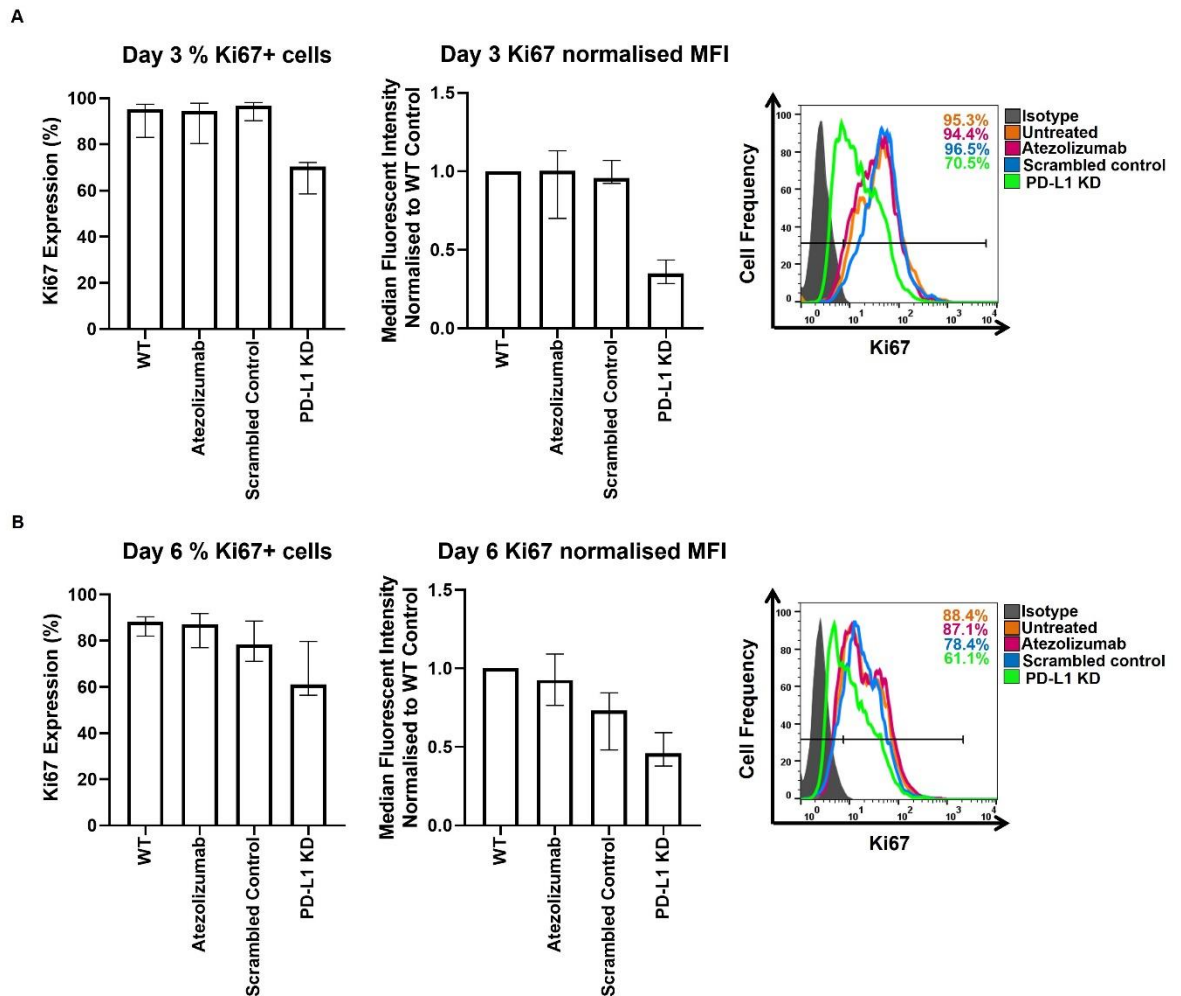
Figure 5.20 PD-L1 knockdown cells display a lower MFI for Ki67 expression compared to WT, Atezolizumab-treated WT, and scrambled control cells at day 3 and 6 of culture. Flow cytometry was used to measure the expression of Ki67 protein by WT, Atezolizumab-treated WT, scrambled control and PD-L1 knockdown cells after **(A)** 3 and **(B)** 6 days of culture. A representative flow cytometry histogram is displayed to illustrate the isotype control (grey) relative to the Ki67 positive population for WT (orange), Atezolizumab-treated (pink), scrambled control (blue) and knockdown cells (green) at each time point. The percentage of cells expressing Ki67 protein is displayed (left) alongside the MFI (right). The MFI was normalised to the MFI of WT cells (control). Data is presented as median ± range. n=3 independent experiments each with 3 technical repeats. Data was analysed by a Kruskal-Wallis followed by a Dunn's multiple comparisons test.

5.3.7 PD-L1 knockdown affects the viability of MDA-MB-231 breast cancer cells in 2D cell culture

It was next determined whether PD-L1 knockdown effected the viability of MDA-MB-231 cells similar to, or more so, than 3 or 6 days of Atezolizumab treatment. The expression of PD-L1 detected by WT, Atezolizumab-treated WT, scrambled control and PD-L1 knockdown cells was investigated simultaneously to cell viability (Appendix Figure 9.16). MDA-MB-231 cells with PD-L1 knocked down displayed significantly more cell death than cells treated with Atezolizumab for 3 days (p=0.007) (Figure 5.21A-C). Importantly, the amount of cell death observed in PD-L1 knockdown cells was significantly higher than the amount of cell death found in WT (p=0.0056) and scrambled control (p=0.036) cells. A similar trend of PD-L1 knockdown cells to exhibit more cell death compared to WT, Atezolizumab-treated WT and scrambled control cells was shown after 6 days of culture (Figure 5.22A-C). As previously shown in Chapter 4 Figure 4.10, after 6 days of Atezolizumab treatment, MDA-MB-231 cells exhibited more cell death than untreated WT cells, but this was not significant.

5.3.8 PD-L1 knockdown affects the cellular activity of MDA-MB-231 breast cancer cells in 2D cell culture

To further investigate the effects of PD-L1 knockdown versus PD-L1 blockade with Atezolizumab on MDA-MB-231 cell viability, ATP levels and NAD(P)H-dependent oxidoreductase enzymes were measured independently as an indicator of cellular metabolic activity, hence cell viability in WT, Atezolizumab-treated WT, scrambled control and PD-L1 knockdown cells cultured for 3 and 6 days. PD-L1 knockdown cells displayed significantly reduced ATP levels compared to WT and Atezolizumab-treated WT cells after 3 (Figure 5.23A) and 6 (Figure 5.23B) of culture. Although the difference in ATP levels between scrambled control and PD-L1 knockdown cells were found not to be statistically significant after 3 and 6 days of culture, PD-L1 knockdown cells cultured for 6 days exhibited substantially lower median ATP levels corresponding to the RLU of 2.85×10^6 (± 0.83) compared to scrambled control cells (4.8×10^6 RLU ± 2.1). Furthermore, whilst PD-L1 knockdown cells displayed similar levels of NAD(P)H-dependent oxidoreductase enzyme activity detected by the MTT assay at day 3 (Figure 5.23C) of culture compared to WT, Atezolizumab-treated WT and scrambled control cells, after 6 days, PD-L1 knockdown cells displayed reduced enzyme activity in comparison to the other cells (Figure 5.23D). However, this

reduction was only found to be significant for PD-L1 knockdown versus WT cells (p=0.0175).
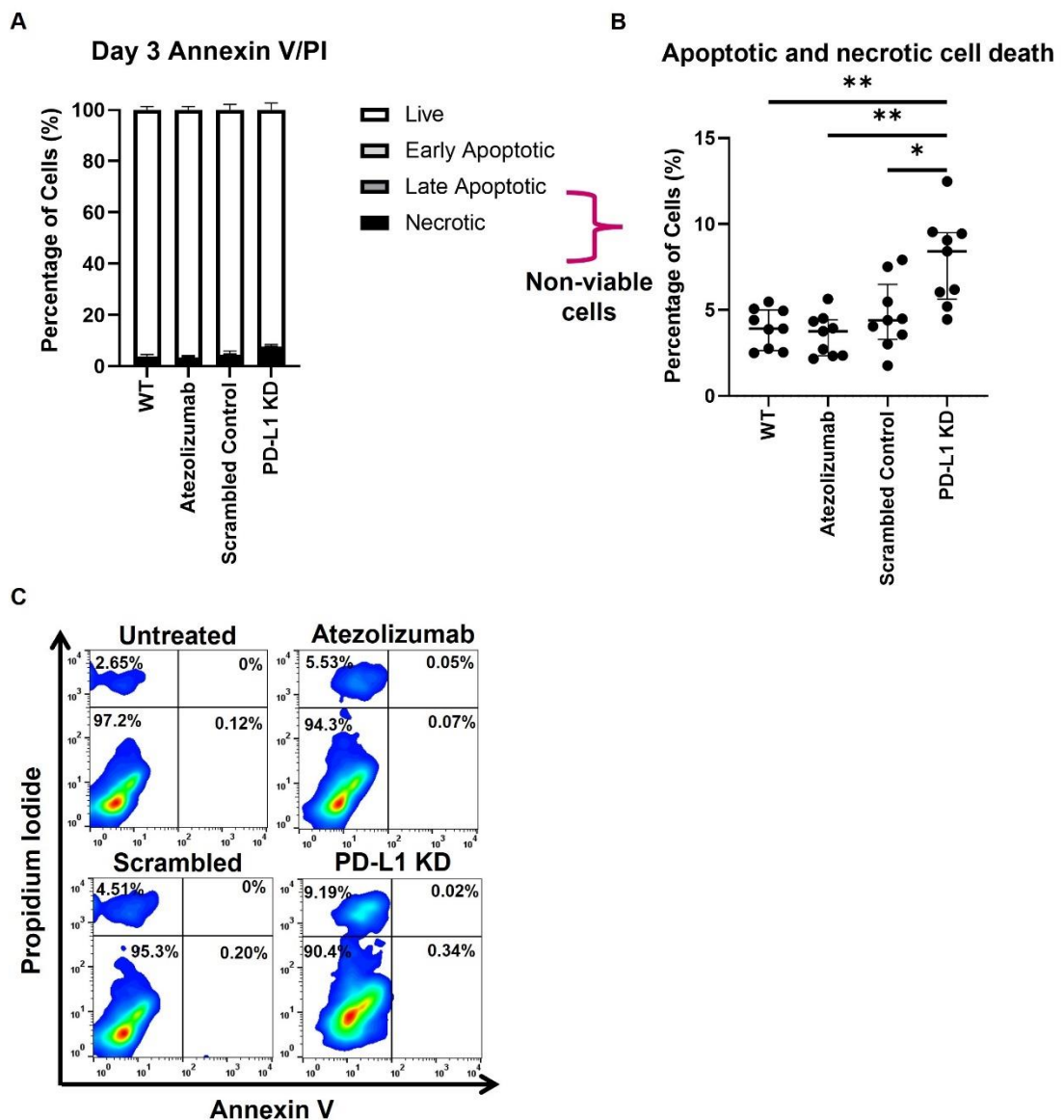
Figure 5.21 PD-L1 knockdown cells display significantly more cell death after 3 days of culture compared to WT, Atezolizumab-treated WT and scrambled control cells. (A) Annexin V/PI staining was used to assess cell viability in MDA-MB-231 WT, Atezolizumab-treated WT, scrambled control and PD-L1 knockdown cells after 3 days of culture. **(B)** The percentage of non-viable cells (AV+/PI-, AV+/PI+, AV-/PI+) is shown separately to demonstrate the statistical significance amongst the different experimental conditions. **(C)** Representative flow cytometry plots show the effects of Atezolizumab and PD-L1 knockdown on cell viability. Data is presented as median ± range. n=3 independent experiments each with 3 technical repeats. Data was analysed by a Kruskal-Wallis followed by Dunn's multiple comparisons test (*P<0.05 and **P<0.01).
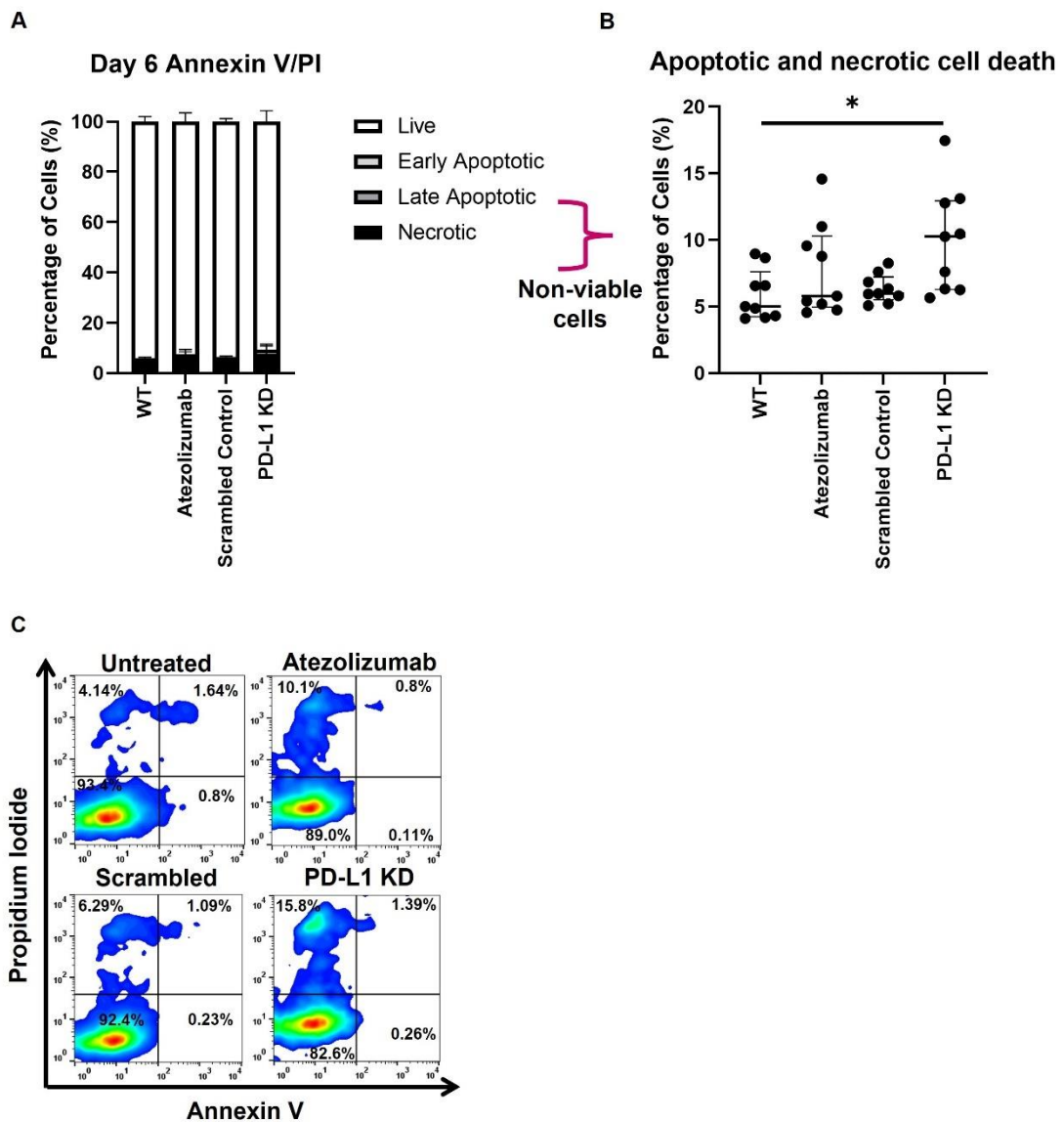
Figure 5.22 PD-L1 knockdown cells display significantly more cell death than WT cells after 6 days of culture. (A) Annexin V/PI staining was used to assess cell viability in MDA-MB-231 WT, Atezolizumab-treated WT, scrambled control and PD-L1 knockdown cells after 6 days of culture. **(B)** The percentage of non-viable cells (AV+/PI-, AV+/PI+, AV-/PI+) is shown separately to demonstrate the difference in the median percentage of non-viable cells amongst the different experimental conditions. **(C)** Representative flow cytometry plots show the effects of Atezolizumab and PD-L1 knockdown on cell viability. Data is presented as median ± range. n=3 independent experiments each with 3 technical repeats. Data was analysed by a Kruskal-Wallis followed by Dunn's multiple comparisons test (*$P<0.05$).
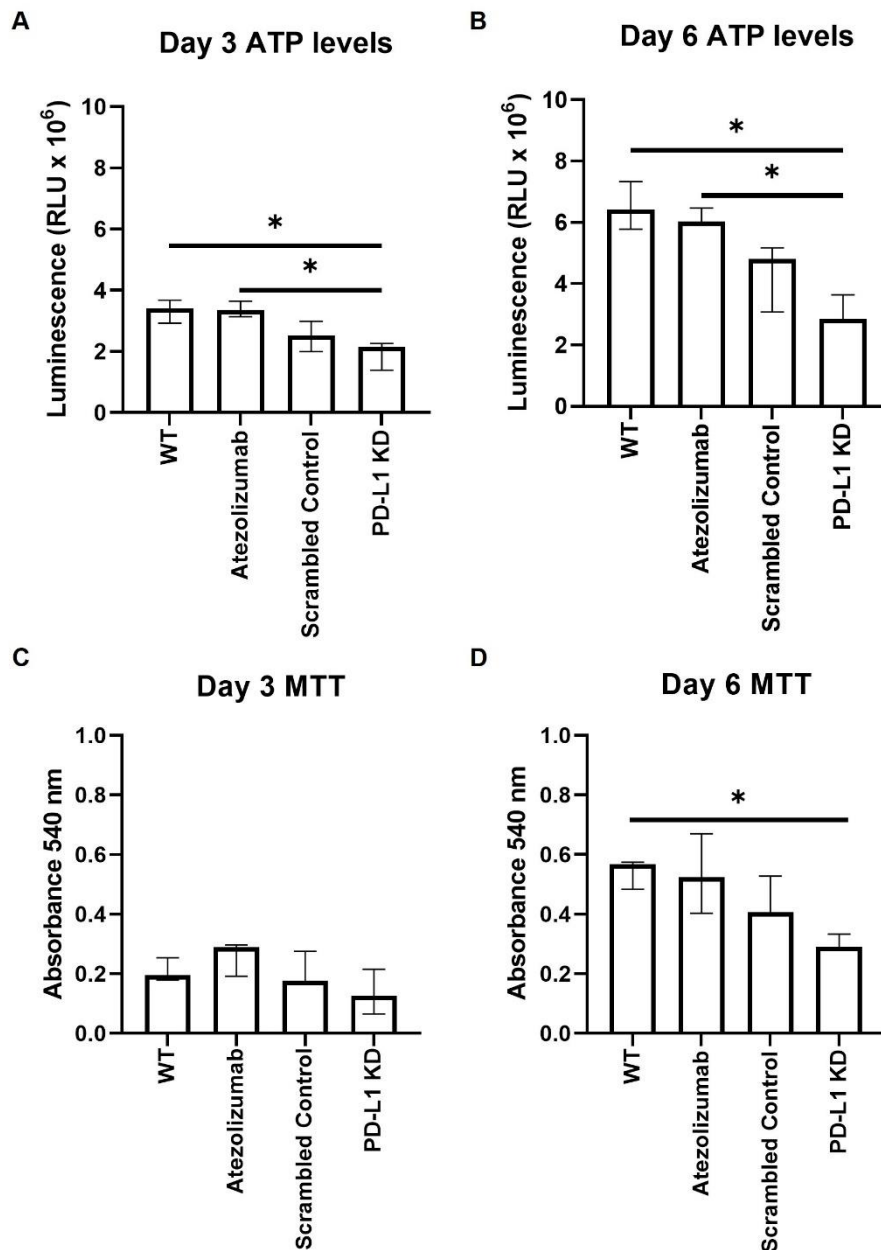
Figure 5.23 PD-L1 knockdown cells display significantly reduced cellular metabolic activity after 3 and 6 days of culture compared to Atezolizumab-treated WT cells. The cellular activity of MDA-MB-231 WT, Atezolizumab-treated WT, scrambled control and PD-L1 knockdown cells was assessed by measuring ATP levels after **(A)** 3 and **(B)** 6 days of culture. MTT assays were also used to measure cellular activity in these cells after **(C)** 3 and **(D)** 6 days of culture. Data is presented as median ± range. n=3 independent experiments each with 6 technical repeats. Data was analysed by a Kruskal-Wallis followed by Dunn's multiple comparisons test (*$P<0.05$).

5.3.9 PD-L1 knockdown affects the growth of MDA-MB-231 breast cancer cells cultured in 3D hanging drop spheroids

Since PD-L1 knockdown effected the growth and proliferation of MDA-MB-231 cells cultured in monolayer, it was next determined whether PD-L1 knockdown impacted the growth, proliferation and spheroid forming capabilities of MDA-MB-231 cells cultured in 3D hanging drop spheroids. Firstly, the diameters of 3D spheroids formed of WT, Atezolizumab-treated WT, scrambled control and PD-L1 knockdown cells were measured after 3 (Figure 5.24A) and 6 (Figure 5.24B) days of culture. After 3 days, PD-L1 knockdown 3D spheroids exhibited a smaller diameter of 1188 μm (± 12) compared to WT (1375μm ± 205), Atezolizumab-treated WT (1351μm ± 162), and scrambled control (1260μm ± 37) 3D spheroids. Similarly, after 6 days, WT, Atezolizumab-treated WT and scrambled control 3D spheroids displayed similar diameters of 1345 μm (± 207), 1323 μm (± 157), and 1279 μm (± 1279) respectively, whereas the diameter of PD-L1 knockdown 3D spheroids were over 100 μm smaller at 1165 μm (± 4). However, this data was found not to be statistically significant.

Images of 3D spheroids stained with Hoechst 33342/PI showed that whilst the staining pattern was similar throughout the different 3D spheroids after 3 days of culture, the outer surface topology of PD-L1 knockdown 3D spheroids were found to be smoother and more spherically shaped than WT, Atezolizumab-treated WT and scrambled control 3D spheroids (Figure 5.25). This difference observed in outer surface topology was also observed after 6 days of culture in PD-L1 knockdown 3D spheroids (Figure 5.26). Additionally, after 6 days PD-L1 knockdown 3D spheroids displayed a lower density of cells stained with Hoechst 33342 throughout the 3D spheroid compared to WT, Atezolizumab-treated WT and scrambled control 3D spheroids which displayed a higher density of cells stained with Hoechst 33342 predominantly in the outermost layers of the spheroids. Appendix Figure 9.17 illustrates further the difference in the density of cells in PD-L1 knockdown versus scrambled control 3D spheroids.

Ki67 expression analysis showed that PD-L1 knockdown 3D spheroids expressed comparable levels of Ki67 protein to WT, Atezolizumab-treated WT and scrambled control 3D spheroids after 3 days of culture (Figure 5.27A). Similarly at day 6, no statistically significant difference in Ki67 expression was observed between any of the 3D spheroids (Figure 5.27B).
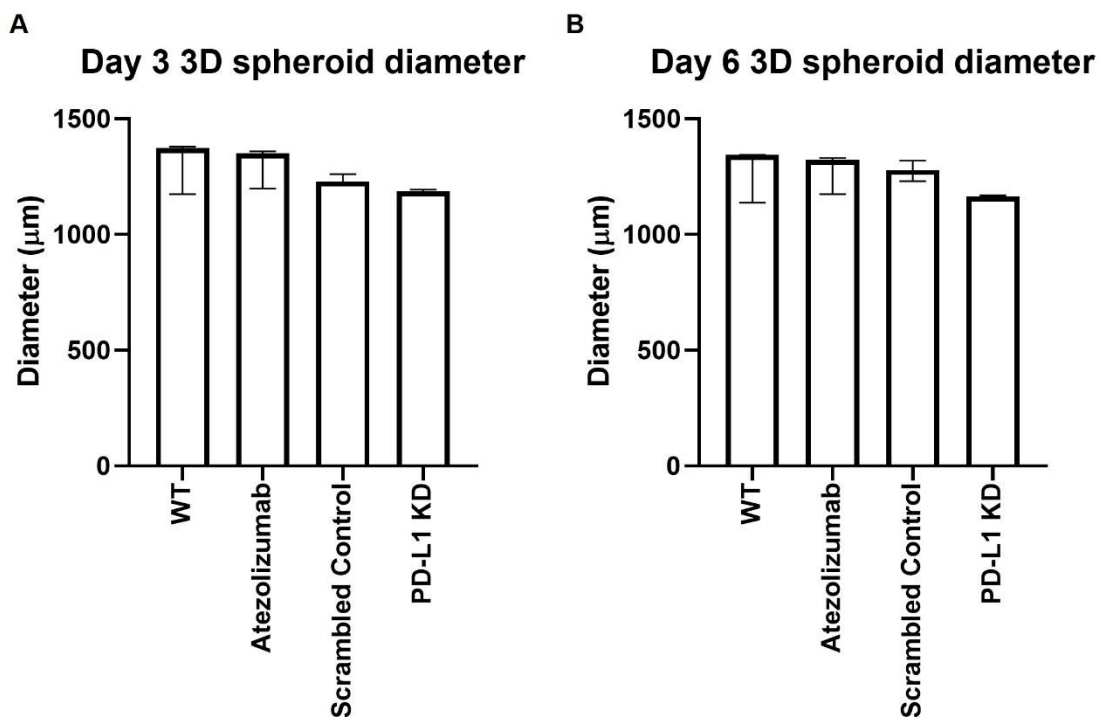
Figure 5.24 PD-L1 knockdown 3D spheroids exhibited the smallest diameter after 3 and 6 days of culture. The diameters of WT, Atezolizumab-treated WT, scrambled control and PD-L1 knockdown 3D spheroids were measured after being cultured for **(A)** 3 and **(B)** 6 days. Data is presented as median ± range. n=3 independent experiments each with 3 technical repeats. Data was analysed by a Kruskal-Wallis followed by a Dunn's multiple comparisons test.
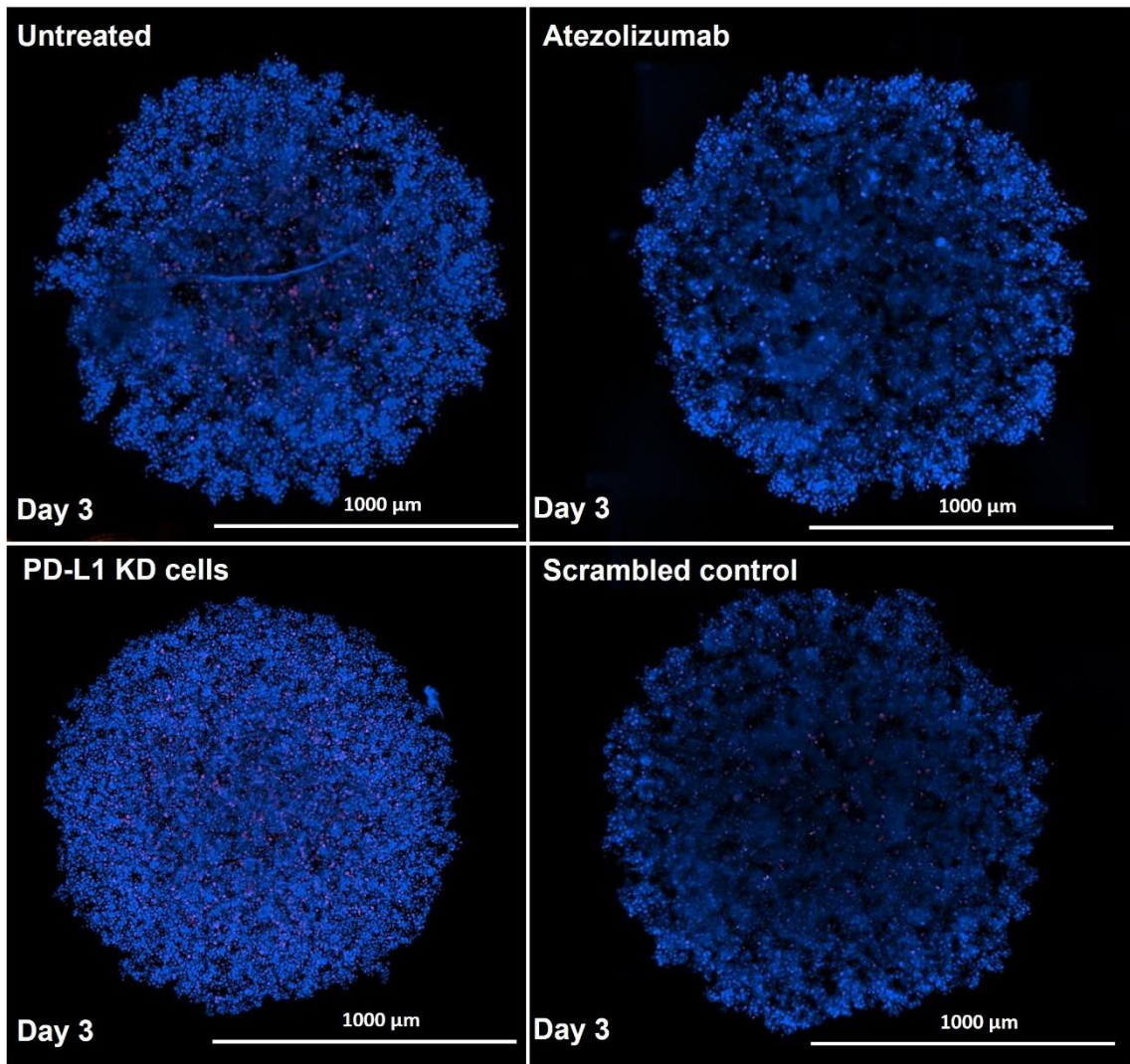
Figure 5.25 PD-L1 knockdown 3D spheroids exhibit a smoother and more spherical outer surface topology after 3 days of culture. Z-stack images were captured of MDA-MB-231 WT, Atezolizumab-treated WT, scrambled control and PD-L1 knockdown cells following culture in 3D spheroids for 3 days and labelling with Hoechst 33342/PI. Scale bar represents 1000 μm. Images represent n=3 independent experiments each with 3 technical repeats.
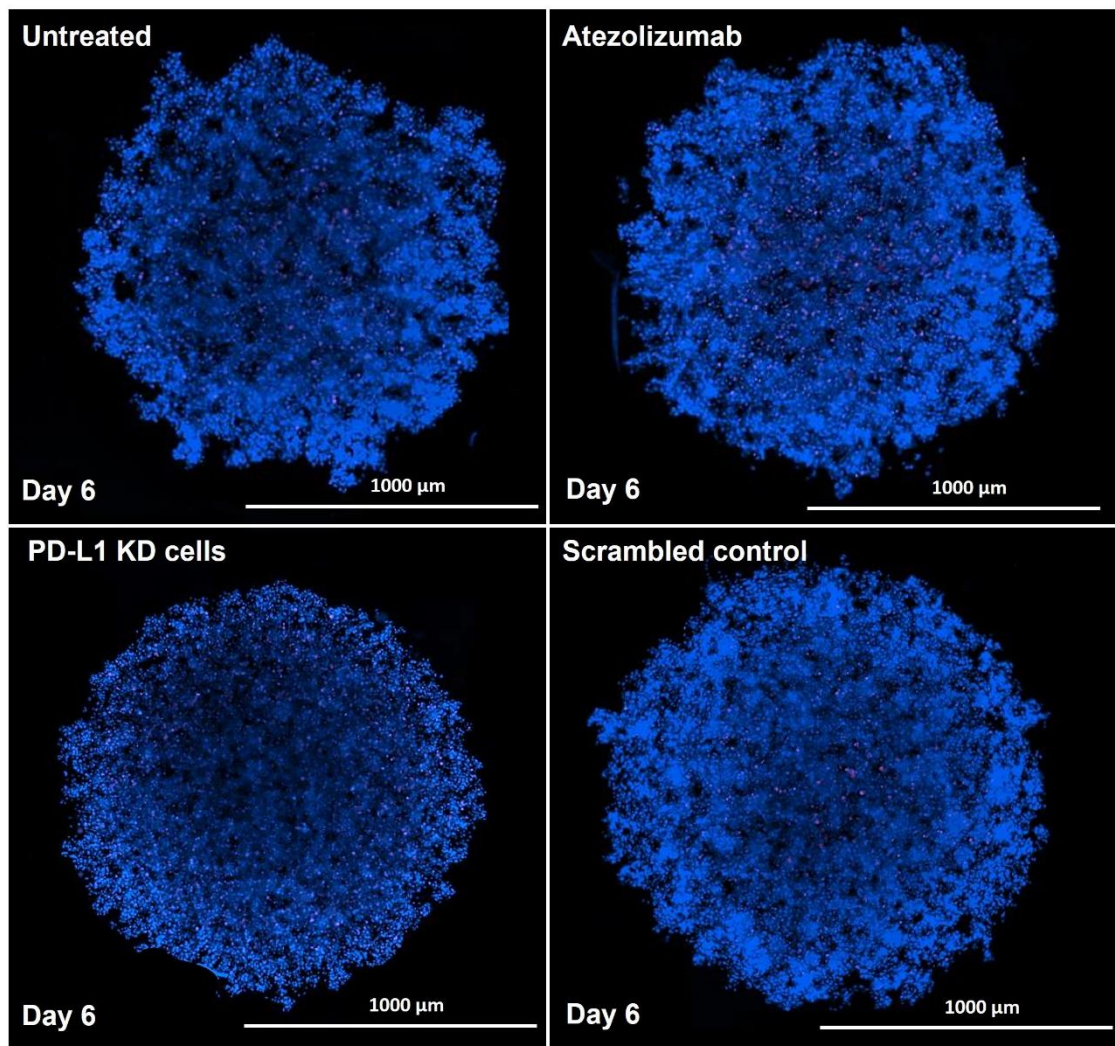
Figure 5.26 PD-L1 knockdown 3D spheroids visually display a smoother outer surface topology and lower density of Hoechst 33342 positive cells in the outer region of the spheroid after 6 days of culture. Z-stack images were captured of MDA-MB-231 WT, Atezolizumab-treated, scrambled control and PD-L1 knockdown cells following culture in 3D spheroids for 6 days and labelling with Hoechst 33342/PI. Scale bar represents 1000 µm. Images represent n=3 independent experiments each with 3 technical repeats.
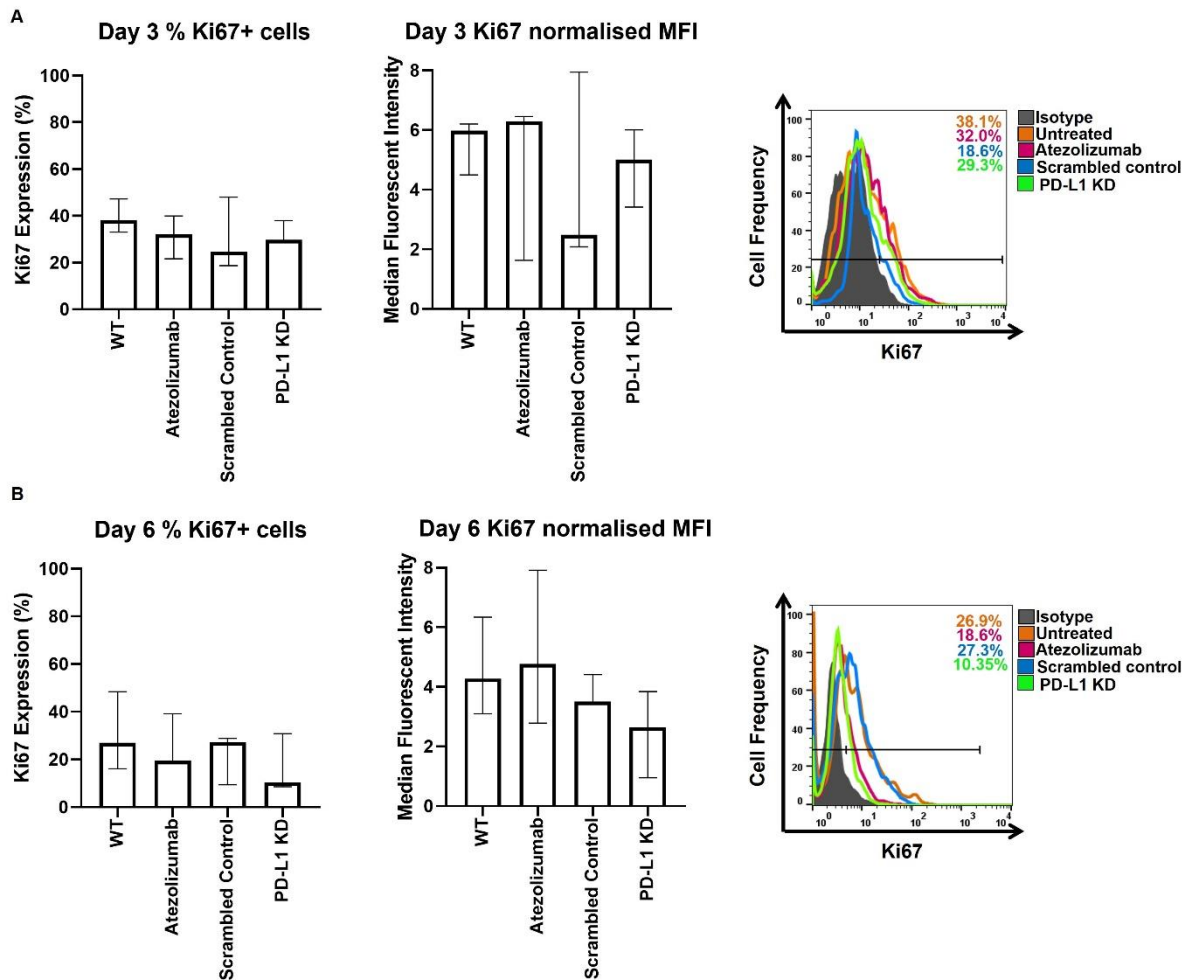
Figure 5.27 Ki67 expression is not significantly altered in PD-L1 knockdown cells cultured for 3 or 6 days in 3D spheroids compared to WT, Atezolizumab-treated WT, and scrambled control cells. Flow cytometry was used to measure the expression of Ki67 protein by WT, Atezolizumab-treated WT, scrambled control and PD-L1 knockdown 3D spheroids after **(A)** 3 and **(B)** 6 days of culture. The percentage of cells expressing Ki67 protein is displayed (left) alongside the MFI (right). The representative flow cytometry histograms illustrate the isotype control (grey) relative to the Ki67 positive population for WT (orange), Atezolizumab-treated WT (pink), scrambled control (blue) and knockdown cells (green) at each time point. Data is presented as median ± range. n=3 independent experiments each with 3 technical repeats. Data was analysed by a Kruskal-Wallis followed by a Dunn's multiple comparisons test.

5.3.10 PD-L1 knockdown affects the viability of MDA-MB-231 breast cancer cells cultured in 3D hanging drop spheroids

Prior to assessing the effects of PD-L1 knockdown on the viability of 3D hanging drop spheroids, PD-L1 expression by WT, Atezolizumab-treated WT, scrambled control and PD-L1 knockdown 3D spheroids was measured to verify PD-L1 blockade by Atezolizumab and PD-L1 knockdown (Appendix Figure 9.16). PD-L1 knockdown 3D spheroids showed a reduction in the percentage of cells expressing PD-L1, similar to the percentage of cells detected positive for PD-L1 in Atezolizumab-treated 3D spheroids. This was not observed in PD-L1 knockdown cells cultured in 2D monolayer to the same extent.

After 3 days, PD-L1 knockdown 3D spheroids displayed significantly more cell death compared to WT (0.0248) and scrambled control (p<0.0012) 3D spheroids (Figure 5.28A-C). Whilst there was no significant difference in cell death found between Atezolizumab-treated WT and PD-L1 knockdown 3D spheroids, it is important to note that there was a great deal of variability between independent experiments. The median percentage of apoptotic and necrotic cells in PD-L1 knockdown spheroids was shown to be 62.5% (± 48.44), which was over 10% higher than cell death induced by 3 days of Atezolizumab treatment in 3D spheroids (50.34% ± 34.5), but due to the variability was still not statistically significant. Similarly, after 6 days of culture, PD-L1 knockdown 3D spheroids displayed more cell death compared to WT, Atezolizumab-treated WT and scrambled control 3D spheroids (Figure 5.29A). However, the amount of cell death induced by knocking down PD-L1 was only statistically significant in comparison to cell death displayed in WT 3D spheroids (p=0.0094) (Figure 5.29B). The median percentage of cell death induced by PD-L1 knockdown in 3D spheroids was 84.8% (± 53.28), compared to 48.28% (± 37.3), 58.5% (± 43.55) and 61.2% (± 55.5) in WT, Atezolizumab-treated WT and scrambled control 3D spheroids after 6 days, respectively. Additionally, after 6 days most cell death amongst WT, Atezolizumab-treated WT, scrambled control and PD-L1 knockdown 3D spheroids was apoptotic (Figure 5.29C). Analysis of the percentage of cells in early and late apoptosis demonstrated that apoptotic cell death in PD-L1 knockdown 3D spheroids was significantly higher in comparison to WT (p=0.0064) and scrambled control (p=0.0336) 3D spheroids (Figure 5.29D). This was also the case for 3D spheroids treated with Atezolizumab for 6 days (P=0.0554). The median percentage of apoptotic cells was higher in Atezolizumab-treated 3D spheroids (43.6% ± 37.29) compared to that of 29.4% (± 27.8) in WT 3D spheroids.
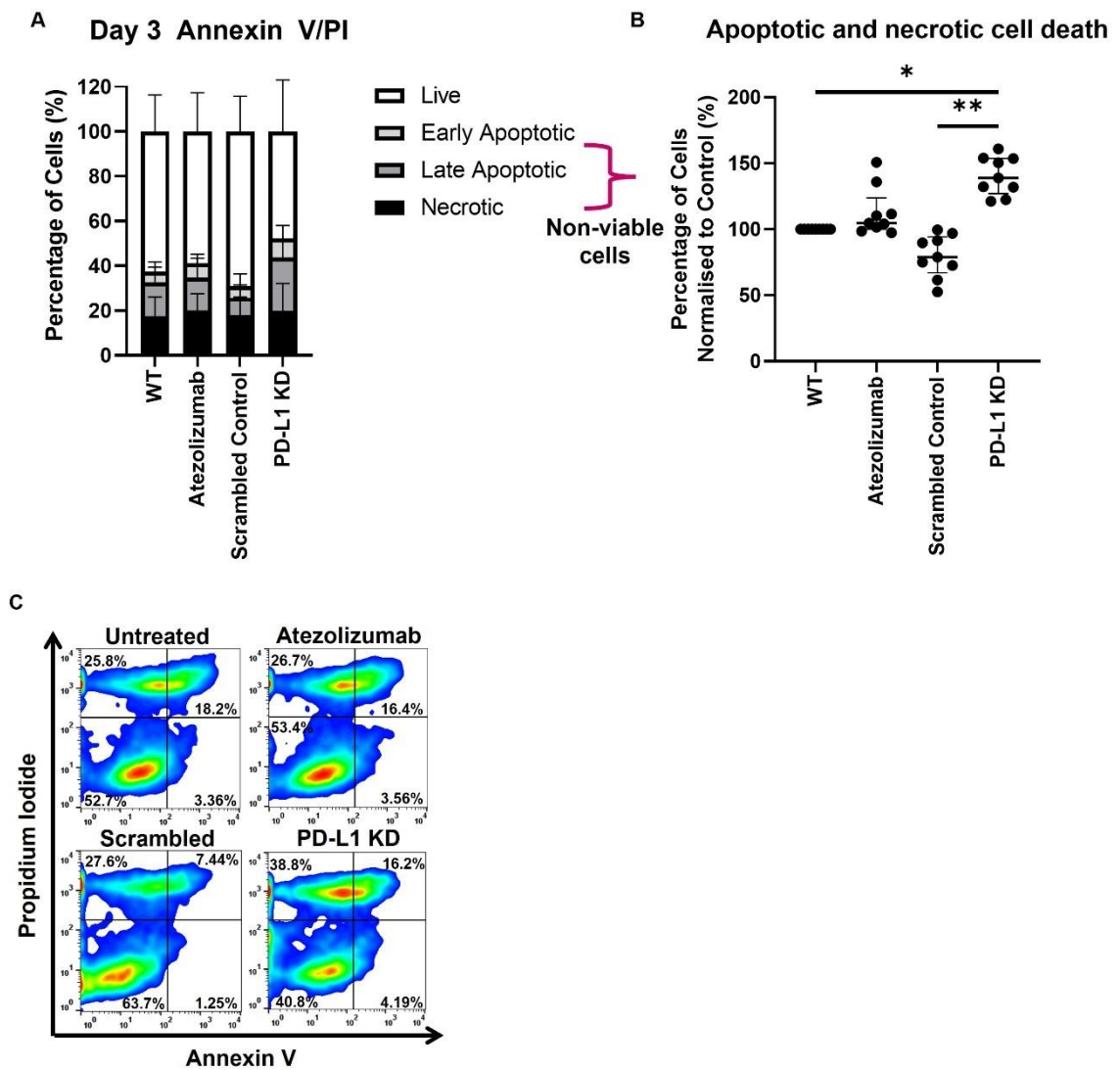
Figure 5.28 PD-L1 knockdown 3D spheroids display significantly more cell death compared to WT and scrambled control 3D spheroids at day 3 of culture. **(A)** Annexin V/PI staining was used to assess cell viability in MDA-MB-231 WT, Atezolizumab-treated WT, scrambled control and PD-L1 knockdown 3D spheroids after 3 days of culture. **(B)** The percentage of non-viable cells (AV+/PI, AV+/PI+, AV-/PI+) is shown separately to show the significant difference between PD-L1 knockdown 3D spheroid viability compared WT and scrambled control 3D spheroids. **(C)** Representative flow cytometry plots show the effect of PD-L1 knockdown on 3D spheroid viability. Data is presented as median ± range. n=3 independent experiments each with 3 technical repeats. Data was analysed by a Kruskal-Wallis followed by Dunn's multiple comparisons test (*P<0.05 and **P<0.01).

A Day 6 Annexin V/PI

B Apoptotic and necrotic cell death

C

D Eary and late apoptotic cell death
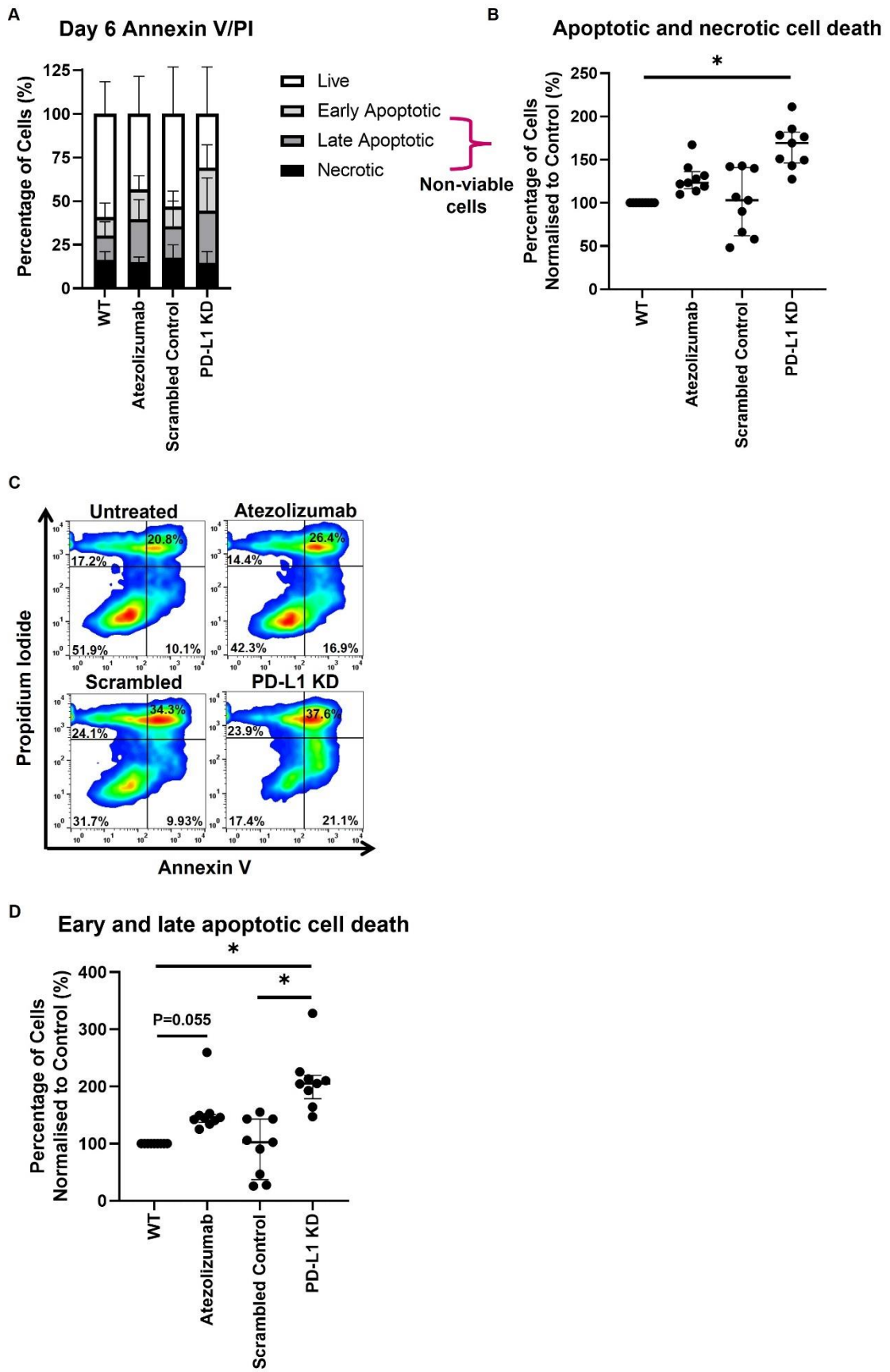
Figure 5.29 Atezolizumab-treated WT and PD-L1 knockdown 3D spheroids display significantly more cell death compared to WT and scrambled control 3D spheroids at day 6 of culture. (A) Annexin V/PI staining was used to assess cell viability in MDA-MB-231 WT, Atezolizumab-treated WT, scrambled control and PD-L1 knockdown 3D spheroids after 6 days of culture. **(B)** The percentage of non-viable cells (AV+/PI-, AV+/PI+, AV-/PI+) is shown separately to display the statistical significance between PD-L1 knockdown and WT 3D spheroids. **(C)** Representative flow cytometry plots demonstrate the effects of Atezolizumab and PD-L1 knockdown on cell viability. **(D)** The percentage of early and late apoptotic cells (AV+/PI-, AV+/PI+) is also shown separately to show the significant difference between Atezolizumab and PD-L1 knockdown 3D spheroids compared to WT and scrambled control 3D spheroids. Data is presented as median ± range. n=3 independent experiments each with 3 technical repeats. Data was analysed by a Kruskal-Wallis followed by Dunn's multiple comparisons test (*P<0.05).

5.3.11 PD-L1 knockdown affects the cellular activity of MDA-MB-231 breast cancer cells cultured in 3D hanging drop spheroids

The effect of PD-L1 knockdown on cellular activity by measuring ATP levels was next investigated as another indicator of the viability of MDA-MB-231 PD-L1 knockdown cells cultured in 3D spheroids compared to WT, Atezolizumab-treated WT and scrambled control 3D spheroids. After 3 days of culture, ATP levels were found to be produced at similar levels in WT, Atezolizumab-treated WT, scrambled control and PD-L1 knockdown 3D spheroids (Figure 5.30A). However, after 6 days ATP levels were significantly reduced in Atezolizumab-treated WT ($p=0.034$) and PD-L1 knockdown ($p=0.0004$) 3D spheroids compared to WT and scrambled control ($p=0.0313$). 3D spheroids (Figure 5.30B). Importantly, after 6 days, PD-L1 knockdown 3D spheroids displayed significantly reduced levels of ATP production compared to 3D spheroids treated with Atezolizumab ($p=0.002$).
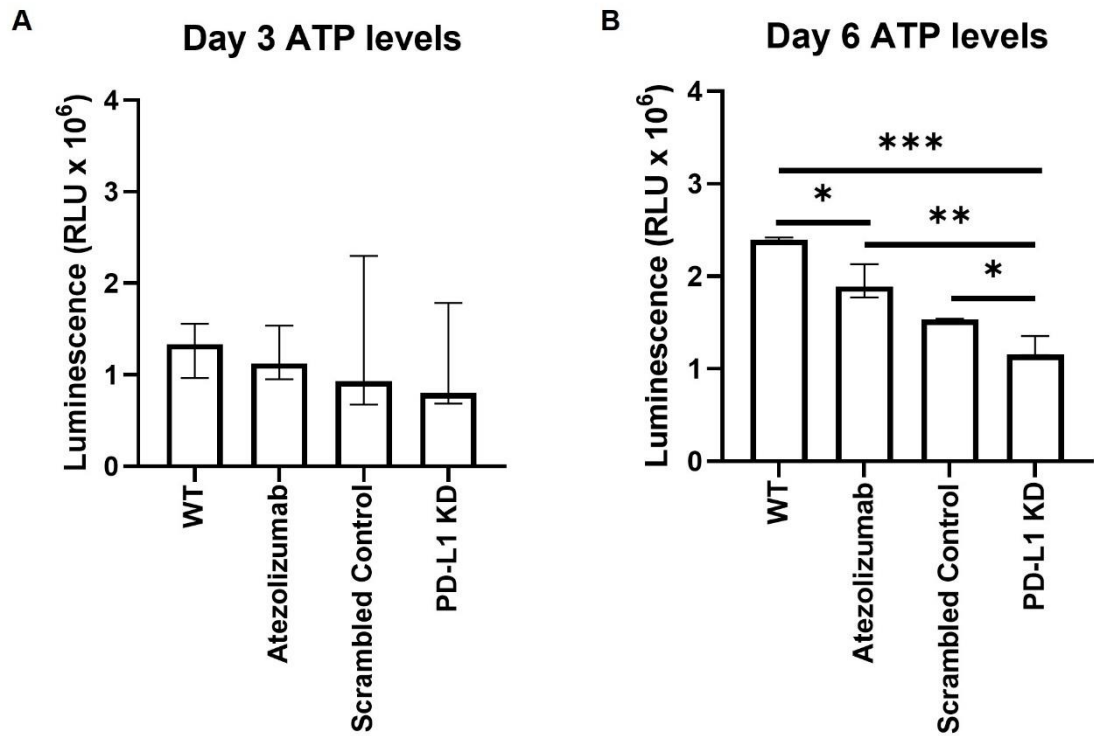
Figure 5.30 PD-L1 knockdown 3D spheroids display significantly reduced levels of ATP after culture for 6 days compared to WT, Atezolizumab-treated WT and scrambled control 3D spheroids. The cellular activity of MDA-MB-231 WT, Atezolizumab-treated WT, scrambled control and PD-L1 knockdown 3D spheroids was assessed by measuring ATP levels at **(A)** day 3 and **(B)** day 6 of culture. Data is presented as median ± range. n=3 independent experiments each with 6 technical repeats. Data was analysed by a Kruskal-Wallis followed by Dunn's multiple comparison test (*P<0.05, **P<0.01 and ***P<0.001).

5.3.12 PD-L1 knockdown effects the growth and proliferation of MDA-MB-231 breast cancer 3D spheroid colonies grown in alginate hydrogel beads

It was next determined whether PD-L1 knockdown affects the growth and proliferation of MDA-MB-231 3D alginate spheroid colonies compared to WT, Atezolizumab-treated WT and scrambled control 3D alginate spheroid colonies. Firstly, the diameters of WT, Atezolizumab-treated WT, scrambled control and PD-L1 knockdown 3D alginate spheroid colonies were measured after 3, 6 and 10 days of culture (Figure 5.31A-C). After day 6 (Figure 5.31B) and 10 (Figure 5.31C) of culture, the diameter of PD-L1 knockdown 3D alginate spheroid colonies were significantly smaller than the diameter of WT, Atezolizumab-treated WT and scrambled control 3D alginate spheroid colonies.

Images captured of whole alginate beads stained with Hoechst 33342/PI demonstrated the differences in the growth of spheroid colonies over the time course of 10 days for WT, Atezolizumab-treated WT, scrambled control and PD-L1 knockdown cells. After 3 days of culture, all cells remained single cells or began to form cell clusters (Figure 5.32). However, after 6 (Figure 5.33) and 10 (Figure 5.34) days the growth of PD-L1 knockdown 3D alginate spheroid colonies were visually different to that of WT, Atezolizumab-treated WT and scrambled control 3D spheroid colonies. PD-L1 knockdown cells were unable to form colonies and remained single cells or formed cell clusters within the alginate (Appendix Figure 9.18). In contrast, WT, Atezolizumab-treated WT and scrambled control cells formed 3D spheroid colonies within the alginate after 10 days of culture.

Whilst the Hoechst 33342/PI staining showed that PD-L1 knockdown seemed to prevent MDA-MB-231 cells from proliferating and forming 3D spheroid colonies over 10 days, Ki67 expression data showed that the frequency of Ki67 was only slightly reduced at day 3 of culture in PD-L1 knockdown cells compared to WT, Atezolizumab-treated WT and scrambled control cells cultured in alginate hydrogel beads (Figure 5.35A-C). The percentage of Ki67 positive PD-L1 knockdown cells cultured in alginate for 3 days was 8.09% (± 10.28) compared to 23.53% (± 7.17), 18.93% (± 10.41), 27.03% (± 9.82) in WT, Atezolizumab-treated WT and scrambled control cells, respectively. Interestingly, in all cells cultured in alginate hydrogel beads, the percentage of Ki67 positive cells was reduced over time, but there were no significant differences between spheroid types.
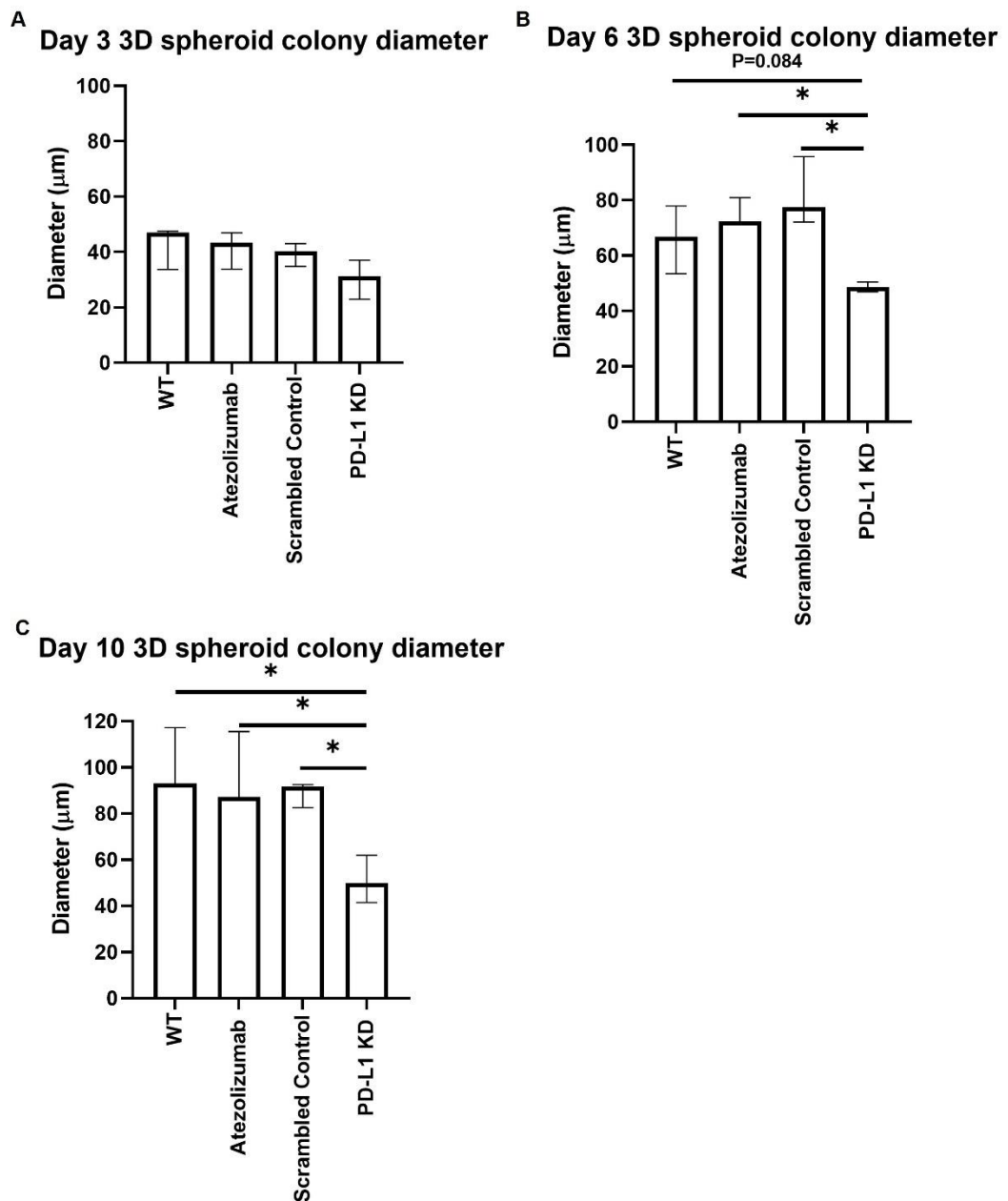
Figure 5.31 PD-L1 knockdown cells exhibit the smallest diameter at day 3, 6 and 10 of culture in alginate. The diameters of WT, Atezolizumab-treated WT, scrambled control and PD-L1 knockdown 3D alginate spheroid colonies were measured at **(A)** day 3, **(B)** day 6 and **(C)** day 10 of culture. Data is presented as median ± range. n=3 independent experiments each with 3 technical repeats. Data was analysed by a Kruskal-Wallis followed by Dunn's multiple comparisons test (*P<0.05).
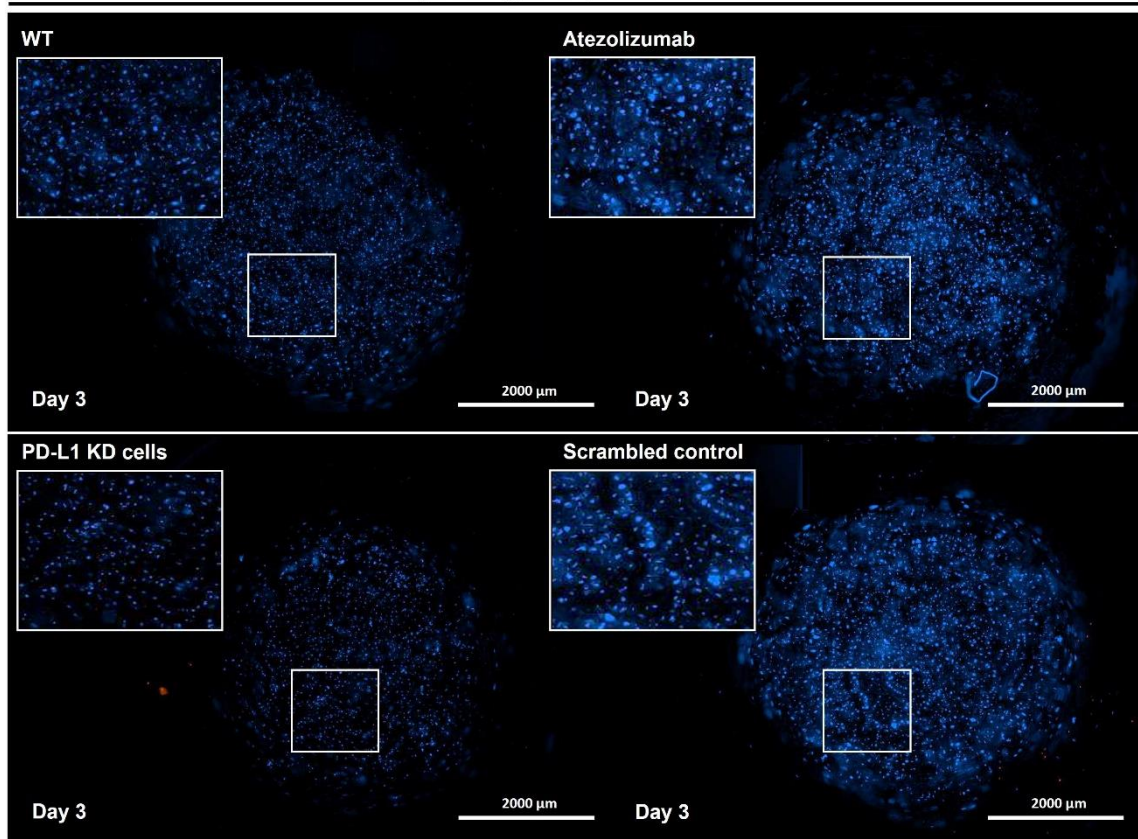
Figure 5.32 WT, Atezolizumab-treated WT, scrambled control and PD-L1 knockdown cells remain single cells or form cell clusters within alginate at day 3 of culture. Images were captured of whole alginate beads stained with Hoechst 33342/PI to show the growth of WT, Atezolizumab-treated WT, scrambled control and PD-L1 knockdown cells within the alginate after 3 days. Scale bar represents 2000 μm. Images represent n=3 independent experiments, each with 3 technical repeats.
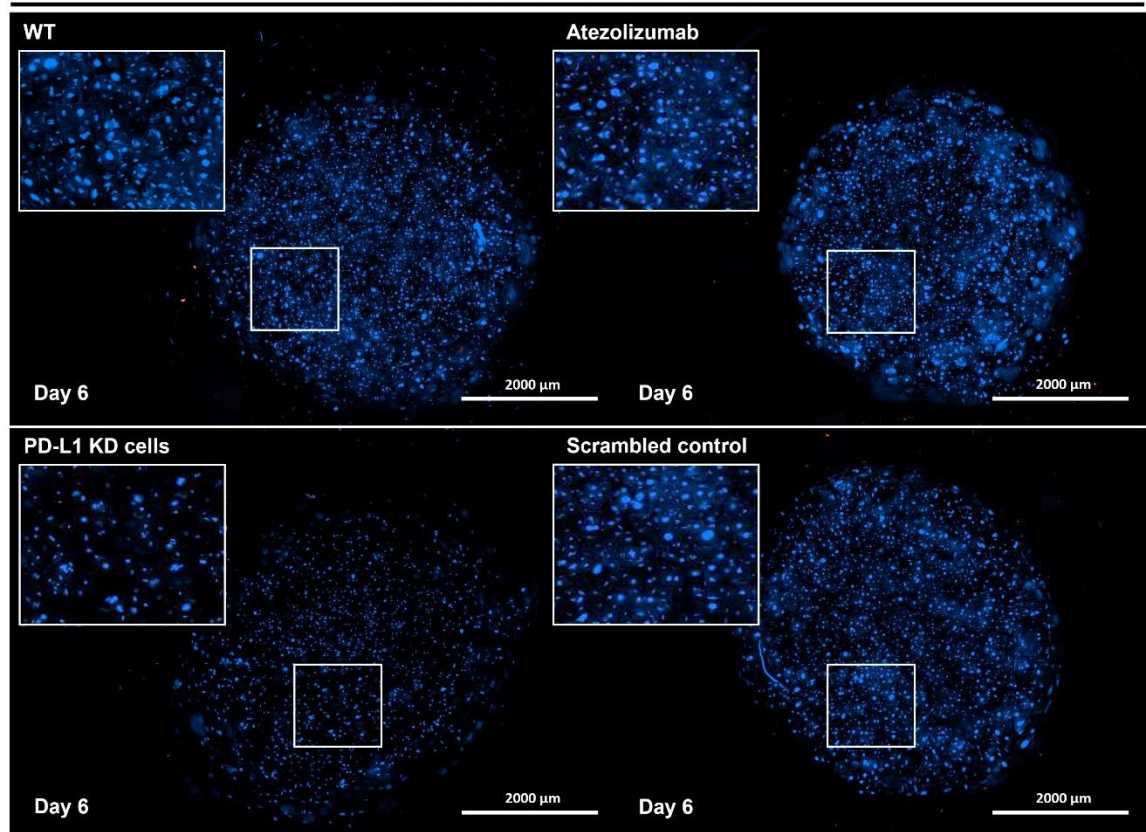
Figure 5.33 Only WT, Atezolizumab-treated WT and scrambled control cells begin to form 3D spheroid colonies within the alginate after 6 days. Images were captured of whole alginate beads stained with Hoechst 33342/PI to show the growth of WT, Atezolizumab-treated WT, scrambled control and PD-L1 knockdown cells within the alginate after 6 days. Scale bar represents 2000 μm. Images represent n=3 independent experiments, each with 3 technical repeats.
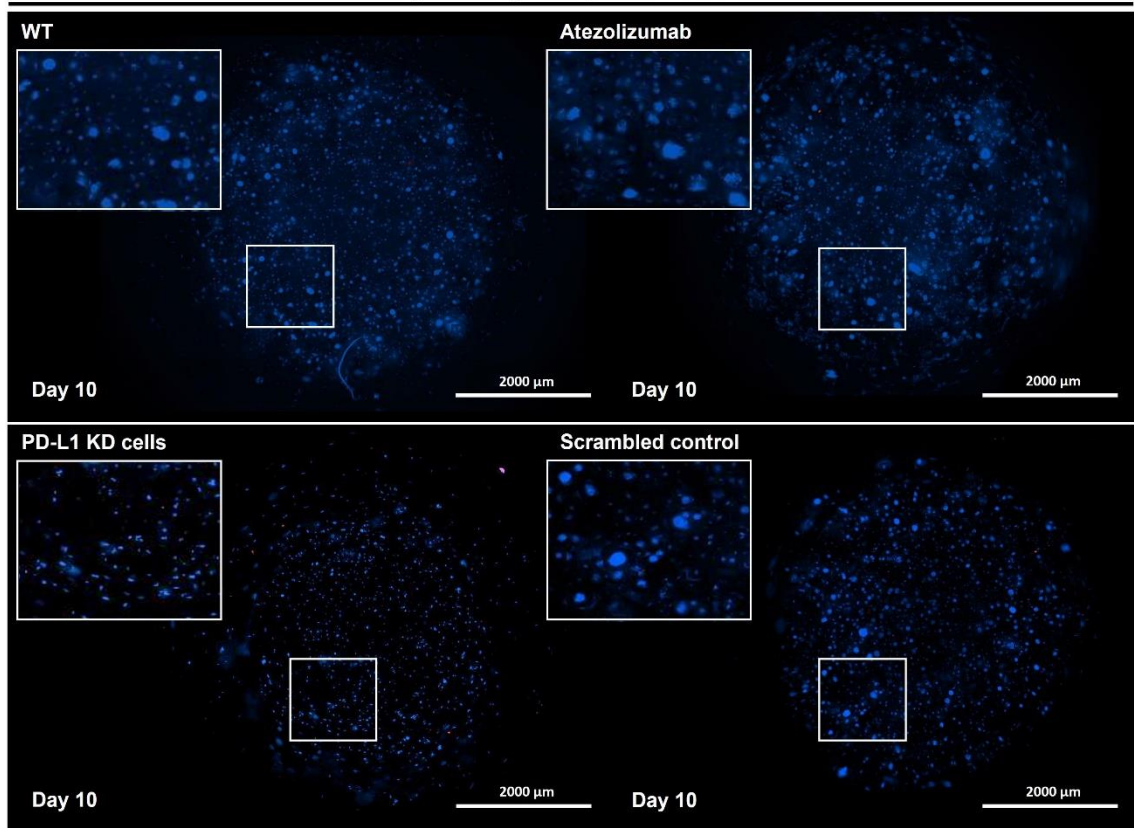
Figure 5.34 PD-L1 knockdown prevents the formation of 3D spheroid colonies forming in alginate over 10 days. Images were captured of whole alginate beads stained with Hoechst 33342/PI to show the differences in growth of WT, Atezolizumab-treated WT, scrambled control and PD-L1 knockdown cells within the alginate after 10 days. Scale bar represents 2000 μm. Images represent n=3 independent experiments each with 3 technical repeats.
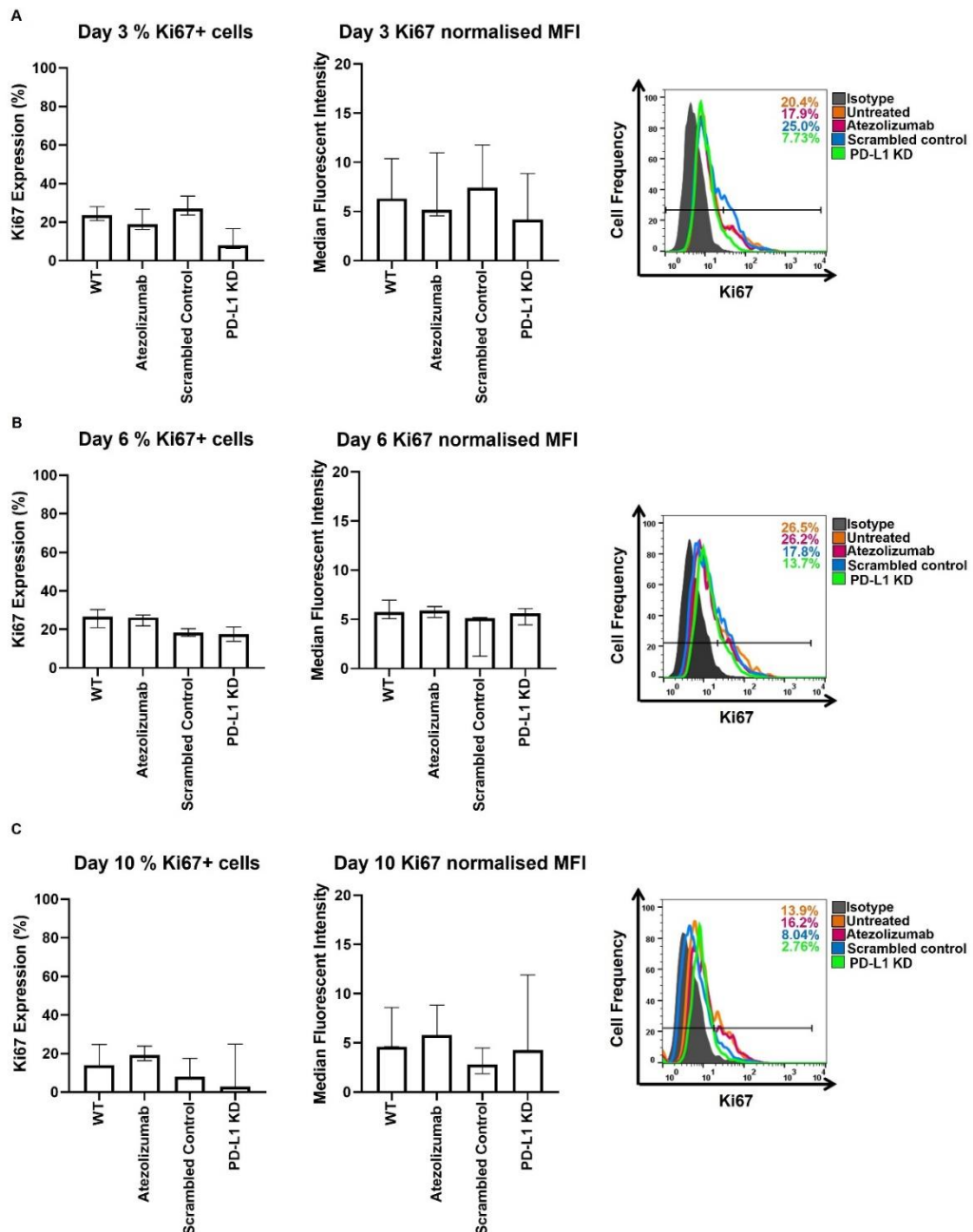
Figure 5.35 PD-L1 knockdown cells display a similar frequency and level of Ki67 expression after 3, 6 and 10 days of culture in alginate. Flow cytometry was used to measure the expression of Ki67 protein by WT, Atezolizumab-treated WT, scrambled control and PD-L1 knockdown cells cultured in alginate for **(A)** 3, **(B)** 6 and **(C)** 10 days. The percentage of cells expressing Ki67 protein is displayed (left) alongside the MFI (right). Representative flow cytometry histograms illustrate the isotype control (grey) relative to the Ki67 positive population for WT (orange), Atezolizumab-treated WT (pink), scrambled control (blue) and PD-L1 knockdown (green) cells at each time point. Data is presented as median ± range. n=3 independent experiments each with 3 technical repeats. Data was analysed by a Kruskal-Wallis and a Dunn's multiple comparisons test.

5.3.13 PD-L1 knockdown affects the viability of MDA-MB-231 breast cancer cells cultured in alginate hydrogel beads

Prior to determining whether PD-L1 knockdown affects the viability of MDA-MB-231 cells cultured in alginate hydrogel beads even more so than Atezolizumab treatment, firstly the expression of PD-L1 was assessed. PD-L1 knockdown cells cultured in 3D alginate spheroid colonies showed the same reduced expression of PD-L1 as observed in PD-L1 knockdown 3D hanging drop spheroids (Appendix Figure 9.16).

After 3 days of culture in alginate hydrogel beads, there was no significant difference in the amount of cell death induced by PD-L1 knockdown and Atezolizumab treatment in MDA-MB-231 cells compared to WT and scrambled control cells (Figure 5.36A and B). In contrast, after day 6 of culture in alginate hydrogel beads, PD-L1 knockdown cells showed slightly more cell death than WT, Atezolizumab-treated WT and scrambled control cells (Figure 5.37A and B). Particularly, PD-L1 knockdown cells exhibited significantly more early apoptotic cell death than WT, Atezolizumab-treated WT and scrambled control cells (Figure 5.37C and D). Importantly, PD-L1 knockdown cells after being cultured for 10 days in alginate exhibited a stronger cell death phenotype than observed after 6 days (Figure 5.38A). PD-L1 knockdown cells in alginate hydrogel beads after 10 days displayed a significantly higher percentage of apoptotic and necrotic cell death than WT, Atezolizumab-treated WT and scrambled control cells (Figure 5.38B and C). Like day 6, the most cell death found by PD-L1 knockdown cells in alginate after 10 days of culture was early apoptotic (Figure 5.38D), which was significantly greater than the percentage of early apoptotic cells found by WT, Atezolizumab-treated WT and scrambled control cells.

5.3.14 PD-L1 knockdown affects the cellular activity of MDA-MB-231 breast cancer cells cultured in alginate hydrogel beads

To further support the cell viability effects of PD-L1 knockdown on MDA-MB-231 cells cultured in alginate hydrogel beads, the levels of ATP produced by the cells were measured and compared to WT, Atezolizumab-treated WT and scrambled control cells cultured in alginate hydrogel beads. PD-L1 knockdown cells cultured for 3 days in alginate displayed similar ATP production to WT, Atezolizumab-treated WT and scrambled control cells (Figure 5.39A). However, after 6 (Figure 5.39B) and 10 (Figure 5.39C) days of culture in alginate, PD-L1 knockdown cells were shown to produce significantly lower levels of ATP compared to WT, Atezolizumab-treated WT and scrambled control cells.
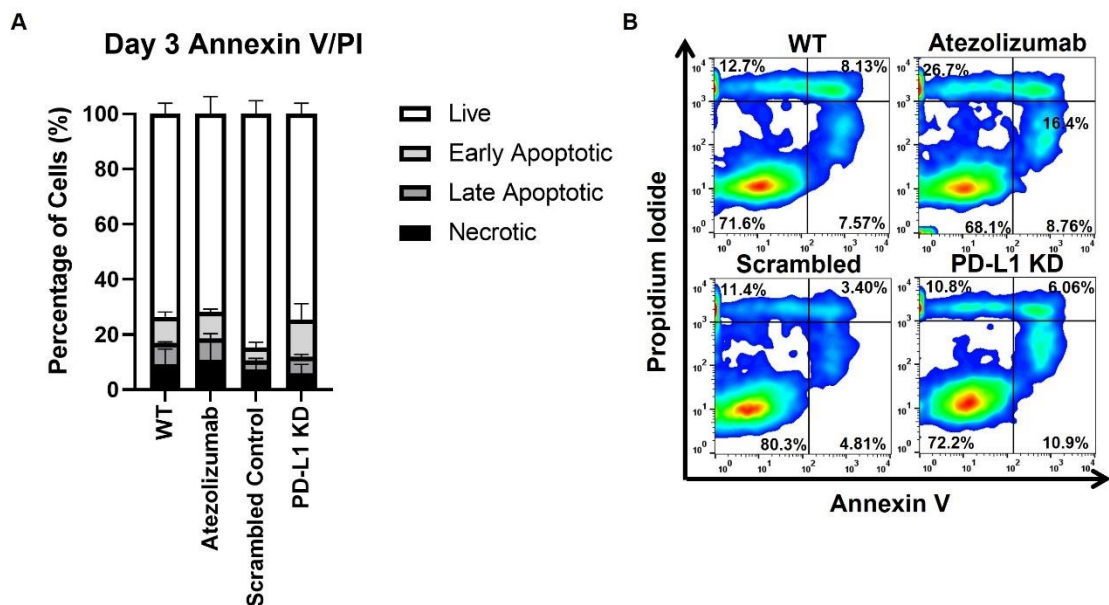
Figure 5.36 After 3 days of culture in alginate, no difference was observed in the amount of cell death amongst all cells. (A) Annexin V/PI staining was used to assess cell viability in MDA-MB-231 WT, Atezolizumab-treated WT, scrambled control and PD-L1 knockdown cells after 3 days of culture in alginate. **(B)** Representative flow cytometry plots demonstrate the minimal effect of Atezolizumab treatment and PD-L1 knockdown on cancer cell viability compared to WT and scrambled control cells cultured in alginate. Data is presented as median ± range. n=3 independent experiments each with 3 technical repeats. Data was analysed by a Kruskal-Wallis followed by a Dunn's multiple comparisons test.

A
Day 6 Annexin V/PI

Legend:
- Live
- Early Apoptotic
- Late Apoptotic
- Necrotic

Non-viable cells

B
Apoptotic and necrotic cell death

C

WT
5.88%   6.48%
80.07%
6.98%

Atezolizumab
5.78%   6.07%
79.1%
9.03%

Scrambled
3.06%   4.41%
85.6%
6.91%

PD-L1 KD
5.11%   7.12%
67.2%
20.6%

Propidium Iodide

D
Early apoptotic cell death

*
P=0.055
****
*
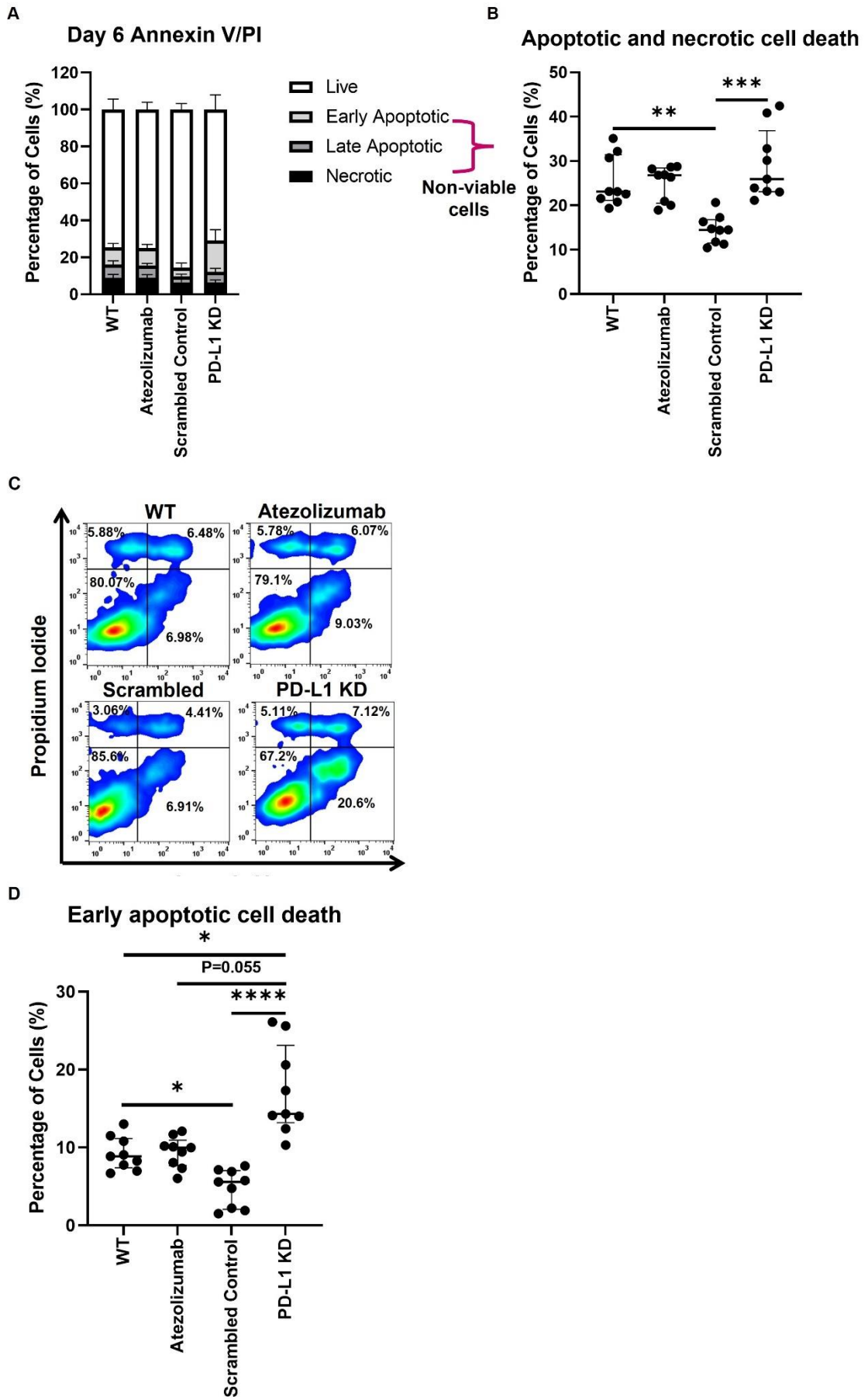
Figure 5.37 PD-L1 knockdown cells display significantly more cell death compared to WT and scrambled control cells after being cultured for 6 days in alginate. (A) Annexin V/PI staining was used to assess cell viability in MDA-MB-231 WT, Atezolizumab-treated WT, scrambled control and PD-L1 knockdown cells after 6 days of culture in alginate. **(B)** The percentage of non-viable cells (AV+/PI-, AV+/PI+, AV-/PI+) is shown separately to display the statistical significance between PD-L1 knockdown cells compared to WT and scrambled control cells in alginate. **(C)** Representative flow cytometry plots demonstrate the effect of Atezolizumab treatment and PD-L1 knockdown on cell viability compared to WT and scrambled control cells. **(D)** The percentage of early apoptotic cells (AV+/PI-) is shown separately to display the statistical significance between PD-L1 knockdown cells compared to WT, Atezolizumab-treated WT and scrambled control cells in alginate. Data is presented as median ± range. n=3 independent experiments each with 3 technical repeats. Data was analysed by a Kruskal-Wallis followed by Dunn's multiple comparison test (*P<0.05, **P<0.01, ***P<0.001 and ****P<0.0001).

A Day 10 Annexin V/PI

B Apoptotic and necrotic cell death

C

WT
3.82%   7.21%
79.4%
9.59%

Atezolizumab
1.89%   4.55%
79.7%
13.9%

Scrambled
3.30%   4.04%
79.5%
13.2%

PD-L1 KD
2.01%   5.14%
59.9%
32.9%

Propidium Iodide
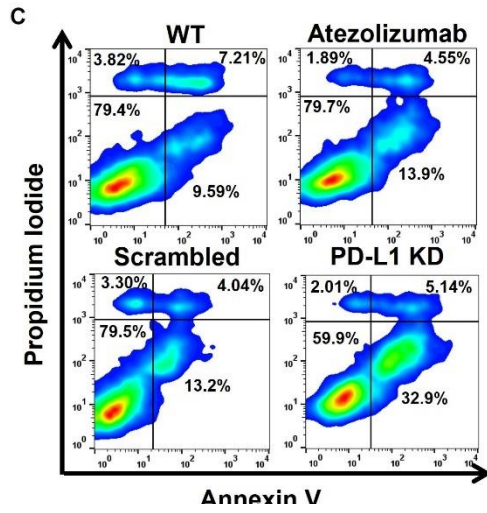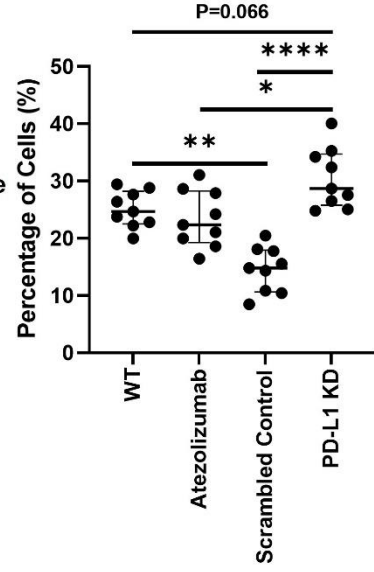
Annexin V

D Early apoptotic cell death

Figure 5.38 PD-L1 knockdown cells display significantly more cell death compared to WT, Atezolizumab-treated WT and scrambled control cells after being cultured in alginate for 10 days. (A) Annexin V/PI staining was used to assess cell viability in MDA-MB-231 WT, Atezolizumab-treated WT, scrambled control and PD-L1 knockdown cells after 10 days of culture in alginate. **(B)** The percentage of non-viable cells (AV+/PI-, AV+/PI+, AV-/PI+) is shown separately to demonstrate the statistical significance between PD-L1 knockdown cells compared WT, Atezolizumab-treated WT and scrambled control cells in alginate. **(C)** Representative flow cytometry plots demonstrate the effect of Atezolizumab treatment and PD-L1 knockdown on cell viability compared to WT and scrambled control cells. **(D)** The percentage of early apoptotic cells (AV+/PI-) is shown separately to display the statistical significance between PD-L1 knockdown cells compared to WT, Atezolizumab-treated WT and scrambled control cells in alginate. Data is presented as median ± range. n=3 independent experiments each with 3 technical repeats. Data was analysed by a Kruskal-Wallis followed by Dunn's multiple comparisons test (*P<0.05, **P<0.01, ***P<0.001, and ****P<0.0001).

Figure 5.39 PD-L1 knockdown cells display significantly reduced ATP levels after 6 and 10 of culture in alginate compared to WT, Atezolizumab-treated WT and scrambled control cells. The cellular activity of MDA-MB-231 WT, Atezolizumab-treated WT, scrambled control and PD-L1 knockdown cells cultured in alginate was assessed by measuring ATP levels after **(A)** 3, **(B)** 6 and **(C)** 10 days of culture. Data is presented as median ± range. n=3 independent experiments each with 3 technical repeats. Data was analysed by a Kruskal-Wallis followed by Dunn's multiple comparisons test (*P<0.05 and **P<0.01).

5.3.15 PD-L1 knockdown cells share some similarities but also display differences to Atezolizumab-treated WT cells in the phosphorylation of different kinases

To determine whether PD-L1 knockdown influences tumour-intrinsic signalling and further understand the mechanism of action of PD-L1 in MDA-MB-231 breast cancer cells, the relative levels of phosphorylation at 37 kinase phosphorylation sites and 2 related total proteins were measured using a Human Phospho-Kinase Array. Out of the 37 kinase phosphorylation sites and 2 total proteins assessed, MDA-MB-231 PD-L1 knockdown cells demonstrated 22 main alterations to kinase phosphorylation in comparison to MDA-MB-231 WT, Atezolizumab-treated WT and scrambled control cells (Figure 5.40). Appendix Table 9.1 displays the coordinates of each target and control on the protein profiler array membranes A and B. Kinase phosphorylation sites in PD-L1 knockdown cells that remained unchanged or showed similar alterations to the level of phosphorylation observed in scrambled control cells can be found in the Appendix (Appendix Figure 9.19A and B).

Based on observations for one array per treatment group only, PD-L1 knockdown cells displayed an increase in the p53 isoforms phosphorylated at S15 and S392 compared to WT and scrambled control cells. Atezolizumab-treated WT cells also showed an increase in p53 isoform phosphorylation at S15 but demonstrated a decrease in phosphorylated p53 isoform at S392 compared to WT and scrambled control cells (Figure 5.41A). Out of the 5 STAT molecules assessed, 4 displayed increased levels of phosphorylation in PD-L1 knockdown cells compared to WT and scrambled control cells (Figure 5.41B). These included STAT5α/β (Y694/Y699), STAT1 (Y701), STAT3 (Y705) and STAT6 (Y641). Atezolizumab-treated WT cells also displayed an increase in STAT1 phosphorylation at Y701 but showed a decrease in phosphorylation levels in the other 3 STAT molecules compared to WT and scrambled control cells. Similarly, in PD-L1 knockdown cells two members of the SFKs, Yes and Fgr, demonstrated reduced phosphorylation levels at sites Y426 and Y421, respectively, compared to WT and scrambled control cells (Figure 5.41C). Interestingly, phosphorylation levels of Yes (Y426) were found to be increased in Atezolizumab-treated WT cells compared to WT and scrambled control cells, whereas Fgr (Y412) showed a similar reduction in phosphorylation levels as PD-L1 knockdown cells.

The phosphorylation of c-Jun (S63) and JNK 1/2/3 (T183/Y185, T221/Y223), molecules associated with Wnt signaling were found to be substantially reduced in PD-L1 knockdown cells compared WT, Atezolizumab-treated WT and scrambled control cells (Figure 5.41D). Similarly, the phosphorylation of molecules associated with PI3K/AKT/mTOR signaling was also affected by knocking down PD-L1 in MDA-MB-231 cells (Figure 5.42A). Phosphorylation sites of AKT 1/2/3 (S473), GSK-3α/β (S21/S9), CREB (S133) and PDGF Rβ (Y751) displayed reduced levels of phosphorylation in PD-L1 knockdown cells compared to WT and scrambled control cells. Whilst Atezolizumab-treated WT cells also displayed a decrease in GSK-3α/β (S21/S9) and PDGF Rβ (Y751) phosphorylation levels, they demonstrated an increase in AKT 1/2/3 (S473) and CREB (S133) phosphorylation levels compared to WT and scrambled control cells. Additionally, phosphorylation sites of eNOS (S1177), PRAS40 (T246) and PYK2 (Y402) demonstrated increased levels of phosphorylation in Atezolizumab-treated WT cells which were further increased in PD-L1 knockdown cells, compared to WT and scrambled control cells. Whilst PD-L1 knockdown cells also displayed increased phosphorylation levels of p70 S6 kinase at sites T389 and T421/S242, Atezolizumab-treated WT cells showed reduced phosphorylation levels compared to WT and scrambled control cells.

Furthermore, the phosphorylation of kinases associated with the MAPK/ERK signaling pathway were also altered substantially in PD-L1 knockdown cells compared to WT and scrambled control cells (Figure 5.42B). p38α (T180/Y182) phosphorylation levels were substantially reduced in PD-L1 knockdown cells compared to WT, Atezolizumab-treated WT and scrambled control cells. Similarly, HSP27 (S78/S82) phosphorylation levels were substantially reduced in PD-L1 knockdown cells compared WT and scrambled control cells. Atezolizumab-treated WT cells showed increased phosphorylation levels of HSP27 (S78/S82). Moreover, RSK1/2 (S221/S227) phosphorylation levels were substantially increased in PD-L1 knockdown cells, whereas for Atezolizumab-treated WT and scrambled control cells, levels of RSK1/2 (S221/S227) phosphorylation were found to be substantially reduced compared to WT cells.
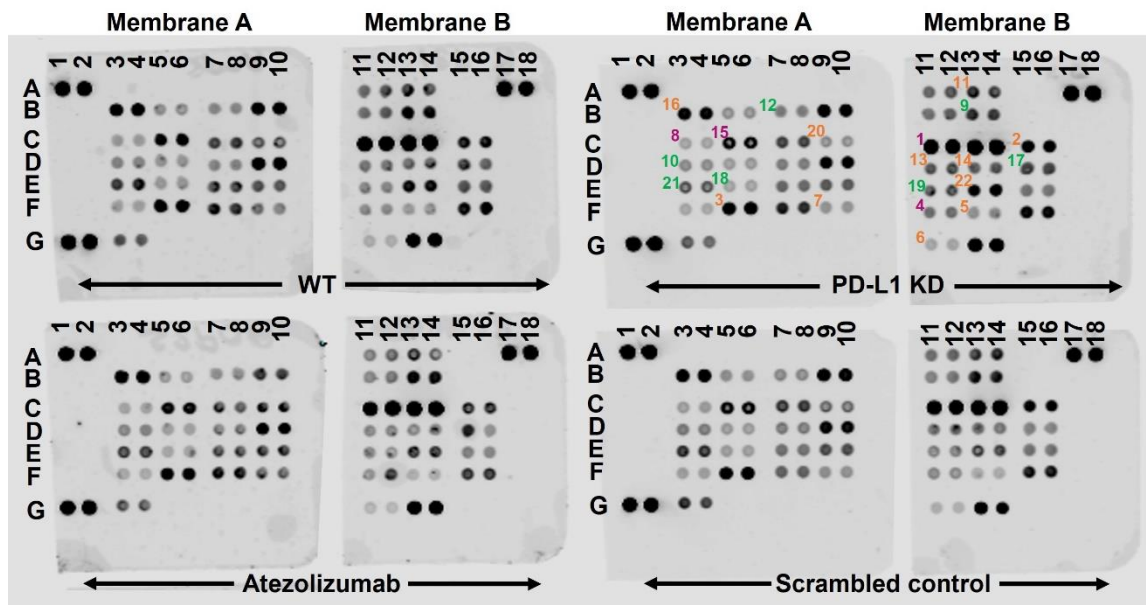
Figure 5.40 PD-L1 knockdown cells display 22 main differences in kinase phosphorylation compared to WT, Atezolizumab-treated WT and scrambled control cells. The Human Phospho-Kinase Array was utilised to measure relative levels of phosphorylation of 37 kinase phosphorylation sites and 2 related total proteins in MDA-MB-231 WT, Atezolizumab-treated WT, scrambled control and PD-L1 knockdown cells. Array membranes A and B that had been treated with cell lysate from WT, Atezolizumab-treated WT, scrambled control and PD-L1 knockdown cells were scanned with LI-COR Odyssey® Infrared Imaging System. The annotated numbers displayed on membranes A and B highlight the 22 main changes in phosphorylation levels detected in PD-L1 knockdown cells compared to the other cells. Each number is located to the left of the target spots that are in duplicate and represents PD-L1 knockdown cells that show similar trend in phosphorylation levels to Atezolizumab-treated WT cells (pink); PD-L1 knockdown cells that show opposing alterations to phosphorylation levels to Atezolizumab-treated WT cells (orange); and PD-L1 knockdown cells that show same trend and larger alterations to phosphorylation levels compared to Atezolizumab-treated WT cells (green).
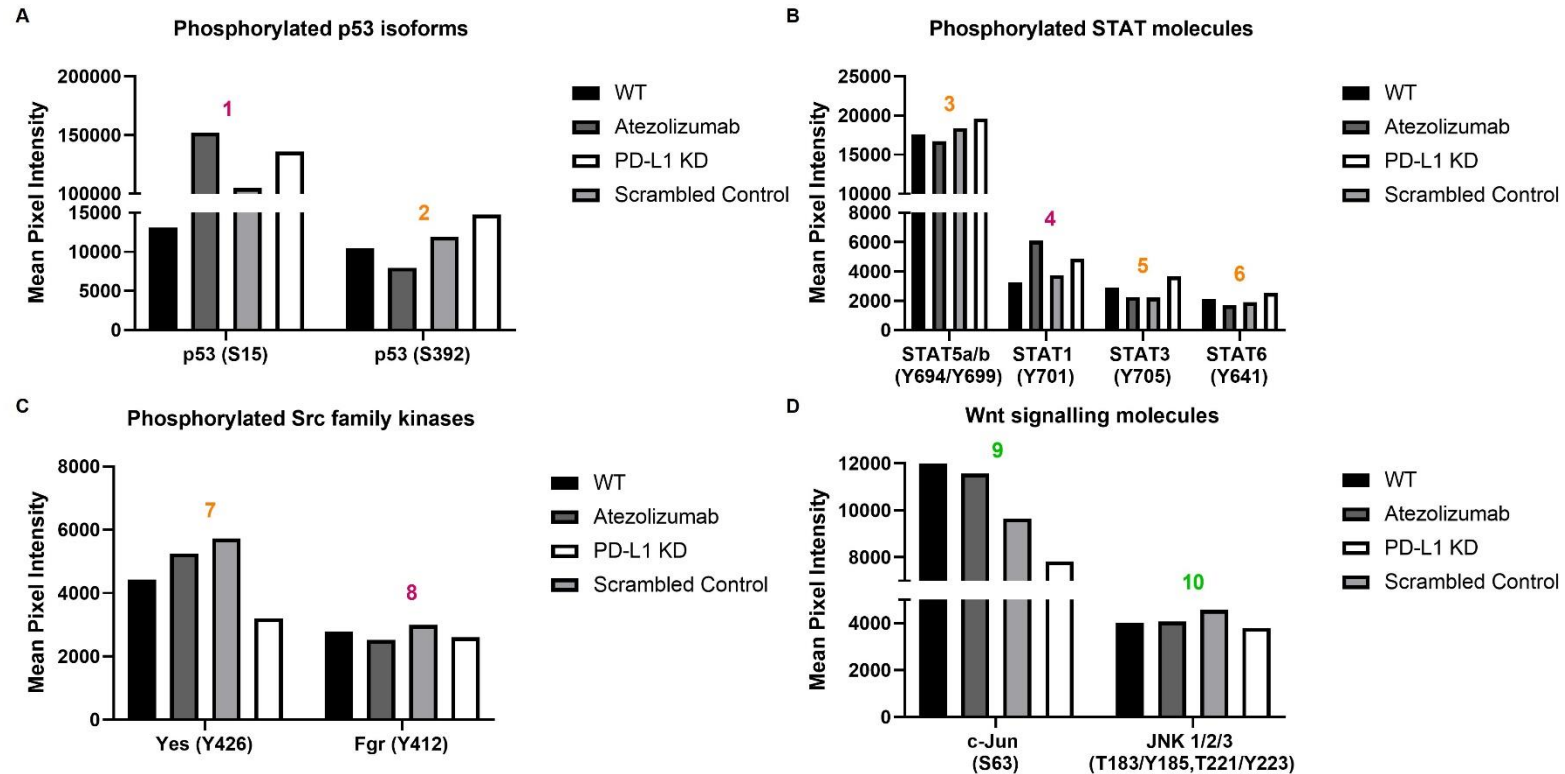
Figure 5.41 PD-L1 knockdown alters the phosphorylation levels of p53 isoforms, STAT molecules, Src family kinases and Wnt signalling molecules. The effects of PD-L1 knockdown on the phosphorylation levels of **(A)** p53 isoforms, **(B)** STAT molecules, **(C)** Src family kinases and **(D)** Wnt signalling molecules were assessed in MDA-MB-231 cells by performing a Human Phospho-Kinase Array. The annotated numbers displayed on the graph correspond to the annotated numbers on the array membrane in Figure 5.40. Data represents n=1 independent experiment with 2 technical repeats shown as the mean pixel intensity.
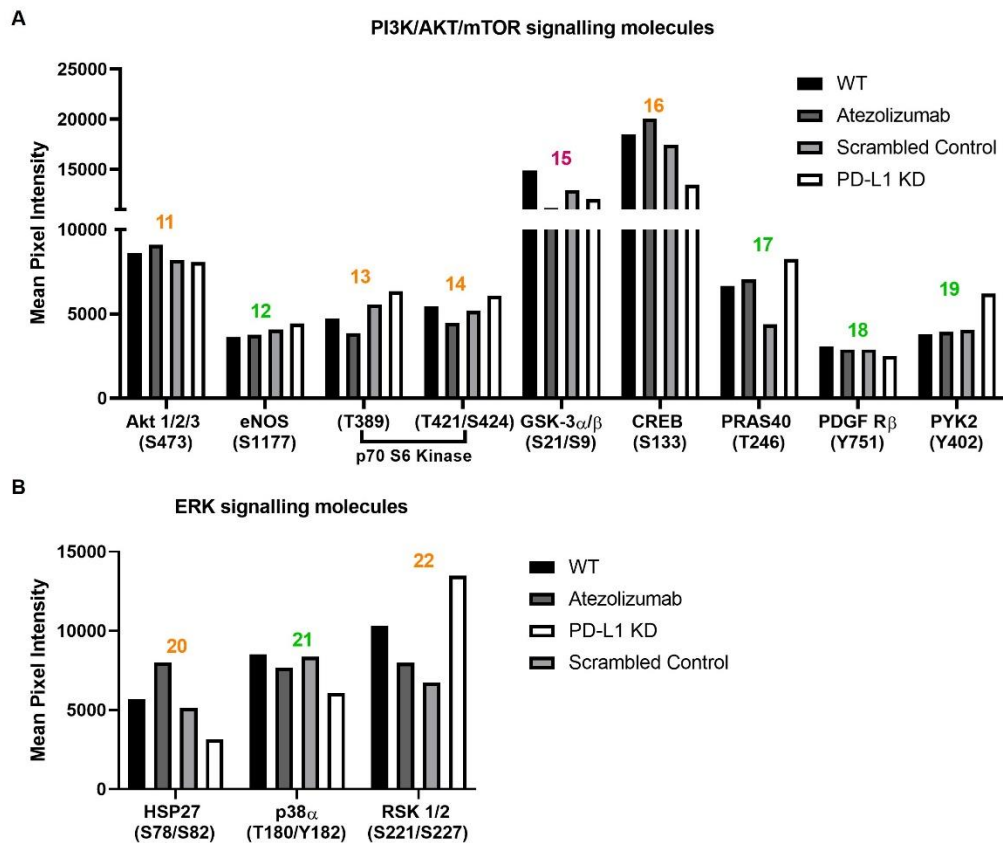
Figure 5.42 PD-L1 knockdown alters the phosphorylation levels of PI3K/AKT/mTOR and MAPK/ERK signalling molecules. The effects of PD-L1 knockdown on the phosphorylation levels of kinases involved in the **(A)** PI3K/AKT/mTOR and **(B)** MAPK/ERK signalling pathways were assessed in MDA-MB-231 cells by performing a Human Phospho-Kinase Array. The annotated numbers displayed on the graph correspond to the annotated numbers on the array membrane in Figure 5.40. Data represents n=1 independent experiment with 2 technical repeats shown as the mean pixel intensity.

5.3.16 The cell viability effects of TNFα treatment on PD-L1 knockdown cells in 2D and 3D cell culture models

Finally, since Atezolizumab treatment in combination with TNFα demonstrated some synergistic effects to induce cell death in MDA-MB-231 in 3D spheroid colonies grown in alginate hydrogel beads, it was next determined whether knocking down PD-L1 as opposed to blocking it at the cell surface with Atezolizumab could enhance the cell death phenotype exhibited by 2D- and 3D-cultured MDA-MB-231 breast cancer cells.

5.3.16.1 Treatment of PD-L1 knockdown 2D-cultured cells and 3D hanging drop spheroids with TNFα

In Chapter 4 Sections 4.3.13.1 and 4.3.13.2, it was shown that PD-L1 blockade with Atezolizumab in combination with cytokine modulation did not induce cell death in MDA-MB-231 cells cultured in monolayer and 3D hanging drop spheroids. Similarly, here the addition of TNFα to Atezolizumab-treated WT and PD-L1 knockdown cells cultured in monolayer (Figure 5.43A-C) or 3D spheroids (Figure 5.44A-C) did not induce a higher cell death phenotype than Atezolizumab treatment and PD-L1 knockdown alone. In both monolayer-cultured cells and 3D spheroids, PD-L1 knockdown cells demonstrated the highest cell death phenotype, despite the addition of TNFα. In 3D spheroids, PD-L1 knockdown cells exhibited more cell death than WT cells and cells treated with TNFα only, Atezolizumab only, and Atezolizumab and TNFα combined. Cell viability effects of TNFα on scrambled control cells cultured in monolayer and 3D spheroids was also investigated concurrently, and representative flow cytometry plots can be found in Appendix Figure 9.20.
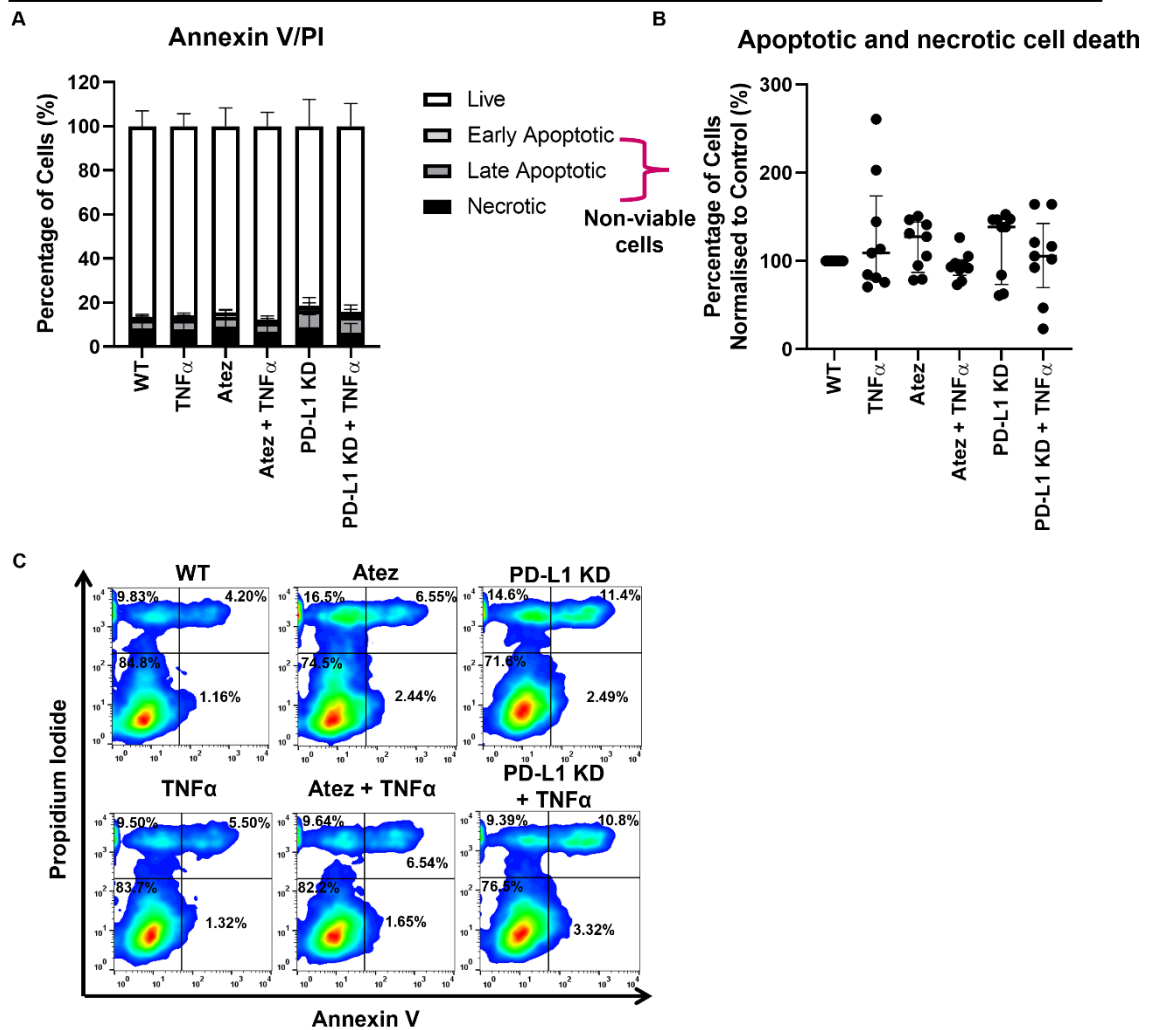
Figure 5.43 TNFα does not enhance the cell death phenotype observed by PD-L1 knockdown in MDA-MB-231 cells in monolayer cell culture. (A) Annexin V/PI staining was used to assess cell viability in Atezolizumab-treated WT and PD-L1 knockdown cells treated with or without TNFα in monolayer cell culture to determine whether TNFα enhanced the cell death phenotype of PD-L1 knockdown cells even more so than Atezolizumab. **(B)** The percentage of apoptotic and necrotic cells (AV+/PI-, AV+/PI+, AV-/PI+) is shown separately for statistical analysis. **(C)** Representative flow cytometry plots demonstrate the effect of Atezolizumab and PD-L1 knockdown on cell viability with or without the addition of TNFα compared to WT cells. Data is presented as median ± range. n=3 independent experiments each with 3 technical repeats. Data was analysed by a Kruskal-Wallis followed by a Dunn's multiple comparisons test.
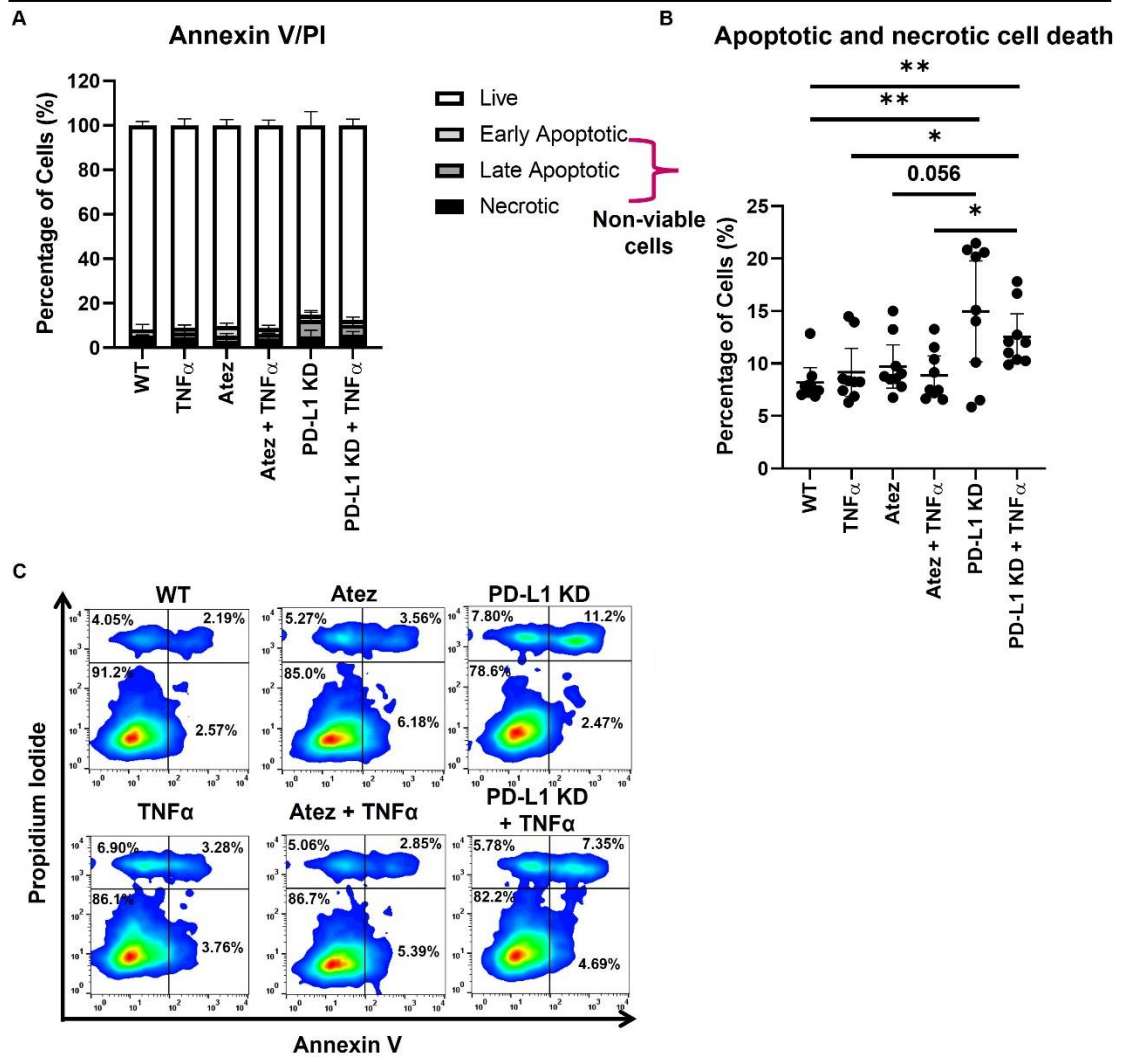
Figure 5.44 TNFα does not enhance the cell death phenotype observed by Atezolizumab and PD-L1 knockdown in MDA-MB-231 3D spheroids. (A) Annexin V/PI staining was used to assess cell viability in Atezolizumab-treated WT and PD-L1 knockdown 3D spheroids treated with or without TNFα to determine whether TNFα enhanced the cell death phenotype of PD-L1 knockdown cells even more so than Atezolizumab. **(B)** The percentage of apoptotic and necrotic cells (AV+/PI-, AV+/PI+, AV-/PI+) is shown separately for statistical analysis. **(C)** Representative flow cytometry plots demonstrate the effect of Atezolizumab and PD-L1 knockdown on cancer cell viability with or without the addition of TNFα. Data is presented as median ± range. n=3 independent experiments each with 3 technical repeats. Data was analysed by a Kruskal-Wallis followed by Dunn's multiple comparisons test (*P<0.05 and **P<0.01).

5.3.16.2 TNFα enhances cell death in Atezolizumab-treated and PD-L1 knockdown cells cultured in alginate hydrogel beads

In contrast to observing no enhanced effect on cell viability with the addition of TNFα to PD-L1 knockdown cells cultured in monolayer and 3D hanging drop spheroids, the addition of TNFα to PD-L1 knockdown cells cultured in alginate hydrogel beads significantly enhanced the cell death phenotype observed after only 3 days of culture (Figure 5.45 A-C). PD-L1 knockdown cells cultured in alginate displayed a similar percentage of cell death to cells treated with TNFα alone or in combination with Atezolizumab which was significantly higher than the percentage of cell death observed by WT cells grown in alginate hydrogel beads. Importantly, PD-L1 knockdown cells showed a significantly higher percentage of cell death than Atezolizumab-treated WT cells in alginate hydrogel beads ($p=0.027$). Additionally, when TNFα was added to PD-L1 knockdown cells 48 hours prior to cell viability assessment, the percentage of cell death observed was significantly higher compared to PD-L1 knockdown cells ($p=0.0387$) as well as WT cells ($p<0.0001$) and cells treated with TNFα only ($p=0.046$), Atezolizumab only and Atezolizumab and TNFα combined ($p=0.0027$). Cell viability effects of TNFα on scrambled control cells cultured in alginate hydrogel beads was also investigated concurrently showing that treatment has no effect, and representative flow cytometry plots can be found in Appendix Figure 9.20.
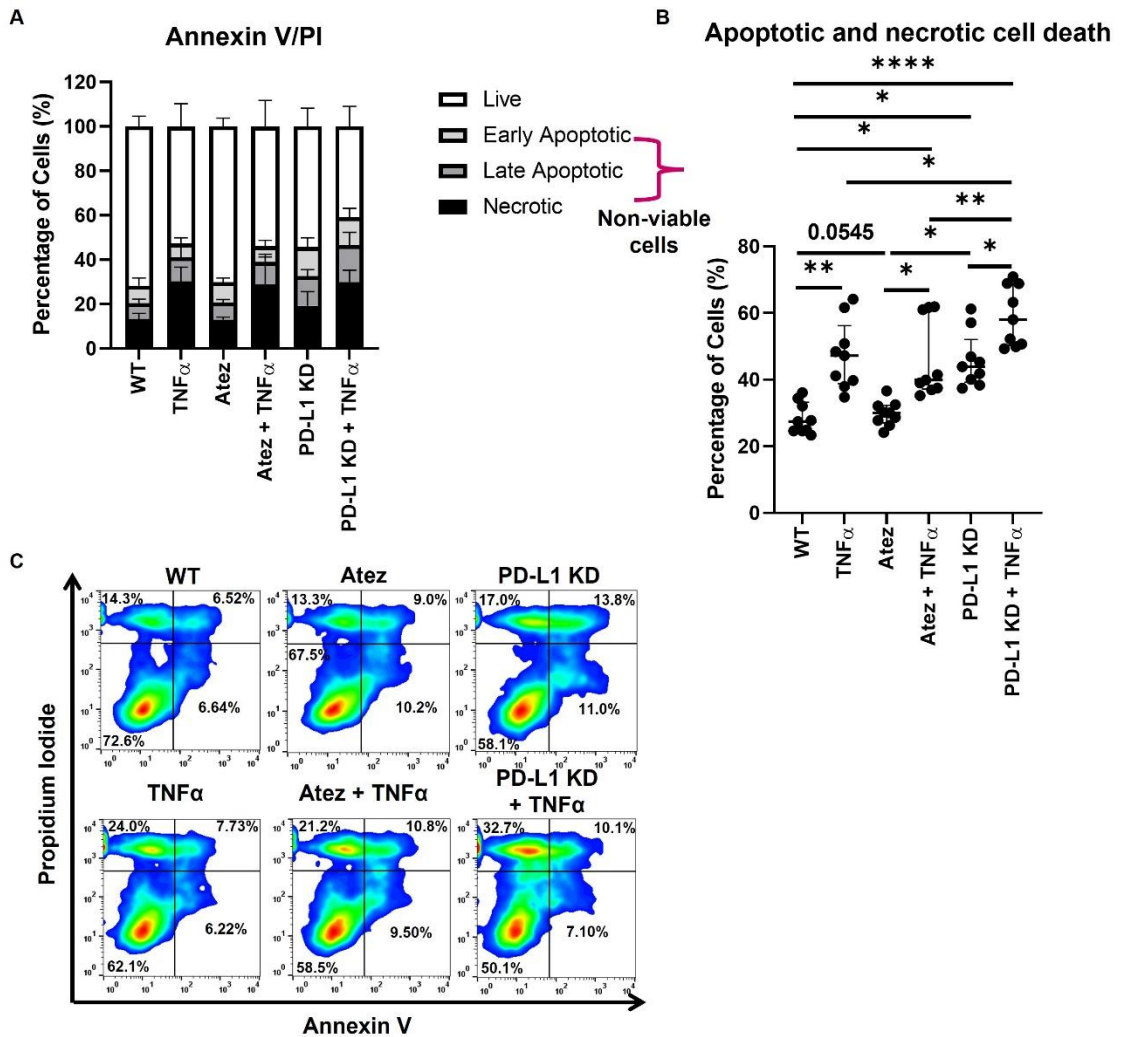
Figure 5.45 TNFα enhances the cell death phenotype observed by PD-L1 knockdown cells after only 3 days of being cultured in alginate hydrogel beads. **(A)** Annexin V/PI staining was used to assess cell viability of PD-L1 knockdown cells treated with or without TNFα when cultured in alginate to determine whether TNFα enhanced the cell death phenotype of PD-L1 knockdown cells even more so than Atezolizumab combined with TNFα. **(B)** The percentage of apoptotic and necrotic cells (AV+/PI-, AV+/PI+, AV-/PI+) is shown separately for statistical analysis. **(C)** Representative flow cytometry plots demonstrate the effect of PD-L1 knockdown on cancer cell viability with or without TNFα. Data is presented as median ± range. n=3 independent experiments each with 3 technical repeats. Data was analysed by a Kruskal-Wallis followed by Dunn's multiple comparison test. (*P<0.05, **P<0.01 and ****P<0.0001).

5.4 Discussion

Triple negative breast cancer has a poor prognosis and conventional chemotherapy has been the gold standard treatment, but responses are often short-lived, and patients have a median overall survival of only 12 to 18 months (Garrido-Castro *et al.,* 2019). Recent approval of Atezolizumab plus nab-paclitaxel for TNBC treatment was based on its capability to improve the median overall survival to 25 months (Schmid *et al.,* 2018). This unprecedented result to prolong patient survival with the use of cancer immunotherapy is encouraging research to focus on understanding how this treatment can be improved further. Understanding the role of PD-L1 in TNBC is a step in the right direction since TNBC tumours present with high PD-L1 expression showing potential for the generation of a robust anti-tumour immune response with the treatment of anti-PD-L1 monoclonal antibodies or other modalities targeting PD-L1.

To understand a specific proteins biological function in a cell it is necessary to use gene silencing or gene knockout approaches to reduce its expression or remove it completely from the cells. RNA interference (siRNA, short hairpin-RNA and miRNA) and CRISPR-Cas9 are widely used technologies in cancer biology to facilitate gene knockdowns and gene knockouts, respectively. In this study we designed miRNA 100% complementary to WT PD-L1 and used a vector-based delivery system that incorporated GFP upstream of our miRNA to allow dual knockdown of PD-L1 and expression of GFP in MDA-MB-231 cells following stable transfection using lipofectamine and Blasticidin selection. miRNAs are endogenously expressed small ssRNA sequences which naturally direct gene silencing (Bartel, 2004) and as discussed briefly in the introduction to this thesis many miRNAs have been shown to regulate the expression of PD-L1 in cancers acting as oncogenes or tumour suppressors. For us has researchers selecting a miRNA-mediated knockdown approach was the most natural way in that our findings could encourage the therapeutic targeting of miRNAs shown to positively regulate PD-L1 expression. Using this approach, we were able to achieve a 70% reduction in PD-L1 expression which allowed us to establish that PD-L1 may in fact be a tumour intrinsic signalling protein in TNBC cells.

Here, PD-L1 knockdown in MDA-MB-231 TNBC cells cultured in 2D monolayer were shown to have reduced growth and proliferation compared to the PD-L1 WT and Atezolizumab-treated cells through assessment of the percentage surface area

covered by cells and Ki67 expression. PD-L1 knockdown in human gastric cancer cell lines SGC-7901 and AGS reduced cell proliferation and induced cell cycle arrest *in vitro* and reduced tumour growth in immunocompromised mice *in vivo* compared to gastric tumours expressing PD-L1 (Li *et al.,* 2017). Similarly, PD-L1 silencing in murine B16 melanoma cells has also been shown to slow tumour growth and reduce metastases to the lungs of immunocompetent mice as well as immunodeficient mice via mechanisms that increase autophagy and reduce mTORC1 signalling (Clark *et al.,* 2016). Chen *et al.,* (2021) very recently reported that MDA-MB-231 cells showed a significant decrease in growth using PD-L1 CRISPR/Cas9 knockout and siRNA knockdown approaches. Indeed, PD-L1 expression has previously been reported to correlate with Ki67 expression in melanoma (Kraft *et al.,* 2017), chondrosarcoma (Yang *et al.,* 2017), breast (Schmidt *et al.,* 2022) and lung (Figueiredo *et al.,* 2021) cancer.

Although the effects of PD-L1 on the cell cycle were not investigated here, through performing a Kinase-Phosphatase Array we were able to show that PD-L1 knockdown cells displayed an increase in the p53 phosphorylated at S15 and S392 compared to PD-L1 WT and scrambled control cells, we could assume that p53 activity may be increased in PD-L1 knockdown cells resulting in cell cycle arrest in these cells since it has been shown to previously (Li *et al.,* 2017). Additionally, phosphorylation of c-Jun transcription factor was shown to be substantially reduced in this study compared to WT and scrambled control cells and c-Jun plays a key role in driving cell cycle progression (Lukey *et al.,* 2016). c-Jun binds directly to the *TP53* gene promoter leading to suppression of p53 and p53-regulated cyclin-dependent kinase inhibitor p21 and therefore downregulation of c-Jun in PD-L1 knockdown cells could in part explain the increase in p53 phosphorylation that was observed in the study. However, further investigations would be required to verify this statement of PD-L1 knockdown affecting the cell cycle and growth in TNBC cells, such as cell cycle analysis, p53 total protein levels, and assessment of downstream targets of p53 such as p21 in PD-L1 knockdown versus WT cells (Loughery *et al.,* 2014; Chen, 2016).

Importantly, for the first time we can report that PD-L1 knockdown inhibits the spheroid forming capabilities of MDA-MB-231 cells differently in two 3D cell culture models. Whilst no significant reduction in Ki67 expression was detected in 3D cell culture models generated from PD-L1 knockdown cells, from the fluorescent images

acquired the effect PD-L1 knockdown on cell growth was evident. A reduction is cell proliferation and thus Ki67 expression is a well-known characteristic of cancer cells when cultured in 3D models compared to 2D and is one of the features that makes using these models more representative of an *in vivo* tumour (Edmondson *et al.,* 2014). Since a reduction in Ki67 expression is observed naturally in 3D-cultured cancer cells we could postulate that our method of assessing its expression in this study (flow cytometry) is not the most sensitive, as very low levels were also detected in PD-L1 WT cells in 3D. Immunohistochemistry/Immunofluorescence to measure the spatial distribution of Ki67 protein may pose has a more appropriate method to assess Ki67 amongst our PD-L1 WT versus knockdown 3D cell culture models. This would highlight the Ki67 positive proliferative cells in the outermost layer of the 3D cultures and could determine whether there was a difference in the distribution and expression of Ki67. Alternatively, the effects on cancer cell growth we observe in 3D following PD-L1 knockdown may be due to other mechanistic changes rather than effects on proliferation marker Ki67.

PD-L1 knockdown 3D hanging drop spheroids showed smoother and more spherical surface topology compared to PD-L1 WT and Atezolizumab-treated 3D spheroids. Surface topology has been shown to be affected by the number of cells used to form the spheroids (Guillaume *et al.,* 2019). The presence of more cells made the outer surface appear rougher than those with less cells. Since 10,000 cancer cells were seeded consistently to form 3D spheroids in our investigations, the data could suggest that PD-L1 knockdown cells may not be proliferating at the outer most layer of the spheroids and may in fact be a similar number of cells as seeded originally. To support this statement the diameter of PD-L1 knockdown 3D spheroids were consistently smaller than those formed of PD-L1 WT and Atezolizumab-treated cells. Liao *et al.,* (2017) has also demonstrated that CRISPR/Cas9 PD-L1 knockout in human osteosarcoma KHOS and MNNG/HOS cells compromised their ability to form 3D spheroids *in vitro*. The diameter of the spheroids formed by PD-L1 knockout cells were significantly decreased compared to the control cells (Liao *et al.,* 2017).

In the 3D alginate hydrogel model used in this study, PD-L1 knockdown cells were unable to form 3D spheroid colonies and remained singled cells or cell clusters of approximately 3-4 cells over the 10-day culture period compared to WT and Atezolizumab-treated cells. Since the alginate model promotes the clonogenic proliferation of cancer cells from a single cell, it is evident that PD-L1 knockdown has

impaired the MDA-MB-231 cells ability to self-renew. Indeed, PD-L1 expression has been positively associated with CSC-like characteristics in head and neck (Lee *et al.,* 2016), lung (Nishino *et al.,* 2017), colorectal (Zhi *et al.,* 2015), ovarian (Gupta *et al.,* 2016), breast cancer (Gao *et al.,* 2019) and melanoma (Gupta *et al.,* 2016) cells. Tumour PD-L1 has been shown to promote the tumour-initiating cell generation in immunocompromised murine melanoma and ovarian cancer mouse models; a phenotype which was also verified in a human ovarian cancer cell xenograft mouse model (Gupta *et al.,* 2016; Kari *et al.,* 2019). PD-L1 was also shown to promote OCT4 and Nanog transcription factor expression via PI3K/AKT pathway signalling which are critical for pluripotency and tumorigenesis in breast CSCs (Almozyan *et al.,* 2017). PD-L1 knockdown compromised the capability of breast CSCs to self-renew themselves *in vitro* and *in vivo* using immune deficient nude mice. In the same study the effects of PD-L1 on cancer stemness were recapitulated using T-47D breast cancer cells which are normally PD-L1 negative. T-47D cells were transfected with PD-L1 which resulted in an increased in OCT4 and Nanog expression confirming their findings in different breast cancer types (Gupta *et al.,* 2016). More recently, lung (H460 and H358) and breast (MDA-MB-231) cancer cells with PD-L1 knocked down were shown to have a weakened ability of forming colonies (Yu *et al.,* 2020; Chen *et al.,* 2021). Interestingly, this study's findings of c-Jun being substantially reduced following PD-L1 knockdown could indicate that OCT4 may also be reduced in our cells as it has previously been shown that c-Jun-mediated transactivation of the OCT4 promoter and vice versa is crucial for promoting cancer development and maintaining cancer stemness in liver and breast cancer (Jiao *et al.,* 2010; Kuo *et al.,* 2016). Additionally, in this study we found that PD-L1 knockdown reduced AKT and CREB phosphorylation which may suggest that PI3K/AKT pathway exhibits reduced activity in these cells which previously reported responsible for cancer stemness in breast cancer cells (Almozyan *et al.,* 2017). Hence why we may observe the inhibited growth of MDA-MB-231 PD-L1 knockdown cells in the 3D alginate model.

PD-L1 knockdown has also been shown to reduce the viability of gastric (Li *et al.,* 2017) and lung (Yu *et al.,* 2020) cancer cells. Here we were able to show for the first time that PD-L1 knockdown significantly reduced the viability of MDA-MB-231 TNBC cells in both 2D monolayer and 3D cell culture models more so than Atezolizumab. Due to the extensive effects of PD-L1 knockdown on the ability of MDA-MB-231 cells to form 3D structures, it was by no surprise that more cell death was observed in 3D cell culture models compared to 2D monolayer, particularly in the alginate model at

day 10. The mechanism by which PD-L1 knockdown may induce cell death in MDA-MB-231 cells could in part be explained by the reduced phosphorylation of heat shock protein (HSP)-27 observed in this study. HSP27 is overexpressed in many cancers and facilitates cellular survival (Lampros *et al.,* 2022). HSP27 either interacts directly with caspase-3 or cytochrome c and inactivates them (Garrido *et al.,* 2006) or upregulates the PI3K/AKT pathway leading to AKT-induced AKT/Bax interaction which eventually blocks Bax translocation to the mitochondria and thus the subsequent Bax-mediated apoptosis cascade (Havasi *et al.,* 2008). The reduction of HSP27 in this study following PD-L1 knockdown coincides with reduced AKT phosphorylation and increased p53 phosphorylation which may imply that HSP27-mediated survival mechanisms are less effective, and that p53-mediated apoptosis may be able to occur in PD-L1 knockdown cells. Additionally, p38-MAPK pathway activation of HSP27 has been reported to be necessary for cancer cell survival in hypoxic conditions (Lin *et al.,* 2012), which could explain why we observed a higher percentage of cell death in our 3D cell culture models consisting of PD-L1 knockdown cells where hypoxia may exist compared to the normoxic conditions of 2D monolayer cultures as shown in Chapter 3.

HSP27 has also been shown to promote chemotherapy resistance via the inhibition of p53-mediated apoptosis (Lampros *et al.,* 2022). This could imply that PD-L1 may regulate HSP27-mediated drug resistance in TNBCs since cells exhibit reduced phosphorylation of HSP27 and associated regulatory molecules (AKT and p38α) following PD-L1 knockdown. PD-L1 has in fact been implicated to promote drug resistance in breast cancer cells previously (Ghebeh *et al.,* 2010; Black *et al.,* 2017).

Accompanied by reduced cell viability with PD-L1 knockdown in MDA-MB-231 was a significant reduction in ATP synthesis even more so than Atezolizumab effects on ATP levels in 2D and 3D cell culture models. Interestingly, shRNA mediated knockdown of PD-L1 or treatment with anti-PD-L1 antibodies was shown to reduce aerobic glycolysis mechanisms in B16 melanoma, MC38 colon cancer and sarcoma cancer cell lines *in vitro* (Chang *et al.,* 2015). Additionally, PD-L1 has been shown to supress type I interferon by promoting a metabolic shift characterized by enhanced glucose uptake and glycolysis rate (Hodgins *et al.,* 2022). These studies support our findings in that tumorigenic PD-L1 has the potential to modulate cancer cells metabolic processes.

Lastly, in Chapter 4 we showed the potential of TNFα to work collectively with Atezolizumab to induce more cell death in MDA-MB-231 cells cultured in 2D and 3D cell culture models than both treatments alone. Our initial theory was that PD-L1 modulation prior to blocking PD-L1 with Atezolizumab may increase the anti-tumour role of Atezolizumab or that the role of TNFα to stabilise PD-L1 expression could explain the beneficial effects of the combination. Here we show that PD-L1 knockdown cells treated with TNFα displayed significantly more cell death than those untreated in cells culture in 2D monolayer and alginate. This therefore suggests that TNFα is eliciting its anti-tumour role via mechanisms independent of PD-L1. Interestingly, in 3D hanging drop spheroids where we observed no changes to cell viability with Atezolizumab and TNFα combined, with PD-L1 knockdown cells treated with TNFα we observed a significant increase in cell death compared to Atezolizumab and TNFα combined but not untreated PD-L1 knockdown cells. This suggests that PD-L1 may be influencing the anti-tumour effects of TNFα in 3D hanging drop spheroids. The mechanism of action of TNFα and PD-L1 knockdown would need to be further investigated but it shows promising results to induce cell death in TNBC cells.

In summary, we have demonstrated for the first time the culturing of TNBC cells with PD-L1 knockdown in 2D cell culture alongside two 3D cell culture models and have compared the biological effects it has on cancer cells to the therapeutically approved monoclonal PD-L1 antibody, Atezolizumab. Here, PD-L1 knockdown in TNBC cells reduced their proliferation, viability, metabolism, and spheroid forming capabilities implicating the role of PD-L1 to intrinsically signal to facilitate growth and tumorigenicity in TNBC cells. Importantly, the negative biological effects that PD-L1 knockdown had on TNBC cells were more prominent than blocking PD-L1 at the cell surface with Atezolizumab. Our preliminary data produced from the Phospho-Kinase Array also suggests that PD-L1 blockade and PD-L1 knockdown may mediated different signalling mechanisms intrinsically, and no doubt led to the activation or deactivation of different signalling pathways to cause these biological changes within TNBC cells. Collectively, these results demonstrate for the first time that blocking PD-L1 in TNBC cells may not be sufficient to prevent tumorigenic signalling of PD-L1 and that other modalities of targeting PD-L1 intrinsically should be investigated. Lastly, we showed for the first-time the dual role of PD-L1 knockdown and TNFα on their ability to induce more cell death than PD-L1 knockdown alone in 2D and more importantly 3D cell culture models, prompting this strategy to be investigated further.

6. Final Discussion

PD-L1 is an immune checkpoint inhibitor which binds to its receptor PD-1 expressed by immune cells to regulate immune responses to prevent exacerbated activation and autoimmunity (Freeman *et al.,* 2000; Johnson and Dong, 2017). Many tumours overexpress PD-L1 to inhibit immune cell effector functions which in turn promotes immune evasion and tumour progression (Hino *et al.,* 2010; Maine *et al.,* 2013; Muenst *et al.,* 2014). Monoclonal antibodies targeting the PD-1/PD-L1 signalling axis have demonstrated unprecedented capabilites to generate robust anti-tumour immune responses in select patients with advanced cancers and have indeed become first-line treatments for some cancers; predominantly in melanoma and NSCLC (Fehrenbacher *et al.,* 2016; Rosenberg *et al.,* 2016; Balar *et al.,* 2017). However, some patients are unresponsive, hyperprogressive or develop resistance, and the mechanisms for this discrepancy remain largely unknown (Wang *et al.,* 2019; Kocikowski *et al.,* 2020).

The recently discovered tumour-intrinsic roles of PD-L1 and its receptor PD-1 are becoming apparent in some cancer types, and their roles may be responsible for the unresponsiveness and drug resistance observed in cancer patients (Wang *et al.,* 2020). Most research elucidating their roles has been carried out in human or mouse cancer cell lines cultured in 2D monolayer or in *in vivo* mouse models which fail to recapitulate the complex microenvironment of human tumours (Hudson *et al.,* 2020). Moreover, elucidating the roles of these proteins in melanoma and NSCLC, where patients exhibit the highest response to PD-1/PD-L1-targeted therapies have been the focus for most researchers to aid in the improvement of the treatment efficacy (Gupta *et al.,* 2016; Kari *et al.,* 2019; Wang *et al.,* 2020; Yu *et al.,* 2020). However, it is crucial to investigate the roles of PD-L1 and PD-1 in all cancer types; and understand how approved immunotherapies may influence their roles to maximise the clinical response to PD-1/PD-L1-targeted therapies across all cancers; particularly those cancers that exhibit low response to treatment, such as breast, prostate, and colorectal cancers.

In Chapter 2 of this thesis, human breast, prostate, and colorectal cancer cell lines were assessed for their expression of PD-L1 and PD-1 at basal levels. Indeed, all cell lines expressed PD-L1, with only colorectal cancer cell lines being the only cell lines to express PD-1. This leads to the suggestion that these cancer cell lines should in theory respond to PD-1/PD-L1-targeted therapies *in vitro*. However, in a clinical

setting these cancer types show only modest responses to PD-1/PD-L1-targeted monotherapies, despite some patient with these cancer types harbouring certain characteristics that usually coincide with positive immunotherapy responses such as immunogenicity and/or mismatch repair deficiency (Topalian *et al.,* 2012; Patnaik *et al.,* 2015; Overman *et al.,* 2017; Schmid *et al.,* 2018; Abida *et al.,* 2018).

In our study, like many others, we were able to show that low PD-L1 expressing cell lines (derived from luminal breast subtype, prostate, and colorectal cancers) could be modulated by IFNγ and/or TNFα treatment to enhance cell surface PD-L1 expression (Lee *et al.,* 2006; Pardoll, 2012; Ye *et al.,* 2017). As for PD-1 modulation, its expression has certainly been reported to be induced by various cytokines in ovarian cancer cells (Osta *et al.,* 2018) and immune cell subsets (Qin *et al.,* 2019), but here we did not investigate PD-1 further than its expression by cancer cell lines. Here we have demonstrated the ability to manipulate the expression of PD-L1 which is a valuable tool to enable the investigation of its intrinsic role within these cancers, and furthermore the utilisation of cytokines to modulate PD-L1 also more closely models the immune-tumour microenvironment (Pardoll, 2012). Cytokine driven PD-1 upregulation has been used in ovarian ES2 cells to show that anti-PD-1 therapy could reduce cancer cell growth (Osta *et al.,* 2018), suggesting that cytokine treatment may make cancer cells more vulnerable to anti-PD-1/PD-L1 therapy. This idea is supported by the finding that vector-induced overexpression of PD-L1 in HEK293T TNBC cells revealed the tumorigenic role of PD-L1 to promote EMT (Chen *et al.,* 2021). Similarly, in H1299 and A549 NSCLC cells overexpressing PD-L1 exhibited increased colony formation and viability compared to H460 and H358 cells with PD-L1 knocked down (Yu *et al.,* 2020), indicating that PD-L1 manipulation is crucial to understand its role in amongst different tumours.

Here, in Chapter 3, we also further demonstrated how implementing human breast, prostate and colorectal cancer cell lines into 3D tumour models could modulate PD-L1 and PD-1 expression. *In vitro* 3D tumour models possess several *in vivo* features of human tumours that would influence responses to PD-1/PD-L1-taregted therapy such as, cell-cell interaction, production/deposition of ECM, hypoxia, genomic and protein alterations, drug penetration and resistance; all of which are not recreated in 2D monolayer cell cultures (Breslin and O'Driscoll, 2013; Knight and Przybors, 2015; Lazzari *et al.,* 2017; Hoarau-Véchot *et al.,* 2018; Di Modugno *et al.,* 2019; Boucherit *et al.,* 2020). Indeed, the expression of immune checkpoint molecules by tumours *in*

vivo have been reported to differ from their expression in 2D monolayer cell culture models (Rom-Jurek *et al.,* 2018; Boucherit *et al.,* 2020); highlighting the benefits of utilising 3D tumour models for investigating the tumorigenic role of PD-L1/PD-1 and immunotherapy responses. Additionally, the two studies which have investigated cell lines in 3D tumour models also demonstrate how mechanical cues via manipulating the ECM stiffness can modulate PD-L1 expression and in turn influence cancer cells response to treatment (Miyazawa *et al.,* 2018; Azadi *et al.,* 2019), further strengthening the argument for using 3D tumour models for PD-L1/PD-1 axis investigations.

In the present study, we utilised a scaffold-free (hanging drop method) and a scaffold-based (alginate hydrogel bead) system to form 3D spheroids and 3D spheroid colonies, respectively, to assess PD-L1 expression by human cell lines compared to their 2D monolayer counterparts. These 3D tumour models have previously been reported to sustain an oxygen and nutrient gradient (Muller-Klieser and Sutherland, 1982; Alessandri *et al.,* 2013; Nunes *et al.,* 2019), encourage increased ECM deposition (Lee and Mooney, 2012; Rios de la Rosa *et al.,* 2018), facilitate genomic and protein alterations (Souza *et al.,* 2017; Souza *et al.,* 2018) and demonstrate increased resistance to anti-cancer therapies, similar to that observed in *in vivo* human tumours (Luca *et al.,* 2013; Riedl *et al.,* 2017; Takahashi *et al.,* 2020; Boucherit *et al.,* 2020).

Our tumour models show the development of a hypoxic core, which could account for the increased expression of PD-L1 we observed in 4 out of the 6 cancer cell lines when grown in 3D, since hypoxia has been reported to positively regulate PD-L1 expression (Barsoum *et al.,* 2014; Johnson and Dong, 2017; Zhou *et al.,* 2019). However, many other factors within the 3D environment could be responsible for the modulation of PD-L1 expression in these cell lines.

It is well known in the literature that a 3D environment promotes increased ECM deposition that will alter the stiffness of the tumour microenvironment in which the cancer cells are growing (Lee and Mooney, 2012; Rios de la Rosa *et al.,* 2018). Epithelial cells i.e. cancer cells connect to the ECM via integrin adhesions which in turn alters the cytoskeletal tension surrounding the cancer cells promoting malignant transformation (Ansardamavandi *et al.,* 2018). Increasing the substrate stiffness has been shown to positively correlate with PD-L1 expression in breast and lung cancer cells (Miyazawa *et al.,* 2018; Azadi *et al.,* 2019). In lung cancer cells, the actin

cytoskeleton was shown to be involved in the mechanisms promoting stiffness-induced PD-L1 expression (Miyazawa *et al.,* 2018). In this study, inhibition of actin polymerisation using cytochalasin D significantly reduced PD-L1 protein levels, suggesting an actin-dependent modulation of PD-L1 expression in lung cancer cells. More recently, αvβ3-integrin expression on tumour cells which positively correlates with metastatic phenotype and stemness, was shown to positively regulate PD-L1 expression in human glioblastoma GMB23 cells (Vannini *et al.,* 2019). Indeed, αvβ3 integrin have previously been shown to enhance breast cancer cell invasion through increasing cellular stiffness and cytoskeletal remodelling which enables the cells to generate and transmit contractile forces to overcome the steric hindrance of 3D ECMs (Mierke *et al.,* 2013). It maybe that in our 3D tumour models, cancer cells exhibit increased αvβ3 integrin expression and hence why we observed increased PD-L1 protein expression in some of our cell lines investigated. Furthermore, Vannini *et al.,* (2019) showed that αvβ3 integrin-deficient tumour cells exhibited a drastic reduction in the growth of primary tumours in an *in vivo* B19 melanoma mouse model which was accompanied by reduced PD-L1 expression resulting in the transition from an immunologically cold tumour to an immunologically hot tumour. Treatment of αvβ3 integrin-deficient tumours with anti-PD-1 therapy led to a durable response in mice compared to tumours with αvβ3 integrin intact, suggesting αvβ3-integrin serves as a critical component of the cancer immune evasion strategy via PD-L1 modulation and therefore warrants further investigation in our 3D tumour models of human cancer.

Here, the alginate model in particular serves as a good model to investigate this further, given that the stiffness of the alginate can be manipulated. Since the behaviours of cancer cells such as proliferation, invasion, metastasis, and their responses to treatments are highly modified by their surrounding environments including mechanical properties (Ansardamavandi *et al.,* 2018), the alginate model used in this study would therefore be more useful than 3D spheroids formed by hanging drop for investigating the effects of ECM stiffness on tumour progression in the different cell lines further. Moreover, the clonal spheroid colonies that are produced in the alginate model would be more representative of early tumour development in terms of stemness and offer more heterogeneous phenotypes to monitor how the 3D environment can influence malignancy and importantly PD-L1 expression.

Nevertheless, the alterations to PD-L1 expression by cancer cells that we observed in this study were consistent across the two different 3D tumour models, which may suggest that the mechanisms for regulating PD-L1 expression in 3D is intrinsic to these cancer cells rather than a result of external stimuli, or perhaps both models although different encourage similar external stimuli that influence the cancer cells in the same way to express these altered levels of PD-L1. It is well studied that culturing cancer cells in 3D can alter the intrinsic signalling of various pathways involved in tumorigenesis leading to the up- or down-regulation of downstream targets that change the cancer cells phenotype (Souza *et al.,* 2017; Souza *et al.,* 2018). Specific cancer cell intrinsic mechanisms that may be responsible for PD-L1 modulation in our 3D models could involve epigenetic modifications (up- or down-regulation of miRNAs that target PD-L1), oncogenic signalling (different cancer cells harbour different genetic mutations that influence tumorigenic pathway signalling that can influence PD-L1 expression), as well as post translational modifications (all reviewed extensively in Section 1.5 of this thesis). Certainly, the reasons for altered levels of PD-L1 in a 3D environment are likely to be cancer cell specific and warrants further investigation in each of the cell lines used in this study.

The fact that basal levels of PD-L1 expression can be manipulated in all these cell lines by using cytokines or more importantly 3D tumour models warrant them eligible for future investigation of the PD-1/PD-L1 signalling axis. In Chapter 4 of this thesis, we briefly demonstrated the implications of modulating PD-L1 expression with cytokines (IFNγ and/or TNFα) in our 3D alginate model to enhance the tumorigenic effects of PD-L1 blockade with Atezolizumab treatment in both high and low PD-L1 expressing breast cancer cell lines, MDA-MB-231 and MCF-7 cells, respectively. Consistently, Osta *et al.,* (2018) used IFNγ to increase PD-1 expression on ovarian cancer cells which potentiated the anti-tumour effects of anti-PD-1 therapy in an immune-independent setting (Osta *et al.,* 2018). The data here collectively support the use of cytokine modulation for increasing the efficacy of PD-1/PD-L1-targeted therapies as well as investigating the influence that treatment may have on tumour-intrinsic signalling. Indeed, cytokine therapy with immune potentiating effects are currently under preclinical and clinical investigations for the treatment solid tumours in combination with PD-1/PD-L1 targeted therapies (Kalateh *et al.,* 2020).

PD-L1 tumour-intrinsic signalling has been shown to promote cancer initiation, metastasis, development, and resistance to therapy in some cancers (Dong *et al.,*

2018; Hudson *et al.,* 2020). In TNBC, it has been established that PD-L1 expression correlates with EMT, cancer metastasis and resistance to apoptosis (Soliman *et al.,* 2014; Black *et al.,* 2016; Sun *et al.,* 2019). However, only recently the effects of anti-PD-L1 monoclonal antibodies on PD-L1 intrinsic signalling are being investigated in 2D-cultured cancer cells (Saleh *et al.,* 2019; Ali *et al.,* 2019; Wang *et al.,* 2020; Chen *et al.,* 2021), and these effects need to be fully elucidated in TNBC utilising 3D tumour models that more closely recapitulate *in vivo* human tumours. Hence, why in this study we utilised 2D and 3D TNBC models and in doing so showed that Atezolizumab can in fact modulate the cancer cells intrinsically resulting in a reduction in viability, ATP synthesis and phosphorylation of a broad range of kinases. This has been shown here for the first time in two different 3D tumour models.

Indeed, Atezolizumab has been reported to show agonistic properties previously (Ali *et al.,* 2019; Jin *et al.,* 2021; Hodgins *et al.,* 2022). Saleh *et al.,* (2019) was the first to report the ability of Atezolizumab to bind PD-L1 on monolayer-cultured MDA-MB-231 breast cancer cells and induce cell death and transcriptomic changes, independent of the immune system. Like in our study, Saleh *et al.,* (2019) demonstrated that Atezolizumab could modulate metabolic changes through downregulating genes involved in ATP synthesis. Here we showed using a functional assay that ATP production was significantly reduced in 2D and 3D tumour models of TNBC. Moreover, the PI3K/AKT and MAPK/ERK signalling pathways have been reported to be affected by PD-L1 blockade in four independent studies (Saleh *et al.,* 2019; Passariello *et al.,* 2019; Wang *et al.,* 2020; Chen *et al.,* 2021). However, these studies show contradictory roles of these signalling pathways following PD-L1 blockade to either promote or inhibit tumour progression. Here we showed that Atezolizumab treatment reduced AKT and ERK phosphorylation; important signalling molecules for conducting downstream signalling and activation of target genes involved in cell proliferation, survival, migration, and invasion (Guo *et al.,* 2020; Rascio *et al.,* 2021). Thus, here we believe the role of PD-L1 may be tumour promoting in TNBC cells (Figure 6.1).

Since Atezolizumab treatment reduced the phosphorylation of AKT in MDA-MB-231 TNBC cells compared to untreated control cells in our study, we can postulate that AKT signal activation may be reduced in these cells. A reduced level of active AKT would reduce downstream AKT-mediated target gene activation. Here, the phosphorylation of p70S6K, a downstream target of AKT signalling, was reduced in

Atezolizumab-treated cells. Previously, p70S6K has been shown to promote cell proliferation and invasion ability of NSCLC cells (Qiu *et al.,* 2016). p70S6K has also been reported to promote tumour growth via regulating protein synthesis and cell cycle progression (Harada *et al.,* 2001). In this study, PLCγ1 phosphorylation at Y783 was also reduced following Atezolizumab treatment, another downstream target of AKT which positively correlates with invasion and metastasis in breast and melanoma tumours (Raimondi *et al.,* 2016; Lattanzio *et al.,* 2019). All together this may suggest that Atezolizumab treatment may reduce the growth, invasion, and metastatic capabilities of TNBC cells via reducing AKT activation resulting in reduced p70S6K and PLCγ1 phosphorylation. Saleh *et al.,* (2019) has in fact demonstrated recently that treatment of MDA-MB-231 cells with Atezolizumab can downregulate genes involved in growth, invasion and metastasis using RNA-Seq. Moreover, PD-L1 silencing in melanoma mouse cells was reported to reduce tumour growth and metastases to the lungs of immunocompetent mice via reducing mTORC1 signalling (Clark *et al.,* 2016); another downstream target of AKT.

Moreover, AKT signalling is a negative regulator of p53 and vice versa (Liu *et al.,* 2015). Therefore, it was not surprising that the reduced phosphorylated AKT in Atezolizumab-treated cells may have resulted in the increased phosphorylation of p53 at Ser15, particularly since we observed changes to the cell's metabolic activity (Jones *et al.,* 2005; Loughery *et al.,* 2014). Activated p53 inhibits AKT signalling preventing glycolysis (Loughery *et al.,* 2014; Liu *et al.,* 2015), which may in part explain why we observed reduced ATP levels in our 2D and 3D TNBC models following Atezolizumab treatment. Chang *et al.,* (2015) reported that an anti-PD-L1 monoclonal antibody (10F.9G2) reduced glycolytic activity in sarcoma tumour cells via inactivation of the PI3K/AKT/mTOR pathway and the translation of glycolytic enzymes that regulate glycolysis within these cells. This may imply that Atezolizumab can induce metabolic changes in TNBC cells. In fact, Hodgins *et al.,* (2022) recently demonstrated that Atezolizumab binding to PD-L1 could reduce glycolysis in TRAMP-C2 prostate cancer cells, thus we are likely observing this same affect in TNBC cells.

Furthermore, the substantial reduction in ERK phosphorylation that we observed in this study also implies that the MAPK/ERK signalling pathway may be being modulated by Atezolizumab treatment in TNBC cells. Interestingly, MDA-MB-231 cells harbour KRAS and BRAF mutations which allow constitutive ERK signalling.

Signalling via this pathway has previously been shown to be inhibited through blocking PD-L1 with monoclonal antibodies (Passariello *et al.,* 2019; Chen *et al.,* 2021) and Chen *et al.,* (2021) demonstrated this also in MDA-MB-231 cells harbouring the two mutations. Here, several downstream targets of ERK also exhibited reduced phosphorylation, which may indeed suggest reduced ERK activation in Atezolizumab-treated cells. RSK1/2 and GSKα/β phosphorylation was reduced following Atezolizumab treatment and both these downstream targets of ERK are well known known to promote cell motility leading to invasion and metastasis via reducing cellular adhesion molecules and actin cytoskeleton remodelling (Sulzmaier and Ramos, 2013; Domoto *et al.,* 2020). Inhibition of both these effector molecules in preclinical studies has been shown to supress tumour growth and metastasis in many different cancer types (Wang *et al.,* 2008; Doehn *et al.,* 2009; Gawecka *et al.,* 2012; Zhang *et al.,* 2018). Similarly, p38α also exhibited reduced phosphorylation, another downstream target of ERK which is involved in promoting cell proliferation, invasion, and metastasis. Chen *et al.,* (2021) also reported p38α to exhibit reduced phosphorylation in response to PD-L1 blockade in TNBC cells which supressed tumour progression *in vivo.* The same study showed that PD-L1 regulates GSKβ phosphorylation via regulating the p38/MAPK pathway to promote EMT and aggressive TNBC phenotype, suggesting that the reduced phosphorylation of p38 and GSKα/β could also be linked in our study. These data collectively suggest that PD-L1 blockade with Atezolizumab may be able to influence the motility of TNBC cells to supress malignancy. A simple scratch assay approach would aid in confirming this claim of PD-L1 blockade to effect motility of TNBC cells. Lastly, MSK1/2 important regulators of cell survival and proliferation activated by ERK signalling as well as p38α (Roux and Blenis, 2004), showed reduced phosphorylation following Atezolizumab treatment, which may indicate that PD-L1 blockade may also influence the viability and proliferative capacity of TNBC cells.
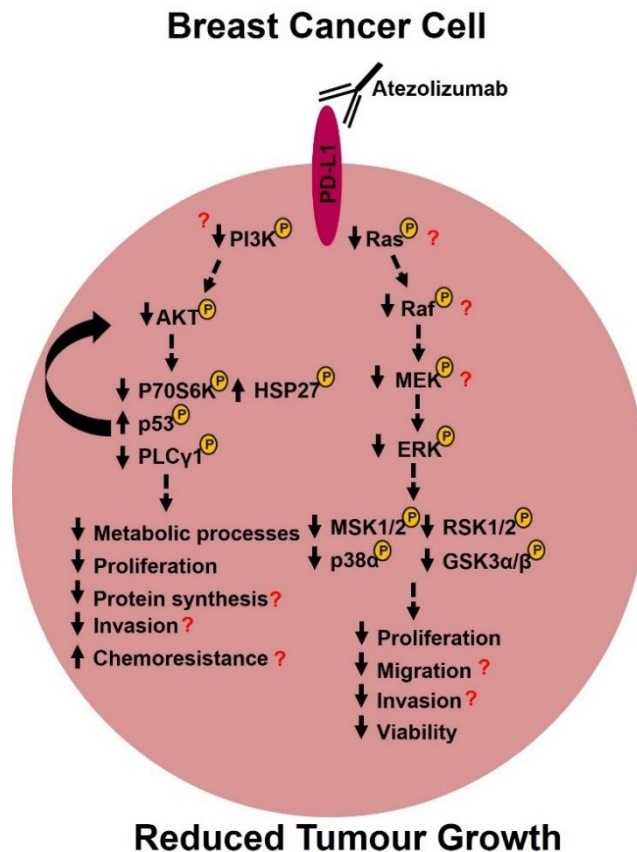
Breast Cancer Cell

Reduced Tumour Growth

Figure 6.1 A schematic representation of the proposed mechanism of PD-L1 intrinsic signalling following Atezolizumab treatment in TNBC cells. Atezolizumab binding to PD-L1 on the surface of TNBC cells potentially induces intrinsic signalling leading to altered phosphorylation levels on several kinases involved in the PI3K/AKT and MAPK/ERK pathways. These alterations may induce or prevent the activation of other downstream signalling molecules, ultimately effecting the transcription of target genes important for metabolic processes, cell proliferation, protein synthesis, cell viability, migration, invasion, and drug resistance. The red question marks indicate parts of the proposed mechanism which would need to be investigated in future experiments to make these potential findings conclusive.

Rather than PD-L1 blockade having a direct effect on the PI3K/AKT and MAPK/ERK pathways as we and a few others may have first thought, a very recent study has shown that PD-L1 engagement with cellular ligands or therapeutically approved antibodies, including Atezolizumab, supresses the type I IFN pathway which is in fact known to regulate these pathways (Hodgins *et al.,* 2022). This may suggest that the PI3K/AKT and MAPK/ERK pathways are affected by PD-L1 blockade indirectly downstream of PD-L1 in cancer cells. Activation of the type I IFN signalling pathway

has various downstream targets including STATs, MAPK, PI3K, p38, MSK1/2 and mTOR, to name a few (David, 2002). Some of these downstream targets were modulated by PD-L1 blockade in our study (Figure 6.1). Hodgins *et al.,* (2022) shows that PD-L1 interacts with CD80 on the surface of cancer cells which in turn inhibited type I IFN responses. They show that PD-L1 regulates the JAK/STAT pathway by decreasing STAT1 and increasing STAT3 phosphorylation (Hodgins at *et al.,* 2022). In our study, PD-L1 blockade with Atezolizumab increased STAT1 and decreased STAT3 phosphorylation, which may imply that Atezolizumab-mediated inhibition of type I IFN response is occurring in our TNBC models. To solidify these findings the type I IFN response pathway would need to be thoroughly investigated in our models by using type I IFNs to stimulate the TNBC cells and assessing downstream signalling with and without PD-L1 blockade with Atezolizumab.

In our functional assays we only observed modest effects on growth and viability of TNBC cells in 2D and 3D tumour models following Atezolizumab treatment. This lack of response here, could be the timepoint in which these parameters were assessed, as the preliminary data generated from the Phospho-Kinase array suggests that proliferation and viability is likely to be affected by Atezolizumab treatment, at least eventually. Our functional assays could be performed at a later timepoint to test this theory, or more robust methodologies could be applied to measure these parameters. For example, spatial distribution of Ki67 in 3D TNBC tumour models would be more informative of the effects of Atezolizumab on proliferation, also tracking proliferation overtime in 2D and 3D TNBC tumour models using labelling dyes such as those used in CellTrace CFSE Cell Proliferation Kit would potentially be more insightful than endpoint analysis.

Alternatively, the lack of response observed in our functional assays could imply that PD-L1 blockade with Atezolizumab may not be sufficient to reduce proliferation or induce cell death in TNBC cells, at least to detectable levels with the functional assays we used in this study. However, consistent with our findings, Mohan *et al.,* (2019) showed that Atezolizumab was unable to inhibit the growth of TNBC cell lines (MDA-MB-231 and BT20) but was able to supress invasion and motility, suggesting that Atezolizumab may be capable of only partially inhibiting tumorigenic PD-L1 in TNBC.

To test this theory, we knocked down PD-L1 in MDA-MB-231 TNBC cells and compared its biological effects to PD-L1 blockade with Atezolizumab. Indeed, we

observed more pronounced effects with PD-L1 knockdown on the growth, viability, metabolic activity, and spheroid forming capabilities of MDA-MB-231 TNBC cells, suggesting that intrinsic targeting of PD-L1 may be more sufficient at supressing the pro-tumour role of PD-L1 in TNBC cells rather than blocking PD-L1 on the cell surface. To our knowledge only one group of researchers have investigated PD-L1 knockdown and PD-L1 blockade with therapeutically approved anti-PD-L1 monoclonal antibodies in the same study (Wang *et al.,* 2020), however they did not make a direct comparison and instead showed that both PD-L1-targeting strategies were capable of inducing tumour-intrinsic signalling; as we have done here. This study also investigated lung and colorectal cancer cell lines cultured in 2D monolayer, whereas our study looked at TNBC cells in both 2D monolayer and 3D tumour models (Wang *et al.,* 2020).

Our study for the first time shows that PD-L1 knockdown reduces the growth, viability, metabolic activity, and spheroid forming capabilities of TNBC cells cultured in two different 3D cell culture models. Demonstrating that PD-L1 has a pro-tumour role in 3D TNBC tumour models further strengthens our and other researcher's conclusions that PD-L1 is tumour promoting in TNBC cells, since 3D tumour models are more representative of *in vivo* human tumours than 2D monolayer cultures. The Phospho-Kinase Array performed in this study also provides insight into the potential mechanisms responsible for these biological effects observed following PD-L1 knockdown in TNBC cells (Figure 6.2). Most studies that have investigated PD-L1 knockdown in tumour cells have demonstrated that the PI3K/AKT/mTOR and MAPK/ERK signalling pathways show reduced activation which was found responsible for the reduced tumour growth, viability, and metabolic activity that they also observed. Here we showed that the phosphorylation of AKT and several kinases downstream of both PI3K/AKT/mTOR and MAPK/ERK pathways were either reduced or enhanced following PD-L1 knockdown, suggesting that our study's findings is in line with the available literature.

A reduction in the growth and viability following PD-L1 knockdown has previously been reported in 2D monolayer cultures or *in vivo* mouse models of melanoma (Clark *et al.,* 2016), osteosarcoma (Liao *et al.,* 2017), gastric (Li *et al.,* 2017), and breast cancer (Ghebeh *et al.,* 2010; Chen *et al.,* 2021). c-Jun plays a key role in driving cell cycle progression and promoting tumour growth (Lukey *et al.,* 2016), and this downstream target of AKT was substantially reduced in PD-L1 knockdown cells in

our study. In line with this, p53 activation which is normally suppressed by c-Jun was increased here in PD-L1 knockdown cells, suggesting that reduced c-Jun activation may have led to the increased p53 phosphorylation, and hence may be responsible for the reduced growth and proliferative capacity of PD-L1 knockdown cells in which we observed, particularly in our 3D alginate model (Figure 6.2). The ability of cancer cells to proliferate from a single cell is an important characteristic required for tumour progression (Jiao *et al.,* 2010; Kuo *et al.,* 2016). Here, in our alginate model, TNBC cells harbouring PD-L1 knockdown were unable to form clonogenic spheroid colonies from single cells in 3D, indicating that PD-L1 expression is required for the spheroid forming capabilities of TNBC cells. Indeed, previous studies have reported that PD-L1 knockdown weakens a cancer cell's ability of forming colonies (Yu *et al.,* 2020; Chen *et al.,* 2021). For the first time we show this in a 3D cell culture environment. Also, other studies have shown that PD-L1 knockdown reduces the CSC phenotype of melanoma, ovarian and breast cancer cells (Gupta *et al.,* 2016; Almozyan *et al.,* 2017). The lack of colony formation that we observed in our 3D alginate model could be explained by PD-L1 knockdown cells exhibiting reduced cancer stemness. This study's findings of c-Jun being substantially reduced following PD-L1 knockdown could indicate that OCT4 may also be reduced in our cells due to it previously been shown that c-Jun-mediated transactivation of the OCT4 promoter and vice versa is crucial for promoting cancer development and maintaining cancer stemness in liver and breast cancer (Jiao *et al.,* 2010; Kuo *et al.,* 2016). Almozyan *et al.,* (2017) showed that PD-L1 expression promoted OCT4 and Nanog expression via the PI3K/AKT/mTOR signalling pathway and therefore this could explain why when we reduced PD-L1 expression via PD-L1 knockdown that AKT and c-Jun activation was reduced and TNBCs cells exhibited an inability to form colonies in alginate.

Interestingly, PYK2 phosphorylation was found to be increased in PD-L1 knockdown cells in this study. PYK2 has been shown to promote apoptosis and reduce cancer cell viability in multiple myeloma, glioblastoma, lung and prostate cancer cells (Shen *et al.,* 2018). In breast cancer though, the role of PYK2 is understood to be an oncogene promoting AKT and ERK signalling (Burdick *et al.,* 2006), but since we observed an increase in PYK2 here and reduced AKT and ERK signalling, it may suggest a dual role of PYK2 in TNBC dependent on the experimental conditions (Figure 6.2). PYK2 may regulate downstream signalling beyond the AKT and ERK pathways. In prostate cancer, PYK2 has been shown to act as a tumour suppressor

and oncogene (Shen *et al.,* 2018), which may support our theory and could explain why we observed reduced viability in PD-L1 knockdown cells in 2D and 3D TNBC tumour models. Furthermore, AKT and/or p38α/ERK signalling have also been shown to regulate the phosphorylation of CREB and HSP27 which have both been shown to promote cancer cell survival (Steven and Seliger, 2016; Lampros *et al.,* 2022). Here, CREB and HSP27 phosphorylation was substantially reduced which could also explain the reduced viability we observed in our 2D and 3D TNBC tumour models.

Although the role of PD-L1 on drug resistance was not investigated in this study, reduced phosphorylation of CREB and HSP27 could indicate that PD-L1 knockdown in TNBC cells may exhibit increased chemosensitivity (Figure 6.2), since high levels of both these signalling molecules have been associated with chemotherapy resistance in tumour cells previously (Steven and Seliger, 2016; Lampros *et al.,* 2022). Interestingly, in this study Atezolizumab treated cells showed the opposite and exhibited increased levels of HSP27 phosphorylation. Hence if our theory was correct, this would mean that PD-L1 blockade with Atezolizumab may in fact promote chemoresistance and hyperprogression, regardless of its other anti-tumour properties. Atezolizumab has been shown previously to promote chemotherapy resistance in lung and colorectal cancer cells via AKT and ERK signalling (Wang *et al.,* 2020). Similarly, in human colorectal cancer cells the targeting of PD-L1 reduced tumour growth *in vitro* and *in vivo* but at the same time supressed the expression of pro-apoptotic proteins which promoted chemotherapy resistance in these cells (Feng *et al.,* 2015). This highlights the importance of understanding the role of PD-L1 in all cancer types to assist in selecting cancer patients eligible for monoclonal antibody treatment. It may also suggest that targeting PD-L1 intrinsically provides the most promise at eradicating the tumorigenic functions of PD-L1. Ghebeh *et al.,* (2010) demonstrated how PD-L1 knockdown in breast cancer cells was able to increase chemotherapy induced apoptosis, and more recently it has been reported that targeting PD-L1 for degradation also enhances chemosensitivity in breast cancer cells (Chen *et al.,* 2021).
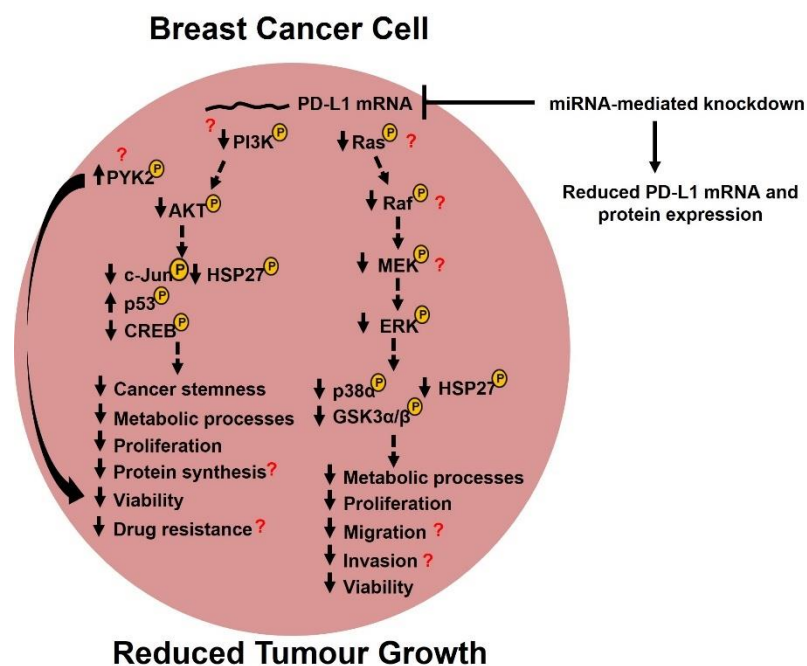
Figure 6.2 A schematic representation of the proposed effects of PD-L1 knockdown in TNBC cells. Reducing PD-L1 expression by miRNA-mediated knockdown potentially induces intrinsic signalling leading to altered phosphorylation levels on several kinases involved in the PI3K/AKT and MAPK/ERK pathways. These alterations may induce or prevent the activation of other downstream signalling molecules, ultimately effecting the transcription of target genes important for metabolic processes, cell proliferation, protein synthesis, cell viability, migration, invasion, and drug resistance. The red question marks indicate parts of the proposed mechanism which would need to be investigated in future experiments to make these potential findings conclusive.

Consistent with our findings, Chen *et al.,* (2021) demonstrated that knocking out PD-L1 in MDA-MB-231 cells achieved a more stable interruption of EMT and their aggressive status compared to PD-L1 knockdown using a siRNA approach. This highlights that the complete removal of PD-L1 expression may be necessary to eradicate the tumorigenic intrinsic functions of PD-L1 completely. In our study, we observed this same difference in the biological interruption of PD-L1 function when we reduced PD-L1 expression via miRNA-mediated knockdown as opposed to only blocking it at the cell surface. Additionally, monoclonal antibodies targeting the degradation of PD-L1 were shown to have similar effects to PD-L1 knockout (Chen

et al., 2021); again, suggesting the removal of PD-L1 from TNBC cells is likely the way forward to eradicate the tumorigenic functions of PD-L1. The influence that therapeutically approved monoclonal antibodies may have on PD-L1 degradation is largely unknown and needs investigating in the future. It could be that some of the approved monoclonal antibodies may exert their anti-tumour effects via this mechanism of initiating PD-L1 degradation as opposed to immune system reactivation alone as scientists first understood.

Since monoclonal antibodies have only proven clinically successful in a limited number of cancer types, recent studies have pointed out that PD-L1 produced by tumour cells is also present in circulating endosomes, the Golgi apparatus, and vesicles in the cells, indicating that PD-L1 may be constantly renewed at the cell surface, replacing inactivated PD-L1, which may be one of the causes of antibody drug failure (Wu *et al.,* 2020). Alternatively, it may be that PD-L1 is being expressed by tumour cells but not being presented on the cell surface and found only in intracellular compartments; conferring resistance to monoclonal antibodies targeting PD-L1 thus allowing PD-L1 to exert its tumorigenic functions. This has certainly been shown to be the case for prostate cancer cells (Poggio *et al.,* 2019). Prostate cancer is well known for its lack of response to PD-1/PD-L1-taregted therapies and scientists have long thought this was due to low PD-L1 expression by the prostate cancer cells (Martin *et al.,* 2015). However, Poggio *et al.,* (2019) demonstrated that prostate cancer cells in fact express high levels of PD-L1 which is released from exosomes that are secreted by the tumour cells. This would also explain why we observed low PD-L1 expression at mRNA and protein levels in LNCaP and PC3 prostate cancer cell lines in the earlier Chapters. The exosomes were shown to travel to the lymph nodes and deactivate immune cells before they could reach the tumour site through releasing PD-L1 (Poggio *et al.,* 2019). Hence, explaining the low response observed in prostate cancer patients. It is also highly likely that drug resistance mediated by exosome-derived PD-L1 is not exclusive to prostate cancer and requires further investigation across all cancer types. Exosome production and the presence of PD-L1 in exosomes could be assessed using confocal microscopy or by using the latest flow cytometry ZE5 Cell Analyzer.

Small molecule inhibitors that inhibit PD-L1 transcription (JQ1 and Osimertinib), translation (eFT508) and promote PD-L1 degradation (Curcumin) are currently under preclinical investigation and have demonstrated their anti-tumour capabilities to

repress tumour growth and migration in many different cancer models *in vitro* and *in vivo* more so than monoclonal antibodies (Zhan *et al.,* 2016; Wu *et al.,* 2020). These small molecules suppress PD-L1 expression and therefore have the potential to eradicate the tumorigenic functions of PD-L1 across all cancer types. They also have the potential to overcome drug resistance, as well as the immune-related adverse effects associated with monoclonal antibody treatment. However, these small molecules are far from entering clinical development due to their low affinity for their target and short half-life (Zhan *et al.,* 2016; Wu *et al.,* 2020). Since it is evident that targeting PD-L1 intrinsically is likely to be more beneficial to suppress tumorigenic PD-L1 functions, future work should focus on screening for small molecules with higher affinity for their targets and investigate approaches of coupling small molecules to cancer cell-specific conjugates that have the potential to increase their therapeutic efficacy by minimising off-target effects.

Other future work should investigate PD-L1 blockade versus intrinsic targeting of PD-L1 in 3D immune cell-cancer cell co-cultures to further elucidate this emerging tumorigenic role of PD-L1 in TNBC cells depicted in this study to determine the effects both strategies may have on immune cell effector function. Since PD-L1 knockdown has a greater impact on the TNBC cell growth, viability, metabolic activity, and spheroid-forming capabilities compared to PD-L1 blockade with Atezolizumab, we could postulate that the TNBC cells would be more susceptible to immune mediated cancer cell killing in an immune co-culture setting. Particularly, the reduction in ATP production that we observed by Atezolizumab-treated cells and even more so with cells harbouring PD-L1 knockdown using the CellTiter-Glo® Assays suggests that the TNBC cells are less metabolically active, and hence using less glucose and oxygen from their surrounding tumour microenvironment. This may therefore suggest that there would be more nutrients available for immune cells which is paramount in order for them to function effectively. It is well known that low nutrients found in solid tumours is inhibitory to immune cell effector functions and hence why immune cells show limited migratory capacity to the core of tumours (Boucherit *et al.,* 2020). Therefore, in a 3D co-culture system with low metabolically active cancer cells, the immune cells in theory should be more cytotoxic towards the cancer cells since there is more nutrients available for them to metabolise and produce more ATP themselves. In support of this, Chang *et al.,* (2015) reported that checkpoint blockade could induce an increase in glucose concentration within a progressive tumour mouse model. This increased glucose concentration enhanced

the glycolytic capacity of tumour infiltrating lymphocytes and increased IFNγ production signifying increased T cell activation (Chang *et al.,* 2015). Similarly, Hodgins *et al.,* (2022) reported that PD-L1 expression directly mediates increased lactate production via glycolysis which inhibited the IFN signalling axis. Targeting PD-L1 using Atezolizumab reduced glycolysis and thus the levels of ATP produced by the TRAMP-C2 prostate cancer cells (Hodgins *et al.,* 2022).

3D spheroids aggregates like those formed by hanging drop in this study are by far the most widely used 3D cell culture model for immune co-culture systems since immune cell migration into the tumour spheroid can be monitored relatively easily (Law *et al.,* 2021). However, scaffold-based systems like the alginate model used in this study allow stiffness modulation and mimic cell-ECM interactions which are important modulators of cancer cell and immune cell function. Tumour stiffness can be a limiting factor for immune cell migration, hence incorporating this component into a 3D co-culture system better recapitulates the *in vivo* tumour microenvironment (Boucherit *et al.,* 2020). Since, PD-L1 knockdown in our alginate model prevented the TNBC cell's ability to form spheroid colonies it would be interesting to investigate how different immune cell types may affect the cancer cells in this setting. For example, tumour-promoting cell types such as MDSCs or Tregs may restore the cancer cell's ability to proliferate or protect them from apoptosis. The paracrine signalling that occurs between tumour cells and immunosuppressive cell types is well known to promote tumour survival and growth (Lorenzo-Sanz and Muñoz, 2019). These types of studies could potentially reveal resistance mechanisms mediated employed by immunosuppressive cell types in tumour microenvironment when therapeutically targeting the PD-L1/PD-1 signalling axis.

Furthermore, in this study we also assessed the expression of HLA-ABC and death receptor expression across a broad range of human cancer cell lines (breast, prostate, and colorectal cancer cell lines) cultured in 2D monolayer and 3D tumour models which has the potential to guide the development of future *in vitro* experiments for investigating the PD-L1/PD-1 signalling axis in a 3D cancer-immune cell setting.

It is important for cancer cells to express MHC-I in order for PD-1/PD-L1-targeted therapies to be able to work efficiently in promoting a CD8+ T cell-mediated anti-tumour immune response. A recent study showed that chemotherapy resistant ovarian cancer cells were less susceptible to CD8+ T cell-mediated killing following

anti-PD-1 therapy because they displayed reduced MHC-I expression (Natoli *et al.,* 2020). From looking at our expression data we could postulate that MCF-7 breast cancer cells cultured in 3D cell culture would be least susceptible to CD8+ T cell-mediated killing and activation of an anti-tumour immune response following PD-1/PD-L1-targeted therapy amongst the different cancer cell lines investigated because of their significant reduction in MHC-I protein expression. Similarly, death receptor expression by cancer cells is also important for immune-mediated killing. TRAIL expressed by T cells, NK cells, dendritic cells and macrophages can bind death receptors on immune cells and promote receptor-mediated apoptosis in cancer cells (Walczak, 2013). In this study, DR5 expression was reduced by MDA-MB-231 breast cancer cells and DR4 was reduced by PC3 prostate and SW620 colorectal cancer cells in both 3D cell culture models, which could suggest that these cells would be less responsive to TRAIL-mediated apoptosis in 3D cell culture than 2D monolayer. Hendricks *et al.,* (2016) showed the potential synergy of co-targeting PD-L1 and TRAIL using a bi-specific protein in monolayer-cultured melanoma cells. These cells underwent PD-L1-directed TRAIL-mediated apoptosis and in a co-culture with T cells the bi-specific protein augmented T cell activation (Hendricks *et al.,* 2016). Since here we showed a high proportion of MDA-MB-231 and PC3 cells express PD-L1 in 3D, they would be good models to use for combining TRAIL and PD-L1 blockade in an 3D immune co-culture model to sensitise these cells to TRAIL-mediated apoptosis. Future studies should investigate this cooperation of TRAIL and PD-L1 targeting in different cancer types. With the cancer specific nature of TRAIL, it makes it appealing to combined with immune checkpoint blockade to potentially reduce the immune adverse effects observed in some patients treated with immunotherapies. HLA-ABC (MHC-I) and death receptor downregulation observed in this studies 3D tumour models emphasises the need to investigate cancer cell-immune cell interactions in a 3D environment that more closely recapitulates the immune evasion mechanisms employed by cancer cells observed in *in vivo* human tumours (Shin *et al.,* 2001; Martínez-Lostao *et al.,* 2015; Chandrasekaran *et al.,* 2014).

7. Final Conclusions

Conclusively, this thesis provides new insights into the expression of immunological and tumorigenic proteins by diverse human cancer cells; demonstrates how PD-L1 blockade with Atezolizumab may influence PD-L1 intrinsic signalling in TNBC cells; and reveals that PD-L1 may in fact exhibit a pro-tumour role in breast cancer cells; not only in 2D monolayer but for the first time in two different 3D cell culture models. Importantly, this study prompts the investigation of PD-L1 blockade versus intrinsic targeting of PD-L1 in 3D immune cell-cancer cell co-cultures and/or *in vivo* mouse models to further elucidate this emerging tumorigenic role of PD-L1 in TNBC; with the hopes to reveal the implications these treatments may have on immune cell function, and potential resistance mechanisms employed by TNBC cells that could be co-targeted with anti-PD-L1 immunotherapies to ultimately improve their efficacy for treating TNBC patients.

8. References

Abida W. Cheng ML. Amernia J. Middha S. Autio KA. Rathkopf DE. *et al.,* Microsatellite instability in prostate cancer and response to immune checkpoint blockade. *J. Clin. Oncol.* 2018; 36:5020. doi: 10.1200/JCO.2018.36.15_suppl.5020

Ahn H. Yang JM. Kim H. Chung JH. Ahn SH. Jeong WJ. *et al.,* Clinicopathologic implications of the miR-197/PD-L1 axis in oral squamous cell carcinoma. *Oncotarget.* 2017; 8(39):66178–94. doi: 10.18632/oncotarget.19842

Akbay EA. Koyama S. Carretero J. Altabef A. Tchaicha JH. Christensen CL. *et al.,* Activation of the PD-1 pathway contributes to immune escape in EGFR-driven lung tumors. *Cancer Discov.* 2013; 3(12):1355–1363. doi: 10.1158/2159-8290.CD-13-0310

Al Tameemi W. Dale TP. Al-Jumaily RMK. Forsyth NR. Hypoxia-modified cancer cell metabolism. *Front. Cell Dev. Biol.* 2019; 7:4. doi: 10.3389/fcell.2019.00004

Alavi S. Stewart AJ. Kefford RF. Lim SY. Shklovskaya E. Rizos H. Interferon Signaling Is Frequently Downregulated in Melanoma. *Front Immunol.* 2018; 9:1414. doi: 10.3389/fimmu.2018.01414

Alessandri K. Sarangi BR. Gurchenkov VV. Sinha B. Kießling TR. Fetler L. *et al.,* Cellular capsules as a tool for multicellular spheroid production and for investigating the mechanics of tumor progression in vitro. *Proc. Natl. Acad. Sci. USA.* 2013; 110 (37):14843. doi:10.1073/pnas.1309482110

Ali MHM. Toor SM. Rakib F. Mall R. Ullah E. Mroue K. *et al.,* Investigation of the Effect of PD-L1 Blockade on Triple Negative Breast Cancer Cells Using Fourier Transform Infrared Spectroscopy. *Vaccines (Basel).* 2019; 7(3):109. doi: 10.3390/vaccines7030109

Almozyan S. Colak D. Mansour F. Alaiya A. Al-Harazi O. Qattan A. *et al.,* PD-L1 promotes OCT4 and Nanog expression in breast cancer stem cells by sustaining PI3K/AKT pathway activation. *Int J Cancer.* 2017; 141:1402–12. doi: 10.1002/ijc.30834

Alsuliman A. Colak D. Al-Harazi O. Fitwi H. Tulbah A. Al-Tweigeri T. *et al.,* Bidirectional crosstalk between PD-L1 expression and epithelial to mesenchymal transition: significance in claudin-low breast cancer cells. *Mol. Cancer.* 2015; 14:149. doi: 10.1186/s12943-015-0421-2

André T. Shiu KK. Kim TW. Jensen BV. Jensen LH. Punt C. *et al.,* Pembrolizumab in Microsatellite-Instability-High Advanced Colorectal Cancer. *N. Engl. J. Med.* 2020; 383(23):2207-2218. doi: 10.1056/NEJMoa2017699

Ansardamavandi A. Tafazzoli-Shadpour M. Shokrgozar MA. Behavioral remodeling of normal and cancerous epithelial cell lines with differing invasion potential induced by substrate elastic modulus. *Cell Adhesion & Migration.* 2018. 12(5): 472-488. doi: 10.1080/19336918.2018.1475803

Ansell SM. Lesokhin AM. Borello I. Halwani A. Scott EC. Gutierrez M. *et al.,* PD-1 blockade with Nivolumab in relapsed and refractory Hodgkin's lymphoma. *N. Engl. J. Med.* 2015; 372:1277–90. doi: 10.1056/NEJMoa1411087

Antonia SJ. López-Martin JA. Bendell J. Ott P., Taylor M. Eder JP. *et al.,* Nivolumab alone and nivolumab plus ipilimumab in recurrent small-cell lung cancer (CheckMate 032): a multicentre, open-label, phase 1/2 trial. *Lancet Oncol.* 2016; 17:883–95. doi: 10.1016/S1470-2045(16)30098-5

Antonia SJ. Villegas A. Daniel D. Vicente D. Murakami S. Hui R. *et al.,* Overall survival with durvalumab after chemoradiotherapy in stage III NSCLC. *N Engl J Med.* 2018; 379:2342–50. doi: 10.1056/NEJMoa1809697

Antonia SJ. Villegas A. Daniel D. Vicente D. Murakami S. Hui R. *et al.,* Overall survival with durvalumab after chemoradiotherapy in stage III NSCLC. *N. Engl. J. Med.* 2018; 379:2342–50. doi: 10.1056/NEJMoa1809697

Aptsiauri N. Cabrera T. Garcia-Lora A. Lopez-Nevot MA. Ruiz-Cabello F. Garrido F. MHC class I antigens and immune surveillance in transformed cells. *Int. Rev. Cytol.* 2007; 256:139-89. doi: 10.1016/S0074-7696(07)56005-5

Arhoma A. Chantry AD. Haywood-Small SL. Cross NA. SAHA-induced TRAIL-sensitisation of Multiple Myeloma cells is enhanced in 3D cell culture. *Exp. Cell Res.* 2017;360(2):226-235. doi: 10.1016/j.yexcr.2017.09.012

Ashkenazi A. Holland P. Eckhardt SG. Ligand-based targeting of apoptosis in cancer: the potential of recombinant human apoptosis ligand 2/Tumour necrosis factor-related apoptosis-inducing ligand (rhApo2L/TRAIL). *J. Clin. Oncol.* 2008; 26(21):3621-30. doi: 10.1200/JCO.2007.15.7198

Ayers M. Lunceford J. Nebozhyn M. Murphy E. Loboda A. Kaufman DR. *et al.,* IFN-γ–related mRNA profile predicts clinical response to PD-1 blockade. *J. Clin. Invest.* 2017; 127(8):2930-2940. doi:10.1172/JCI91190.

Azadi S. Es HA. Bazaz SR. Thiery JP. Asadnia M. and Warkiani ME. Upregulation of PD-L1 Expression in Breast Cancer Cells Through the Formation of 3D Multicellular Cancer Aggregates Under Different Chemical and Mechanical Conditions. *Biochim. Biophys. Acta. Mol. Cell. Res.* 2019;1866(12):118526. doi: 10.1016/j.bbamcr.2019.118526

Azuma T. Yao S. Zhu G. Flies AS. Flies SJ. and Chen L. B7-H1 is a ubiquitous antiapoptotic receptor on cancer cells. *Blood.* 2008; 111(7):3635-3643. doi: 10.1182/blood-2007-11-123141

Baas P. Scherpereel A. Nowak AK. Fujimoto N. Peters S. Tsao AS. *et al.,* First-line nivolumab plus ipilimumab in unresectable malignant pleural mesothelioma (CheckMate 743): a multicentre, randomised, open-label, phase 3 trial. *Lancet.* 2021; 397(10272):375-386. doi: 10.1016/S0140-6736(20)32714-8

Bae J. Hideshima T. Tai YT. Song Y. Richardson P. Raje N. *et al.,* Histone deacetylase (HDAC) inhibitor ACY241 enhances anti-tumor activities of antigen-specific central memory cytotoxic T lymphocytes against multiple myeloma and solid tumors. *Leukemia.* 2018; 32(9):1932–1947. doi: 10.1038/s41375-018-0062-8

Bai J. Goa Z. Li X. Dong L. Han W. Nie J. Regulation of PD-1/PD-L1 pathway and resistance to PD-1/PD-L1 blockade. *Oncotarget.* 2017; 8:110693–707. doi: 10.18632/oncotarget.22690

Balar AV. Castellano D. O'Donnell PH. Grivas P. Vuky J. Powels T. *et al.,* First-line pembrolizumab in cisplatin-ineligible patients with locally advanced and unresectable or metastatic urothelial cancer (KEYNOTE-052): A multicentre, single-arm, phase 2 study. *Lancet Oncol.* 2017; 18(11): 1483-1492. doi: 10.1016/S1470-2045(17)30616-2

Barretina. J. Caponigro G. Stransky N. Venkatesan K. Margolin AA. Kim S. *et al.,* The Cancer Cell Line Encyclopedia enables predictive modelling of anticancer drug sensitivity. *Nature.* 2021; 483, 603–607. doi: 10.1038/nature11003

Barrett MT. Anderson KS. Lenkiewicz E. Andreozzi M. Cunliffe HE. Klassen CL. *et al.,* Genomic amplification of 9p24.1 targeting JAK2, PD-L1, and PD-L2 is enriched in high-risk triple negative breast cancer. *Oncotarget.* 2015; 6(28):26483–26493. doi: 10.18632/oncotarget.4494

Barsoum IB. Smallwood CA. Siemens DR. and Graham CH. A mechanism of hypoxia-mediated escape from adaptive immunity in cancer cells. *Cancer Res.* 2014; 74(3):665–674. doi: 10.1158/0008-5472.CAN-13-0992

Bartel DP. MicroRNAs: genomics, biogenesis, mechanism, and function. *Cell.* 2004; 116(2):281-97. doi: 10.1016/s0092-8674(04)00045-5

Bass AJ. Thorsson V. Shmulevich I. Reynolds SM. Miller M. Bernard B. *et al.,* Comprehensive molecular characterization of gastric adenocarcinoma. *Nature.* 2014; 513(7517):202–209. doi: 10.1038/nature13480

Bauml J. Seiwert TY. Pfister DG. Worden F. Liu SV. Gilbert J. *et al.,* Pembrolizumab for platinum- and cetuximab-refractory head and neck cancer: results from a single-arm, phase II study. *J. Clin. Oncol.* 2017; 35:1542–9. doi: 10.1200/JCO.2016.70.1524

Beatty GL, Gladney WL. Immune escape mechanisms as a guide for cancer immunotherapy. *Clin. Cancer. Res.* 2015; 15;21(4):687-92. doi: 10.1158/1078-0432

Bellucci R. Martin A. Bommarito D. Wang K. Hansen SH. Freeman GJ. *et al.,* Interferon-γ-induced activation of JAK1 and JAK2 suppresses tumor cell susceptibility to NK cells through upregulation of PD-L1 expression. *Oncoimmunol.* 2015; 4(6):e1008824. doi: 10.1080/2162402X.2015.1008824

Bertucci F. Gonçalves A. Immunotherapy in Breast Cancer: the Emerging Role of PD-1 and PD-L1. *Curr Oncol Rep.* 2017; 19(10):64. doi: 10.1007/s11912-017-0627-0

Bianco SR. Sun J. Fosmire SP. Hance K. Padilla ML. Ritt MG. *et al.,* Enhancing antimelanoma immune responses through apoptosis. *Cancer Gene Ther.* 2003; 10(9):76-36. doi: 10.1038/sj.cgt.7700625

Black M. Barsoum IB. Truesdell P. Cotechini T. Macdonald-Goodfellow SK. Petroff M. *et al.,* Activation of the PD-1/PD-L1 immune checkpoint confers tumor cell chemoresistance associated with increased metastasis. *Oncotarget.* 2016; 7:10557–15567. doi: 10.18632/oncotarget.7235

Booth L. Roberts JL. Poklepovic A. Dent P. [pemetrexed + sildenafil], via autophagy-dependent HDAC downregulation, enhances the immunotherapy response of NSCLC cells. *Cancer Biol. Ther.* 2017; 18(9):705-714. doi: 10.1080/15384047.2017.1362511

Booth L. Roberts JL. Poklepovic A. Kirkwood J. Dent P. HDAC inhibitors enhance the immunotherapy response of melanoma cells. *Oncotarge*t. 2017; 8(47):83155–70. doi: 10.18632/oncotarget.17950

Boucherit N. Gorvel L. Olive D. 3D Tumor Models and Their Use for the Testing of Immunotherapies. *Front. Immunol.* 2020. doi: 10.3389/fimmu.2020.603640

Brahmer J. Reckamp KL. Baas P. Crinò L. Eberhart WEE. Poddubskaya E. *et al.,* Nivolumab versus docetaxel in advanced squamous-cell non-small-cell lung cancer. *N Engl J Med.* 2015; 373:1803–13. doi: 10.1056/NEJMoa1504627

Breslin S. O'Driscoll L. Three-dimensional cell culture: The missing link in drug discovery. *Drug Discov.* 2013; 18(5-6): 240-249. doi: 10.1016/j.drudis.2012.10.003

Briere D. Sudhakar N. Woods DM. Hallin J. Engstrom LD. Aranda R. *et al.,* The class I/IV HDAC inhibitor mocetinostat increases tumor antigen presentation, decreases immune suppressive cell types and augments checkpoint inhibitor therapy. *Cancer Immunol. Immunother.* 2018;67(3):381-392. doi: 10.1007/s00262-017-2091-y

Buchbinder E. Desai A. CTLA-4 and PD-1 Pathways Similarities, Differences and Implications of Their Inhibition. *Am. J. Clin. Oncol.* 2016; 39(1):98-106. doi: 10.1097/COC.0000000000000239

Budczies J. Bockmayr M. Denkert C. Klauschen F. Gröschel S. Darb-Esfahani S. *et al.,* Pan-cancer analysis of copy number changes in programmed death-ligand 1 (PD-L1, CD274) – associations with gene expression, mutational load, and survival. *Gene Chromosome Canc.* 2016; 55(8):626-639. doi: 10.1002/gcc.22365

Budczies J. Mechtersheimer G. Denkert C. Klauschen F. Mughal SS. Chudasama P. *et al.,* PD-L1 (CD274) copy number gain, expression, and immune cell infiltration as candidate predictors for response to immune checkpoint inhibitors in soft-tissue

sarcoma. *OncoImmunol.* 2017; 6(3):e1279777. doi: 10.1080/2162402X.2017.1279777

Burdick AD. Ivnitski-Steele ID. Lauer FT. Burchiel SW. PYK2 mediates anti-apoptotic AKT signaling in response to benzo[a]pyrene diol epoxide in mammary epithelial cells. *Carcinogenesis.* 2006; 27(11):2331-40. doi: 10.1093/carcin/bgl083

Burgess EF. Livasy C. Hartman A. Robinson MM. Symanowski J. Naso C. *et al.,* Discordance of high PD-L1 expression in primary and metastatic urothelial carcinoma lesions. *Urol. Oncol.* 2019; 37(5):299.e19−299.e25. doi: 10.1016/j.urolonc.2019.01.002

Calcinotto A. Grioni M. Jachetti E. Curnis F. Mondino A. Parmiani G. *et al.,* Targeting TNF-α to neoangiogenic vessels enhances lymphocyte infiltration in tumors and increases the therapeutic potential of immunotherapy. *J Immunol.* 2012; 188:2687–94. doi: 10.4049/jimmunol.1101877

Cao X. Zhao Y. Wang J. Dai B. Gentile E. Lin J. *et al.,* TUSC2 downregulates PD-L1 expression in non-small cell lung cancer (NSCLC). *Oncotarget.* 2017; 8(64):107621–107629. doi: 10.18632/oncotarget.22581

Carbotti G. Barisione G. Airoldi I. Mezzanzanica D. Bagnoli M. Ferrero S. *et al.,* IL-27 induces the expression of IDO and PD-L1 in human cancer cells. *Oncotarget.* 2015; 6 (41):43267-43280. doi: 10.18632/oncotarget.6530

Casey SC. Tong L. Li Y. Do R. Walz S. Fitzgerald KN. *et al.,* MYC regulates the antitumor immune response through CD47 and PD-L1. *Science.* 2016; 352(6282):227-231. doi: 10.1126/science.aac9935

Castrogiovanni C. Waterschoot B. De Backer O. Dumont P. Serine 392 phosphorylation modulates p53 mitochondrial translocation and transcription-independent apoptosis. *Cell Death Differ.* 2018; 25:190–203. doi: 10.1038/cdd.2017.143

Cervera-Carrascon V. Siurala M. Santos JM. Havunen R. Tähtinen S. Karell P. *et al.,* TNFa and IL-2 armed adenoviruses enable complete responses by anti-PD-1 checkpoint blockade. *Oncoimmunology.* 2018; 7:e1412902. doi: 10.1080/2162402X.2017.1412902

Chakrabarti J. Holokai L. Syu LJ. Steele NG. Chang J. Wang J. Hedgehog signaling induces PD-L1 expression and tumor cell proliferation in gastric cancer. *Oncotarget.* 2018; 9:37439–37457. doi: 10.18632/oncotarget.26473

Cham CM. Driessens G. O'Keefe JP. Gajewski TF. Glucose deprivation inhibits multiple key gene expression events and effector functions in CD8+ T cells. *Eur. J. Immunol.* 2008; 38:2438–50. doi: 10.1002/eji.200838289

Champiat S. Dercle L. Ammari S. Massard C. Hollebecque A. Postel-Vinay S. *et al.,* Hyperprogressive disease is a new pattern of progression in cancer patients treated

by anti-PD-1/PD-L1. *Clin. Cancer Res.* 2017; 23:1920–8. doi: 10.1158/1078-0432.CCR-16-1741

Chan DA. Sutphin PD. Denko NC. Giaccia AJ. Role of prolyl hydroxylation in oncogenically stabilized hypoxia-inducible factor-1alpha. *J. Biol. Chem.* 2002; 277(42):40112-7. doi: 10.1074/jbc.M206922200

Chandrakesan P. Panneerselvam J. May R. Weygant N. Qu D. Berry WR. *et al.,* DCLK1-Isoform2 Alternative Splice Variant Promotes Pancreatic Tumor Immunosuppressive M2-Macrophage Polarization. *Mol. Cancer Ther.* 2020; 19:1539–1549. doi: 10.1158/1535-7163.MCT-19-0776

Chandrasekaran S. Marshall JR. Messing JA. Hsu J-W. King MR. TRAIL-Mediated Apoptosis in Breast Cancer Cells Cultured as 3D Spheroids. *PLoS ONE.* 2014; 9(10):e111487. doi: 10.1371/journal.pone.0111487

Chang CH. Qui J. O'Sullivan D. Buck MD. Noguchi T. Curtis JD. *et al.,* Metabolic competition in the tumor microenvironment is a driver of cancer progression. *Cell.* 2015; 162:1229–41. doi: 10.1016/j.cell.2015.08.016

Chaudhri A. Xiao Y. Klee AN. Wang X. Zhu B. and Freeman GJ. PD-L1 Binds to B7-1 Only In Cis on the Same Cell Surface. *Cancer Immunol. Res.* 2018; 6(8):921-929. doi: 10.1158/2326-6066.CIR-17-0316

Chen C. Li S. Xue J. Qi M. Liu X. Huang Y. *et al.,* PD-L1 tumor-intrinsic signaling and its therapeutic implication in triple-negative breast cancer. *JCI Insight.* 2021; 6(8):e131458. doi: 10.1172/jci.insight.131458.

Chen J. The Cell-Cycle Arrest and Apoptotic Functions of p53 in Tumor Initiation and Progression. *Cold Spring Harb. Perspect. Med.* 2016; 6(3):a026104. doi: 10.1101/cshperspect.a026104

Chen L. Gibbons DL. Goswami S. Cortez MA. Ahn YH. Byers LA. *et al.,* Metastasis is regulated via microRNA-200/ZEB1 axis control of tumour cell PD-L1 expression and intratumoral immunosuppression. *Nat. Commun.* 2014; 5:5241. doi: 10.1038/ncomms6241

Chen R. Zinzani PL. Fanale MA. Armand P. Johnson NA. Brice P. *et al.,* Phase II Study of the Efficacy and Safety of Pembrolizumab for Relapsed/Refractory Classic Hodgkin Lymphoma. *J. Clin. Oncol.* 2017; 35(19):2125-2132. doi: 10.1200/JCO.2016.72.1316

Chen S. Crabill GA. Pritchard TS. McMiller TL. Wei P. Pardoll DM. *et al.,* Mechanisms regulating PD-L1 expression on tumor and immune cells. *JITC.* 2019; 7:305. doi: 10.1186/s40425-019-0770-2

Chocarro de Erauso L. Zuazo M. Arasanz H. Bocanegra A. Hernandez C. Fernandez G. *et al.,* Resistance to PD-L1/PD-1 blockade immunotherapy. A tumor-intrinsic or tumor-extrinsic phenomenon? *Front Pharmacol.* 2020; 11:441. doi: 10.3389/fphar.2020.00441

Choueiri TK. Powles T. Burotto M. Escudier B. Bourlon MT. Zurawski B. *et al.,* Nivolumab plus Cabozantinib versus Sunitinib for advanced renal-cell carcinoma. *N. Engl. J. Med.* 2021; 384:829–41. doi: 10.1056/NEJMoa2026982

Chung HC. Ros W. Delord JP. Perets R. Italiano A. Shapira-Frommer R. *et al.,* Efficacy and safety of pembrolizumab in previously treated advanced cervical cancer: results from the phase II KEYNOTE-158 study. *J. Clin. Oncol.* 2019; 37:1470–8. doi: 10.1200/JCO.18.01265

Clambey ET. McNamee EN. Westrich JA. Glover LE. Campbell EL. Jedlicka P. *et al.,* Hypoxia-inducible factor-1 alpha–dependent induction of FoxP3 drives regulatory T-cell abundance and function during inflammatory hypoxia of the mucosa. *PNAS.* 2012; 109(41):E2784-E2793. doi: 10.1073/pnas.1202366109

Clark CA. Gupta HB. Sareddy G. Pandeswara S. Lao S. Yuan B. *et al.,* Tumor-Intrinsic PD-L1 Signals Regulate Cell Growth, Pathogenesis, and Autophagy in Ovarian Cancer and Melanoma. *Cancer Res.* 2016; 76(23):6964-6974. doi: 10.1158/0008-5472.CAN-16-0258

Clayer M. Bouralexis S. Evdokiou A. Hay S. Atkins GJ. Findlay DM. Enhanced apoptosis of soft tissue sarcoma cells with chemotherapy: A potential new approach using TRAIL. *J. Ortho. Sur.* 2001; 9(2):19–22. doi: 10.1177/230949900100900205

Courau T. Bonnereau J. Chicoteau J. Bottois H. Remark R. Assante Miranda L. *et al.,* Cocultures of human colorectal tumor spheroids with immune cells reveal the therapeutic potential of MICA/B and NKG2A targeting for cancer treatment. *J. Immunother. Cancer.* 2019; 7:74. doi: 10.1186/s40425-019-0553-9

Crane CA. Panner A. Murray JC. Wilson SP. Xu H. Chen L. *et al.,* PI(3) kinase is associated with a mechanism of immunoresistance in breast and prostate cancer. *Oncogene.* 2009; 28(2):306-12. doi: 10.1038/onc.2008.384

Cruceriu D. Baldasici O. Balacescu O. Berindan-Neagoe I. The dual role of tumor necrosis factor-alpha (TNF-α) in breast cancer: molecular insights and therapeutic approaches. *Cell Oncol.* 2020; 43:1–18. doi: 10.1007/s13402-019-00489-1

Curnis F. Sacchi A. Borgna L. Magni F. Gasparri A. Corti A. Enhancement of tumor necrosis factor alpha antitumor immunotherapeutic properties by targeted delivery to aminopeptidase N (CD13). *Nat Biotechnol.* 2000; 18:1185–90. doi: 10.1038/81183

Dang CV. MYC on the path to cancer. *Cell.* 2012; 149(1):22-35. doi: 10.1016/j.cell.2012.03.003

David, M. Signal transduction by type I interferons. *Biotechniques.* 2002; Suppl:58-65.

De Andrade LF. En Tay R. Pan D. Luoma AM. Ito Y. Badrinath S. *et al.,* Antibody-mediated inhibition of MICA and MICB shedding promotes NK cell-driven tumor immunity. *Science.* 2018; 359:1537–1542. doi: 10.1126/science.aao0505

de Carvalho-Neto PB. Santos Md. de Carvalho MB. Mercante AMdC. Santos VPPd. Severino P. *et al.*, FAS/FASL Expression Profile as a Prognostic Marker in Squamous Cell Carcinoma of the Oral Cavity. *PLoS ONE.* 2013; 8(7):e69024. doi: 10.1371/journal.pone.0069024

de Visser KE. Eichten A. Coussens LM. Paradoxical roles of the immune system during cancer development. *Nat. Rev. Cancer.* 2006; 6(1):24-37. doi: 10.1038/nrc1782

Debela DT. Muzazu SG. Heraro KD. Ndalama MT. Mesele BW. Haile DC. *et al.,* New approaches and procedures for cancer treatment: Current perspectives. *SAGE Open Med.* 2021; 9:20503121211034366. doi: 10.1177/20503121211034366

Del Re M. Vivaldi C. Rofi E. Salani F. Crucitta S. Catanese S. *et al.,* Gemcitabine Plus Nab-Paclitaxel Induces PD-L1 mRNA Expression in Plasma-Derived Microvesicles in Pancreatic Cancer. *Cancers (Basel).* 2021; 13(15):3738. doi: 10.3390/cancers13153738

Dellagatta JL. Steelman S. Sougnez C. Cibulskis K. Kiezun A. Hacohen N. *et al.,* Comprehensive analysis of cancer-associated somatic mutations in class I HLA genes. *Nat. Biotechnol.* 2015; 33(11):1152-8. doi: 10.1038/nbt.3344

Deng L. Liang H. Burnette B. Beckett M. Darga T. Weichselbaum RR. *et al.,* Irradiation and anti-PD-L1 treatment synergistically promote antitumor immunity in mice. *J. Clin. Invest.* 2014; 124(2):687-95. doi: 10.1172/JCI67313

Dhatchinamoorthy K. Colbert JD. Rock KL. Cancer Immune Evasion Through Loss of MHC Class I Antigen Presentation. *Front. Immunol.* 2021; 12. doi: 10.3389/fimmu.2021.636568

Di Modugno F. Colosi C. Trono P. Antonacci G. Ruocco G. Nistic, P. 3D models in the new era of immune oncology: Focus on T cells, CAF and ECM. *J. Exp. Clin. Cancer Res.* 2019; 38: 117. doi: 10.1186/s13046-019-1086-2

Doehn U. Hauge C. Frank SR. Jensen CJ. Duda K. Nielsen JV. *et al.,* RSK is a principal effector of the RAS-ERK pathway for eliciting a coordinate promotile/invasive gene program and phenotype in epithelial cells. *Mol. Cell.* 2009; 35(4): 511-22. doi: 10.1016/j.molcel.2009.08.002

Domoto T. Uehara M. Bolidong D. Minamoto T. Glycogen Synthase Kinase 3β in Cancer Biology and Treatment. *Cells.* 2020; 9(6):1388. doi: 10.3390/cells9061388

Donato NJ. Klostergaard J. Distinct stress and cell destruction pathways are engaged by TNF and ceramide during apoptosis of MCF-7 cells. *Exp Cell Res.* 2004; 294(2):523-33. doi: 10.1016/j.yexcr.2003.11.021

Dong H. Strome SE. Salomao DR. Tamura H. Hirano F. Flies DB. *et al.,* Tumor-associated B7-H1 promotes T-cell apoptosis: A potential mechanism of immune evasion. *Nat. Med.* 2002;8(8): 793-800. doi: 10.1038/nm730

Dong P. Xiong Y. Yu J. Chen L. Tao T. Yi S. *et al.,* Control of PD-L1 expression by miR-140/142/340/383 and oncogenic activation of the OCT4-miR-18a pathway in cervical cancer. *Oncogene.* 2018;37(39):5257-5268. doi: 10.1038/s41388-018-0347-4

Dong P. Xiong Y. Yue J. Hanley SJB. Watari H. Tumor-Intrinsic PD-L1 Signaling in Cancer Initiation, Development and Treatment: Beyond Immune Evasion. *Front. Oncol.* 2018; 8:386. doi: 10.3389/fonc.2018.00386

Dong P. Xiong Y. Yue J. Hanley SJB. Watari H. Tumor-intrinsic PD-L1 signaling in cancer initiation, development and treatment: beyond immune evasion. *Front Oncol.* 2018; 8:386. doi: 10.3389/fonc.2018.00386

Dong W. Wu X. Ma S. Wang Y. Nalin AP. Zhu Z. *et al.,* The mechanism of anti-PD-L1 antibody efficacy against PD-L1 negative tumors identifies NK cells expressing PD-L1 as a cytolytic effector. *Cancer Discov.* 2019; 9(10):1422-1437. doi: 10.1158/2159-8290.CD-18-1259

Doublier S. Belisario DC. Polimeni M. Annaratone L. Riganti C. Allia E*. et al.,* HIF-1 activation induces doxorubicin resistance in MCF7 3-D spheroids via P-glycoprotein expression: a potential model of the chemo-resistance of invasive micropapillary carcinoma of the breast. *BMC Cancer.* 2012; 12(4). doi: 10.1186/1471-2407-12-4

Du S. McCall N. Park K. Guan Q. Fontina P. Ertel A. *et al.,* Blockade of tumor-expressed PD-1 promotes lung cancer growth. *Oncoimmunology.* 2018; 7:e1408747. doi: 10.1080/2162402X.2017.1408747

Edmondson R. Broglie JJ. Adcock AF. Yang L. Three-dimensional cell culture systems and their applications in drug discovery and cell-based biosensors. *Assay Drug Dev. Technol.* 2014; 12(4):207-18. doi: 10.1089/adt.2014.573.

Elia AR. Grioni M. Basso V. Curnis F. Freschi M. Corti A. *et al.,* Targeting tumor vasculature with TNF leads effector T cells to the tumor and enhances therapeutic efficacy of immune checkpoint blockers in combination with adoptive cell therapy. Clin *Cancer Res.* 2018; 24:2171–81. doi: 10.1158/1078-0432.CCR-17-2210

El-Khoueiry AB. Sangro B. Yau T. Crocenzi TS. Kudo M. Hsu C. *et al.,* Nivolumab in patients with advanced hepatocellular carcinoma (CheckMate 040): an open-label, non-comparative, phase 1/2 dose escalation and expansion trial*. Lancet.* 2017; 389:2492–502. doi: 10.1016/S0140-6736(17)31046-2

Elmore S. Apoptosis: a review of programmed cell death. *Toxicol. Pathol.* 2007; 35(4):495-516. doi: 10.1080/01926230701320337

Escors D. Gato-Cañas M. Zuazo M. Arasanz H. Gracía-Granda MJ. Vera R. *et al.,* The intracellular signalosome of PD-L1 in cancer cells. *Signal Transduct. Target Ther.* 2018; 3:26. doi: 10.1038/s41392-018-0022-9

Falschlehner C. Schaefer U. Walczak H. Following TRAIL's path in the immune system. Immunology. 2009; 127(2):145-54. doi: 10.1111/j.1365-2567.2009.03058.x

Fashoyin-Aje L. Donoghue M. Chen H. He K. Veeraraghavan J. Goldberg K.B. *et al.,* FDA Approval Summary: Pembrolizumab for Recurrent Locally Advanced or Metastatic Gastric or Gastroesophageal Junction Adenocarcinoma Expressing PD-L1. *Oncologist.* 2019; 24(1):103-109. doi: 10.1634/theoncologist.2018-0221

Fehrenbacher L. Spira A. Ballinger M. Kowanetz M. Vansteenkiste J. Mazieres J. *et al.,* Atezolizumab versus docetaxel for patients with previously treated non-small-cell lung cancer (POPLAR): a multicentre, open-label, phase 2 randomised controlled trial. *Lancet.* 2016; 387(10030): 1837-1846. doi: 10.1016/S0140-6736(16)00587-0

Feng D. Qin B. Pal K. Sun L. Dutta S. Dong H. *et al.,* BRAF V600E-induced, tumour intrinsic PD-L1 can regulate chemotherapy-induced apoptosis in human colorectal cancer cells and in tumour xenografts. *Oncogene.* 2019; 38:6752–66. doi: 10.1038/s41388-019-0919-y

Feng Y. Spezia M. Huang S. Yuan C. Zeng Z. Zhang L. *et al.,* Breast cancer development and progression: Risk factors, cancer stem cells, signaling pathways, genomics, and molecular pathogenesis. *Genes Dis.* 2018; 5(2):77-106. doi: 10.1016/j.gendis.2018.05.001

Ferris RL. Goncalves A. Baxi SS. Martens UM. Gauthier H. Langenburg M. *et al.,* LBA46 - an open-label, multicohort, phase 1/2 study in patients with virus-associated cancers (CheckMate 358): safety and efficacy of neoadjuvant nivolumab in squamous cell carcinoma of the head and neck. *Ann. Oncol.* (2017) 28:605–49. doi: 10.1093/annonc/mdx440.041

Figueiredo MI. Ladeirinha A. Alarcão A. Sousa V. Carvalho L. PD-L1, Vimentin and Ki-67 Acting as Immunotherapy Predictive Biomarkers in Pulmonary Carcinomas Transthoracic and Bronchial Biopsies. *Res. J. Onco.* 2022; 6(2):8-15. doi: 10.21203/rs.3.rs-1135697/v1

Finn RS. Qin S. Ikeda M. Galle PR. Ducreux M. Kim TY. *et al.,* Atezolizumab plus Bevacizumab in Unresectable Hepatocellular Carcinoma. *N. Engl. J Med.* 2020; 382:1894–905. doi: 10.1056/NEJMoa1915745

Fitzgerald AA. Li E. Weiner LM. 3D Culture Systems for Exploring Cancer Immunology. *Cancers (Basel).* 2020; 13(1):56. doi: 10.3390/cancers13010056

Flint LE. Hamm G. Ready JD. Ling S. Duckett, CJ. Cross NA. *et al.,* Characterization of an Aggregated Three-Dimensional Cell Culture Model by Multimodal Mass Spectrometry Imaging. *Anal. Chem.* 2020; 92(18):12538-12547. doi: 10.1021/acs.analchem.0c02389

Florczyk SJ. Kievit FM. Wang K. Erickson AE. Ellenbogen RG. Zhang M. 3D Porous Chitosan-Alginate Scaffolds Promote Proliferation and Enrichment of Cancer Stem-Like Cells. *J. Mater. Chem. B.* 2016;14; 4(38):6326-6334. doi: 10.1039/C6TB01713D

Fournel L. Wu Z. Stadler N. Samotte D. Lococo F. Boulle G. *et al.,* Cisplatin increases PD-L1 expression and optimizes immune check-point blockade in non-small cell lung cancer. *Cancer Letters.* 2019; 464:5-14. doi: 10.1016/j.canlet.2019.08.005

Franzen A. Vogt TJ. Müller T. Dietrich J. Schröck A. Golletz C. *et al.,* PD-L1 (CD274) and PD-L2 (PDCD1LG2) promoter methylation is associated with HPV infection and transcriptional repression in head and neck squamous cell carcinomas. *Oncotarget.* 2017; 9(1):641–650. doi: 10.18632/oncotarget.23080

Freeman GJ. Long AJ. Iwai Y. Bourque K. Chernova T. Nishimura H. *et al.,* Engagement of the PD-1 immunoinhibitory receptor by a novel B7 family member leads to negative regulation of lymphocyte activation. *J. Exp. Med.* 2000; 192: 1027-1034. 10.1084/jem.192.7.1027

Friedrich J. Seidel C. Ebner R. Kunz-Schughart LA. Spheroid-based drug screen: considerations and practical approach. *Nat. Protoc.* 2009; 4(3):309-24. doi: 10.1038/nprot.2008.226

Fujita Y. Yagishita S. Hagiwara K. Yoshioka Y. Kosaka N. Takeshita F. *et al.,* The clinical relevance of the miR-197/CKS1B/STAT3-mediated PD-L1 network in chemoresistant non-small-cell lung cancer. *Mol. Ther.* 2015; 23(4):717-727. doi: 10.1038/mt.2015.10

Gabrilovich DI. Chen HL. Girgis KR. Cunningham HT. Meny GM. Nadaf S. *et al.,* Production of vascular endothelial growth factor by human tumors inhibits the functional maturation of dendritic cells. *Nat. Med.* 1996; 2(10):1096-1103. doi: 10.1038/nm1096-1096

Gadgeel SM. Stevenson J. Langer CJ. Gandhi L. Borghaei H. Patnaik A. *et al.,* Pembrolizumab (pembro) plus chemotherapy as front-line therapy for advanced NSCLC: KEYNOTE-021 cohorts A-C. *J. Clin. Oncol.* 2017;34(15):9016-9016. doi: 10.1200/JCO.2016.34.15_suppl.9016

Gajewski TF. Schreiber H. Fu YX. Innate and adaptive immune cells in the tumour microenvironment. *Nat. Immunol.* 2013; 14:1014–22. doi: 10.1038/ni.2703

Galon J. Costes A. Sanchez-Cabo F. Kirilovsky A. Mlecnik B. Lagorce-Pagès C. *et al.,* Type, density, and location of immune cells within human colorectal tumors predict clinical outcome. *Sci.* 2006;313(5795):1960–1964. doi: 10.1126/science.1129139

Gao L. Guo Q. Li X. Yang X. Ni H. Wang T. MiR-873/PD-L1 axis regulates the stemness of breast cancer cells. *EBioMedicine.* 2019; 41:395–407. doi: 10.1016/j.ebiom.2019.02.034

Garcia-Diaz A. Shin DS. Moreno BH. Saco J. Escuin-Ordinas H. Rodriguez GA. *et al.,* Interferon receptor signaling pathways regulating PD-L1 and PD-L2 expression. *Cell Rep.* 2017; 19(6):1189-1201. doi: 10.1016/j.celrep.2017.04.031

Garnett MJ. Edelman EJ. Heidorn SJ. Greenman CD. Dastur A. Lau KW. *et al.,* Systematic identification of genomic markers of drug sensitivity in cancer cells. *Nature.* 2012; 483(7391):570-5. doi: 10.1038/nature11005

Garon EB. Rizvi NA. Hui R. Leighl N. Balmanoukian AS. Eder JP. *et al.,* Pembrolizumab for the treatment of non-small-cell lung cancer. *N. Engl. J. Med.* 2015; 372:2018–28. doi: 10.1056/NEJMoa1501824

Garrido C. Brunet M. Didelot C. Zermati Y. Schmitt E. Kroemer G. Heat shock proteins 27 and 70: anti-apoptotic proteins with tumorigenic properties. *Cell Cycle.* 2006; 5(22):2592-601. doi: 10.4161/cc.5.22.3448

Garrido F. Aptsiauri N. Cancer immune escape: MHC expression in primary tumours versus metastases. *Immunology.* 2019; 158: 255-266. doi: 10.1111/imm.13114

Garrido-Castro AC. Lin NU. Polyak K. Insights into Molecular Classifications of Triple-Negative Breast Cancer: Improving Patient Selection for Treatment. *Cancer Discov.* 2019; 9(2):176-198. doi: 10.1158/2159-8290.CD-18-1177

Gatalica Z. Snyder C. Maney T. Ghazalpour A. Holterman DA. Xiao N. *et al.,* Programmed Cell Death 1 (PD-1) and Its Ligand (PD-L1) in Common Cancers and Their Correlation with Molecular Cancer Type. *Cancer Epidemiol. Biomarkers Prev.* 2014; 23(12):2965-2970. doi: 10.1158/1055-9965.EPI-14-0654

Gato-Cañas M. Zuazo M. Arasanz H. Ibañez-Vea M. Lorenzo L. Fernandez-Hinojal G. *et al.,* PDL1 Signals through Conserved Sequence Motifs to Overcome Interferon-Mediated Cytotoxicity. *Cell Rep.* 2017; 20(8):1818-1829. doi: 10.1016/j.celrep.2017.07.075

Gawecka JE. Young-Robbins SS. Sulzmaier FJ. Caliva MJ. Heikkilä MM. Matter ML. *et al.,* RSK2 protein suppresses integrin activation and fibronectin matrix assembly and promotes cell migration. *J. Biol. Chem.* 2012; 287(52): 43424-37. doi: 10.1074/jbc.M112.423046

George J. Saito M. Tsuta K. Iwakawa R. Shiraishi K. Scheel AH. *et al.,* Genomic amplification of CD274 (PD-L1) in small-cell lung cancer. *Clin. Cancer Res.* 2017; 23(5):1220-1226. doi: 10.1158/1078-0432.CCR-16-1069

Georgiou K. Chen L. Berglund M. Ren W. de Miranda NF. Lisboa S. *et al.,* Genetic basis of PD-L1 overexpression in diffuse large B-cell lymphomas. *Blood.* 2016; 127(24):3026-3034. doi: 10.1182/blood-2015-12-686550

Gettinger S. Hellmann MD. Chow LQM. Borghaei H. Antonia S. Brahmer JR. *et al.,* Nivolumab Plus Erlotinib in Patients With EGFR-Mutant Advanced NSCLC. *J. Thorac. Oncol.* 2018; 13(9)1363-1372. doi: 10.1016/j.jtho.2018.05.015.

Gevensleben H. Holmes EE. Goltz D. Dietrich J. Sailer V. Ellinger J. *et al.,* PD-L1 promoter methylation is a prognostic biomarker for biochemical recurrence-free survival in prostate cancer patients following radical prostatectomy. *Oncotarget.* 2016; 7(48):79943–79955. doi: 10.18632/oncotarget.13161

Ghebeh H. Lehe C. Barhoush E. Al-Romaih K. Tulbah A. Al-Alwan M. *et al.,* Doxorubicin downregulates cell surface B7-H1 expression and upregulates its

nuclear expression in breast cancer cells: role of B7-H1 as an anti-apoptotic molecule. Breast *Cancer Res.* 2010; 1(4)48. doi: 10.1186/bcr2605

Goltz D. Gevensleben H. Dietrich J. Dietrich D. PD-L1 (CD274) promoter methylation predicts survival in colorectal cancer patients. *Oncoimmunol.* 2017; 6(1):e1257454. doi: 10.1080/2162402X.2016.1257454

Goltz D. Gevensleben H. Grünen S. Dietrich J. Kristiansen G. Landsberg J. *et al.,* PD-L1 (CD274) promoter methylation predicts survival in patients with acute myeloid leukemia. *Leukemia.* 2017; 31(3):738-743. doi: 10.1038/leu.2016.328

Gowrishhankar K. Gunatilake D. Gallagher SJ. Tiffen J. Rizos H. Hersey P. Inducible but not constitutive expression of PD-L1 in human melanoma cells is dependent on activation of NF-κB. *PLoS One.* 2015; 10(4):e0123410. doi: 10.1371/journal.pone.0123410

Green MR. Monti S. Rodig SJ. Juszczynski P. Currie T. O'Donnell E. *et al.,* Integrative analysis reveals selective 9p24.1 amplification, increased PD-1 ligand expression, and further induction via JAK2 in nodular sclerosing Hodgkin lymphoma and primary mediastinal large B-cell lymphoma. *Blood.* 2010; 116(17):3268-3277. doi: 10.1182/blood-2010-05-282780

Green MR. Rodig S. Juszczynski P. Ouyang J. Sinha P. O'Donnell E. *et al.,* Constitutive AP-1 activity and EBV infection induce PD-L1 in Hodgkin lymphomas and posttransplant lymphoproliferative disorders: implications for targeted therapy. *Clin. Cancer Res.* 2012; 18:1611-1618. doi: 10.1158/1078-0432.CCR-11-1942

Grob JJ. Gonzalez R. Basset-Seguin N. Vornicova O. Schachter J. Joshi A. *et al.,* Pembrolizumab Monotherapy for Recurrent or Metastatic Cutaneous Squamous Cell Carcinoma: A Single-Arm Phase II Trial (KEYNOTE-629). *J. Clin. Oncol.* 2020; 38(25):2916-2925. doi: 10.1200/JCO.19.03054

Gros A. Robbins PF. Yao X. Li YF. Turcotte S. Tran E. *et al.,* PD-1 identifies the patient-specific CD8^{+} tumor-reactive repertoire infiltrating human tumors. *J. Clin. Invest.* 2014; 124(5):2246-59. doi: 10.1172/JCI73639

Grywalska E. Pasiarski M. Góźdź S. Rolińsk J. Immune-checkpoint inhibitors for combating T-cell dysfunction in cancer. *Onco. Targets Ther.* 2018; 11:6505-6524. doi: 10.2147/OTT.S150817

Guillaume L. Rigal L. Fehrenbach J. Severac C. Ducommun B. Lobjois V. Characterization of the physical properties of tumor-derived spheroids reveals critical insights for pre-clinical studies. *Sci. Rep.* 2019; 9:6597. doi: 10.1038/s41598-019-43090-0

Guo YJ. Pan WW. Liu SB. Shen ZF. Xu Y. Hu LL. ERK/MAPK signalling pathway and tumorigenesis (Review). *Exp. Ther. Med.* 2020; 19:1997-2007. doi: 10.3892/etm.2020.8454

Gupta HB. Clark CA. Yuan B. Sareddy G. Pandeswara S. Padron AS. *et al.,* Tumor cell-intrinsic PD-L1 promotes tumor-initiating cell generation and functions in melanoma and ovarian cancer. *Signal Transduct Tar.* 2016; 1:16030. doi: 10.1038/sigtrans.2016.30

Gutzmer R. Stroyakovskiy D. Gogas H. Robert C. Lewis K. Protsenko S. *et al.,* Atezolizumab, vemurafenib, and cobimetinib as first-line treatment for unresectable advanced BRAFV600 mutation-positive melanoma (IMspire150): primary analysis of the randomised, double-blind, placebo-controlled, phase 3 trial. *Lancet.* 2020; 395(10240):1835-1844. doi: 10.1016/S0140-6736(20)30934-X

Haile ST. Bosch JJ. Agu NI. Zeender AM. Somasundaram P. Srivastava MK. *et al.,* Tumor cell programmed death ligand 1-mediated T cell suppression is overcome by coexpression of CD80. *J. Immunol.* 2011; 186:6822–9. doi: 10.4049/jimmunol.1003682

Haile ST. Bosch JJ. Agu NI. Zeender AM. Somasundaram P. Srivastava MK. *et al.,* Tumor Cell Programmed Death Ligand 1-Mediated T Cell Suppression Is Overcome by Coexpression of CD80. *J. Immunol.* 2011; 186(12):6822-6829. doi: 10.4049/jimmunol.1003682

Hanahan D. and Weinberg RA. Hallmark of Cancer: The Next Generation. *Cell.* 2011; 144(5):646-674. doi: 10.1016/j.cell.2011.02.013

Harada H. Andersen JS. Mann M. Terada N. Korsmeyer SJ. p70S6 kinase signals cell survival as well as growth, inactivating the pro-apoptotic molecule BAD. PNAS. 2001; 98(17): 9666-70. doi: 10.1073/pnas.171301998

Havasi A. Li Z. Wang Z. Martin JL. Botla V. Ruchalski K. *et al.,* Hsp27 inhibits Bax activation and apoptosis via a phosphatidylinositol 3-kinase-dependent mechanism. *J. Biol. Chem.* 2008; 283(18):12305-13. doi: 10.1074/jbc.M801291200

Heiland DH. Haaker G. Delev D. Mercas B. Masalha W. Heynckes S. *et al.,* Comprehensive analysis of PD-L1 expression in glioblastoma multiforme. *Oncotarget.* 2017; 8(26):42214–42225. doi: 10.18632/oncotarget.15031

Hellmann MD. Nathanson T. Rizvi H. Creelan BC. Sanchez-Vega F. Ahuja A. *et al.,* Genomic Features of Response to Combination Immunotherapy in Patients with Advanced Non-Small-Cell Lung Cancer. *Cancer Cell.* 2018; 33(5):843-852. Doi: 10.1016/j.ccell.2018.03.018

Hellmann MD. Paz-Ares L. Caro RB. Zurawski B. Kim S. Costa EC. *et al.,* Nivolumab plus Ipilimumab in Advanced Non–Small-Cell Lung Cancer. *N. Engl. J. Med.* 2019; 381:2020-2031 doi 10.1056/NEJMoa1910231

Hellwig-Bürgel T. Rutkowski K. Metzen E. Fandrey J. Jelkmann W. Interleukin-1beta and tumor necrosis factor-alpha stimulate DNA binding of hypoxia-inducible factor-1. *Blood.* 1999; 94(5):1561-7.

Hendriks D. He Y. Koopmans I. Wiersma VR. van Ginkel RJ. Samplonius DF. *et al.*, Programmed Death Ligand 1 (PD-L1)-targeted TRAIL combines PD-L1-mediated checkpoint inhibition with TRAIL-mediated apoptosis induction. *Oncoimmunology*. 2016; 5(8):e1202390. doi: 10.1080/2162402X.2016.1202390

Herbst R. Eckhardt S. Kurzrock R. Ebbinghaus S. O'Dwyer P. Gordon M. Phase I Dose-Escalation Study of Recombinant Human Apo2L/TRAIL, a Dual Proapoptotic Receptor Agonist, in Patients With Advanced Cancer. *J. Clin. Oncol.* 2010; 28(17): 2839-2846. doi: 10.1200/JCO.2009.25.1991

Hino R. Kabashima K. Kato Y. Yagi H. Nakamura M. Honjo T. *et al.,* Tumour cell expression of programmed cell death-1 ligand 1 is a prognostic factor for malignant melanoma. *Cancer*. 2010;116(7):1757-66. doi: 10.1002/cncr.24899

Hoarau-Véchot J. Rafii A. Pasquier J. Halfway between 2D and animal models: Are 3D cultures the ideal tool to study cancer-microenvironment interactions? *Int. J. Mol. Sci.* 2018; 19(1): 181. doi: 10.3390/ijms19010181

Hodgins JJ. Abou-Hamad J. Hagerman A. Yakubovich E. Tanese de Souza C. Marotel M. *et al.,* More than a ligand: PD-L1 promotes oncolytic virus infection via a metabolic shift that inhibits the type I interferon pathway. *bioRxiv*. 2022. doi: 10.1101/2022.08.31.506095

Hodi FS. O'Day SJ. McDermott DF. Weber RW. Sosman JA. Haanen JB. *et al.,* Improved survival with ipilimumab in patients with metastatic melanoma. *New Engl. J. Med.* 2010; 363(8):711–723. doi: 10.1056/NEJMoa1003466

Horn L. Gettinger SN. Gordon MS. Herbst RS. Gandi L. Felip E. *et al.,* Safety and clinical activity of atezolizumab monotherapy in metastatic non-small-cell lung cancer: final results from a phase I study. *Eur J Cancer.* 2018; 101:201–9. doi: 10.1016/j.ejca.2018.06.031

Hsu JM. Li CW. Lai YJ. Hung MC. Posttranslational Modifications of PD-L1 and Their Applications in Cancer Therapy. *Cancer Res.* 2018;78(22):6349-6353. doi: 10.1158/0008-5472.CAN-18-1892

Hudson K. Cross N. Jordan-Mahy N. Leyland R. The Extrinsic and Intrinsic Roles of PD-L1 and Its Receptor PD-1: Implications for Immunotherapy Treatment. *Front. Immunol.* 2020. doi: 10.3389/fimmu.2020.568931

Hwang WL. Pike LRG. Royce TJ. Mahal BA. Loeffler JS. Safety of combining radiotherapy with immune-checkpoint inhibition. *Nat. Rev. Clin. Oncol.* 2018; 15(8):477-494. doi: 10.1038/s41571-018-0046-7

Igney FH. Krammer PH. Death and anti-death: tumour resistance to apoptosis. *Nat. Rev. Cancer.* 2002; 2(4):277-88. doi: 10.1038/nrc776

Ikeda S. Okamoto T. Okano S. Umemoto Y. Tagawa T. Morodomi Y. *et al.,* PD-L1 Is Upregulated by Simultaneous Amplification of the PD-L1 and JAK2 Genes in Non-

Small Cell Lung Cancer. *J Thorac Oncol.* 2016; 11(1):62-71. doi: 10.1016/j.jtho.2015.09.010

Imai D. Yoshizumi T. Okano S. Itoh S. Ikegami T. Harada N. *et al.,* IFN-γ promotes epithelial-mesenchymal transition and the expression of PD-L1 in pancreatic cancer. *J. Surg. Res.* 2019; 240:115-123. doi: 10.1016/j.jss.2019.02.038

Imamura Y. Mukohara T. Shimono Y. Funakoshi Y. Chayahara N. Toyoda M. *et al.,* Comparison of 2D- and 3D-culture models as drug-testing platforms in breast cancer. *Oncol. Rep.* 2015; 33:1837–1843. doi: 10.3892/or.2015.3767

Inman BA. Sebo TJ. Frigola X. Dong H. Bergstralh EJ. Frank I. *et al.,* PD-L1 (B7-H1) expression by urothelial carcinoma of the bladder and BCG-induced granulomata: associations with localized stage progression. *Cancer.* 2007; 109(8):1499–1505. doi: 10.1002/cncr.22588

Inoue Y. Yoshimura K. Mori K. Kurabe N Kahyo T. Mori H. *et al.,* Clinical significance of PD-L1 and PD-L2 copy number gains in non-small-cell lung cancer. *Oncotarget.* 2016; 7(22):32113-32128. doi: 10.18632/oncotarget.8528

Itoh N. Yonehara S. Ishii A. Yonehara M. Mizushima S. Sameshima M. The polypeptide encoded by the cDNA for human cell surface antigen Fas can mediate apoptosis. *Cell.* 1991; 66(2):233–243. doi: 10.1016/0092-8674(91)90614-5

Janse van Rensburg HJ. Azad T. Ling M. Hao Y. Snetsinger B. Khanal P. *et al.,* The Hippo Pathway Component TAZ Promotes Immune Evasion in Human Cancer through PD-L1. *Cancer Res.* 2018; 78(6):1457-1470. doi: 10.1158/0008-5472.CAN-17-3139

Ji X. Wang E. Tian F. MicroRNA-140 suppresses osteosarcoma tumor growth by enhancing anti-tumor immune response and blocking mTOR signaling. *Biochem. Biophys. Res. Commun.* 2018; 495(1):1342–8. doi: 10.1016/j.bbrc.2017.11.120

Jiang X. Wang J. Deng X. Xiong F. Ge J. Xiang B. Wu X. *et al.,* Role of the tumor microenvironment in PD-L1/PD-1-mediated tumor immune escape. *Mol. Cancer.* 2019; 18:10. Doi: 10.1186/s12943-018-0928-4

Jiang X. Zhou J. Giobbie-Hurder A. Wargo J. and Hodi FS. The activation of MAPK in melanoma cells resistant to BRAF inhibition promotes PD-L1 expression that is reversible by MEK and PI3K inhibition. *Clin. Cancer Res.* 2013; 19(3):598–609. doi: 10.1158/1078-0432.CCR-12-2731

Jiao X. Katiyar S. Willmarth NE. Liu M. Ma X. Flomenberg N. *et al.,* c-Jun induces mammary epithelial cellular invasion and breast cancer stem cell expansion. *J. Biol. Chem.* 2010; 285(11):8218-26. doi: 10.1074/jbc.M110.100792

Jin H. D'Urso V. Neuteboom B. McKenna SD. Schweickhardt R. Gross AW. *et al.,* Avelumab internalization by human circulating immune cells is mediated by both Fc gamma receptor and PD-L1 binding. *Oncoimmunology.* 2021; 10(1):1958590. doi: 10.1080/2162402X.2021.1958590

Jin X. Ding D. Yan Y. Li H. Wang B. Ma L. *et al.*, Phosphorylated RB promotes cancer immunity by inhibiting NF-κB activation and PD-L1 expression. *Mol. Cell.* 2018; 73(1):22–35. doi: 10.1016/j.molcel.2018.10.034

Johnson RMG. and Dong H. Functional expression of programmed death-ligand 1 (B7-H1) by immune cells and tumor cells. *Front Immunol.* 2017;8.

Jones RG. Plas DR. Kubek S. Buzzai M. Mu J. Xu Y. *et al.*, AMP-activated protein kinase induces a p53-dependent metabolic checkpoint. *Mol. Cell.* 2005; 18(3):283-93. doi: 10.1016/j.molcel.2005.03.027

Ju X. Zhang H. Zhou Z. Wang Q. Regulation of PD-L1 expression in cancer and clinical implications in immunotherapy. *Am. J. Cancer. Res.* 2020; 10(1):1–11.

Kallio PJ. Pongratz I. Gradin K. McGuire J. Poellinger L. Activation of hypoxia-inducible factor 1alpha: posttranscriptional regulation and conformational change by recruitment of the Arnt transcription factor. *Proc. Natl. Acad. Sci. USA.* 1997; 94(11):5667-72. doi: 10.1073/pnas.94.11.5667

Karachaliou N. Gonzalez-Cao M. Crespo G. Drozdowskyj A. Aldeguer E. Gimenez-Capitan A. *et al.*, Interferon gamma, an important marker of response to immune checkpoint blockade in non-small cell lung cancer and melanoma patients. *Ther. Adv. Med. Oncol.* 2018; 10:1758834017749748. doi: 10.1177/1758834017749748

Kari SC. Kancharla A. Gupta HB. Risinger A. Curiel TJ. Tumor-intrinsic PD-L1 reduces actin cytoskeleton polymerization to promote mTORC1 signals driving tumor stemness. *J. Immunol.* 2019; 202:137–8.

Kato K. Cho BC. Takahashi M. Okada M. Lin CY. Chin K *et al.*, Nivolumab versus chemotherapy in patients with advanced oesophageal squamous cell carcinoma refractory or intolerant to previous chemotherapy (ATTRACTION-3): a multicentre, randomised, open-label, phase 3 trial. *Lancet Oncol.* 2019; 20(11):1506-1517. doi: 10.1016/S1470-2045(19)30626-6

Kaufman HL. Russell J. Hamid O. Bhatia S. Terheyden P. D'Angelo SP. *et al.*, Avelumab in patients with chemotherapy-refractory metastatic Merkel cell carcinoma: a multicentre, single-group, open-label, phase 2 trial. *Lancet Oncol.* 2016; 17:1374–85. doi: 10.1016/S1470-2045(16)30364-3

Kaufman HL. Russell JS. Hamid O. Bhatia S. Terheyden P. D'Angelo SP. *et al.,* Updated efficacy of avelumab in patients with previously treated metastatic merkel cell carcinoma after greater than or equal to 1 year of follow-up: JAVELIN merkel 200, a phase 2 clinical trial. *J. ImmunoTher. Cancer.* 2018; 6:7. doi: 10.1186/s40425-017-0310-x

Kelley SK. Ashkenazi A. Targeting death receptors in cancer with Apo2L/TRAIL. *Curr. Opin. Pharmacol.* 2004; 4(4):333-9. doi: 10.1016/j.coph.2004.02.006

Kelm JM. Timmins NE. Brown CJ. Fussenegger M. Nielsen LK. Method for generation of homogeneous multicellular tumor spheroids applicable to a wide variety of cell types. *Biotechnol. Bioeng.* 2003; 83(2):173-80. doi: 10.1002/bit.10655

Khair DO. Bax HJ. Mele S. Crescioli S. Pellizzari G. Khiabany A. *et al.,* Combining Immune Checkpoint Inhibitors: Established and Emerging Targets and Strategies to Improve Outcomes in Melanoma. *Front. Immunol.* 2019;10:453. doi: 10.3389/fimmu.2019.00453

Kim YS. Park GB. Lee HK. Song H. Choi IH. Lee WJ. *et al.,* Cross-linking of B7-H1 on EBV-transformed B cells induces apoptosis through reactive oxygen species production, JNK signaling activation, and fasL expression. *J. Immunol.* 2008; 181:6158-6169. doi: 10.4049/jimmunol.181.9.6158

Kleffel S. Posch C. Barthel SR. Mueller H. Schlapbach C. Guenova E, *et al.,* Melanoma cell-intrinsic PD-1 receptor functions promote tumor growth. *Cell.* 2015; 162:1242–56. doi: 10.1016/j.cell.2015.08.052

Knight E. Przybors S. Advances in 3D cell culture technologies enabling tissue-like structures to be created in vitro. J. Anat. 2015; 227(6): 746-756. doi: 10.1111/joa

Kocikowski M. Dziubek K. Parys M. Hyperprogression under immune checkpoint-based immunotherapy-current understanding, the role of PD-1/PD-L1 tumour-intrinsic signalling, future directions and a potential large animal model. *Cancers (Basel).* 2020; 12:e804. doi: 10.3390/cancers12040804

Kogure Y. Kataoka K. Genetic alterations in adult T-cell leukemia/lymphoma. Cancer Sci. 2017; 108(9):1719–1725. doi: 10.1111/cas.13303

Kong T. Ahn R. Yang K. Zhu X. Fu Z. Morin G. *et al.,* CD44 promotes PD-L1 expression and its tumor-intrinsic function in breast and lung cancers. *Cancer Res.* 2019; 80:444–57. doi: 10.1158/0008-5472.CAN-19-1108

Kotredes KP. Gamero AM. Interferons as inducers of apoptosis in malignant cells. *J Interferon Cytokine Res.* 2013; 33(4):162-70. doi: 10.1089/jir.2012.0110

Kraft S. Fernandez-Figueras MT. Richarz NA. Flaherty KT, Hoang MP. PDL1 expression in desmoplastic melanoma is associated with tumor aggressiveness and progression. *J. Am. Acad. Dermatol.* 2017; 77(3):534–542. doi: 10.1016/j.jaad.2017.05.007

Kuen J. Darowski D. Kluge T. Majety M. Pancreatic cancer cell/fibroblast co-culture induces M2 like macrophages that influence therapeutic response in a 3D model. *PLoS ONE.* 2017; 12:e0182039. doi: 10.1371/journal.pone.0182039

Kuo KK. Lee KT. Chen KK. Yang YH. Lin YC. *et al.,* Positive Feedback Loop of OCT4 and c-JUN Expedites Cancer Stemness in Liver Cancer. *Stem Cells.* 2016; 34(11):2613-2624. doi: 10.1002/stem.2447

Kurimoto R. Iwasawa S. Ebata T. Ishiwata T. Sekine I. Tada Y. *et al.,* Drug resistance originating from a TGF-beta/FGF-2-driven epithelial-to-mesenchymal transition and its reversion in human lung adenocarcinoma cell lines harboring an EGFR mutation. *Int. J. Oncol.* 2016; 48(5):1825-1836. doi: 10.3892/ijo.2016.3419

Lampros M. Vlachos N. Voulgaris S. Alexiou GA. The Role of Hsp27 in Chemotherapy Resistance. *Biomedicines.* 2022;1 0(4):897. doi: 10.3390/biomedicines10040897

Lanuza PM. Vigueras A. Olivan S. Prats AC. Costas S. Llamazares G. *et al.,* Activated human primary NK cells efficiently kill colorectal cancer cells in 3D spheroid cultures irrespectively of the level of PD-L1 expression. Oncoimmunology. 2018; 7(4):e1395123. doi: 10.1080/2162402X.2017.1395123

Larkin J. Chiarion-Sileni V. Gonzalez R. Grob JJ. Cowey L. Lao CD. *et al.,* Combined nivolumab and ipilimumab or monotherapy in untreated melanoma. *N Engl J Med.* 2015; 373:23–4. doi:10.1056/NEJMoa1504030

Lastwika KJ. Wilson W 3rd. Li QK. Norris J. Xu H. Ghazarian SR. *et al.,* Control of PD-L1 expression by oncogenic activation of the AKT-mTOR pathway in non-small cell lung cancer. *Cancer Res.* 2016; 76(2):227–38. doi: 10.1158/0008-5472.CAN-14-3362

Lattanzio R. Iezzi M. Sala G. Tinari N. Falasca M. Alberti S. *et al.,* PLC-gamma-1 phosphorylation status is prognostic of metastatic risk in patients with early-stage Luminal-A and -B breast cancer subtypes. *BMC Cancer.* 2019; 19, 747. doi: 10.1186/s12885-019-5949-x

Law AMK. Rodriguez de la Fuente L. Grundy TJ. Fang G. Valdes-Mora F. Gallego-Ortega D. Advancements in 3D Cell Culture Systems for Personalizing Anti-Cancer Therapies. *Front. Oncol.* 2020; 11:782766. doi: 10.3389/fonc.2021.782766

Lazzari G. Couvreur P. Mura S. Multicellular tumor spheroids: A relevant 3D model for the in vitro preclinical investigation of polymer nanomedicines. *Polym. Chem.* 2017; 8(34): 4947-4969. doi: 10.1039/c7py00559h

Lee KY. Mooney DJ. Alginate: properties and biomedical applications. *Prog. Polym. Sci.* 2012;37(1): 106-126. doi: 10.1016/j.proppolymsci.2011.06.003

Lee SH. Shin MS. Park WS. Kim SY. Kim HS. Han JY. *et al.,* Alterations of Fas (Apo-1/CD95) gene in non-small cell lung cancer. *Oncogene.* 1999; 18(25):3754-60. doi: 10.1038/sj.onc.1202769

Lee SJ. Jang BC. Lee SW. Yang YI. Suhb SI. Park YM. *et al.,* Interferon regulatory factor-1 is prerequisite to the constitutive expression and IFN-γ-induced upregulation of B7-H1 (CD274). *FEBS Lett.* 2006; 580(3):755-762. doi: 10.1016/j.febslet.2005.12.093

Lee Y. Shin JH. Longmire M. Wang H. Kohrt HE. Chang HY. *et al.,* CD44+ cells in head and neck squamous cell carcinoma suppress T-cell-mediated immunity by selective constitutive and inducible expression of PD-L1. *Clin. Cancer Res.* 2016; 22:3571–81. doi: 10.1158/1078-0432.CCR-15-2665

Leong S. Cohen RB. Gustafson DL. Langer CJ. Camidge DR. Padavic K. *et al.,* Mapatumumab, an Antibody Targeting TRAIL-R1, in Combination With Paclitaxel and Carboplatin in Patients With Advanced Solid Malignancies: Results of a Phase I

and Pharmacokinetic Study. *J. Clin. Oncol.* 2009; 27(26):4413-4421. doi: 10.1200/JCO.2008.21.7422

Leuci V., Donini C., Grignani G., Rotolo R., Mesiano G., Fiorino E., Gammaitoni L., D'ambrosio L., Merlini A., Landoni E., et al. CSPG4-Specific CAR.CIK Lymphocytes as a Novel Therapy for the Treatment of Multiple Soft-Tissue Sarcoma Histotypes. *Clin. Cancer Res.* 2020 doi: 10.1158/1078-0432.CCR-20-0357.

Li CW. Lim SO. Xia W. Lee HH. Chan LC. Kuo CW. *et al.,* Glycosylation and stabilization of programmed death ligand-1 suppresses T-cell activity. *Nat Commun.* 2016; 7:12632. doi: 10.1038/ncomms12632

Li H. Li X. Liu S. Guo L. Zhang B. Zhang J. *et al.,* Programmed cell death-1 (PD-1) checkpoint blockade in combination with a mammalian target of rapamycin inhibitor restrains hepatocellular carcinoma growth induced by hepatoma cell-intrinsic PD-1. *Hepatology.* 2017; 66:1920–19933. doi: 10.1002/hep.29360

Li H. Zhu H. Xu CJ. Yuan J. Cleavage of BID by caspase 8 mediates the mitochondrial damage in the Fas pathway of apoptosis. *Cell.* 1998; 94(4):491-501. doi: 10.1016/s0092-8674(00)81590-1

Li J. Chen L. Xiong Y. Zheng X. Xie Q. Zhou Q. *et al.,* Knockdown of PD-L1 in human gastric cancer cells inhibits tumor progression and improves the cytotoxic sensitivity to CIK therapy. *Cell Physiol. Biochem.* 2017; 41:907–20. doi: 10.1159/000460504

Li N. Wang J. Zhang N. Zhuang M. Zong Z. Zou J. *et al.,* Cross-talk between TNF-alpha and IFN-gamma signaling in induction of B7-H1 expression in hepatocellular carcinoma cells. *Cancer Immunol. Immunother.* 2018; 67:271-283. doi: 10.1007/s00262-017-2086-8

Li W. Qian L. Lin J. Huang G. Hao N. Wei X. *et al.,* CD44 regulates prostate cancer proliferation, invasion and migration via PDK1 and PFKFB4. *Oncotarget.* 2017; 8(39):65143-65151. doi: 10.18632/oncotarget.17821

Li Y. Patel SP. Roszik J. Qin Y. Hypoxia-Driven Immunosuppressive Metabolites in the Tumor Microenvironment: New Approaches for Combinational Immunotherapy. *Front. Immunol.* 2018; 9:1591. doi: 10.3389/fimmu.2018.01591

Li Y. Wang J. Li C. Ke XY. Contribution of PD-L1 to on cogenesis of lymphoma and its RNAi-based targeting therapy. *Leuk. Lymphoma.* 2012; 53:2015–23. doi: 10.3109/10428194.2012.673228

Liao Y. Chen L. Feng Y. Shen J. Gao Y. Cote G. *et al.,* Targeting programmed cell death ligand 1 by CRISPR/Cas9 in osteosarcoma cells. *Oncotarget.* 2017; 8:30276–87. doi: 10.18632/oncotarget.16326

Lienlaf M. Perez-Villarroel P. Knox T. Pabon M. Sahakian E. Powers J. *et al.,* Essential role of HDAC6 in the regulation of PD-L1 in melanoma. *Mol. Oncol.* 2016; 10(5):735-750.10:735–50. doi: 10.1016/j.molonc.2015.12.012

Lim JY. Gerber SA. Murphy SP. Lord EM. Type I interferons induced by radiation therapy mediate recruitment and effector function of CD8(+) T cells. *Cancer Immunol. Immunother.* 2014; 63:259–71. doi: 10.1007/s00262-013-1506-7

Lim SO. Li CW. Xia W. Cha JH. Chan LC. Wu Y. *et al.,* Deubiquitination and Stabilization of PD-L1 by CSN5. *Cancer Cell.* 2016; 30(6):925-939. doi: 10.1016/j.ccell.2016.10.010

Lin SP. Lee YT. Wang JY. Miller SA. Chiou SH. Hung MC. *et al.,* Survival of cancer stem cells under hypoxia and serum depletion via decrease in PP2A activity and activation of p38-MAPKAPK2-Hsp27. *PLoS One.* 2012; 7(11):e49605. doi: 10.1371/journal.pone.0049605

Liu J. Zhang C. Hu W. Feng Z. Tumor suppressor p53 and its mutants in cancer metabolism. *Cancer Lett.* 2015; 356(2): 197-203. doi: 10.1016/j.canlet.2013.12.025

Liu S. Chen S. Yuan W. Wang H. Chen K. Li D. et al.. PD-1/PD-L1 interaction up-regulates MDR1/P-gp expression in breast cancer cells via PI3K/AKT and MAPK/ERK pathways. *Oncotarget.* 2017; 8:99901–12. doi: 10.18632/oncotarget.21914

Liu X. Lukowski JK. Flinders C. Kim S. Georgiadis RA. Mumenthaler SM. Hummon AB. MALDI-MSI of Immunotherapy: Mapping the EGFR-Targeting Antibody Cetuximab in 3D Colon-Cancer Cell Cultures. *Anal. Chem.* 2018; 90:14156–14164. doi: 10.1021/acs.analchem.8b02151

Llosa NJ. Cruise M. Tam A. Wicks EC. Hechenbleikner EM. Taube JM. The vigorous immune microenvironment of microsatellite instable colon cancer is balanced by multiple counter-inhibitory checkpoints. *Cancer Discov.* 2015; 5(1):43-51. doi: 10.1158/2159-8290.CD-14-0863

Loetscher H. Pan YC. Lahm HW. Gentz R. Brockhaus M. Tabuchi H. *et al.,* Molecular cloning and expression of the human 55 kd tumor necrosis factor receptor. *Cell.* 1990; 61(2):351–359. doi: 10.1016/0092-8674(90)90815-v

Lorenzo-Sanz L, Muñoz P. Tumor-Infiltrating Immunosuppressive Cells in Cancer-Cell Plasticity, Tumor Progression and Therapy Response. Cancer Microenviron. 2019 Dec;12(2-3):119-132. doi: 10.1007/s12307-019-00232-2

Loughery J. Cox M. Smith LM. Meek DW. Critical role for p53-serine 15 phosphorylation in stimulating transactivation at p53-responsive promoters. *Nucleic Acids Res.* 2014; 42(12):7666-80. doi: 10.1093/nar/gku501

Luca AC. Merch S. Deenen R. Schmidt S. Messner I. Schafer K. Impact of the 3D Microenvironment on Phenotype, Gene Expression, and EGFR Inhibition of Colorectal Cancer Cell Lines. *PLoS One.* 2013; 8(3):e59689. doi: 10.1371/journal.pone.0059689

Lukey MJ. Greene KS. Erickson JW. Wilson KF. Cerione RA. The oncogenic transcription factor c-Jun regulates glutaminase expression and sensitizes cells to

glutaminase-targeted therapy. *Nat Commun.* 2016; 7:11321. doi: 10.1038/ncomms11321

Lv D. Xing C. Cao L. Zhuo Y. Wu T. and Gao N. PD-L1 gene promoter methylation represents a potential diagnostic marker in advanced gastric cancer. *Oncol Lett.* 2020; 19(2):1223–1234. doi: 10.3892/ol.2019.11221

Maeda T. Hiraki M. Jin C. Rajabi H. Tagde A. Alam M. MUC1-C Induces PD-L1 and Immune Evasion in Triple-Negative Breast Cancer. *Cancer Res.* 2017; 78(1):205-215. doi: 10.1158/0008-5472.CAN-17-1636

Maher J. Davies ET. Targeting cytotoxic T lymphocytes for cancer immunotherapy. *Br. J. Cancer.* 2004; 91(5):817-21. doi: 10.1038/sj.bjc.6602022

Mahmoud SM. Paish EC. Powe DG. Macmillan RD. Grainge M J. Lee AH. *et al.,* Tumor-infiltrating CD8+ lymphocytes predict clinical outcome in breast cancer. J. Clin. Oncol. 2011; 29(15):1949-55. doi: 10.1200/JCO.2010.30.5037

Mahon KL. Lin HM. Castillo L. Lee BY. Lee-Ng M. Chatfield MD. *et al.,* Cytokine profiling of docetaxel-resistant castration-resistant prostate cancer. *Br. J. Cancer.* 2015; 112(8):1340-1348. doi: 10.1038/bjc.2015.74

Maine CJ. Aziz NH. Chatterjee J. Hayford C. Brewig N. Whilding L. *et al.,* Programmed death ligand-1 over-expression correlates with malignancy and contributes to immune regulation in ovarian cancer. *Cancer Immunol. Immunother.* 2013; 63(3):215-24. doi: 10.1007/s00262-013-1503-x

Mak MP. Tong P. Diao L. Cardnell RJ. Gibbons DL. William WN. *et al.,* A patient-derived, pan-cancer EMT signature identifies global molecular alterations and immune target enrichment following epithelial to mesenchymal transition. *Clin. Cancer Res.* 2016; 22(3): 609-620. doi: 10.1158/1078-0432.CCR-15-0876

Makker V. Rasco D. Vogelzang NJ. Brose MS. Cohn AL. Mier J. *et al.,* Lenvatinib plus pembrolizumab in patients with advanced endometrial cancer: an interim analysis of a multicentre, open-label, single-arm, phase 2 trial. *Lancet Oncol.* 2019; 20:711–8. doi: 1016/S1470-2045(19)30020-8

Mansfield AS. Każarnowicz A. Karaseva N. Sánchez A. De Boer R. Andric Z. *et al.,* Safety and patient-reported outcomes of atezolizumab, carboplatin, and etoposide in extensive-stage small-cell lung cancer (IMpower133): a randomized phase I/III trial. *Ann. Oncol.* 2020; 31(2):310-317. doi: 10.1016/j.annonc.2019.10.021

Marabelle A. Le DT. Ascierto PA. Di Giacomo AM. De Jesus-Acosta A. Delord JP. *et al.,* Efficacy of Pembrolizumab in Patients With Noncolorectal High Microsatellite Instability/Mismatch Repair-Deficient Cancer: Results From the Phase II KEYNOTE-158 Study. *J. Clin. Oncol.* 2020; 38(1):1-10. doi: 10.1200/JCO.19.02105

Marinelli O. Annibali D. Morelli MB. Zeppa L. Tuyaerts S. Aguzzi C. *et al.,* Biological Function of PD-L2 and Correlation With Overall Survival in Type II Endometrial Cancer. *Front Oncol.* 2020; 10:538064. doi: 10.3389/fonc.2020.538064

Mark C. Czerwinski T. Roessner S. Mainka A. Hörsch F. Heublein L. *et al.,* Cryopreservation impairs 3-D migration and cytotoxicity of natural killer cells. *Nat. Commun.* 2020; 11(1):5224. doi: 10.1038/s41467-020-19094-0

Markham A. Atezolizumab: First Global Approval. *Drugs.* 2016; 76(12):1227-32. doi: 10.1007/s40265-016-0618-8

Martin AM. Nirschl TR. Nirschl CJ. Francica BJ. Kochel CM. van Bokhoven A. *et al.,* Paucity of PD-L1 expression in prostate cancer: Innate and adaptive immune resistance. *Prostate Cancer Prostatic Dis.* 2015; 18(4):325-332. doi: 10.1038/pcan.2015.39

Martínez-Lostao L. Anel A. Pardo J. How Do Cytotoxic Lymphocytes Kill Cancer Cells? *Clin. Cancer Res.* 2015; 21(22): 5047–56. doi: 10.1158/1078-0432.CCR-15-0685

Marxsen JH. Stengel P. Doege K. Heikkinen P. Jokilehto T. Wagner T. *et al.,* Hypoxia-inducible factor-1 (HIF-1) promotes its degradation by induction of HIF-alpha-prolyl-4-hydroxylases. *Biochem. J.* 2004; 381(Pt 3):761-7. doi: 10.1042/BJ20040620

Marzec M. Zhang Q. Goradia A. Raghunath PN. Liu X. Paessler M. *et al.,* Oncogenic kinase NPM/ALK induces through STAT3 expression of immunosuppressive protein CD274 (PD-L1. B7-H1). *PNAS.* 2008; 105:20852-20857. doi: 10.1073/pnas.0810958105

Massi D. Brusa D. Merelli B. Ciano M. Audrito V. Serra S. *et al.,* PD-L1 marks a subset of melanomas with a shorter overall survival and distinct genetic and morphological characteristics. *Ann Oncol.* 2014; 25:2433–42. doi: 10.1093/annonc/mdu452

McGowan M. Hoven AS. Lund-Iversen M. Solberg S. Helland Å. Hirsch FR. *et al.,* PIK3CA mutations as prognostic factor in squamous cell lung carcinoma. Lung *Cancer.* 2017; 103:52-57. doi:10.1016/j.lungcan.2016.11.018

Metzen E. Zhou J. Jelkmann W. Fandrey J. Brüne B. Nitric oxide impairs normoxic degradation of HIF-1alpha by inhibition of prolyl hydroxylases. *Mol Biol Cell.* 2003; 14(8):3470-81. doi: 10.1091/mbc.e02-12-0791

Mezzadra R. Sun C. Jae LT. Gomez-Eerland R. de Vries E. Wu W. *et al.,* Identification of CMTM6 and CMTM4 as PD-L1 protein regulators. *Nature.* 2017; 549:106–110. doi: 10.1038/nature23669

Micevic G. Thakral D. McGeary M. and Bosenberg MW. PD-L1 methylation regulates PD-L1 expression and is associated with melanoma survival. *Pigment Cell Melanoma Res.* 2018; 32(3):435-40. doi: 10.1111/pcmr.12745

Mierke CT. The integrin alphav beta3 increases cellular stiffness and cytoskeletal remodeling dynamics to facilitate cancer cell invasion. *New J. Phys.* 2013; 15(1): 015003. doi: 10.1088/1367-2630/15/1/015003

Migone TS. Zhang J. Luo X. Zhuang L. Chen C. Hu B. *et al.,* TL1A is a TNF-like ligand for DR3 and TR6/DcR3 and functions as a T cell costimulator. *Immunity.* 16(3):479-92. doi: 10.1016/s1074-7613(02)00283-2.

Mirabelli P. Coppola L. Salvatore M. Cancer Cell Lines Are Useful Model Systems for Medical Research. *Cancers (Basel).* 2019; 11(8):1098. doi: 10.3390/cancers11081098

Mittendorf EA. Philips AV. Meric-Bernstam F. Qiao N. Wu Y. Harrington S. *et al.,* PD-L1 expression in triple-negative breast cancer. *Cancer Immunol. Res.* 2014; 2(4):361–370. doi: 10.1158/2326-6066.CIR-13-0127

Miyazawa A. Ito S. Asano S. Tanaka I. Sato M. Kondo M. Hasegawa, Y. Regulation of PD-L1 expression by matrix stiffness in lung cancer cells. *Biochem. Biophys. Res. Commun.* 2018; 495(3):2344-2349. doi: 10.1016/j.bbrc.2017.12.115

Modiano JF. Bellgrau D. Fas Ligand Based Immunotherapy: A Potent and Effective Neoadjuvant with Checkpoint Inhibitor Properties, or a Systemically Toxic Promoter of Tumor Growth? *Discov. Med.* 2016; 21(114):109-116.

Modiano JF. Bellgrau D. Cutter GR. Lana SE. Ehrhart NP. Ehrhart E. *et al.,* Inflammation, apoptosis, and necrosis induced by neoadjuvant fas ligand gene therapy improves survival of dogs with spontaneous bone cancer. *Mol. Ther.* 2012; 20(12):2234-43. doi: 10.1038/mt.2012.149

Mohammad GRKS. Ghahremanloo A. Soltani A. Fathi E. Hashemy SI. Cytokines as potential combination agents with PD-1/PD-L1 blockade for cancer treatment. *J. Cell Physiol.* 2020; 235(7-8): 5449-5460. doi: 10.1002/jcp.29491

Mohan N. Hosain S. Zhao J. Shen Y. Luo X. Jiang J. *et al.,* Atezolizumab potentiates Tcell-mediated cytotoxicity and coordinates with FAK to suppress cell invasion and motility in PD-L1+ triple negative breast cancer cells. *OncoImmunology.* 2019; 8:9. doi: 10.1080/2162402X.2019.1624128

Montfort A. Colacios C. Levade T. Andrieu-Abadie N. Meyer N. Ségui B. The TNF Paradox in Cancer Progression and Immunotherapy. *Front. Immunol.* 2019; 10:1818. doi: 10.3389/fimmu.2019.01818

Moon JW. Kong SK. Kim BS. Kim HJ. Lim H. Noh K. *et al.,* IFNγ induces PD-L1 overexpression by JAK2/STAT1/IRF-1 signaling in EBV-positive gastric carcinoma. *Sci Rep.* 2017;7:17810. doi: 10.1038/s41598-017-18132-0

Motzer RJ. Escudier B. McDermott DF. George S. Hammers HJ. Srinivas S. *et al.,* Nivolumab versus everolimus in advanced renal-cell carcinoma. *N. Engl. J. Med.* 2015; 373:1803–13. doi: 10.1056/NEJMoa1510665

Motzer RJ. Robbins PB. Powles T. Albiges L. Haanen JB. Larkin J. *et al.,* Avelumab plus axitinib versus sunitinib in advanced renal cell carcinoma: biomarker analysis of the phase 3 JAVELIN renal 101 trial. *Nat. Med.* 2020; 26:1733–41. doi: 10.1038/s41591-020-1044-8

Mueller-Klieser WF. Sutherland RM. Oxygen tensions in multicellular spheroids of two cell lines. *Br. J. Cancer.* 1982; 45(2):256. doi:10.1038/bjc.1982.41

Muenst S. Schaerli A. Gao F. Däster S Trella E. Droeser R. *et al.,* Expression of programmed death ligand 1 (PD-L1) is associated with poor prognosis in human breast cancer. *Breast Cancer Res. Treat.* 2014; 146(1):15-24. doi: 10.1007/s10549-014-2988-5

Natoli M. Bonito N. Robinson JD. Ghaem-Maghami S. Mao Y. Human ovarian cancer intrinsic mechanisms regulate lymphocyte activation in response to immune checkpoint blockade. *Cancer Immunol. Immunother.* 2020; 69:1391–401. doi: 10.1007/s00262-020-02544-5

Neal JT. Li X. Zhu J. Giangarra V. Grzeskowiak CL. Ju J. *et al.,* Organoid modelling of the tumor immune microenvironment. *Cell.* 2018; 175:1972–88. doi: 10.1016/j.cell.2018.11.021

Newsom-Davis T. Prieske S. Walczak H. Is TRAIL the holy grail of cancer therapy? *Apoptosis.* 2009; 14(4):607–623. doi: 10.1007/s10495-009-0321-2

Ng HY. Li J. Tao L. Lam AK. Chan KW. Ko JMY. *et al.,* Chemotherapeutic Treatments Increase PD-L1 Expression in Esophageal Squamous Cell Carcinoma through EGFR/ERK Activation. *Transl Oncol.* 2018; 11(6):1323-1333. doi: 10.1016/j.tranon.2018.08.005

Nghiem PT. Bhatia S. Lipson EJ. Kudchadkar RR. Miller NJ. Annamalai L. *et al.,* PD-1 blockade with pembrolizumab in advanced merkel-cell carcinoma. *N. Engl. J. Med.* 2016; 374:2542–52. doi: 10.1056/NEJMoa1603702

Nishino M. Ozaki M. Hegab AE. Hamamoto J. Kagawa S. Arai D. *et al.,* Variant CD44 expression is enriching for a cell population with cancer stem cell-like characteristics in human lung adenocarcinoma. *J. Cancer.* 2017; 8:1774–85. doi: 10.7150/jca.19732

Noman MZ. Desantis G. Janji B. Hasmim M. Karray S. Dessen P. *et al.,* PD-L1 is a novel direct target of HIF-1α, and its blockade under hypoxia enhanced MDSC-mediated T cell activation. *J. Exp. Med.* 2014; 211(5):781-790. doi: 10.1084/jem.20131916

Noman MZ. Hasmim M. Messai Y. Terry S. Kieda C. Janji B. *et al.,* Hypoxia: a key player in antitumor immune response. A Review in the Theme: Cellular Responses to Hypoxia. *Am. J. Physiol. Cell Physiol.* 2015; 309(9):C569-79. doi: 10.1152/ajpcell.00207.2015

Nomi T. Sho M. Akahori T. Hamada K. Kubo A. Kanehiro H. et al.. Clinical significance and therapeutic potential of the programmed death-1 ligand/programmed death-1 pathway in human pancreatic cancer. *Clin. Cancer Res.* 2007; 13:2151–7. doi: 10.1158/1078-0432.CCR-06-2746

Nunes AS. Barros AS. Costa EC. Moreira AF. Correia IJ. 3D tumor spheroids as in vitro models to mimic in vivo human solid tumors resistance to therapeutic drugs. *Biotechnol. Bioen.* 2019; 116(1):206-226. doi: 10.1002/bit.26845

Nusinow DP. Szpyt J. Ghandi M. Rose CM. McDonald ER 3rd. Kalocsay M. *et al.,* Quantitative Proteomics of the Cancer Cell Line Encyclopedia. *Cell.* 2020; 180(2):387-402.e16. doi: 10.1016/j.cell.2019.12.023

Oda K. Arakawa H. Tanaka T. Matsuda K. Tanikawa C. Mori T. *et al.,* p53AIP1, a potential mediator of p53-dependent apoptosis, and its regulation by Ser-46-phosphorylated p53. *Cell.* 2000; 102(6):849-62. doi: 10.1016/s0092-8674(00)00073-8

Ohtsukasa S. Okabe S. Yamashita H. Iwai T. Sugihara K. Increased expression of CEA and MHC class I in colorectal cancer cell lines exposed to chemotherapy drugs. *J. Cancer Res. Clin. Oncol.* 2003;1 29(12):719-726. doi: 10.1007/s00432-003-0492-0

Oshima Y. Tanimoto T. Yuji K. Tojo A. EGFR-TKI-associated interstitial pneumonitis in Nivolumab-treated patients with non-small cell lung Cancer. *JAMA Oncol.* 2018;4:1112–5. doi: 10.1001/jamaoncol.2017.4526

Osta E, Gupta HB, Zhang D, Kornepati A, Clark CA, Curiel TJ. Tumor cell-intrinsic programmed death protein 1 expression and induction in human cancer cell lines. *J. Immunol.* 2018; 200:178.

Ott PA. Elez E. Hiret S. Kim DW. Morosky A. Saraf S. *et al.,* Pembrolizumab in patients with extensive-stage small-cell lung cancer: results from the phase Ib KEYNOTE-028 study. *J. Clin. Oncol.* 2017; 5:3823–9. doi: 10.1200/JCO.2017.72.5069

Overman MJ. Lonardi S. Wong KYM. Lenz HJ. Gelsomino F. Aglietta M. *et al.,* Durable Clinical Benefit With Nivolumab Plus Ipilimumab in DNA Mismatch Repair-Deficient/Microsatellite Instability-High Metastatic Colorectal Cancer. *J. Clin. Oncol.* 2018; 36(8):773-779. doi: 10.1200/JCO.2017.76.9901

Overman MJ. McDermott R. Leach JL. Lonardi S. Lenz HJ. Morse MA. *et al.,* Nivolumab in patients with metastatic DNA mismatch repair-deficient or microsatellite instability-high colorectal cancer (CheckMate 142): an open-label, multicentre, phase 2 study. *Lancet Oncol.* 2017; 18:1182–91. doi: 10.1016/S1470-2045(17)30422-9

Pacheco JM. Camidge R. Doebele RC. and Schenk E. A Changing of the Guard: Immune Checkpoint Inhibitors With and Without Chemotherapy as First Line Treatment for Metastatic Non-small Cell Lung Cancer. *Front. Oncol.* 2019; 9:195. doi: 10.3389/fonc.2019.00195

Pardoll DM. The blockade of immune checkpoints in cancer immunotherapy. Nature Rev. *Cancer.* 2012; 12: 252–264.

Park JJ. Thi EP. Carpio VH. Bi Y. Cole AG. Dorsey BD. *et al.,* Checkpoint inhibition through small molecule-induced internalization of programmed death-ligand 1. Nat Commun. 2021; 12:1222. doi: 10.1038/s41467-021-21410-1

Parsa AT. Waldron JS. Panner A. Crane CA. Parney IF. Barry JJ. *et al.,* Loss of tumor suppressor PTEN function increases B7-H1 expression and immunoresistance in glioma. *Nat Med.* 2007; 13(1):84–88. doi: 10.1038/nm1517

Passariello M. D'Alise AM. Esposito A. Vetrei C. Froechlich G. Scarselli E. *et al.,* Novel Human Anti-PD-L1 mAbs Inhibit Immune-Independent Tumor Cell Growth and PD-L1 Associated Intracellular Signalling. *Sci Rep.* 2019; 9:13125. doi: 10.1038/s41598-019-49485-3

Patel MR. Ellerton J. Infante JR. Agrawal M. Gordon M. Aljumaily R. *et al.,* Avelumab in metastatic urothelial carcinoma after platinum failure (JAVELIN Solid Tumor): pooled results from two expansion cohorts of an open-label, phase 1 trial. *Lancet Oncol.* 2017; 19:51–64. doi: 10.1016/S1470-2045(17)30900-2

Patnaik A. Kang SP. Rasco D. Papadopoulos KP. Elassaiss-Schaap J. Beeram M. *et al.,* Phase I study of pembrolizumab (MK-3475; anti-PD-1 monoclonal antibody) in patients with advanced solid tumours. *Clin. Cancer Res.* 2015; 21:4286–93. doi: 10.1158/1078-0432.CCR-14-2607

Paz-Ares L. Luft A. Vicente D. Tafreshi A. Gümüş M. Mazières J. *et al.,* Pembrolizumab plus Chemotherapy for Squamous Non-Small-Cell Lung Cancer. *N. Engl. J. Med.* 2018; 379(21): 2040-2051. doi: 10.1056/NEJMoa1810865

Peled M. Tocheva AS. Sandigursky S. Nayak S. Philips EA. Nichols KE. *et al.,* Affinity purification mass spectrometry analysis of PD-1 uncovers SAP as a new checkpoint inhibitor. *PNAS.* 2018; 115:E468–77. doi: 10.1073/pnas.1710437115

Peter M. Hadji A. Murmann A. Brockway S. Putzbach W. Pattanayak A. *et al.,* The role of CD95 and CD95 ligand in cancer. *Cell Death Differ.* 2015; 22:549-559. doi: 10.1038/cdd.2015.3

Petrylak DP. Powles T. Bellmunt J. Braiteh FY. Morales-Barrera R. *et al.,* Atezolizumab (MPDL3280A) monotherapy for patients with metastatic urothelial cancer long-term outcomes from a phase 1 study. *JAMA Oncol.* 2018; 4:537–44. doi: 10.1001/jamaoncol.2017.5440

Pitti RM. Marsters SA. Ruppert S. Donahue CJ. Moore A. Ashkenazi A. Induction of apoptosis by Apo-2 ligand, a new member of the tumor necrosis factor cytokine family. *J. Biol. Chem.* 1996; 271(22):12687–12690. doi: 10.1074/jbc.271.22.12687.

Plate JM. Plate AE. Shott S. Bograd S. Harris JE. Effect of gemcitabine on immune cells in subjects with adenocarcinoma of the pancreas. *Cancer Immunol. Immunother.* 2005;54(9):915-25. doi: 10.1007/s00262-004-0638-1

Poggio M. Hu T. Pai CC. Chu B. Belair CD. Chang A. *et al.,* Suppression of Exosomal PD-L1 Induces Systemic Anti-tumor Immunity and Memory. *Cell.* 2019; 177(2):414-427.e13. doi: 10.1016/j.cell.2019.02.016.

Powles T. O'Donnell PH. Massard C. Arkenau HT. Friedlander TW. Hoimes CJ. *et al.,* Efficacy and safety of durvalumab in locally advanced or metastatic urothelial carcinoma: updated results from a phase 1/2 open-label study. *JAMA Oncol.* 2017; 3(9):e172411. doi: 10.1001/jamaoncol.2017.2411

Prakash O. Gill J. Farr G. Immune disorders and susceptibility to neoplasms. *Ochsner J.* 2002;4(2):107-11.

Pyzer AR. Stroopinsky D. Rosenblatt J. Anastasiadou E. Rajabi H. Washington A. *et al.,* MUC1 inhibition leads to decrease in PD-L1 levels via upregulation of miRNAs. Leukemia. 2017; 31(12):2780–90. doi: 10.1038/leu.2017.163

Qiao X. Wang X. Shang Y. Li Y. Azithromycin enhances anticancer activity of TRAIL by inhibiting autophagy and up-regulating the protein levels of DR4/5 in colon cancer cells in vitro and in vivo. *Cancer Commun.* 2018; 38(43):1-13. doi: 10.1186/s40880-018-0309-9

Qin W. Hu L. Zhang X. Jiang S. Li J. Zhang Z. *et al.,* The diverse function of PD-1/PD-L pathway beyond cancer. *Front. Immunol.* 2019; 10:2298. doi: 10.3389/fimmu.2019.02298

Qiu Z-X. Sun R-F. Mo X-M. Li W-M. The p70S6K Specific Inhibitor PF-4708671 Impedes Non-Small Cell Lung Cancer Growth. *PLOS ONE.* 2016; 11(1): e0147185. doi: 10.1371/journal.pone.0147185

Raghavan S. Mehta P. Xie Y. Lei YL. Mehta G. Ovarian cancer stem cells and macrophages reciprocally interact through the WNT pathway to promote pro-tumoral and malignant phenotypes in 3D engineered microenvironments. *J. Immunother. Cancer.* 2019; 7:190. doi: 10.1186/s40425-019-0666-1

Raimondi C. Calleja V. Ferro R. Fantin A. Riley AM. Potter BVL. *et al.,* A Small Molecule Inhibitor of PDK1/PLCγ1 Interaction Blocks Breast and Melanoma Cancer Cell Invasion. *Sci Rep.* 2016; 6, 26142. doi: 10.1038/srep26142

Rascio F. Spadaccino F. Rocchetti MT. Castellano G. Stallone G. Netti GS. *et al.,* The Pathogenic Role of PI3K/AKT Pathway in Cancer Onset and Drug Resistance: An Updated Review. *Cancers.* 2021; 13(16):3949. doi: 10.3390/cancers13163949

Ribas A. Hu-Lieskovan S. What does PD-L1 positive or negative mean? *J. Exp. Med.* 2016; 213(13):2835-2840. doi: 10.1084/jem.20161462

Riedl A. Schlederer M. Pudelko K. Stadler M. Walter S. Unterleuthner D. Comparison of cancer cells in 2D vs 3D culture reveals differences in AKT–mTOR–S6K signaling and drug responses. *J. Cell Sci.* 2017; 130(1): 203-218. doi: 10.1242/jcs.188102

Rios de la Rosa JM. Wubetu J. Tirelli N. Tirella A. Colorectal tumor 3D in vitro models: Advantages of biofabrication for the recapitulation of early stages of tumour development. *Biomed. Phys. Eng. Expr.* 2018; 4(4):045010. doi: 10.1088/2057-1976/aac1c9

Robert C. Schachter J. Long GV. Arance A. Grob JJ. Mortier L. *et al.,* Pembrolizumab versus ipilimumab in advanced melanoma. *N Engl J Med.* 2015; 372:2521–32. doi: 10.1056/NEJMoa1503093

Robert C. Schachter J. Long GV. Arance A. Grob JJ. Mortier L. *et al.,* Pembrolizumab versus ipilimumab in advanced melanoma. *N. Engl. J. Med.* 2015; 372:2521–32. doi: 10.1056/NEJMoa1503093

Rodallec A. Sicard G. Giacometti S. Carré M. Pourroy B. Bouquet F. *et al.,* From 3D spheroids to tumor bearing mice: Efficacy and distribution studies of trastuzumab-docetaxel immunoliposome in breast cancer. *Int. J. Nanomed.* 2018; 13:6677–6688. doi: 10.2147/IJN.S179290.10.3389/fonc.2021.782766

Romano E. Honeychurch J. Illidge TM. Radiotherapy-Immunotherapy Combination: How Will We Bridge the Gap Between Pre-Clinical Promise and Effective Clinical Delivery? *Cancers (Basel).* 2021; 13(3):457. doi: 10.3390/cancers13030457

Rom-Jurek EM. Kirchhammer N. Ugocsai P. Ortmann O. Wege AK. Brockhoff G. Regulation of Programmed Death Ligand 1 (PD-L1) Expression in Breast Cancer Cell Lines In Vitro and in Immunodeficient and Humanized Tumor Mice. *Int. J. Mol. Sci.* 2018; 19(2):563. doi: 10.3390/ijms19020563

Rosenberg JE. Hoffman-Censits J. Powles T. van der Heijden MS. Balar AV. Necchi A. *et al.,* Atezolizumab in patients with locally advanced and metastatic urothelial carcinoma who have progressed following treatment with platinum-based chemotherapy: a single-arm, multicentre, phase 2 trial. *Lancet.* 2016; 387(10031): 1909-1920. doi: 10.1016/S0140-6736(16)00561-4

Roux PP. Blenis J. ERK and p38 MAPK-activated protein kinases: a family of protein kinases with diverse biological functions. *Microbiol. Mol. Biol. Rev.* 2004; 68(2): 320-44. doi: 10.1128/MMBR.68.2.320-344.2004

Sabatier R. Finetti P. Mamessier E. Adelaide J. Chaffanet M. Ali H. *et al.,* Prognostic and predictive value of PDL1 expression in breast cancer. *Oncotarget.* 2015; 6: 5449-5464. doi: 10.18632/oncotarget.3216

Saleh R. Taha RZ. Sasidharan Nair V. Alajez NM. Elkord E. PD-L1 blockade by atezolizumab downregulates signaling pathways associated with tumor growth, metastasis, and hypoxia in human triple negative breast cancer. *Cancers.* 2019; 11:1050. doi: 10.3390/cancers11081050

Sansom DM. Walker LSK. Dimers Aren't Forever: CD80 Breaks up with PD-L1. *Immunity.* 2019; 51(6):972-974. doi: 10.1016/j.immuni.2019.11.011

Satelli A. Batth IS. Brownlee Z. Rojas C. Meng QH. Kopetz S. Li S. Potential role of nuclear PD-L1 expression in cell-surface vimentin positive circulating tumor cells as a prognostic marker in cancer patients. *Sci. Rep.* 2016; 6:28910. doi: 10.1038/srep28910

Sato E. Olson SH. Ahn J. Bundy B. Nishikawa H. Qian F. *et al.,* Intraepithelial CD8+ tumor-infiltrating lymphocytes and a high CD8+/regulatory T cell ratio are associated

with favorable prognosis in ovarian cancer. *PNAS*. 2005; 102 (51):18538–18543. doi: 10.1073/pnas.0509182102

Schaafsma E. Fugle CM. Wang X. Cheng C. Pan-cancer association of HLA gene expression with cancer prognosis and immunotherapy efficacy. *Br. J. Cancer.* 2021; 125, 422-432. doi: 10.1038/s41416-021-01400-2

Scharping NE. Menk AV. Whetstone RD. Zeng X. Delgoffe GM. Efficacy of PD-1 blockade is potentiated by metformin-induced reduction of tumor hypoxia. *Cancer Immunol. Res.* 2017; 5(1):9-16. doi: 10.1158/2326-6066

Schmid P. Adams S. Rugo HS. Schneeweiss A. Barrios CH. Iwata H. *et al.,* Atezolizumab and nab-paclitaxel in advanced triple-negative breast cancer. *N Engl J Med.* 2018; 379(22):2108-2121. doi: 10.1056/NEJMoa1809615

Schmidt G. Guhl MM. Solomayer EF. Wagenpfeil G. Hammadeh ME. Juhasz-Boess I. *et al.,* Immunohistochemical assessment of PD-L1 expression using three different monoclonal antibodies in triple negative breast cancer patients. *Arch. Gynecol. Obstet.* 2022. doi: 10.1007/s00404-022-06529-w

Senbanjo LT. Chellaiah MA. CD44: A Multifunctional Cell Surface Adhesion Receptor Is a Regulator of Progression and Metastasis of Cancer Cells. *Front. Cell Dev.* Biol. 2017; 5:18. doi: 10.3389/fcell.2017.00018

Shah NJ. Kelly WJ. Liu SV. Choquette K. Spira A. Product review on the Anti-PD-L1 antibody atezolizumab. *Hum Vaccin Immunother.* 2018; 14(2):269-276. doi: 10.1080/21645515.2017.1403694

Shang B. Lui Y. Jiang S. Lui Y. Prognostic value of tumor-infiltrating FoxP3+ regulatory T cells in cancers: a systematic review and meta-analysis. *Sci Rep.* 2015; 5:15179. doi: 10.1038/srep15179

Sharma P. Retz M. Siefker-Radtke A. Baron A. Necchi A. Bedke J. *et al.,* Nivolumab in metastatic urothelial carcinoma after platinum therapy (CheckMate 275): a multicentre, single-arm, phase 2 trial. *Lancet Oncol.* 2017; 18:312–22. doi: 10.1016/S1470-2045(17)30065-7

Sharma P. Shen Y. Wen S. Yamada S. Jungbluth AA. Gnjatic S. *et al.,* CD8 tumor-infiltrating lymphocytes are predictive of survival in muscle-invasive urothelial carcinoma. *PNAS*. 2007;104(10):3967–3972. doi: 10.1073/pnas.0611618104

Shen X. Zhang L. Li J. Li Y. Wang Y. and Xu ZX. Recent Findings in the Regulation of Programmed Death Ligand 1 Expression. *Front. Immunol*. 2019; 10:1337. doi: 10.3389/fimmu.2019.01337

Sheridan JP. Marsters SA. Pitti RM. Gurney A. Skubatch M. Baldwin D. *et al.,* Control of TRAIL-induced apoptosis by a family of signaling and decoy receptors. *Science.* 1997; 277(5327):818–821. doi: 10.1126/science.277.5327.818

Shi Y. Chang M. Wang F. Ouyang X. Jia Y. Du H. Role and mechanism of hypoxia-inducible factor-1 in cell growth and apoptosis of breast cancer cell line MDA-MB-231. *Oncol Lett.* 2010; 1(4):657-662. doi: 10.3892/ol_00000115

Shin DS. Zaretsky JM. Escuin-Ordinas H. Garcia-Diaz A. Hu-Lieskovan S. Kalbasi A. *et al.,* Primary resistance to PD-1 blockade mediated by JAK1/2 mutations. *Cancer Discov.* 2017; 7:188–201. doi: 10.1158/2159-8290.CD-16-1223

Shin MS. Kim HS. Lee SH. Park WS. Kim SY. Park JY. *et al.,* (2001). Mutations of tumour necrosis factor-related apoptosis-inducing ligand receptor 1 (TRAIL-R1) and receptor 2 (TRAIL-R2) genes in metastatic breast cancers. *Cancer Res.* 2001; 61(13): 4942-4946.

Showalter A. Limaye A. Oyer JL. Igarashi R. Kittipatarin C. Copik AJ. *et al.,* Cytokines in immunogenic cell death: Applications for cancer immunotherapy. *Cytokine.* 2017; 97, 123–132. doi: 10.1016/j.cyto.2017.05.024

Simeone E. Grimaldi AM. Festino L. Giannarelli D. Palla M. Caracò C. *et al.,* Correlation between BRAF mutational status and clinical response to pembrolizumab in advanced melanoma patients. *J. Immunother. Cancer.* 2015; 3(2):P134. doi: 10.1186/2051-1426-3-S2-P134

Simstein R. Burow M. Parker A. Weldon C. Beckman B. Apoptosis, chemoresistance, and breast cancer: insights from the MCF-7 cell model system. *Exp Biol Med (Maywood).* 2003; 228(9):995-1003. doi: 10.1177/153537020322800903

Socinski MA. Jotte RM. Cappuzzo F. Orlandi F. Stroyakovskiy D. Nogami N. *et al.,* Atezolizumab for First-Line Treatment of Metastatic Nonsquamous NSCLC. *N. Engl. J. Med.* 2018; 378(24):2288-2301. doi: 10.1056/NEJMoa1716948

Soliman H. Khalil F. Scott A. PD-L1 expression is increased in a subset of basal type breast cancer cells. *PLoS One.* 2014; 9(2):e88557. doi: 10.1371/journal.pone.0088557

Song M. Chen D. Lu B. Wang C. Zhang J. *et al.,* PTEN Loss Increases PD-L1 Protein Expression and Affects the Correlation between PD-L1 Expression and Clinical Parameters in Colorectal Cancer. *PLoS ONE.* 2013; 8(6):e65821. doi: 10.1371/journal.pone.0065821

Souza AG. Silva IBB. Campos-Fernández E. Barcelos LS. Souza JB. Marangoni K. Comparative assay of 2D and 3D cell culture models: Proliferation, gene expression and anticancer drug response. *Curr. Pharm. Des.* 2018; 24:1-6. doi: 10.2174/1381612824666180404152304

Steven A. Seliger B. Control of CREB expression in tumors: from molecular mechanisms and signal transduction pathways to therapeutic target. *Oncotarget.* 2016 ; 7(23):35454-65. doi: 10.18632/oncotarget.7721

Sulzmaier FJ. Ramos JW. RSK isoforms in cancer cell invasion and metastasis. *Cancer Res.* 2013; 73(20): 6099-105. doi: 10.1158/0008-5472.CAN-13-1087

Sun C. Lan P. Han Q. Huang M. Zhang Z. Xu G. *et al.,* Oncofetal gene SALL4 reactivation by hepatitis B virus counteracts miR-200c in PD-L1-induced T cell exhaustion. *Nat Commun.* 2018; 9(1):1241. doi: 10.1038/s41467-018-03584-3

Sun JM. Shen L. Shah MA. Enzinger P. Adenis A. Doi T. *et al.,* Pembrolizumab plus chemotherapy versus chemotherapy alone for first-line treatment of advanced oesophageal cancer (KEYNOTE-590): A randomised, placebo-controlled, phase 3 study. *Lancet.* 2021; 398:759–771. doi: 10.1016/S0140-6736(21)01234-4.

Sun LL. Yang RY. Li CW. Chen MK. Shao B. Hsu JM. *et al.,* Inhibition of ATR downregulates PD-L1 and sensitizes tumor cells to T cell-mediated killing. *Am. J. Cancer Res.* 2018; 8:1307–1316.

Tai S. Sun Y. Squires JM. Zhang H. Oh WK. Liang CZ. *et al.,* PC3 is a cell line characteristic of prostatic small cell carcinoma. *Prostate.* 2011; 71(15):1668-79. doi: 10.1002/pros.21383

Takahashi N. Cho P. Selfors LM. Kuiken HJ. Kaul R. Fujiwara T. *et al.,* 3D Culture Models with CRISPR Screens Reveal Hyperactive NRF2 as a Prerequisite for Spheroid Formation via Regulation of Proliferation and Ferroptosis. *Mol. Cell.* 2020; 80:828-844.e6. doi: 10.1016/j.molcel.2020.10.010

Tamai K. Nakamura M. Mizuma M. Mochizuki M. Yokoyama M. Endo H. *et al.,* Suppressive expression of CD274 increases tumorigenesis and cancer stem cell like phenotypes in cholangiocarcinoma. *Cancer Sci.* 2014;105(6):667–674. doi: 10.1111/cas.12406

Tang D. Zhao D. Wu Y. Yao R. Zhou L. Lu L. *et al.,* The miR-3127-5p/p-STAT3 axis up-regulates PD-L1 inducing chemoresistance in non-small-cell lung cancer. *J. Cell Mol. Med.* 2018; 22(8):3847–3856. doi: 10.1111/jcmm.13657

Tawfik O. Kimler BF. Karnik T. Shehata, P. Clinicopathological correlation of PD-L1 expression in primary and metastatic breast cancer and infiltrating immune cells. *Hum. Pathol.* 2018; 80:170-178. doi: 10.1016/j.humpath.2018.06.008

Teng MWL. Galon J. Fridman WH. Smyth MJ. From mice to humans: developments in cancer immunoediting. *J. Clin. Invest.* 2015; 125(9):3338–46. doi: 10.1172/JCI80004

Teo PY. Yang C. Whilding LM. Parente-Pereira AC. Mhaer J. George AJT. *et al.,* Ovarian cancer immunotherapy using PD-L1 siRNA targeted delivery from folic acid-functionalized polyethylenimine: strategies to enhance T cell killing. *Adv. Healthc. Mater.* 2015; 4(8):1180-1189. doi: 10.1002/adhm.201500089

Theivanthiran B. Evans KS. DeVito NC. Plebanek M. Sturdivant M. Wachsmuth LP. *et al.,* A tumor-intrinsic PD-L1-NLRP3 inflammasome signaling pathway drives resistance to anti-PD-1 immunotherapy. *J. Clin. Invest.* 2020; 130:2570–86. doi: 10.1172/JCI133055

Thompson RH. Kuntz SM. Leibovich BC. Dong H. Lohse CM. Webster WS. et al.. Tumor B7-H1 is associated with poor prognosis in renal cell carcinoma patients with long-term follow-up. *Cancer Res*. (2006) 66:3381–5. doi: 10.1158/0008-5472

Thorburn A. Tumor necrosis factor-related apoptosis-inducing ligand (TRAIL) pathway signaling. *J. Thorac. Oncol.* 2007; 2(6):461-465. doi:10.1097/JTO.0b013e31805fea64

Todaro M. Lombardo Y. Francipane MG. Alea MP. Cammareri P. Iovino F. Di Stefano AB. Di Bernardo C. Agrusa A. Condorelli G. Walczak H. Stassi G. Apoptosis resistance in epithelial tumors is mediated by tumor-cell-derived interleukin-4. *Cell Death Differ.* 2008; 15(4):762-72. doi: 10.1038/sj.cdd.4402305

Topalian SL. Hodi FS. Brahmer JR. Gettinger SN. Smith DC. McDermott DF. *et al.,* Safety, activity, and immune correlates of anti-PD-1 antibody in cancer. *N. Engl. J. Med.* 2012; 366:2443–54. doi: 10.1056/NEJMoa1200690

Trauth BC. Klas C. Peters AM. Matzku S. Moller P. Falk W. *et al.,* Monoclonal antibody-mediated tumor regression by induction of apoptosis. *Science*. 1989; 245(4915):301-5. doi: 10.1126/science.2787530

Tsai YP. Wu KJ. Hypoxia-regulated target genes implicated in tumor metastasis. *J. Biomed. Sci.* 2012; 19(1):102. doi: 10.1186/1423-0127-19-102

Tumeh PC. Harview CL. Yearley JH. Shintaku PI. Taylor EJM. Robert L. *et al.,* PD-1 blockade induces responses by inhibiting adaptive immune resistance. *Nature.* 2014; 515:568–571. doi: 10.1038/nature13954

Tur V. van der Sloot AM. Reis C R. Szegezdi E. Cool RH. Samali A. *et al.,* DR4-selective tumor necrosis factor-related apoptosis-inducing ligand (TRAIL) variants obtained by structure-based design. *J. Biol. Chem.* 2008; 283(29):20560. doi:10.1074/jbc.M800457200

Twa DDW. Chan FC. Ben-Neriah S. Woolcock BW. Mottok A. Tan KL. *et al.,* Genomic rearrangements involving programmed death ligands are recurrent in primary mediastinal large B-cell lymphoma. *Blood.* 2014; 123(13):2062–2065. doi: 10.1182/blood-2013-10-535443

Vanneman M. Dranoff G. Combining immunotherapy and targeted therapies in cancer treatment. *Nat. Rev. Cancer.* 2012; 12(4): 237-51. doi: 10.1038/nrc3237

Vanneman M. Dranoff G. Combining immunotherapy and targeted therapies in cancer treatment. *Nat. Rev. Cancer.* 2012; 12(4):237-51. doi: 10.1038/nrc3237.

Vannini A. Leoni V. Barboni C. Sanapo M. Zaghini A. Malatesta P. *et al.,* αvβ3-integrin regulates PD-L1 expression and is involved in cancer immune evasion. PNAS. 2019; 116(40):20141-20150. doi: 10.1073/pnas.1901931116

Villa-Morales M. Fernández-Piqueras J. Targeting the Fas/FasL signaling pathway in cancer therapy. *Expert Opin. Ther. Targets.* 2012; 16(1):85-101. doi: 10.1517/14728222.2011.628937

Votanopoulos KI. Forsythe S. Sivakumar H. Mazzocchi A. Aleman J. Miller L. *et al.,* Model of Patient-Specific Immune-Enhanced Organoids for Immunotherapy Screening: Feasibility Study. *Ann. Surg. Oncol.* 2020; 27:1956–1967. doi: 10.1245/s10434-019-08143-8

Walczak H. Miller RE. Ariail K. Gliniak B. Griffith TS. Kubin M. *et al.,* Tumoricidal activity of tumor necrosis factor-related apoptosis-inducing ligand in vivo. *Nat. Med.* 1999; 5(2):157–163. doi: 10.1038/5517

Wang D. Lin J. Yang X. Long J. Bai Y. Yang X. et al.. Combination regimens with PD-1/PD-L1 immune checkpoint inhibitors for gastrointestinal malignancies. *J Hematol Oncol.* 2019; 12:42. doi: 10.1186/s13045-019-0730-9

Wang JS. Wang CL. Wen JF. Wang YJ. Hu YB. Ren HZ. Lithium inhibits proliferation of human esophageal cancer cell line Eca-109 by inducing a G2/M cell cycle arrest. *World J. Gastroenterol.* 2008; 14(1):3982–3989. doi: 10.3748/wjg.14.3982

Wang S. Xu L. Che X. Li C. Xu L. Hou K. *et al.,* E3 ubiquitin ligases Cbl-b and c-Cbl downregulate PD-L1 in EGFR wild-type non-small cell lung cancer. *FEBS Lett.* 2018; 592(4):621-630. doi: 10.1002/1873-3468.12985

Wang W. Sun J. Li F. Li R. Gu Y. Liu C. *et al.,* A frequent somatic mutation in CD274 3'-UTR leads to protein over-expression in gastric cancer by disrupting miR-570 binding. *Hum Mutat.* 2012;33(3):480-484. doi: 10.1002/humu.22014

Wang X. Schoenhals JE. Li A. Valdecanas DR. Ye H. Zang F. *et al.,* Suppression of type I IFN signaling in tumors mediates resistance to anti-PD-1 treatment that can be overcome by radiotherapy. *Cancer Res.* 2017; 77(4):839–50. doi: 10.1158/0008-5472

Wang X. Teng F. Kong L. Yu J. PD-L1 expression in human cancers and its association with clinical outcomes. *Onco Targets Ther.* 2016; 9:5023-39. doi: 10.2147/OTT.S105862

Wang X. Yang L. Huang F. Zhang Q. Liu S. Ma L. *et al.,* Inflammatory cytokines IL-17 and TNF-α up-regulate PD-L1 expression in human prostate and colon cancer cells. *Immunol. Lett.* 2017; 184: 7-14. doi: 10.1016/j.imlet.2017.02.006

Wang X. Yang X. Zhang C. Wang Y. Cheng T. Duan L. *et al.,* Tumor cell-intrinsic PD-1 receptor is a tumor suppressor and mediates resistance to PD-1 blockade therapy. *Proc. Natl. Acad. Sci. USA.* 2020; 117(12): 6640-6650. doi: 10.1073/pnas.1921445117

Wang Y. Wang X. Zhao H. Liang B. Du Q. Clusterin confers resistance to TNF-alpha-induced apoptosis in breast cancer cells through NF-kappaB activation and Bcl-2 overexpression. *J. Chemother.* 2012; 24(6):348-357. doi: 10.1179/1973947812Y.0000000049

Wang YF. Liu F. Sherwin S. Farrelly M. Yan XG. Croft A. *et al.,* Cooperativity of HOXA5 and STAT3 Is critical for HDAC8 inhibition-mediated transcriptional

activation of PD-L1 in human melanoma cells. *J. Invest. Dermatol.* 2018; 138(4):922–32. doi: 10.1016/j.jid.2017.11.009

Weber J. Mandala M. Del Vecchio M. Gogas HJ. Arance AM. Cowey CL, *et al.,* Adjuvant nivolumab versus ipilimumab in resected stage III or IV melanoma. *N. Engl. J. Med.* 2017; 377:1824–35. doi: 10.1056/NEJMoa1709030

Weber JS. D'Angelo SP. Minor D. Hodi FS. Gutzmer R. Neyns B. *et al.,* Nivolumab versus chemotherapy in patients with advanced melanoma who progressed after anti-CTLA-4 treatment (CheckMate 037): a randomised, controlled, open-label, phase 3 trial. *Lancet Oncol.* 2015; 16:375–84. doi: 10.1016/S1470-2045(15)70076-8

West H. McCleod M. Hussein M. Morabito A. Rittmeyer A. Conter HJ. *et al.,* Atezolizumab in combination with carboplatin plus nab-paclitaxel chemotherapy compared with chemotherapy alone as first-line treatment for metastatic non-squamous non-small-cell lung cancer (IMpower130): a multicentre, randomised, open-label, phase 3 trial. *Lancet Oncol.* 2019; 20(7):924-937. doi: 10.1016/S1470-2045(19)30167-6

Wiley SR. Schooley K. Smolak PJ. Din WS. Huang CP. Nicholl JK. *et al.,* Identification and characterization of a new member of the TNF family that induces apoptosis. *Immunity.* 1995; 3: 673–682. Doi: 10.1016/1074-7613(95)90057-8.

Wu Q. Jiang L. Li SC. He QJ. Yang B. Cao J. Small molecule inhibitors targeting the PD-1/PD-L1 signaling pathway. *Acta Pharmacol Sin.* 2021; 42, 1–9. doi: 10.1038/s41401-020-0366-x

Wu X. Li Y. Liu X. Chen C. Harrington SM. Cao S. *et al.,* Targeting B7-H1 (PD-L1) sensitizes cancer cells to chemotherapy. *Heliyon.* 2018; 4(12):e01039. doi: 10.1016/j.heliyon.2018.e01039

Wu Y. Gu W. Jiang L. Chen C. and Xu ZP. Silencing PD-1 and PD-L1 with nanoparticle-delivered small interfering RNA increases cytotoxicity of tumour-infiltrating lymphocytes. *Nanomedicine.* 2019; 14(8):955-967. Doi: 10.2217/nnm-2018-0237

Xiao G. Jin LL. Liu CQ. Wang YC. Meng YM. Zhou ZG. *et al.,* EZH2 negatively regulates PD-L1 expression in hepatocellular carcinoma. *J. Immunother. Cancer.* 2019; 7:300. doi: 10.1186/s40425-019-0784-9

Xu C. Fillmore CM. Koyama S. Wu H. Zhao Y. Chen Z. *et al.,* Loss of Lkb1 and Pten leads to lung squamous cell carcinoma with elevated PD-L1 expression. *Cancer Cell.* 2014; 259(5):590–604. doi: 10.1016/j.ccr.2014.03.033

Yang H. Zhou X. Sun L. Mao Y. Correlation Between PD-L2 Expression and Clinical Outcome in Solid Cancer Patients: A Meta-Analysis. *Front Oncol.* 2019; 13;9:47. doi: 10.3389/fonc.2019.00047

Yang J. Yan J. Liu B. Targeting VEGF/VEGFR to Modulate Antitumor Immunity. *Front. Immunol.* 2018; 9:978. doi: 10.3389/fimmu.2018.00978

Yang X. Zhu G. Yang Z. Zeng K. Liu F. Sun J. Expression of PD-L1/PD-L2 is associated with high proliferation index of Ki-67 but not with TP53 overexpression in chondrosarcoma. *Int. J. Biol. Markers.* 2018; 33(4):507-513. doi: 10.1177/1724600818774464

Yao H. Wang H. Li C. Fang J. and Xu J. Cancer Cell-Intrinsic PD-1 and Implications in Combinatorial Immunotherapy. *Front Immunol.* 2018; 9:1774. doi: 10.3389/fimmu.2018.01774

Yasuda M. Tanaka Y. Fujii K. Yasumoto K. CD44 stimulation down-regulates Fas expression and Fas-mediated apoptosis of lung cancer cells. *Int Immunol.* 2001; 13(10):1309-19. doi: 10.1093/intimm/13.10.1309

Yau T. Kang Y. Kim T. El-Khoueiry AB. Santoro A. Sangro B. *et al.,* Efficacy and Safety of Nivolumab Plus Ipilimumab in Patients With Advanced Hepatocellular Carcinoma Previously Treated With Sorafenib: The CheckMate 040 Randomized Clinical Trial. *JAMA Oncol.* 2020; 6(11):e204564. doi:10.1001/jamaoncol.2020.4564

Yee D. Shah KM. Coles MC. Sharp TV. Lagos D. MicroRNA-155 induction via TNF-α and IFN-γ suppresses expression of programmed death ligand-1 (PD-L1) in human primary cells. *J. Biol. Chem.* 2017; 292(50):20683–20693. doi: 10.1074/jbc.M117.809053

Yi M. Jiao D. Xu H. Liu Q. Zhao W. Han X. *et al.,* Biomarkers for predicting efficacy of PD-1/PD-L1 inhibitors. *Mol Cancer.* 2018; 17:129. doi: 10.1186/s12943-018-0864-3

Yi M. Zheng X. Niu M. Zhu S. Ge H. Wu K. Combination strategies with PD-1/PD-L1 blockade: current advances and future directions. *Mol. Cancer.* 2022; 21(1):28. doi: 10.1186/s12943-021-01489-2

Young CD. Lewis AS. Rudolph MC. Ruehle MD. Jackman MR. Yun UJ. *et al.,* Modulation of glucose transporter 1 (GLUT1) expression levels alters mouse mammary tumor cell growth in vitro and in vivo. *PLoS One.* 2011; 6(8):e23205. doi: 10.1371/journal.pone.0023205

Yu S. Wang Y. He P. Shao B. Liu F. Xiang Z. *et al.,* Effective Combinations of Immunotherapy and Radiotherapy for Cancer Treatment. *Front. Oncol.* 2022; 12:809304. doi: 10.3389/fonc.2022.809304

Yu W. Hua Y. Qiu H. Hao J. Zou K. Li Z. *et al.,* PD-L1 promotes tumor growth and progression by activating WIP and β-catenin signaling pathways and predicts poor prognosis in lung cancer. *Cell Death Dis.* 2020; 11:506. doi: 10.1038/s41419-020-2701-z

Zaretsky JM. Garcia-Diaz A. Shin DS. Escuin-Ordinas H. Hugo W. Hu-Lieskovan S. *et al.,* Mutations Associated with Acquired Resistance to PD-1 Blockade in Melanoma. *N. Engl. J. Med.* 2016; 375(9):819-829. doi: 10.1056/NEJMoa1604958

Zeng Z. Shi F. Zhou L. Zhang MN. Chen Y. Chang XJ. et al.. Upregulation of circulating PD-L1/PD-1 is associated with poor post-cryoablation prognosis in patients with HBV-related hepatocellular carcinoma. *PLoS ONE.* 2011; 6:e23621. doi: 10.1371/journal.pone.0023621

Zhan MM. Hu XQ. Liu XX. Ruan BF. Xu J. Liao C. From monoclonal antibodies to small molecules: the development of inhibitors targeting the PD-1/PD-L1 pathway. *Drug Discov. Today.* 2016; 21(6):1027-36. doi: 10.1016/j.drudis.2016.04.011

Zhang F. Qi X. Wang X. Wei D. Wu J. Feng L. *et al.,* Structural basis of the therapeutic anti-PD-L1 antibody atezolizumab. *Oncotarget.* 2017; 8(52):90215-90224. doi: 10.18632/oncotarget.21652

Zhang J. Bu X. Wang H. Zhu Y. Geng Y. Nihira NT. *et al.,* Cyclin D-CDK4 kinase destabilizes PD-L1 via cullin 3-SPOP to control cancer immune surveillance. *Nature.* 2018; 553:91-95. doi: 10.1038/nature25015

 Zhang JY. Zhao YL. Lv YP. Cheng P. Chen W. Duan M. *et al.,* Modulation of CD8(+) memory stem T cell activity and glycogen synthase kinase 3β inhibition enhances anti-tumoral immunity in gastric cancer. *Oncoimmunol.* 2018; 7: e1412900. doi: 10.1080/2162402X.2017.1412900

Zhang X. Zeng Y. Qu Q. Zhu J. Liu Z. Ning W. *et al.,* PD-L1 induced by IFN-gamma from tumor-associated macrophages via the JAK/STAT3 and PI3K/AKT signaling pathways promoted progression of lung cancer. *Int. J. Clin. Oncol.* 2017; 22:1026-1033. doi: 10.1007/s10147-017-1161-7

Zhang Y. Xiang C. Wang Y. Duan Y. Liu C. and Zhang Y. PD-L1 promoter methylation mediates the resistance response to anti-PD-1 therapy in NSCLC patients with EGFR-TKI resistance. *Oncotarget.* 2017; 8(60):101535–101544. doi: 10.18632/oncotarget.21328

Zhao Y. Lee CK. Lin CH. Gassen RB. Xu X. Huang Z. *et al.,* PD-L1:CD80 Cis-Heterodimer Triggers the Co-stimulatory Receptor CD28 While Repressing the Inhibitory PD-1 and CTLA-4 Pathways. *Immunity.* 2019; 51(6):1059-1073. doi: 10.1016/j.immuni.2019.11.003

Zheng H. Zhao W. Yan C. Watson CC. Massengill M. Xie M. *et al.,* HDAC inhibitors enhance T cell chemokine expression and augment response to PD-1 immunotherapy in lung adenocarcinoma. *Clin Cancer Res.* 2016; 22(16):4119-4132. doi: 10.1158/1078-0432.CCR-15-2584

Zhi Y. Mou Z. Chen J. He Y. Dong H. Fu X. *et al.,* B7H1 expression and epithelial-to-mesenchymal transition phenotypes on colorectal cancer stem-like cells. *PLoS ONE.* 2015; 10:e0135528. doi: 10.1371/journal.pone.0135528

Zhong F. Cheng X. Sun S. Zhou J. Transcriptional activation of PD-L1 by Sox2 contributes to the proliferation of hepatocellular carcinoma cells. *Oncol Rep.* 2017; 37(5):3061-3067. doi: 10.3892/or.2017.5523.

Zhou J. Schmid T. Brüne B. Tumor necrosis factor-alpha causes accumulation of a ubiquitinated form of hypoxia inducible factor-1alpha through a nuclear factor-kappaB-dependent pathway. *Mol Biol Cell.* 2003; 14(6):2216-25. doi: 10.1091/mbc.e02-09-0598

Zhou L. Cha G. Chen L. Yang C. Xu D. and Ge M. HIF1α/PD-L1 axis mediates hypoxia-induced cell apoptosis and tumor progression in follicular thyroid carcinoma. *Onco. Targets Ther*. 2019;12:6461–6470. doi: 10.2147/OTT.S203724

Zhu AX. Finn RS. Edeline J. Cattan S. Ogasawara S. Palmer D. *et al.,* KEYNOTE-224 investigators. Pembrolizumab in patients with advanced hepatocellular carcinoma previously treated with sorafenib (KEYNOTE-224): a non-randomised, open-label phase 2 trial. *Lancet Oncol.* 2018; 19:940–52. doi: 10.1016/S1470-2045(18)30351-6

Zhu J. Chen L. Zou L. Yang P. Wu R. Mao Y. *et al.,* MiR-20b, -21, and -130b inhibit PTEN expression resulting in B7-H1 over-expression in advanced colorectal cancer. *Hum Immunol.* 2014; 75(4):348-353. doi: 10.1016/j.humimm.2014.01.006

Zinzani P. Thieblemont C. Melnichenko V. Osmanov D. Bouabdallah K. Walewski J. *et al.,* Efficacy and safety of pembrolizumab in relapsed/refractory primary mediastinal large B-cell lymphoma (rrPMBCL): interim analysis of the KEYNOTE-170 phase 2 trial. *Hematol. Oncol.* 2017; 35:62–3. doi: 10.1002/hon.2437_49

Ziogas AC. Gavalas NG. Tsiatas M. Tsitsilonis O. Politi E. Terpos E. *et al.,* VEGF directly suppresses activation of T cells from ovarian cancer patients and healthy individuals via VEGF receptor Type 2. *Int. J. Cancer.* 2012;130(4):857–864. doi: 10.1002/ijc.26094

9. Appendices

Appendix Figure 9.1.
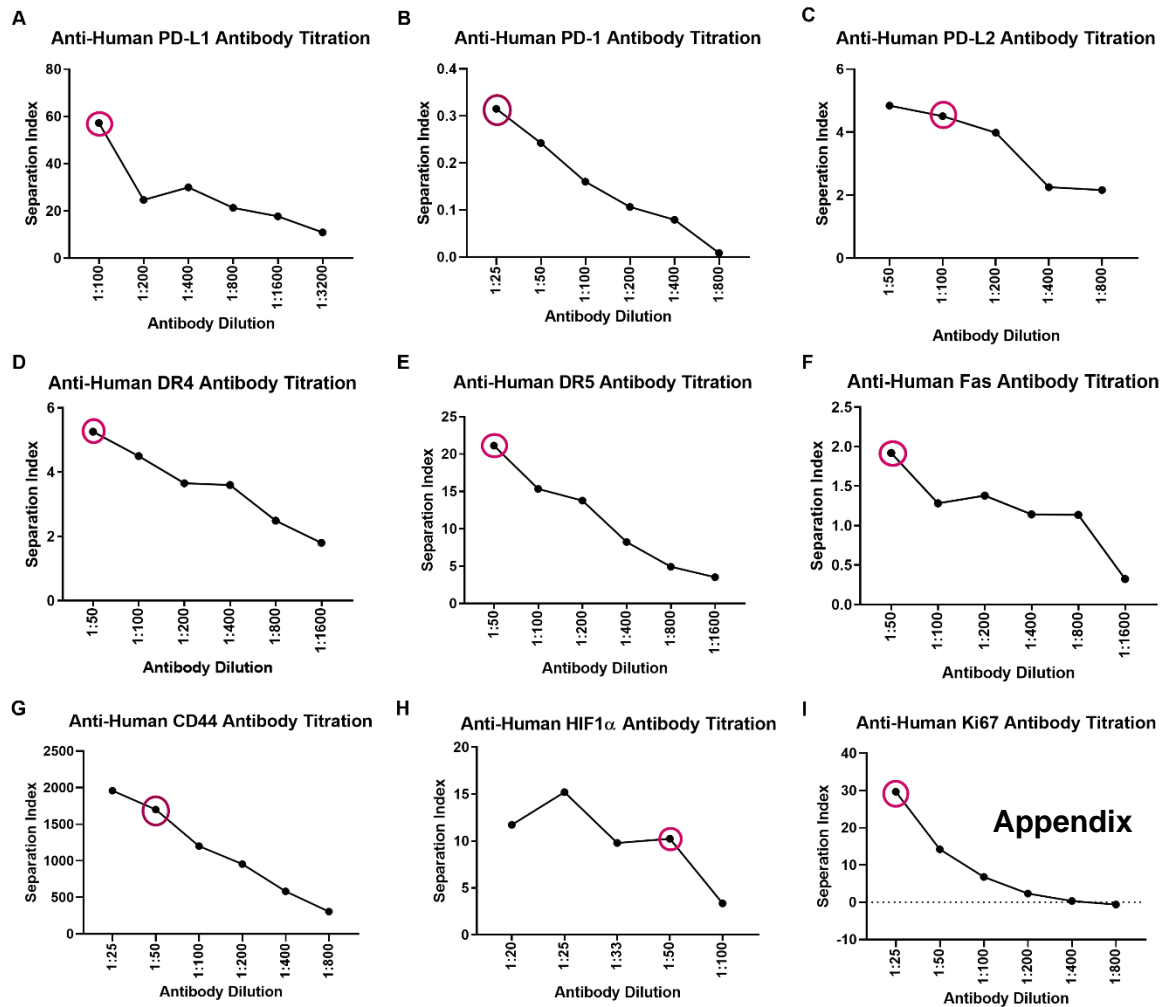
**Figure 9.1. Antibody titrations of the different antibodies used in this study.** Antibodies used in this study were titrated prior to carrying out the main experiments to determine the separation index and optimal concentration of antibody to use. Antibody concentrations were decided by using the manufacturer's recommendations and/or prior published antibody concentrations. Antibody titrations were performed for **(A)** anti-human PD-L1, **(B)** anti-human PD-1, **(C)** anti-human PD-L2, **(D)** anti-human DR4, **(E)** anti-human DR5, **(F)** anti-human Fas, **(G)** anti-human CD44, **(H)** anti-human HIF1α, and **(I)** anti-human Ki67. Data here represents n=1.

Appendix Figure 9.2

A

B
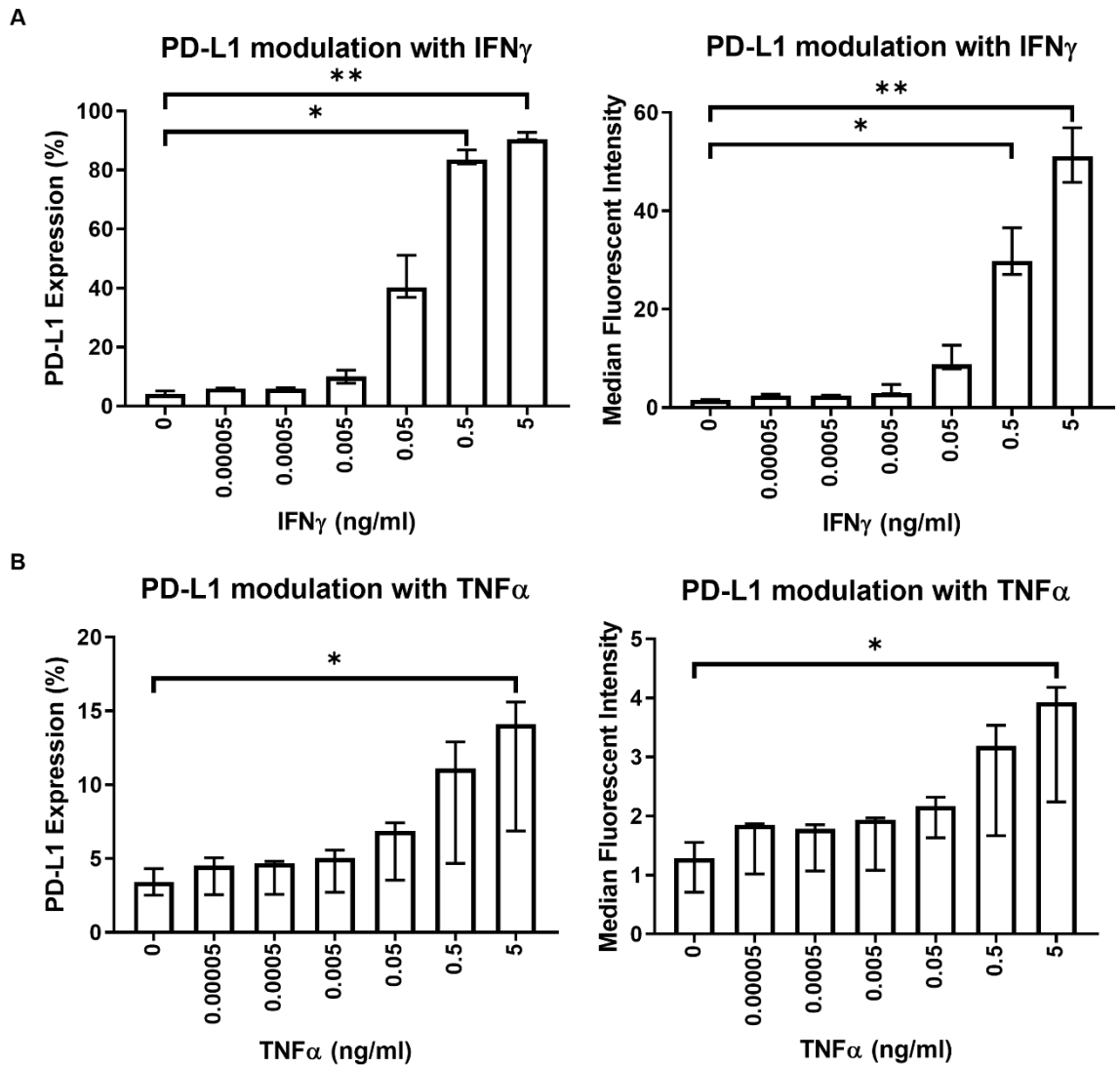
Appendix Figure 9.2 The lowest significant doses of IFNγ (0.5 ng/ml) and TNFα (5 ng/ml) required to modulate cell surface PD-L1 expression on SW620 colorectal cancer cells cultured in monolayer. SW620 colorectal cancer cells that express low baseline levels of PD-L1 were treated with **(A)** IFNγ and **(B)** TNFα at concentrations ranging from 5 ng/ml to 0 ng/ml in 10-fold dilutions for 48 hours to determine the lowest significant dose of each cytokine. The percentage of cells expressing PD-L1 is displayed alongside the MFI for untreated and cytokine-treated SW620 cells. Data is presented as median ± range. n=3 independent experiments each with 3 technical repeats. Data was analysed by a Kruskal-Wallis followed by Conover-Iman multiple comparisons test (*P<0.05).
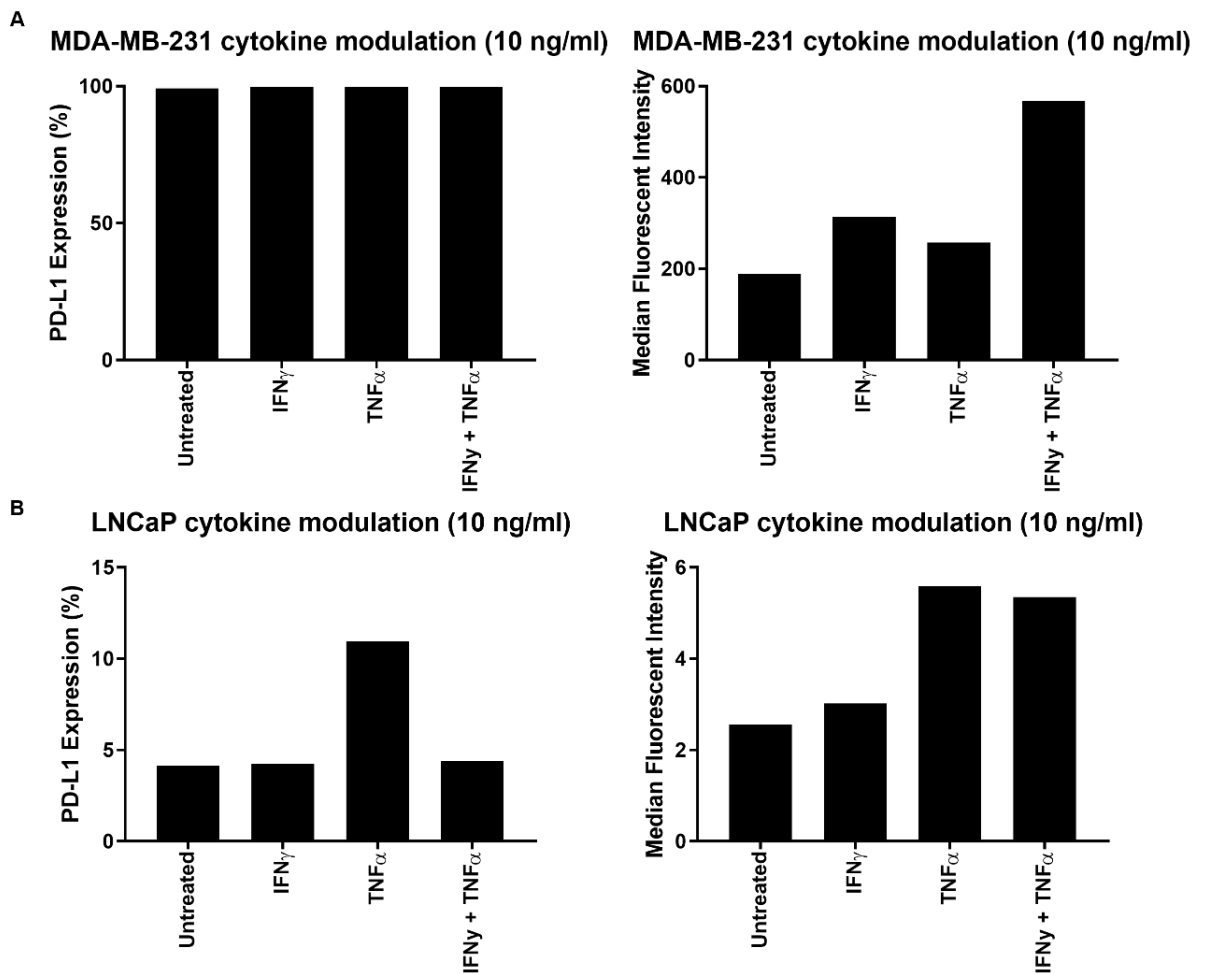
Appendix Figure 9.3

Appendix Figure 9.3 MDA-MB-231 breast and LNCaP prostate cancer cell lines treated with 10 ng/ml IFNγ and TNFα display a similar proportion of cells expressing PD-L1 and MFI of PD-L1 expression to cancer cells treated with the lowest significant doses. (A) MDA-MB-231 breast and **(B)** LNCaP prostate cancer cell lines were treated with 10 ng/ml IFNγ and TNFα to maximise the cytokine response for PD-L1 modulation. The percentage of cells expressing PD-L1 is displayed alongside the MFI for untreated and cytokine-treated MDA-MB-231 and LNCaP cells cultured in 2D monolayer. Data is presented as median ± range. n=1 independent experiment with 3 technical repeats.
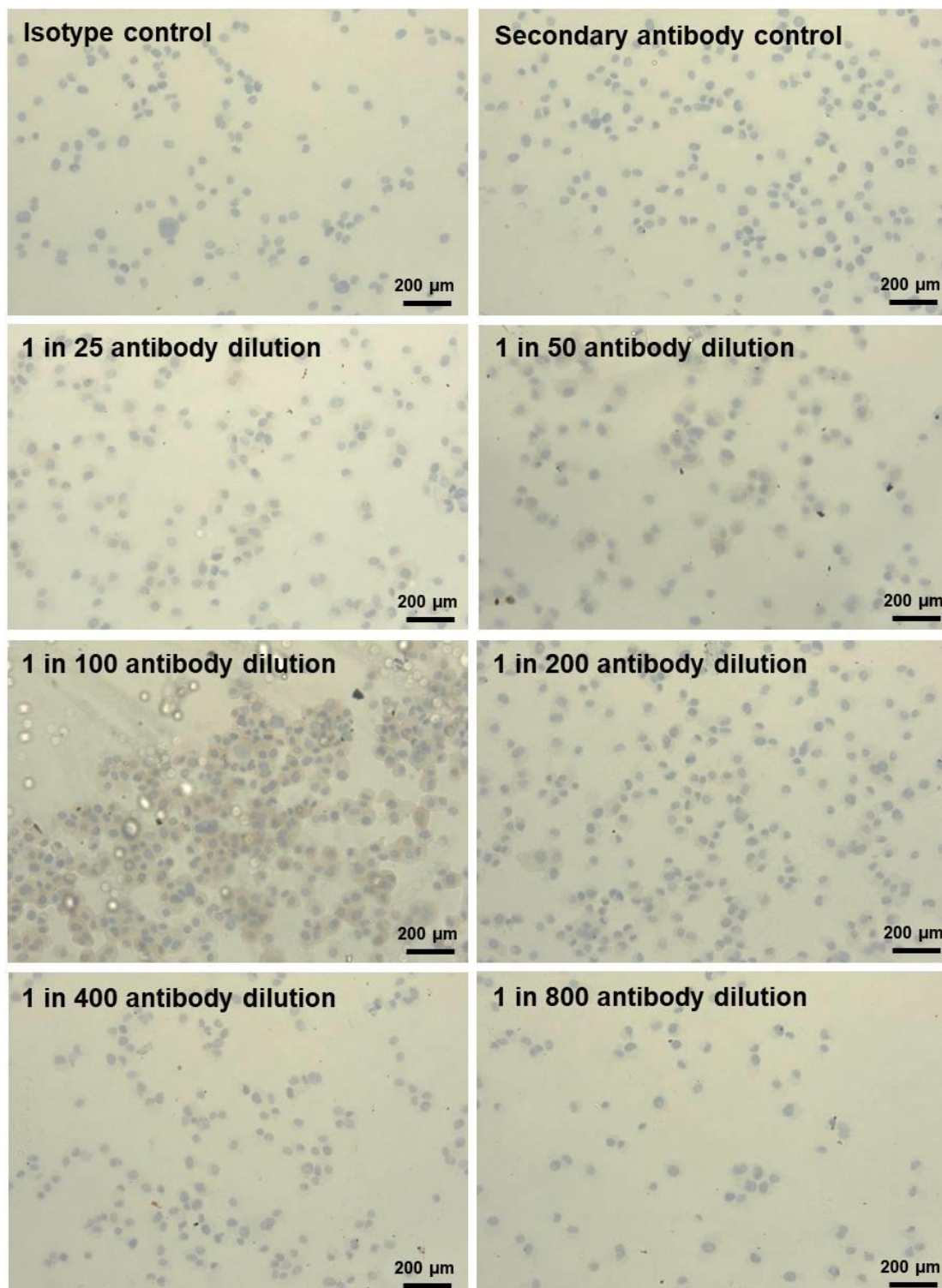
Appendix Figure 9.4 Anti-human PD-L1 antibody optimisation. Cytospins of MDA-MB-231 breast cancer cells were prepared and stained for PD-L1 using different antibody concentrations (1:25 to 1:800 dilution). Isotype control and secondary antibody controls were used. Brightfield images were captured of stained samples. Scale bar represents 200 μm. Images represent n=2 repeats.

Appendix Figure 9.5
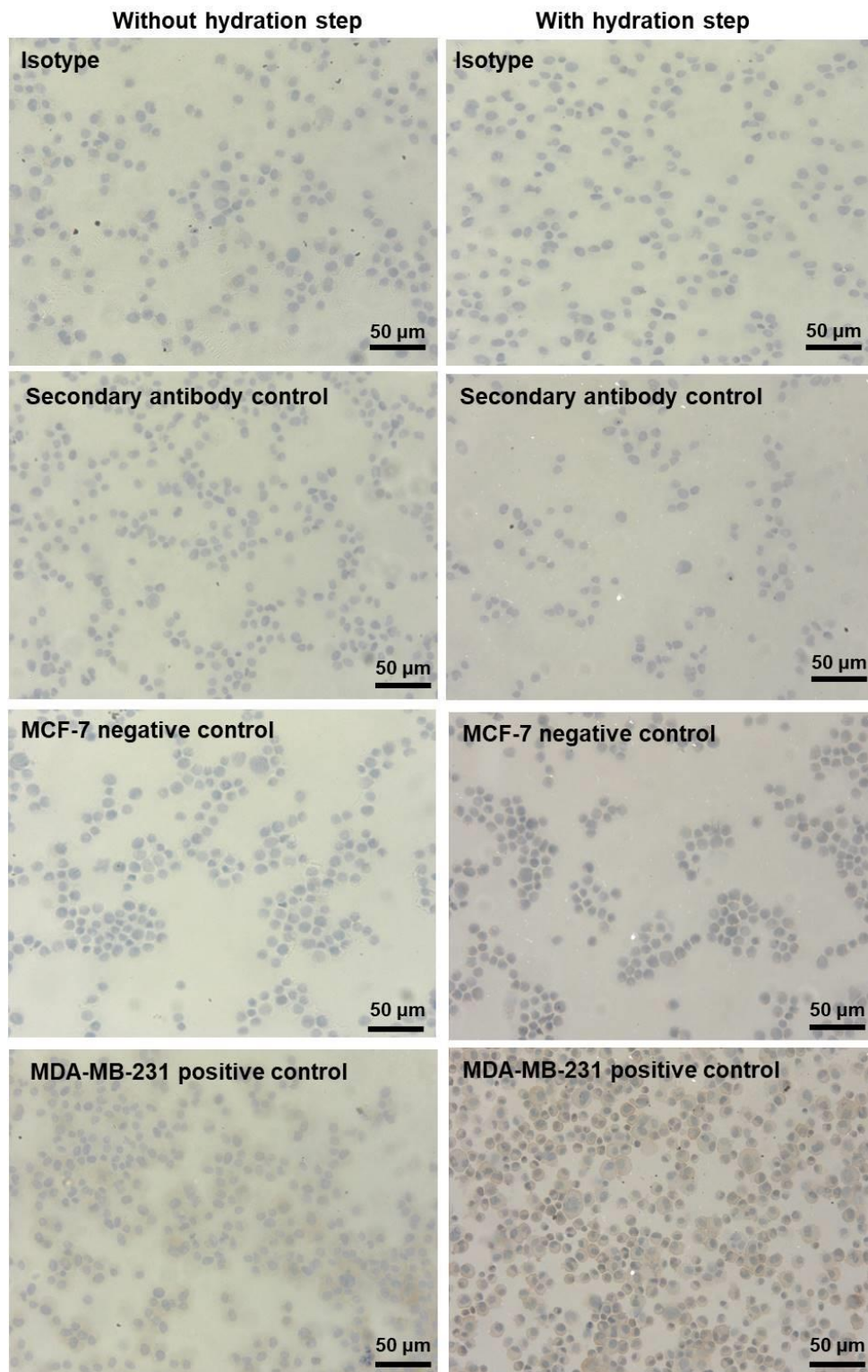
Appendix Figure 9.5 The hydration step increases the intensity of the PD-L1 stain. Cytospins of MDA-MB-231 breast cancer cells were prepared and stained for PD-L1 with or without a hydration step at the end of the staining protocol. The hydration step increases stain intensity. Scale bar represents 50 µm. Images represent n=3 repeats.

Appendix Figure 9.6
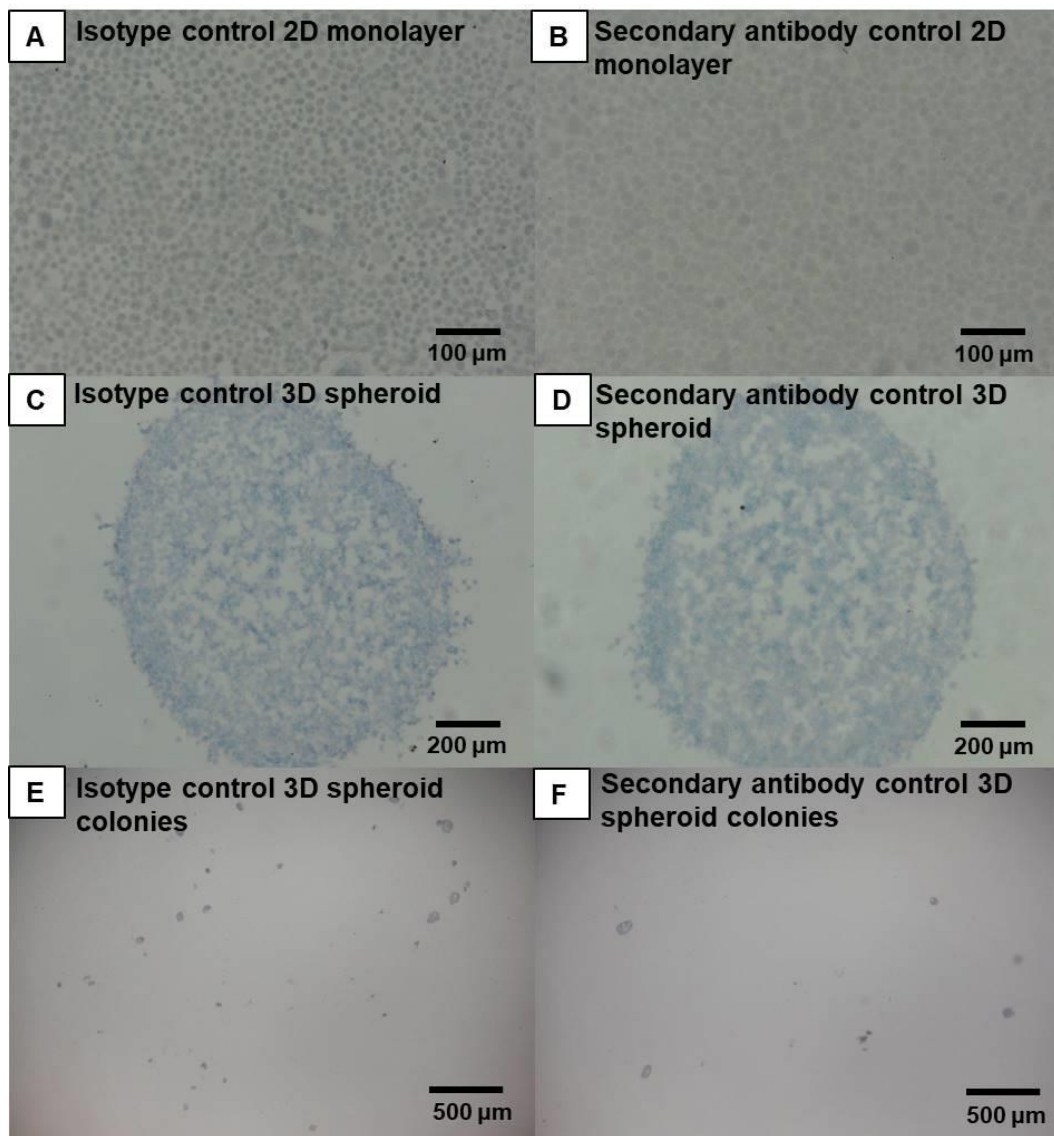
Appendix Figure 9.6 Controls used for immunohistochemical staining of PD-L1 in 2D monolayer, 3D hanging drop spheroids and 3D alginate spheroid colonies. Isotype and secondary antibody controls were run alongside each staining experiment to ensure PD-L1 detection was specific when staining: **(A, B)** 2D monolayer cells, **(C, D)** 3D hanging drop spheroids, and **(E, F)** 3D alginate spheroid colonies. Brown DAB staining was not observed in any of the controls. Scale bar represents 100 µm (cytospins), 200 µm (3D hanging drop spheroids) and 500 µm (3D alginate spheroid colonies). Images represent controls from n=3 independent experiments.

Cytospins of 2D Monolayer Cells
Haematoxylin/PD-L1
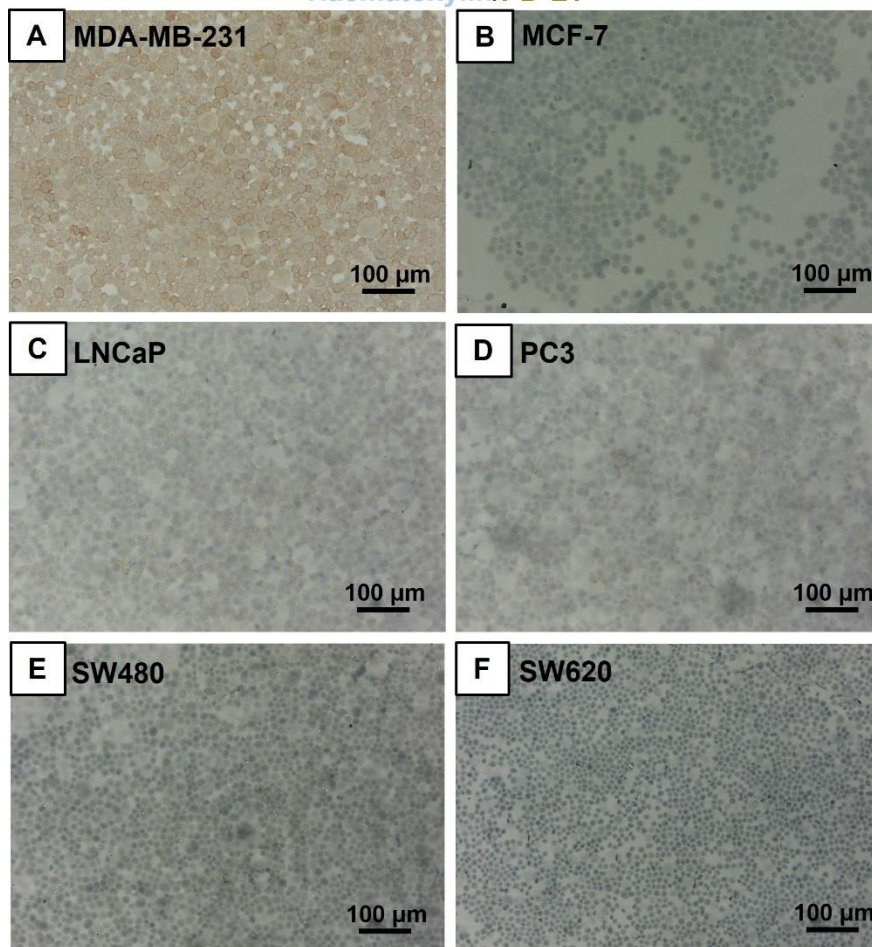
Appendix Figure 9.7 PD-L1 expression can be detected in cytospins of MDA-MB-231, LNCaP, PC3, and SW480 2D monolayer-cultured cells. Immunohistochemical staining of PD-L1 was performed on MDA-MB-231 **(A)**, MCF-7 **(B)**, LNCaP **(C)**, PC3 **(D)**, SW480 **(E)** and SW620 **(F)** cancer cells cultured in monolayer to assess PD-L1 expression and distribution within the cell populations. Images of cytospins were captured. Scale bar represents 100 µm. n=3 independent experiments each with 3 technical repeats.
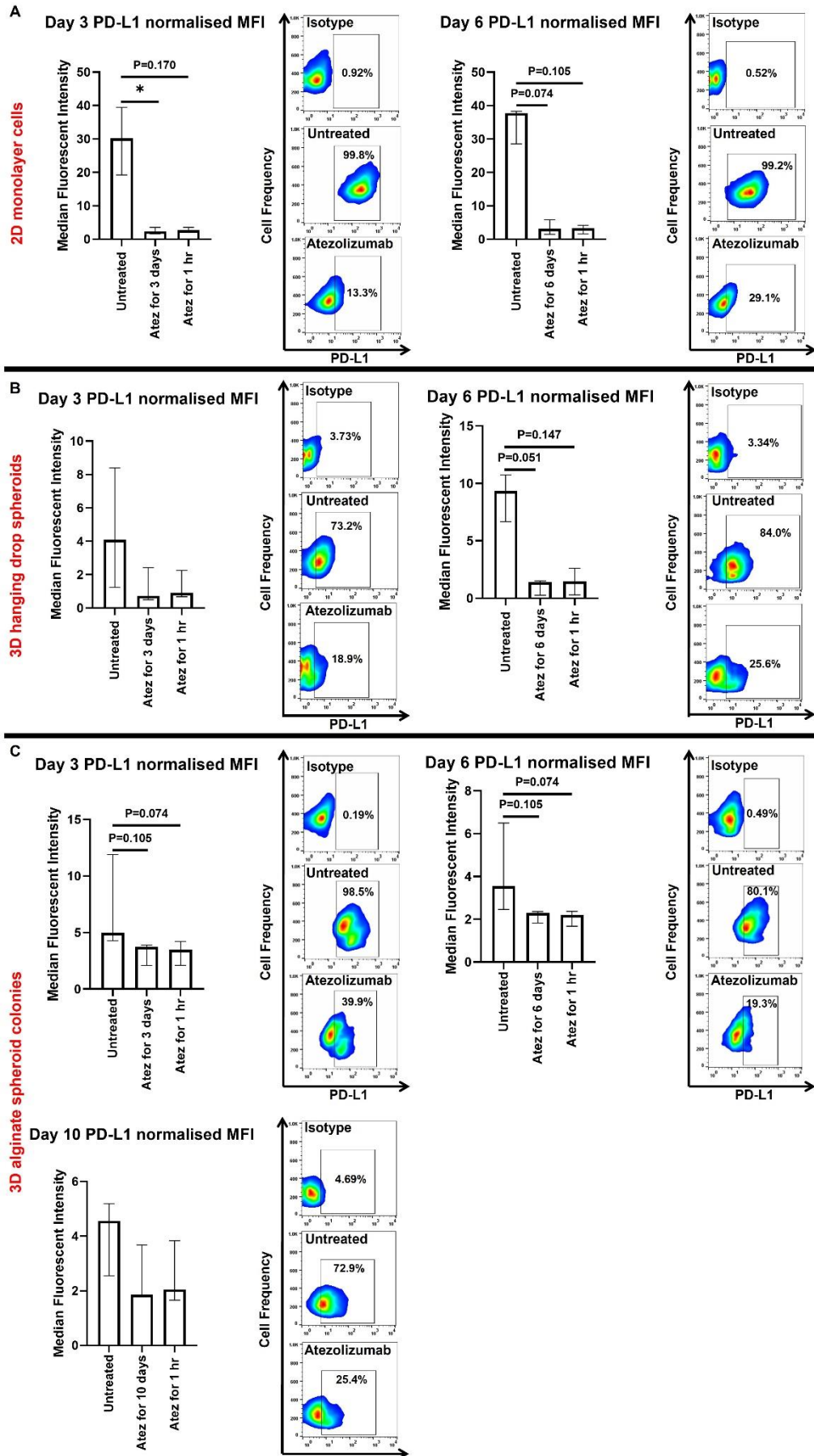
Appendix Figure 9.8. Atezolizumab treatment reduces the level of PD-L1 expression detected in both 2D and 3D cell culture models at all timepoints assessed. PD-L1 expression was measured by MDA-MB-231 cells cultured in **(A)** 2D monolayer, **(B)** 3D hanging drop spheroids and **(C)** 3D alginate spheroid colonies that were treated with or without Atezolizumab to verify PD-L1 blockade at all timepoints investigated in other assays. The MFI of PD-L1 expression is shown for all cultures at all the different timepoints. Representative flow cytometry plots for each timepoint show the degree of PD-L1 blockade by Atezolizumab. Data is presented as median ± range. n=3 independent experiments each with 3 technical repeats. Data was analysed by a Kruskal-Wallis and Dunn's multiple comparisons test.

Appendix Table 9.1

Membrane/Coordinates	Target/Control	Phosphorylation Site
A-A1, A2	Reference Spot	___
A-E3, E4	p38α	T180/Y182
B-A11, A12	Akt 1/2/3	T308
B-A13, A14	Akt 1/2/3	S473
B-A17, A18	Reference Spot	___
A-B3, B4	CREB	S133
A-B5, B6	EGF R	Y1086
A-B7, B8	eNOS	S1177
A-B9, B10	ERK1/2	T202/Y204, T185/Y187
B-B11, B12	Chk-2	T68
B-B13, B14	c-Jun	S63
A-C3, C4	Fgr	Y412
A-C5, C6	GSK-3α/β	S21/S9
A-C7, C8	GSK-3β	S9
A-C9, C10	HSP27	S78/S82
B-C11, C12	p53	S15
B-C13, C14	p53	S46
B-C15, C16	p53	S392
A-D3, D4	JNK 1/2/3	T183/Y185, T221/Y223
A-D5, D6	Lck	Y394
A-D7, D8	Lyn	Y397
A-D9, D10	MSK1/2	S376/S360
B-D11, D12	p70 S6 Kinase	T389
B-D13, D14	p70 S6 Kinase	T421/S424
B-D15, D16	PRAS40	T246
A-E3, E4	p38α	T180/Y182
A-E5, E6	PDGF Rβ	Y751
A-E7, E8	PLC-γ1	Y783
A-E9, E10	Src	Y419

Membrane/Coordinates	Target/Control	Phosphorylation Site
B-E11, E12	PYK2	Y402
B-E13, E14	RSK1/2	S221/S227
B-E15, E16	RSK1/2/3	S380/S386/S377
A-F3, F4	STAT2	Y689
A-F5, F6	STAT5a/b	Y694/Y699
A-F7, F8	WNK1	T60
A-F9, F10	Yes	Y426
B-F11, F12	STAT1	Y701
B-F13, F14	STAT3	Y705
B-F15, F16	STAT3	S727
A-G1, G2	Reference Spot	___
A-G3, G4	β-Catenin	___
A-G9, G10	PBS (Negative Control)	___
B-G11, G12	STAT6	Y641
B-G13, G14	HSP60	___
B-G17, G18	PBS (Negative Control)	___

Appendix Table 9.1 Human Phospho-Kinase Protein Profiler Array coordinates. Columns display the coordinates of each target or control located on membranes A or B, the targets, and controls to which the coordinates correspond, and the phosphorylation site which was being assessed for each target.
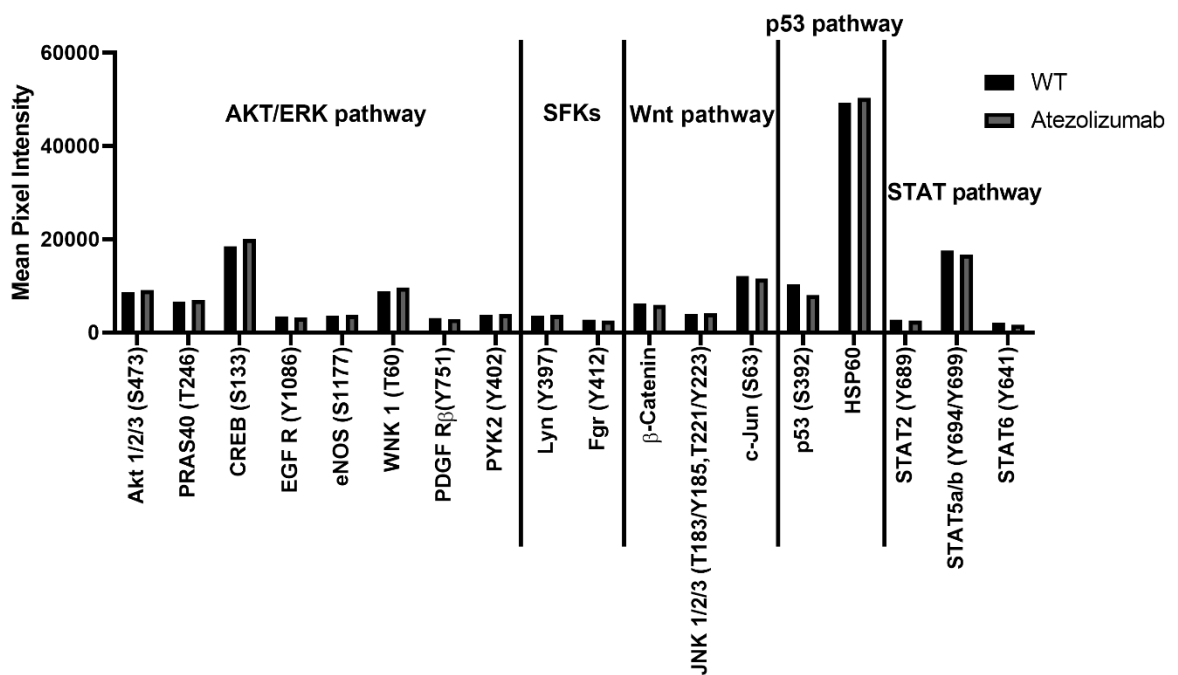
Appendix Figure 9.9 Kinases and total proteins that show similar phosphorylation levels in MDA-MB-231 breast cancer cells treated with or without Atezolizumab. The Human Phospho-Kinase Array was used to investigate the effects of Atezolizumab on phosphorylation of 37 different kinases and 2 total proteins. The kinases and proteins in MDA-MB-231 cells treated with Atezolizumab that displayed similar levels of phosphorylation to untreated MDA-MB-231 cells are displayed in the graph. Each target molecule has been grouped depending on the pathways that it has previously shown to be involved in. n=1 independent experiment with 2 technical repeats.
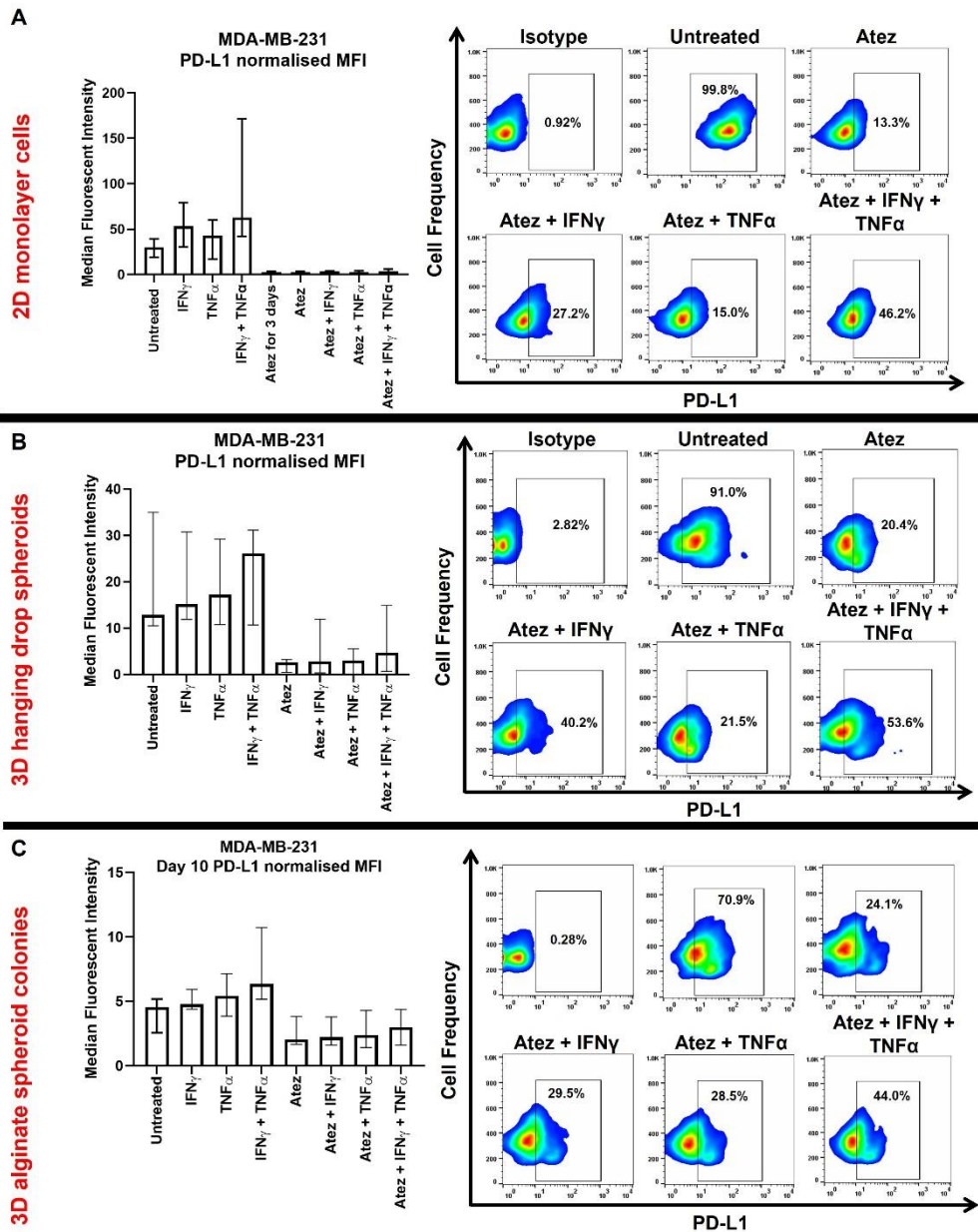
Figure 9.10. Atezolizumab reduces the level of PD-L1 expression detected in MDA-MB-231 2D and 3D cell culture models despite cytokine modulation prior to treatment. PD-L1 expression was measured by MDA-MB-231 cells cultured in **(A)** 2D monolayer, **(B)** 3D hanging drop spheroids and **(C)** 3D alginate spheroid colonies that were treated with Atezolizumab with or without prior cytokine modulation to verify PD-L1 blockade. The MFI of PD-L1 expression is shown for all cultures. Representative flow cytometry plots show the degree of PD-L1 blockade by Atezolizumab with or without cytokine modulation. Day 10 data is shown for 3D alginate spheroid colonies which is representative of all timepoints assessed. Data is presented as median ± range. n=3 independent experiments each with 3 technical repeats. Data was analysed by a Kruskal-Wallis test.
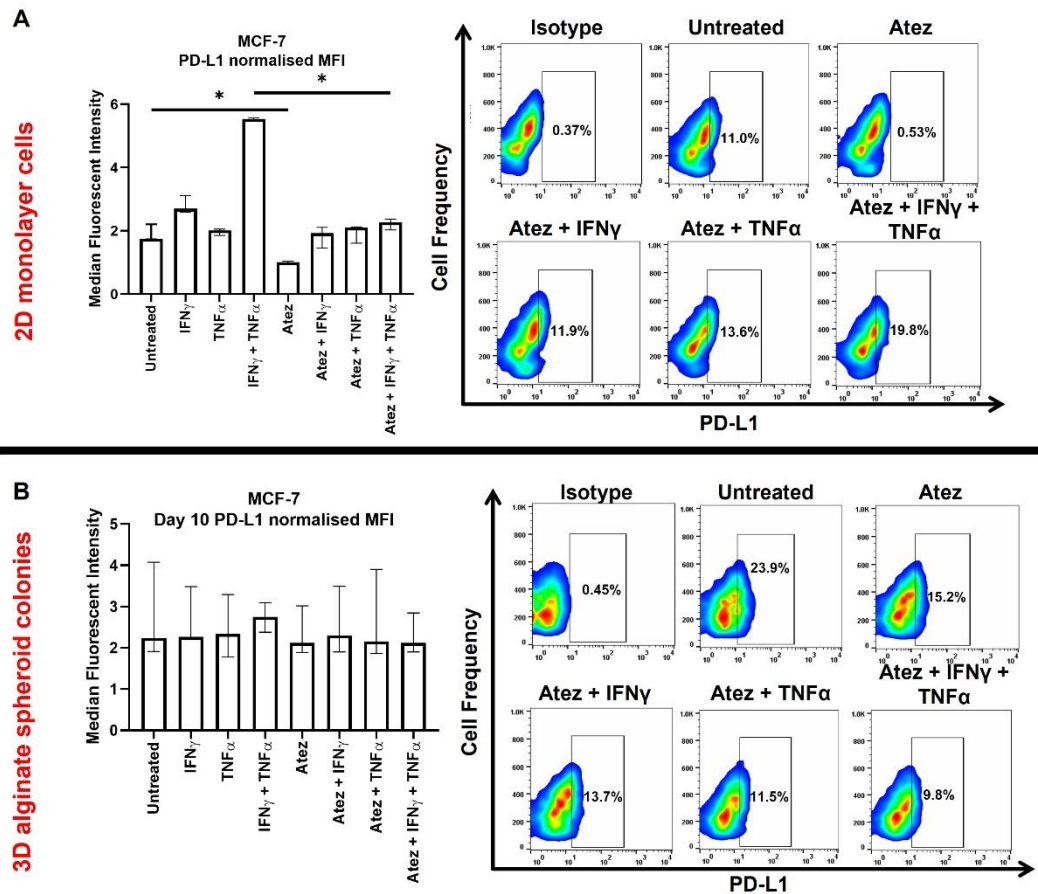
Appendix Figure 9.11. Atezolizumab reduces the level of PD-L1 expression detected in both MCF-7 2D and 3D alginate cultures despite cytokine modulation prior to treatment. PD-L1 expression was measured by MCF-7 cells cultured in **(A)** 2D monolayer and **(B)** 3D alginate spheroid colonies that were treated with Atezolizumab with or without prior cytokine modulation to verify PD-L1 blockade. The MFI of PD-L1 expression is shown for both cultures. Representative flow cytometry plots show the degree of PD-L1 blockade by Atezolizumab with or without cytokine modulation. Data is presented as median ± range. n=3 independent experiments each with 3 technical repeats. Data was analysed by a Kruskal-Wallis followed by a Dunn's multiple comparisons test (*P<0.05).
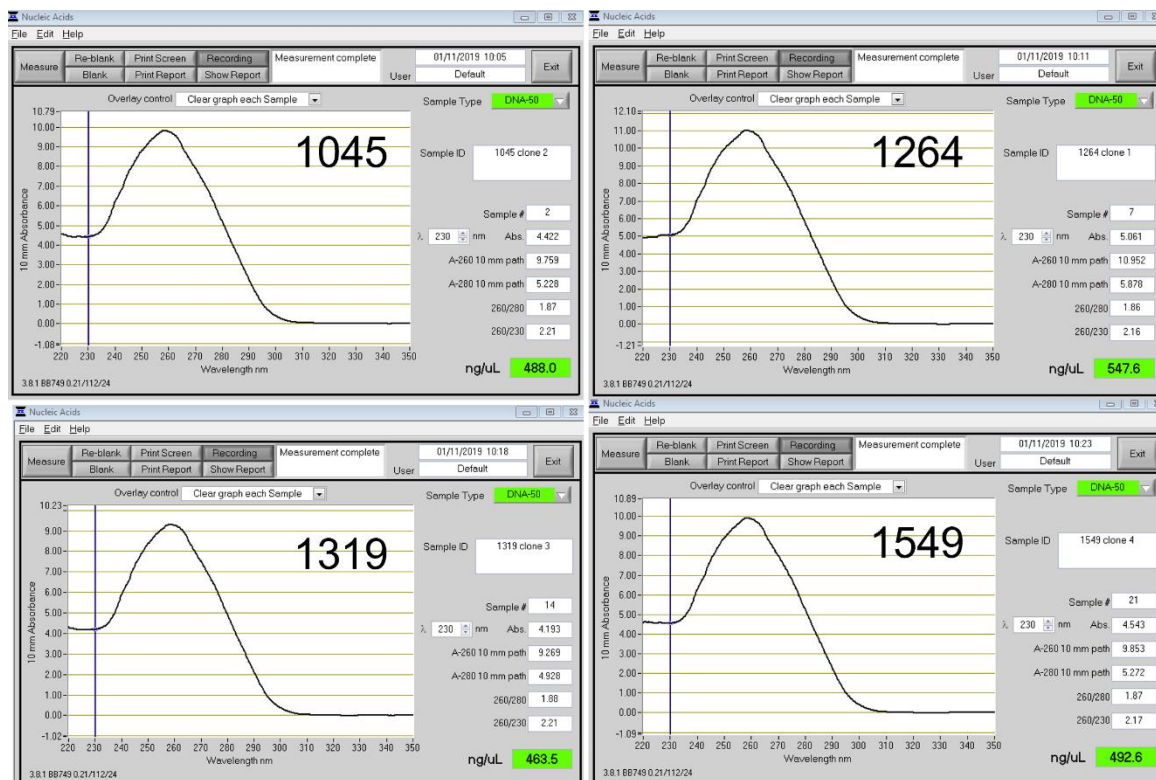
Appendix Figure 9.12 Plasmid DNA purification profiles of selected clones sent for Sanger Sequencing highlighting the quantity and quality of plasmid DNA isolated from transformed *E. coli*. Out of the 5 individual colonies of transformed *E. coli* selected for plasmid DNA isolation for each vector construct (1045, 1264, 1319 and 1549), only 1 clone of the highest purity was sent for Sanger Sequencing for each vector construct which was subsequently used for MDA-MB-231 cell transfection. The purity of the isolated plasmid DNA was determined by observing the 260/230 ratio and comparing it to the expected range for nucleic acids (2.0-2.2).

6 days post transfection

**Brightfield/EmGFP combined**
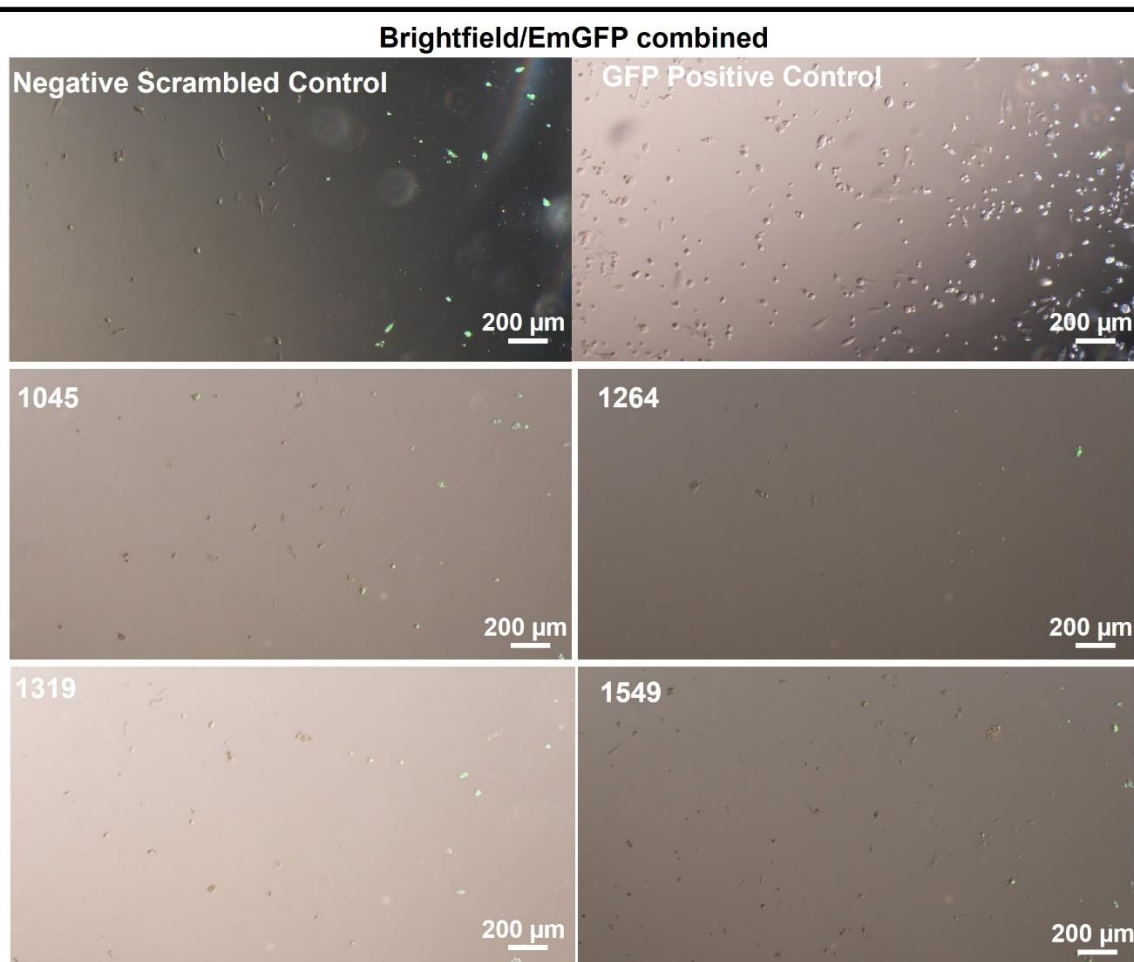
 Appendix Figure 9.13 MDA-MB-231 cells show less GFP positivity 6 days post transfection. MDA-MB-231 cells were cultured in selection medium following nucleofection with plasmid DNA for the negative scrambled control, GFP positive control and the 4 different vector constructs 1045, 1264, 1319 and 1549. The expression of EmGFP was assessed 6 days post transfection. Images in brightfield and FITC were captured and were shown combined. Scale bar represents 200 µm. Images represent n=2 transfection procedures.
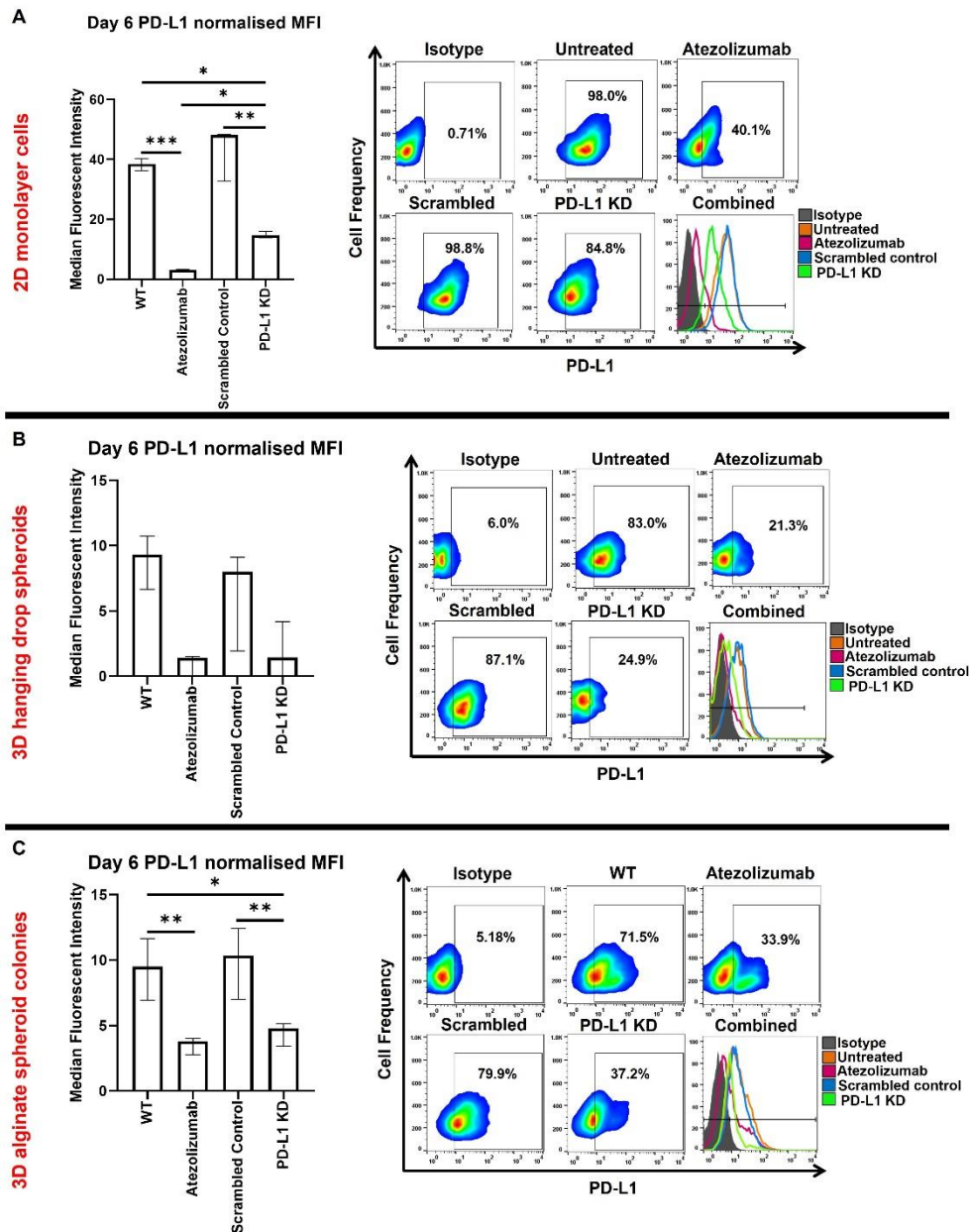
Appendix Figure 9.14
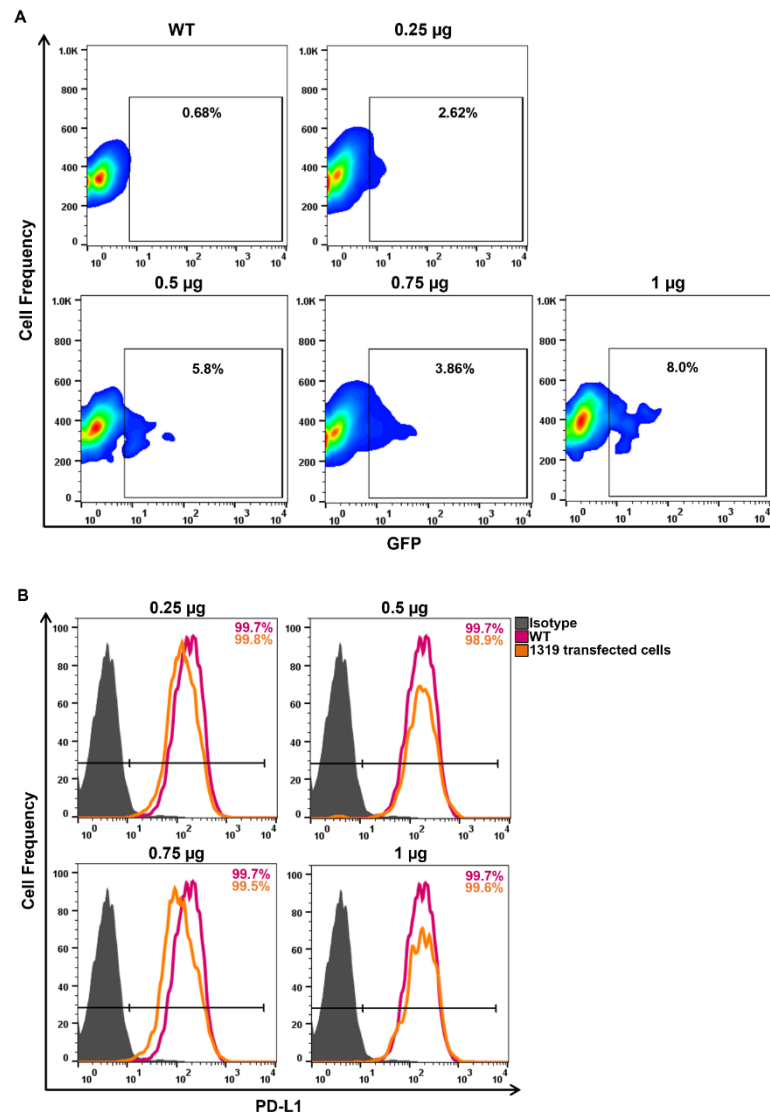
Appendix Figure 9.14 The amount of 1319 plasmid DNA used to transfect MDA-MB-231 breast cancer cells did not improve the stable transfection efficacy in relation to GFP positivity and PD-L1 knockdown. MDA-MB-231 breast cancer cells were transfected with different amounts of 1319 plasmid DNA to determine whether stable transfection efficacy could be improved. **(A)** Flow cytometry plots showing the GFP positivity present within the transfected cell population for each plasmid DNA amount investigated. **(B)** Flow cytometry histograms demonstrating the percentage and level of PD-L1 expression by transfected cells at each plasmid DNA amount investigated relative to the isotype control and MDA-MB-231 WT cells. Data represents n=1 independent transfection with 3 technical repeats.
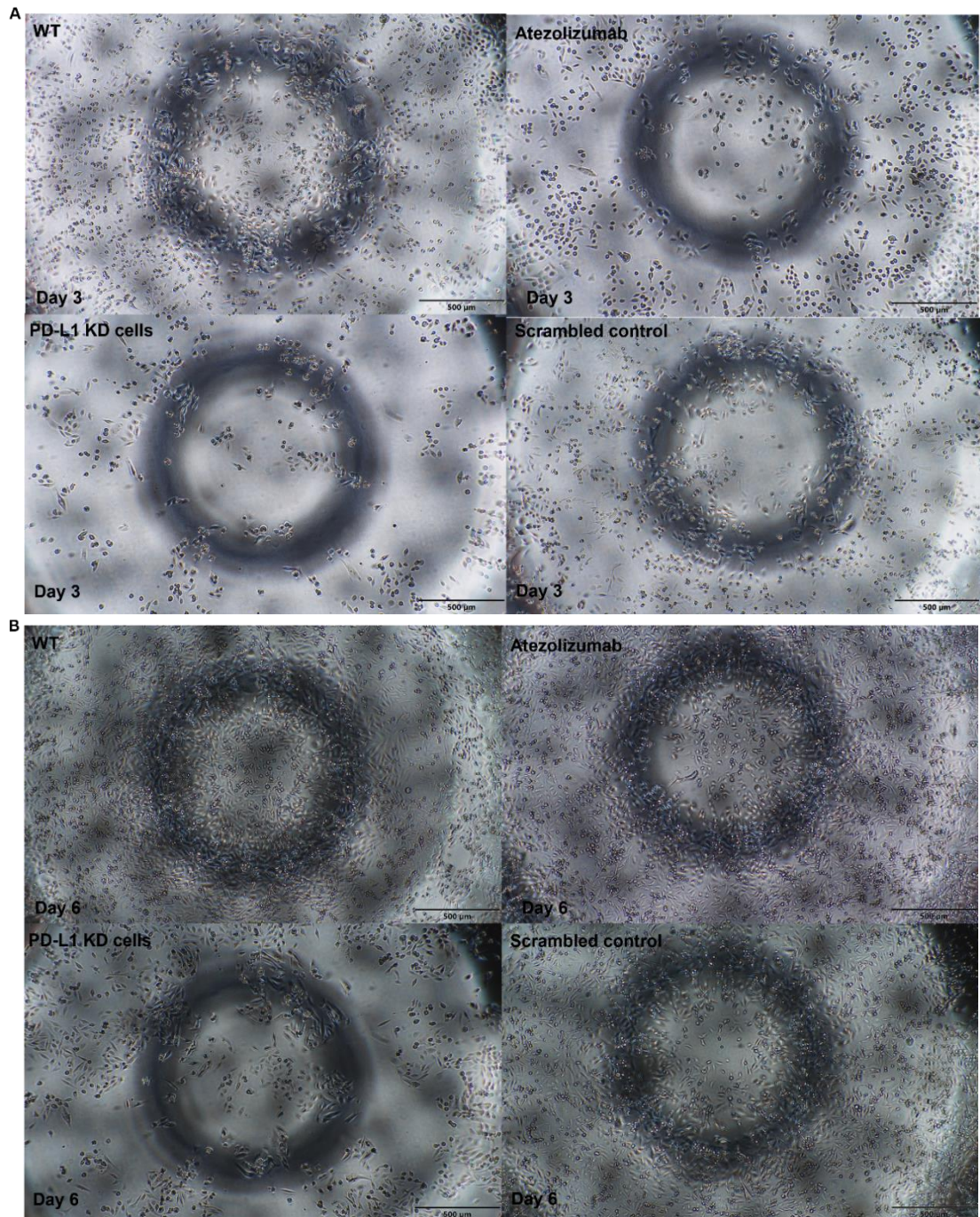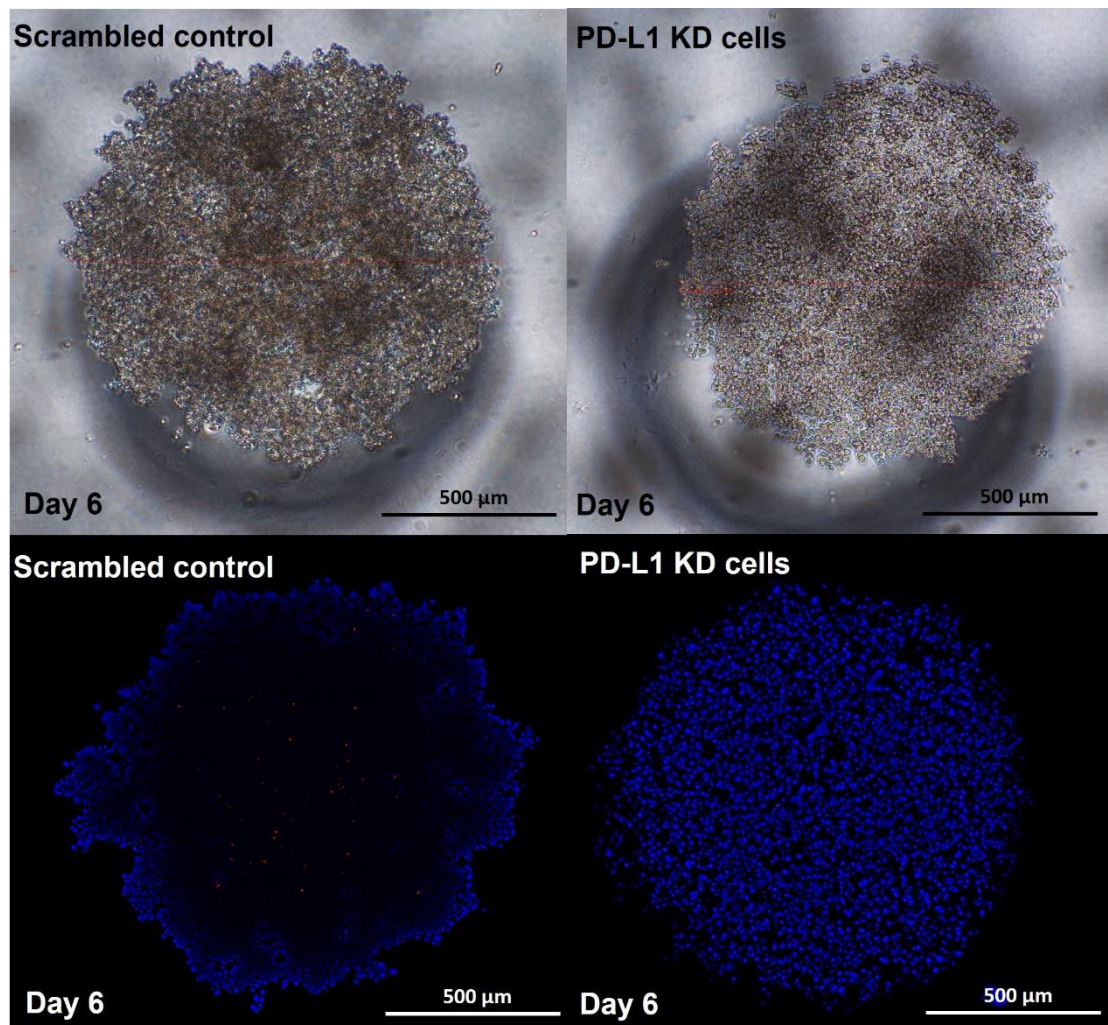
Appendix Figure 9.15 Brightfield images captured at day 3 and 6 showed that PD-L1 knockdown cells were less confluent than WT, Atezolizumab-treated and scrambled control cells after 3 days of culture. Brightfield images were taken of MDA-MB-231 WT, Atezolizumab-treated, scrambled control and PD-L1 kncockdown cells cultured in a 96-well plate for **(A)** 3 and **(B)** 6 days. Scale bar represents 500 μm. Images are represetative of n=3 independnt experiments each with 3 technical repeats.
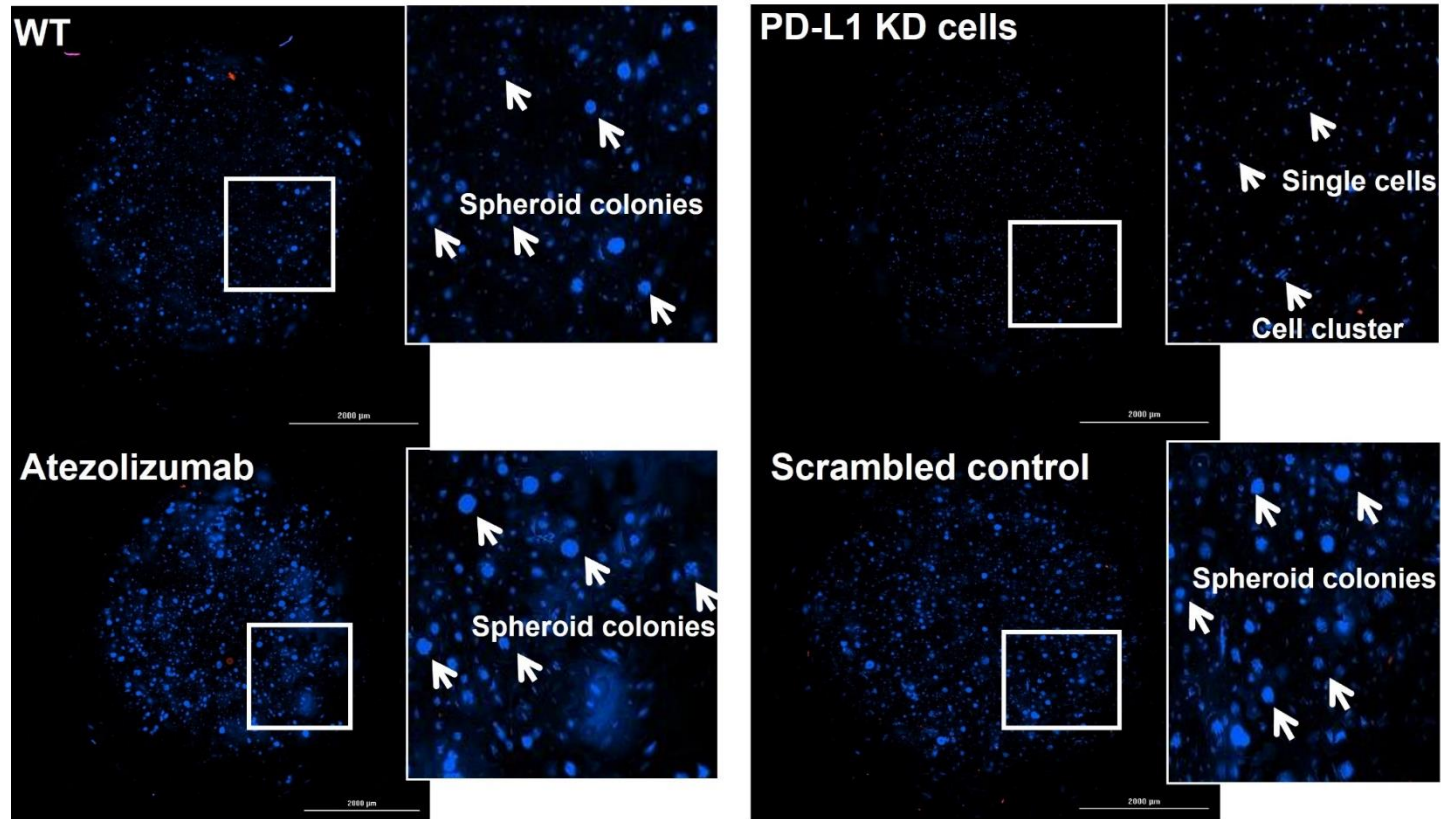
Appendix Figure 9.16

Appendix Figure 9.16. PD-L1 detection is reduced in Atezolizumab-treated WT and PD-L1 knockdown cells compared to WT and scrambled control cells in 2D and 3D cell culture models. PD-L1 expression was measured for MDA-MB-231 WT, Atezolizumab-treated WT, scrambled control and PD-L1 knockdown cells cultured in **(A)** 2D monolayer, **(B)** 3D hanging drop spheroids and **(C)** 3D alginate spheroid colonies. The MFI of PD-L1 expression is shown alongside representative flow cytometry plots that show the degree of PD-L1 reduction. Day 6 data is shown here which is representative of all timepoints assessed. Data is presented as median ± range. n=3 independent experiments each with 3 technical repeats. Data was analysed using a Kruskal-Wallis followed by Dunn's multiple comparisons test (*P<0.05 and **P<0.01).

390

Appendix Figure 9.17

Appendix Figure 9.17 PD-L1 knockdown 3D spheroids visually display a lower density of cells, appear less compact and smooth on the outer surface compared to scrambled control 3D spheroids at day 6. Representative brightfield images are displayed for MDA-MB-231 3D spheroids formed with scrambled control cells and PD-L1 knockdown cells at day 6 (top images). Representative images of scrambled control and PD-L1 knockdown 3D spheroids stained with Hoechst 33342 and PI are also shown at day 6 (bottom). Images were captured using 4X magnification and represent a Z-slice of a Z-stack image to capture cell density in one plane. Scale bar represents 500 µm. Images represent n=3 independent experiments each with 3 technical repeats.
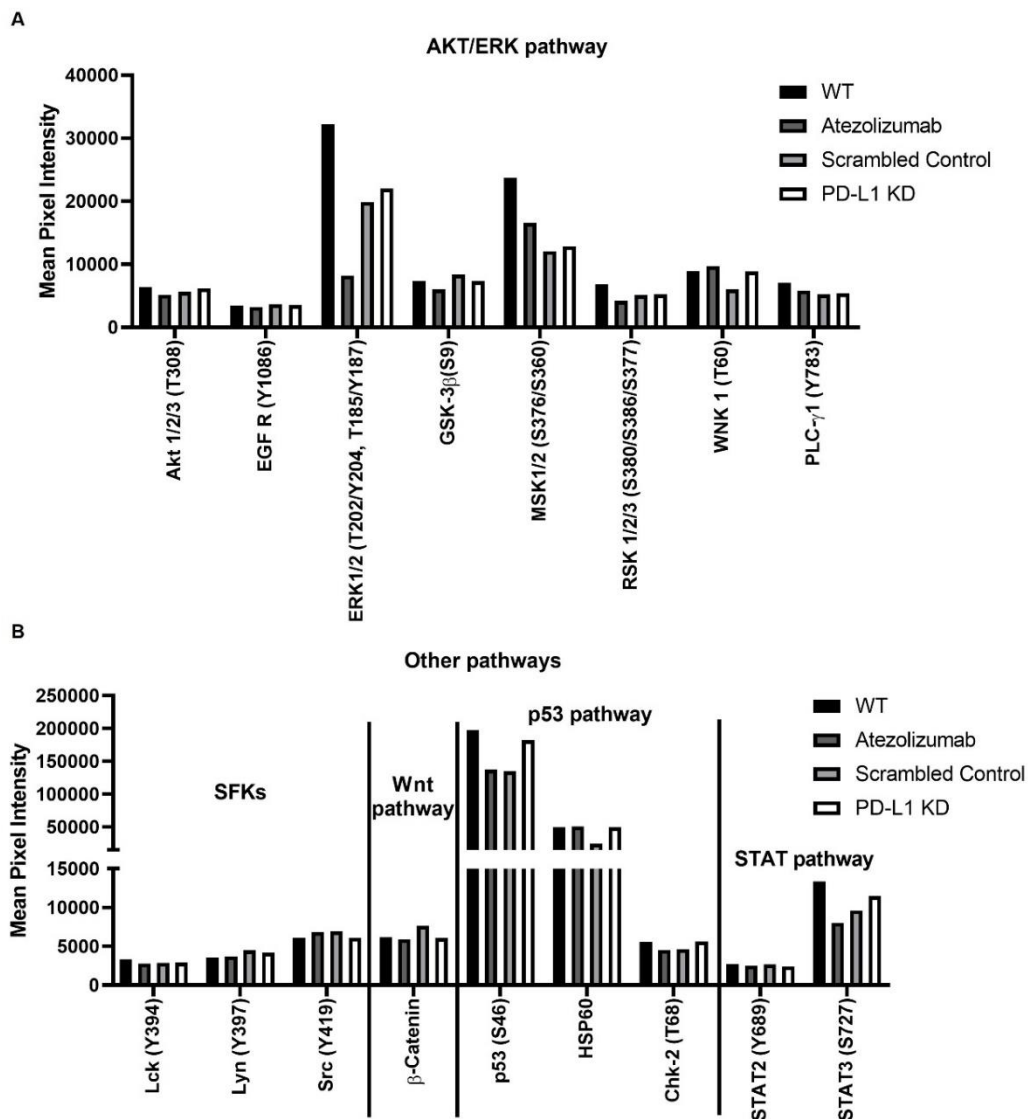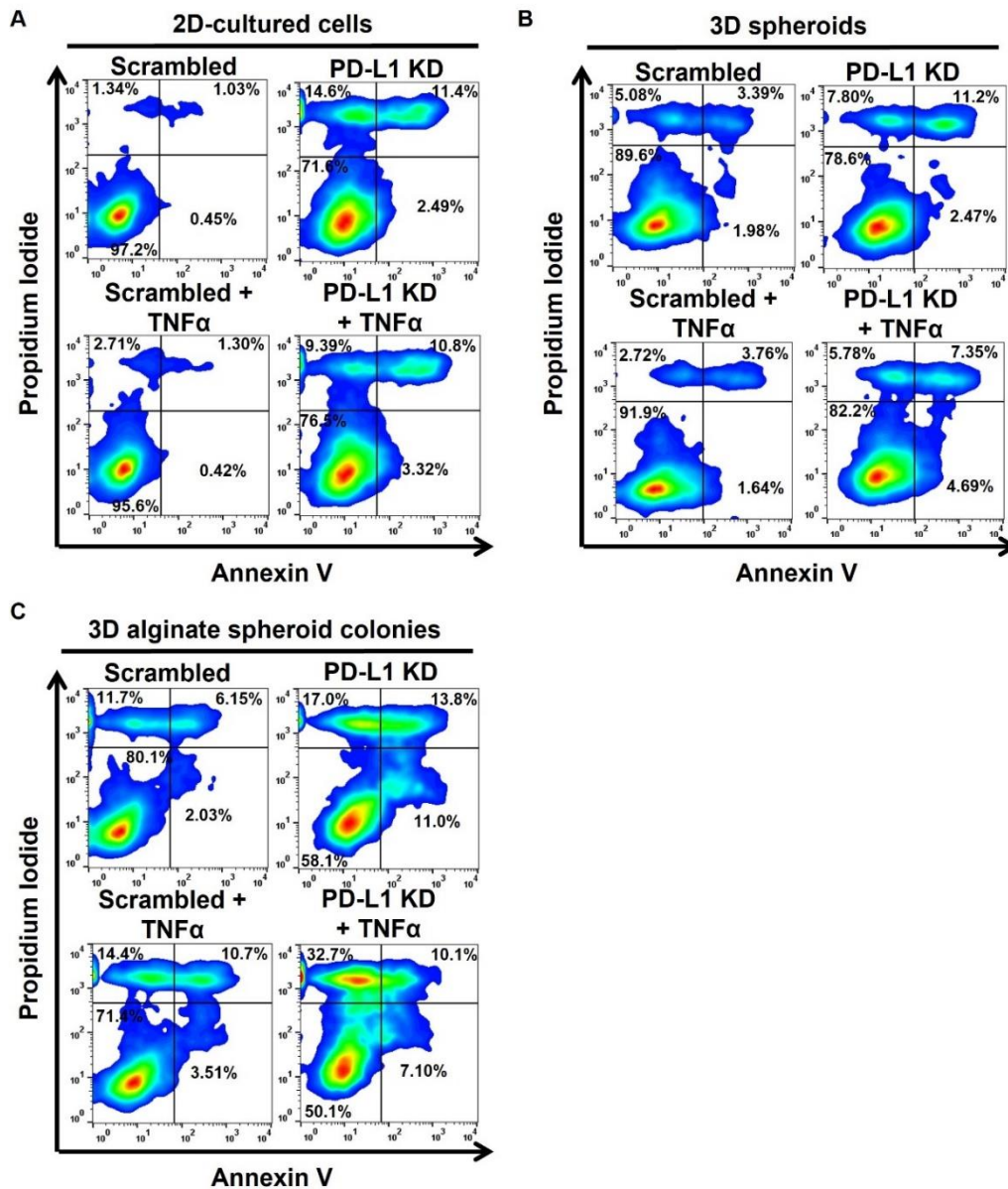
Appendix Figure 9.18

Appendix Figure 9.18 PD-L1 knockdown cells do not grown to form 3D spheroid colonies in alginate hydrogel beads after 10 days of culture. Images were captured of whole alginate beads stained with Hoechst 33342 and PI to show the difference in the growth of WT, Atezolizumab-treated, scrambled control and PD-L1 knockdown cells within the alginate after 10 days of culture. Scale bar represents 2000 µm. Images represent n=3 independent experiments, each with 3 technical repeats.

Appendix Figure 9.19 The phosphorylation levels of some kinases alter in scrambled control cells more so than PD-L1 knockdown cells. The Human Phospho-Kinase Array was used to investigate the effects of PD-L1 knockdown in MDA-MB-231 breast cancer cells on phosphorylation of 37 different kinases and 2 total proteins. The kinases and proteins in PD-L1 knockdown cells that displayed similar levels of phosphorylation to WT, Atezolizumab-treated and scrambled control cells are displayed in the graph. Also, kinases and proteins in scrambled control cells that altered more so than in PD-L1 knockdown cells are displayed in the graph. Each target molecule has been grouped depending on the pathways that it has previously shown to be involved in including **(A)** AKT/ERK signalling pathways and **(B)** several other pathways.

Appendix Figure 9.20

Appendix Figure 9.20 Scrambled control cells treated with or without TNFα remain highly viable in 2D and 3D cell culture models. The viability of scrambled control cells treated with or without TNFα was assessed alongside that of PD-L1 knockdown cells treated with or without TNFα to ensure that cell death was not being observed at a similar or higher level than PD-L1 knockdown cells in both 2D and 3D cell culture models. Representative flow cytometry plots for scrambled control and PD-L1 knockdown cells treated with or without TNFα are shown for **(A)** 2D-cultured cells, **(B)** 3D hanging drop spheroids and **(C)** 3D alginate spheroid colonies following staining with Annexin V/PI. Representative flow cytometry plots represent n=3 independent experiments, each with 3 technical repeats.